Springer Complexity

Springer Complexity is an interdisciplinary program publishing the best research and academic-level teaching on both fundamental and applied aspects of complex systems – cutting across all traditional disciplines of the natural and life sciences, engineering, economics, medicine, neuroscience, social and computer science.

Complex Systems are systems that comprise many interacting parts with the ability to generate a new quality of macroscopic collective behavior the manifestations of which are the spontaneous formation of distinctive temporal, spatial or functional structures. Models of such systems can be successfully mapped onto quite diverse "real-life" situations like the climate, the coherent emission of light from lasers, chemical reaction-diffusion systems, biological cellular networks, the dynamics of stock markets and of the internet, earthquake statistics and prediction, freeway traffic, the human brain, or the formation of opinions in social systems, to name just some of the popular applications.

Although their scope and methodologies overlap somewhat, one can distinguish the following main concepts and tools: self-organization, nonlinear dynamics, synergetics, turbulence, dynamical systems, catastrophes, instabilities, stochastic processes, chaos, graphs and networks, cellular automata, adaptive systems, genetic algorithms and computational intelligence.

The three major book publication platforms of the Springer Complexity program are the monograph series "Understanding Complex Systems" focusing on the various applications of complexity, the "Springer Series in Synergetics", which is devoted to the quantitative theoretical and methodological foundations, and the "SpringerBriefs in Complexity" which are concise and topical working reports, case-studies, surveys, essays and lecture notes of relevance to the field.

In addition to the books in these three core series, the program also incorporates individual titles ranging from textbooks to major reference works.

Understanding Complex Systems

Founding Editor: S. Kelso

Future scientific and technological developments in many fields will necessarily depend upon coming to grips with complex systems. Such systems are complex in both their composition – typically many different kinds of components interacting simultaneously and nonlinearly with each other and their environments on multiple levels – and in the rich diversity of behavior of which they are capable.

The Springer Series in Understanding Complex Systems series (UCS) promotes new strategies and paradigms for understanding and realizing applications of complex systems research in a wide variety of fields and endeavors. UCS is explicitly transdisciplinary. It has three main goals: First, to elaborate the concepts, methods and tools of complex systems at all levels of description and in all scientific fields, especially newly emerging areas within the life, social, behavioral, economic, neuro- and cognitive sciences (and derivatives thereof); second, to encourage novel applications of these ideas in various fields of engineering and computation such as robotics, nano-technology and informatics; third, to provide a single forum within which commonalities and differences in the workings of complex systems may be discerned, hence leading to deeper insight and understanding.

UCS will publish monographs, lecture notes and selected edited contributions aimed at communicating new findings to a large multidisciplinary audience.

For further volumes:
http://www.springer.com/series/5394

Luiz A.O. Rocha • Sylvie Lorente • Adrian Bejan
Editors

Constructal Law and the Unifying Principle of Design

Springer

Editors
Luiz A.O. Rocha
Federal University of Rio Grande
do SUL-UFRGS
Porto Alegre, RS, Brazil

Sylvie Lorente
LMDC, INSA
University of Toulouse
Toulouse, France

Adrian Bejan
Duke University
Durham, NC, USA

ISSN 1860-0832
ISBN 978-1-4614-5048-1
DOI 10.1007/978-1-4614-5049-8
Springer New York Heidelberg Dordrecht London

ISSN 1860-0840 (electronic)
ISBN 978-1-4614-5049-8 (eBook)

Library of Congress Control Number: 2012952264

Printed on acid-free paper

Springer is part of Springer Science+Business Media (www.springer.com)

Preface

Constructal Law, Design in Nature, and Complexity

This book is about the Constructal Law of design in nature and the state of the field that is growing around this law of physics. It explores the unifying power of the Constructal Law and its applications in all the domains of design generation and evolution, from biology and geophysics to globalization, engineering, sustainability, and security. This growing activity covers the board, from physics and biology to social organization and technology evolution.

The Constructal Law has generated a worldwide movement toward design as science, i.e., design as a physics phenomenon as captured in 1996 by the Constructal Law: "For a finite-size flow system to persist in time (to live), its configuration must evolve in such a way that it provides easier access to the imposed (global) currents that flow through it."

Life is movement and the persistent morphing of the configuration of this movement. The Constructal Law identifies (a) life, design and evolution (changes in configuration) as a physics phenomenon and (b) captures the time direction of design generation and evolution. Reviews of this growing field are available in refs. 1–7.

To place the Constructal Law and its field in the greater framework of scientific inquiry, it is timely to review what we mean by design in nature and by other words that refer to design in nature: complexity, networks, diversity, chance, turbulence, etc. These words are old and numerous because the fascination with the surroundings has inspired human curiosity and creativity throughout history. Science is only the latest and most powerful mental construct that came out of this natural human tendency to understand and use the surroundings in order to move more easily, farther, and more persistently in time through the surroundings.

Design has two meanings in English. The first is the noun, which means shape, structure, configuration, pattern, drawing, figure, rhythm, motif, architecture, and

many more words that represent the mental viewing of an image—black lines on a background of a different color. Design in nature is about this. Science began with images: geometry (the science of figures) and mechanics (the science of contrivances made out of moving figures). We think, we create, and we speak in terms of images. Design in nature is about this, the images. The very fact that these images have names—river basin, lung, snowflake—means that we all know what they are individually even though they all look like trees.

The second meaning is the verb "to design," which is about the human activity of creating images and contrivances that are useful. This verb refers strictly to what people do on a design project, for example in engineering, where along with the verb "to design" comes "the designer" as one or many. This second meaning is not the object of this book or of any other application of the Constructal Law. Design in nature is not about "to design" and "the designer."

The Constructal Law is about predicting the design (the flow configuration) and its evolution in time. The Constructal Law is about why geometry happens. Constructal theory is the view that the Constructal Law is correct and reliable in a predictive sense. The use of constructal theory to discover flow configurations that offer greater access is constructal design.

Constructal theory and design are predictive, not descriptive. This is the big difference between the Constructal Law and other views of design in nature. Previous attempts to explain design in nature are based on empiricism: observing first and explaining after. They are backward looking, descriptive, and at best explanatory. They are not predictive theories even though some are called theories. Examples are complexity theory, network theory, chaos theory, power laws (allometric scaling rules), general models, and optimality statements (minimum, maximum, optimum).

The Constructal Law is not about optimality, destiny, or end design. It is about the fact that the generation and evolution of design never ends. With the Constructal Law we anticipate the evolving design and its direction in time. Complexity and scaling rules are discovered, not observed. Complexity is finite (modest), and is part of the description of the constructal design that emerges. If the flows are between points and areas or volumes, the constructal designs that are discovered are tree-shaped networks. The "networks" are discovered, not observed, and not postulated. Networks, scaling rules, and complexity are part of the description of the world of constructal design that emerges predictively from the Constructal Law.

Based on selected papers presented at the 2011 Constructal Law Conference in Porto Alegre, Brazil, this book illustrates the life, vigor, and growth of the research field that is stimulated today by the Constructal Law. The samples selected for presentation cover the broad range of science, from physics and biology to technology and human dynamics. The first part of the book is devoted to fundamentals and how the Constructal Law can be used to predict design in nature, the generation of design and the evolution of design. The second part takes the reader into the world of applications, where the constructal configurations are placed in processes and

systems that are useful. Together, the constructal fundamentals and applications are an invitation to new research with the Constructal Law, in new directions that so far are waiting to be brought under the tent of "design as science," which the Constructal Law holds firmly.

Porto Alegre, RS, Brazil — Luiz A.O. Rocha
Toulouse, France — Sylvie Lorente
Durham, NC, USA — Adrian Bejam

References

1. A Bejan, JP Zane. Design in nature. How the constructal law governs evolution in biology, physics, technology and social organization. New York:Doubleday; 2012
2. A Bejan, S Lorente. Design with constructal theory. Hoboken:Wiley; 2008
3. A Bejan, S Lorente. The constructal law and the evolution of design in nature. Phy Life Rev. 2011;8:209–240
4. A Bejan, S Lorente. The constructal law of design and evolution in nature. Phil Trans R Soc B. 2010;365:1335–1347
5. AH Reis. Constructal theory: from engineering to physics, and how flow systems develop shape and structure. Appl Mech Rev. 2006;59:269–282
6. L. Chen. Progress in the study on constructal theory and its applications. Sci China Tech Sci. 2012;55(3):802–820
7. T. Basak. The law of life. Phy Life Rev. 2011;8:249–252

Contents

Contributors

Y. Azoumah LESEE-2iE, Laboratoire Energie Solaire et Economie d'Energie, Institut International d'Ingénierie de l'Eau et de l'Environnement, Ouagadougou, Burkina Faso

A. Bejan Department of Mechanical Engineering and Materials Science, Duke University, Durham, NC, USA

T. Bello-Ochende Department of Mechanical and Aeronautical Engineering, University of Pretoria, Hatfield, South Africa

P. Bieupoude LESEE-2iE, Laboratoire Energie Solaire et Economie d'Energie, Institut International d'Ingénierie de l'Eau et de l'Environnement, Ouagadougou, Burkina Faso

C. Biserni Dipartimento di Ingegneria Energetica, Nucleare e del Controllo Ambientale, Università degli Studi di Bologna, Bologna, Italy

A.L.G. Correia Escola de Engenharia (EE), Universidade Federal de Rio Grande (FURG), Rio Grande, RS, Brazil

J.A.V. Costa Escola de Química e Engenharia de Alimentos, Universidade Federal do Rio Grande, Rio Grande, RS, Brazil

D.C. Cunha Instituto Federal de Educação, Ciência e Tecnologia do Rio Grande do Sul, Campus Rio Grande, Rio Grande, RS, Brazil

Weizhong Dai Mathematics and Statistics, College of Engineering and Science, Louisiana Tech University, Ruston, LA, USA

M.R. Errera Department of Environmental Engineering, Federal University of Paraná, Curitiba, Brazil

F.L. Garcia Departamento de Engenharia Mecânica, Universidade Federal do Rio Grande do Sul, Porto Alegre, RS, Brazil

M.N. Gomes Departamento de Engenharia Mecânica, Centro Politécnico, Universidade Federal do Paraná, Curitiba, PR, Brazil

L.A. Isoldi Escola de Engenharia (EE), Universidade Federal de Rio Grande (FURG), Rio Grande, RS, Brazil

M. Letzow Programa de Pós-Graduação em Modelagem Computacional, Universidade Federal do Rio Grande, Rio Grande, RS, Brazil

X. Liu School of Energy and Power Engineering, Nanjing University of Science and Technology, Nanjing, Jiangsu, China

N. Lopes Escola de Engenharia (EE), Universidade Federal de Rio Grande (FURG), Rio Grande, RS, Brazil

Sylvie Lorente LMDC (Laboratoire Matériaux et Durabilité des Constructions), Université de Toulouse, INSA, Toulouse, France

G. Lorenzini Dipartimento di Ingegneria Industriale, Università degli Sudi di Parma, Parma, Italy

B.N. Machado Escola de Engenharia (EE), Universidade Federal de Rio Grande (FURG), Rio Grande, RS, Brazil

C.A. Marin Companhia de Saneamento do Paraná–SANEPAR, Curitiba, Brazil

C.H. Marques Escola de Engenharia (EE), Universidade Federal de Rio Grande (FURG), Rio Grande, RS, Brazil

J.P. Meyer Department of Mechanical and Aeronautical Engineering, University of Pretoria, Hatfield, South Africa

A.F. Miguel Department of Physics and Geophysics Center of Évora, University of Évora, Évora, Portugal

P. Neveu Laboratoire Procédés Matériaux et Energie Solaire, PROMES-CNRS UPR 8521, Rambla de la thermodynamique, Tecnosud Université de Perpignan, Perpignan cedex, France

O.T. Olakoyejo Department of Mechanical and Aeronautical Engineering, University of Pretoria, Hatfield, South Africa

J.C. Ordonez Department of Mechanical Engineering and Center for Advanced Power Systems, Florida State University, Tallahassee, FL, USA

S. Périn OCTO Technology, Paris, France

Achintya Kumar Pramanick Department of Mechanical Engineering, National Institute of Technology Durgapur, West Bengal, India

M.V. Real Escola de Engenharia (EE), Universidade Federal de Rio Grande (FURG), Rio Grande, RS, Brazil

A.H. Reis Department of Physics and Évora Geophysics Centre, University of Évora, Évora, Portugal

L.A.O. Rocha Departamento de Engenharia Mecânica (DEMEC), Universidade Federal do Rio Grande do Sul (UFRGS), Porto Alegre, RS, Brazil

E.D. dos Santos Escola de Engenharia (EE), Universidade Federal de Rio Grande (FURG), Rio Grande, RS, Brazil

J.A. Souza Department of Mechanical Engineering and Center for Advanced Power Systems, Florida State University, Tallahassee, FL, USA

G. Stanescu Departamento de Engenharia Mecânica, Centro Politécnico, Universidade Federal do Paraná, Curitiba, Paraná, Brazil

P.R.F. Teixeira Escola de Engenharia (EE), Universidade Federal de Rio Grande (FURG), Rio Grande, RS, Brazil

J.V.C. Vargas Departamento de Engenharia Mecânica, Universidade Federal do Paraná, Curitiba, Paraná, Brazil

J. Vaz Escola de Engenharia (EE), Universidade Federal de Rio Grande (FURG), Rio Grande, RS, Brazil

R. Xiong School of Energy and Power Engineering, Nanjing University of Science and Technology, Nanjing, Jiangsu, China

H. Zhang School of Energy and Power Engineering, Nanjing University of Science and Technology, Nanjing, Jiangsu, China

S. Zhu School of Energy and Power Engineering, Nanjing University of Science and Technology, Nanjing, Jiangsu, China

Chapter 1
The Constructal Design of Humanity on the Globe

A. Bejan and Sylvie Lorente

1.1 The Water and Energy Problem

Energy and water are commonly described as "problems," like not having enough money in the bank. In this chapter we show that energy and water are not "commodities," rather they are flows that sustain human life. They are not two flows but one flow, which is responsible for all the needs of human life (movement, heating, cooling, fresh water). This single flow represents wealth and is the reason why the annual economic activity of a country (the GDP) is proportional to the annual consumption of fuel in that country.

All things move because they are driven. All the live systems (animate and inanimate) function as engines connected to brakes, such that the ultimate effect of fuel consumption is movement on the world map. To be most effective, this movement is hierarchical: *few large and many small* engines connected to brakes, all forming a multiscale tapestry (vasculature) of movement on the globe. The tapestry is a superposition of numerous distributing and collecting flow architectures, all linking discrete points with finite spaces (areas and volumes). The spaces covered by collecting and distributing flows grow in time in accord with S-shaped curves, which unite all the animate and inanimate flow designs on the landscape, and are predicted entirely based on the constructal law.

The opening ceremony of a recent conference commemorating "World Water Day 2011" in Muscat, Oman, began with one of those lines with which nobody

A. Bejan (✉)
Department of Mechanical Engineering and Materials Science, Duke University, Durham, NC 27708-0300, USA
e-mail: abejan@duke.edu

S. Lorente
LMDC (Laboratoire Matériaux et Durabilité des Constructions), Université de Toulouse, 135, avenue de Rangueil, Toulouse, Cedex 04 F-31 077, France
e-mail: lorente@insa-toulouse.fr

L.A.O. Rocha et al. (eds.), *Constructal Law and the Unifying Principle of Design*, Understanding Complex Systems, DOI 10.1007/978-1-4614-5049-8_1,

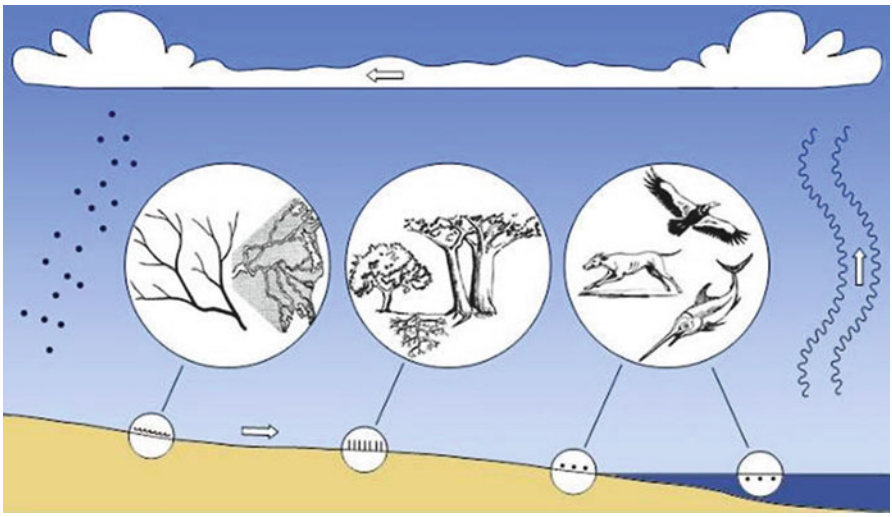

Fig. 1.1 Water in nature circulates with flow configurations: atmospheric currents, rain, river basins and deltas, vegetation, rising plumes, and animal locomotion [3]

could disagree: "Life would not exist without water." Yes, but incomplete. Life would not exist without *the flow* of water.

The keynote event at the ASME 2011 International Mechanical Engineering Congress & Exposition was "Energy and Water: Two Vital Commodities." This is not accurate either. Vital yes, commodities no. There is plenty of water in a swamp, and plenty of solar energy in the Sahara. Neither is precious because neither is *flowing* through the space inhabited by human life [1, 2].

We and the entire animate realm are an integral part of the circuit that water completes as it flows on earth (Fig. 1.1). The best known parts of this loop are the downward flow (the rain) and the flow along the landscape (the river basins, deltas, underground seepage, ocean currents). Less known is the upward flow, which is vehicled by evaporation from the land and water surface, and from the vegetation that covers the land (this flow design is why "trees like water"). Even less known is that the biosphere too is a design for water flow on the world map. When this flow stops, life stops.

Humanity is one of an immense number of biological water flow systems on earth. It is the most potent of them all, in fact, the more advanced we become the more water we move on the landscape. We change the landscape to such degrees that we are constructing and witnessing our own geological age on Earth: the human age.

Like all world problems, the world water problem is not distributed evenly on the globe (Fig. 1.2) [4]. There are stressed regions, and there are regions of plenty. Why then are North America and Europe not stressed? These are regions that do not break records of rainfall. The Congo is. North America and Europe are not regions without agriculture; in fact they serve as bread baskets for the whole world. Why is it that the water problem is distributed so unevenly?

Fig. 1.2 The world map of fraction of fresh water withdrawal for agriculture in 2000 [4]

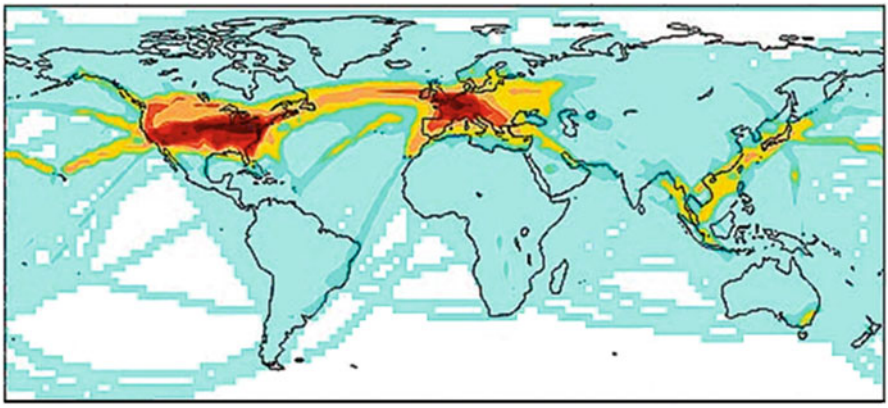

Fig. 1.3 The world map of human air mass transit. Where aircraft flew in 1992 [5]

One clue is that the unevenness of the water problem matches the unevenness of the human movement on the globe (Fig. 1.3) [5]. Advanced means advanced in everything (movement, water flow, science, technology, etc.), and this is where thermodynamics and the constructal law come in. Advancement ultimately means only one thing: moving greater currents on the landscape more easily.

1.2 Movement, Economics, and Wealth

Things flow because they are driven. On earth, all the flows are driven by the heat engine that operates between heating from the sun and heat rejection to the cold sky. Take our own movement (Fig. 1.4). Work is produced by the global heat engine, but

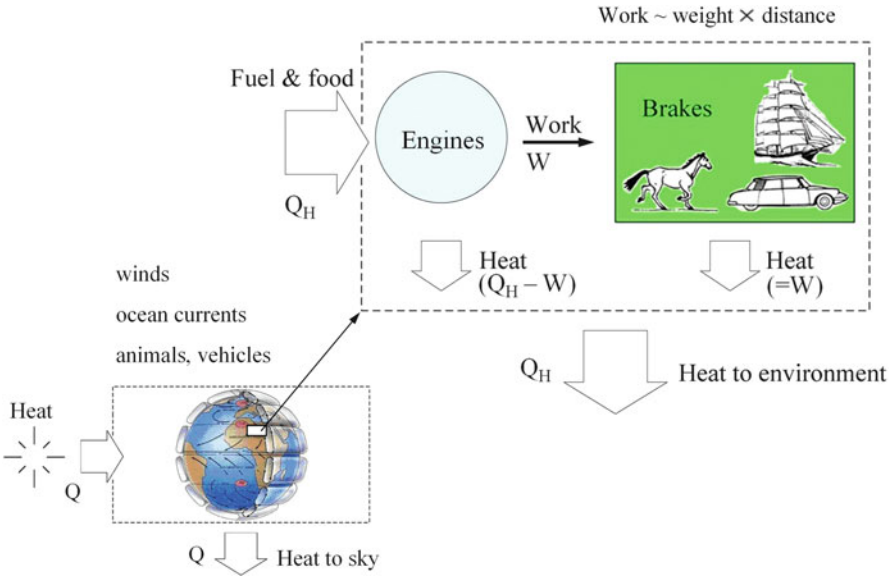

Fig. 1.4 Everything that moves on earth is driven. It moves as an engine that dissipates its work output into a brake [1]

there is no taker for this work. Instead, all the work is dissipated (destroyed) into heat, in the brakes shown in Fig. 1.4. The net effect of the flow of heat from hot to cold is movement, in this case human locomotion.

All the human needs are reducible to this thermodynamic conclusion, and they are put together in Fig. 1.5. The need to have heating, i.e., a room temperature above the ambient temperature, requires the flow of heat from the fire to the ambient. The better we configure this heat flow, the more the heat flow passes through our living space before it is dumped into the ambient. The need to have air conditioning and refrigerated spaces to store food is satisfied in the same manner. It is all about facilitating our movement on the landscape and increasing our staying power.

In animal design, as in our own evolution as *the human and machine species* [6, 7], the design for greater flow access on the globe calls not only for decreasing some flow resistances but also for increasing others. To facilitate movement, animals must have body insulation, i.e., thermal resistances. Our engines, homes, and refrigerators must also be covered by insulation. This is because what flows *through* animals, humans, and vehicles must proceed along certain channels. This means less resistance *along* each channel and more resistance *across* the channel. This apparent contradiction of less resistance and more resistance is what "channel" means.

Completely analogous is the need to have water flow in the living space. The building of infrastructure for water delivery and removal requires work, which comes from power plants that consume fuel. The need to have food (another water stream into the living space) is met through agriculture and irrigation, which require

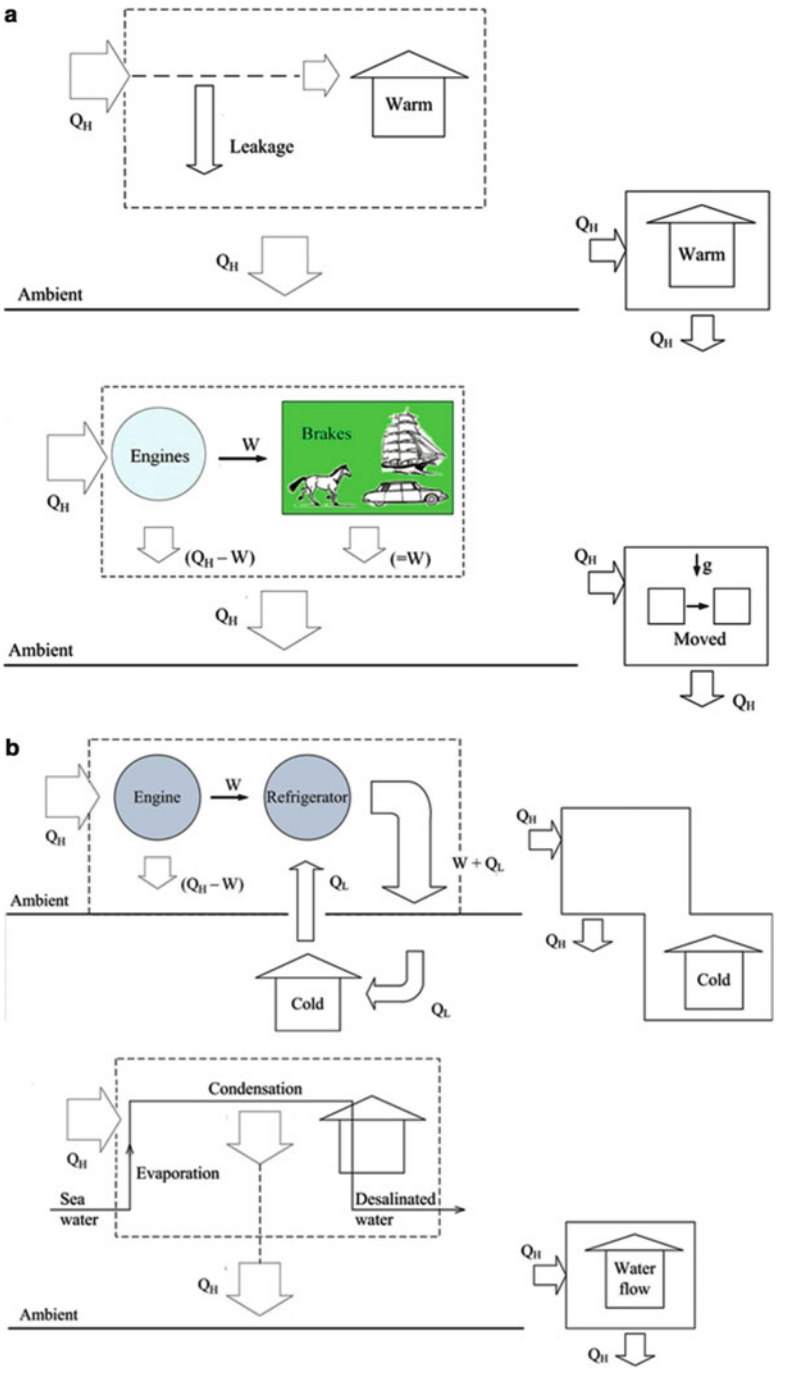

Fig. 1.5 All the needs of humanity can be reduced to the model of Fig. 1.4. Heat flows through the human space, from high temperature to ambient temperature, and the effect is beneficial for human life: heating, transportation, cooling, water, etc.

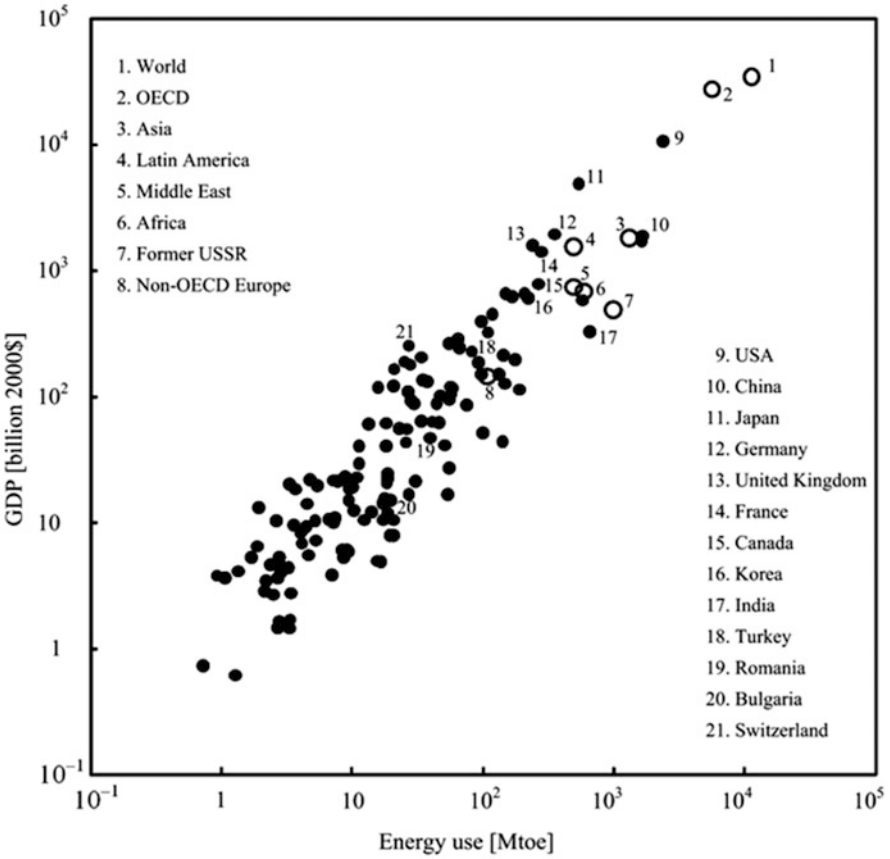

Fig. 1.6 The *bottom line* of Fig. 1.5 is that economic activity means the burning of fuel for human needs [1]. This is demonstrated by the annual GDP of countries all over the globe, which is proportional to the fuel burned in those countries (data from International Energy Agency. Key World Energy Statistics, 2006)

work. In the arid and populated regions of the globe the water supply comes largely from desalination. This too requires work from fuel.

All together, the needs that define modern living are streams driven by work, or power. In time, these streams swell as the society becomes more advanced, civilized, and affluent. Better living conditions (food, water, heating, cooling) are achieved not only through the use of more fuel but also through configuring better the designs (i.e., science and technology) of all the things that flow and move. We see this most clearly in the comparison of countries according to wealth (GDP) and fuel consumption (Fig. 1.6) [1]. Wealth is power, literally, the power used to drive all the currents that constitute the economic activity. The need to have water is the need to have power.

All the moving and flowing systems evolve in time toward constructal designs (Fig. 1.4). The movement is the result of dissipating the work produced by the heat current as it passes from high temperature to the temperature of the ambient.

Movement and flow mean "work ~ weight × distance," as highlighted in Fig. 1.4. This summarizing formula holds for the work needed to drive the water flow through all the river channels, and the animals on all their paths on the world map. It holds not only for the inanimate and animate weight that sweeps the globe horizontally, but also for the weight of humanity—all the people, goods, and communications (assemblies of people and goods moving together, globally). We see the actual flow of this human and machine species in Fig. 1.3, which shows the design that has emerged naturally to facilitate human movement on earth. This global river basin—this vasculature—is driven by the burning of fuel. Like the movement that it drives, the burning of fuel is nonuniform, organized into few large channels and many small channels, just like the architecture of river basins, vascular tissues, and the animal kingdom.

Wealth means movement today, not some gold hidden in a cave and forgotten. This view places the concept of "wealth" in physics. A country is wealthy (developed, advanced) because it moves more material and people than the underdeveloped. Fuel that flows (extracted, sold, burned) is wealth (e.g., Fig. 1.6), because it sustains the movement of people and goods, in accord with the constructal-law tendency to morph to move more easily. Fuel saved in the ground is not wealth, because it does not create movement. Likewise, money that is being spent (to drive the flow of fuel, which generates movement) is wealth; money that is hoarded (not spent) is not wealth. In sum, the view provided by the constructal law (Fig. 1.6) is the physics law of the natural design phenomenon known as economics and business.

With the constructal law, biology and economics become like physics—law-based, exact, and predictable [2].

The burning of fuel and the resulting movement are not the only streams that represent wealth. There is also the creation of knowledge (science, education, information), technology and paths of communication. These streams and flow architectures happen because they are integral parts of the design of moving people and goods more effectively. The flow of knowledge is an integral part of the material flow architecture on the globe, and it also means wealth—more, farther, more efficiently, all measurable in physics. This is why the map of the distribution of scientific ideas (Fig. 1.7) [8] is essentially the same as the map of the distribution of human movement (Fig. 1.3) and wealth (Fig. 1.6).

1.3 Few Large and Many Small

The power of this mental viewing rests in its implications in the design needed by the underdeveloped to move more, to have better roads, education, information, economies, peace, and security. How is this to be done? By attaching the

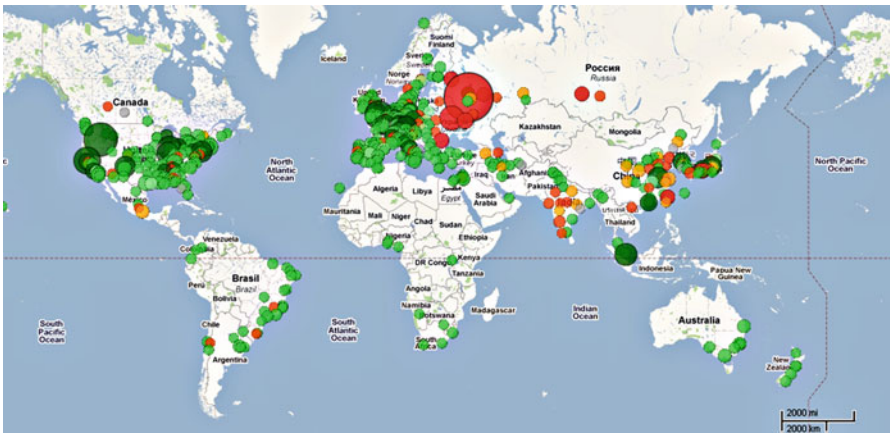

Fig. 1.7 The distribution of regions with highly cited scientific publications over the world [8]

underdeveloped areas and groups better (with better flowing channels placed in better locations) to the trunks and big branches of the flow of economy on the globe. For these attachments to flow, the grand design needs the big rivers. It needs the advanced. This is how to control the size of the gap between the developed and the underdeveloped, so that the whole design is efficient, stable, and beneficial to all its components.

The few large and many small flow together, because this is how movement is facilitated the most on the landscape. The movement of goods has evolved into a tapestry of few large roads and many small streets (Fig. 1.8), and few large trucks and many small vehicles (Fig. 1.9) [9]. The few large and many small is also the secret of the design of all animal mass flow on the landscape (Fig. 1.10). In biology and common language this is better known as the food chain, the fast catches the slow, and the large eats the small (which is correct, because the larger animals are faster, on land, in water, and in the air [10–12]).

Few large and many small are all the streams that sweep the globe. They are hierarchical, like a circulatory system with one heart with two chambers, Europe and North America (Fig. 1.3). Fuel consumption, economic activity, and wealth (Fig. 1.6) are other names for this natural design.

1.4 Distributed Energy Systems: The Global Design

Seen through the lens of the constructal law, the future design of globalization is clear. It is an energy and water future, a design of channels with diffusion perpendicular to the channels. The human activity toward this design proceeds on three fronts:

1. The development of water and fuel resources.
2. The development of water production and energy conversion methods.

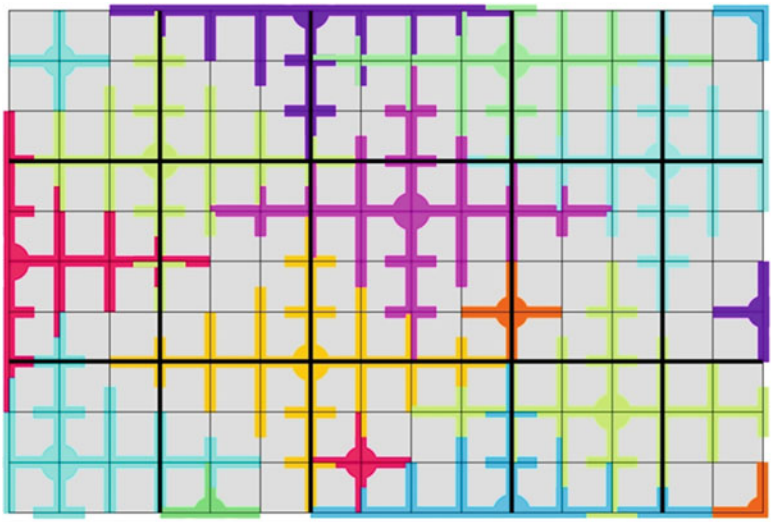

Fig. 1.8 The movement on the landscape appears complicated because it leaves marks (paths) that crisscross and form grids. This is particularly evident in the evolving designs of urban traffic. Less evident is the actual flow of people and goods on the area. Each flow is tree shaped, from the area to the point of interest or from another point to the same area. The grid is the solid (but not permanent) infrastructure that accommodates all the possible and superimposed tree-shaped flows. The superposition of the big branches of the trees forms the grid of avenues and highways. The superposition of the tree canopies forms the grid of streets and alleys. The few large and many small of urban design has its origin in the natural design of tree-shaped flow on the landscape

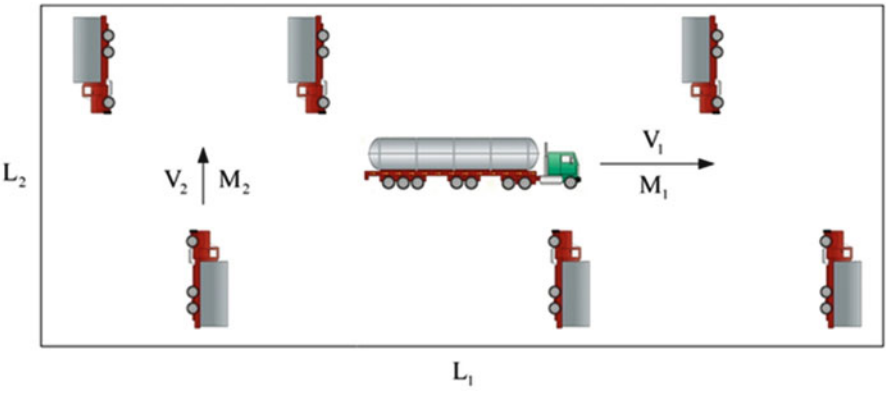

Fig. 1.9 Few large and many small in the movement of freight on vehicles on the landscape [9]. The movement is enhanced when a certain balance is established between the number of small vehicles allocated to a large vehicle, and the balance (L_1/L_2) between the distances (L_1, L_2) traveled by the few and the many

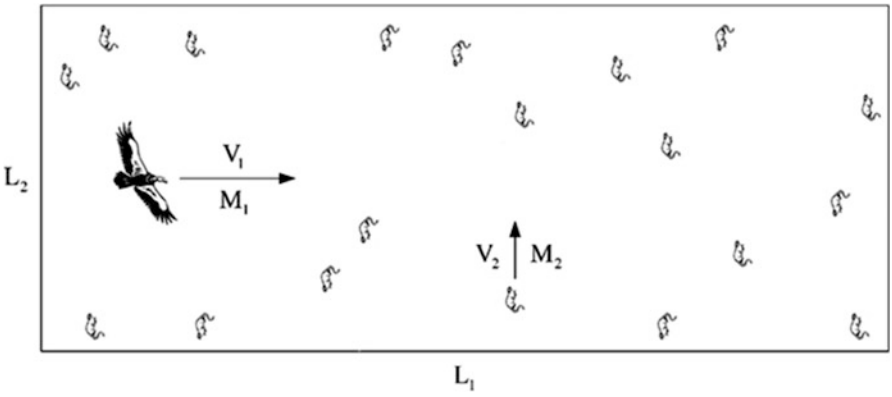

Fig. 1.10 Few large and many small in how animal mass is moving on the globe, on land, in water, and in the air. Note the analogy between this design and Fig. 1.9. The design of animal mass flow is the precursor to our own design as human and machines (vehicles) sweeping the globe

3. The global design of water and fuel production and consumption, hand in glove with the global design of generation, distribution, and consumption (destruction).

Most important but least recognized is the third front, because it resonates in the daily debates about globalization, sustainability, and environmental impact. Work on the third front adds a fundamental component to water and energy initiatives in government, which has enormous impact on science, education, and industry.

The global flow system is a tapestry of nodes of production embedded in areas populated by users and environment, distributing and collecting flow systems, all linked, and sweeping the earth with their movement. Constructal theory and design [13] is showing that the whole basin is flowing better (with fewer obstacles globally) when the production nodes and the channels are allocated in certain ways to the covered areas (the environment). This is how the inhabited globe becomes a live system—a living tissue—and why its best future can be designed based on principle. With the constructal law, this design can be pursued predictively.

Distribution, allocation, and the consumption of power should be considered together on fronts 1–3, as equal partners. This holistic view includes fields such as housing and transportation, building materials, heating and air conditioning, lighting, and water distribution. In the university, it serves as a healthy unifier of mechanical, civil, and electrical engineering with environmental science. Taken together, all these concerns allow the global design to emerge with balance between the fuel streams that sustain our society on earth.

Once again, few large and many small is the secret of the global design, because we showed recently that larger flow systems must be more efficient than smaller systems [9, 14]. This is in accord with the recorded performance of steam turbine power plants [15], gas turbine power plants [14], individual turbines [15], and refrigeration and liquefaction installations [16]. Samples of these data are presented in Fig. 1.11. This size effect is predictable from the argument that larger body sizes

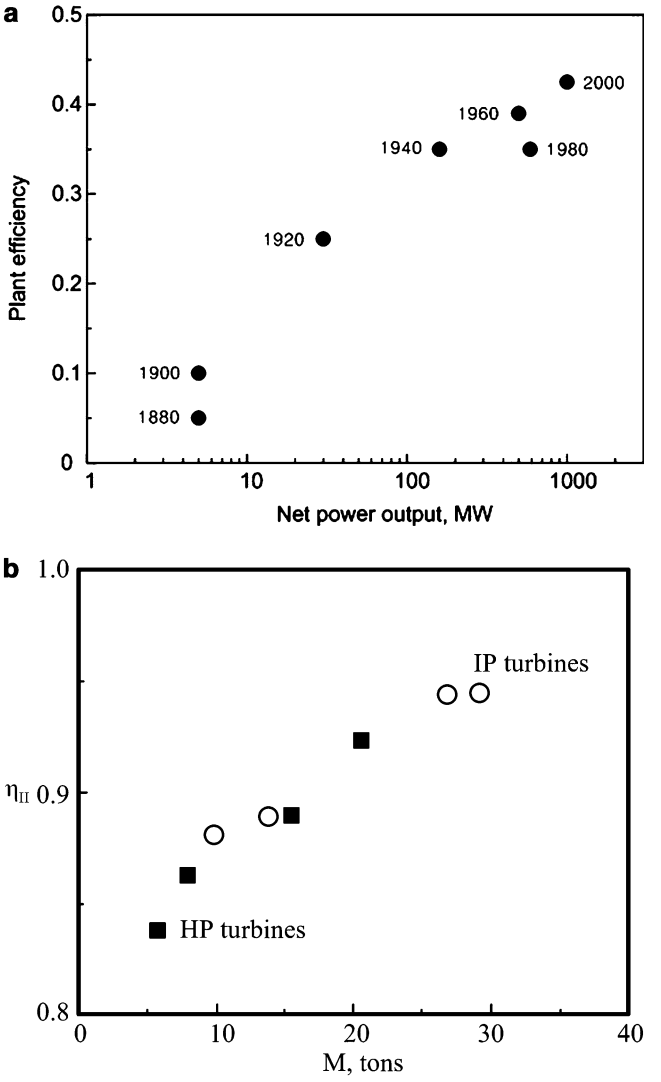
a
0.5
0.4
0.3
0.2
0.1
0
Plant efficiency
2000
1960
1940
1980
1920
1900
1880
1
10
100
1000
Net power output, MW
b
1.0
0.9
0.8
η_{II}
IP turbines
HP turbines
0
10
20
30
40
M, tons

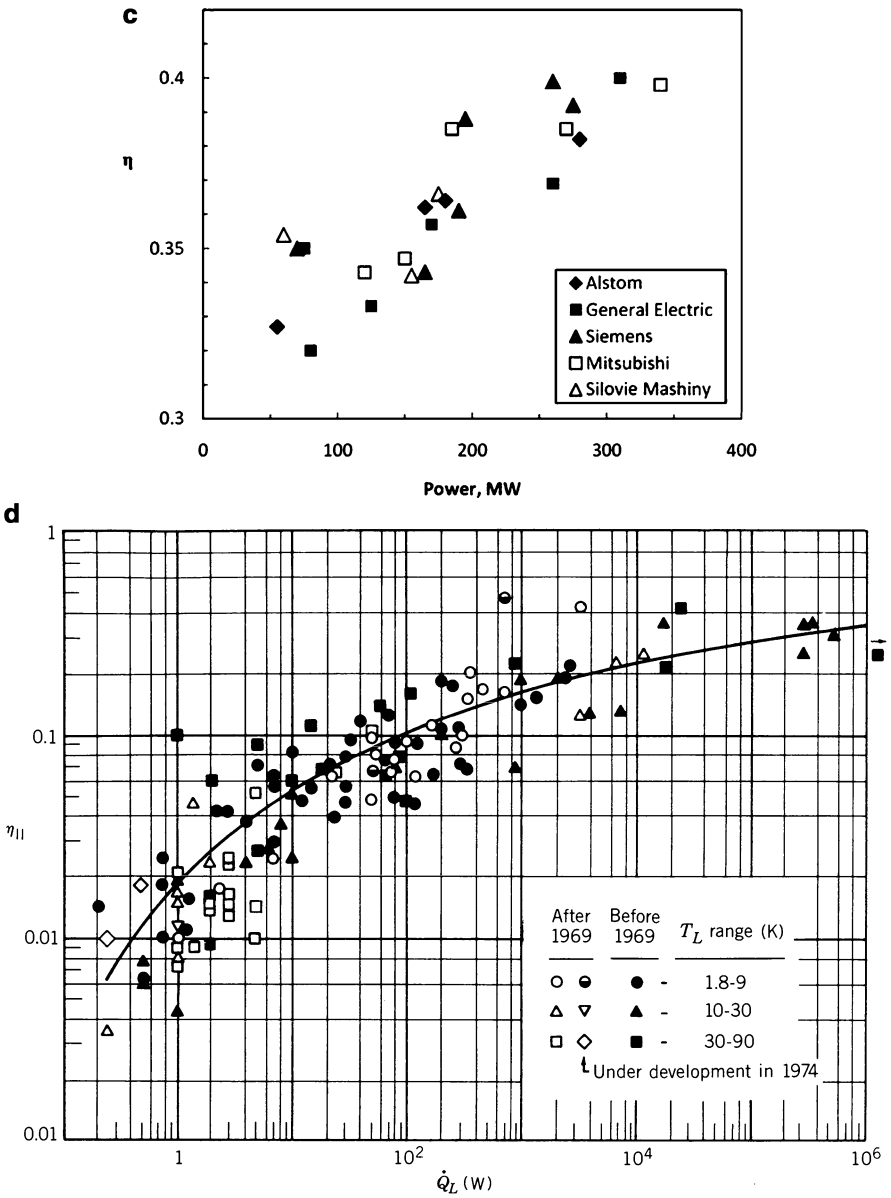

Fig. 1.11 The effect of size on efficiency [14]: (**a**) steam turbine power plants ; (**b**) individual steam turbines; (**c**) gas turbine units; (**d**) refrigeration and liquefaction plants

accommodate ducts with larger cross-sections and larger surfaces for heat and mass transfer, which represent lower resistances for the flow of fluids and heat and mass currents. This holds equally for power plants and animal design, and is summarized in an efficiency formula of the form $\eta_{II} = C_1 M^{\alpha}$, where η_{II} is the second law efficiency, C_1

is a constant, M is the body mass, and $\alpha \tilde{<} 1$. This also predicts the efficiency of animal design as a transportation system for animal mass on the landscape.

For example this effect of "economies of scale" can be predicted by considering even simpler flow systems. We showed that when heating water in a central facility the loss of heat from the water mass m is proportional to the surface of the water tank (i.e., $m^{2/3}$), and consequently the heat loss per unit of heated water mass decreases as $m^{-1/3}$ as the body size m increases [13]. Another example is the power output of solar chimney power plants, which increases in proportion with $A^{3/2}$, where A is the land area occupied by the roof of the power plant [17].

At first glance, this size effect suggests that bigger is always better. We showed that this is incorrect because the efficient system must serve a population of users distributed on an area. When the system is large, the area is large and the users are many. The distribution lines that connect the central system with the users are plagued by losses that increase in proportion with the length scale of the area. From this point of view, smaller is better. There is a fundamental tradeoff between the two effects, and its chief result is that a balance always emerges between the size of the central system and the number of users that the system serves. We demonstrated this for the generating and distribution of power on a land area [18], refrigeration and air conditioning [19], and heating [13, 20].

In sum, the landscape emerges as a tapestry of nodes of production and lines of distribution. The nodes are few and large, and the branches that reach the users are many and small. We also discovered that this tapestry must be woven according to a vascular design that depends on the size of the whole system. For example, while distributing heated water from a central heater to a square area with N uniformly distributed users, the flow architecture can be radial (r), dichotomous (2), or a construct (4) based on a quadrupling rule, Fig. 1.12. The lower part of the figure shows that the total heat loss per user (i.e., the loss at the center and along the distribution lines) decreases as the size of the landscape (N) increases. In the pursuit of efficiency (less fuel required per user), the flow architecture must change stepwise from (r) to (2), and finally to (4) as the overall size increases. The stepwise evolutionary design of vasculature covers all scales, including the water and energy design of the inhabited globe.

1.5 Designs for Distributing and Collecting: The S-Curve Phenomena

The flows that bathe and connect the live landscape are united not only by the tapestry of tree-shaped flows (Figs. 1.8 and 1.9) but also by the unsteady (nonmonotonic) manner in which these flow architectures spread. When the covered territory is plotted vs. time, the histories of spreading and collecting flows are S-shaped curves.

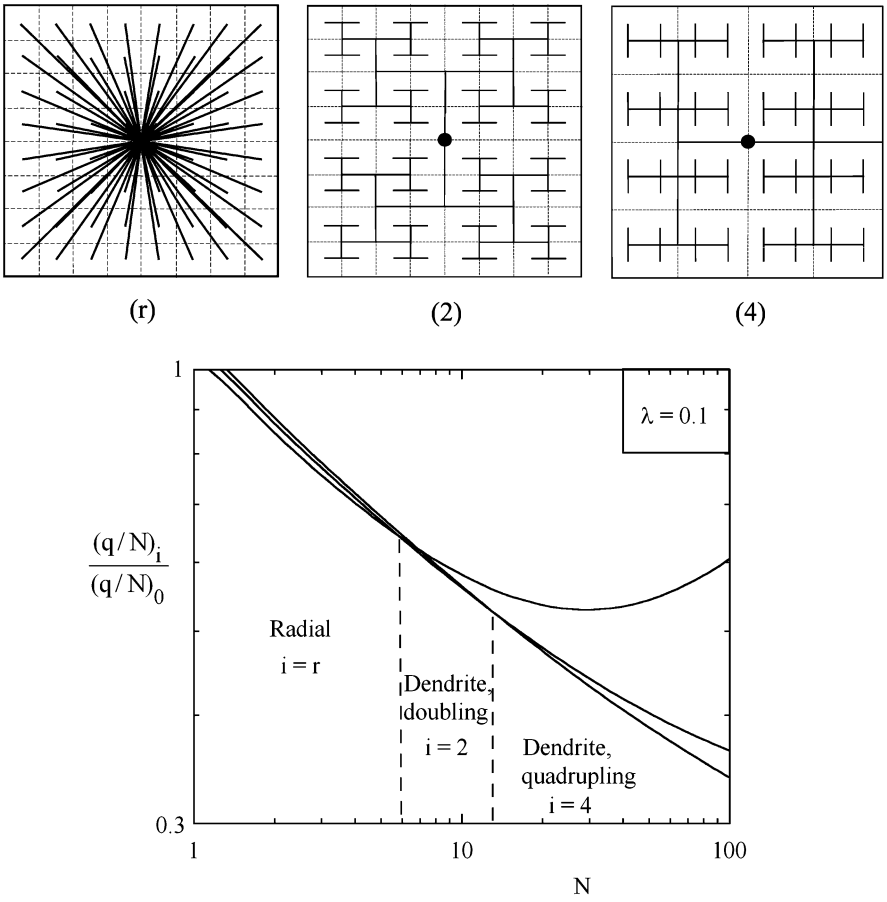

Fig. 1.12 The effect of size on the vasculature design of distributed heating on the landscape [20]. The total heat loss per user decreases as the size of the inhabited area increases. The heat loss per user is lower when the architecture evolves stepwise from radial to dendritic as N increases

In the beginning, the covered territory grows slowly, but the rate of territory coverage increases in time. The growth rate is maximum at the point where the S-curve is the steepest. Later, the growth rate decreases monotonically and the covered territory tends to a plateau, which is the upper end of the S (see the examples of Fig. 1.13).

When a heat pump cools a home during the hot and humid season, it must dump a multiple of that heat current into the ambient. Where the human settlement is sparse, the dumping of the heat is not a critical design feature. The atmosphere—the big sewer in the sky—will do. The same "environment" serves the heat pump during the cold season, when the heat pump must draw a heat current from the ambient and inject it (multiplied) into the home. What was sewer in summer is manna from heaven in winter.

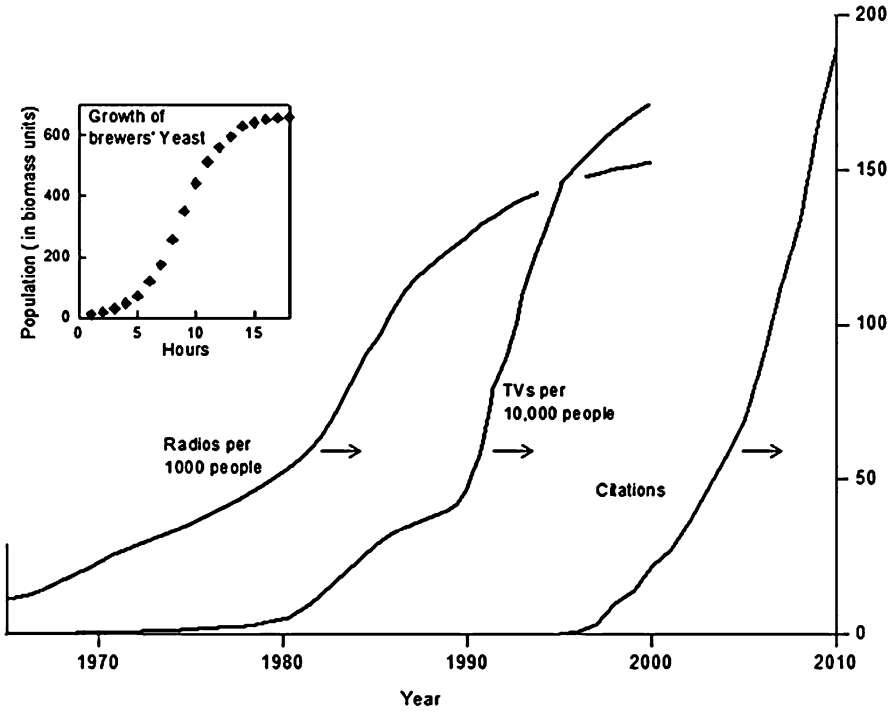

Fig. 1.13 Examples of S-curve phenomena: the growth of brewer's yeast, the spreading of radios and TVs, and the growth of the readership of scientific publications [21]

It is not nearly as easy when the human settlement is dense. No one wants to live in somebody else's exhaust. In this evolutionary direction (which, by the way, is the future of all humanity), the "environment" is as dear as the plot of land on which the home is built. The heat pumps of the future must dump heat to and suck heat from the ground.

How to spread a heat current from one point (the heat pump) to a finite-size volume (the soil around the home) is a constructal design problem that we solved by using the constructal law [21]. First, the heat must be spread by fluid flow, through tree-shaped pipes, throughout the territory. During this initial "invasion" phase, the volume of the heated soil is small (Fig. 1.14), but it increases at a growing rate. Second, after the hot fluid has *invaded* all the channels on the territory, the heat is transmitted from the channels perpendicularly to the neighboring soil. This is the "consolidation" phase, where the theme "solid" in the word consolidation suggests the reality of the heat current filling the soil interstices held between neighboring channels.

The history of the volume of heated soil vs. time is an S-shaped curve (Fig. 1.14) that is entirely deterministic, i.e., predictable. Everything about this S curve is known because both phases, the invasion and the consolidation, are known. We also

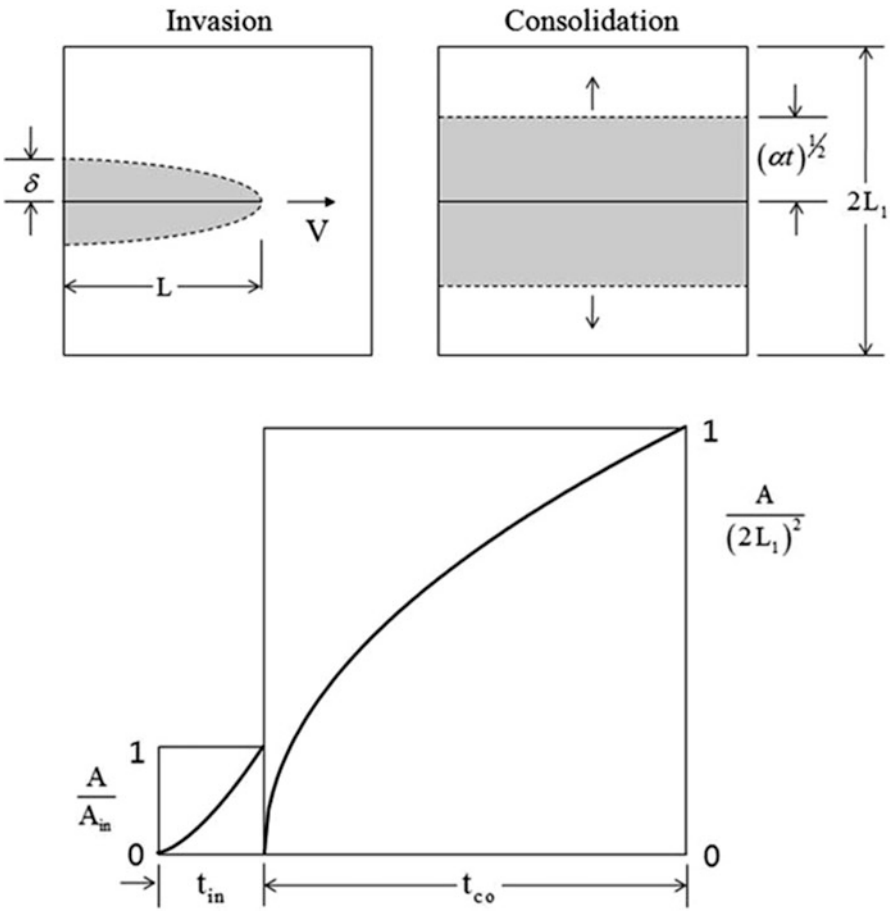

Fig. 1.14 Line-shaped invasion, followed by consolidation by transversal diffusion. The predicted history of the area covered by diffusion reveals the S-shaped curve [21]

predicted that when the invading channels are tree-shaped (Fig. 1.15) as opposed to single channels (Fig. 1.14), the entire flow from point to volume occurs faster, more easily, along a steeper S curve.

In summary, and in accord with the constructal law, the S curves of nature are manifestations (history records) of tree-shaped invasion (not line invasion) on areas and volumes that are eventually filled during consolidation by transversal diffusion.

This discovery of the S curve is important for two reasons. First, the S curve was predicted from the constructal law before there was any reason to look outside to see many diverse S curves and try to predict them in order to unite them. This first part of the story is about the meaning of pure theory. It is images in the mind, in that imaginary movie theater.

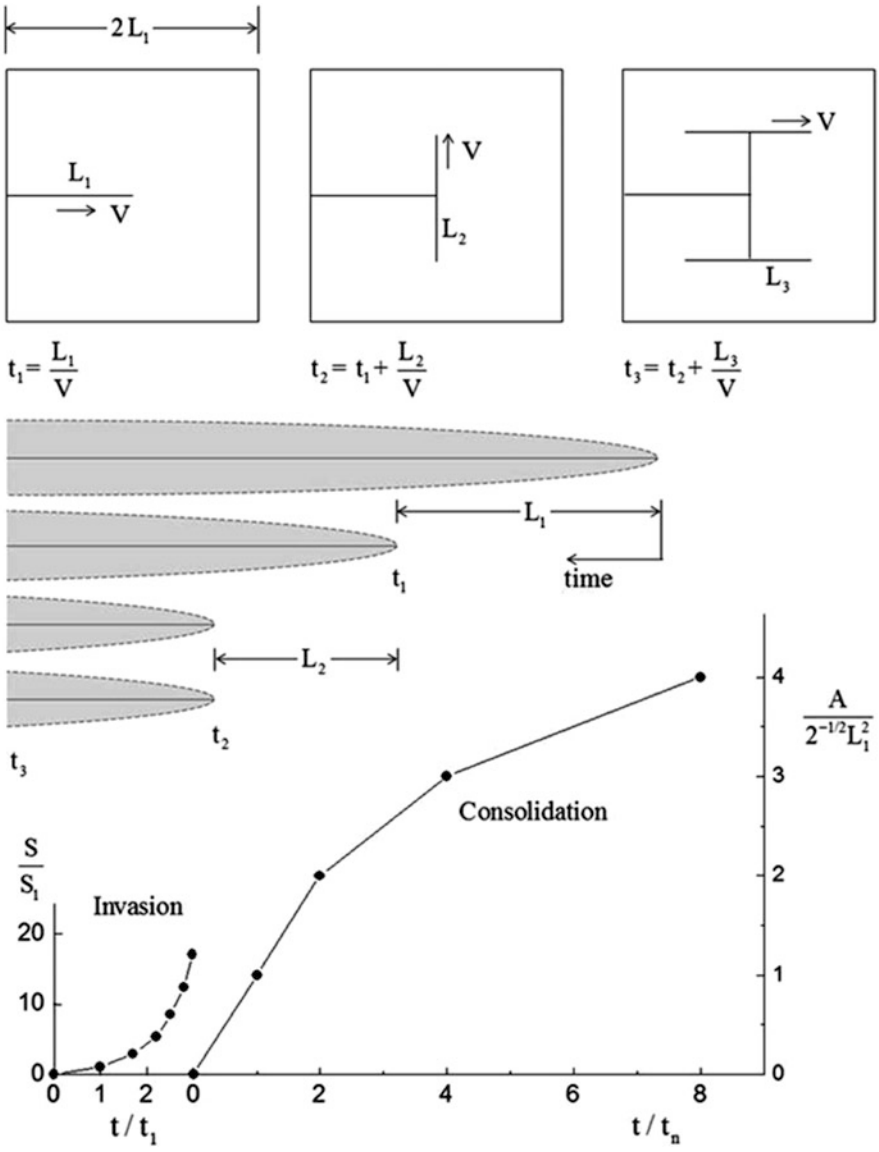

Fig. 1.15 Tree-shaped invasion, showing the narrow regions covered by diffusion in the immediate vicinity of the invasion lines [21]

The second part is about the practical value of this power to predict. When anything spreads on a territory, the curve of territory size vs. time is S-shaped: slow initial growth is followed by much faster growth, and finally by slow growth again. The corresponding curve of the rate of spreading vs. time is bell shaped.

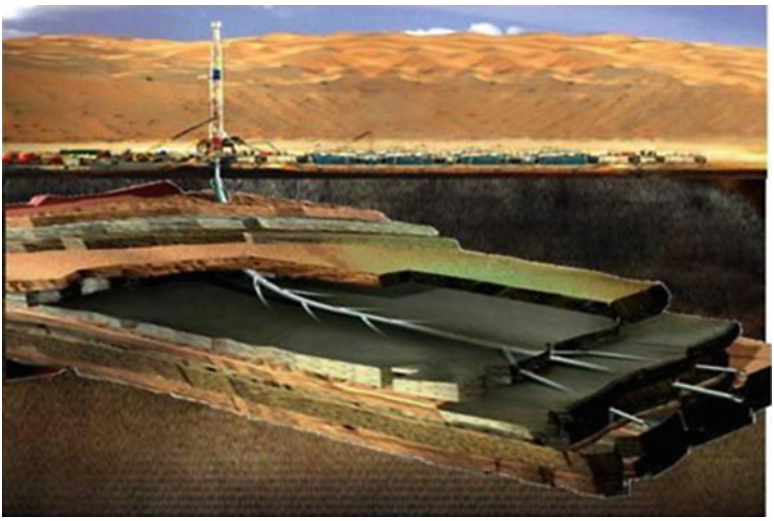

Fig. 1.16 The evolution of human-made volume-point flow underground: drilling and oil extraction pattern under the Empty Quarter, Saudi Arabia (Courtesy of Aramco). This tree-shaped design is an icon of all mining that occurs worldwide: coal, gas, metals, etc. [21]

This phenomenon is so common that it has generated entire fields of research that seem unrelated: the spreading of biological populations, cancer tumors, chemical reactions, contaminants, languages, news, information, innovations, technologies, infrastructure, and economic activity (e.g., Fig. 1.13).

The natural S-curve phenomenon is not a particular mathematical expression for the S-shaped curve. In fact, we showed that the S-shaped curves are not unique [21]. The natural phenomenon is the observation that in many and highly diverse flow systems the covered territory increases in time according to a curve that *resembles* an S.

The prevalence of S-curve phenomena in nature rivals that of tree-shaped flows, which also unite the animate, inanimate, and human realms. This is not a coincidence. Both phenomena are manifestations of the natural tendency of flow systems to generate evolving designs that allow them to flow, spread, and collect more easily. This tendency is summarized by the constructal law.

All these predictions apply equally to the behavior of collecting flows, which extract mass or energy from areas or volumes and carry them to discrete points. For collecting flows, the scales of the S inflection point indicate the all important regime of peak production rate, known as the "Hubbert peak" in oil extraction. It is not a coincidence that oil extraction technology has evolved from single-line invasion (the single well) to tree invasion, e.g., Fig. 1.16.

The S-curve phenomenon and its physics principle unite the spreading flows with the collecting flows, and the animate flows with the inanimate flows. In the human realm, they unite the designs for urban infrastructure with the underground architectures for mining (coal, metals, etc.), and teach the physics of "limits to

growth" and when a spreading population and technology can be expected to "hit the wall." They also cover the periodic phenomena of spreading and collecting, such as respiration (inhaling, exhaling), drug delivery, excretion, rain water (from river basin to delta), and blood circulation.

There is a lot of doomsday talk today about the world being in an "explosion" phase, or on an "exponential growth" curve. In view of the constructal-law origin of the S curve, all such talk is about the first part of the actual S-curve phenomenon. What looks like explosion today, will look like hitting the wall tomorrow.

Let's return to the discussion of how a new technology spreads [22]. The invasion-consolidation scenario happens naturally, not because industry and government leaders dictate it. Decades ago, only a few companies made autos—now everybody makes autos, but the advanced companies are making them with better designs and methods. Each such design is the start of its own S curve of how it spreads on the globe. It is the same with aircraft, although here the consolidation phase is yet to become visible. Agriculture is a much older example. The invasion was from Mesopotamia to Europe, and the consolidation followed: now everybody plants and reaps something.

All these phenomena are covered (in their own language) by our prediction of their S curves [21, 22]. If translated correctly, they reveal that their "exponential growth" must end and be replaced by "hitting the wall." China, by the way, will hit the wall too.

References

1. Bejan A, Lorente S. The constructal law and the evolution of design in nature. Phys Life Rev. 2011;8:209–40.
2. Bejan A, Lorente S. The constructal law makes biology and economics be like physics. Phys Life Rev. 2011;8:261–3.
3. Bejan A, Lorente S, Lee J. Unifying constructal theory of tree roots, canopies and forests. J Theor Biol. 2008;254:529–40.
4. Fraction of freshwater withdrawal for agriculture, UNEP/GRID; 2002.
5. Gierens K, Sausen R, Schumann U. A diagnostic study of the global distribution of contrails. Part 2: Future air traffic scenarios. Theor Appl Climatol. 1999;63:1–9.
6. Bejan A. Shape and structure, from engineering to nature. Cambridge: Cambridge University Press; 2000.
7. Bejan A, Zane PJ. Design in nature. How the constructal law governs evolution in biology, physics, technology and social organization. New York, NY: Doubleday; 2012.
8. Bornmann L. Leydesdorff L. Walch-Solimena C. E++1 C. J. Infometrics 2011; 5: 537–546.
9. Lorente S, Bejan A. Few large and many small: hierarchy in movement on Earth. Int J Des Nat Ecodyn. 2010;5:254–67.
10. Bejan A, Marden JH. Unifying constructal theory for scale effects in running, swimming and flying. J Exp Biol. 2006;209:238–48.
11. Charles JD, Bejan A. The evolution of speed, size and shape in modern athletics. J Exp Biol. 2009;212:2419–25.
12. Bejan A, Jones EC, Charles JD. The evolution of speed in athletics: why the fastest runners are black and swimmers white. Int J Des Nat Ecodyn. 2010;5:199–211.

13. Bejan A, Lorente S. Design with constructal theory. Hoboken, NJ: Wiley; 2008.
14. Bejan A, Lorente S, Yilbas BS, Sahin AS. The effect of size on efficiency: power plants and vascular designs. Int J Heat Mass Transfer. 2011;54:1475–81.
15. Kim YS, Lorente S, Bejan A. Distribution of size in steam turbine power plants. Int J Energy Res. 2009;33:989–98.
16. Bejan A. Advanced engineering thermodynamics. 3rd ed. Hoboken, NJ: Wiley; 2006.
17. Lorente S, Koonsrisuk A, Bejan A. Constructal distribution of solar chimney power plants: few large and many small. Int J Green Energy. 2010;7:577–92.
18. Lorente S, Bejan A. Global distributed energy systems. In: Brebbia CA, Jovanovic N, Tiezzi E, editors. Management of natural resources, sustainable development and ecological hazards II. Southampton: WIT Press; 2010. p. 251–69.
19. Xia L, Lorente S, Bejan A. Constructal design of distributed cooling on the landscape. Int J Energy Res. 2010. doi:10.1002/er.1743.
20. Rocha LAO, Lorente S, Bejan A. Distributed energy tapestry for heating the landscape. J Appl Phys. 2010;108:124904.
21. Bejan A, Lorente S. The constructal law origin of the logistics S curve. J Appl Phys. 2011;110:024901.
22. Bejan A. Lorente S. The physics of spreading ideas. Int. J. Heat Mass Transfer 2012; 55: 802–807.

Chapter 2
Toward a Quantitative Unifying Theory of Natural Design of Flow Systems: Emergence and Evolution

A.F. Miguel

2.1 Quality Design Prevalence in Natural Systems

The idea of beauty and quality of design of the natural systems found a broad consensus in the natural philosophers [1]. This is because living systems are wonderfully adaptable and can survive in a complex natural environment. Attempts to imitate living systems have been made since ancient times. The identification of animals as streamlined bodies with applications to manufactured devices for drag comes from Renaissance period [2, 3]. Leonardo da Vinci recognized the importance of the relationship between design and function. He noticed that a fish could move through water with little resistance because its streamlined shape allowed the water to flow smoothly over the afterbody without prematurely separating [4]. Da Vinci's flying machines powered by man were drawn in the 1490s based on the observation of birds [2] (Fig. 2.1).

In the seventeenth century, Borelli, together with Robert Boyle, René Descartes, Niels Stensen, and others, was the founder of an important intellectual movement known as iatromechanism [5]. According to Thomas Hall [5] "For Borelli, living bodies are machines. The life of the machine is the totality of movements exhibited by the moving parts and by the machine as a whole. The whole machine is an assemblage of smaller component machines." Borelli [6] also attempted to copy animal characteristics in a submarine design. Buoyancy control was based on the swim bladders of fish and propulsion control was obtained by oars acting similarly to paddling feet of geese or frogs.

The adherence to biological principles and designs for an enhanced performance influenced different areas of knowledge and last until today [7, 8]. The slogan "form follows function" became the tune of modern architecture [9]. This idea influenced

A.F. Miguel
Department of Physics & Geophysics Center of Évora, University of Évora,
Rua Romão Ramalho 59, Évora 7000-671, Portugal
e-mail: afm@uevora.pt

L.A.O. Rocha et al. (eds.), *Constructal Law and the Unifying Principle of Design*,
Understanding Complex Systems, DOI 10.1007/978-1-4614-5049-8_2,

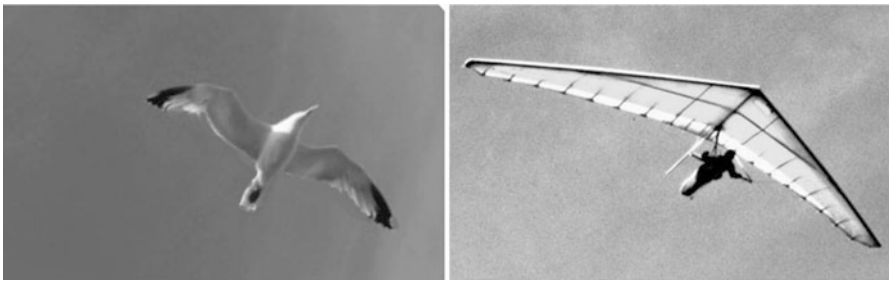

Fig. 2.1 A bird and a flying machine

the organic architecture of Frank Lloyd Wright and follows. In modern engineering, the idea is also to use biological inspiration to engineer machines that emulate the performance of animals. This biomimetic approach[1] [10] attempts to seek solutions for increased efficiency and specialization because consider that living systems have already performed the cost–benefit analysis (i.e., optimizing specific design for particular functions) due to process of "natural selection." Not long ago, scientists designed an electronic camera that mimics the shape of the human eye for improved imaging [12]. This design prevents the distortion that normally occurs at the edges of flat lenses.

The designs exhibited by natural systems may be target for technology transfer and to reduce the time of development of innovative solutions. Although, strict adherence to these designs is not always synonymous of good practical results [13, 14]. To prevent failures, a clear understanding of why a particular design is successful and the circumstances that make it successful is needed.

2.2 Design and Physics Principles

Since Anaximenes of Miletus (585–528 B.C.) laws are considered operative throughout the Nature [15]. This constitutes a magnificent triumph of reason and observation: laws tell us how things operate and can guide us in the quest for news knowledge. The invariance provides a structure and coherence to the laws just as the laws provide a structure and coherence to the set of natural events. In fact, the invariance of the laws of Nature under space–time translations allows applying them at different times and places. So, laws form the bedrock of Physics.

During the last century, quantum theory and relativity have profoundly modified the laws of mechanics. The whole body of thermodynamics, instead, has remained

[1] The term "biomimetics" was conceived by Otto H. Schmitt in 1969 from "bios" meaning life and "mimesis" meaning to imitate [11]. Other term that is often used is "biomimicry," which has been put forward as a method of working that seeks sustainable solutions by emulating nature's patterns and strategies (e.g., a photovoltaic cell inspired by the structure of a leaf).

untouchable.[2] The zeroth law defines a useful property "temperature" (and states that the equality of temperature as necessary and sufficient condition for thermal equilibrium), the first law defines a useful property "energy" (and asserts that energy is conserved), the second law asserts the existence of an extensive property "entropy" (and states that the entropy of an adiabatically isolated system never decreases in time), and the third law define a state known as "absolute zero" (and relates the entropy of a systems to its absolute temperature).

The generation of configuration (design) is a universal phenomenon that occurs in every flow system. In the struggle to understand this phenomenon, Adrian Bejan comes to a new and comprehensive law of design generation—the constructal law. The ubiquitous generation of configuration is, like other phenomena, covered by a physics law that states that "For a finite-size flow system to persist in time (to live) it must evolve such that it provides greater and greater access to the currents that flow through it" [17, 18].

The generation of flow design (configuration, shape, and structure) belongs in thermodynamics [19–22], and completes the four solid metacarpal bones (i.e., previous four laws) that form the structural frame of the hand that holds the modern science. This new law asserts that for any flow system there is a property "configuration" (and relates the generation of configuration to its greater access to flow[3]). Flows occur against resistances (imperfections) that constantly try to slow down. Design is the constructal path to persist in time (to survival). Each system acquires configuration (design), in time, by replacing an existing configuration by a design that best allocate imperfection (resistances), providing an easier flow access. Therefore, the mastery of this law is essential in the analysis of systems far from equilibrium.

2.3 Thermodynamics Laws, Time, and (A)Symmetry

Regarding the influence of the time, laws may be separated into two components: the description of the set of states that the system can be in at any given time and how states change with time. In mechanics these two components are called "kinematics" and "dynamics," respectively. The question about preferred direction of action in time or time symmetry/asymmetry can be regarded within this framework.

[2] "The law that entropy always increases, holds, I think, the supreme position among the laws of Nature. If someone points out to you that your pet theory of the universe is in disagreement with Maxwell's equations—then so much the worse for Maxwell's equations. If it is found to be contradicted by observation—well, these experimentalists do bungle things sometimes. But if your theory is found to be against the second law of thermodynamics, I can give you no hope; there is nothing for it but to collapse in deepest humiliation"—Eddington [16].

[3] "Maximum flow access" corresponds to minimum travel time or minimum transfer time [23]. Therefore, "for a finite-size flow system to persist in time it must evolve such that it provides a minimum travel time to currents that flow through it."

Although all processes must take place in accordance with the first law, the principle of conservation of energy is, by itself, insufficient for an unambiguous description of the behavior of a system. Specifically, there is no mention that every natural process has preferred directions of action in time. For example, in the formation of Benard cells (i.e., far from equilibrium phenomenon), the flow of heat occurs naturally from hotter to colder sites, and as the temperature of the bottom layer is increased, a stage is reached (critical temperature) where the liquid overcomes its internal resistance (viscosity) and begins to undergo bulk motion. The concept of energy (and energy conservation) is not sufficient to explain these things. Both, the reverse flow (cold to hot) and the immutability of configuration, are not in violation of the first law. In addition, so far as that law is concerned, the heat is transferred into the system and increases its internal energy, but if the heat source is disconnected, it undergoes a decrease in temperature and returns to the same internal energy state. Since it is possible to take the same amount of internal energy back, there is symmetry of state of the system.

The second law of thermodynamics points that the "forward" and "backward" for heat is not allowed in the sense that heat always flows from hotter to colder sites (i.e., energy always gets dissipated as heat—irreversibility). There is a "time asymmetry" or a "direction of time" or an "arrow of time." The second law states that $\frac{\mathrm{d}S}{\mathrm{d}t} \geq 0$, where S is the entropy and t is the time, and expresses a time asymmetry of the state of the system (i.e., "kinematics").

The constructal law points to another "arrow of time": an existing configuration morph toward easier flowing configurations to assure its survival (i.e., designs that provide less access to the currents are not allowed). This law tells how configuration changes with time in the quest for greater flow access (i.e., "dynamics"). Cells emerge when the temperature of the bottom reaches a critical temperature because cells facilitate heat to flow more efficiently into the colder sites. But they disappear as soon as the temperature drops below the critical temperature because cells are not the constructal paths that provide an easier flow access. The constructal law, as others "dynamical laws," admits time reversal symmetry.

It becomes apparent that the emergence of configuration, defined by the constructal law, requires that the entropy changes, rather than staying the same. Consider a Poiseuille-type resistive flow. The rate of entropy generated, S_{g}, is

$$\frac{\mathrm{d}S_{\mathrm{g}}}{\mathrm{d}t} = \frac{VI}{T}. \tag{2.1}$$

Here V is the potential, I is the current I, and T is the absolute temperature. In terms of flow resistance R, (2.1) may be rewritten as

$$\frac{\mathrm{d}S_{\mathrm{g}}}{\mathrm{d}t} = \frac{V^2}{RT} \quad \text{or} \quad R = \frac{V^2}{\left(\mathrm{d}S_{\mathrm{g}}/\mathrm{d}t\right)T}, \tag{2.2}$$

$$\frac{\mathrm{d}S_{\mathrm{g}}}{\mathrm{d}t} = \frac{RI^2}{T} \quad \text{or} \quad R = \frac{T\left(\mathrm{d}S_{\mathrm{g}}/\mathrm{d}t\right)}{I^2}. \tag{2.3}$$

Maximum flow access means minimum resistance under constraints: constraint of constant I or constraint of constant V. According to the (2.2), minimizing the flow resistance for a specified potential, V, corresponds to maximization of the entropy generation rate. On the other hand, minimizing the flow resistance under a constant current, I, corresponds to minimizing the entropy generation rate (2.3). The meaning of (2.2) and (2.3) is double-fold: (1) the constructal law is connected with the maximization and minimization of entropy generation rate principles, and (2) as second law of thermodynamics is diverse of the principle of maximization/minimization of entropy generation rate, the constructal law is distinct of the second law of thermodynamics.

In summary, the constructal law may be connected with minimization/maximization of entropy generation rate and is essentially different from the second law of thermodynamics. Both laws share a preferred direction of action in time ("arrow of time") but with distinct time symmetry.

2.4 Natural (Constructal) Design of the Large and Small

Natural flow systems are complex and diverse. They cover several orders of magnitude in length and in mass.

Inanimate systems such as Nile and Amazon basins have lengths of 6,850 km and 6,700 km, respectively, and drain more than 3×10^6 km^2 [24, 25]. In the opposite length scales are the aerosols. Aerosols are solid or liquid particles suspended in air or other gaseous environment. Their particles sizes are in the micrometer and sub-micrometer range, and tend to combine with each other (agglomerate) to form larger particles. Living organisms cover more than 27 orders of magnitude in mass from molecules of the genetic code to whales and sequoias [26]. Even though, life uses the same reactions and chemical elements to generate a remarkable variety of forms and dynamical behaviors. Do these systems follow the same law of configuration (design)?

The constructal law is grounded on the idea that flow systems are not purposeless (the ultimate target is to persist) and are free to morph in time (evolve), under global constraints, to accomplish their purpose. Configuration is the constructal path to carry fluid, heat, mass, information, people, etc., in order to persist in the "arrow of time." Is this law of design real? Does it belongs to the world or merely reflect the way we speak about it? All scientific efforts are based on the existence of universality, which manifests itself in diverse ways and scales. In this section, we arbitrarily partitioned the scale spectrum into microscale, mesoscale, and macroscale [27] and reviewed some advances in the emergence of configuration, within these scales, in the light of constructal law. This is not an exhaustive list of examples, but it does reveal the depth that this law embodies.

2.4.1 Natural Design into Microscale Flow Systems

Nano- and micron-particle agglomerates often have dendritic shapes instead of spherical shapes. Why does it occur?

Consider that there are not electrically neutral surfaces in contact with the air [28], and the forces that make aerosol particles stick onto previously deposited particles are of the electrical type. Observation shows that there are two kinds of configurations: spherical and conically. The volume growth in time of a spherical agglomerate shape, V_{sph}, is given by [29]

$$V_{\text{sph}} \sim K^2 t^2, \tag{2.4}$$

while the volume growth in time of an agglomerate of particles with the conical shape, V_{con}, is

$$V_{\text{con}} \sim \left(\frac{q_{\text{el}} K^{14/3}}{\mu_{\text{el}}}\right)^{1/2} t^{7/3}, \tag{2.5}$$

where μ_{el} is the dipole moment, q_{el} is the charge and K is a quantity that depends of the particle size, dipole moment, electric charge, Cunningham correction factor, electric permittivity of the air, surface density of charge, and air viscosity.

According to the constructal law, the architecture of the aggregate of particles evolves in time in such a way that the global rate of accumulation of the particles is maximized (i.e., agglomerates the particles in the fastest way possible). The temporal evolution of the accumulation volume is presented in Fig. 2.2. This plot shows that at the critical time, t_{critical}, the volume of conical agglomerates overtakes the volume of spherical agglomerates. According to (2.4) and (2.5)

$$t_{\text{critical}} \sim \left(\frac{\mu_{\text{el}}}{q_{\text{el}} K^{2/3}}\right)^{3/2}. \tag{2.6}$$

This means that the agglomerate must first grow as a sphere ($t < t_{\text{critical}}$) and then change to a conical shape. The initial design (spherical) is replaced by a design (conical, tree-shaped) that agglomerates more easily. Experimental measurements reported in the literature confirm the main features of this constructal development [29].

Liquid droplet impact on a solid surface may present a disk configuration or develops needles that grow radially (Fig. 2.3). Bejan and Gobin [30] reveal that liquid droplet impact is a manifestation of the constructal law and also present a dimensionless number that governs the selection of geometry. This number is defined by the ratio of two lengths, the final radius of the disc that dies viscously, divided by the radius of the still inviscid ring that just wrinkles.

Transportation systems for the long-distance delivery and distribution of biofluids are essential for the multicellular organisms. The fluid with some

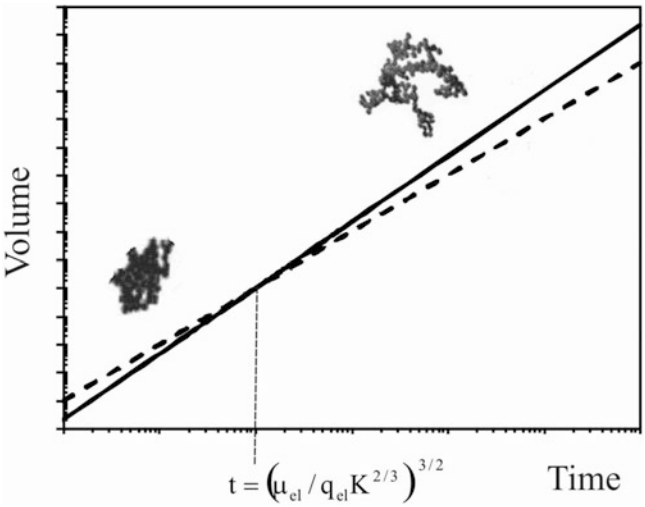

Fig. 2.2 Time evolution of the volume corresponding to conical (*line*) and spherical (*dashed line*) agglomerates

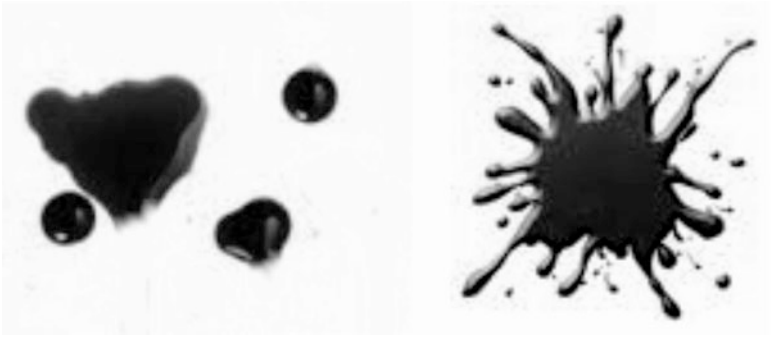

Fig. 2.3 Liquid droplet impact on a solid surface

dissolved components (oxygen, carbonic acid, mineral, and organic nutrients) must be delivered to a distributed set of consumers (cells, tissues, organs). Galen who lived in the second century A.D. and spent part of his lifetime in observation of the human body and its functioning, described the blood vessels as "trunks divided into many branches and twigs" that nourished the body [31]. Tree-shaped networks of tubes with decreased caliber are used to deliver these fluids (Fig. 2.4). It can be found in mammals, plants, invertebrates, and some others. In spite of their complicated topology and sizes (i.e., tubes may vary in diameter from micrometer to decimeter), they reveal a common design principle of construction in the nature. Vast measurements on different systems (i.e., arterial, venous, and respiratory systems; plant leaves; etc.) show that [18, 21, 31]

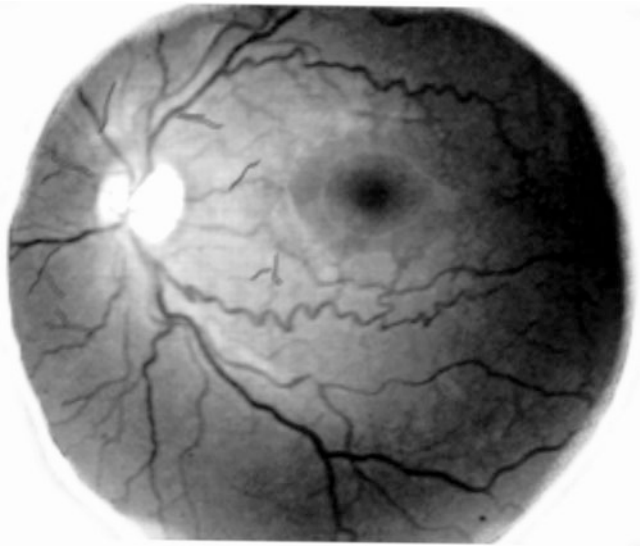

Fig. 2.4 Network of branching blood vessels in the eye (courtesy of UNL)

$$D_o^n = D_1^n + D_2^n, \tag{2.7}$$

where D_0, D_1, and D_2 are the diameters of the parent and daughter's vessels at a bifurcation, respectively, and the power exponent n was found to be 3, except when the flow is not laminar ($n = 2.3$). Equation (2.7) is usually termed as Murray or Hess–Murray law.

Bejan et al. [32] focused on a stream that branch into tributaries streams in a constrained space. A steady incompressible flow through an assembly of ducts (T- and Y-shaped assembly depicted in Fig. 2.5) with negligible pressure losses[4] at bifurcation was considered. The objective was the maximization of the system performance by minimizing the global flow resistance of the fluid stream. They found that the exponent n of Equation (2.7) depends on the flow regime but it is independent of geometry of the configuration: for laminar flow n is 3 but for turbulent flow n is 7/3 (~2.3). Bejan et al. [32] also studied the relationship between the lengths of the parent and daughter's vessels (L_0, L_1, and L_2). They found that the lengths are described by an equation similar to that of (2.7) (i.e., ${L_0}^n = {L_1}^n + {L_2}^n$): for laminar flow n is 3 and for turbulent flow n is 7. These are new results provided by the constructal theory [32].

[4] Wechsatol et al. [33] studied the effect of junction losses on the optimal geometry of bifurcation. For laminar flow, the junction losses have sizable effects on the optimal diameter ratio at each node of bifurcation only when the dimensionless parameter called svelteness, defined by the ratio between the external and internal length scales, is lower than the square root of 10.

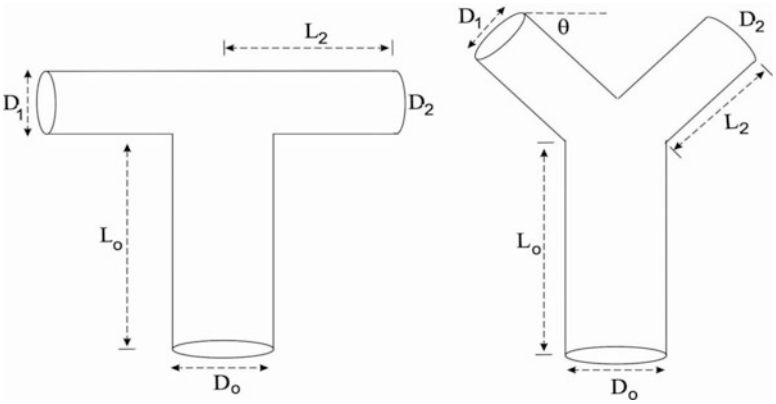

Fig. 2.5 T- and Y-shaped assembly of ducts (adapted from Bejan et al. [32])

Tree-shaped networks are also a manifestation of the constructal law. Bejan [34] and Bejan and Lorente [35] showed that the tree-shaped networks of tubes with decreased caliber, found in mammals, plants, invertebrates, and some others, occur if the purpose is to connect one point (source or sink) with an infinity of points (volume, area, and line), and what flows (i.e., fluid, heat, people, goods, or other) exhibit at least two regimes (e.g., slow and fast).

Snowflakes configuration is a manifestation of the constructal law and the explanation is also provided by Bejan [18, 36]. If the fluid temperature is slightly below the solidification temperature at an immobile fluid medium, latent heat is released at the solidification site and flows into the subcooled medium. The tree-shaped configuration of the snowflake is the one that makes it easier for the heat currents to flow from small areas to the entire volume. Turbulent eddy configuration has also a similar foundation: the trade-off between diffusion and convection (streams) mechanisms [18, 37].

2.4.2 Natural Design into Mesoscale Flow Systems

Lungs, kidneys, circulatory system, etc., and also colonies of living organisms (e.g., stony corals) are also examples of ordered solid configurations. Lungs, for example, are the organs specialized for oxygen and carbon dioxide exchange between air and blood [31]. Two flow mechanisms may accomplish this objective: diffusion and convection (streams). Therefore, the lung could be a ducts system or a simple single sac open to the external air from which the oxygen and carbon dioxide diffuses between the air and the blood. A duct system has a higher friction resistance than a sac (volume) open to external air [31]. Besides, the access time for a gas concentration to travel by diffusion and by "streams," through a characteristic length L, is $\sim L^2/D$ and $\sim L/u$, respectively, where D is the diffusion coefficient and u the gas

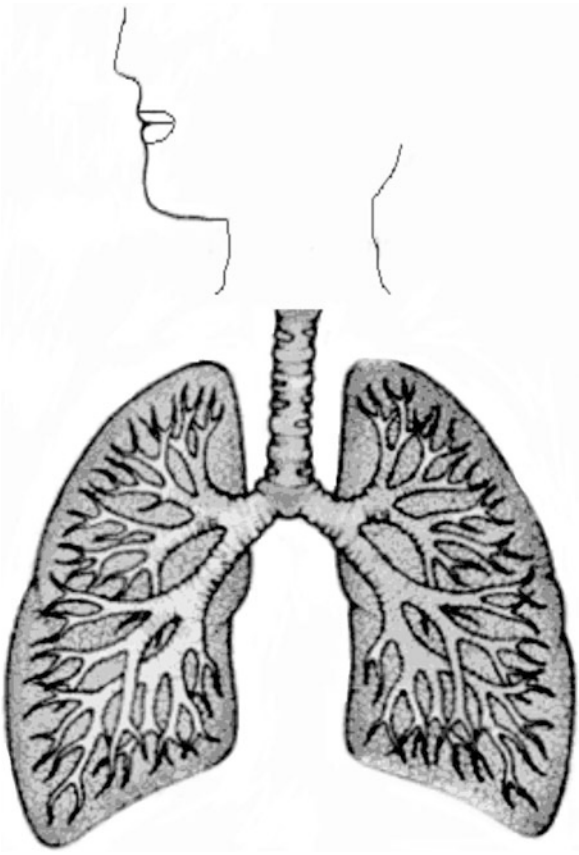

Fig. 2.6 Anatomy of the lungs

speed [31]. Consequently, the possibility of a simple single sac is clearly noncompetitive as compared to a ducts system: the former has an access time for streams flow of ~1 s (characteristics length ~0.5 m and gas speed ~0.5 m/s) whereas the latter has an access time of ~10^4 s (diffusion coefficient ~10^{-5} m^2/s). In summary, a duct system has a large friction resistance to airflow whereas the single sac has a large spreading resistance. Why are lungs tree-like structures?

The answer is provided by Bejan [18] based on the constructal law: as mentioned in the last section, if the aim is to connect one point with an infinity of points and there are different flow mechanisms to accomplish the purpose, the constructal path that emerges is a tree (Fig. 2.6). Tree-shaped networks act as basic supportive flow paths along which flows need to survive are propagated [18]. But what are the tree characteristics that provide the easiest way to supply oxygen to the blood and the drainage of carbon dioxide from it?

Dichotomy (pairing or bifurcation) is an optimized result in tree-flow structures provided by the constructal law (see for example, Bejan [18], Bejan and Lorente [21], Miguel [31]), as well as the relationship between successive duct sizes

(see Sect. 2.4.1). The exact number of bifurcations was studied via the constructal law [31, 38, 39]. Assuming a Hagen–Poiseuille flow through the network, the global resistance to fluid flow after minimization yields the optimal number of bifurcations, N_{opt},

$$N_{opt} = 2.164 \ln \left[\frac{0.000235 D_0^4 R_{air} T_{air}}{\nu_{air} D_g L_0^2} \left(\frac{\phi_{g,0}}{\phi_g} - 1 \right) \right], \tag{2.8}$$

where ν_{air} is the kinematic viscosity of the air, L_0 is the trachea length, D_0 is the trachea diameter, D_g is the diffusivity of the gas (e.g., oxygen or carbon dioxide) in the air, R_{air} is the air constant, T_{air} is the temperature, and ϕ_g and $\phi_{g,0}$ are the relative concentration of gas in the alveoli and in the outside air, respectively. Based on data available in the literature for L_0, D_0 and ϕ_g, the optimal number of bifurcations is obtained by assuming a body temperature of 36 °C and taking all pertinent values at this temperature. Using these values in the previous formula, N_{opt} is 23.4 and 23.2 for O_2 and CO_2 transport, respectively. As the number of bifurcations must be an integer, the optimal number of bifurcations of the respiratory tree must be 23, which is a very well-known result in pulmonary physiology. In summary, the best configuration for lung is a tree with 23 levels of bifurcation (i.e., ducts system with a lower spreading resistance) that ends with alveolar sacs.

All the living beings are subjected to the same average environmental parameters. Therefore, the constructal law also predicts that it must exists a characteristic length ${D_0}^2/L_0$ (i.e., the ratio of the square of trachea diameter to its length) that is representative for humans [38, 39]

$$\frac{D_0^2}{L_0} = 8.63 \frac{LA}{V} \frac{\nu_{air} D_g \phi_g}{R_{air} T_{air} (\phi_{g,0} - \phi_g)}. \tag{2.9}$$

Here A is the alveolar area required for gas exchange, V is the volume allocated to the respiratory system and L is the length of the respiratory tree. Equations (2.8) and (2.9) clearly demonstrate that the number of bifurcations of the respiratory tree is determined by the characteristic length ${D_0}^2/L_0$, and this length is determined by the dimensionless number LA/V.

Stony corals and other colonies of living organisms (e.g., bacterial colonies) that cope with hostile environmental conditions (e.g., growing in sheltered sites or nutrient-poor water) develop branched configurations. Stony corals, for example, may present two flow "mechanisms" of growth: diffusion (compact and massive) and streams (tree-shaped). Besides, diffusion and convection (streams) mechanisms may also drive the water, with nutrients, that bath the colony. Configuration is the constructal path to survival by increasing flow access (performance). At sheltered sites, diffusion (high access time; high spreading resistance) is the dominant mechanism that drives the nutrients. Therefore, the action of the constructal law is evident: corals must grow as "bio-streams" (low spreading resistance) which provide the most direct path to the slow (diffusive) regions of nutrient transport [40]. On

the other hand, at nutrient-rich water currents (i.e., streams with low spreading resistance) corals grow as compact structures (i.e., more effective to fill space) [40]. This subject will be further addressed at Sect. 2.5.

The majority, if not all, of complex systems have at least one common feature: they have a propensity to exhibit scaling properties [7, 26, 41]. The identifying signature of a scaling property is an allometric scaling law. These laws capture essential features such as configuration, organization, and dynamics of natural flow systems [7]. Therefore, they should be a manifestation of the constructal law.

Metabolic rate (or rate of energy use) is essential and limits almost all biological processes in microbes but also in mammals, birds, or plants. Since the important study of Kleiber in 1932 [7, 41], it has been known that the metabolic rate in most living organisms scales as approximately the 3/4 power of body mass. In 2001, this empirical allometric law was derived based on the constructal law [42]. Bejan and coauthors [21, 42] also showed that living organisms are built from the same "constructal paths" under the existence of the same powerful constraints at every level of biological organization (e.g., optimized space-filling, tree networks) because they have survived the process of natural selection.

Speed of flyers, land animals, and swimmers are in proportion to their masses raised to the power 1/6 and body movement frequencies (stride, flapping, and fishtailing) decrease with their mass raised to power $(-1/6)$. These allometric laws are also covered by the constructal law [43, 44] and clearly demonstrate that the locomotion design in living creatures is ruled by the same law. The generation of constructal configuration in also visible on the allometric scaling laws for the breathing, the heart beating, hair coats of animals, etc. [18, 21], as well as, in several main features of vegetation, from root and canopy to forest, such as the scaling laws for the tree length, the tree flow conductance, and the ratio between leaf volume and total tree volume. [45].

2.4.3 Natural Design into Macroscale Flow Systems

The atmosphere is the blanket of air surrounding our Planet. Its circulation has configuration and is also a manifestation of the constructal law. The middle latitude atmosphere is filled of eddies, which manifest themselves as traveling weather system. As explained by Bejan [18, 46], eddies represent the best paths for the flow of momentum. Reis and Bejan [47] relied on the constructal law to predict the latitude of the boundary between the Hadley and the Ferrel cells, and between the Ferrel and the Polar cells (Fig. 2.7). These latitudes constitute the constructal partitioning of the Earth's surface with respect to the heat flow along the meridian. Other quantities such as the average temperature of the earth surface and the convective conductance in the horizontal direction are also determined based on constructal law. They also concluded that the poleward heat transfer is determinant on the flow structure.

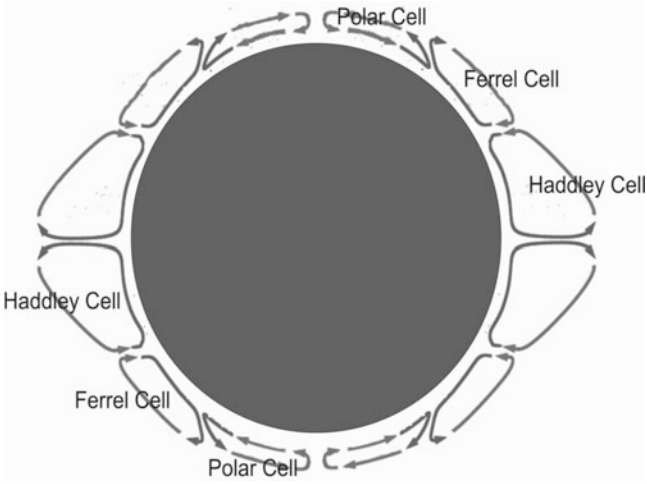

Fig. 2.7 The circulation of the atmosphere

Fig. 2.8 Tagus river basin through the Iberian Peninsula

The river basins are another class of tree-shaped configuration, like lungs, snowflakes, and corals (Fig. 2.8). The reason for this particular configuration is the same as for the lungs, snowflakes, and corals: the maximization of access for the flowing currents. The balance between dissimilar flow mechanisms (i.e., timescale

of seepage down the hill ~ residence time in the entire basin) provides the maximization of flow access between one point and infinity of points, and vice versa [22].

River basins present geometrical features which can be measured, namely the area (measured on the vertical projection), the elongation ratio (the diameter of a circle with the same area as the drainage basin, divided by the basin maximum length), the relief (the difference of elevation between the highest and the lowest points of the drainage area) and the relief ratio (the basin relief divided by the maximum length of the basin). Scaling these geometrical features typically follows a simple power law (scaling law). These laws constitute the bond which united all of river basins. Well-known empirical allometric laws were derived from the constructal law as a result of minimization of the overall flow resistance [37, 48]: (1) the ratios of lengths of consecutive streams predicted by the constructal approach match Horton's law for the same ratio, (2) the number of consecutive streams match Horton's law of ratios of consecutive stream numbers, and (3) both Hack's and Melton's laws are predicted and the exponent evaluated accurately.

Cities are characterized by specific shape and dynamics. In time, they increase in size and number (evolve). Cities possess self-similar structures that repeat over a hierarchy of scales [49, 50]. Cities and countries are "giant" living organisms, which acquire and consume resources, produce and discard wastes, all the while employing energy for a variety of tasks: transportation, communication, maintenance, and reproduction of the complexity and organization.

In 1949, George Zipf devised his simple distribution law to explain the size cities in a country [28]. Giesen and Südekum [51] showed that Zipf's law not only satisfies the cities hierarchy but also German regions. Zipf distribution of city ranks versus city sizes can be derived from the constructal law in the same fashion as patterns of natural flow systems. Bejan [37] shows that this distribution can be obtained from the optimal allocation of flow paths to areas. This and others distributions have their origin on tree-shaped flow systems with patterns optimally allocated in space, in a similar way to scaling laws of river basins.

Another study shows that the carbon dioxide emissions to the atmosphere and the gross domestic product (GDP) from different countries scale with their "body" mass [41]. Countries have a body (structure in space), but also a rhythm (structure in time). Miguel [41] based on the idea of similarity between living organisms and countries presented several optimal features of intermittent flows (rhythmicities) for countries.

In summary, the emergence of scaling laws in river basins, cities, and countries (inanimate flow systems) is similar to the emergence of allometric laws in living beings. In both cases, they reveal similar basic supportive flow paths along which "order" need to survive is propagated. Therefore, scaling laws are a synonym of constructal systems.

2.5 Intraspecific Variability of Configurations (in Similar Systems) as a Manifestation of the Constructal Law

Micro, meso, and macroscales house diverse examples of intraspecific variability of configurations inside similar systems. Bacterial and stony corals colonies that cope with hostile environmental conditions develop branched configurations, while colonies that enjoy environments loaded with nutrients develop a compact shape instead [52–54]. Plants in soil have more open and more thinly branched roots than specimens of the same species which are growing under hydroponics regime [55]. Pedestrians typically prefer to move freely [56]. But in crowded spaces or when a stationary crowd stands in their way and needs to be overcome, pedestrians naturally organize themselves into streams (lanes).

Complexity is associated with an increased use of communication signals to organize a cooperative behavior [8, 57–59]. These signals do not elicit specific responses in themselves, but rather operate in a general manner to alter the probability that individuals will respond to other stimuli. For example, pheromone communication is an effective means of coordinating the activities of insect colonies such as ants, including food gathering, alarm, and defense, and even reproduction [59]. The growth of the coral or bacteria colonies also requires communication (i.e., sharing of information): between cells to create the individual polyp or bacterium, and between polyps or bacteria to create the colony. They must rely on chemical signals, electrical impulses, vibration signals, or other [8]. An organized collective behavior is also based on a coordinated and orchestrated interaction between people. They must share information—communicate. The communication can be verbal (i.e., communication that uses words) but also non-verbal (i.e., communication that includes eye contact, body posture and motions, positioning within groups, etc.) [8]. Therefore, pedestrians rely on communication to control specific pattern formation. Vision (and sometimes verbal communication) guarantees a precise control of the pedestrian position in space and time. In summary, communication signals are necessary for a specific pattern formation. The question to be answered is why they develop a particular configuration?

All these systems are not purposeless (i.e., they have objectives, functions to fulfill), and they are free to morph. So, according to the constructal law they should develop designs that represent the most competitive configuration for survival. A spherical massive volume (diffusive) is the more effective way to fill space and extract nutrients from the surrounding environment [40, 60]. But in a low-nutrient environment (or a hard agar surface or in a crowded open space) the formation of branches (i.e., bio-lanes, bio-streams, bio-rivers, or rivers of people) provide the constructal paths with low spreading resistance that enable coral and bacteria to thrive inside the nutrient rich region or pedestrians to penetrate the crowds [40, 60, 61].

Consider, for example, stony corals growing at a rate, u_c, of a few cm/year in a sheltered site, where water currents are practically absent and diffusion is the most important nutrient transport mechanism. The biological system starts to grow at its birth. Immediately after, nutrients close to the system are quickly depleted.

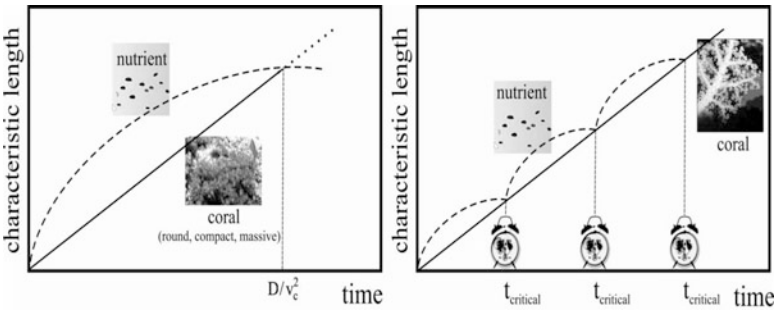

Fig. 2.9 Nutrient propagation and coral growth

This consumption of nutrients in the surroundings of the stony coral causes a decrease of nutrient concentration which triggers a diffusive wave of nutrients defined by a speed of propagation, v_d,

$$v_d \sim \left(\frac{D}{t}\right)^{1/2} \tag{2.10}$$

where D is the he nutrient diffusion coefficient and t is the time. The initial speed of propagation is greater than any growth speed of the living system, but decreases with the inverse of the square root of time. Consequently, the speed of nutrient propagation drops below the growth speed of the living system when $t_{critical} > D/u_c^2$. For $t_{critical} < D/u_c^2$, the round (massive) shape is the most effective arrangement for filling the flow space [40] but when $t_{critical} > D/u_c^2$, the coral begins to grow outside the nutrient diffusion region (Fig. 2.9). Then, branches (bio-streams, bio-lanes, or bio-rivers) develop because are low-resistance paths for nutrient access (i.e., the access time for stream paths is much lower than for diffusive paths; see also Sect. 2.4.2). As soon as the critical time is reached, the system comes out of the nutrient region. Then, each branch generates a new group of branches and the global feature of this scenario is the tree-shaped pattern (Fig. 2.9). In open sites where convection currents are important, the fluid velocity surrounding corals is much larger than the growth speed of the coral. Therefore, the critical time is never reached, and the system grows always inside a region where nutrients are ready available developing a round and compact design which is the most effective arrangement for filling the space [40].

Countries are also complex systems that are far from equilibrium because they are "alive" [41]. Prominent areas—the hubs of thinkers, makers, and traders—pump flows of energy, information and goods across the country. Night-time satellite images show that while these flows present a more massive configuration of brightly lit areas in developed countries/areas (i.e., resource-rich environments), they lead to a substantially more branched configuration of lights (light-lanes, light-streams) in underdeveloped ones [41, 62, 63]. Similarly to what happens in corals or bacteria or plant roots, the configurations of human activity appear to be optimally designed to fulfill their purpose, given the local constraints of economic development.

2.6 Survival in the World of Flow Configuration (Design)

> The task is, not so much to see what no one has yet seen, but to think what nobody has yet thought, about that which everybody sees.
> Arthur Schopenhauer (1788–1860) cited by L. von Bertalanffy's "Problems of Life" 1952.

Design—configuration, architecture, shape, structure, pattern, rhythm—is omnipresent in nature because all things have a design. The answer for the phenomenon of design generation lies directly in the constructal law of Adrian Bejan which constitutes an important contribution to the development of thermodynamics. Flow configuration emerges as a necessary consequence of being effective in a game plan catered to system strengths. Systems out of equilibrium, with internal freedom to morph, develop in time constructal paths which mean survival by increasing flow access (performance). The body of work reviewed here is not supposed to be exhaustive. For reviews that include the constructal view of manmade flow systems and social organization, see for example Bejan and Zane [64], Bejan and Lorente [21, 22, 62], Bejan and Merkx [65], Bejan et al. [7, 28], and Bejan [18, 37, 46, 66].

In summary, the evolution of systems is strictly connected with the possibility of their morphing configuration, permitting that the new configurations replace existing configurations, to perform better (constructal law). This self-standing law of design has both local and global significance. It shows a fascinating connection between the Nature as a whole and what this law holds in our world. The paths of all natural flow systems (i.e., animate and inanimate systems) are drawn together and can be described and understood under a unified view.

References

1. Crowe MJ. Mechanics from Aristotle to Einstein. Santa Fe: Green Lion Press; 2007.
2. Laurenza D. Leonardo's machines: Da Vinci's inventions revealed. Roma: Giunti Editori; 2005.
3. Miguel AF. Constructal patterns formation in nature, pedestrian motion and epidemics propagation. In: Bejan, Merkx, editors. Constructal theory of social dynamics. New York: Springer; 2007. p. 85–114.
4. Guillen M. Five equations that changed the world: the power and poetry of mathematics. New York: Hyperion; 1996.
5. Hall TS. Ideas of life and matter: studies in the history of general physiology, 600 BC–1900AD. Chicago: University of Chicago Press; 1969.
6. Borelli GA. De motu animalium (The movement of animals). Rome: AngeloBernabo; 1680.
7. Bejan A, Lorente S, Miguel AF, Reis AH, editors. Constructal human dynamics, security and sustainability, Series Human and Societal Dynamics, Vol. 50, IOS Press, Amsterdam 2009.
8. Miguel AF. Natural flow systems: acquiring their constructal morphology. Int J Des Nat Ecodyn. 2010;5:230–41.
9. Sullivan LH. The autobiography of an idea. New York: Dover Books on Architecture; 2008.
10. Bar-Cohen Y. Biomimetics: biologically inspired technologies. Boca Raton: CRC Press; 2005.
11. Sarikaya M, Aksay IA, editors. Biomimetics: design and processing of materials. Woodbury, New York: AIP Press; 1995.

12. Charles K. Curved electronic eye created. Nature. doi:10.1038/News.2008.1004
13. Vogel S. Cat's paws and catapults. New York: W.W. Norton; 1998.
14. Sarikaya M, Tamerler C, Jen AK-Y, Schulten K, Baney F. Molecular biomimetics: nanotechnology through biology. Nat Mater. 2003;2:577–85.
15. Waterfield R. The first philosophers: the presocratics and sophists. Oxford world's classics. Oxford: Oxford University Press; 2009.
16. Eddington A. The nature of the physical world. Michigan: University of Michigan Press; 1981.
17. Bejan A. Street network theory of organization in nature. J Adv Transport. 1996;30:85–107.
18. Bejan A. Shape and structure from engineering to nature. Cambridge: Cambridge University Press; 2000.
19. Bejan A, Lorente S. The constructal law and the thermodynamics of flow systems with configuration. Int J Heat Mass Tran. 2004;47:3203–14.
20. Bejan A, Lorente S. Constructal theory of generation of configuration in nature and engineering. J Appl Phys. 2006;100:041301.
21. Bejan A, Lorente S. Design with constructal theory. Hoboken: Wiley; 2008.
22. Bejan A, Lorente S. The constructal law of design and evolution in nature. Phil Trans R Soc B. 2010;365:1335–47.
23. Bejan A, Ledezma GA. Streets tree networks and urban growth: optimal geometry for quickest access between a finite-size volume and one point. Physica A. 1998;255:211–7.
24. Biswas AK, Cordeiro NV,. Brage BPF, editors. Management of Latin American river basins: Amazon, Plata, and São Francisco, Water resources management and policy series. United Nations University; 1999
25. Mamdouh S. Hydrology of the Nile river basin. New York: Elsevier; 1985.
26. West GB, Brown JH. The origin of allometric scaling laws in biology from genomes to ecosystems: towards a quantitative unifying theory of biological structure and organization. J Exp Biol. 2005;208:1575–92.
27. Liljenström H, Svedin U, editors. Micro, meso, macro: addressing complex systems couplings. Singapore: World Scientific Publishing; 2005.
28. Bejan A, Lorente S, Miguel AF, Reis AH. Along with Constructal Theory, UNIL · FGSE Workshop Series No. 1, J. Hernandez and M. Cosinschi, editors. Lausanne: University of Lausanne, Faculty of Geosciences and the Environment, 2006.
29. Reis AH, Miguel AF, Bejan A. Constructal theory of particle agglomeration and design of air-cleaning devices. J Phys D. 2006;39:2311–8.
30. Bejan A, Gobin D. Constructal theory of droplet impact geometry. Int J Heat Mass Tran. 2006;49:2412–9.
31. Miguel AF. Lungs as a natural porous media: architecture, airflow characteristics and transport of suspended particles. In: Heat and mass transfer in porous media, Advanced Structured Materials Series. Berlin: Springer. 2012;13: 115–37
32. Bejan A, Rocha LAO, Lorente S. Thermodynamic optimization of geometry: T- and Y-shaped constructs of fluid streams. Int J Therm Sci. 2000;39:949–60.
33. Wechsatol W, Lorente S, Bejan A. Tree-shaped flow structures with local junction losses. Int J Heat Mass Tran. 2006;49:2957–64.
34. Bejan A. Constructal tree network for fluid flow between a finite-size volume and one source or sink. Revue Générale de Thermique. 1997;36:592–604.
35. Bejan A, Lorente S. Constructal tree-shaped flow structures. Appl Therm Eng. 2007;27:755–61.
36. Bejan A. Advanced engineering thermodynamics. 2nd ed. New York: Wiley; 1997.
37. Bejan A. Advanced engineering thermodynamics. 3rd ed. Hoboken: Wiley; 2006.
38. Reis AH, Miguel AF, Aydin M. Constructal theory of flow architecture of the lungs. Med Phys. 2004;31:1135–40.
39. Reis AH, Miguel AF. Constructal theory and flow architectures in living systems. Therm Sci. 2006;10:57–64.

40. Miguel AF, Bejan A. The principle that generates dissimilar patterns inside aggregates of organisms. Physica A. 2009;388:727–31.
41. Miguel AF. Quantitative study of the CO_2 emission to atmosphere from biological scaling laws. Int J Global Warming. 2009;1:129–43.
42. Bejan A. The tree of convective heat streams: its thermal insulation function and the predicted ¾ power relation between body heat loss and body size. Int J Heat Mass Tran. 2001;44:699–704.
43. Bejan A, Marden JH. Unifying constructal theory for scale effects in running, swimming and flying. J Experiment Biol. 2006;209:238–48.
44. Bejan A, Marden JH. Constructing animal locomotion from new thermodynamics theory. Am Sci. 2006;94:342–9.
45. Bejan A, Lorente S, Lee J. Unifying constructal theory of tree roots, canopies and forests. J Theor Biol. 2008;254:529–40.
46. Bejan A. Constructal theory of pattern formation. Hydrol Earth Syst Sci. 2007;11:753–68.
47. Reis AH, Bejan A. Constructal theory of global circulation and climate. Int J Heat Mass Tran. 2006;49:1857–75.
48. Reis AH. Constructal view of scaling laws of river basins. Geomorphology. 2006;78:201–6.
49. Alexander C, Ishikawa S, Silverstein M, Jacobson M, Fiksdahl-King I, Angel S. A pattern language. New York: Oxford University Press; 1977.
50. Krier L. Architecture: choice or fate. Berkshire: Windsor; 1998.
51. Giesen K, Südekum J. Zipf's law for cities in the regions and the country. J Econ Geogr. 2011;11:667–86.
52. Ben-Jacob E, Cohen I, Shochet O, Aronson I, Levine H, Tsimering L. Complex bacterial patterns. Nature. 1995;373:566–7.
53. Merks R, Hoekstra A, Kaandorp J, Sloot P. Models of coral growth: spontaneous branching, compactification and the laplacian growth assumption. J Theor Biol. 2003;224:153–66.
54. Thar R, Kuhl M. Complex pattern formation of marine gradient bacteria explained by a simple computer model. FEMS Microbiol Lett. 2005;246:75–9.
55. Howard M. Hydroponic Food Production. Santa Barbara: Woodbridge Press; 1994.
56. Schreckenberg M, Sharma SD, editors. Pedestrian and evacuation dynamics. New York: Springer; 2002.
57. Anderson C, McShea DW. Individual versus social complexity, with particular reference to ant colonies. Biol Rev Camb Philos Soc. 2001;76:211–37.
58. Hyland KM, Cao TT, Malechuk AM, Lewis LA, Schneider SS. Vibration signal behaviour and the use of modulatory communication in established and newly founded honeybee colonies. Anim Behav. 2007;73:541–51.
59. Tumlinson JH, Silverstein RJ, Moser JC, Brownlee RG, Ruth JM. Identification of the trail pheromone of a leaf-cutting ant Atta texana. Nature. 1971;234:348–9.
60. Miguel AF. Constructal pattern formation in stony corals, bacterial colonies and plant roots under different hydrodynamics conditions. J Theor Biol. 2006;242:954–61.
61. Miguel AF. Constructal theory of pedestrian dynamics. Phys Lett A. 2009;373:1734–8.
62. Bejan A, Lorente S. The constructal law and the evolution of design in nature. Phys Life Rev. 2011;8:209–40.
63. Miguel AF. The physics principle of the generation of flow configuration, comment on "The constructal law and the evolution of design in nature" by Bejan & Lorente. Phys Life Rev. 2011;8:243–4.
64. Bejan A, Zane JP. Design in nature: how the constructal law governs evolution in biology, physics, technology, and social organization. New York: Doubleday; 2012.
65. Bejan A, Merkx GW, editors. Constructal theory of social dynamics. New York: Springer; 2007.
66. Bejan A. Constructal self-organization of research: empire building versus the individual investigator. Int J Des Nat Ecodyn. 2008;3:1–13.

Chapter 3
Leaf Shapes and Venation Patterns

A.H. Reis

3.1 Plant Leaves, Power Generation, and Distribution

Plant life is fuelled by solar radiation through photosynthesis, by processes in which leaves act as power generators, main factories, and dispensers of organic substances. Leaves store energy in organic compounds (mainly carbohydrates) that are redistributed within the plant system, thus keeping all metabolic and transport processes active and maintaining and developing plant structure. Water availability is essential both for metabolic processes and for keeping the sap flowing throughout the whole plant system.

Leaf shape and structure generation have been analyzed from various perspectives, ranging from genetics [1] and auxin sources and signaling [2] to transport of water and carbohydrates [3, 4]. Because leaves display such a startling diversity of shapes and venation structures one hardly conceives that this fact might be understood based on some basic principle.

In this chapter we present an analysis of the shape and venation structure generation of leaves based on a new concept of the process by which water ascends in trees, together with the assumption that plant flow structures have been optimized in time (evolution) in order to "provide easier and easier access to the currents that flow through them" (Constructal Law, Bejan, 1997) [5]. The Constructal Law has been successfully applied to various natural (and engineered) systems (see [6–8]) and is seen more and more as a law of Nature that basically expresses the evolution of flow architectures towards reduction of global resistances to internal flows under the existing constraints.

A.H. Reis
Department of Physics and Évora Geophysics Centre, University of Évora,
Rua Ramalho, 59, 7000-671 Évora, Portugal
e-mail: ahr@uevora.pt

L.A.O. Rocha et al. (eds.), *Constructal Law and the Unifying Principle of Design*,
Understanding Complex Systems, DOI 10.1007/978-1-4614-5049-8_3,

3.2 Driving Potential for Sap Flow in Plants

The process by which water ascends up to 100 m height in trees is not well understood yet. Many modern plant physiologists accept Cohesion Theory [9] put forward by Joly (1895) that states that water ascent in trees is achieved by the tension created in the xylem vessels by the transpirational pull. This implies that water flow is not disrupted anywhere and that water can stay liquid and stable under negative pressures of order 0.1 MPa, and higher in the tallest trees. In addition to the fact that water in such conditions would be in a metastable state, there is considerable experimental evidence that Cohesion Theory is not tenable. In result, Multi-force Theory [10] (1995) has been developed to account for a multiplicity of factors such as osmotic pressure [11, 14], gel-supported water lift [12], electrical double layers [13], and Marangoni-streaming [14]. However, it is not clear yet how all these factors might work together (see [14]).

In the following we present a possible very simple mechanism which may provide the adequate driving potential for water ascent in trees. The detailed explanations of this mechanism as well as the experimental evidences that support it are developed in another paper [15]. Here we just summarize its basic features.

The ground is usually electrically negative with respect to the nearby atmosphere, leading to the existence of an electric field directed downwards. Therefore, the ohmic component of the Maxwell current that flows between the ionosphere and the Earth's surface is composed of a downward flux of positive ions, together with an upward flux of negative ions. We put forward the assumption that trees operate as branches of this global circuit by carrying positive atmospheric ions to the ground and absorbing negative ions from the soil. Among the positive ions that are likely absorbed by the tree leaves is hydronium (H_3O^+), which results from dissociation of water ($2H_2O \rightleftharpoons OH^- + H_3O^+$). On the other hand, the negative hydroxide ions (OH^-) that are absorbed in the roots namely in the form of plant nutrients (e.g., KOH, $Zn_5(CO_3)_2(OH)_6$, $Cu_4(OH)_6SO_4$, $Cu_3(OH)_4SO_4$, $Ca(OH)_2$, and $CaMg(OH)_4$) move upwards in plants, where combination with hydronium ions generate liquid water. As the consequence of different concentrations of soluble ions of all kinds, water and nutrients flow within the plant systems (sap flows).

Because plants have much less resistance to ohmic currents than the air, they provide a preferential way for the $OH^- + H_3O^+$ current to flow in the neighborhood of the ground. In this way, the electric potential of leaves is very much close to that of the ground than that of the nearby air, thus enhancing electric fields in the leaves' vicinity. The electric fields are particularly intense in the vicinity of the leaf apex and of the leaf margin, where almost all hydronium ions are expected to be absorbed. This aspect completes the picture put forward for water absorption and, as a consequence, water intake by plants is proportional to the number of leaves times the average length of leaf margins.

Recent work [16] supports the above idea and, namely, that by Koppán and coworkers, [17] which refers "a remarkable correlation between electric potential differences and the water potential of air".

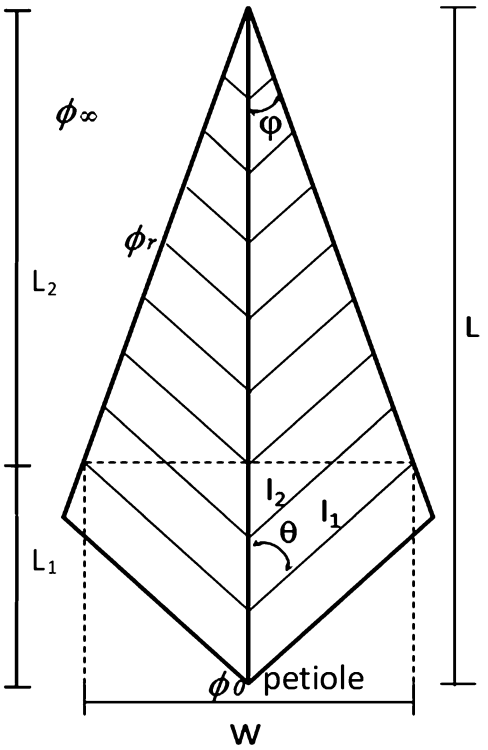

Fig. 3.1 Representation of a symmetric leaf. $\emptyset_\infty$, $\emptyset_r$, and $\emptyset_0$ represent the electric potential in free atmosphere, at the leaf margin, and at the petiole, respectively

3.3 Leaf Morphology and Structure

The geometric representation of a symmetric leaf is shown in Fig. 3.1. The analysis developed in the following holds for leafs that exhibit such symmetry. We have: $l_1 = W/(2\sin\theta)$, $L_1 = W/(2\mathrm{tg}\theta)$, and $L = L_1 + L_2$.

According to the flow model developed in the previous section, hydronium ions are absorbed at the leaf margin and travel in the vein structure to meet the hydroxide ions that enter the petiole. As observed in Fig. 3.1, the leaf flow tree is composed of veins of different resistivities (a for the central vein, and b for its tributaries). In this way, the resistance of each vein is proportional to its length, $R_0 = aL$, $R_n = bl_n$, where l_n denotes the length of vein n. Therefore, if N denotes the number of secondary veins in the leaf, the global resistance R_v of the vein tree is given by $1/R_\mathrm{v} = \sum_{n=1}^{N} (bl_n + aL(2n/N))^{-1}$. For N sufficiently large, the summation may be approached by the integral of the same function. Then, by defining leaf slenderness as $S = L/W$, we obtain the resistance of the vein tree in the form:

$$R_\mathrm{V} = Lb\left[\frac{a}{b} - \frac{1}{S\sin\theta}\right] / \ln[((1 + (2/N)(b/aS\sin\theta))/(2/N + (b/(aS\sin\theta)] \quad (3.1)$$

The electric field strength is higher near the leaf margin. We assume that hydronium ions are driven to the leaf margin by a potential difference $\Delta\emptyset = \emptyset_r - \emptyset_\infty$ between the leaf margin and the average potential of the air at a point at the same height and free of trees (see Fig. 3.1). The potential $\Delta\emptyset$ increases with hydronium ions concentration in the air, which in turn increases with water vapor concentration (absolute humidity).

As indicated before, we assume that the flow of hydronium ions is proportional to the length of the leaf margin, $\sim l_1 + W/\sin\varphi$. Therefore, if α denotes the appropriate constant of proportionality, the resistance to flow of hydronium ions reads:

$$R_h = (\Delta\emptyset)/\left[\alpha W\left(\frac{1}{\sin\theta}\right) + \frac{1}{\sin\varphi}\right] \tag{3.2}$$

The global resistance R of the circuit in which the ions OH^- and H_3O^+ flow is given by $R = R_v + R_h$. By denoting $S\ \sin\theta = 1/x$ and by making L dimensionless trough $\tilde{L} = L/(\Delta\emptyset a\alpha)^{1/2}$, the dimensionless global resistance $R/bL = \tilde{R}$ can be rewritten in the form:

$$\tilde{R} = (a/b - x)/\ln[(1 + (2/N)(b/a)x)/(2/N + (b/a)x)] + a/[\tilde{L}^2 bsx(1 + \sin\theta/\sin\varphi)] \tag{3.3}$$

Equation (3.3) shows that with respect to leaf morphology the global resistance depends on $\tilde{L}$, x, N, and φ.

The N veins convey water and nutrients to the cells in the leaf through a secondary vein network, which works differently from a tree. We assume that, regarding each specific secondary vein network, the resistivity ratio b/a reflects already the arrangement that corresponds to the way by which this process is carried out with minimum flow resistance.

3.4 Minimization of the Global Resistance

For fixed L, x, and φ, the global resistance to flow decreases monotonically with the number of veins, N. By inspecting (3.3) we see that R diverges at the lower limit ($N = 2$), which is a consequence of having approached the summation in (3.3) by the correspondent integral. Therefore, the following analysis will be accurate, as N is greater than 2. As an acceptable approach we also assume that $\sin\theta/\sin\varphi \sim 1$, which is fairly confirmed by observation.

According to the Constructal Law we assume that leaves have evolved in time, such as to provide easier and easier access to the currents that flow through them. In this way for fixed L, N, a/b, $\Delta\emptyset$, and α, the leaf shape x will take the value that minimizes the global resistance. Then, we have: $(\partial\tilde{R}/\partial x)_{\tilde{L},N,a/b} = 0$.

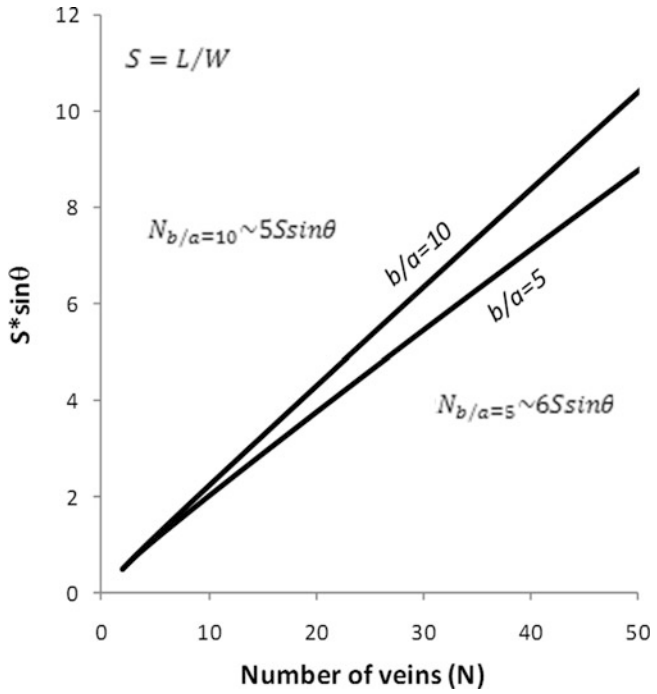

Fig. 3.2 Leaf slenderness and vein angle in relation to number of veins (dry environments). The curves for resistivity ratios 5 and 10 are approached by functions represented in the figure

With the purpose of simplification we further assume that $R_h \ll R_v$ which means very low driving potential $\Delta\emptyset$ [see (3.2)] for the hydronium ions (dry environments), and that $b/a \ll 2/N$. Then from (3.3) we obtain the number of veins N in relation with x in the form:

$$N_{\tilde{L},N,a/b} \approx 2\left\{x - \frac{a}{b} - \ln\left[\left(1 + \frac{2b}{Na}x\right)/\left(\frac{2}{N} + \frac{b}{a}x\right)\right]\right\}/$$
$$\left\{\left(1 - \frac{b}{a}x\right)(x-1) + x\frac{b}{a}\ln\left[\left(1 + \frac{2b}{Na}x\right)/\left(\frac{2}{N} + \frac{b}{a}x\right)\right]\right\}. \quad (3.4)$$

Figure 3.2 shows curves (N, x) for two resistivity ratios: $b/a = 5$ and $b/a = 10$. We can observe that with good approximation the number of veins increases with $S\ \sin\theta$. Therefore, (3.4) predicts that in dry environments the number of veins increases with slenderness S and vein insertion angle θ. This result matches the observational data, at least in a qualitative way. Also, from Fig. 3.2 we may anticipate that for fixed x, the number of veins moderately decreases with resistivity ratio.

Now, for any $\tilde{L}$, and for fixed leaf shape x and driving potential $\Delta\emptyset$ (i.e., same environmental conditions), we see from (3.3) that the global resistance R may also

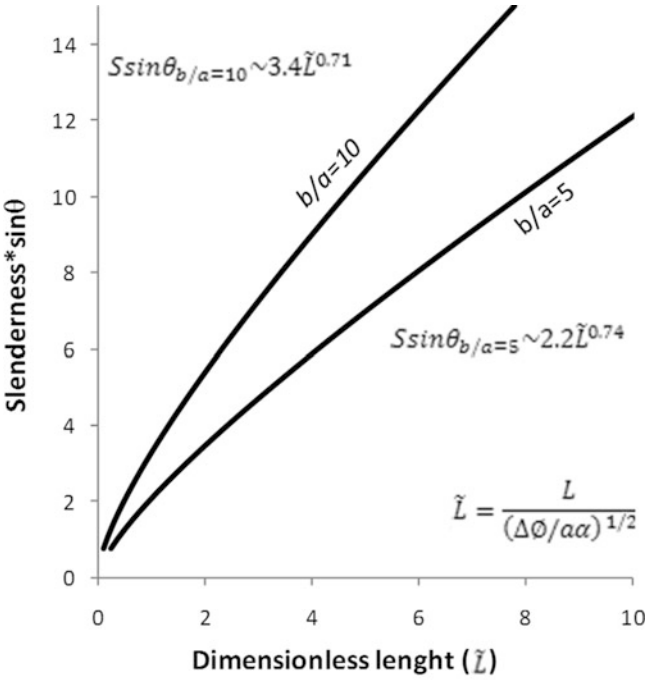

Fig. 3.3 Leaf slenderness and vein angle in relation to dimensionless length. The curves for resistivity ratios 5 and 10 are approached by functions represented in the figure

be minimized against leaf length, L. In this case, the condition for minimum resistance reads: $(\partial R/\partial L)_{x,N,a/b,\Delta\emptyset} = 0$. With (3.3) one obtains:

$$\tilde{L}_{x,N,a/b,\Delta\emptyset} = \left\{ \frac{\ln[(1 + (2/N)(b/a)x)/(2/N + (b/a)x)]}{2x(1 - xb/a)} \right\}^{1/2} \tag{3.5}$$

Equation (3.5) enables us to draw the curves $(S \sin\theta = 1/x; \tilde{L})$ represented in Fig. 3.3 for two resistivity ratios: $b/a = 5$ and $b/a = 10$. We note again that $\tilde{L}$ represents the ratio of leaf real length (L) to $(\Delta\emptyset/\alpha\alpha)^{1/2}$, which represents the environmental conditions at the leaf margin.

Therefore, in dry environments, for the same L and θ, $\tilde{L}$ will be greater than in humid environments. Hence, (3.5) predicts that leaves of plants in dry environments will be slender than those of humid climates (see Fig. 3.3), which corresponds to observations. On the other hand, for the same reason, (3.5) predicts that in dry environments leaves with the same x (slenderness; insertion angle) and N will be shorter than those of plants living in humid environments. Additionally, in this case leaf length decreases with resistivity ratio.

In Fig. 3.4, the number of veins N is represented against $\tilde{L}$ for the same values of x. By analyzing the curves in Fig. 3.4 we anticipate that leaves of the same length

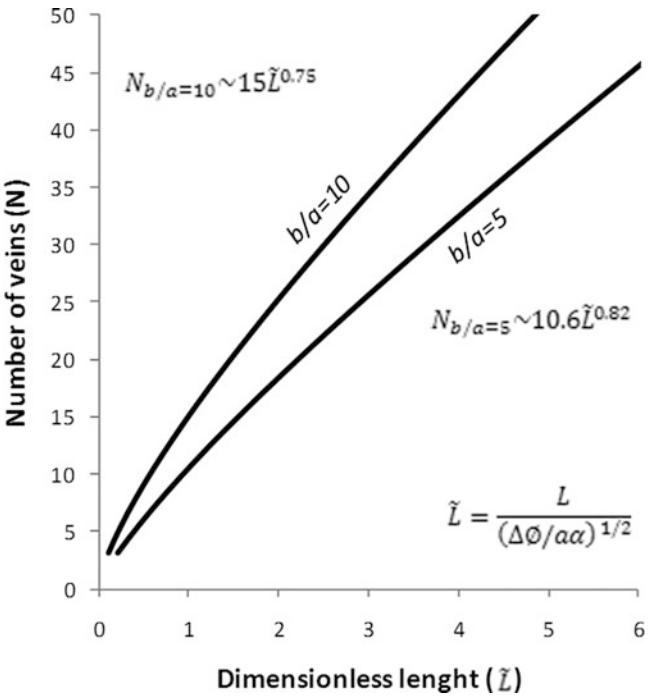

Fig. 3.4 Number of veins in relation to dimensionless length. The curves for resistivity ratios 5 and 10 are approached by functions represented in the figure

L will have more veins in dry climates (low $\Delta\emptyset$) with respect to those of humid environments, and vice versa. It is also evident that in either case the number of veins increases with resistivity ratio and the resistivity, a, of the central vein.

The resistivity ratio may also be optimized with the purpose of allowing minimum global flow resistance. In this case, a relationship between b/a and $S\sin\theta$ emerges, which we will not explore in this chapter.

3.5 Analysis of Real Leaves

The theory put forward in this paper needs to be extensively tested with field data in order to validate it. In the following we present just the application of the theory to symmetric leaves though they are very different in shape.

Figure 3.5 shows leaves of rosebush (*rosa cornelia*), escallonia (*escallonia yveyi*), and babylon willow (*salix babylonica*) taken in Alentejo, Portugal, (relatively dry environment). Also represented are the respective geometric parameters that are important with respect to application of (3.4).

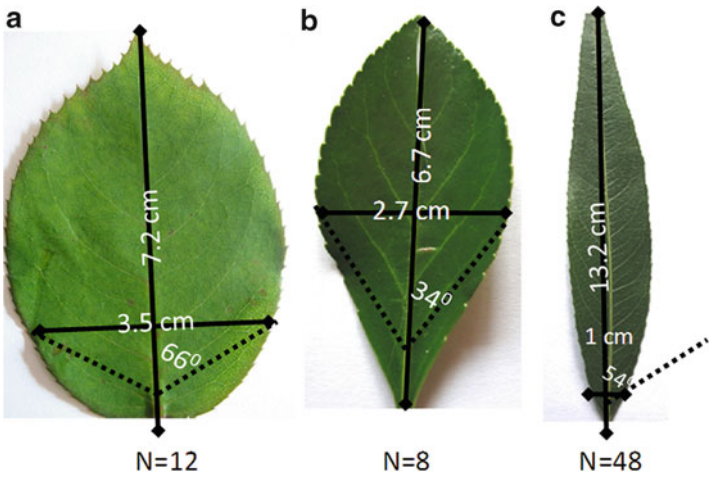

Fig. 3.5 Leaves of (**a**) rosebush (*rosa cornelia*), (**b**) escallonia (*escallonia yveyi*), (**c**) babylon willow (*salix babylonica*) (not to scale)

In fact, contrary to (3.5), (3.4) is suitable for an immediate test because the former requires the availability of the values of $\Delta\emptyset$ and α, whose determination is not easy.

Hence, by taking into account the geometric parameters of the leaves in Fig. 3.5, together with the resistivity ratio (b/a) considered to be appropriate (by visual inspection), (3.4) (see Fig. 3.2) yields the following results for the number of veins: rosebush ($b/a = 5$), $N = 11$ (11.3); escallonia ($b/a = 5$), $N = 8$ (8.3); and babylon willow ($b/a = 5$), $N = 53$ (53.4).

We can observe that the number of veins of each leaf anticipated by the theory is close to the real one shown in Fig. 3.5.

3.6 Conclusions

Though extensive testing is still needed, the new idea of the process by which water and nutrient flow in plants that was put forward in this chapter together with Constructal Law appears to explain the shapes and venation patterns of symmetric leaves. Basically that idea assumes that hydronium ions are taken by leafs in points where the atmospheric electric field is most intense (e.g., leaf margins and apex) and then flow downwards to meet hydroxide ions that are absorbed in the roots. The different concentrations of both ions drive internal water flows that redistribute water and nutrients within the plant. The atmospheric electric field existing near the ground is basic to this process.

The analysis of leaf shapes and venation patterns was based on the assumption that leaf shapes and leaf venation patterns have evolved in time such as to provide

easier and easier access to the internal currents that flow within (Constructal Law). Then, by minimizing the global resistance to flow we anticipated the number of veins in relation to leaf shape (slenderness and vein insertion angle) and prevalent environmental conditions (represented by the potential for leaf water intake from the atmosphere). We also anticipated that leaves in dry environments will be slender and shorter and with more veins as compared with those of plants adapted to humid environments.

The theory was applied to three symmetric but very different leaves with fairly good results.

References

1. Dengler N, Kang J. Vascular patterning and leaf shape. Curr Opin Plant Biol. 2001;4:50–6.
2. Runions N, Fuhrer M, Lane B, Federl P, Rolland-Lagan AG, Prusinkiewicz P. Modeling and visualization of leaf venation patterns. ACM Transactions on Graphics. 2005;24(3):702–11.
3. Zimmerman U, Meinzer F, Bentrup FW. How does water ascend in tall trees and other vascular plants? Ann Bot. 1995;76:545–51.
4. Jackson RB, Sperry JS, Dawson TE. Root water uptake and transport: using physiological processes in global predictions. Trends Plant Sci. 2000;5(11):482–8.
5. Bejan A. Advanced engineering thermodynamics, Chap. 13. 2nd ed. New York: Wiley; 1997.
6. Bejan A. Shape and structure, from engineering to nature. Cambridge: Cambridge University Press; 2000.
7. Reis AH. Constructal theory: from engineering to physics, or How flow systems develop shape and structure. Appl Mech Rev. 2006;59:269–82.
8. Bejan A, Lorente S. Design with constructal theory. Hoboken: Wiley; 2008.
9. Dixon HH, Joly J. On the ascent of sap. Phil Trans R Soc Lond B. 1895;186:563–76.
10. Canny MJ. A new theory for the ascent of sap-cohesion supported by tissue pressure. Ann Bot. 1995;75:343–57.
11. Balling A, Zimmerman U. Comparative measurements of xylem pressure of Nicotiana plants by means of the pressure bomb and pressure probe. Planta. 1990;182:325–38.
12. Plumb RC, Bridgman WB. Ascent of sap in trees. Science. 1972;179:1129–31.
13. Cary JW, Jensen ME, Fisher HD. Physical state of water in plant xylem vessels. Agronomy J. 1968;60:167–9.
14. Zimmerman U, Haase A, Langbein D, Meinze FC. Mechanisms of long-distance water transport in plants: a re-examination of some paradigms in the light of new evidence. Phil Trans R Soc Lond B. 1993;341:19–31.
15. Reis AH. A natural potential for sap ascent in plants, (to appear in Plant J, 2012); 2012.
16. Gibert D, Le Moue JL, Lambs L. Sap flow and daily electric potential variations in a tree trunk. Plant Sci. 2006;171:572–84.
17. Koppán A, Fenyves A, Szarka L, Wesztergom V. Measurement of electric potential difference on trees. Acta Biologica Szegediensis. 2002;46(3–4):37–8.

Chapter 4
Drainage Basins Evolution with Non-erodible Regions

M.R. Errera and C.A. Marin

4.1 Introduction

Drainage basins are systems that collect water over a finite area and convey it to lower altitudes by gravity. Large-scale basins are so important that they became subject of a scientific field called hydrology (e.g., [1]). Small-scale basins, like the ephemeral set of channels present in superficial runoff water, are also important since they carry over nutrients, organisms, and even pollutants rested on the ground (non-point-source pollution).

Of great interest are drainage systems that evolve to build a path network in which two flow regimes are present. Slow flow regime that takes place over almost all the collecting area and fast flow regime that is observed in channels. They both are essential parts of a drainage basin. How drainage basins acquire such form and structure is the subject of the field known as river geomorphology (e.g., [2]).

One specific topology of networks is shaped as tree, found on a broad range of types of systems, e.g., blood vessels network, nerves in leaves, bronchial trees, and tree roots and canopies [3]. There are also intangible tree networks, that is, nonmaterial, such as in human social dynamics and mutualistic pollination networks [4].

Nature's preference in developing and maintaining tree-like networks in all realms can be interpreted as a consequence of some global principle [5]. If so, one expects predictability at some extent.

Features of river basins have been widely known and published in geophysics and hydrology treatises (e.g., [2, 6–8]). River architectures exhibit similarities

M.R. Errera (✉)
Department of Environmental Engineering, Federal University of Paraná,
CP 190110, Curitiba PR 81531-990, Brazil
e-mail: errera@ufpr.br

C.A. Marin
Companhia de Saneamento do Paraná–SANEPAR, Rua Marechal Deodoro,
3081, Curitiba, PR 80045-375, Brazil
e-mail: cesaugmarin@gmail.com

L.A.O. Rocha et al. (eds.), *Constructal Law and the Unifying Principle of Design*,
Understanding Complex Systems, DOI 10.1007/978-1-4614-5049-8_4,

among a diverse and wide range of basins. Those patterns were computed in the form of scaling laws such as the Horton's Laws, Melton's Law, and Hack's Law [7]. Alternatively, the fractal approach introduced other scaling properties of channels which are based on statistical factors [9].

Early models of river network formation were fully random [6, 10] but they failed to agree with empirical scaling correlations verified in real river basins, as noted by ref. [11]. Later the concept of minimum energy expenditure was introduced by the method of the Optimal Channel Networks (OCN). In the latter approach, OCNs are created in algorithms that begin with an initial randomly selected network from a wide range of possible combinations of given channels. The search for the OCN of the basin proceeds by testing random replacement of channel by channel (branch by branch) in the network. Changes are accepted only if the new configuration reduces the value of overall energy expenditure [11, 12]. The optimization does yield configurations that follow the scaling laws parameters found in nature. That is somewhat expected since the features of landscape and the geometry of the channels are already considered beforehand. The OCNs approach does use physical principles but starts with the prior assumption that the network *will be there* and thus structural complexity.

There are also deterministic models of fluvial landform evolution [13, 14] that consider the effects of mass diffusion, erosion, and tectonic uplift in the shape of the landforms. Nevertheless, the networks appear only because of the initial conditions or because of random erodibility [14]. In other words, it also fails to explain why nature "chooses" to use a tree-like network instead of another configuration to drain a given area (e.g., parallel straight channels, network of lakes or ponds, or a single broad channel).

In ref. [15] the topic geomorphology of river basins was also approached in view of its dynamics. In another different approach [16] and [17] relied on the mean elevation of the basin to describe morphological characteristics of basins. While the former associated elevation with statistical self-similarity, the latter further associated it to information entropy and potential energy.

Recently it was shown that the principal scaling laws of resulting river networks could be predicted [18]. The *existence* of an ordering scheme was still assumed.

An important piece of information has been overlooked though: *dendron*-like drainage networks also occur in ephemeral small-scale systems [20]. For instance, the superficial runoff flow from rainfall over a homogenous terrain or soaked coffee grounds in conic paper filter (Fig. 13.30 of [21] and Fig. 1 of [22]). Tree networks were first approached by Constructal Theory (CT) with an analytical formulation based on several simplifying assumptions, such as right angles between stems and tributaries, fully developed laminar flow, a chosen construction sequence, and constant-thickness branches [5, 19, 23]. Subsequently most of the assumptions were relaxed and the same problem was solved numerically [24, 25]. The resulting networks in those works are consequence of the need to connecting an infinite amount of points (e.g., a volume, an area, or a line) to a single point (a point-source or a line-sink) while offering the least global resistance possible [26]. In all those cases the tree network pattern was assumed and the configuration of such networks was built by optimization procedures.

References [26] and [27] are two recent reviews that show a wide array of configurations of natural phenomena that can be predicted by CT in both inanimate systems (e.g., duct cross sections, open channel cross sections, turbulent flow structure, global circulation, and climate) and animate systems (e.g., allometric laws of body size, flying, running, swimming, and breathing), along with applications in engineering (e.g., heat conduction, heat exchangers, fluid flow). Overall CT has successfully demonstrated the *why* of the very existence of the various types of flow configurations in nature, and it did it in a completely deterministic approach.

The *very origin* of networks in drainage basins was successfully approached in [22], when CT was first applied on the subject. The network appeared spontaneously based only on an erosion model, with no assumption of ordering scheme or initial forms or structures. In sum, the basin *self-constructed* its drainage network in a progressive step-by-step pace responding only to an external forcing term (rainfall).

The erosion mechanism was modeled as replacement of high flow-resistance patches by low flow-resistance patches (blocks). This process leads to a reduction of the global mass flow-resistance. Such reduction takes place first because the placing of lower flow resistance blocks on space previously occupied by higher flow resistance is a process that reduces the global resistance per se. A second reduction comes to play due to the selection of which space is converted to low-resistance flow.

The relative contribution of both parcels was addressed in [28], where the evolution by random removal was compared with evolution by erosion and by optimization processes. Two random cases were considered. One was fully random, in the sense that any block across the basin could be turned into low-resistance flow medium, and the other case considered that only the blocks adjacent to low-resistance blocks could be turned.

Reference [22] covered a wide range of configurations and degrees of freedom. Nevertheless, conditions were to homogenous flow resistance (permeability) in each part of the basin.

This chapter covers how a drainage network would evolve if there were impermeable non-erodible regions within the basin. Such drainage void spaces may represent rocky terrains in large scales [29] or pebbles or other solid compact objects in small scales.

Two types of voids were tested separately. One of them is squared and the other long shaped (Fig. 4.1). They were placed in three different parts of the basin to investigate the role of the position of the voids and their spatial range of influence. Simulations followed the procedure developed in [30] and published earlier in [22]. The simulation methods are presented in the next section.

4.2 Simulation Methods

We adapted the erosion model of [22] in order to include an impermeable domain within the original basin. The bottom of Fig. 4.1 briefly represents the new problem statement. A basin of surface area of $A = H \times L$ and fixed shape $H/L = 1$ is initially

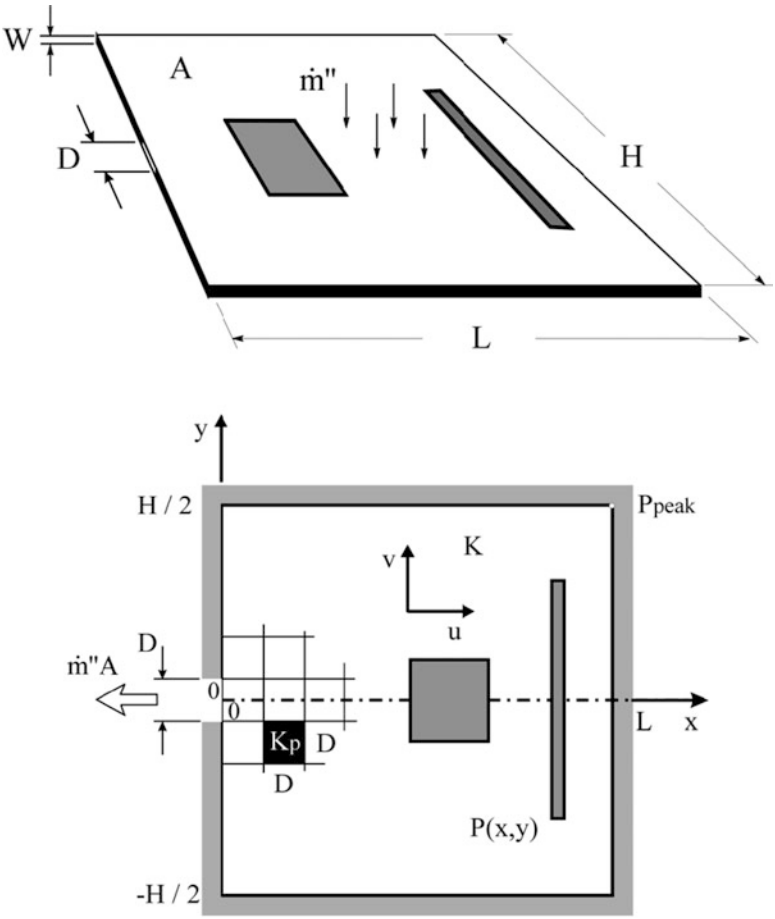

Fig. 4.1 (*top*) Two-dimensional model of an area-to-point flow with non-erodible zones (*gray*) and (*bottom*) the soil simulated as composition of square blocks of side D, which can be dislodged to form a low-resistance path (*black*) [22]

coated with a homogeneous isotropic porous layer of permeability K with voids (in gray shades). The basin thickness W is relatively very small, that is, $W \ll (H, L)$.

A uniform mass flow rate $\dot{m}''$ of an incompressible Newtonian fluid baths the basin area A. The basin then conveys the entire fluid load to a small outlet of size $D \times W$ placed symmetrically along one of the edges. The load thus creates a hydraulic potential $P(x,y)$ (piezometric head, pressure field) that drives the fluid to the outlet. The flow through the K- and Kp-media is modeled as Darcy flow that is further combined with the continuity equation in order to obtain a Poisson type equation for the pressure field:

$$\frac{\partial^2 P}{\partial x^2} + \frac{\partial^2 P}{\partial y^2} + \frac{\dot{m}'' v}{WK} = 0, \tag{4.1}$$

where v is the kinematic viscosity of the fluid.

Spaces with low flow resistance (high permeability, Kp) are created because the high flow resistance soil blocks (low permeability, K) can be dislodged (Fig. 4.1, bottom). That happens when the force created by the pressure field acting on the block (~ΔPDW) is larger than the cohesion force of the soil (τD^2, where τ is the maximum shear stress supported by a K-block). In view of that force balance, Equation (4.1) is modified to a dimensionless form as below:

$$\frac{\partial^2 \tilde{P}}{\partial \tilde{x}^2} + \frac{\partial^2 \tilde{P}}{\partial \tilde{y}^2} + M = 0, \tag{4.2}$$

where:

$$(\tilde{x}, \tilde{y}) = \frac{(x, y)}{D}; \tilde{P} = \frac{P}{\tau D/W}; M = \dot{m}'' \frac{vD}{\tau K}. \tag{4.3}$$

Equation (4.2) is further adjusted for the higher permeability domain (in black) by multiplying the forcing term M by the ratio K/Kp.

If s is the direction of the resulting force acting on the block, the block is dislodged when:

$$\left(\frac{\partial \tilde{P}}{\partial \tilde{s}}\right) > 1. \tag{4.4}$$

In every step (n) of the simulation, this condition was checked for all the K-blocks that had one of the sides facing to a Kp-block (black domain). The first block to be removed is always the one facing the outlet at the origin of the coordinate system.

Blocks are removed one by one until the condition (4.4) no longer holds for any of the eligible blocks. The hydraulic potential $P(x,y)$ is then updated for the just formed drainage basin, and condition (4.4) tested again in a process that stops only when no more blocks can be removed. In that moment, it is fair to say there is a constrained equilibrium with the current environment.

At such point, only environmental changes will lead to dislodge more K-blocks. The model simulates such external changes by the parameter M, the dimensionless forcing term.

Equation (4.4) will be then tested again after a new pressure field is calculated under a new higher value of M. The forcing term is increased in a prescribed small amount, ΔM.

In order to identify the influence of impermeable not erodible voids, we selected a set of parameters of one of the simulations presented in [22], namely, $H = L = 51$D, and permeability ratio of K/Kp $= 0.1$. All parameters are set before the simulations start ($n = 0$). The procedure goes on with no one's intervention until the end ($n = 800$, for illustration purposes). Some of the results of the former work are reproduced in Fig. 4.2.

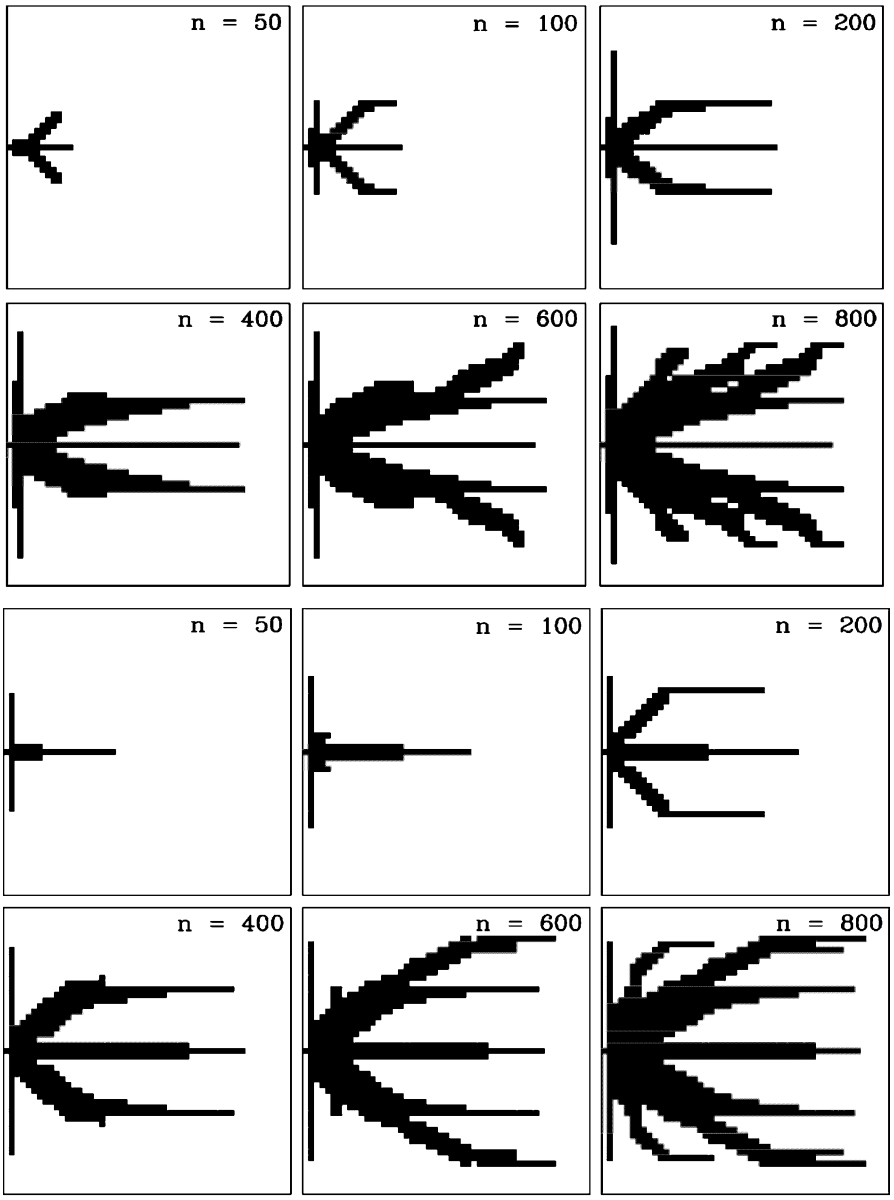

Fig. 4.2 Evolution of the basin by erosion for $K/K\mathrm{p} = 0.1$ with $\Delta\mathrm{M} = 10^{-3}$ (*top*) and $\Delta\mathrm{M} = 10^{-4}$ (*bottom*) until 800 steps (Figs. 4.7 and 4.8 [22])

We tested each kind of impermeable zone separately. The square-shaped void was placed in the middle distance to the outlet and at the thirds, and the tall-shaped void was placed at the middle, at the first third, and at the closest 1/7th to the exit slot.

The first of the K-blocks is removed at a critical value M_c of 0.00088932 [30]. The forcing term progressively increases in $\Delta M = 10^{-3}$ or 10^{-4} steps. We therefore carried out a set of 12 numerical experiments.

We considered symmetry with respect to the x-axis due to computational restrictions.

The constructal law is monitored by the global flow resistance, which is measured by the ratio between the peak pressure (highest pressure difference across the domain) and the forcing term:

$$\text{Flow Resistance} \propto \frac{\max\left(\tilde{P}\right)}{M} = \frac{\tilde{P}_{\text{peak}}}{M}. \tag{4.5}$$

Equation (4.5) holds because Darcy flow given Equation (4.2) is linear for a uniform M.

There are two simulations in progress, namely, the steady-state Darcy flow for each configuration at step n, and the evolution of the design of the drainage network. Continuous time plays no role, only historic *design* sequence matters.

The model and the computer code were updated for today's computational capabilities and versions of C and Pascal compilers, GPL-Octave and FIDAP®. FIDAP® helped turn the simulations feasible because it contains bi-quadratic (nine nodes) interpolation model for each element of the Finite Element Method (FEM). It also provides ways of successful interaction with external procedures. For instance, the simulation shown on the top of Fig. 4.2 took nearly 400 FEM different calculations of the pressure field that in each time was exported to an Octave routine in order to evaluate the condition set forth in Equation (4.4).

Detailed information of the validation of the recently updated code was documented in [31].

4.3 Results and Discussion

Results will be discussed first with regard to morphological evolution of the drainage basin, and subsequently we address the evolution in view of the performance given by the global flow resistance.

We first present the results with the square-shaped void, which was selected to cover nearly 9 % of the basin surface area (15D × 15D). Figure 4.3 shows three sets of six frames of the evolution the basin for $\Delta M = 10^{-3}$ and Fig. 4.4 shows the evolution for $\Delta \mathrm{M} = 10^{-4}$.

The plain basin of the top of Fig. 4.2 and the upper two sequences of Fig. 4.3 present resemblance until the 200th step, but with a striking difference in the occurrence of a central horizontal finger. It means that the void was felt even when the low flow resistance (Kp) path was still far from it. Later on, a minor central horizontal finger would appear in both cases above.

When the void was placed in the left-most third (bottom of Fig. 4.3), it drove the Kp-path to surround it. Another interesting feature was the appearance of a clump of low flow resistance blocks near the top and bottom boundaries.

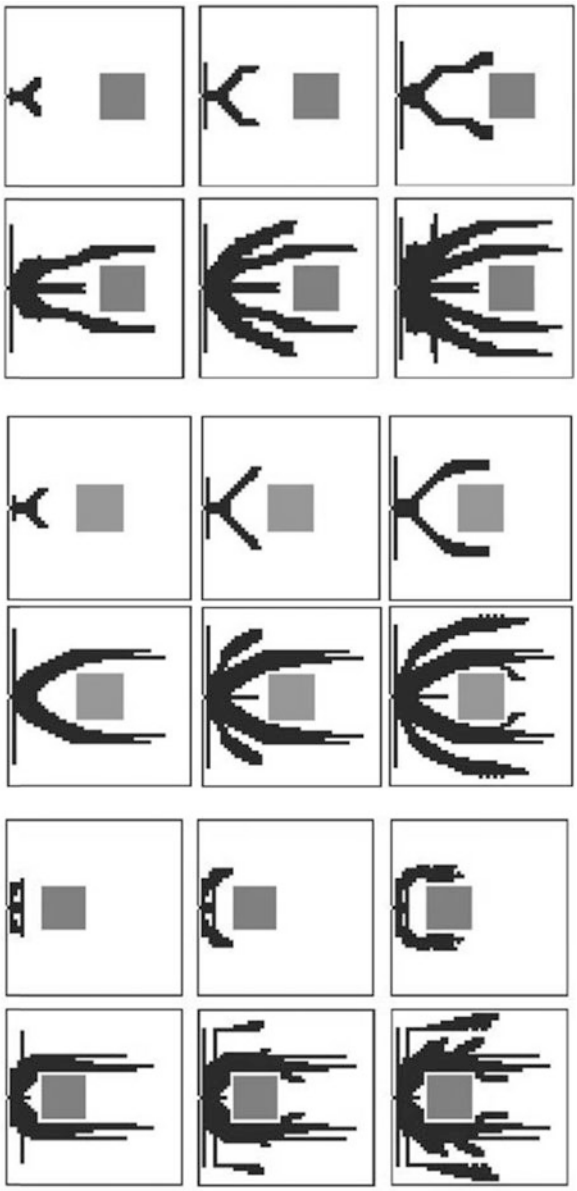

Fig. 4.3 Three evolutions of the basin for $K/K\mathrm{p} = 0.1$ and $\Delta M = 10^{-3}$, with a 15D × 15D area void, until 800 steps of evolution by erosion model in six frames ($n = 50$, 100, 200, 400, 600, and 800, respectively)

We next present the evolution of the basin under a smaller step $\Delta M = 10^{-4}$, Fig. 4.4. The case in which the void was located at the second third of the x-axis (Fig. 4.4, top) held high resemblance to the simulation of its counterpart shown at the bottom of Fig. 4.2 until $n = 400$. At the end the drainage path started to contour the not erodible impermeable zone. One can also note the central horizontal finger almost touched the void.

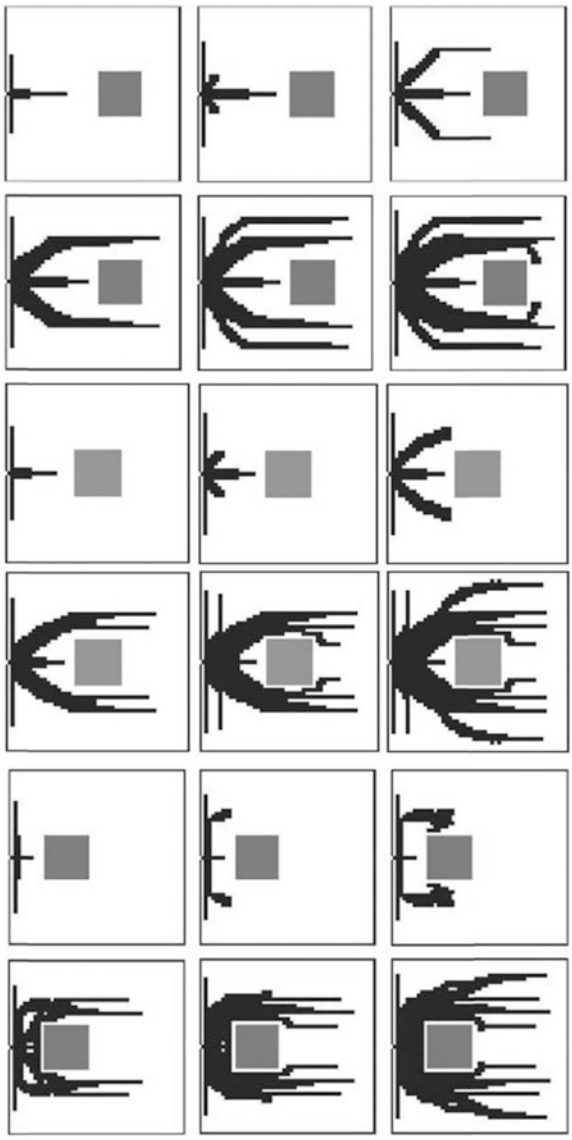

Fig. 4.4 Three evolutions of the basin for $K/K\mathrm{p} = 0.1$ and $\Delta\mathrm{M} = 10^{-4}$, with a 15D × 15D area void, until 800 steps of evolution by erosion model in six frames (n = 50, 100, 200, 400, 600, and 800, respectively)

The sequence at the middle of Fig. 4.4 shows again the low-resistance path surrounding the void near the end. Arched fingers arose seeking the farthermost corner of the basin.

In not one of the six simulations of Figs. 4.3 and 4.4 did the low flow resistance path fully embrace the non-erodible impermeable region until 800 steps of design evolution.

Next we present the results of the simulations with the tall-shaped void that was intended to work as flow barrier. It was sized to be as thin as possible and to lay on

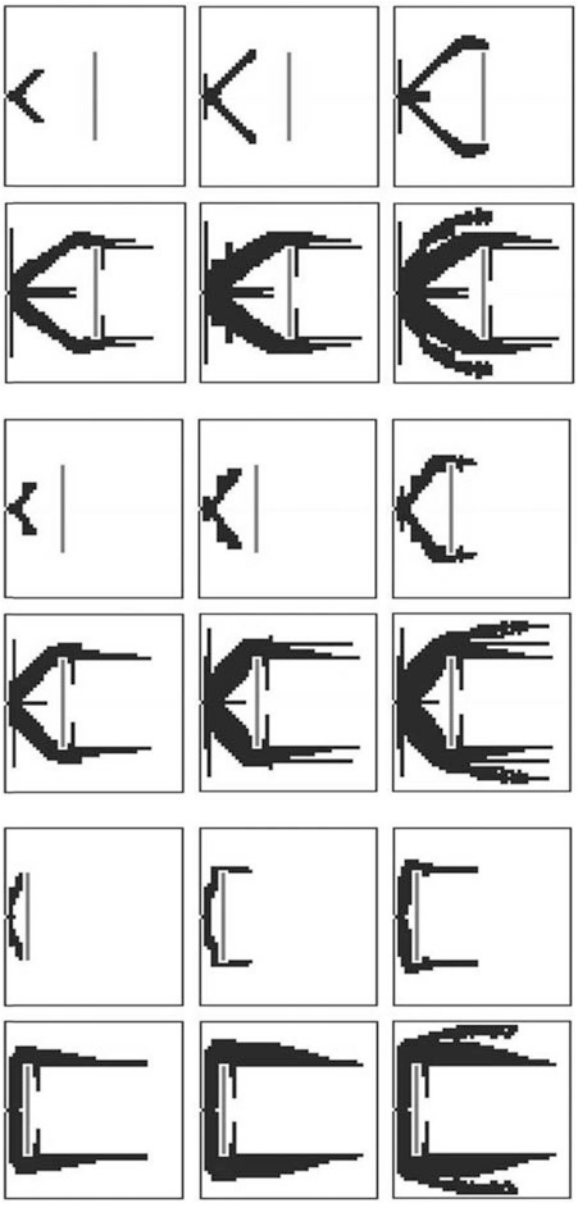

Fig. 4.5 Three evolutions of the basin for $K/K\mathrm{p} = 0.1$ and $\Delta\mathrm{M} = 10^{-3}$, with a 1D × 25D area barrier, until 800 steps of evolution by erosion model in six frames ($n = 50$, 100, 200, 400, 600, and 800, respectively)

half of the *y*-length, hence its area of nearly 1 % (1D × 25D) of the whole basin area. Figure 4.5 shows the evolution of the basin for $\Delta M = 10^{-3}$ and Fig. 4.6 the evolution for $\Delta M = 10^{-4}$.

The two superior sequences of Fig. 4.5 are *topologically* similar until the 600th step when a second pair of channel appears near the outlet (top sequence) and

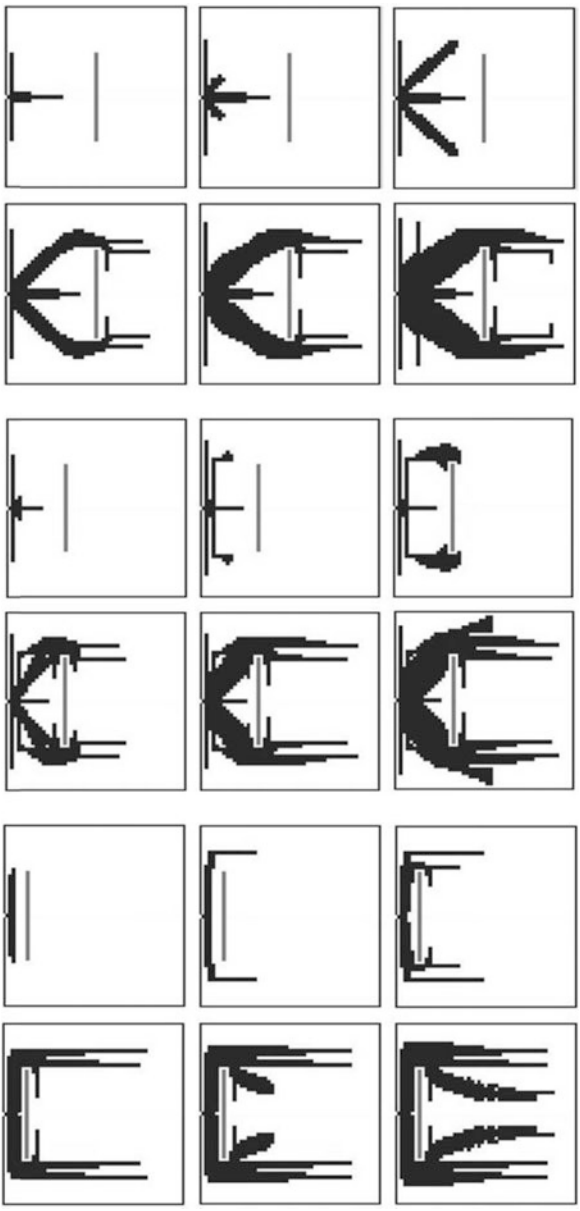

Fig. 4.6 Three evolutions of the basin for $K/K\mathrm{p} = 0.1$ and $\Delta\mathrm{M} = 10^{-3}$, with a 1D $\times$ 25D area barrier, until 800 steps of evolution by erosion model in six frames ($n = 50$, 100, 200, 400, 600, and 800, respectively)

beyond the barrier in the sequence placed at the middle. The bottom sequence of Fig. 4.5 in which the barrier is close to the outlet port shows that the *K*p-path fills all available space in front of the barrier and thickens beyond it. Nevertheless, a central area behind the barrier remained uncovered up to $n = 800$.

The smallest step of increase in the forcing term lead to the formation of momentary "isles" that were "flooded" later on by the *K*p-path (Fig. 4.6, middle sequence, $n = 400$). Another interesting feature is the high resemblance between the upper sequences of Figs. 4.5 and 4.6 in steps 400 and 600. They grew to be different in the final 200 steps when a pair of secondary arched channel appears.

Also worth noting is the growth of the pair of fingers to cover the central region of the basin that lies behind the barrier (bottom, Fig. 4.6).

A further understanding of the influence of not erodible regions on the evolution of the basin is provided by the progress of the forcing term and the maximum pressure (piezometric head). In ref. [20] we pointed out there are different moments in the morphological evolution of a drainage basin.

There are moments in which new features appear with little or no variation whatsoever of the forcing term, and moments that the current configuration *morphs* only under steep increase of the forcing term. In other words we have identified points of *morphological stability* (tenacity, good fitness) *and instability* (need to morph in order to achieve fitness and sustain external stress). Furthermore, there are times that the global flow resistance is more affected than others.

In Fig. 4.7 we show selected specific cases of the 12 simulations in order to stress the claim set forth above.

In the early 100 steps of the bottom sequence of Fig. 4.2, almost every single removal of K-block required an increase in the forcing term M (shown in the top, Fig. 4.7). In other words, the structure only *morphs* under larger external stress, thus being *tenacious*. After the 100th step, a different pace of changes in *K*p-path took place, that is, almost a 100 K-blocks were removed with nearly the same value of forcing term (a plateau in the $M \times n$ plot). We called that early structure to be *morphologically unstable* because two new diagonal fingers appeared to sustain a slightly more severe external condition.

Instability phase also took place between $n = 400$ and 550, when secondary fingers emerged. Those fingers grew (thickened) during another tenacity stage until $n = 600$ when a tertiary pair of finger appears in a short instability phase.

The M and $\tilde{P}_{\text{peak}}$ curves of the upper two plots of Fig. 4.7 are very similar until $n = 600$ when the influence of the impermeable but not erodible region is magnified.

The "extreme" case of an impermeable non-erodible barrier close the outlet port, which sequence is shown at the bottom of Fig. 4.6, lead to two great moments of instability, namely, in the early steps in order to bypass the barrier and near the half of the simulation when the two major fingers grew diagonally towards the right end of the basin.

One last argument is presented in Fig. 4.8 where we show the evolution of the global resistance of the selected simulations shown in Fig. 4.7. One can notice that two of the sequences present different configurations but fairly the same global performance. One then may ask whether it means the local factors do play important role in the final configuration.

Still in regard to Fig. 4.8, the sequence with the barrier closest to the outlet port never reaches the level of performance of the other two. The global resistance in

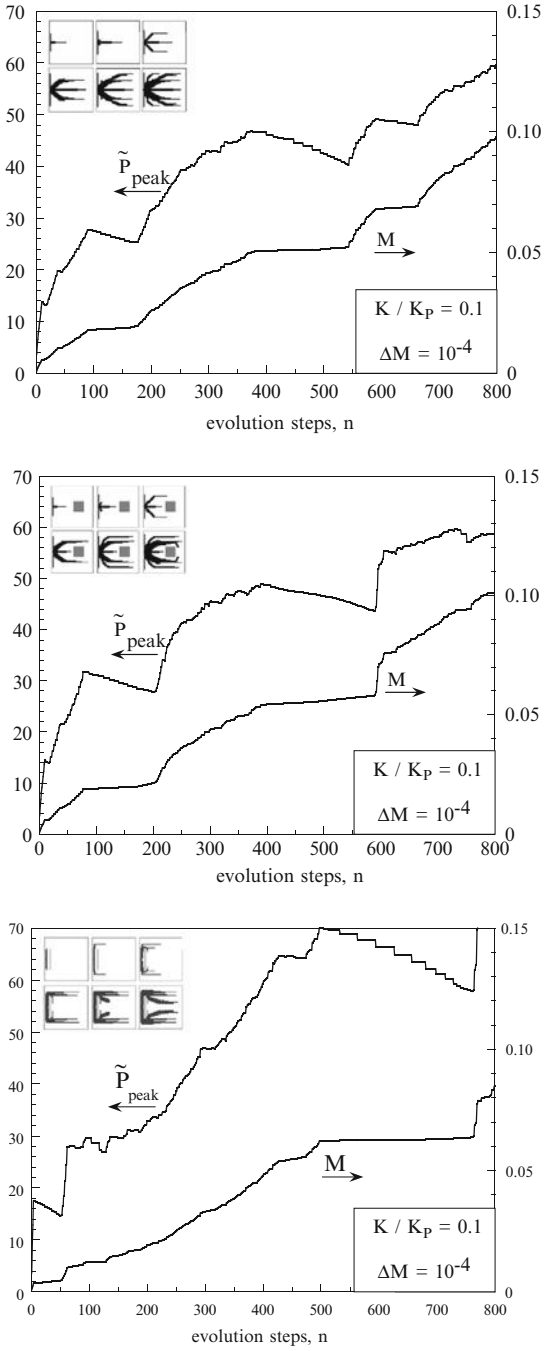

Fig. 4.7 Variation of the forcing term M and maximum pressure over the basin along evolution steps n. (top, related to the bottom of Fig. 4.2; middle, related to bottom of Fig. 4.4; bottom, related to the sequence at bottom of Fig. 4.6)

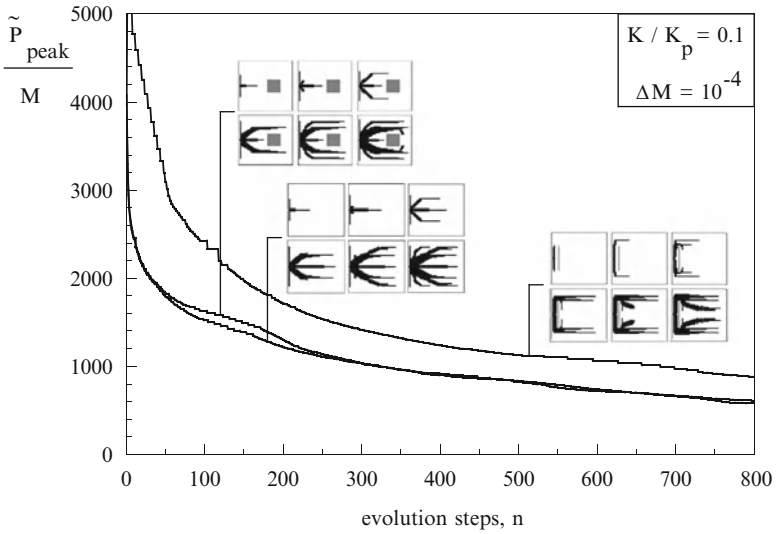

Fig. 4.8 Variation of global flow resistance in the evolution process of the erosion model for selected sequences of Fig. 4.7

this case could not benefit of the channel thickening near the outlet that was present in the other simulations.

Now when one looks to Figs. 4.7 and 4.8 together, one notices the basin of bottom of Fig. 4.6 underwent changes with lower levels of the forcing term. The highest level was 0.85, and yet the maximum pressure observed was always higher.

4.4 Concluding Remarks

In this chapter we addressed the influence of impermeable non-erodible regions in the evolution (formation) of a drainage basin by numerical simulations. The evolution was driven by erosion modeled as dislodging blocks according to earlier work [30] and [22]. Two steps of increase of the forcing term (rainfall) were considered for a fixed ratio of permeability and a square-shaped basin. We performed 12 different simulations.

Relatively large square-shaped voids placed along the centerline did influence the configuration of the *K*p-path but it did not affect dramatically the global flow resistance of the basin. The basin evolved to place more *K*p-blocks near the outlet rather than encircle the obstacles, as it had done in the original case.

On the other hand, tall-shaped voids (flow barriers) played a major role in both the configuration and performance of the basin. The most adverse situation, when the barrier was placed near the outlet port, lead the *K*p-path to grow and thicken beyond the barrier and towards the middle of the basin.

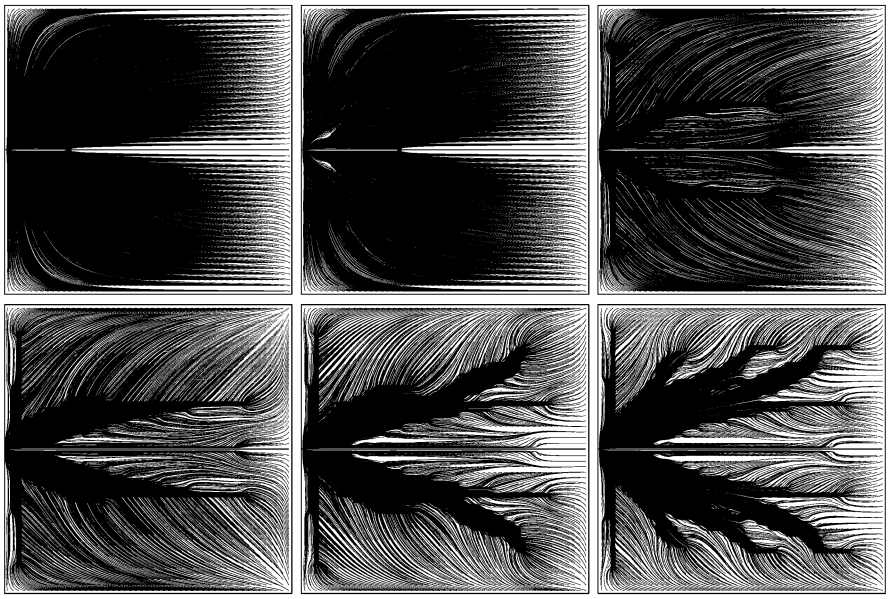

Fig. 4.9 Massless streamlines over the basin simulated for $K/K\mathrm{p} = 0.1$ and $\Delta M = 10^{-3}$, until 800 steps of evolution by erosion ($n = 50$, 100, 200, 400, 600, and 800, respectively)

Simulations considered only the events that caused changes in the internal design of the basin and they were counted in discrete n-steps.

The interaction between external environment and the basin took place solely by the progressive increase of the forcing term M in two different steps of increase. For large-scale basins, however, one expects that the external environment be also affected by the way the basin convey water to the outlet port. For instance, the precipitation $\dot{m}''$would be affected by the heterogeneity of the basin and probably would vary spatially across the basin.

In addition to the growth and formation of the low flow-resistance path there is another morphological process in progress that is not evident, namely, the rearrangement of the flow field after each morphological change in the Kp-path. In order to illustrate such process we selected the simulation whose sequence is shown at the top of Fig. 4.2 to trace the massless streamlines (Fig. 4.9).

In the early steps the flow goes nearly straight towards left, then towards the centerline, and finally to the outlet. Flow directions across the basin change as the internal structure does.

One can notice the organization of the flow from a diffusive ("blurry") pattern to a well-defined sub-basins system. At the end, one can count 11 different sub-basins in the case shown in Fig. 4.9.

Further conclusions can be drawn beyond the special cases simulated in this chapter. They relate to some trends in the way the basin evolution process takes

place in the simulations. First one observes the development of internal configuration of basins occurs in different paces with respect to the progress of an external forcing term. There are times in which a little increase of the forcing term leads to substantial change in the topology, as if a threshold was surpassed. Those instances are the beginning of *a morphological instability* phase that in turn is often followed by *morphological stagnation* stages, when the current topology is just enhanced (thickened or consolidated).

Sometimes morphological stagnation phases just end with another extreme morphological move; one that requires a very large increase in the external stress in order to change the current design. In other words, the design in those stagnation phases sustain large perturbations before yielding to new morphological changes. It is fair to say that such design state is tenacious.

In the design evolution process addressed in our work only K-blocks can be turned into *K*p-blocks, never the other way around. Hence, there is a logical sequence that can only go forward and leaves a trail. This is design with *memory*: a system can only morph on top of its current design, which in turn was the consequence of the history that had brought it there. Furthermore if the external stress is suppressed (e.g., no more rain), there will be a *fossil* structure as pointed out in ref. [32]

Let us compare this class of design process with the streamlines design in the classic heat transfer problem of natural convection in square cavity driven by one heated vertical wall (e.g., [34]). Initially the system is at rest. When one of the sidewalls is heated up to a prescribed temperature, the fluid starts to move until a steady pattern of streamlines and a temperature field are reached. The system evolved and an internal structure has been set. Nevertheless, once the wall is no longer heated, the system will gradually return to its initial design state at rest. This is evolution of configuration with no memory, as no trace of the internal structure will be found in the future.

Indeed the evolution by erosion covered in this chapter relates to a design process that is path dependent and shows memory effect. Nevertheless, unlikely biological systems, the simulated basins cannot inherit traits from a pool of individuals and a selective process. It just morphs on its own.

These features are important because they may complement the Thermodynamic Equilibrium analogy proposed by ref. [33].

Results also indicate that the global performance is significant in the shaping of the *K*p-path, but does not fully explain the entire *design* phenomenon. This claim is supported by the plots of Fig. 4.8, where one can notice two distinctive internal configurations perform progressively similar.

The bounds between performances of different internal configurations were first addressed in [28]. The lower limit is given by randomly replacing K-blocks by *K*p-blocks regardless of the external stresses, and the upper bound is determined by the step-by-step optimization.

In sum, local factors do play a role in shaping internal configuration, even though they may not be relevant to global performance.

We finally draw attention that the internal structure with rational complexity in [22] has been developed with no assumption of the existence of any network whatsoever. Complex structures can indeed be derived from simpler ones, in fact the simplest (a plain uniform drainage basin). This is a strong argument against the doctrine so called "irreducible complexity" that claims large networks can only be consequence of other simpler or smaller networks.

Future applications of erosion-type models may exceed the realm of drainage basins and aid predicting the growth of new blood vessels (angiogenesis) of new tissues or tumors.

Acknowledgements C.A.M. is thankful for his scholarship granted by Coordenação de Aperfeiçamento de Pessoal de Ensino Superior (CAPES) of the Brazilian Government during his years at Water Resources and Environmental Engineering Graduate Program (PPGERHA). We acknowledge Duke University's support on the use of the FIDAP® software and its computers. We are especially grateful for Prof. Luiz A. O. Rocha's support.

References

1. Maidment DR, editor. Handbook of hydrology. New York: McGraw-Hill Professional; 1993.
2. Rodríguez-Iturbe I, Rinaldo A. Fractal river basins. New York: Cambridge University Press; 1997.
3. Bejan A. Shape and structure, from engineering to nature. Cambridge: Cambridge University Press; 2000.
4. Proulx SR, Promislow DEL, Phillips PC. Network thinking in ecology and evolution. Trends Ecol Evol. 2005;20(6):345–53.
5. Bejan A. Constructal-theory network of conducting paths for cooling a heat generating volume. Int J Heat Mass Transfer. 1997;40:799–816.
6. Chorley RJ, Schumm SA, Sugden DE. Geomorphology. New York: Methuen and Co.; 1984.
7. Leopold LB, Wolman MG, Miller JP. Fluvial processes in geomorphology. San Francisco: W. H Freeman and Company; 1964.
8. Chow VT, Maidment DR, Mays LW. Applied hydrology. New York: McGraw-Hill Inc; 1988.
9. Maritan A, Rinaldo A, Rigon R, Giacometti A, Rodriguez-Iturbe I. Scaling laws for river networks. Phys Rev E Stat Phys Plasmas Fluids Relat Interdiscip Topics. 1996;53:1510–5.
10. Cieplak M, Giacometti A, Maritan A, Rinaldo A, Rodriguez-Iturbe I, Banavar JR. Models of fractal river basins. J Stat Phys. 1998;91:1–14.
11. Rinaldo A, Rodriguez-Iturbe I, Rigon R. Channel networks. Annu Rev Earth Planet Sci. 1998;26:289–327.
12. Rinaldo A, Banavar JR, Maritan A. Trees, networks, and hydrology. Water Resour Res. 2006;42:1–19.
13. Howard AD. Badland morphology and evolution: interpretation using a simulation model. Earth Surf Proc Land. 1997;22:211–27.
14. Pelletier JD. Fractal behavior in space and time in a simplified model of fluvial landform evolution. Geomorphology. 2007;91:291–301.
15. Rosa RN, Reis AH, Miguel AF, editors. River basins: geomorphology and dynamics. Proceedings of the symposium on Bejan's Constructal Theory of Shape and Structure; Évora Geophysics Center, University of Évora, Évora, Portugal: 2004. pp. 15-47.
16. Gupta VK, Waymire EC. Stastical self-similarity in river networks parameterized by elevation. Water Resour Res. 1989;25:463–76.

17. Fiorentino M, Claps P, Singh VP. An entropy-based morphological analysis of river basin networks. Water Resour Res. 1993;29(4):1215–24.
18. Reis AH. Constructal view of scaling laws of river basins. Geomorphology. 2006;78:201–6.
19. Bejan A, Errera MR. Deterministic tree networks for fluid flow: geometry for minimal flow resistance between a volume and one point. Fractals. 1997;5:685–95.
20. Errera MR, Marin CA. Numerical simulation of drainage basins formation in small-scale porous media with an unalterable region, Proceedings of ENCIT 2010, 13th Brazilian Congress of Thermal Sciences and Engineering, ABCM; 2010 December 05–10, Uberlandia, Brazil
21. Bejan A. Advanced engineering thermodynamics. 2nd ed. New York: Wiley; 1997.
22. Errera MR, Bejan A. Deterministic tree networks for river drainage basins. Fractals. 1998;6:245–61.
23. Bejan A. Constructal tree network for fluid flow between a finite-size volume and one source sink. Rev Gen Therm. 1997;36:592–604.
24. Ledezma GA, Bejan A, Errera MR. Constructal tree networks for heat transfer. J Appl Phys. 1997;82:89–100.
25. Errera MR, Bejan A. Tree networks for minimal flow resistance to volume-to-point flows in composite porous media. J Porous Media. 2000;2:1–18.
26. Bejan A, Lorente S. Constructal theory of generation of configuration in nature and engineering. J Appl Phys. 2006;100:1–27.
27. Bejan A. Constructal theory of pattern formation. Hydrol Earth Syst Sc. 2007;11:753–68.
28. Marin CA, Errera MR. A comparison between random and deterministic tree networks for river drainage basins. Proceedings of Third Southern Conference on Computational Modeling (3MCSUL, 2009), IEEE Proceedings; 2010. pp. 18–23.
29. Bejan A, Personnal communication on the possible impacts of impermeable non erodible regions in the evolution of drainage basins.February, 2007.
30. Errera MR. Geometric optimization of flow systems with irreversibilities. Ph.D. thesis, Duke University (published and copyrighted by UM); 1999.
31. Marin CA. Numerical study of the influences of impermeable parcels in drainage basins. M Sc. Thesis. Water Resources and Environmental Engineering Graduate Program (PPGERHA), UFPR, Curitiba, Brazil; 2010.
32. Bejan A, Lorente S. The constructal law of design and evolution in nature. Philos Trans R Soc Lond B Biol Sci. 2010;365(1545):1335–47.
33. Bejan A, Lorente S. The constructal law and the thermodynamics of flow systems with configuration. Int J Heat Mass Tran. 2004;47:3203–14.
34. Bejan A. Convection heat transfer. 2nd ed. New York: Wiley; 1995.

Chapter 5
Software Evolution and the Constructal Law

S. Périn

5.1 Software Evolution

The evolution of software programs, which could be defined as the change process occurring in software programs in time, is a domain widely studied, now for decades, but the relatively recent development of both Internet and Open Source Software (OSS) offered new perspectives on this domain, thanks to the tremendous amount of data now easily available to the researchers.

In 1985, M. M. Lehman and L. A. Belady published what had been a reference for years in the domain of software evolution [1]. In their book, gathering works written mainly in the 1970s and 1980s, Lehman and Belady proposed a general framework to understand the evolution of software programs, along with discussions on afferent topics such as growth dynamics or software maintainability. More particularly, in the 1970s, they proposed initially three laws, later extended to eight, known as Lehman's laws of E-type systems evolution—where the term E-type system represents a large class of software programs, E meaning "Evolutionary." The first three of these laws are [1, 2]:

1. The law of continuous change: An E-type system must be continually adapted otherwise it becomes progressively less satisfactory in use.
2. The law of increasing complexity, also called the law of increasing entropy: As an E-type system is evolved its complexity increases unless work is done to maintain or reduce the complexity.
3. The law of statistically smooth growth or law of self-regulation: Global E-type system evolution is regulated by feedback.

   For our purpose, we will also cite the sixth law [2]:

6. The law of continuing growth: The functional capability of E-type systems must be continually enhanced to maintain user satisfaction over the system lifetime.

S. Périn
OCTO Technology, 58 Avenue des Champs-Élysées, Paris 75008, France
e-mail: sperin@octo.com

L.A.O. Rocha et al. (eds.), *Constructal Law and the Unifying Principle of Design*,
Understanding Complex Systems, DOI 10.1007/978-1-4614-5049-8_5,

Today, software evolution is still a hot topic, because, in time, a software application needs to accommodate continuous changes to fit the needs of its users, and this continuous process usually increase the complexity of the system, meanwhile frequently degrading its overall quality, and finally threatening the survival of the software application due to the increasing costs of maintenance [1, 3]. This process underlies Lehman's Laws, which try to capture its essence.

The validity of Lehman's laws for OSS was recently studied, and the conclusion asked for a revision of the Lehman's laws [2], since very few of the eight laws were systematically experimentally verified. In their conclusion, Fernandez-Ramil et al. [2] suggest that "it could well be that we are facing a paradigm-shift in our understanding of software evolution."

We believe that the Constructal Theory [4, 5] of global optimization under local constraints could provide such a paradigm-shift, and provide new keys to better understand—or even optimize—the process of software evolution.

Stated in 1996, the Constructal Law [6, 7] is now sustained by a large and increasing body of evidence [8]. The Constructal Law states that "For a finite-size flow system to persist in time (to live), its configuration must evolve such that it provides easier and easier access to its currents."

Since software systems are complicated flow systems, we propose here to study the relevancy of Constructal theory to this field of engineering. The rest of the chapter is dedicated to the experimental discovery of constructal patterns in the evolution of a software system, and to the explanation of the emergence of these patterns thanks to Constructal theory. For our study, we will use the source code of the core of the Java Platform.

5.2 The Java Development Kit

The Java platform is both a programming language and a very rich set of software libraries allowing software programmers to develop standalone applications, Web applications, mobile applications, enterprise applications, etc. Several sub-platforms (Software Development Kit, or SDK) are provided to the programmers' community, in addition to the core of the system, known as the Java Development Kit (JDK), such as the Java ME SDK (Java Micro Edition Platform) or the JEE SDK (Java Enterprise Edition). The first version (v1.0) of the JDK was publicly released in 1996, and the last one (v7) in July 2011.

The Java platform is widely used in the domain of software development, especially for Enterprise Application development, and at a worldwide scale. Many factors can contribute to explain this success: of course, one of the more important is probably the support of the company which initially developed the Java platform, Sun Microsystems, Inc. (now ORACLE). Among the many factors of success, we can list probably, and for instance: the similarity of its syntax with the ones of the C and C++ languages, thus facilitating the learning of the language for already experimented developers, the automatic garbage collection, liberating the

developer from the tedious task of memory management, a rich ecosystem of OSS applications or libraries, especially in the domain of software engineering, and the gratuitousness of the technology.

The success of this platform is the main reason for choosing it as object of our study (with the availability of many software metrics calculation tools). Effectively, the Constructal Law is supposed to concern finite-size flow systems persisting in time. Since the Java platform succeeded to persist during the last 15 years and even became one of the main languages used worldwide [9–11], we considered Java as a choice of predilection.

A contrario, the Go programming language (http://golang.org), developed by Google, Inc. and launched in 2007 cannot be considered such a success 4 years later, if compared to the Java platform, in term of adoption by the software developers' community—all other thing being equals.

Our study focused thus on the main following research questions: How does the size of JDK evolve in time? Does the growth of the JDK display characteristic patterns? If yes, are the growth patterns of the JDK understandable in the light of the Constructal Law?

5.3 Source Code and Experiment

In order to try to answer to these questions, we study the evolution of the JDKs 1.0–7, over 15 years. We strictly restricted our study to the Java source code of the JDK classes. Other software artifacts of the platform were ignored (XML files, C/C++ source code, etc.) The objective of the experiment was to collect the required metrics on each of the JDK version for study.

For versions 1.0–6, the binary files of the JDK, containing the source code root directory, were downloaded from the current Oracle Java Archive (http://www.oracle.com), or from the previous Web site of Sun Microsystems, Inc. (http://java.sun.com). For the seventh version, the source code was retrieved from the Java.net community site (http://jdk7.java.net/), now the official source of the JDK, since the release of its source code under the GNU General Public License (GPL) in 2006.

Regarding the release dates used, we considered the dates of the major releases of the several versions of the JDKs that we used, as listed in Table 5.1, and used in Figs. 5.3, 5.8, 5.9, and 5.11, but the JDK versions that we analyzed were sometimes the minor versions, for reasons linked to the availability of the major versions of the JDKs, at the time of the download of the JDKs binary files (namely, versions 1.0.2, 1.1.3.beta, 1.2.2.12, 7b147). For our purpose, and as a hypothesis, we considered the differences in lines of code between a major release version and one of its minor versions as negligible, since they consist usually mainly in bug fixes and minor API evolutions (changes in methods signatures, renaming of fields, etc.)

The first JDK was released in January 1996, but the project started ca. 5 years earlier, under the code name Oak as part of the Green project [12, 13], at Sun Microsystems, Inc.

Table 5.1 Time between the JDK releases, inception

JDK version	Release date (mm/dd/yyyy)	Time between releases (years)
1.0	01/23/1996	4.5–5.1[b]
1.1	02/19/1997	1.1
1.2	12/08/1998	1.8
1.3	05/08/2000	1.4
1.4	02/06/2002	1.8
1.5	09/30/2004	2.6
6	12/11/2006	2.2
7[a]	07/28/2011	4.6

[a]Open JDK
[b]Depending on the start date considered (Dec. 1990 or June 1991)

We retained the date of December the 1st, 1990 for the calculation of the v1.0 release time, since "Java, whose original name was Oak, was developed as a part of the Green project at Sun. It was started in December 1990 by Patrick Naughton, Mike Sheridan and James Gosling" according to J. Gosling, considered as the father of the Java language [12, 14].

Another possible start date to consider is mid-1991, when J. Gosling started effectively to work on the Oak language interpreter, i.e., to program it. But for our purpose, we are mainly interested in the order of magnitude.

5.4 Tools and Software Metrics

We use different and complementary tools in order to calculate the several software metrics used in this study. The tools used were CLOC 1.53, http://cloc.sourceforge.net, SourceMonitor 2.6, http://www.campwoodsw.com, and JHawk 5, http://www.virtualmachinery.com.

Due to the very recent release of the JDK 7 at the time of this study, we were not able to calculate all required metrics on the JDK 7 source code. Effectively, the grammar of the Java language has evolved between the version 6 and 7, and all tools were not yet supporting this too recent evolution of the Java platform.

The metrics used concern more especially the number of different types of lines of code (comment, blank, non comment or blank ...) and some Object Oriented (OO) metrics regarding the number of packages, classes, and methods [15]:

- BLOC, Blank Line of Code
- CLOC, Comment Line of Code
- LOC, Line of Code
- NCLOC, Non-comment Line of Code
- NOC, Number of Classes
- NOSCF, Number of Source Code Files
- NOM, Number of Methods
- NOP, Number of Packages

5.5 Results and Discussion

The global sizes in lines of code of the JDK, listed in Table 5.2, are displayed in a more detail bar-chart in Fig. 5.1, whereas Fig. 5.2 shows a log–log plot of the distribution of the size of the JDK files, expressed in NCLOC, for the eight versions studied.

The overall NCLOC size of the JDK was multiplied by ca. 74 from version 1.0 to version 7. Every JDK is bigger than the previous one, as visible in Fig. 5.1 and on the log–log plot provided by Fig. 5.2, where, on this last plot, the distributions move

Table 5.2 Files and lines of code metrics for eight of the main versions of the JDK

JDK version[a]	NOSCF	NCLOC	CLOC	NOC
1.0.2	216	15,343	17,370	227
1.1.3b	644	58,619	70,030	673
1.2.2.12	1,650	214,948	226,930	2,814
1.3.0	1,878	242,662	271,918	3,266
1.4.0	3,882	506,653	530,703	6,209
1.5.0	6,558	833,995	824,545	10,092
6	7,069	896,746	897,798	10,879
7b147	7,490	1,142,189	1,017,027	12,111
Total	29,387	3,856,321	3,911,155	46,271

[a]"b" indicates a beta version

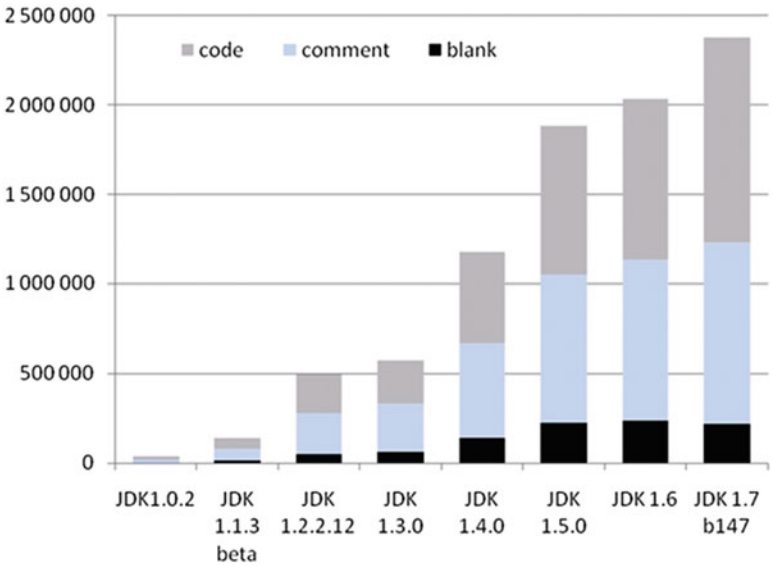

Fig. 5.1 Evolution of the overall size, in lines of code, of the JDK, showing the repartition between NCLOC, NCLOC, and BLOC

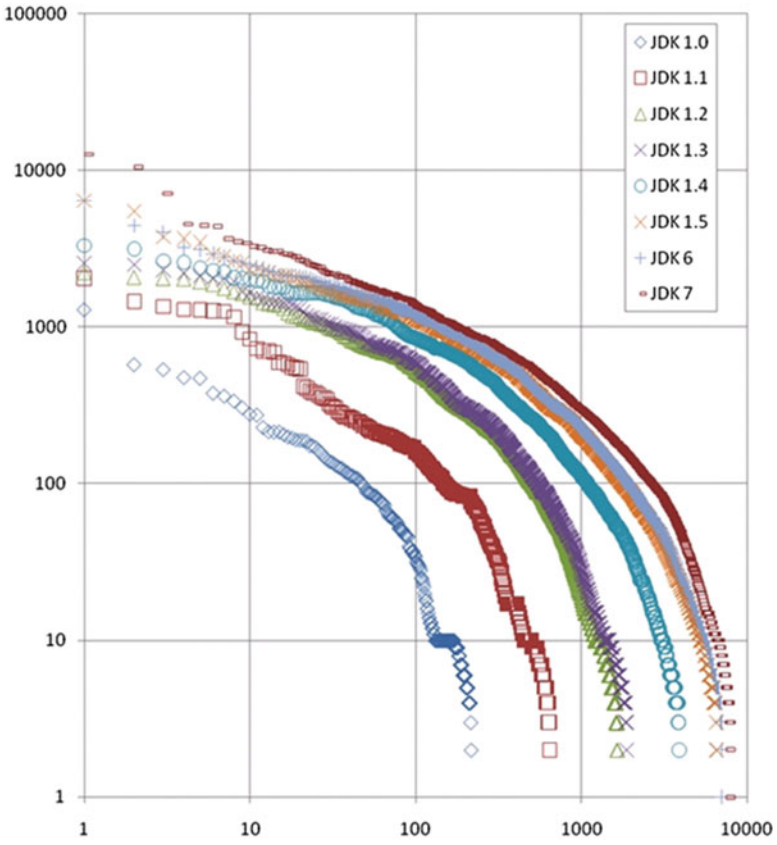

Fig. 5.2 Log–log plot of the NCLOC metric, for eight JDK versions, ranked for every source file. The period between the first and last distribution covers ca. 15.5 years

up, and extend to the right of the figure (the long tail of the distribution is extending). The size of the overall system only increases, and never decreases, over the last 15 years. By the way, the sixth law of Lehman seems verified for the evolution of the JDK, but it is not our point here.

One of the main interests of a log–log plot is to visually check the tendency of this kind of rank-size distribution. Very often, the distribution is almost linear on several decades-depending of the size of the sampling-with divergence on the tail and on the head of the distribution.

Frequently, a power-law distribution is fitted with such kind of distribution. But in our case, it is obvious that these rank-size distributions do not fit well a log–log "linear" power law distribution of the following form, where $p > 0$:

$$\mathrm{f}(x) = k \cdot x^{-p}. \tag{5.1}$$

This kind of distributions is identifiable thanks to its linear shape on a log–log graph, where p dictates the slope of the curve.

On the log–log plot, the JDKs' distributions are in fact clearly curved, quasi-parabolic, and the more recent the version, the smoother the curvature. In our case, trying to fit this kind of curves with a power-law will obviously not be satisfying.

This kind of curved distribution on log–log plot is in fact extremely frequent in different domains such as galactic intensities, city sizes, or petroleum systems [16]. Often, the curvature is explained by the finite size of the system: "The fact that most of the natural distributions display a log–log curved plot, avoiding the divergence and leading to thinner tails than predicted by a power law, has mostly been interpreted in terms of finite-size effects." [17].

J. Laherrere proposed to name such distributions Parabolic Fractal (PF), and proposed also to fit them with a polynomial power-law relation as follow [16]:

$$\ln(y_n) = a \cdot \ln(x_n)^2 + b \cdot \ln(x_n)c. \tag{5.2}$$

with

$$c = \ln(y_1) \tag{5.3}$$

where y_1 is the ordinate of the first value of the distribution, $a < 0$, is the coefficient of curvature, and $b < 0$ the slope at the first rank.

Laherrere discusses also the King effect, which is described as the effect explaining the frequent divergence of the data with the PF distribution for the first ranks. The abnormality of the plot of Paris on the log–log distribution of French city sizes [15] is thus explained thanks to this effect: "the new King kills the barons to avoid competition and to acquire a wealth above the commoners" [17]. This effect exacerbates so the concentration of the population in the first ranks. To best fit the data with the model, the first rank must be ignored, in this case.

Another alternative model, the stretched exponential, complementary to the power-law and PF models was also proposed [17]. Usually, power-law, Zipfian distribution, FP, etc., are interpreted as the result of a stochastic growth process, with birth and death mechanism [17, 18]. And because of the clustering of high-rank values close to the x-axis, values are sometimes grouped into buckets of exponentially increasing size in order to improve the accuracy of the regression [19].

We could of course try to fit the JDKs' Java files size distributions with a power-law, a PF, a stretched exponential, etc., and discuss their adequateness to describe the observed phenomenon.

But we propose to consider instead a radical new approach to understand the potential mechanism generating such a great variety of distributions such as Zipfian, power-law, PF, and stretched exponential, as discussed here below.

For this, we need first to consider the evolution of the global LOC size of the JDK versions in time, as depicted in Fig. 5.3a, b, for, respectively, the Java files and the Java classes. The curve displays a typical S-shape profile, frequently observed in many phenomena of natural, social, or other origin [8].

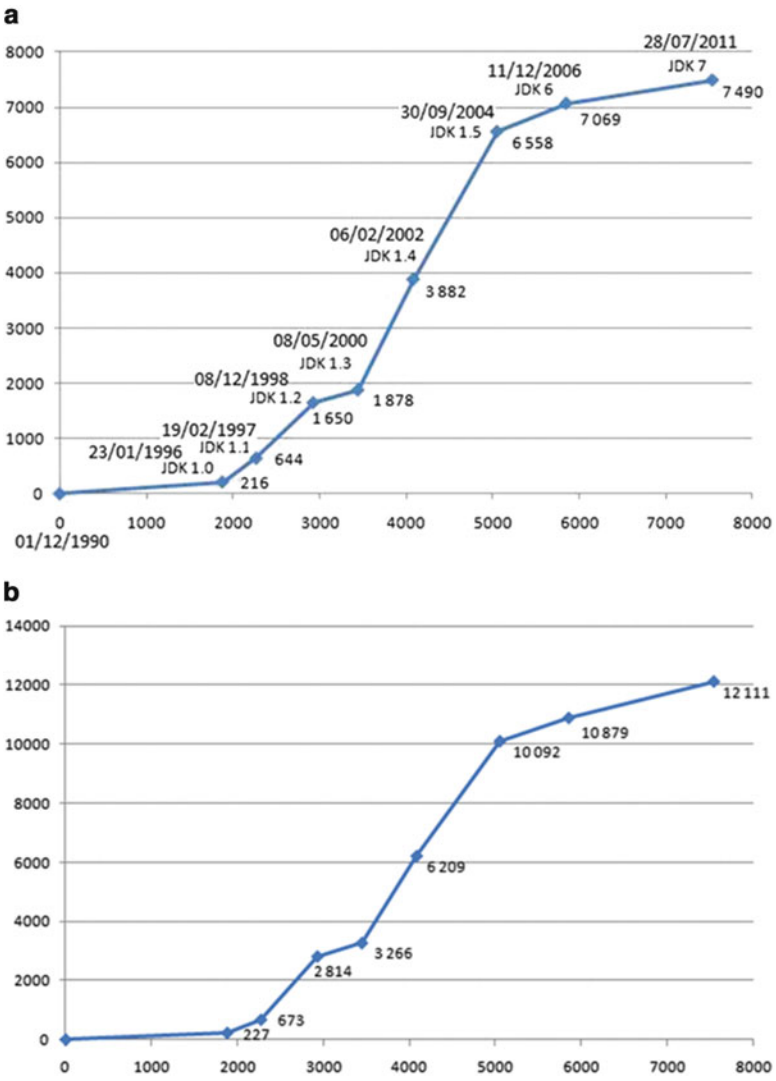

Fig. 5.3 Approximation of the evolution, in time (number of days), of the number of Java files (**a**) and classes (**b**) for each of the main versions of the JDK, since the project inception and until the last release

In the domain of software development, the existence of S-curve had been documented, as cumulative-flow diagrams (CFD) usually follow this shape [20, 21]. CFD are used to track the progress of a software development project, especially for projects following an Agile method or using a Software Kanban, and a lot of information can be extracted just by looking at a project's CFD.

It is thus not surprising that the evolution of the JDK, which is a software development project, conforms to the S-shape of the logistic function.

S-curves are also typical of technological adoption curves. In our case, the JDK is a technology that has pervaded inside the software developer community for 15 years and reached a state of massive and worldwide adoption. This consideration reinforces our conclusion, since the increasing adoption of the Java technology contributed in return to the good development of the software project in charge of the JDK.

It must be observed that since the version 1.5, the growth rhythm of the platform seems to approach a plateau, indicating maybe a now great level of maturity of the platform, and the richness of all its features.

Bejan and Lorente showed recently [8] that S-curves can be theorized in terms of a constructal invasions of a territory by a flow system. Tree-shaped invasion were also identified in the same publication as an optimization of the invasion mechanism.

Furthermore, Queiros-Conde et al. [22] showed that a constructal tree structure exhibits a parabolic scaling of its geometry.

5.6 Constructal Tree-Shaped Invasion of a Territory by a Growing Population

On the basis of the fact that Zipfian power-law distributions are theoretized by the constructal distribution of city sizes [23], that the logistic (S-curve) function can be predicted thanks to the constructal invasion of a territory, and considering that constructal trees develop a parabolic scaling distribution of their geometry [22, 24], we thus propose to consider the generation of curved power-law distribution of the size of a population (such as PF or stretched exponential) as the combination of the constructal tree-shaped invasion of a territory by a growing population, as explained here below.

The mechanism is depicted in Fig. 5.4. Initially, a population occupies a small fraction (A_0) of a bigger territory (A), as shown in Fig. 5.4a. As a hypothesis, the distribution of the population assumes a power-law distribution according to the Constructal Theory documented in [23]. As time progress, the territory colonized by the population extends, and the initial distribution of the population is replicated to another A_0-sized territory. Now a part $A_1 = 2A_0$ of the territory is invaded (Fig. 5.4b). Meanwhile, the first population has grown of a factor g_0.

Then, another part of the territory of A_1-size is invaded by a new population assuming the same distribution as the initial one (Fig. 5.4c). During the same period, the populations occupying the A_1 territory have grown of a factor g_1. This mechanism replicates until the whole A territory is invaded (Fig. 5.4d).

Furthermore, at the time of invasion, the invaded territory can already house one or several constructal flow systems, such as a hydrographic basin (for a geological system), this last obeying to the Horton's Law predicted by the Constructal theory [25, 26]. Such kind of flow system, as sketched in Fig. 5.5, can facilitate both the invasion on the territory and dictate also the progression of

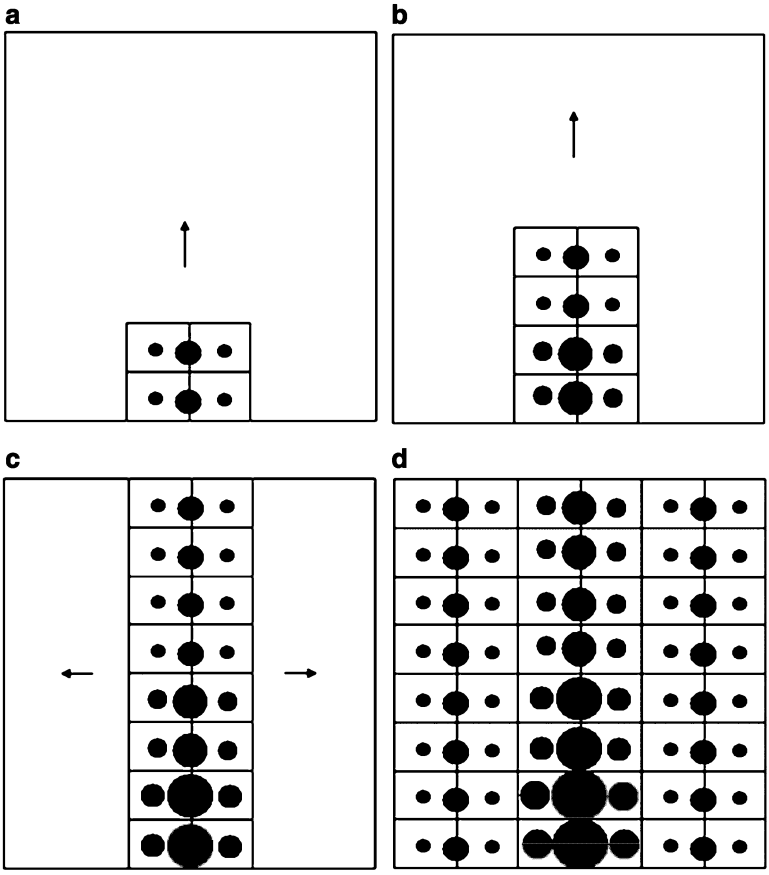

Fig. 5.4 Constructal tree-shaped invasion of a territory

the invasion, as they constitute usually the paths of least resistance to progress into the system.

In order to challenge this idea, we run very simple simulations of this mechanism, with hundred initial values, distributed according to a power-law, as shown in Fig. 5.6, and iterated six times the constructal-invasion mechanism discussed here above, with growth rates of 100 % (doubling). The resulting distributions are plotted altogether in Fig. 5.6, whereas the resulting S-curve for the overall size of the population is displayed in Fig. 5.7. For the simulation whose results are displayed in Fig. 5.6a, where the curvature is exacerbated, each new generation N is a replica of the previous generation, whereas, for Fig. 5.6b, the new kth generation N is composed of $2k - 1$ replicas of the initial N_0 generation.

As expected, the rank-size distributions progressively deviates from the initial power-law, and develop a curved tail, whereas the first ranks become more stepped.

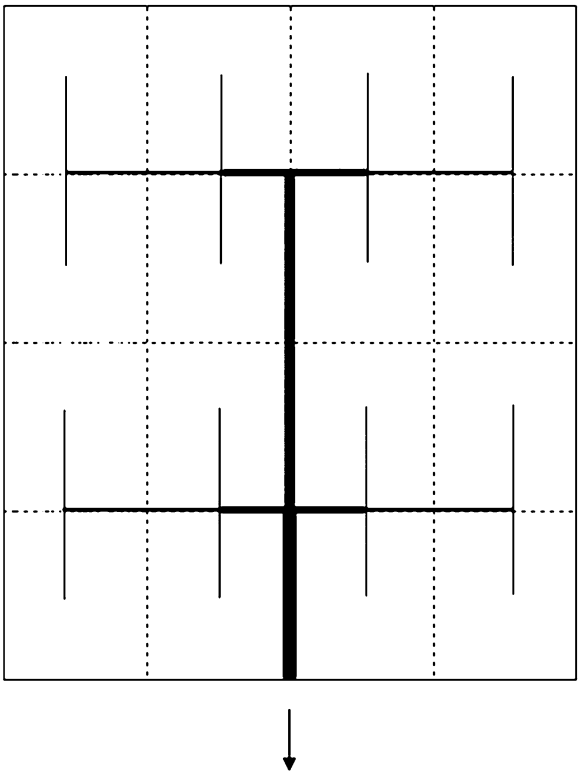

Fig. 5.5 Constructal model of a river basin

What's accounted for here is the general trend of the distribution resulting from the proposed mechanism, and not the specific fit with a PF, a stretched exponential, or another distribution function.

History, local and global factors, heterogeneity, etc., account for the uniqueness of each rank-size distribution. For instance, it accounts for the "King Effect" in the French cities-sizes distribution [15].

One consequence of our proposed model is the rejection of the assumption that the finite-size effects of a natural system can be accounted for the curvature often encountered in pseudo-power-law distributions [17]. In our proposed mechanism, the main origin of the curvature resides in the conjunction of growth of older generations, i.e., the upward shift of old plots, with the development of new generations. Because they are more recent, they start smaller, and tend to accumulate at this end of the distribution (in the long tail), closer to the x-axis, and exacerbating the curvature.

Similarly, the King Effect results, in the here above proposed mechanism, in a greater upward shift (growth) of the first and older concentration points of the distribution, and where the growth is exacerbated.

We now come back to our initial object of study: How is this related to the evolution of the JDK lineage? We think that the tree-shaped invasion of a functional

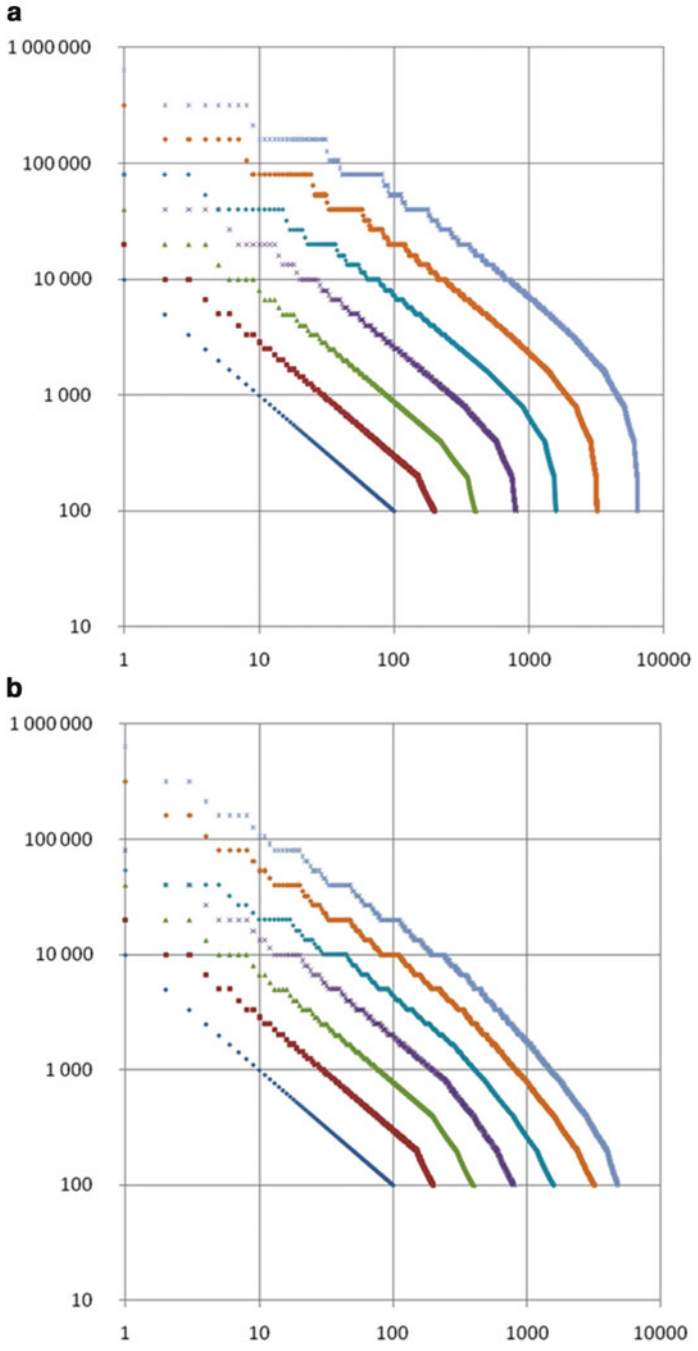

Fig. 5.6 Two simulated Constructal tree-shaped invasions of a territory: rank (x) versus size (y) distributions

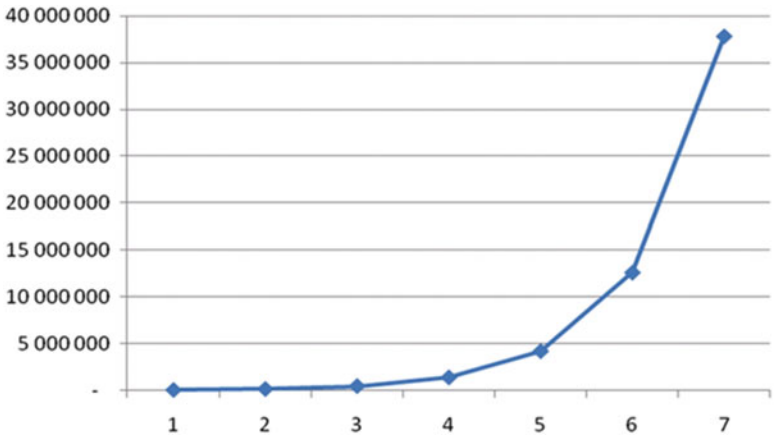

Fig. 5.7 Constructal tree-shaped invasion of a territory: cumulated size of the simulated population

Table 5.3 NOP metric for seven JDK versions

JDK version	NOP
1.0.2	10
1.1.3 beta	28
1.2.2.12	67
1.3.0	78
1.4.0	202
1.5.0	370
6	421

space (the territory) is directly visible in the package structure of the JDK. Each Java package if usually a micro-framework, regrouping a set of classes (i.e., Java programs) addressing a specific functional need (e.g., IO, networking, mathematics, text manipulation, data structures, etc.) The number of Java packages grown from ten packages in the v1.0–421 packages in the v6, as listed in Table 5.3. These packages are organized in hierarchical tree with functional organization. For instance, the new packages of the v2 include a new Graphic User Interface library (Swing), whose source code is located in the src/javax/swing/source directory, which contains nine subdirectories, with one of these directory (src/javax/swing/plaf/) containing three subdirectories, etc. Furthermore, there is also another complex tree—or graph—made of the dependencies between the JDK's classes, i.e., files (at compile time).

The evolution of the total number of packages, visible in Fig. 5.8, also follows a S-curve. Hence, in time, the JDK extended it functional space or territory, by developing new packages inside its source files' tree, populated by new Java classes, meanwhile the older Java classes were often subject to size increase, from one version to a newer. For instance, the GregorianCalendar class, which

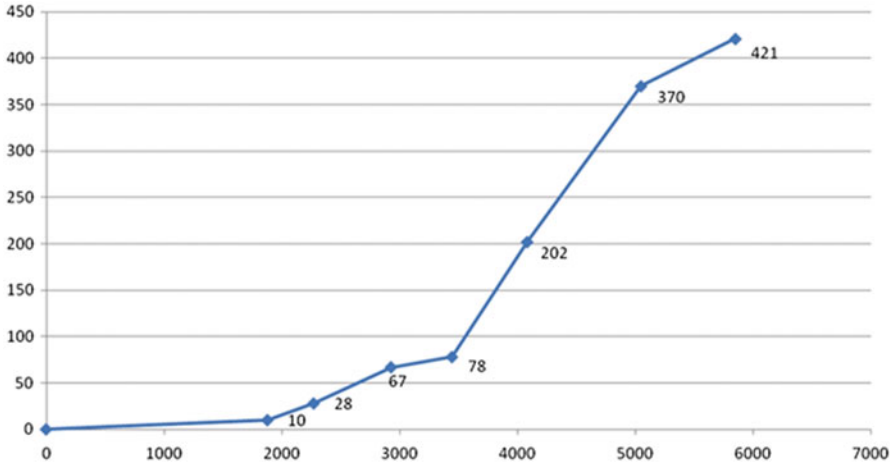

Fig. 5.8 Evolution of the number of Java packages of the JDK

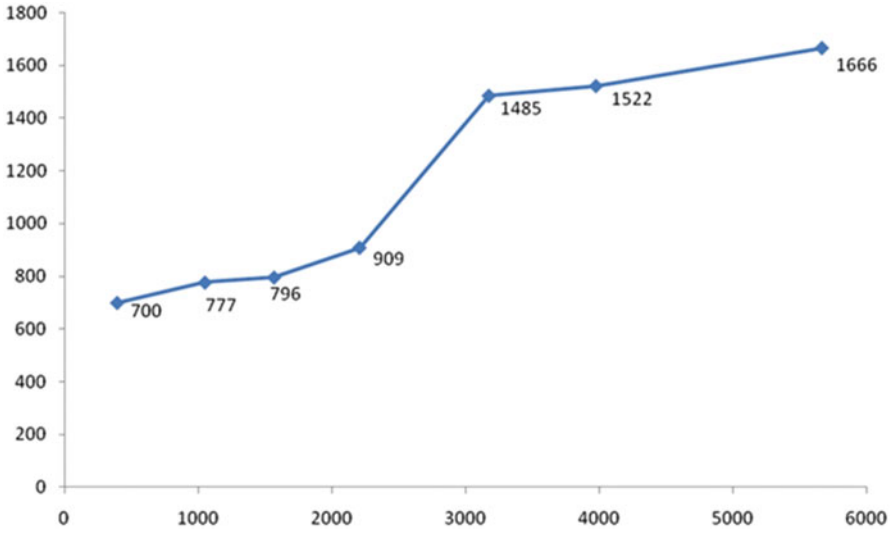

Fig. 5.9 Evolution in time (days) of the NCLOC size of the GregorianCalendar class from the JDK version 1 to version 7

appeared in the JDK 1.1, more than doubled its NCLOC size in the JDK 7, as visible in Fig. 5.9.

Before concluding our discussion on the JDK, we propose to briefly study if this kind of distribution could, maybe, be specific to the JDK lineage's source code. We thus performed the same analysis on the source code of the Zend Framework (ZF) platform. The ZF is an open-source object-oriented (OO) software framework,

Table 5.4 NOSCF and NCLOC metrics for nine ZF's versions, aggregated at the framework size level

ZF version	NOSCF	NCLOC
0.1.3.0	236	15,758
0.2.0	301	25,349
0.6.0	363	31,854
0.8.0	507	49,343
1.0	690	64,377
1.5.0	1,074	94,728
1.8.0	1,684	149,523
1.11.0	2,368	209,196
1.11.9	2,376	210,606
Total	9,599	850,734

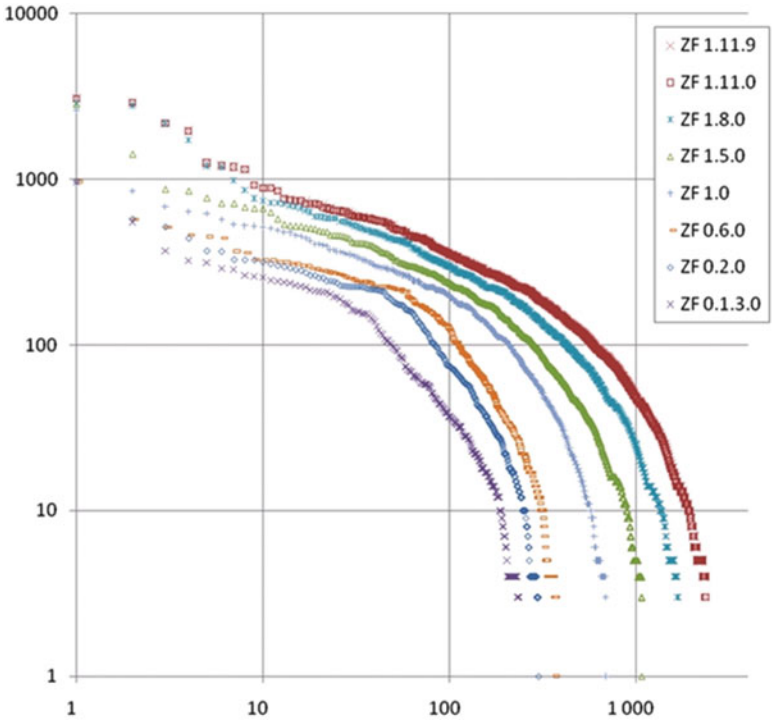

Fig. 5.10 Log–log plot of the NCLOC metric, for eight versions of the ZF over ca. 6.5 years, ranked for every source file

programmed with the PHP language, and based on the PHP platform. The ZF is more specifically dedicated to the development of Web applications.

Similarly to the JDK, the ZF is a very successful software framework, widely used by the PHP developers' community.

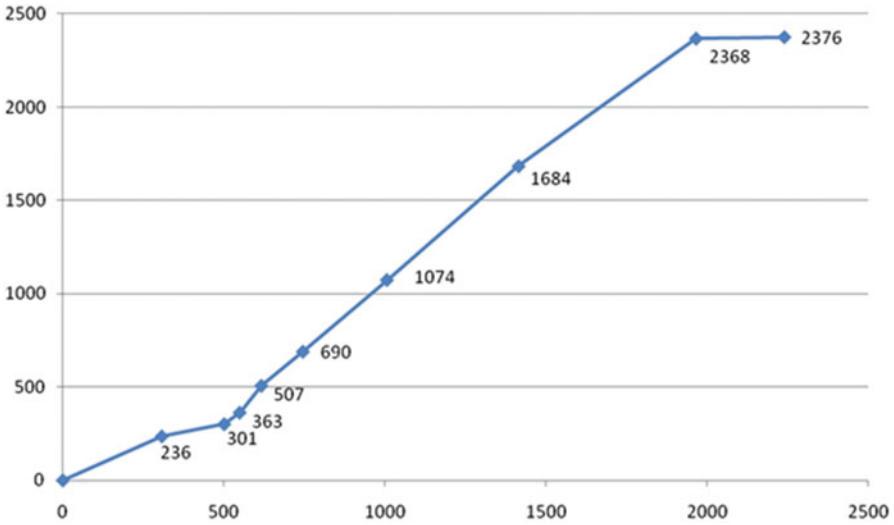

Fig. 5.11 Approximation of the evolution, in time (number of days), of the number of PHP source files for nine version of the ZF

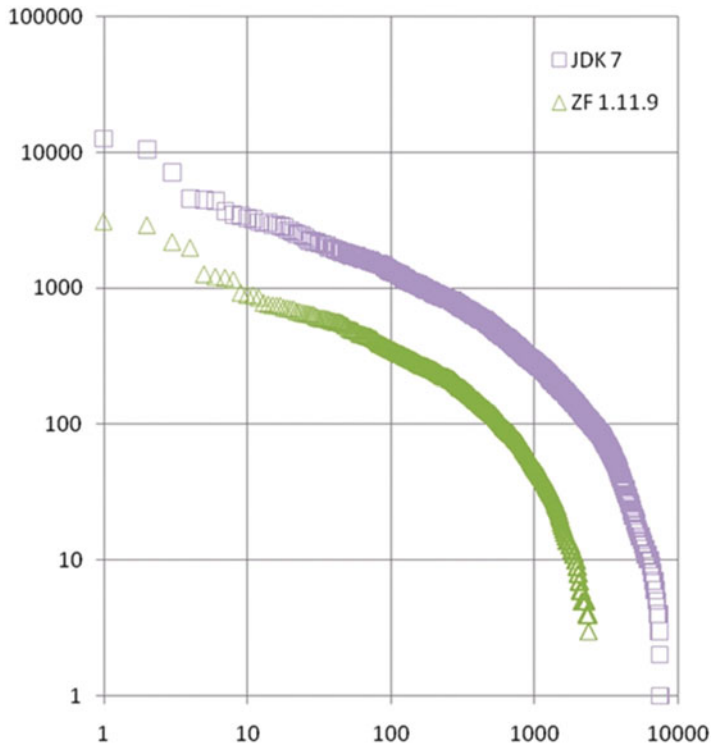

Fig. 5.12 Log–log plot of the ranked distribution of the NCLOC metric of the Java and PHP source files, respectively, for the JDK 7 and ZF 1.11.9

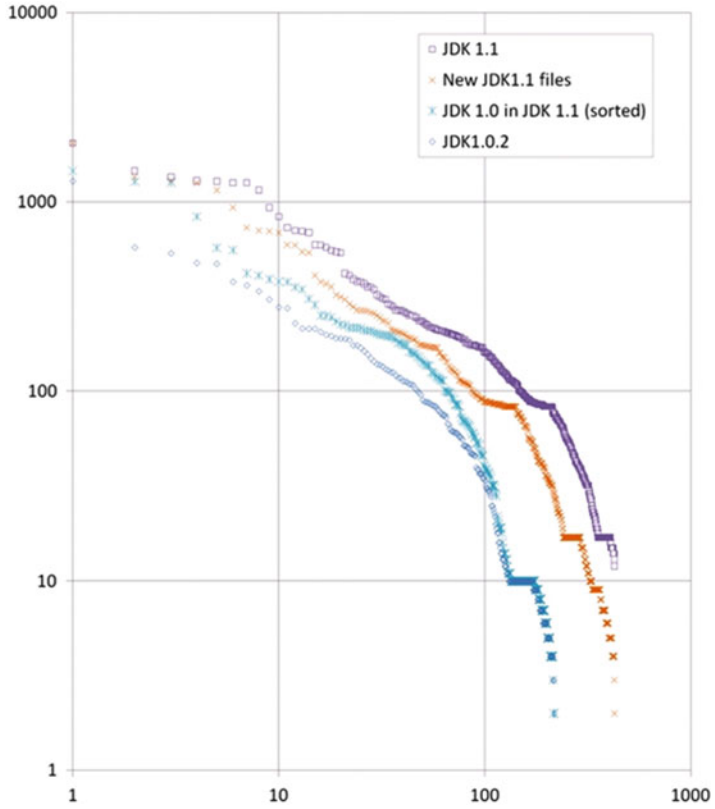

Fig. 5.13 Log–log plot of the ranked distribution of the NCLOC metric of the JDK 1.0 and 1.1 files, showing the old files and new files evolution.

The source code was retrieved from the ZF archive Web page [27]. We used CLOC to calculate the LOC metrics of nine versions of the ZF, aggregated in Table 5.4, released over 6.5 years, between the summer 2005, date when the development started [28] and the last version to date, released in August 2011 (v1.11.9).

Figures 5.10 and 5.11 clearly show that the ZF developed, in time, similar source code size distribution patterns as the JDK's one: a S-curve and a parabolic scaling of the distribution of the ranking of the source code files' sizes. Figure 5.12 displays the distributions of both frameworks, in their last version to date.

These phenomenologically recurring patterns are strong evidences of a same underlying mechanism, and we consider the Constructal Law as an adequate candidate for this purpose.

We also studied the evolution of the size of the Java source files between two consecutive JDK's versions. We considered the JDK 1.0 and 1.1 for this purpose, and the results are shown in Figs 5.13 and 5.14. Interestingly, the 15,343 NCLOC of

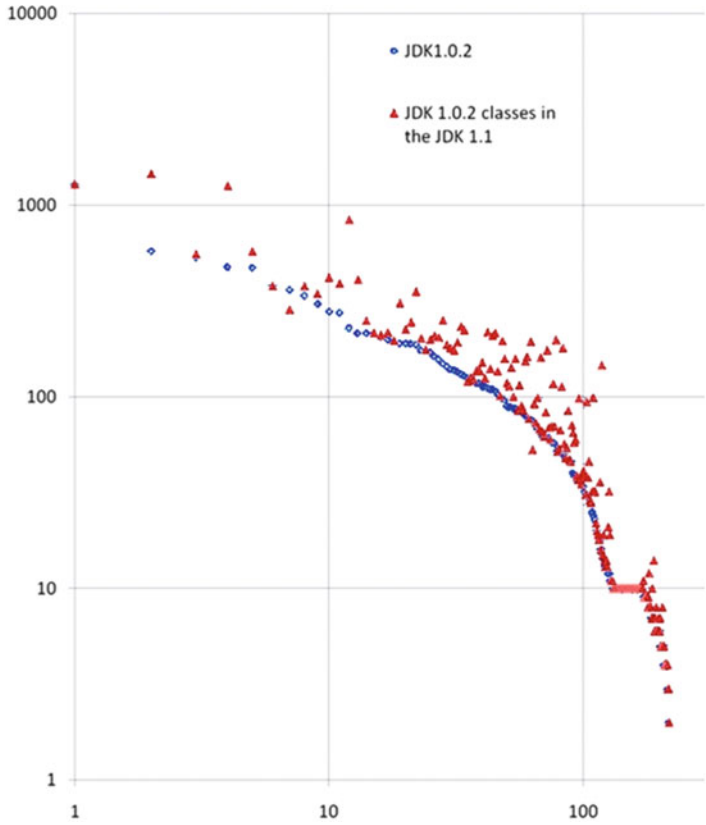

Fig. 5.14 Log–log plot of the ranking distribution of the NCLOC metric for the JDK 1.0 files for both the JDK1.0 and 1.1 version, highlighting the tendency of evolution towards a greater size of the source files between the two versions

the JDK 1.0 source files are 41 % bigger in the JDK 1.1: 6,348 NCLOC were added on 105 files of the 216 initial files, whereas 105 remain at the same size, and 6 files (3 %) decreased in size (total of −114 NCLOC). In the same time, 435 new files appeared in the JDK 1.1, for a total of 38,108 NCLOC. These two facts confirm that, as sketched here above, two mechanisms contribute to the evolution of the rank-size distribution: the growth of the initial source code files, and the adjunction of new source code files, following a distribution similar to the first one. In the specific case of the JDK 1.1, the new Java files constitute a distribution even greater than the initial source files of the JDK 1.0. It must be noticed that the releases of these two versions are separated by ca. 1 year, thus constitute snapshots of the source code very distant in time.

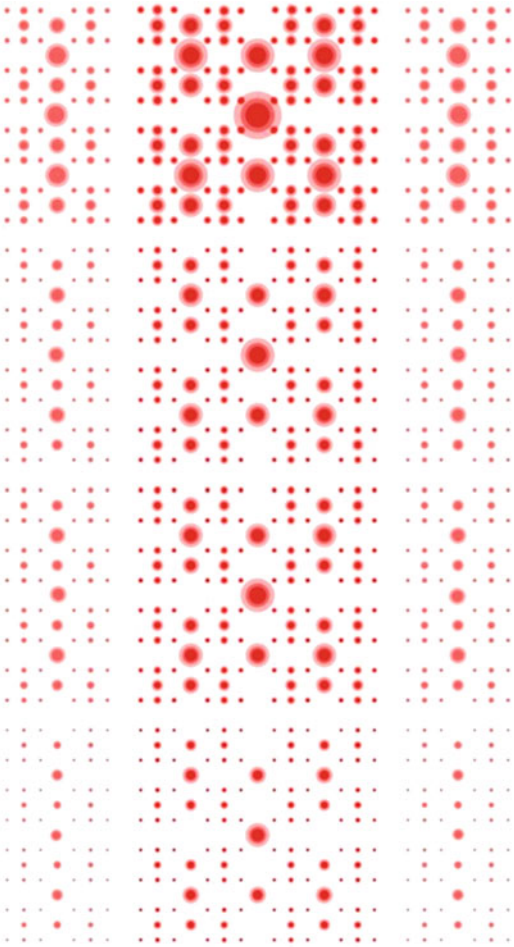

Fig. 5.15 Resulting geometry of a population distribution generated by a simulation of the constructal growth and tree-shaped invasion mechanism

5.7 Conclusion

We have shown in this chapter that during the last 15 years, the rank-size distributions of the source file sizes of the successive versions of the JDK developed typical evolutionary patterns such as a parabolic scaling, and that the cumulated NCLOC or number of classes of the Java source code follows a typical sigmoid shape (S-curve), and we have also shown that these patterns are shared by at least one other OO framework (ZF) with a different functional scope, of a smaller size, developed by a different software developers' community, and based on different language (PHP). These patterns (parabolic scaling, S-curve) are characteristic of Constructal flow systems, as demonstrated by Bejan and Lorente [8], and Queiros-Conde et al. [22].

In order to explain the emergence of parabolic scaling in a constructal flow system, we proposed to consider the constructal tree-shaped invasion of territory combined with the constructal rank-size distribution of a growing population as the mechanism potentially generating a wide variety of population distributions, subject to external factors, and we have shown experimentally, thanks to several numeric simulations, that this mechanism generates distributions with a shorter, curved tail, similar to a parabolic scaling of the distribution. The resulting geometry of a population distribution generated by such a mechanism on a two-dimensional area is depicted in Fig. 5.15.

In the case of the JDK, the functional scope addressed by the successive versions of the platform, assimilated to a functional space to invade, continuously increased in time. The development of the JDK's functional packages hierarchy is interpreted as the constructal tree structure followed by the invasive flow.

It is worth noticing that we do not pretend that the mechanism proposed here accounts for all parabolically scaling distributions encountered in natural, social, or engineered (man-made) systems, but this mechanism seems to fit quite well the domain of software development and is generic enough to cover a wide variety of other phenomena.

According to K. Beck, the father of the Test Driven Design (TDD), "We're just beginning to understand software evolution. [...] How can I maintain focus as I make larger changes in small, safe steps over a long period of time, interleaved with feature development?" [29]. We hope that our study will contribute to a better understanding of the mechanisms and laws underlying the processes of software evolution.

In conclusion, all the elements here above advocate to consider the Constructal Law as the main driver behind the evolution of software programs and call both for the revision of Lehman's law on the basis of this first constructal principle and for further studies on this subject.

References

1. Lehman MM, Belady LA. Program evolution; processes of software change, A.P.I.C. Studies in Data Processing. Vol. 27. Academic; 1985.
2. Fernandez-Ramil et al, Empirical studies of open source evolution, Empirical studies of open source evolution, T. Mens and S. Demeyer eds., *Software Evolution*, Berlin, Springer, 2008, pp. 263–288.
3. Mens T, et al. Software Evolution, Guest Editor Introduction, Software Evolution. IEEE Software. 2010;27(4):22–5.
4. Bejan A. Shape and Structure, from Engineering to Nature. Cambridge: Cambridge University Press; 2000.
5. Bejan A, Lorente S. Design with constructal theory. Wiley; 2008.
6. Bejan A. Constructal-theory network of conducting paths for cooling a heat generating volume. Int J Heat Mass Transfer. 1996;40:799.
7. Bejan A. Advanced Engineering Thermodynamics. 2nd ed. New York: Wiley; 1997. p. 807.

8. Bejan A, Lorente S. The constructal law origin of the logistics S curve. J Appl Phys. 2011;110 (2):024901.
9. Ohloh, Compare Languages, 2011. http://www.ohloh.net/languages/compare. Accessed 10 Sept. 2011
10. TIOBE Software, TIOBE Programming Community Index for September, 2011. http://www.tiobe.com/index.php/content/paperinfo/tpci/index.html. Accessed 10 Sept. 2011
11. Conway D. Ranking the popularity of programming languages, dataist.com. http://www.dataists.com/2010/12/ranking-the-popularity-of-programming-langauges/. Accessed 10 sept. 2011.
12. Gosling J. A brief history of the green project. http://java.sun.com/people/jag/green/index.html. Accessed October 1998.
13. FirstPerson, Inc., Oak Language Specification, Palo Alto, CA 1994.
14. Byous J. Java technology: an early history. 1998. java.sun.com/features/1998/05/birthday.html. Accessed 05 Sept. 2011
15. Henderson-Sellers B. Object-oriented metrics: measures of complexity. Prentice Hall Inc., Upper Saddle River, NJ; 1995.
16. Laherrere J. Distributions de type fractal parabolique dans la Nature. Comptes-Rendus de l'Académie des Sciences, Série IIa n°7-4. 1996;322:535–41.
17. Laherrere J, Sornette D. Stretched exponential distributions in nature and economy: "fat tails" with characteristic scales. Eur Phys J B. 1998;2:525–39.
18. Maillart T, et al. Empirical Tests of Zipf's Law Mechanism in Open Source Linux Distribution. Phys Rev Lett. 2008;101(21):218701.
19. Wheeldon R, Counsell S. Power law distributions in class relationships, eprint arXiv:cs/0305037, To appear in proceedings of third IEEE international workshop on source code analysis and manipulation, 2003, 0:45–54
20. Anderson DJ. Using cumulative flow diagrams, Borland Developer Network, 2004. http://edn.embarcadero.com/article/32410, http://bdn.borland.com/coadletter/agilemanagement. Accessed 25 July 2011
21. Anderson DJ. The S-curve explained, Agile Management, Borland Developer Network, 2004. http://edn.embarcadero.com/article/32411, http://bdn.borland.com/coadletter/agilemanagement. Accessed 25 July 2011
22. Queiros-Conde D, et al. Parabolic scaling of tree-shaped constructal network. Physica A: Statistical Mechanics and its Applications. 2007;384(2):719–24.
23. Bejan A, et al. Section 13.4 Constructal theory of distribution of city sizes. In: Advanced engineering thermodynamics. 3rd ed. Wiley, New York: 2006, p. 774–82.
24. Queiros-Conde D, Feidt M. Constructal theory and multi-scale geometries; theory and applications in energetics, chemical engineering and materials. Les Actes, ENSTA, 2010, p. 117–30
25. Reis AH. Constructal view of scaling laws of river basins. Geomorphology. 2006;78 (3–4):201–6.
26. Bejan A, et al. Constructal distribution of river sizes. In: Advanced engineering thermodynamics. 3rd ed. Wiley, New York; 2006, p. 779–82.
27. Zend Technologies Ltd., Zend Framework Download, Every public release of Zend Framework, all in one place, 2011. http://framework.zend.com/download/archives. Accessed 18 Oct. 2011
28. Weier O'Phinney M, Schindler R. Introducing Zend Framework 2.0, 2010. http://www.slideshare.net/weierophinney/introducing-zend-framework-20. Accessed 18 Oct. 2011
29. Beck K. The inevitability of evolution, software evolution. IEEE Software. 2010;27(4):28–9.

Chapter 6
Constructal Design of High-Conductivity Inserts

J.A. Souza and J.C. Ordonez

6.1 Introduction

Bejan presented the Constructal Theory by solving an optimization problem for the cooling of a heat generating volume [1]. The proposed problem was "how to collect and channel to one point the heat generated volumetrically in a low conductivity volume of given size." The proposed approach defined an elemental construct for which the geometry was optimized. The elemental construct had rectangular shape and consisted of two regions: one region with a low-conductivity material and heat generation and a second region with high-conductivity material that was used to conduct the generated heat to the exterior through one end (Fig. 6.1a). The fraction of high-conductivity material was fixed. More complex forms (assemblies) were obtained by combining the optimized elemental form as shown in Fig. 6.1b–d.

Based on Constructal Theory, a number of authors have solved similar problems for different geometries and assembly levels. These solutions are not restricted to heat conduction, they cover a wide variety of optimization problems where the flow resistance of a given entity can be minimized. The flowing entity can be energy in the form of heat [2], fluid [3, 4], aggregates of organisms [5] or even people [6].

According to Ledezma et al. [7], the major difficulty with the optimization of higher order assembles is the increasing number of degrees of freedom to be optimized. This difficulty is one of the motivations for the present work.

The idea is to develop a solution strategy and an optimization algorithm capable of searching for a geometry that leads to near optimal performance in a computationally efficient way for a heat conduction problem similar to the one of Fig. 6.1.

The proposed strategy, following Constructal Theory, optimizes the cooling solution by minimization of the heat flow resistance. The domain is divided in small

J.A. Souza • J.C. Ordonez (✉)
Department of Mechanical Engineering and Center for Advanced Power Systems
Florida State University, 2525 Pottsdamer St., Room 229, Tallahassee, FL 32310-6046, USA
e-mail: jasouza1974@gmail.co; ordonez@caps.fsu.edu

L.A.O. Rocha et al. (eds.), *Constructal Law and the Unifying Principle of Design*,
Understanding Complex Systems, DOI 10.1007/978-1-4614-5049-8_6,

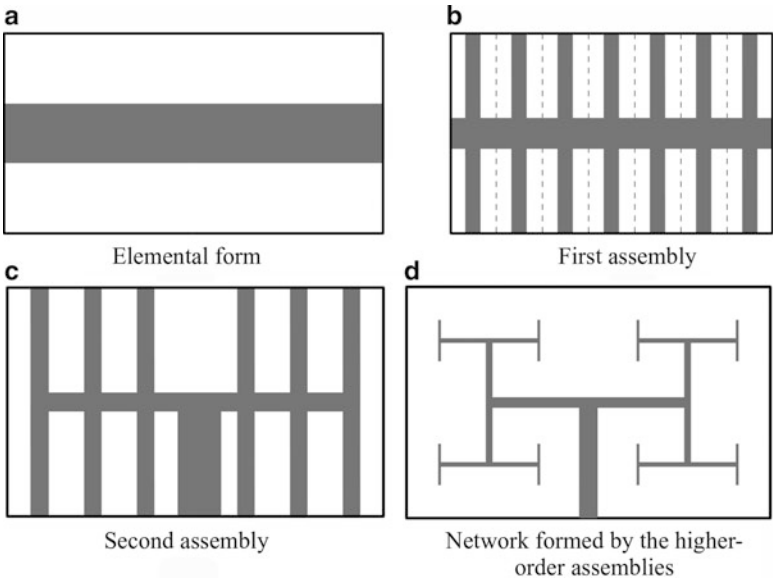

Fig. 6.1 Constructal assemblies [1]

elements and the solution starts with all elements having low conductivity k_0. The temperature and temperature gradient fields are computed and the group of elements (or element) with the highest temperature gradient and low conductivity are exchanged by element(s) with high conductivity k_p. This procedure is repeated until all available high-conductivity material (k_p) has been placed in the computational domain.

There are in the literature similar algorithms. In the work of Errera and Bejan [8] dendritic patterns formed by low-resistance channels in a river drainage basin were reproduced by a porous media model where the drainage channels were predicted using Constructal Theory. In their solution, Darcy's Law was used to formulate the problem and the computational domain was divided in small blocks which were initialized with a base permeability k_0. The first step of the methodology was to determine the pressure field inside the computational domain and use it to estimate the pressure gradients. The process started with the replacement of the block that has the outlet port as one of its four sides. In a second step, the pressure gradient of all neighboring blocks were calculated. If one or more of these gradients was higher than a predefined maximum value, the respective block was replaced by a higher permeability block. The procedure was then repeated for a defined number of steps. This algorithm produced a tree-like forms similar to the patterns observed in a coffee sediment on a concave surface.

Ordonez et al. [9] studied a similar porous media problem. Two criteria, highest pressure and highest pressure gradient, were used to choose the replacement sequence among elements that share at least one face with the high-permeability region. The comparison of these two criteria led to the conclusion that better results can be obtained using the pressure gradient option.

In the present study, both the highest temperature and highest temperature gradient were considered to select the elements that should have their thermal conductivity increased. Better results were obtained using the highest temperature gradient and only those are reported in the following sections.

A more recent work [10] presented an algorithm, called automaton by the authors, that searches for an optimized solution for the problem of how to effectively cool a heat generating surface by arranging the configuration of high-conductivity material inside a fixed area. This algorithm is similar to the one proposed in this work. It discretized the domain in simple elements and uses the temperature gradient to determine the location where high-conductivity material should be positioned, however, it differs from the present approach in how the high-conductivity material is placed inside the domain. In [10] all the high-conductivity material was initially placed inside the computational domain and, at each solution step, elements with high conductivity exchanged their position with elements with low conductivity. In the present work, inspired by the work of Ordonez et al. [9] and Errera and Bejan [8], initially the computational domain has only low-conductivity material (k_0). The high-conductivity material is added to the domain based on the calculated temperature gradient at each solution step. Boichot et al. [10] did not explore if the automaton algorithm is capable of treating the problem in the same way considered here. Another difference between the two methods is that while in the present methodology it is allowed for one element to be placed in isolation, i.e., new elements added to the computational domain do not need to share edges with other high-conductivity elements, in [10] the exchanged elements must be connected, by at least one edge, with the high-conductivity tree. The methods differ also in the numerical approach used to compute the temperature gradient.

6.2 Problem Description

The problem to be solved consists on a solid 2D plate built with two different materials: a low-conductivity and a high-conductivity one. Heat sources are present inside the plate and one or more heat sinks are used to dissipate the heat generated to the ambient. The maximum temperature is monitored and the main goal of the optimization problem is to determine the best possible configuration (location) for the high- and low-conductivity materials in the plate such that the maximum temperature can be minimized. The total amount of available high-conductivity material is constrained. Due to the computational challenge of trying all possible configurations (especially in large domains), we follow an approach similar to Ordonez et al. [9] to search for a nearly optimal configuration.

Figure 6.2 shows one possible geometric configuration for the problem. A rectangular plate with a single heat sink. The internal shaded region represents the high-conductivity material and the white (empty) region represents the low-conductivity material. In this particular example, the heat generation is applied

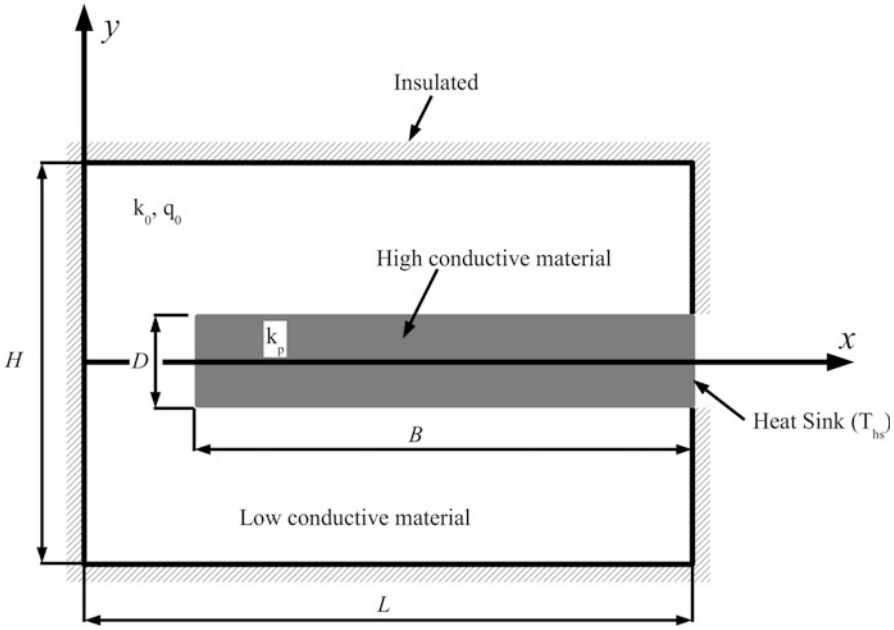

Fig. 6.2 Problem description

only in the regions with low-conductivity material. The dimensions of the plate may vary, however for the optimization problem the plate area is kept constant and equal to $H \times L$.

The problem presented in Fig. 6.2 was first proposed by Bejan as one of the applications of Constructal Theory [1]. The goal is to determine the best shape (H/L) and structure of the high-conductivity material placed within the low-conductivity material in such a way that the heat removed through the heat sink is maximized.

The governing equation for the problem illustrated in Fig. 6.2 is given by

$$k_0 \frac{\partial^2 T}{\partial x^2} + k_0 \frac{\partial^2 T}{\partial y^2} + \frac{q_0}{(A_0 - A_\mathrm{p})W} = 0, \tag{6.1}$$

for the region with low-conductivity material, and

$$k_\mathrm{p} \frac{\partial^2 T}{\partial x^2} + k_\mathrm{p} \frac{\partial^2 T}{\partial y^2} = 0, \tag{6.2}$$

for the region with high-conductivity material.

In (6.1) and (6.2), T is the temperature (K), x and y are the Cartesian coordinates (m) and q_0 is the heat generation rate (W).

In order to compare the present solution with previous work [7, 11] (6.1) must be rewritten in a nondimensional form. Defining the following nondimensional variables

$$(\tilde{x}, \tilde{y}) = \frac{(x, y)}{A_0^{(1/2)}}, \quad \tilde{T} = \frac{T - T_{\text{hs}}}{q''' A_0 / k_0}, \quad \varphi = \frac{A_{\text{p}}}{A_0}, \tag{6.3}$$

where A is the area (m^2), φ the ratio between the areas of the high- and low-conductivity material and the subscripts 0, p and hs indicate low-conductivity material, high- conductivity material and heat sink, respectively.

A constant heat generation rate is present only in the low-conductivity material, Fig. 6.2. The relationship between this heat (q_0) and the volumetric heat generation that appears in (6.3) (q''') is given by

$$q''' = \frac{q_0}{A_0} = \frac{q_0}{HLW}, \tag{6.4}$$

where H is the height, L the length and $W = 1$ the thickness of the computational domain.

Combining (6.1)–(6.4), the nondimensional governing equation for the low-conductivity material is given by

$$\frac{\partial^2 \tilde{T}}{\partial \tilde{x}^2} + \frac{\partial^2 \tilde{T}}{\partial \tilde{y}^2} + \frac{1}{1 - \varphi} = 0 \tag{6.5}$$

and for the high-conductivity material

$$\frac{\partial^2 \tilde{T}}{\partial \tilde{x}^2} + \frac{\partial^2 \tilde{T}}{\partial \tilde{y}^2} = 0. \tag{6.6}$$

Equations (6.5) and (6.6) should be applied in a nondimensional computational domain defined by the variables

$$(\tilde{H}, \tilde{L}, \tilde{D}) = \frac{(H, L, D)}{A_0^{1/2}}, \tag{6.7}$$

which satisfy the nondimensional constant area constraint given by

$$\tilde{H}\tilde{L} = 1. \tag{6.8}$$

The search for the minimization of the maximum temperature in similar problems to the one described in this section has been reported by [7, 10, 11].

6.3 Mathematical and Numerical Formulation

6.3.1 Proposed Algorithm

In a sequential form, the present algorithm can be described as

Stage 1: discretize the computational domain in small elements;
Stage 2: assign the low conductivity (k_0) to the whole computational domain;
Stage 3: set boundary conditions and internal heat generation;
Stage 4: calculate the temperature gradients;
Stage 5: determine, among regions with low-conductivity material, the location of the highest gradients (N_c of them);
Stage 6: set the N_c highest temperature gradient elements with high-conductivity material;
Stage 7: check if $A_p/A_0 < \varphi$;
if true → return to stage 4;
if false → end.

Stages 1–3 define the geometry, grid and boundary conditions. The grid refinement necessary to solve the problem is not only associated with the numerical solution of (6.5) and (6.6), but also with the search for the regions where the high-conductivity material should be placed. Since the high-conductivity material is gradually placed on the regions with higher temperature gradients, it is expected that more refined grids will lead to solutions closer to the optimal one (i.e., the maximum temperature approaches its minimal value). The boundary conditions are set as described in Fig. 6.2.

In *stage 4* the temperature gradients must be evaluated. The temperature profile inside the computational domain is obtained with a Control Volume Finite Element method [12, 13], hereafter referred to as CVFES (Control Volume Finite Element Solver).

Figure 6.3 shows a grid element, built with four points. A local coordinate system (s, t) is used to interpolate the temperature and calculate the pressure gradients inside the element. The shape functions for this element are

$$\left\{\begin{array}{l} N_1 = (s,t) = 0.25(1+s)(1+t) \\ N_2 = (s,t) = 0.25(1-s)(1+t) \\ N_3 = (s,t) = 0.25(1-s)(1-t) \\ N_4 = (s,t) = 0.25(1+s)(1-t) \end{array}\right\}. \tag{6.9}$$

Knowing the four node temperatures T_1, T_2, T_3, and T_4, the temperature at a specific position (s, t) inside the element can be approximated as

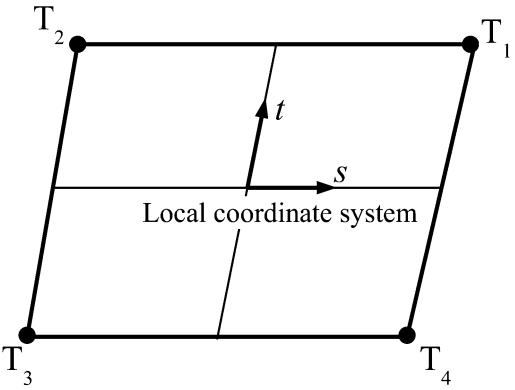

Fig. 6.3 Grid element: temperature gradient calculation

$$T(s,t) = \sum_{i=1}^{4} N_i(s,t) T_i \tag{6.10}$$

and the temperature gradients in the x and y directions can be computed as

$$\left.\frac{\partial T}{\partial x}\right|_{s,t} = \sum_{i=1}^{4} \left.\frac{\partial N_i}{\partial x}\right|_{s,t} T_i, \tag{6.11}$$

$$\left.\frac{\partial T}{\partial y}\right|_{s,t} = \sum_{i=1}^{4} \left.\frac{\partial N_i}{\partial y}\right|_{s,t} T_i, \tag{6.12}$$

where s and t define the local coordinate system, N is the shape function and i the index for the element nodes. A more detailed description of the variables and derivatives interpolations inside the element can be found in [12–14].

For the present analysis, a positive scalar derivative field needs to be calculated. Since, for each element, two derivatives are computed (in the x and y directions) and both may assume a positive or a negative value, a new scalar variable, θ, is defined as

$$\theta = \max\left(\left|\frac{\partial T}{\partial x}\right|, \left|\frac{\partial T}{\partial y}\right|\right). \tag{6.13}$$

In *stage 5*, the scalar field defined by (6.13) will guide the sequential procedure of replacing the low-conductivity elements with the high-conductivity ones.

The sequential substitution procedure is illustrated in Fig. 6.4. Step 0 represents the first temperature field calculation. At this moment, all elements have low conductivity (k_0). In step 1, based on the temperature gradient calculated in step 0, the two ($N_c = 2$) elements, with the highest θ will be replaced by elements with high conductivity (*stage 6*). The procedure is repeated until the number of

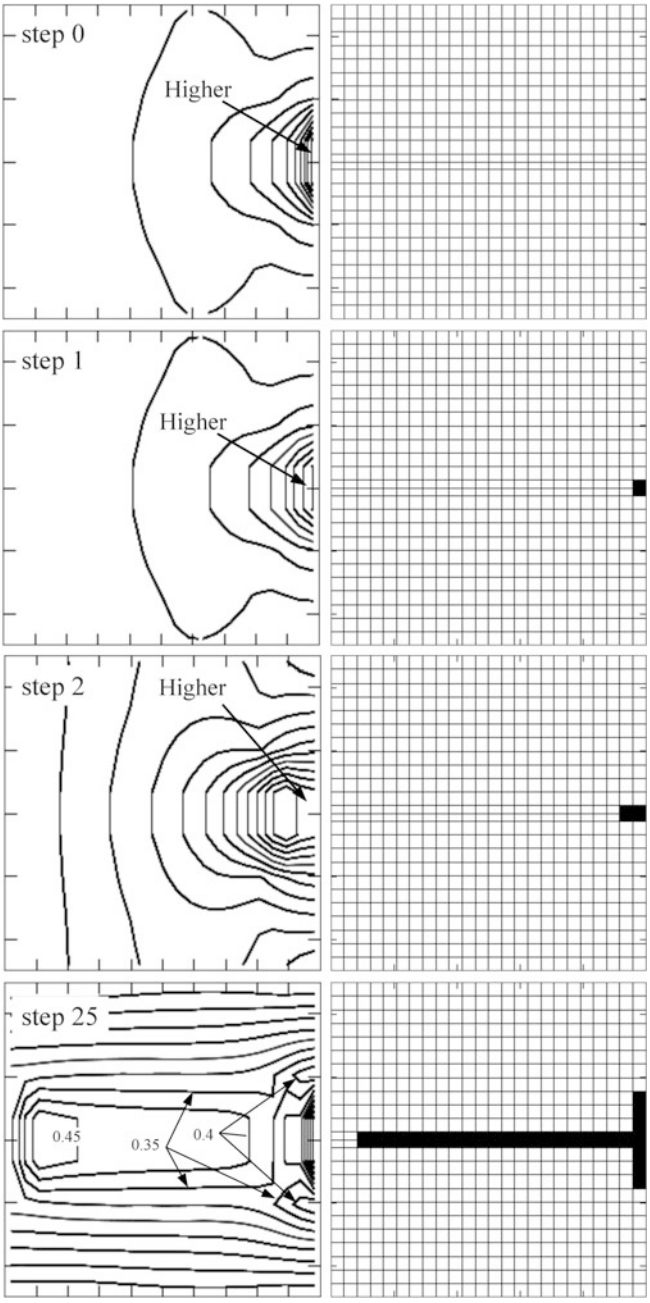

Fig. 6.4 High-conductivity material placing sequence; *left*: temperature gradients (θ), *right*: position of the high-conductivity material ($N_c = 2$, 1,056 elements, $k_p/k_0 = 10$)

Table 6.1 Comparison between the highest temperature results calculated with the CVFES and the FE [11] ($\varphi = 0.1$, $H/L = 1$ (square) and $D/B = 0.15$)

k_p/k_0	CVFES	FE	Difference (%)*
1,000	0.128465	0.128236	0.18
300	0.136147	0.135924	0.16
100	0.157437	0.157219	0.14
30	0.225056	0.224812	0.11
10	0.375526	0.374893	0.17

* difference = 100 * (CVFES-FE)/CVFES

high-conductivity elements is such that $A_p/A_0 > \varphi$ (*stage 7*). Steps 2 and 25 are also shown in Fig. 6.4.

6.3.2 Finite Volume Solver Validation

Equations (6.5) and (6.6) were solved using a CVFES method [12–14]. The validity of the CVFES solution was tested by comparing its solution with the solution obtained with a Finite Element solver in a similar problem [11] shown in Fig. 6.2. All dimensions in Fig. 6.2 are presented in a nondimensional form and the computational domain discretization was performed with rectangular elements. The solution grid independence was tested by assuming square elements with side length $l = 0.005$, 0.01 and 0.015. The grid is built mainly of square elements of edge l, however, since more than one subdomain exists, in some cases the elements are not perfect squares.

The comparison with the problem described in [11] showed a difference between the two solutions (for the maximum temperature inside the geometry) smaller than 0.2 % when the grids with $l = 0.01$ and $l = 0.005$ were used, thus the grid with $l = 0.01$ (approximately 10,000 elements) was selected for the computation of the temperature field. Table 6.1 contains a comparison between the CVFES and the FE [11] solutions for a problem with $\varphi = 0.1$, $H/L = 1$ (square) and $D/B = 0.15$. The grid with $l = 0.01$ was used in this comparison.

6.3.3 Algorithm Validation

The algorithm proposed here is validated by comparing the results obtained for the problem shown in Fig. 6.2 and the solutions presented in [7] and [11] for the elemental, first and second constructs. The main goal of this section is not to completely reproduce the results obtained in by [7] and [11], but only to show that the present solution is capable of generating optimized geometries following a sequential procedure.

The problem considered is a square geometry ($\tilde{H}/\tilde{L} = 1$), with $\varphi = 0.1$ and $k_p/k_0 = 300$. From Almogbel and Bejan [11], it is known that the optimized value

Table 6.2 Validation of the proposed algorithm ($k_p/k_0 = 300$, $\varphi = 0.1$)

Present work[a]		Previous work	
$\tilde{T}_{min}$	Construct	$\tilde{T}_{min}$	Reference
0.0379 ($l = 0.01$)	0	0.125[a]	[11]—Table 3
	0	~0.08[b]	[7]—Fig. 4
0.03357 ($l = 0.005$)	1	0.031[b]	[7]—Table 2
	2	0.0312[b]	[7]—Page 99

[a]Square domain ($\tilde{H}/\tilde{L} = 1$ with optimized $\tilde{D}/\tilde{B} = 0.11$)
[b]Optimized H/L

of $\tilde{D}/\tilde{B}$ for this problem is 0.11. Combining this information, it is possible to set a system of equations:

$$\begin{cases} \dfrac{\tilde{H}}{\tilde{L}} = 1 \\ \tilde{H}\tilde{L} = 1 \\ \dfrac{\tilde{D}}{\tilde{B}} = 0.11 \\ \varphi = \dfrac{\tilde{D}\tilde{B}}{\tilde{H}\tilde{L}} = 0.1 \end{cases} . \tag{6.14}$$

The solution of (6.14) will result in $\tilde{L} = 1, \tilde{H} = 1, \tilde{D} = 0.104881$ and $\tilde{B} = 0.953463$. Note that $\tilde{B}$ is not used in the present solution.

Table 6.2 present a comparison between the proposed solution with optimized solutions of the elemental, first and second constructs. Only one problem has been solved here, the square geometry with fixed heat sink height ($D = 0.104881$), and it is compared with four different solutions obtained by [7] and [11]. The first column in Table 6.2 indicates the minimum hot-spot temperature found following the proposed approach using two different meshes ($l = 0.01$ and $l = 0.005$). The second column contains the construct level, and the third and fourth columns correspond to results reported in [7] and [11]. The first row contains the optimized solution for a square geometry and the elemental construct. This is the simplest possible configuration and has the highest minimum temperature among the cases being compared. Row 2 shows that only changing the external shape (H/L) leads to a lower maximum temperature. Increasing the complexity of the system, i.e., increasing the construct level, will lead to lower maximum temperatures inside the computational domain. This can be seen in rows 3 and 4 of Table 6.2, with the first and second constructs, respectively.

In Table 6.2 is also possible to see that increasing the complexity of the problem, either by refining the grid in the present solution or by increasing the construct level, leads to approximately the same maximum (nondimensional) temperature of 0.03.

Figure 6.5 shows the high-conductivity material distribution inside the computational domain. The symmetry is obtained automatically when $N_c = 2$ is selected.

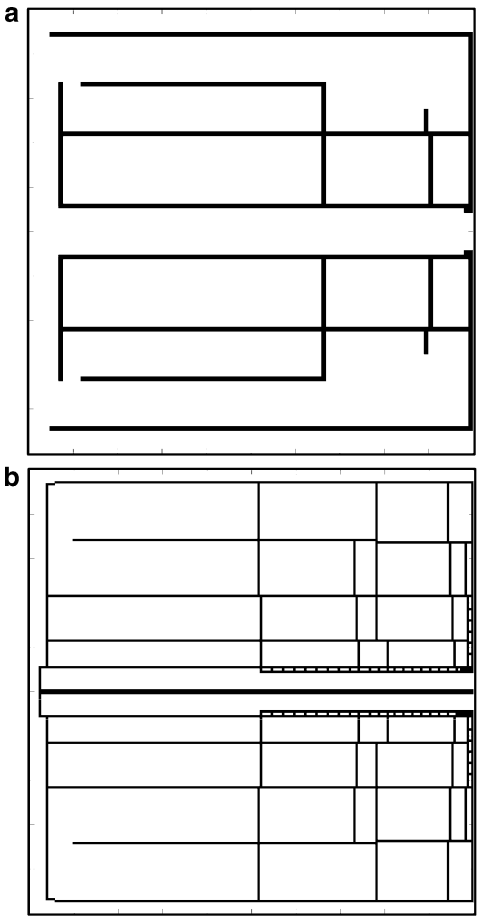

Fig. 6.5 Geometry obtained for the validation solution ($N_c = 1$, $k_p/k_0 = 300$, $\varphi = 0.1$, $\tilde{L} = 1$, $\tilde{H} = 1$, $\tilde{D} = 0.104881$ and $\tilde{B} = 0.953463$); a: grid $l = 0.01$, b: grid $l = 0.005$

This means that at every simulation step, two low-conductivity elements will be replaced by two high-conductivity elements. There is no need to impose any kind of symmetry verification in the code. Other interesting point that can be observed in Fig. 6.5 is that as predicted by the Constructal Theory, heat channels form naturally to facilitate the overall system cooling. Again, there is no imposition made to the algorithm to force that the new high-conductivity elements be placed next to an already existent high-conductivity element.

6.4 Influence of k_p/k_0 and N_c on the Solution

The shape of the high-conductivity insert that results with the present algorithm depends on both the ratio k_p/k_0 and the number of elements with low-conductivity material replaced (in every solution step) by elements with high-conductivity material, N_c. Figure 6.6 illustrates a map of the solution (maximum temperature)

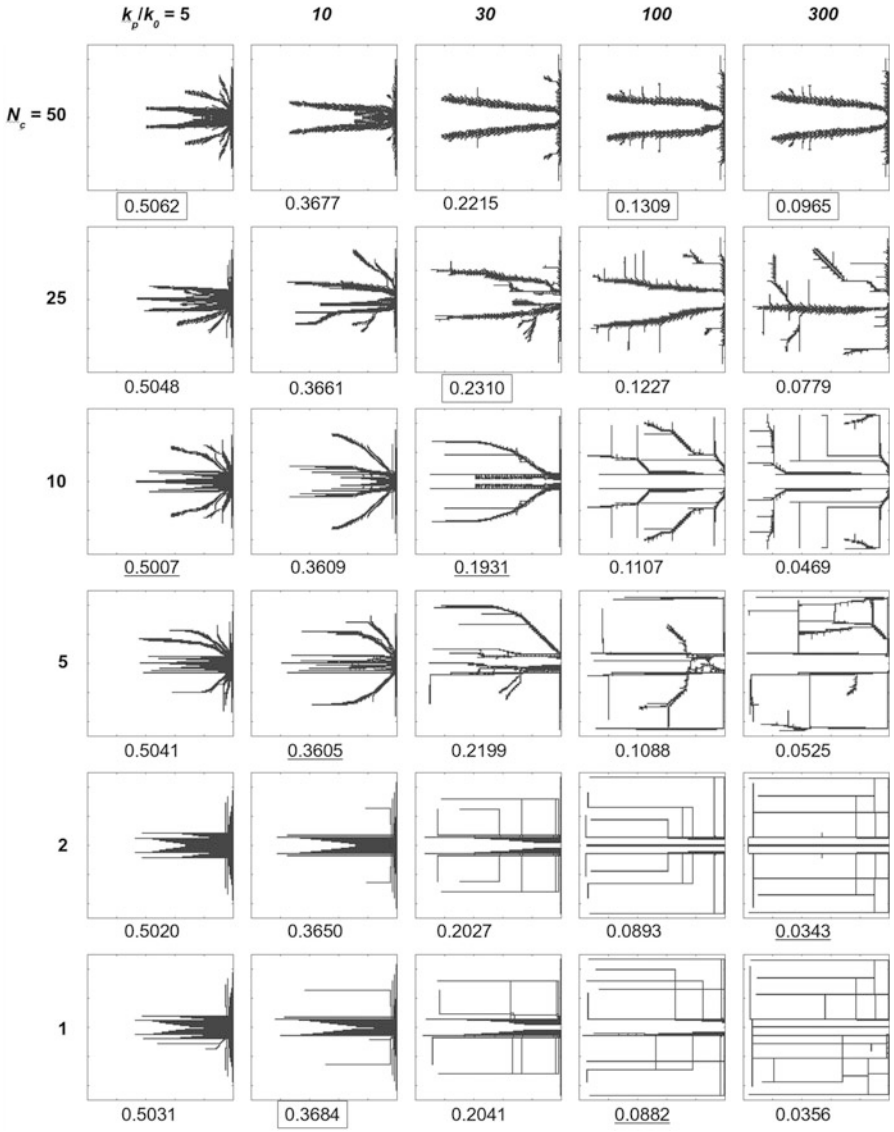

Fig. 6.6 Analysis of the N_c and k_p/k_0 parameters influence on the tree like patterns formation ($\varphi = 0.1$, grid with 19,880 element)

for $k_p/k_0 = 5$, 10, 30, 100 and 300 and $N_c = 1$, 2, 5, 10, 20 and 50. In each column, the highest and lowest minimum temperatures are highlighted in Fig. 6.6 with a border box and underlined text, respectively.

In Fig. 6.6, it can be observed that tree-like geometries, like those predicted by Constructal Theory are formed naturally (recall that we do not force the elements to

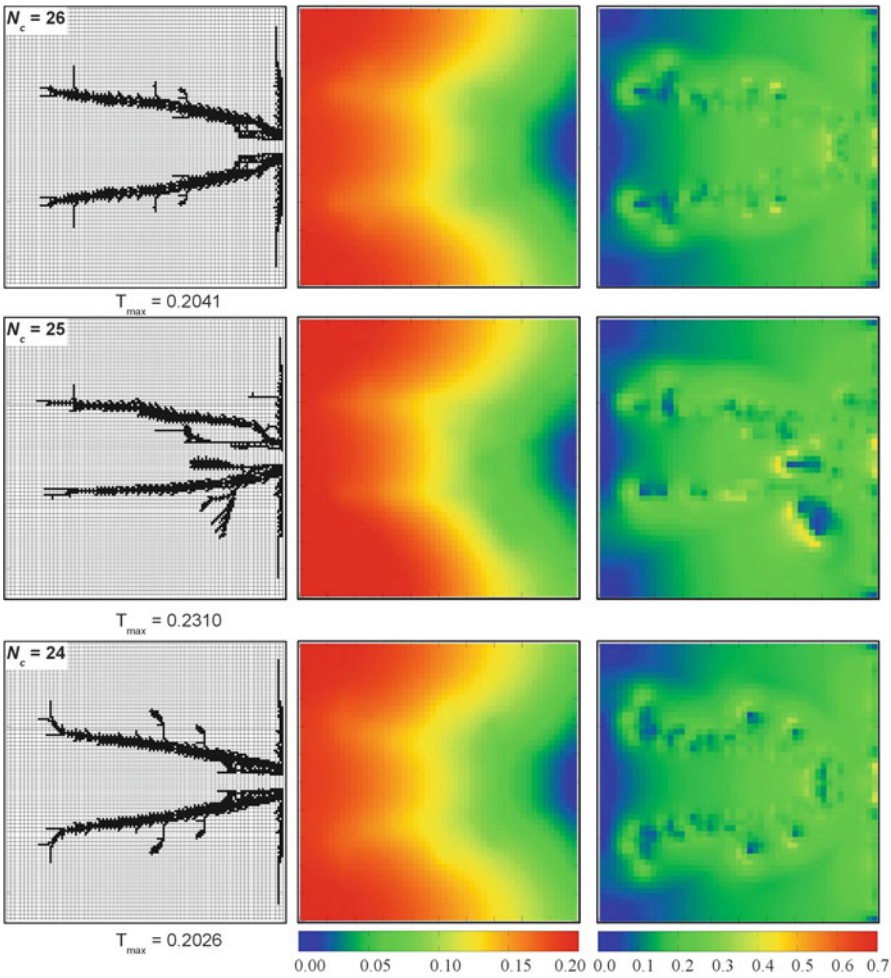

Fig. 6.7 Pattern formation, temperature and temperature gradient for $N_c = 24$, 25 and 26 ($k_p/k_0 = 30$, $\varphi = 0.1$, $\tilde{L} = 1$, $\tilde{H} = 1$, $\tilde{D} = 0.104881$ and $\tilde{B} = 0.953463$)

be adjacent). Also in Fig. 6.6 it can be noticed that an even N_c produces a symmetric structure while and odd N_c will produce an asymmetric one.

An unexpected result in Fig. 6.6 is that the best solution among the cases considered is not associated with the lowest N_c. Further studies are necessary to fully explore this behavior. It must be remembered that the time needed to solve the problem is inversely proportional to N_c. In this way, if a high N_c is used, it is possible to get a fast solution that is close to the optimal one.

Figure 6.7 illustrates the resulting high conductivity patterns (left), the temperature field (center) and the temperature gradient (right) for three consecutive values of N_c ($N_c = 24$, 25 and 26) and a thermal conductivity ratio $k_p/k_0 = 30$. Tree like

structures are observed for all three cases. It is also possible to notice that for the cases considered, the peak temperature does not monotonically decrease with the decrease of N_c.

6.5 Nonuniform Heat Generation

In this section, the cooling of a rectangular plate with one or more heat sources is considered. The problem is to determine the positioning of the high-conductivity material that will produce the minimum maximum temperature. The problem differs from the ones of previous sections by the fact that the heat generation is no longer uniform through the low-conductivity domain, but localized in given location(s). Both high- and low-conductivity materials can be placed in these regions.

The problem of how to assemble a number of heat sources on a plate of given area and ensure that the maximum temperature is kept below an acceptable value can be treated in at least two ways. The first, and more common [15–17], is to determine the best location for these heat sources inside the available area in order to minimize the maximum temperature. The second situation occurs when the heat source locations have a predetermined position and cannot be moved. In this case it is necessary to find other ways to minimize the maximum temperature. Possible solutions are to increase the cooling rate with the inclusion of fins, a fan, or exchange the plate material with a material with higher conductivity. In this work, this second type of problems is analyzed. The idea is not to exchange the whole plate with one of higher conductivity (and likely more expensive) material, but to optimize the use of this high-conductivity material by adding just the needed quantity of it in a low-conductivity (low cost) material plate.

6.5.1 One Source Problem

First, a one source problem (Fig. 6.8) is analyzed. The computational domain is a rectangular area with dimensions L and H with a rectangular heat source (with side length D_s). The heat source center point is located at (x_s, y_s). The total heat being generated within the source is constant and equal to q_{gen}.

Again, the constant total area constraint is applied ($LH = A_0$). The problem is also solved in a nondimensional form. Additional nondimensional variable needed are:

$$\tilde{D}_s = \frac{D_s}{A_0^{1/2}}, \quad \varphi_s = \frac{A_s}{A_0} = \frac{\tilde{D}_s^2}{\tilde{H}\tilde{L}}\tilde{x}, \quad \tilde{y} = \frac{x, y}{A_0^{1/2}}. \tag{6.15}$$

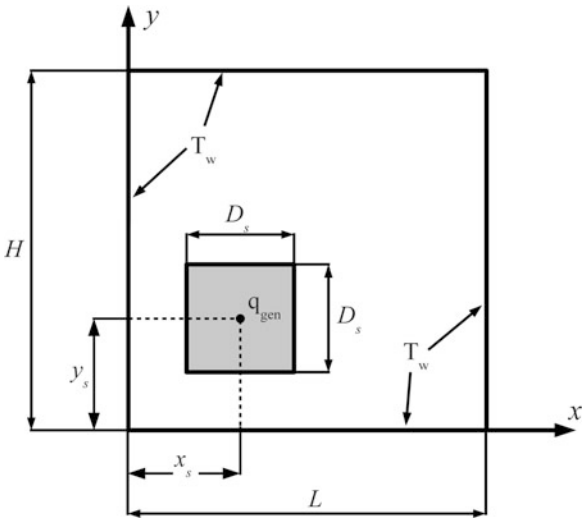

Fig. 6.8 The one source problem sketch

In a general form, (6.1) can be rewritten as

$$k\frac{\partial^2 T}{\partial x^2} + k\frac{\partial^2 T}{\partial y^2} + q''' = 0, \tag{6.16}$$

where k can assume values of k_0 or k_p. The volumetric heat generation term, q''', is defined as

$$q''' = \frac{q_{gen}}{A_s W}, \tag{6.17}$$

where W is the plate thickness and equal to 1 m. Combining (6.3), (6.15), (6.16) and (6.17), the resulting heat conduction equation for the regions with heat generation will be:

$$\frac{\partial^2 \tilde{T}}{\partial \tilde{x}^2} + \frac{\partial^2 \tilde{T}}{\partial \tilde{y}^2} + \frac{k_0}{k} = 0 \tag{6.18}$$

and for regions without heat generation:

$$\frac{\partial^2 \tilde{T}}{\partial \tilde{x}^2} + \frac{\partial^2 \tilde{T}}{\partial \tilde{y}^2} = 0. \tag{6.19}$$

In this section all boundaries are kept at $\tilde{T}_w = 0$.

Figure 6.9 illustrates different solutions to the one source problem. Figure 6.9a–c illustrate three basic solutions to be compared with the proposed algorithm. The heat generation (source) is uniformly distributed in a square area of central

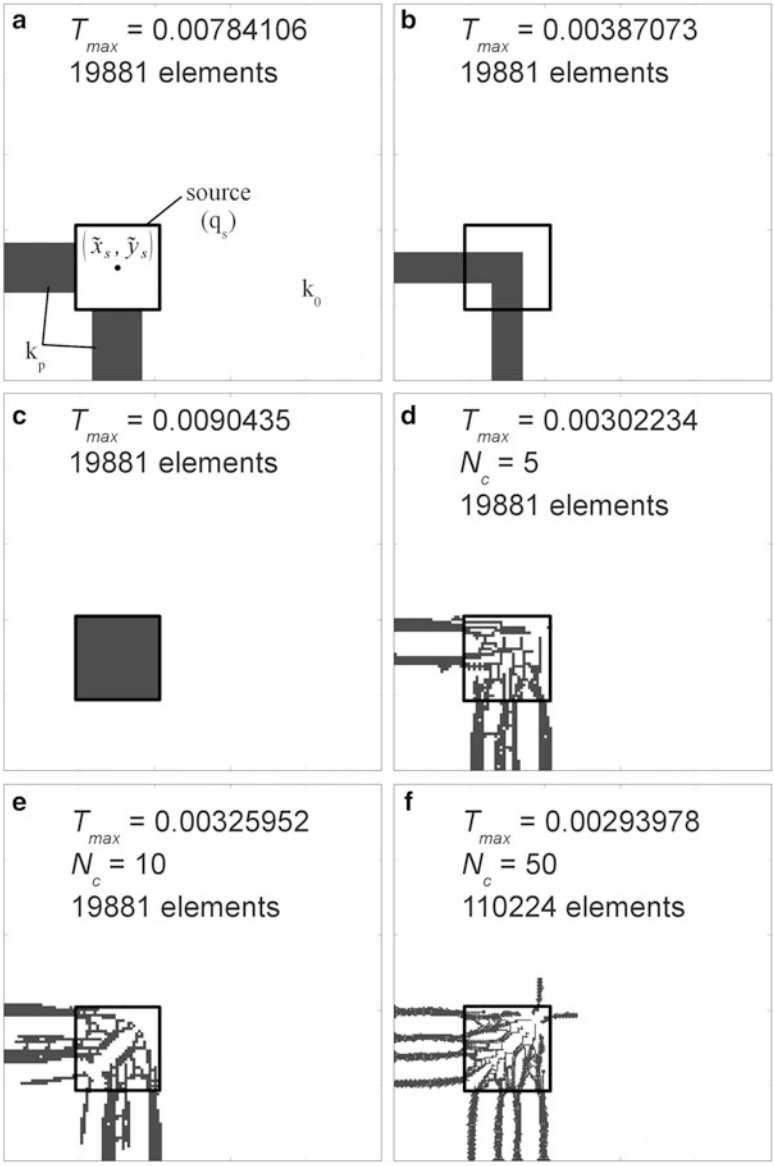

Fig. 6.9 The one source problem solution ($\varphi = \varphi_s = 0.05$, $k_p/k_0 = 30$, $\tilde{x}_s = 0.3$, $\tilde{y}_s = 0.3$)

coordinates $\tilde{x}_s = 0.3$ and $\tilde{y}_s = 0.3$ and the computational domain is also square ($H = L$).

In Fig. 6.9a, the heat source is connected by two "heat channels" with the two closest domain walls at temperature $\tilde{T}_w = 0$. When compared with results presented in Fig. 6.9d, it is clear that a lower maximum temperature can be obtained with the

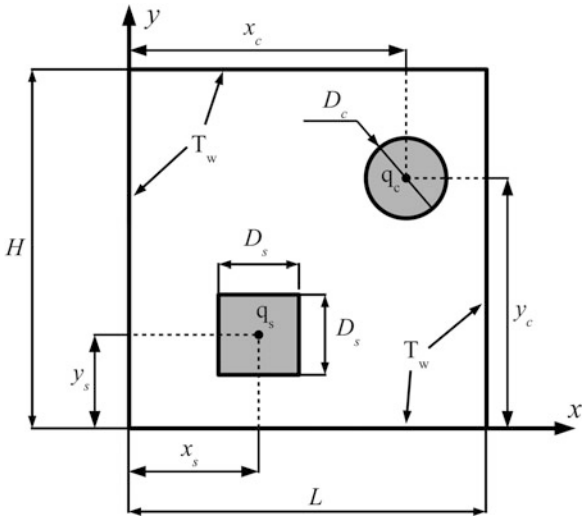

Fig. 6.10 The two sources problem sketch

same amount of high-conductivity material. The analysis of Fig. 6.9d suggests that part of the high-conductivity material should be placed inside the heat source area, thus a second configuration, Fig. 6.9b, was tested and the maximum temperature obtained with this second configuration was reduced to 0.00387073. The extreme is to place all high-conductivity material inside the heat source region (Fig. 6.9c), however this configurations is not optimal because there are no heat channels connecting the heat generation with the domain walls (heat sink).

In Fig. 6.9e, f the same analysis of Fig. 6.9d is performed for $N_c = 10$ and 50. As already discussed in this work, if the problem has a symmetry axis, the use of an even N_c will lead to a symmetrical solution.

In Fig. 6.9f a very refined grid was used. It shows a geometry similar to the geometry shown in Fig. 6.9e, however the four small legs (connections) that do not touch the domains walls in Fig. 6.9e are now complete and better formed. With the more refined grid, the proposed algorithm was capable of building four well formed connections between the heat source area and the domain walls (heat sink). This configuration led to the minimum maximum temperature of all configurations shown in Fig. 6.9.

6.5.2 The Two Sources Problem

In this section, a second source is added to the problem presented in Fig. 6.8. The new problem is illustrated in Fig. 6.10. Now, the same computational domain ($H \times L$) has two sources, one square with side length D_s, and one circular with diameter D_c, both shown in Fig. 6.10. The two heat sources have their center points

located at (x_s, y_s) and (x_c, y_c), respectively. The total heat being generated within the two sources is constant and equal to $q_{gen} = q_c + q_s$.

Additional nondimensional variables are:

$$\tilde{D}_c = \frac{D_c}{A_0^{1/2}}, \quad \varphi_c = \frac{A_c}{A_0} = \frac{\tilde{D}_c^2}{\tilde{H}\tilde{L}}. \tag{6.20}$$

Equation (6.16) applies to regions with heat generation. The new volumetric heat generation term assumes the form

$$q''' = \frac{q_{gen}}{(A_c + A_s)W}. \tag{6.21}$$

Applying (6.21) to the areas A_c and A_s, the volumetric heat sources can be calculated as

$$q'''_c = \frac{q_{gen}}{(A_c + A_s) \times 1} \frac{A_c}{(A_c + A_s) \times 1} = \frac{q_{gen} A_c}{(A_c + A_s)^2} \tag{6.22}$$

and

$$q'''_s = \frac{q_{gen}}{(A_c + A_s) \times 1} \frac{A_s}{(A_c + A_s) \times 1} = \frac{q_{gen} A_s}{(A_c + A_s)^2}. \tag{6.23}$$

Combining (6.15), (6.16), (6.18), (6.21)–(6.23) the resulting heat conduction equations for the square and circular source regions are given by

$$k\frac{\partial^2 \tilde{T}}{\partial x^2} + k\frac{\partial^2 \tilde{T}}{\partial y^2} + k_0 \left[\frac{\pi}{4}\left(\frac{\tilde{D}_c}{\tilde{D}_s}\right)^2 + 1\right]^{-1} = 0, \tag{6.24}$$

$$k\frac{\partial^2 \tilde{T}}{\partial x^2} + k\frac{\partial^2 \tilde{T}}{\partial y^2} + k_0 \left[\frac{4}{\pi}\left(\frac{\tilde{D}_s}{\tilde{D}_c}\right)^2 + 1\right]^{-1} = 0. \tag{6.25}$$

Results for various N_c and k_p/k_0 parameters are shown in Fig. 6.11. In this figure, the central coordinates of the square and circular sources are $(\tilde{x}_s, \tilde{y}_s) = (0.3, 0.2)$ and $(\tilde{x}_c, \tilde{y}_c) = (0.65, 0.55)$, respectively. These values were chosen to guarantee the asymmetry of the problem. From Fig. 6.11 it is possible to observe that each source establishes a high-conductivity channel connection with the two closest walls (heat sinks) and that this connection is stronger (wider channel or multiple channels) with the closest wall. This phenomenon can be more clearly visualized for small k_p/k_0 and large N_c values. The bottom wall is the closest to the squared source and the right wall is the closest to the circular source.

Similarly to Fig. 6.6, it is not possible to associate the best performance with the N_c variable (possibly due to mesh limitations). In the solutions highlighted in

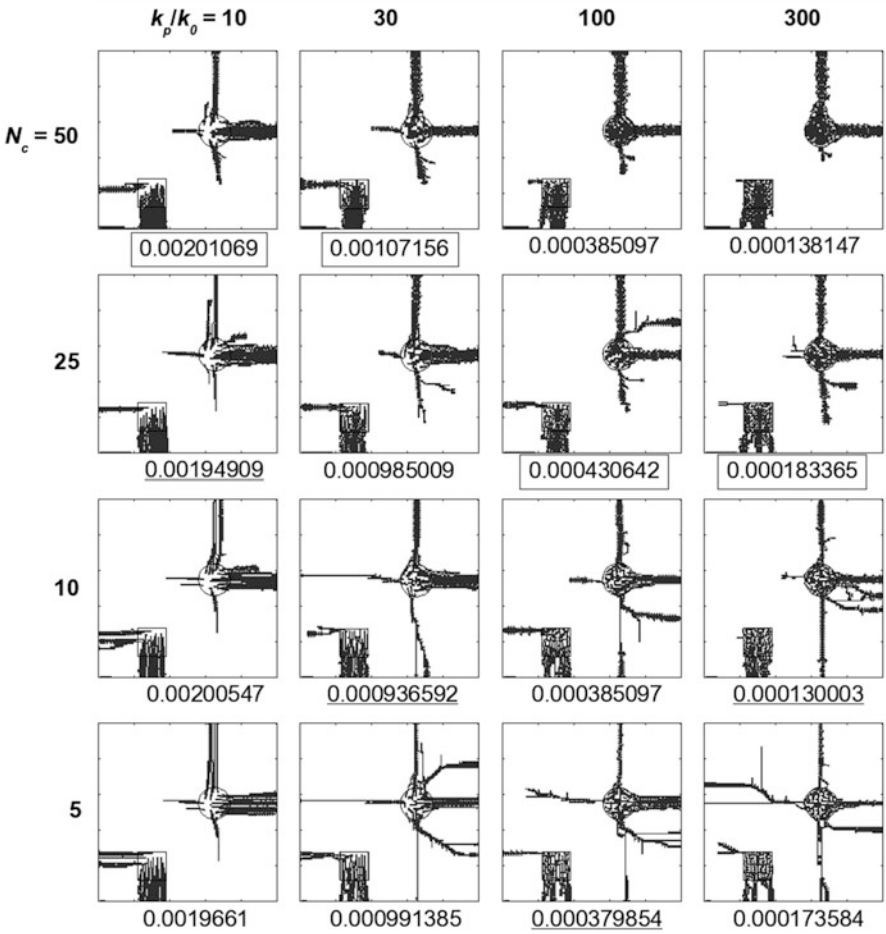

Fig. 6.11 The two sources problem maximum temperature analysis for various N_c and k_p/k_0 ($\varphi = 0.1$, $\varphi_c = \varphi_s = 0.025$, $(\tilde{x}_s, \tilde{y}_s) = (0.3, 0.2)$, $(\tilde{x}_c, \tilde{y}_c) = (0.65, 0.55)$, 18,360 elements)

Fig. 6.6 with the temperatures values inside a box (worst case in each column), it is possible to observe unfinished heat channels that do not reach the domain walls. The best solutions (underlined temperatures), seem to be associated with narrow and mostly complete heat channels.

6.6 Conclusions

A methodology, based in the Constructal Law, was proposed to implement a simple and efficient numerical algorithm that with a non iterative procedure is capable of generating optimized geometries for composite plates consisting of two materials of different thermal conductivities with uniform or localized heat sources. Starting

from an homogeneous plate with conductivity k_0 and one or more heat sources; the plate is divided in small elements and then, based on the computed temperature derivative field, one or more low-conductivity elements are exchanged with elements of higher conductivity k_p. The procedure is repeated until that all available high-conductivity material is placed inside the computational domain. The main goal of the optimization is to minimize the maximum temperature inside the plate. Previous solutions for a plate with uniform heat generation are used to validate the proposed algorithm.

It is possible to see the proposed approach as one in which the elemental construct geometry is given by the size and shape of the elements being replaced (dictated by the mesh) and the assembly levels (higher constructs) correspond to the number of times that N_c low-conductivity elements have been placed within the domain.

The results have been validated by comparison with previous constructal solutions. Results showed that:

- The structures obtained are a function of the grid and the number of elements exchanged in each solution step (N_c).
- The structures that emerge are highly dependent upon the thermal conductivity ratio of the two materials.
- For a symmetric problem, if an even number of element, N_c is replaced, the resulting structure will exhibit symmetry. If N_c is an odd number an asymmetric structure will appear.
- The methodology does not preclude isolated high-conductivity patches from appearing, however the results indicate that the tree-like and dendritic structures arise naturally.

At the end, two cases of localized heat sources are considered to demonstrate the capability of the proposed methodology to determine desirable structures for the high-conductivity paths. They also demonstrate that an increase in the complexity of the problem does not significantly increase the complexity of the present approach.

References

1. Bejan A. Constructal-theory network of conducting paths for cooling a heat generating volume. Int J Heat Mass Transfer. 1997;40:799–816.
2. Wei S, Chen L, Sun F. The area-point constructal optimization for discrete variable cross-section conducting path. Appl Energy. 2009;86:1111–8.
3. Wechsatol W, Ordonez JC, Kosaraju S. Constructal dendritic geometry and the existence of asymmetric bifurcation. J Appl Phys. 2006;100:113514.
4. Rocha LAO, Lorente S, Bejan A. Tree-shaped vascular wall designs for localized intense cooling. Int J Heat Mass Transfer. 2009;52:4535–44.
5. Miguel AF, Bejan A. The principle that generates dissimilar patterns inside aggregates of organisms. Phys A: Stat Mech Appl. 2009;388:727–31.

6. Reis AH. Constructal view of the scaling laws of street networks—the dynamics behind geometry. Phys A: Stat Mech Appl. 2008;387:617–22.
7. Ledezma G, Bejan A, Errera M. Constructal tree networks for heat transfer. J Appl Phys. 1997;82:89–100.
8. Errera M, Bejan A. Deterministic tree networks for river drainage basins, fractals—an interdisciplinary. Fractals 1998;6:245–61.
9. Ordonez J, Bejan A, Cherry R. Designed porous media: optimally nonuniform flow structures connecting one point with more points. Int J Therm Sci. 2003;42:857–70.
10. Boichot R, Luo L, Fan Y. Tree-network structure generation for heat conduction by cellular automaton. Energy Convers Manage. 2009;50:376–86.
11. Almogbel M, Bejan A. Conduction trees with spacings at the tips. Int J Heat Mass Transfer. 1999;42:3739–56.
12. Souza JA. Implementação de um método de volumes finitos com sistema de coordenadas locais para a solução acoplada das equações de navier-stokes. Universidade Federal de Santa Catarina - UFSC; 2000.
13. Schneider GE, Raw MJ. Control volume finite-element method for heat-transfer and fluid-flow using colocated variables 1: computational procedure. Numer Heat Transfer. 1987;11:363–90.
14. Souza JA, Maliska CR. Analysis of a volume based finite element methodology in view of the interpolation function employed and coupling characteristics. In: 12th Brazilian Congress of Thermal Sciences and Engineering - ENCIT Porto Alegre-RS, 2000.
15. Hengeveld DW, Braun JE, Groll EA, Williams AD. Optimal placement of electronic components to minimize heat flux nonuniformities. J Spacecraft Rockets. 2011;48:556–63.
16. Jeevan K, Quadir G, Seetharamu K, Azid I. Thermal management of multi-chip module and printed circuit board using fem and genetic algorithms. Microelectron Int. 2005;22:3–15.
17. Felczak M, Wiecek B, De Mey G. Optimal placement of electronic devices in forced convective cooling conditions. Microelectron Reliab. 2009;49:1537–45.

Chapter 7
Constructal Design of T-Shaped Water Distribution Networks

P. Bieupoude, Y. Azoumah, and P. Neveu

7.1 Water and Water Distribution Networks

More than one billion people do not have access to clean drinking water both in urban and rural areas in the world. This is why, according to a number of scientists involved in drinking water engineering, hundreds of kilometers of networks for water distribution will be constructed or rehabilitated in the coming decades because of both population growth and the crucial need of water services. Therefore the need to optimally design these systems will be increasing everywhere (North and South) and will keep on increasing, in particular in developing countries, very poorly equipped and in need to make strong efforts for the construction of such systems. According to literature, the three main design constraints that are generally met in water distribution projects are water quality, pumping energy, and investment cost [1–4]. In most of the cases, the design problem formulates as follows: "a certain population of density σ_p grouped in households, distributed over a given area, needs to be supplied in drinking water through a distribution network. A lot of technically acceptable solutions can be found to this problem. Some methods differ from the others in terms of total head losses, overall residence time, initial or total investment due to the design" [5]. The challenge for engineers relies on how to optimally design the network in terms of pumping energy and the evolution of water quality in the network.

P. Bieupoude (✉) • Y. Azoumah
LESEE-2iE, Laboratoire Energie Solaire et Economie d'Energie, Institut International d'Ingénierie de l'Eau et de l'Environnement, 01 BP 594 Ouagadougou 01, Burkina Faso
e-mail: pascal.bieupoude@gmail.com; yao.azoumah@2ie-edu.org

P. Neveu
Laboratoire Procédés Matériaux et Energie Solaire, PROMES-CNRS UPR 8521, Université de Perpignan, Rambla de la thermodynamique, Tecnosudm, 66100 Perpignan cedex, France
e-mail: neveu@univ-perp.fr

L.A.O. Rocha et al. (eds.), *Constructal Law and the Unifying Principle of Design*, Understanding Complex Systems, DOI 10.1007/978-1-4614-5049-8_7,

Previous works showed that intensive efforts have been made [1–5] and robust hydraulic models have been developed [1–4, 6–9]. Several points are evoked in these computer-based methods: cost optimization [10], water quality monitoring [11], and reliability studies [12, 13]. So far, the geometric optimization of network architectures remains a challenge in water and other fluids engineering. This fact explains the success of the constructal design that derives from the constructal theory of Bejan and his coworkers [14–20].

During the last decade, the constructal theory has advanced the design based on geometry and today it has a wide range of applications [15–25]. The theory is now well known in literature [15], and thence we will not focus on its description but refer readers to the above references noting that excellent references have been earlier proposed by the theory's authors [15].

Former works that used constructal approach in water networks design addressed T-shaped, Y-shaped, size-limited, or looped networks [22–31] and presented the constructal design as a geometric and multi-scale optimization method. Though these works presented successfully geometric optimization of the network architectures, they did not go clearly in the direction topology by focusing on the optimization of both internal (diameters, lengths) and external (spatial occupation) variables. Gosselin evoked diameters and surfaces [29], but dealt with the surface of the network and not with the total surface that is influenced by the geometry of the network. Some other authors [24] examined how to optimally add new users to an existing network, but did not analyze scale variability/invariance, of a parameter that may govern the global geometry of an optimal network.

The aim of this paper is to optimize T-shaped networks by considering the global geometry of the flow architecture, evoking then topologic (spatial) optimization. The constructal sequence [16, 31] is used by progressing from simpler structures to more constructed ones, and the mathematical resolution was performed through global optimization by using the Lagrange multipliers [5, 18].

7.2 T-Shaped Networks

To some former works that focused only on internal dimension optimization [30, 31] subject to an environmental constraint (related to water quality degradation in the network) we have added here a supplementary optimization criterion: spatial optimization. The present study becomes then a complete version of a former illustrative application that was not generalized [32]. We considered that the network has a rectangular geometry of surface S_T that is constant. We defined a shape factor $f = h/H$. In practice, this situation is met when a network is being extended in order to supply new users or during a new housing estate, to position new users on a new area (not yet occupied). Then this optimization can be performed by designers in order to find the optimal distribution of the new network branches to be constructed for the future users. This is to say that the objective is not

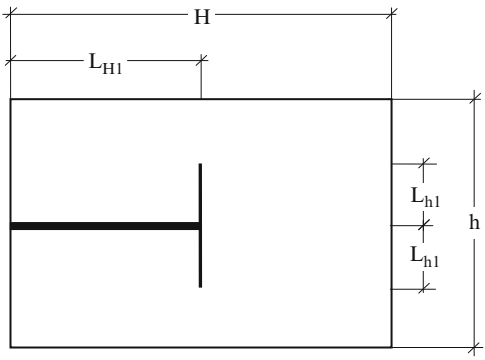

Fig. 7.1 First-order construct [32]

Table 7.1 Optimization results for the first construction

Diameters ratio	$\frac{D_{H_1}}{D_{h_1}} = 2^{\gamma}$
Optimal shape factor	$\left(\frac{h}{H}\right)_{\text{opt}} = 2^{n+1-m\gamma} = f_{\text{opt}_1}$
Diameter of the pipe in the direction h	$D_{h_1} = (4tQ_{h_1}/\pi)^{1/2}\Psi_1^{-1/2}$
Diameter of the pipe in the direction H	$D_{H_1} = 2^{\gamma}(4tQ_{h_1}/\pi)^{1/2}\Psi_1^{-1/2}$
$\psi_1 = \sqrt{S_{\text{T}}(f_{\text{opt}_1})^{-1}}(2^{2\gamma-2} + 2^{-2}f_{\text{opt}_1})$	

only to optimize pipe diameters but also to allocate space optimally so that the network that fits this space minimizes the objective function which is the total head losses, considered as a factor of the pumping power, when the total water demand is constant. It means that it is a search of diameters scaling laws with an additional ratio h/H that we call optimal shape factor f_{opt}, based on the spatial optimization.

7.3 First Construct

To start, we considered a simpler situation where the surface $S_{\text{T}} = h \times H$ is irrigated through two points, as shown in Fig. 7.1 (h and H are geometric dimensions displayed in Fig. 7.1).

The optimization problem consisted in minimizing the head losses subject to two constraints (the water residence time and the surface S_{T} of the area). The mathematical development of the optimization is presented in Appendix (First construct). It yielded in the optimal shape factor f_{opt_1}, diameters ratio, and dimensions that we presented in Table 7.1.

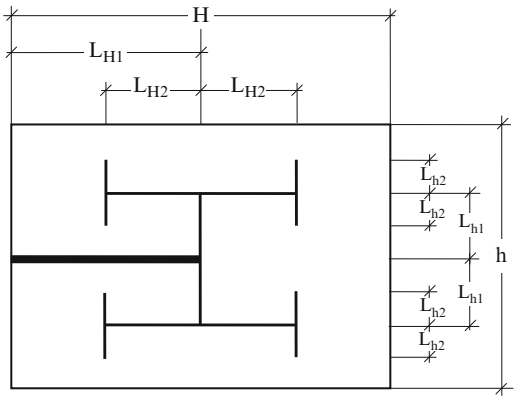

Fig. 7.2 Second order-construct [32]

Table 7.2 Optimization results of the second construction

Diameters ratio	$\frac{D_{H_1}}{D_{h_1}} = \frac{D_{h_1}}{D_{H_2}} = \frac{D_{H_2}}{D_{h_2}} = 2^{\gamma}$
Optimal shape factor	$\left(\frac{h}{H}\right)_{\text{opt}} = \frac{2^{3n-1-3m\gamma}+2^{n-m\gamma-2}}{2^{-3}+2^{2n-2-2m\gamma}} = f_{\text{opt}_2}$
Diameter of the pipe in the direction h	$D_{h_1} = 2^{2\gamma}(4tQ_{h_2}/\pi)^{1/2}\Psi_2^{-1/2}$ $D_{h_2} = (4tQ_{h_2}/\pi)^{1/2}\Psi_2^{-1/2}$
Diameter of the pipe in the direction H	$D_{H_1} = 2^{3\gamma}(4tQ_{h_2}/\pi)^{1/2}\Psi_2^{-1/2}$ $D_{H_2} = 2^{\gamma}(4tQ_{h_2}/\pi)^{1/2}\Psi_2^{-1/2}$
$\psi_2 = \sqrt{S_{\text{T}}(f_{\text{opt}_2})^{-1}}\left((2^{2\times 3\gamma-4}+2^{2\gamma-3})+f_{\text{opt}_2}(2^{2\times 2\gamma-4}+2^{-3})\right)$	

7.4 Second Construct

After the first element of Fig. 7.1 we moved to the second construct shown in Fig. 7.2. It is composed of three levels of pairing. We decided to respect the symmetry of the branching in directions h and H. The surface S_{T} is irrigated through eight service points. For this new system, the earlier Lagrangian function changes as shown in Appendix. In fact, as shown in Fig. 7.2, we have ($L_{h_1} = h/2^2$; $L_{h_2} = h/2^3$) and ($L_{H_1} = H/2^1$;$L_{H_2} = H/2^2$); λ_1 and λ_2 are Lagrange multipliers; t is the residence time, and S_{T} is the total surface ($S_{\text{T}} = h \times H$). The mathematical resolution is detailed in Appendix (Second-order construct) and results are presented in Table 7.2.

7.5 The *k*th Construct

To generalize the method, a more ramified network constructed by the same method of construction by branching in T (Fig. 7.2) is considered and illustrated in Fig. 7.3. We called it the kth-order construct (k is taken odd to keep symmetry in the

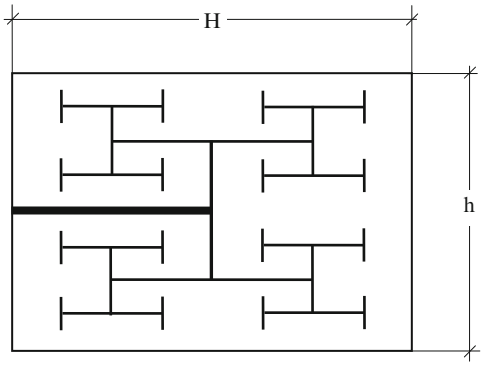

Fig. 7.3 High order-construct

Table 7.3 Optimization results for construct k

Diameters ratio	$\frac{D_{H_1}}{D_{h_1}} = \frac{D_{h_1}}{D_{H_2}} = \frac{D_{H_2}}{D_{h_2}} = \frac{D_{h_2}}{D_{H_3}} = \cdots = \frac{D_{H_k}}{D_{hk}} = 2^{\gamma}$
Optimal shape factor	$\left(\frac{h}{H}\right)_{\text{opt}} = \frac{\left(\sum_{i=1}^{k} 2^{(2k-(2i-1))n-m(2k-(2i-1))\gamma-i}\right)}{\sum_{i=1}^{k} 2^{(2k-(2i))n-m(2k-(2i))\gamma-(i+1)}} = f_{\text{opt}_k}$
Diameter of the pipe in the direction h	$D_{h_k} = (4tQ_{h_k}/\pi)^{1/2}\Psi_k^{-1/2}$ $D_{h_j} = 2^{(2(k-j)\gamma}(4tQ_{h_k}/\pi)^{1/2}\Psi_k^{-1/2}$
Diameter of the pipe in the direction H	$D_{H_j} = 2^{(2(k-j)+1)\gamma}(4tQ_{h_k}/\pi)^{1/2}\Psi_k^{-1/2}$
$\psi_k = \sqrt{\frac{S_T}{f_{\text{opt}_k}}}\left(\sum_{i=1}^{k} 2^{2(2(k-i)+1)\gamma-(2(k-i)+1)-i} + f_{\text{opt}_k}\sum_{i=1}^{k} 2^{2(2(k-i))\gamma-(2(k-i))-(i+1)}\right)$	

directions of h and H). The Lagrangian function of the system to minimize the total head losses subject to the residence time and the surface S_T writes in its general form as we presented in Appendix (the kth-order construct). The optimization results are presented in Table 7.3.

7.6 Results and Significance

The numerical evaluation of the optimal shape factor $f_{\text{opt}} = (h/H)_{\text{opt}}$ given in Table 7.3 showed its scale-invariance for any order of constructs. This optimal shape factor was found close to 1.81, when we considered the head losses parameters given by the Darcy–Weisbach formula where $m = 5$ and $n = 2$ [33]. With the Hazen–Williams formula [33] ($m = 4.871$ and $n = 1.852$), we found $f_{\text{opt}} = 1.78$ and with the Manning–Strickler equation of head losses, [33] ($m = 5.33$ and $n = 2$), we found $f_{\text{opt}} = 1.76$. Note that all these values of m and n are found in

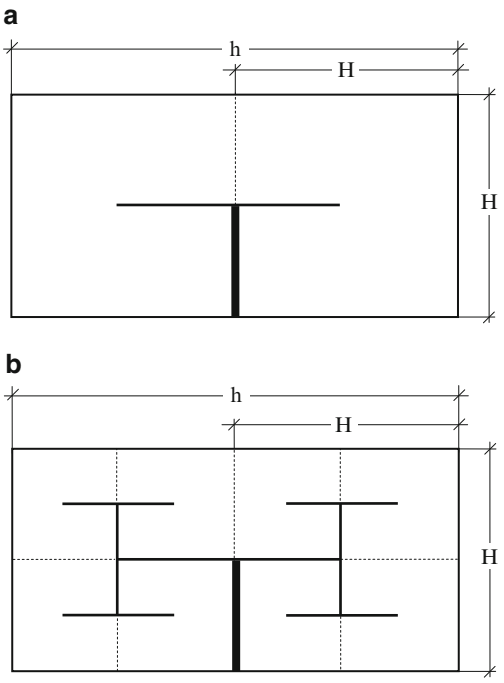

Fig. 7.4 Optimal architectures of T-shaped networks $S_T = hH = 2H^2$: (a) First element, (b) second element

drinking water literature [34] as head losses parameters and are used in the well-known pioneering hydraulic design software called EPAnet [35].

For practical reasons during implementations, one can take $f_{opt} = (h/H)_{opt} \approx 2$. This result of $(h/H)_{opt}$ teaches that the way to supply optimally users spread over an area is to place them in the center of small rectangles (Fig. 7.4) in such a way that the total surface influenced by networks obeys to the f_{opt_k} relation given in Table 7.3. This ratio $f_{opt} \approx 2$ teaches that a T-shaped network fed by a unique entry stream is better when it fits a rectangle of surface $S_T = hH = 2H^2$ composed by two identical square areas of surface ($S_{sqr} = S_T/2 = H^2$) and when the diameter distribution in the network obeys to the relations offered in Table 7.3. This is an important outcome for the optimal design of drinking water networks respectful of energy saving since the head losses are related to pumping power.

7.7 Concluding Remarks

The main objective of this conceptual study was to optimize flow configurations for drinking water distribution subject to some operational constraints by using the multi-scale design of constructal theory [15, 36].

The paper achieved the determination of an optimal geometry for T-shaped water distribution networks and this leads to the definition of an optimal shape

factor, finally found close to $f_{\text{opt}} = (h/H)_{\text{opt}} \approx 2$ for the layout of the networks. This factor f_{opt} that was earlier established in an introductive study [32] for the first two constructs has been determined for the most general case of construct k and the analytical optimization method has been fully developed.

The study is dedicated to new urban areas of cities in extension or semi-urban areas where city planners are developing new building sites on uninhabited zones (designers have freedom to position optimally users in order to obtain an effective network). This means that the area is not yet occupied by users but will be later occupied (very frequent situations in Africa [5]).

This study is in the direction of optimal use of energy by minimizing the pumping power which is a very critical issue in developing countries that are in need of strong efforts for the construction of such urban systems.

Some earlier works showed that minimizing head losses (or pressure drops) is not equivalent to minimizing pumping power [28], but for situations evoked in this paper, when the total water demand is constant, then the pumping power is proportional to the total head losses according to hydraulic literature [33].

Note finally that reliability by adding loops in networks [13] or stochastic questions [9] were not evoked in this paper because they were not targeted but authors did not overlook them as important topics in the design of drinking water networks. This is why authors consider this work as an introductive one that will be continued.

Acknowledgements The International Institute for Water and Environmental Engineering 2iE, 01 BP 594 Ouagadougou 01, Burkina Faso (www.2ie-edu.org), and its financial partners are gratefully acknowledged for their supports that permitted to successfully achieve this work.

Appendix: First-Order Construct

We consider the network shown in Fig. 7.1. The Lagrangian function written to minimize the head losses subject to the residence time and the total surface writes as follows:

$$L_{\text{g}} = a\frac{Q_{H_1}^n}{D_{H_1}^m}\frac{H}{2^1} + a\frac{Q_{h_1}^n}{D_{h_1}^m}\frac{h}{2^2} + \lambda_1\left(\frac{\pi D_{H_1}^2}{4Q_{H_1}}\frac{H}{2^1} + \frac{\pi D_{h_1}^2}{4Q_{h_1}}\frac{h}{2^2} - t\right) + \lambda_2(hH - S_T). \quad (7.1)$$

By differentiating L_{g} with respect to $D_{h_1}, D_{H_1}, h, H, \lambda_1$, and λ_2, and cancelling all the derivatives, we obtain

$$-am\frac{Q_{H_1}^n}{D_{H_1}^{m+1}}\frac{H}{2^1} + 2\frac{\pi}{4}\lambda_1\frac{D_{H_1}}{Q_{H_1}}\frac{H}{2^1} = 0, \quad (7.2a)$$

$$-am\frac{Q_{h_1}^n}{D_{h_1}^{m+1}}\frac{h}{2^2}+2\frac{\pi}{4}\lambda_1\frac{D_{h_1}}{Q_{h_1}}\frac{h}{2^2}=0, \tag{7.2b}$$

$$a\frac{Q_{H_1}^n}{D_{H_1}^m}\frac{1}{2^1}+\lambda_1\frac{\pi D_{H_1}^2}{4Q_{H_1}}\frac{1}{2^1}+\lambda_2 h=0, \tag{7.2c}$$

$$a\frac{Q_{h_1}^n}{D_{h_1}^m}\frac{1}{2^2}+\lambda_1\frac{\pi D_{h_1}^2}{4Q_{h_1}}\frac{1}{2^2}+\lambda_2 H=0, \tag{7.2d}$$

$$\frac{D_{H_1}^2}{Q_{H_1}}\frac{H}{2^1}+\frac{D_{h_1}^2}{Q_{h_1}}\frac{h}{2^2}=\frac{4t}{\pi}, \tag{7.2e}$$

$$\frac{\partial L_{\mathrm{g}}}{\partial\lambda_2}=0\Rightarrow hH-S_{\mathrm{T}}=0. \tag{7.2f}$$

From (7.2a) and (7.2b), we can write

$$\frac{am\frac{Q_{H_1}^n}{D_{H_1}^{m+1}}\frac{H}{2^1}}{am\frac{Q_{h_1}^n}{D_{h_1}^{m+1}}\frac{h}{2^2}}=\frac{2\frac{\pi}{4}\lambda_1\frac{D_{H_1}}{Q_{H_1}}\frac{H}{2^1}}{2\frac{\pi}{4}\lambda_1\frac{D_{h_1}}{Q_{h_1}}\frac{h}{2^2}}. \tag{7.3}$$

This yields in

$$\frac{D_{h_1}^{m+2}}{D_{H_1}^{m+2}}=\frac{Q_{h_1}^{n+1}}{Q_{H_1}^{n+1}}. \tag{7.4}$$

And, noting that because of the symmetry in the structure $2Q_{h_1}=Q_{H_1}$, then we have

$$\frac{D_{H_1}}{D_{h_1}}=2^{\gamma}\ \text{with}\quad \gamma=(n+1)/(m+2). \tag{7.5}$$

From (7.2a) and (7.2b), λ_1 can be expressed as follows:

$$\lambda_1=\frac{2am}{\pi}\frac{Q_{H_1}^{n+1}}{D_{H_1}^{m+2}}=\frac{2am}{\pi}\frac{Q_{h_1}^{n+1}}{D_{h_1}^{m+2}}. \tag{7.6}$$

By introducing λ_1 in (7.2c) and in (7.2d) we obtain

$$a\frac{Q_{H_1}^n}{D_{H_1}^m}\frac{1}{2^1}+\left(\frac{2am}{\pi}\frac{Q_{H_1}^{n+1}}{D_{H_1}^{m+2}}\right)\frac{\pi D_{H_1}^2}{4Q_{H_1}}\frac{1}{2^1}=-\lambda_2 h, \tag{7.7}$$

$$a\frac{Q_{h_1}^n}{D_{h_1}^m}\frac{1}{2^2}+\left(\frac{2am}{\pi}\frac{Q_{h_1}^{n+1}}{D_{h_1}^{m+2}}\right)\frac{\pi D_{h_1}^2}{4Q_{h_1}}\frac{1}{2^2}=-\lambda_2 H. \tag{7.8}$$

This yields in

$$\left(a+\frac{am}{2}\right)\frac{Q_{H_1}^n}{D_{H_1}^m}\frac{1}{2^1}=-\lambda_2 h, \tag{7.9}$$

$$\left(a+\frac{am}{2}\right)\frac{Q_{h_1}^n}{D_{h_1}^m}\frac{1}{2^2}=-\lambda_2 H. \tag{7.10}$$

By dividing member by member (7.9) by (7.10), we obtain

$$\frac{h}{H}=2\frac{Q_{H_1}^n}{Q_{h_1}^n}\frac{D_{h_1}^m}{D_{H_1}^m}. \tag{7.11}$$

Considering (7.5) and the fact that $2Q_{h1}=Q_{H1}$, (7.11) gives

$$\frac{h}{H}=2^{n+1-m\gamma}=f_{\mathrm{opt}_1}. \tag{7.12}$$

Considering (7.12) and (7.2f), we have

$$\begin{cases} hH-S_{\mathrm{T}}=0, \\ \dfrac{h}{H}=2^{n+1-m\gamma}=f_{\mathrm{opt}_1}. \end{cases} \tag{7.13}$$

This allow writing, by eliminating h,

$$H^2=\frac{S_{\mathrm{T}}}{f_{\mathrm{opt}_1}}\Rightarrow H=\sqrt{S_{\mathrm{T}}\left(f_{\mathrm{opt}_1}\right)^{-1}}. \tag{7.14}$$

And then, with (7.12), we can determine h as follows:

$$h=f_{\mathrm{opt}_1}\sqrt{S_{\mathrm{T}}\left(f_{\mathrm{opt}_1}\right)^{-1}}. \tag{7.15}$$

From (7.2e), we can write (by multiplying (7.2e) by the quantity $Q_{h1}/D^2{}_{h1}$)

$$\frac{D_{H_1}^2}{D_{h_1}^2}\frac{Q_{h_1}}{Q_{H_1}}\frac{H}{2^1}+\frac{h}{2^2}=\frac{4tQ_{h_1}}{\pi D_{h_1}^2}. \tag{7.16}$$

This yields, by considering (7.15) and (7.13), in

$$2^{2\gamma-2}\sqrt{S_{\mathrm{T}}\left(f_{\mathrm{opt}_1}\right)^{-1}}+2^{-2}f_{\mathrm{opt}_1}\sqrt{S_{\mathrm{T}}\left(f_{\mathrm{opt}_1}\right)^{-1}}=\frac{4tQ_{h_1}}{\pi D_{h_1}^2}. \tag{7.17}$$

And then

$$\begin{aligned} D_{h_1} &= \sqrt{\frac{4tQ_{h_1}/\pi}{\sqrt{S_{\mathrm{T}}\left(f_{\mathrm{opt}_1}\right)^{-1}}\left(2^{2\gamma-2}+2^{-2}f_{\mathrm{opt}_1}\right)}};D_{H_1} \\ &= 2^{\gamma}\sqrt{\frac{4tQ_{h_1}/\pi}{\sqrt{S_{\mathrm{T}}\left(f_{\mathrm{opt}_1}\right)^{-1}}\left(2^{2\gamma-2}+2^{-2}f_{\mathrm{opt}_1}\right)}}. \end{aligned} \tag{7.18}$$

Second-Order Construct

In the same manner as the previous case, the Lagrangian function writes as follows:

$$\begin{aligned} L_{\mathrm{g}} =& \left(a\frac{Q_{H_1}^n}{D_{H_1}^m}\frac{1}{2^1}+a\frac{Q_{H_2}^n}{D_{H_2}^m}\frac{1}{2^2}\right)H+\left(a\frac{Q_{h_1}^n}{D_{h_1}^m}\frac{1}{2^2}+a\frac{Q_{h_2}^n}{D_{h_2}^m}\frac{1}{2^3}\right)h+ \\ & \lambda_1\left(\left(\frac{\pi D_{H_1}^2}{4Q_{H_1}}\frac{1}{2^1}+\frac{\pi D_{H_2}^2}{4Q_{H_2}}\frac{1}{2^2}\right)H+\left(\frac{\pi D_{h_1}^2}{4Q_{h_1}}\frac{1}{2^2}+\frac{\pi D_{h_2}^2}{4Q_{h_2}}\frac{1}{2^3}\right)h-t\right)+\lambda_2(hH-S_{\mathrm{T}}). \end{aligned} \tag{7.19}$$

By differentiating L_{g} with respect to D_{H_1}, D_{H_2}, D_{h_1}, D_{h_2}, h, H, λ_1, and λ_2, and cancelling the derivatives, we obtain

$$\left(a\frac{Q_{H_1}^n}{D_{H_1}^m}\frac{1}{2^1}+a\frac{Q_{H_2}^n}{D_{H_2}^m}\frac{1}{2^2}\right)+\lambda_1\left(\frac{\pi D_{H_1}^2}{4Q_{H_1}}\frac{1}{2^1}+\frac{\pi D_{H_2}^2}{4Q_{H_2}}\frac{1}{2^2}\right)=-\lambda_2 h, \tag{7.20a}$$

$$\left(a\frac{Q_{h_1}^n}{D_{h_1}^m}\frac{1}{2^2}+a\frac{Q_{h_2}^n}{D_{h_2}^m}\frac{1}{2^3}\right)+\lambda_1\left(\frac{\pi D_{h_1}^2}{4Q_{h_1}}\frac{1}{2^2}+\frac{\pi D_{h_2}^2}{4Q_{h_2}}\frac{1}{2^3}\right)=-\lambda_2 H, \tag{7.20b}$$

$$ma\frac{Q_{H_1}^n}{D_{H_1}^{m+1}}\frac{1}{2^1}=2\lambda_1\frac{\pi D_{H_1}}{4Q_{H_1}}\frac{1}{2^1}, \tag{7.20c}$$

$$ma\frac{Q_{H_2}^n}{D_{H_2}^{m+1}}\frac{1}{2^2}=2\lambda_1\frac{\pi D_{H_2}}{4Q_{H_2}}\frac{1}{2^2}, \tag{7.20d}$$

$$ma\frac{Q_{h_1}^n}{D_{h_1}^{m+1}}\frac{1}{2^2}=2\lambda_1\frac{\pi D_{h_1}}{4Q_{h_1}}\frac{1}{2^2}, \tag{7.20e}$$

$$ma\frac{Q_{h_2}^n}{D_{h_2}^{m+1}}\frac{1}{2^3}=2\lambda_1\frac{\pi D_{h_2}}{4Q_{h_2}}\frac{1}{2^3}, \tag{7.20f}$$

$$\left(\frac{D_{H_1}^2}{Q_{H_1}}\frac{1}{2^1}+\frac{D_{H_2}^2}{Q_{H_2}}\frac{1}{2^2}\right)H+\left(\frac{D_{h_1}^2}{Q_{h_1}}\frac{1}{2^2}+\frac{D_{h_2}^2}{Q_{h_2}}\frac{1}{2^3}\right)h=\frac{4t}{\pi}, \tag{7.20g}$$

$$hH=S_{\mathrm{T}}. \tag{7.20h}$$

From (7.20c), (7.20d), (7.20e), and (7.20f), one can express λ_1 as follows:

$$\lambda_1=\frac{2ma}{\pi}\frac{Q_{H_i}^{n+1}}{D_{H_i}^{m+2}}=\frac{2ma}{\pi}\frac{Q_{h_i}^{n+1}}{D_{h_i}^{m+2}}\quad i=1,2. \tag{7.21}$$

By combining terms of (7.21), one can write (given that $Q_{H1}/Q_{h1}=2$, $Q_{H2}/Q_{h2}=2$, and $Q_{h1}/Q_{H2}=2$ because of the symmetry)

$$\frac{D_{H_1}}{D_{h_1}}=\frac{D_{h_1}}{D_{H_2}}=\frac{D_{H_2}}{D_{h_2}}=2^{\gamma}. \tag{7.22}$$

By introducing these expressions of λ_1 defined in (7.21), (7.20a), and (7.20b), we obtain

$$\begin{cases}\left(a+\dfrac{ma}{2}\right)\left(\dfrac{Q_{h_1}^n}{D_{h_1}^m}\dfrac{1}{2^2}+\dfrac{Q_{h_2}^n}{D_{h_2}^m}\dfrac{1}{2^3}\right)=-\lambda_2 H,\\ \left(a+\dfrac{ma}{2}\right)\left(\dfrac{Q_{H_1}^n}{D_{H_1}^m}\dfrac{1}{2^1}+\dfrac{Q_{H_2}^n}{D_{H_2}^m}\dfrac{1}{2^2}\right)=-\lambda_2 h.\end{cases} \tag{7.23}$$

From (7.23), when we eliminate λ_2, we can obtain by multiplying the numerator and denominator by the quantity $D_{h_2}^m/Q_{h_2}^n$

$$\left(\frac{h}{H}\right)=\frac{\left(\frac{D_{h_2}}{D_{H_1}}\right)^m\left(\frac{Q_{H_1}}{Q_{h_2}}\right)^n\frac{1}{2^1}+\left(\frac{D_{h_2}}{D_{H_2}}\right)^m\left(\frac{Q_{H_2}}{Q_{h_2}}\right)^n\frac{1}{2^2}}{\frac{1}{2^3}+\frac{1}{2^2}\left(\frac{D_{h2}}{D_{h_1}}\right)^m\left(\frac{Q_{h_1}}{Q_{h_2}}\right)^n}. \tag{7.24}$$

By considering (7.22), we finally obtain

$$\left(\frac{h}{H}\right)_{\text{opt}} = \frac{2^{3n-1-3m\gamma} + 2^{n-m\gamma-2}}{2^{-3} + 2^{2n-2-2m\gamma}} = f_{\text{opt}_2}. \tag{7.25}$$

By considering (20 h), and (7.25), the expression of H can be obtained:

$$H = \sqrt{S_{\text{T}}\left(f_{\text{opt}_2}\right)^{-1}}. \tag{7.26}$$

And then

$$h = f_{\text{opt}2}\sqrt{S_{\text{T}}\left(f_{\text{opt}_2}\right)^{-1}}. \tag{7.27}$$

By multiplying (20 g) by the quantity $Q_{h2}/D^2{}_{h2}$ we obtain

$$\begin{aligned}&\left(\frac{D_{H_1}^2}{D_{h_2}^2}\frac{Q_{h_2}}{Q_{H_1}}\frac{1}{2^1} + \frac{D_{H_2}^2}{D_{h_2}^2}\frac{Q_{h_2}}{Q_{H_2}}\frac{1}{2^2}\right)\sqrt{S_{\text{T}}\left(f_{\text{opt}_2}\right)^{-1}} \\ &+ \left(\frac{D_{h_1}^2}{D_{h_2}^2}\frac{Q_{h_2}}{Q_{h_1}}\frac{1}{2^2} + \frac{1}{2^3}\right)f_{\text{opt}_2}\sqrt{S_{\text{T}}\left(f_{\text{opt}_2}\right)^{-1}} = \frac{4tQ_{h_2}}{\pi D_{h_2}^2}.\end{aligned} \tag{7.28}$$

From this, we can write

$$\left(2^{2\times3\gamma-4} + 2^{2\gamma-3}\right)\sqrt{S_{\text{T}}\left(f_{\text{opt}_2}\right)^{-1}} + \left(2^{2\times2\gamma-4} + 2^{-3}\right)f_{\text{opt}2}\sqrt{S_{\text{T}}\left(f_{\text{opt}_2}\right)^{-1}} = \frac{4tQ_{h_2}}{\pi D_{h_2}^2}. \tag{7.29}$$

And then

$$D_{h_2} = \left(4tQ_{h_2}/\pi\right)^{1/2}{\Psi_2}^{-1/2}. \tag{7.30}$$

We finally obtain D_{h2}, D_{H1}, and D_{H2} from (7.22) and from (7.30):

$$D_{H_2} = 2^{\gamma}\left(4tQ_{h_2}/\pi\right)^{1/2}{\Psi_2}^{-1/2}, \tag{7.31}$$

$$D_{h_1} = 2^{2\gamma}\left(4tQ_{h_2}/\pi\right)^{1/2}{\Psi_2}^{-1/2}, \tag{7.32}$$

$$D_{H_1} = 2^{3\gamma}\left(4tQ_{h_2}/\pi\right)^{1/2}{\Psi_2}^{-1/2}, \tag{7.33}$$

$$\Psi_2 = \sqrt{S_{\text{T}}\left(f_{\text{opt}_2}\right)^{-1}}\left(\left(2^{2\times3\gamma-4} + 2^{2\gamma-3}\right) + f_{\text{opt}_2}\left(2^{2\times2\gamma-4} + 2^{-3}\right)\right). \tag{7.34}$$

The *k*th-Order Construct

Consider the situation presented in Fig. 7.2, but taken in a more general form where the network is more and more ramified and has D_0, D_1 until D_k. From the dimension h and H, of Fig. 7.3, one can group the pipes into two groups of index h (those in the direction of h) and of index H (those in the direction of H). To understand, see the first and second constructs that are displayed in Figs. 7.1 and 7.2.

In the same way as in previous cases, the Lagrangian function writes

$$L_{\mathrm{g}} = Ha\sum_{i=1}^{k}\frac{Q_{H_i}^{n}}{D_{H_i}^{m}}\frac{1}{2^i} + ha\sum_{i=1}^{k}\frac{Q_{h_i}^{n}}{D_{h_i}^{m}}\frac{1}{2^{i+1}} + \lambda_1\left(H\sum_{i=1}^{k}\frac{\pi D_{H_i}^2}{4Q_{H_i}}\frac{1}{2^i} + h\sum_{i=1}^{k}\frac{\pi D_{h_i}^2}{4Q_{h_i}}\frac{1}{2^{i+1}} - t\right) + \lambda_2(hH - S_{\mathrm{T}}). \tag{7.35}$$

Note that k is the number of pipes in direction of H, or in the direction of h. It is important to mention that, in order to facilitate calculus, we did not consider constructions in which there are i pipes in the direction of H and $i + 1$ pipes in the direction of h (and vice versa). In this view, on the first construction of Fig. 7.1, $k = 1$ and on the second construction of Fig. 7.2, $k = 2$.

By differentiating L_{g} with respect to D_{h_i}, D_{H_i}, h, H, λ_1, and λ_2, and cancelling all the derivatives, we obtain

$$ma\frac{Q_{H_i}^{n}}{D_{H_i}^{m+1}} = 2\lambda_1\frac{\pi D_{H_i}}{4Q_{H_i}}, \tag{7.36a}$$

$$ma\frac{Q_{h_i}^{n}}{D_{h_i}^{m+1}} = 2\lambda_1\frac{\pi D_{h_i}}{4Q_{h_i}}, \tag{7.36b}$$

$$a\sum_{1}^{k}\frac{Q_{H_i}^{n}}{D_{H_i}^{m}}\frac{1}{2^i} + \lambda_1\sum_{1}^{k}\frac{\pi D_{H_i}^2}{4Q_{H_i}}\frac{1}{2^i} = -\lambda_2 h, \tag{7.36c}$$

$$a\sum_{1}^{k}\frac{Q_{h_i}^{n}}{D_{h_i}^{m}}\frac{1}{2^{i+1}} + \lambda_1\sum_{1}^{k}\frac{\pi D_{h_i}^2}{4Q_{h_i}}\frac{1}{2^{i+1}} = -\lambda_2 H, \tag{7.36d}$$

$$H\sum_{1}^{k}\frac{D_{H_i}^2}{Q_{H_i}}\frac{1}{2^i} + h\sum_{1}^{k}\frac{D_{h_i}^2}{Q_{h_i}}\frac{1}{2^{i+1}} = \frac{4t}{\pi}, \tag{7.36e}$$

$$hH = S_{\mathrm{T}}. \tag{7.36f}$$

From (7.36a), and (7.36b), we can express λ_1 as follows:

$$\lambda_1 = \frac{2ma}{\pi}\frac{Q_{H_1}^{n+1}}{D_{H_1}^{m+2}} = \frac{2ma}{\pi}\frac{Q_{H_2}^{n+1}}{D_{H_2}^{m+2}} = \cdots = \frac{2ma}{\pi}\frac{Q_{h_1}^{n+1}}{D_{h_1}^{m+2}} = \frac{2ma}{\pi}\frac{Q_{h_2}^{n+1}}{D_{h_2}^{m+2}} = \cdots \tag{7.37}$$

By combining terms of (7.37), we obtain (given that $Q_{H1}/Q_{h1} = 2$, $Q_{H2}/Q_{h2} = 2$, …, because of the symmetry of the structure)

$$\frac{D_{H_1}}{D_{h_1}} = \frac{D_{h_1}}{D_{H_2}} = \frac{D_{H_2}}{D_{h_2}} = \frac{D_{h_2}}{D_{H_3}} = \cdots = \frac{D_{H_k}}{D_{h_k}} = 2^{\gamma}. \tag{7.38}$$

By introducing the expressions of λ_1 (defined in (7.37), (7.36c), and (7.36d)), we obtain

$$\left(a + \frac{ma}{2}\right)\sum_{1}^{k}\frac{Q_{H_i}^{n}}{D_{H_i}^{m}}\frac{1}{2^i} = -\lambda_2 h, \tag{7.39}$$

$$\left(a + \frac{ma}{2}\right)\sum_{1}^{k}\frac{Q_{h_i}^{n}}{D_{h_i}^{m}}\frac{1}{2^{i+1}} = -\lambda_2 H. \tag{7.40}$$

By dividing member by member, the terms of (7.39) and (7.40), we obtain

$$\left(\frac{h}{H}\right)_{\text{opt}} = \frac{\sum_{1}^{k}\frac{Q_{H_i}^{n}}{D_{H_i}^{m}}\frac{1}{2^i}}{\sum_{1}^{k}\frac{Q_{h_i}^{n}}{D_{h_i}^{m}}\frac{1}{2^{i+1}}}. \tag{7.41}$$

By multiplying both the numerator and denominator of (7.41) by the quantity ${D_{h_k}}^m/{Q_{h_k}}^n$, as follows

$$\left(\frac{h}{H}\right)_{\text{opt}} = \frac{\frac{Q_{H_1}^{n}}{D_{H_1}^{m}}\frac{1}{2^1}\frac{D_{h_k}^{m}}{Q_{h_k}^{n}} + \cdots + \frac{Q_{H_k}^{n}}{D_{H_k}^{m}}\frac{1}{2^k}\frac{D_{h_k}^{m}}{Q_{h_k}^{n}}}{\frac{Q_{h_1}^{n}}{D_{h_1}^{m}}\frac{1}{2^{1+1}}\frac{D_{h_k}^{m}}{Q_{h_k}^{n}} + \cdots + \frac{Q_{h_k}^{n}}{D_{h_k}^{m}}\frac{1}{2^{k+1}}\frac{D_{h_k}^{n}}{Q_{h_k}^{n}}}, \tag{7.42}$$

and by taking into account (7.38), we obtain

$$\left(\frac{h}{H}\right)_{\text{opt}} = \frac{\sum_{i=1}^{k} 2^{(2k-(2i-1))n - m(2k-(2i-1))\gamma - i}}{\sum_{i=1}^{k} 2^{(2k-(2i))n - m(2k-(2i))\gamma - (i+1)}} = f_{\text{opt}_k}. \tag{7.43}$$

Verifications

Construction 1: $k = 1$ leads to

$$\left(\frac{h}{H}\right)_{\text{opt}} = 2^{n+1-m\gamma}. \tag{7.44}$$

Construction 2: $k = 2$ leads to

$$\left(\frac{h}{H}\right)_{\text{opt}} = \frac{2^{3n-1-3m\gamma} + 2^{n-2-m\gamma}}{2^{2n-2-2m\gamma} + 2^{-3}}. \tag{7.45}$$

By posing that $(h/H)_{\text{opt}} = f_{\text{opt}_k}$, we obtain from (7.43) and from (7.36f) the expressions of H and h as follows:

$$H = \sqrt{S_{\text{T}}\left(f_{\text{opt}_k}\right)^{-1}}, \tag{7.46}$$

$$h = f_{\text{opt}_k}\sqrt{S_{\text{T}}\left(f_{\text{opt}_k}\right)^{-1}}. \tag{7.47}$$

In order to make Q_{h_k}/Q_{H_i}, Q_{h_k}/Q_{h_i}, D_{H_i}/D_{h_k} and D_{h_i}/D_{h_k} appear, we multiply (7.36e) by $Q_{h_k}/D_{h_k}^2$, and we obtain

$$\sqrt{\frac{S_{\text{T}}}{f_{\text{opt}_k}}}\sum_{i=1}^{k}\frac{D_{H_i}^2}{D_{h_k}^2}\frac{Q_{h_k}}{Q_{H_i}}\frac{1}{2^i} + f_{\text{opt}_k}\sqrt{\frac{S_{\text{T}}}{f_{\text{opt}_k}}}\sum_{i=1}^{k}\frac{D_{h_i}^2}{D_{h_k}^2}\frac{Q_{h_k}}{Q_{h_i}}\frac{1}{2^{i+1}} = \frac{4tQ_{h_k}}{\pi D_{h_k}^2}. \tag{7.48}$$

Noting that

$$\frac{D_{H_i}^2}{D_{h_k}^2} = \left(\frac{D_{H_i}^2}{D_{h_i}^2}\times\frac{D_{h_i}^2}{D_{H_{i+1}}^2}\times\cdots\times\frac{D_{h_{k-1}}^2}{D_{H_k}^2}\times\frac{D_{H_k}^2}{D_{h_k}^2}\right) = 2^{2(2(k-i)+1)\gamma}, \tag{7.49}$$

$$\frac{D_{h_i}^2}{D_{h_k}^2} = \frac{D_{h_i}^2}{D_{H_{i+1}}^2}\times\frac{D_{H_{i+1}}^2}{D_{h_{i+1}}^2}\times\cdots\times\frac{D_{h_{k-1}}^2}{D_{H_k}^2}\times\frac{D_{H_k}^2}{D_{h_k}^2} = 2^{2(2(k-i))\gamma}, \tag{7.50}$$

$$\frac{Q_{H_i}}{Q_{h_k}} = \frac{Q_{H_i}}{Q_{h_i}}\times\frac{Q_{h_i}}{Q_{H_{i+1}}}\times\cdots\times\frac{Q_{h_{k-1}}}{Q_{Hk}}\times\frac{Q_{Hk}}{Q_{h_k}} = 2^{2(k-i)+1}, \tag{7.51}$$

and

$$\frac{Q_{h_i}}{Q_{h_k}} = \frac{Q_{h_i}}{Q_{H_{i+1}}}\times\frac{Q_{H_{i+1}}}{Q_{h_{i+1}}}\times\cdots\times\frac{Q_{h_{k-1}}}{Q_{H_k}}\times\frac{Q_{H_k}}{Q_{h_k}} = 2^{2(k-i)}, \tag{7.52}$$

equation (7.48) can be rewritten as follows:

$$\sqrt{\frac{S_T}{f_{opt_k}}}\sum_{i=1}^{k} 2^{2(2(k-i)+1)\gamma-(2(k-i)+1)-i} + f_{opt_k}\sqrt{\frac{S_T}{f_{opt_k}}}\sum_{i=1}^{k} 2^{2(2(k-i))\gamma-(2(k-i))-(i+1)} = \frac{4tQ_{h_k}}{\pi D_{h_k}^2}. \tag{7.53}$$

From this, we finally obtain

$$D_{h_k} = (4tQ_{h_k}/\pi)^{1/2}{\Psi_k}^{-1/2}, \tag{7.54}$$

where

$$\Psi_k = \sqrt{\frac{S_T}{f_{opt_k}}}\left(\sum_{i=1}^{k} 2^{2(2(k-i)+1)\gamma-(2(k-i)+1)-i} + f_{opt_k}\sum_{i=1}^{k} 2^{2(2(k-i))\gamma-(2(k-i))-(i+1)}\right). \tag{7.55}$$

Then, considering (7.38), and for any j ranging from 1 to k, we obtain

$$D_{h_j} = 2^{2(k-j)\gamma}(4tQ_{h_k}/\pi)^{1/2}{\Psi_k}^{-1/2} \tag{7.56}$$

and

$$D_{H_j} = 2^{(2(k-j)+1)\gamma}(4tQ_{h_k}/\pi)^{1/2}{\Psi_k}^{-1/2}. \tag{7.57}$$

References

1. Gupta I, Bassin J, Gupta A, Khanna P. Optimization of water distribution systems. Environ Softw. 1993;8:101–13.
2. Savic D, Walters G. Genetic algorithms for least-cost design of water distribution networks. J Water Res Pl-ASCE. 1997;123:67–77.
3. Gupta I, Gupta A, Khanna P. Genetic algorithm for optimization of water distribution systems. Environ Modell Softw. 1999;14:437–46.
4. Klempous R, Kotowski J, Nikodem J, Ulasiewicz J. Optimization algorithms of operative control in water distribution systems. J Comput Appl Math. 1997;84:91–9.
5. Bieupoude P. Approche constructal pour l'optimisation de réseaux hydrauliques, Thèse de doctorat, Université de Perpignan, France et 2iE Institut International d'Ingénierie de l'Eau et de l'Environnement; Ouagadougou, Burkina Faso; 2011
6. Chu C, Lin M, Liu G, Sung Y. Application of immune algorithms on solving minimum-cost problem of water distribution network. Math Comput Model. 2008;48:1888–900.

7. Baños R, Bans R, Gil C, Reca J, Montoya F. A memetic algorithm applied to the design of water distribution networks. Appl Soft Comput. 2010;10:261–6.
8. Mustonen S, Tissari S, Huikko L, Kolehmainen M, Lehtola M, Hirvonen A. Evaluating online data of water quality changes in a pilot drinking water distribution system with multivariate data exploration methods. Water Res. 2008;42:2421–30.
9. Bolognesi A, Bragalli C, Marchi A, Artina S. Genetic heritage evolution by stochastic transmission in the optimal design of water distribution network. Adv Eng Softw. 2010;41:792–801.
10. Simpson A, Dandy G, Murphy L. Genetic algorithm compared to other techniques for pipe optimization. J Water Res Pl-ASCE. 1994;120:423–43.
11. Kohpaei J, Sathasivan A. Chlorine decay prediction in bulk water using the parallel second order model: an analytical solution development. Chem Eng J. 2011;171:232–41.
12. Bai D, Pei-jun Yang P, Song L. Optimal design method of looped water distribution network. Systems Engineering – Theory and Practice. 2007;27:137–43.
13. Todini E. Looped water distribution networks design using a resilience index based heuristic approach. Urban Water. 2000;2:115–22.
14. Bejan A. Shape and structure from engineering to nature. UK: Cambridge; 2000.
15. Bejan A, Lorente S. Design with constructal theory. Hoboken: Wiley; 2008.
16. Azoumah Y, Mazet N, Neveu P. Constructal network for heat and mass transfer in a solid-gas reactive porous medium. Int J Heat Mass Tran. 2004;47:2961–70.
17. Azoumah Y, Neveu P, Mazet N. Constructal design combined with entropy generation minimization for solid–gas reactors. Int J Therm Sci. 2006;45:716–28.
18. Tondeur D, Fan Y, Luo L. Constructal optimization of arborescent structures with flow singularities. Chem Eng Sci. 2009;64(2009):3968–82.
19. Miguel A. Dendridic structures for fluid flow: laminar turbulent and constructal design. J Fluid Struc. 2010;26:330–5.
20. Bejan A, Marden H. The constructal unification of biological and geophysical design. Phys Life Rev. 2009;6:85–102.
21. Bejan A, Lorente S. The constructal law and the evolution of design in nature. Phys Life Rev. 2011;8:209–40.
22. Bejan A, Rocha L, Lorente S. Thermodynamic optimization of geometry: T- and Y-shaped constructs of fluid streams. Int J Therm Sci. 2000;39:949–60.
23. Wechsatol W, Lorente S, Bejan A. Tree-shaped insulated designs for the uniform distribution of hot water over an area. Int J Heat Mass Tran. 2001;44:3111–23.
24. Wechsatol W, Lorente S, Bejan A. Development of tree-shaped flows by adding new users to existing networks of hot water pipes. Int J Heat Mass Tran. 2002;45:723–33.
25. Wechsatol W, Lorente S, Bejan A. Tree-shaped network with loops. Int J Heat Mass Tran. 2005;48:573–83.
26. Wechsatol W, Lorente S, Bejan A. Tree-shaped flow structures with local junction losses. Int J Heat Mass Tran. 2006;49:2957–64.
27. Gosselin L, Bejan A. Tree networks for minimal pumping power. Int J Therm Sci. 2005;44:53–63.
28. Gosselin L. Optimization of tree-shaped fluid networks with size limitations. Int J Therm Sci. 2007;46:434–43.
29. Bieupoude P, Azoumah Y, Neveu P. Environmental optimization of tree-shaped water distribution networks. Water resources management VI. Proceedings of the sixth International Conference on Sustainable Water Resources Management; California 23-25 May; 2011. p. 99–109
30. Bieupoude P, Azoumah Y Neveu P. Constructal tree-shaped water distribution networks by an environmental approach. Int J Des Nat Ecodyn. (Forthcoming 2011)
31. Bieupoude P, Azoumah Y, Neveu P. Perspectives to urban water networks computer-based optimization methods by integrating the constructal design. Comp Environ Urban. (Forthcoming 2012)

32. Chase D, Savic D, Walski T. Haestad methods. In: Water distribution modeling. USA: Haestad press; 2001
33. Carlier M. Hydraulique générale et appliquée. Paris: Eyrolles; 1972.
34. Rossman L. EPANET 2 Users manual, Chapter 1. Cincinnati; 2000 EPA, United States.
35. Bejan A, Lorente S. La loi constructale. Paris: L'Harmattan; 2005.
36. Azoumah Y, Bieupoude P, Neveu P. Optimal design of tree-shaped water distribution network using constructal approach: T-shaped and Y-shaped architectures optimization and comparison. Int Commun Heat Mass. 2012;39:182–9.

Chapter 8
The Constructal Theory of Electrokinetic Transport Through a Porous System

Sylvie Lorente

8.1 Introduction

Electrokinetic transfer results from applying an electrical current or an electrical field to a medium in order to accelerate and control the transfer of charged species. The applications of such techniques are widespread, ranging from drug delivery [1] to ground cleanup [2, 3] to chloride and nuclear decontamination [4–6].

Constructal theory is a theory of evolution of flow architectures in time, in the direction of greater flow access or less global flow resistances: "for a finite system to persist in time, it must evolve in such a way that it provides access to the currents that flow through it" [7]. The universality of the approach invites us to envisage multi-scale applications such as the cooling of electronics [8–11], micro-heat exchangers [12], urban design [13], and fuel cells [14].

More recently, constructal theory has been used to describe particles agglomeration [15], the tree architecture of stony coral [16, 17], global circulation and climate [18], and vascularized smart materials with self-healing functionality [19–22].

This paper reviews the main advances on the application of constructal theory to electrokinetic transport. It is demonstrated that the maximization of ionic transfer leads not only to the optimization of electrokinetic transfer in time but also to the discovery of the optimal geometry of the system.

S. Lorente (✉)
LMDC (Laboratoire Matériaux et Durabilité des Constructions), INSA, Université de Toulouse, 135, avenue de Rangueil, Toulouse, Cedex 04 F-31 077, France
e-mail: lorente@insa-toulouse.fr

L.A.O. Rocha et al. (eds.), *Constructal Law and the Unifying Principle of Design*, Understanding Complex Systems, DOI 10.1007/978-1-4614-5049-8_8,

8.2 Time-Dependent Scale Analysis

Two electrolyte reservoirs are initially separated by a wall. One of the reservoirs contains ionic species that will be transferred through the reservoir 2 once the separation wall is removed. The transfer will be enhanced by an electrical field applied between two electrodes placed on both ends of reservoir 2 (Fig. 8.1). The electrical potential difference is applied as soon as the separation wall is removed. The continuity equation is

$$\frac{\partial c_i}{\partial t} = D_i \left(\frac{\partial^2 c_i}{\partial x^2} + z_i \frac{F}{RT} \frac{\partial \varphi}{\partial x} \frac{\partial c_i}{\partial x} \right) \tag{8.1}$$

where i is the ionic species, c is the concentration, D is the effective diffusion coefficient, z is the charge number, F is the Faraday constant, R is the ideal gas constant, T is the absolute temperature, and φ is the electrical potential.

The time scales can be obtained by applying scale analysis [23] to the preceding equation,

$$\frac{\Delta c}{t} \approx D_0 \left(\frac{\Delta c}{L^2} \right), D_0 \left(\frac{F}{RT} \frac{\Delta \varphi}{L} \frac{\Delta c}{L} \right) \tag{8.2}$$

where Δc and $\Delta \varphi$ are respectively the maximum concentration difference and potential difference, while D_0 represents an effective diffusivity of reference. Therefore, the characteristic times for a species to be transferred along a distance L is

$$t_{\text{diff},L} \approx \frac{L^2}{D_0} \tag{8.3a}$$

$$t_{\text{electrodiff},L} \approx \frac{RTL^2}{F \Delta \varphi D_0} \tag{8.3b}$$

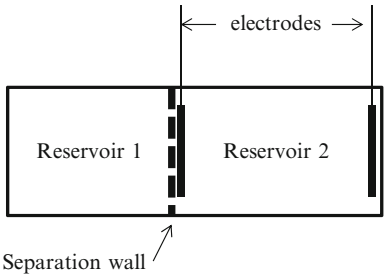

Fig. 8.1 Electrolyte reservoirs

On the very first moments when the potential difference is applied, the scale analysis must be conducted differently [24]. Because of the initially infinite concentration gradient, the length scale for diffusion is x initially, and not L. Here x is the thickness from the near-surface layer previously in contact with the separation wall. We write

$$\frac{\Delta c}{t} \approx \frac{D_0}{x}\left(\frac{\Delta c}{x}\right), \ \frac{D_0}{x}\left(\frac{F}{RT}\frac{\Delta\varphi}{L}\Delta c\right) \tag{8.4}$$

and from this we find

$$t_{\text{diff}} \approx \frac{x^2}{D_0} \tag{8.5a}$$

$$t_{\text{electrodiff}} \approx \frac{RTLx}{F\Delta\varphi D_0} \tag{8.5b}$$

The intersection of (8.5a) and (8.5b) gives the transition time, $t_{\text{transition}}$, corresponding to the transition from diffusion driven transport to migration (electrodiffusion) driven transport. This leads to

$$t_{\text{transition}} = \left(\frac{RTL}{F\Delta\varphi}\right)^2 \frac{1}{D_0} \tag{8.6}$$

When the time is smaller than $t_{\text{transition}}$, the transport of the ionic species is mainly driven by diffusion, and the corresponding depth is given by

$$x \approx (D_0)^{1/2} t^{1/2} \tag{8.7}$$

On the other hand, when $t > t_{\text{transition}}$, migration prevails and the order of magnitude of the depth is given by

$$x \approx \frac{F\Delta\varphi}{RTL} D_0 t \tag{8.8}$$

The maximum depth from the separation wall position for which diffusion drives the transport is given at the intersection of the two curves corresponding to (8.7) and (8.8). We obtain $x_{\text{transition}} = \frac{RTL}{F\Delta\varphi}$. This transition depth is independent of the ionic diffusivity. It is linked only to the electrical field: the higher the electrical field, the smaller the transition depth.

The combination of diffusion at the initial state and migration after a transition time does not occur by chance. The penetration of ionic species is driven by the search for the maximization of ionic transfer, i.e., the maximization of the approach to equilibrium. In the beginning, diffusion is preferred because it leads to a higher

propagation of ions. It is only when the transition depth $x_{\text{transition}}$ is reached that migration becomes a stronger driving force, and the penetration depth increases linearly with time.

Electrodiffusion is an engineered process. Yet other process that are found in nature aim at the same objective: the maximization of transfers not only by the combination of two mechanisms but also by the use of the best of these mechanisms at the best moment. As shown by Bejan [7] as an illustration of the constructal law, the growth of snowflakes is due to diffusion (spherical wave of thermal diffusion) followed by convection (needles). The same pair of mechanisms rules coral growth, as demonstrated in the works of Miguel [16]. In these three examples (electrodiffusion, snowflakes and corals), the initial propagation rate $\partial x/\partial t$ decreases with $t^{-1/2}$. In time, the convection term, represented in this work by $\frac{F\Delta\varphi D_0}{RTL}$ in (8.8), finally overtakes the initial propagation rate.

8.3 Applications to Porous Systems

8.3.1 Radial Positioning

Assume a porous material in which a central electrode is positioned in the center, while electrodes with opposite polarization are located equidistantly on a circle. The radius of the circle is the distance between the central electrode and one of the electrodes on the perimeter. The electrodes on the perimeter are linked electrically to each other, and this link is external to the material [25].

For the sake of simplicity the configuration is modelled as two-dimensional. We search for the optimal number of electrodes to implement for a given uniform concentration contamination level, and for a given electrical current. Because of the symmetry of the configuration, the optimization of the number of electrodes to implement can be reduced to the optimization of α, which is the angle of the sector of radius L presented in Fig. 8.2.

When an electrical current I is imposed between the two electrodes of Fig. 8.2, the ionic species from the entire sector are entrained and transported. A main stream forms along the radius L separating the two electrodes. From the scale analysis of

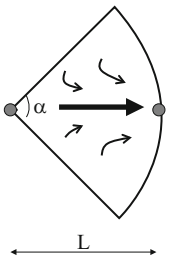

Fig. 8.2 Elemental sector described by the distance between anode and cathode, and the angle α [25]

the Nernst–Planck equation, and assuming that diffusion is negligible compared with the electrical effects in the radial direction L (from anode to cathode), the longitudinal flow rate of species $\dot{m}_{\text{longitudinal}}$ is given by

$$\dot{m}_{\text{longitudinal}} \sim D_0 \frac{F}{RT} \Delta c \Delta \varphi L \alpha \tag{8.9}$$

where $L\alpha$ is the transversal area crossed by the flux from electrode to electrode. The order of magnitude of the current density is

$$j \sim \frac{I}{L\alpha} \tag{8.10}$$

and

$$\frac{\partial \varphi}{\partial x} \sim \frac{RT}{F^2} \frac{j}{D_0 \Delta c} \tag{8.11}$$

Combining (8.9)–(8.11) together, we obtain

$$\dot{m}_{\text{longitudinal}} \sim \frac{I}{F} \tag{8.12}$$

The associated time scale can be obtained from the scale analysis of the law of conservation of mass

$$t_{\text{longitudinal}} \sim \frac{\Delta c F L^2 \alpha}{I} \tag{8.13}$$

In the direction perpendicular to this main direction of transport, the flux is mainly diffusive (Fig. 8.2). Yet the strength of the convective flux is such that close to the main stream of ionic flux the diffusive transport exhibits a longitudinal component. Such a configuration possesses analogies in nature. See for example the flow of ground water close to a river bed (*infero-flux*).

The order of magnitude of the transversal flow rate is also provided by the scale analysis of the Nernst–Planck equation

$$\dot{m}_{\text{transversal}} \sim \frac{D_0 \Delta c}{\alpha} \tag{8.14}$$

The corresponding time scale is obtained from the mass conservation

$$t_{\text{transversal}} \sim \frac{L^2 \alpha^2}{D_0} \tag{8.15}$$

We write according to Bejan [7] that the optimal geometry is the one that corresponds to the equipartition of times of transport. In other words, the angle of the sector is optimal when the time scale of longitudinal transport is of the order of magnitude of the time scale of transversal transport. Therefore,

$$\alpha_{\text{optimal}} \sim \frac{\Delta c F D_0}{I} \tag{8.16}$$

The same optimal angle can be calculated by writing that the longitudinal and transversal flow rates are equal. The result obtained in (8.16) may seem counter-intuitive because it indicates that the optimal angle decreases if the current increases. If the current increases, the amount of ionic species transferred per unit time longitudinally increases. The only possibility to transfer the same amount transversally is to increase the concentration gradient. Because the concentration level is fixed (Δc), increasing the concentration gradient means to decrease the angle α.

The above analysis can be repeated for the case where the electrical potential difference ΔU is fixed instead of the current. The corresponding electrical field is, in an order of magnitude sense, $\Delta U/L$, leading to

$$\dot{m}_{\text{longitudinal}} \sim D_0 \frac{F}{RT} \Delta c \Delta U \alpha \tag{8.17}$$

The transversal ionic flow rate is given by (8.14). Setting the two ionic flow rates equal gives the optimal angle α

$$\alpha_{\text{optimal}} \sim \frac{RT}{F \Delta U} \tag{8.18}$$

Again, increasing the electrical effects (ΔU in this case) means to decrease the value of α.

8.3.2 Source-to-Point Case

Consider a two-dimensional porous material as the one presented in Fig. 8.3 [26]. The material thickness is L_y, and the length is L_x. The material is in contact with a reservoir supplying the ionic species all along the external electrode. The targeted zone inside the material is represented by the shaded area. The objective is to drive and concentrate the ionic species from the outside reservoir to the targeted zone. To reach this goal, migration is used.

Because the objective is to bathe a specific zone, an electrode is inserted in the material perpendicular to Fig. 8.3. Another electrode is placed at the interface

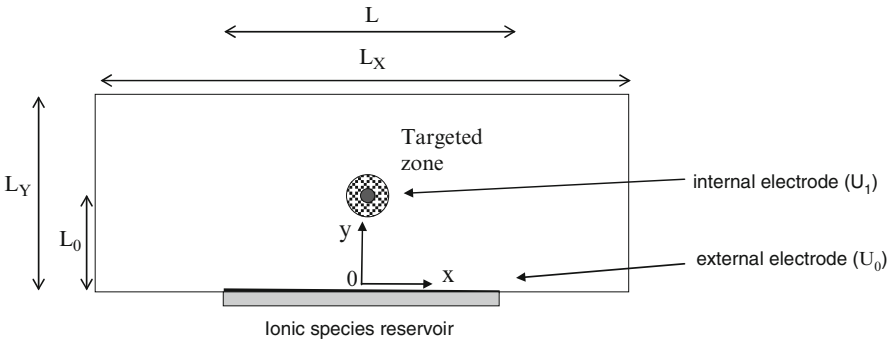

Fig. 8.3 Two-dimensional porous material with an external electrode and an internal one [26]

between the porous medium and the ionic species reservoir. The length of this electrode is L, and its potential is U_0. We assign an x-axis to this electrode, so that $x = 0$ corresponds to a perpendicular touching the targeted zone, which is at $y = L_0$. The two electrodes are connected to an external DC power supply. The applied constant potential difference is $\Delta U = U_1 - U_0$.

Assume that the porous material is saturated and made of a solid that can be considered nonconductive electrically. Assume also that the ionic concentration is initially zero throughout the material, while in the reservoir the concentration is Δc. Therefore, the ionic species entering the porous network under the influence of the applied electrical potential difference obey:

$$j = \frac{I}{A} = F \sum_I z_i J_i \tag{8.19}$$

The flux is given by the Nernst–Planck equation:

$$J_i = -D_i \left(\nabla c_i + z_i \frac{F}{RT} c_i \Delta \Phi \right) \tag{8.20}$$

where Φ is an electrical potential due to the membrane potential, i.e., the electrical potential created by the transport of the ionic species [27] and the external electrical potential ΔU.

In the case of natural diffusion of ionic species, the membrane potential gradient can be calculated by stating that the left-hand side of the current law (8.19) is equal to zero. We obtain:

$$\nabla \Phi = -\frac{RT}{F} \frac{\sum_i z_i D_i \nabla c_i}{\sum_i z_i^2 D_i c_i} \tag{8.21}$$

Combining (8.19) and (8.20), we arrive at:

$$j = \frac{I}{A} = -F \sum_i D_i z_i \nabla c_i - \frac{F^2}{RT} \nabla \Phi \sum_i z_i^2 D_i c_i \tag{8.22}$$

When the porous material situated between the ionic species reservoir and the targeted zone is saturated with the ionic species, the ionic concentration is a constant and $\nabla c_i = 0$. As a consequence, the first term on the right of (8.22) vanishes and the membrane potential becomes zero [see (8.21)]. The electrical potential (which is due to the membrane potential and the external electrical source) becomes $\Delta U/L'$, where L' is the distance between the two electrodes in the plane of Fig. 8.3.

$$j = \frac{I}{A} = -\frac{F^2}{RT} \frac{\Delta U}{L'} \sum_i z_i^2 D_i c_i \tag{8.23}$$

By analogy with Ohm's law, we write:

$$\Delta U = -L' \frac{RT}{F^2} \frac{1}{\sum_i z_i^2 D_i c_i} \frac{L}{A} \tag{8.24}$$

Because the sign of the applied ΔU is negative, the global resistance of the flow configuration is:

$$R_{\text{net}} = \frac{RT}{F^2} \frac{1}{\sum_i z_i^2 D_i c_i} \frac{L'}{A} \tag{8.25}$$

We learned from constructal theory that the architecture of a flow system is the result of the search for greater of global flow access, i.e., the minimization of all the flow resistances together, and the spatial distribution of all resistances. In the present problem the minimization of flow resistances means that we search for paths of least electrical resistance. Because the order of magnitude of the ionic diffusion coefficient is D_0, the order of magnitude of the concentrations is Δc, and A can be represented by L in Fig. 8.3, (8.25) becomes:

$$R_{\text{net}} \sim \frac{RT}{F^2} \frac{1}{D_0 \Delta c} \frac{L'}{L} \tag{8.26}$$

R_{net} is the smallest when $L' = L'(x)$ is minimum, i.e., when $L' = L_0$. This defines an optimal aspect ratio $\left(\frac{L_0}{L}\right)$ that was used later in the numerical simulations. Along this preferred path (L_0) there will be an accumulation of ionic species. The domain bathed between the reservoir and the targeted zone can be expected to have the symmetrical shape sketched in Fig. 8.4.

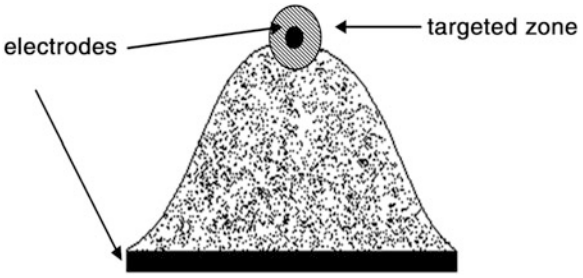

Fig. 8.4 Domain bathed by the ionic species [26]

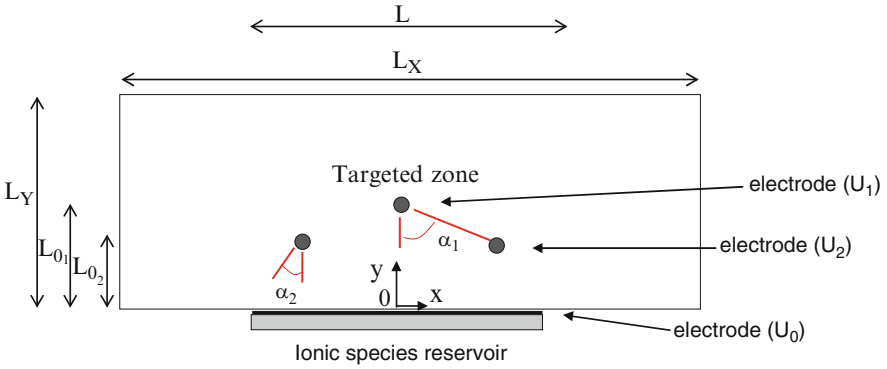

Fig. 8.5 Two-dimensional porous material with an external electrode and a second bed of electrodes [26]

In conclusion, the use of a single line-to-point flow is sufficient to meet objective (a), which was to reach a targeted zone. However, objective (b) is not met because there remains a nonuniform distribution of the species over the domain between the outside (the reservoir), and the target.

Next, a second level of electrodes is designed inside the material, between the external electrode and the first internal electrode of potential U_1. Inspired by previous work on the distribution of fluid flow from a source to an infinite number of sinks [8, 9, 13], which showed that pairing (dichotomy) is the optimal assembly rule, in the second layer of electrodes we place two electrodes. These are positioned symmetrically relative to the y-axis (Fig. 8.5).

The electrical resistance corresponding to the one-electrode design (8.26) is

$$R_{\text{net opt}} \sim \frac{RT}{F^2}\frac{1}{D_0 \Delta c}\frac{L_{0_1}}{L} \tag{8.27}$$

where the optimal aspect ratio was $\frac{L_{0_1}}{L}$. Now, if the two new electrodes are located at $x = \pm\frac{L}{4}$, and the corresponding optimal aspect ratio is $\frac{L_{0_2}}{L/2}$. It is worth noting that

one additional degree of freedom can be included in this analysis, by varying the position of the second layer of electrodes along the y-axis. A uniform distribution of ionic species over the bathed domain means that the electrical resistance between the second layer of electrodes and the reservoir must balance the one given by (8.27)

$$R_{\text{net opt 2}} \sim \frac{RT}{F^2}\frac{1}{D_0 \Delta c}\frac{2L_{0_2}}{L} \tag{8.28}$$

therefore

$$L_{0_2} = \frac{L_{0_1}}{2} \tag{8.29}$$

The corresponding ionic fluxes are, in an order of magnitude sense,

$$J_1 \sim D_0 \frac{F}{RT}\Delta c \frac{\Delta U_1}{L_{0_1}} \tag{8.30}$$

and

$$J_2 \sim D_0 \frac{F}{RT}\Delta c \frac{\Delta U_2}{L_{0_2}} \tag{8.31}$$

These two fluxes have to be equal in order to generate a more uniform ionic distribution. Combining (8.29)–(8.31), we obtain the optimal potential difference $\Delta U_2 = \frac{\Delta U_1}{2}$. The analysis can be repeated further by increasing the number of electrode levels, i.e., by creating a cascade of electrical potential differences.

8.4 Conclusion

The constructal law is the law of maximization of flow access under global constraints in freely morphing flow systems. The constructal law was applied in this study to the case of ionic transfer through porous media under an electrical source, namely, electrokinetic transfer. This principle leads to the discovery of the architecture of flow systems.

References

1. Hsieh S. Drug Permeation Enhancement, Theory and Applications.Marcel Dekker, Inc. New York, USA; 1994
2. Probstein RF, Hicks RE. Removal of contaminants from soils by electric fields. Science. 1993;260:498–503.

3. Sogorka DB, Gabert H, Sogorka B. Emerging technologies for soils contaminated with metals—electrokinetic remediation. Hazard Ind Waste. 1998;30:673–85.
4. Dickenson KS, Ally MR, Brown CH, Morris MI, Wilson-Nichols MJ. Demonstration recommendations for accelerated testing of concrete decontamination methods. Washington: DOE; 1995.
5. DePaoli DW, Harris MT, Morgan IL, Ally MR. Investigation of electrokinetic decontamination of concrete. Symposium on separation science and technology for energy applications, Vol. 32, pp. 387–404; 1997
6. Frizon F, Lorente S, Ollivier JP, Thouvenot P. Modeling the decontamination by electromigration of a porous medium. J Porous Media. 2004;7(3):213–27.
7. Bejan A. Shape and structure, from engineering to nature. Cambridge: Cambridge University; 2000.
8. Wechsatol W, Lorente S, Bejan A. Development of tree-shaped flows by adding new users to existing networks of hot water pipes. Int J Heat Mass Transfer. 2002;45:723–33.
9. Rocha LAO, Lorente S, Bejan A. Constructal design for cooling a disc-shaped area by conduction. Int J Heat Mass Transfer. 2002;45:1643–52.
10. Lorente S, Wechsatol W, Bejan A. Tree-shaped flow structures designed by minimizing path lengths. Int J Heat Mass Transfer. 2002;45:3299–312.
11. Lorente S, Bejan A. Svelteness, freedom to morph, and constructal multi-scale flow structures. Int J Therm Sci. 2005;44(12):1123–30.
12. da Silva AK, Lorente S, Bejan A. Constructal tree heat exchangers. J Appl Phys. 2004;96 (3):1709–18.
13. Wechsatol W, Lorente S, Bejan A. Optimal tree-shaped networks for fluid flow in a disc-shaped body. Int J Heat Mass Transfer. 2002;45:4911–24.
14. Vargas JVC, Ordonez JC, Bejan A. Constructal PEM fuel cell stack design. Int J Heat Mass Transfer. 2005;48(21–22):4410–27.
15. Reis AH, Miguel AF, Bejan A. Constructal theory of particle agglomeration and design of air-cleaning devices. J Phys D: Appl Phys. 2006;39(10):2311–8.
16. Miguel AF. Constructal pattern formation in stony corals, bacterial colonies and plant roots under different hydrodynamics conditions. J Theor Biol. 2006;242(4):954–61.
17. Miguel AF. Shape and complexity in living systems. In: Bejan A, Lorente S, Miguel AF, Reis AH, editors. Along with constructal theory. Presses de l'Université de Lausanne, Lausanne, Switzerland; 2007
18. Reis AH, Bejan A. Constructal theory of global circulation and climate. Int J Heat Mass Transfer. 2006;49(11–12):1857–75.
19. Wang KM, Lorente S, Bejan A. Vascularized networks with two optimized channel sizes. J Phys D: Appl Phys. 2006;39:3086–96.
20. Bejan A, Lorente S, Wang KM. Networks of channels for self-healing composite materials. J Appl Phys. 2006;100:033528 1–6.
21. Kim S, Lorente S, Bejan A. Vascularized materials: tree-shaped flow architectures matched canopy to canopy. J Appl Phys. 2006;100: 063525 1–8.
22. Lorente S, Bejan A. Heterogeneous porous media as multiscale structures for maximum flow access. J Appl Phys. 2006;100:114909.
23. Bejan A. Convection heat transfer. 3rd ed. Hoboken: Wiley Hoboken, New Jersey, USA; 2004.
24. Bégué P, Lorente S. Migration versus diffusion through porous media: time dependent scale-analysis. J Porous Media. 2006;9(7):637–50.
25. Lorente S. Constructal view of electrokinetic transfer through porous media. J Phys D: Appl Phys. 2007;40:2941–7.
26. Auger J, Yssorche-Cubaynes MP, Lorente S, Cussigh F, Demillecamps L. Ionic access through porous media with distributed electrodes. J Appl Phys. 2008;104:084913.
27. Révil A. Ionic diffusivity, electrical conductivity, membrane and thermoelectric potentials in colloids and granular porous media: a unified model. J Colloid Interface Sci. 1999;212:503–22.

Chapter 9
Constructal Theory Applied to Vascular Countercurrent Networks

Weizhong Dai

9.1 Introduction

Heat transfer within the human skin is a complicated process involving metabolic heat generation, heat conduction and blood perfusion in tissue, convection and perfusion of the arterial-venous blood through the capillary, and interaction with the environment. Modeling of heat-related phenomena such as bioheat transfer is important in the development of biological and biomedical technologies, such as thermotherapy of skin cancer and the design of heating or cooling garments, as well as protecting human life in cases of accidental or natural disasters [1, 2].

As pointed out in a recent article of Bergman et al. [3], which summarizes the recommendation on the topic matter of an NSF-sponsored workshop on the Frontier in Transport Phenomena Research and Education, engineering has the responsibility to bring to bear our quantitative approaches and strengths in modeling upon biological discoveries so that biological systems can be described, modeled, predicted, and manipulated.

Living skin is a hierarchically organized, active, and heterogeneous medium [4]. It consists of two subsystems: the cellular tissue treated as a multilayered medium and a highly branching hierarchical vascular network involving arterial and venous beds. Blood flow through the arterial bed supplies the cellular tissue with oxygen, nutritious products, etc., and controls heat balance in the system. Through the venous bed, blood flow withdraws products resulting from the life activity of the cellular tissue. The vascular network is embedded into the cellular tissue and in spite of its small relative volume the vascular network mainly determines heat and mass propagation.

W. Dai (✉)
Mathematics and Statistics, College of Engineering and Science, Louisiana Tech University, Ruston, LA 71272, USA
e-mail: dai@coes.latech.edu

L.A.O. Rocha et al. (eds.), *Constructal Law and the Unifying Principle of Design*, Understanding Complex Systems, DOI 10.1007/978-1-4614-5049-8_9,

Modeling thermal phenomena in living skin requires an accurate assessment of energy dissipation in tissue [5]. Blood flow plays an important role in determining the heat transfer and temperature distribution in skin tissues. Knowledge of the interaction between blood flow and bio-heat transfer is important for the prediction of the physiological response of tissues to high, external thermal radiation. Based on the histological knowledge about the blood circulation within the skin, the largest blood vessels of the skin are arranged in the form of a flat network in the subcutaneous tissue, immediately below the dermis. From the vascular network, branches of the blood vessels pass both inwardly and outwardly. Those that pass outwardly (arteries) supply the blood for the skin, while those that pass inwardly (veins) collect the blood returned from the skin [6].

Due to the vessel system being hierarchically organized, blood flow distribution over the vascular network, as well as over the tissue domain, has to be characterized by strong correlations between different hierarchy levels and by spatial correlations. Therefore, in order to describe the blood flow effect on heat transfer, one should take into account the vascular network as a whole, rather than just consider vessels of different levels individually [4]. However, it is impossible to describe heat transfer in living skin as a whole, including blood flow distribution over its systemic circulation, in the context of continuous theory. Therefore, we should specify a minimal region of living skin for which a complete mathematical model of heat transfer can be developed. In other words, such a model has to describe, in a self-consistent way, the distribution of the tissue temperature as well as the blood flow rate over the tissue domain under consideration [4]. In our research, we consider heat transfer in a domain of living skin that contains a complete vessel system forming a single microcirculatory bed. Such a single microcirculatory bed with several levels of arterial and venous beds is then embedded completely in the subcutaneous layer of a three-dimensional triple layered skin structure. The dimensions of and blood flow in the multilevel blood vessels are determined based on the recently developed constructal theory of multiscale tree-shaped heat exchangers [7–11].

The constructal theory [10] is the view that the generation of a flow configuration is a phenomenon that can be based on the following physical principle (the constructal law): “For a finite-size flow system to persist in time (to survive) its configuration must evolve in such a way that it provides an easier access to the currents that flow through it.” This principle predicts natural configurations across the board: river basins, turbulence, animal design (allometry, vascularization, and locomotion), cracks in solids, dendritic solidification, Earth’s climate, droplet impact configuration, etc. The same principle yields new designs for electronics, fuel cells, and tree networks for the transport of people, goods, and information.

In the following sections, we will show how the constructal theory of multiscale tree-shaped heat exchangers has been applied to the design of a vascular countercurrent network embedded in a 3D triple-layered skin structure [12–16]. Based on the designed vascular countercurrent network, we will present the mathematical models and numerical results for predicting skin burn injury induced by intense

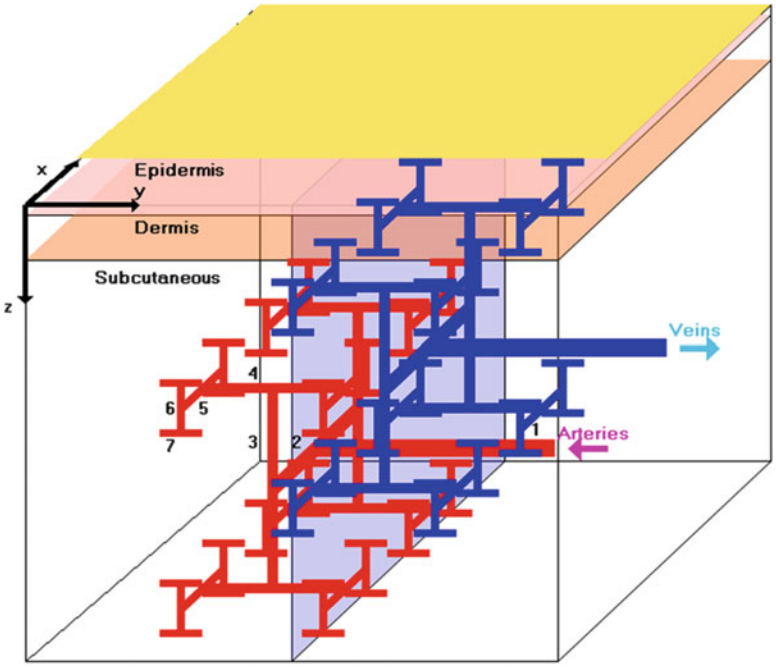

Fig. 9.1 3D triple-layered skin structure embedded with seven levels of countercurrent vasculature network [16]

radiation heating such as intense fire [13, 16], and for optimizing skin temperature induced by laser or electromagnetic radiations related to hyperthermia cancer treatments [12, 14, 15].

9.2 Vascular Countercurrent Network

Since there can be up to seven levels of blood vessels [17], we considered the skin tissue to be a rectangular structure embedded with a seven-level countercurrent vascular network, which is a highly branching and hierarchical network in the subcutaneous layer (Fig. 9.1). In the figure, the red color dendritic network represents arteries while the blue color dendritic network represents veins, where all are considered as slim cuboids for simplicity. Levels of arteries are designed such that the first-level artery comes from right to left running lengthwise in the y-coordinate, the second-level artery branches from the left end of the first-level artery running lengthwise in the x-coordinate, the third-level artery has 2 vessels branching from the two ends of the second-level artery running lengthwise in the z-coordinate, there are four fourth-level arteries branching from the four ends of the third-level arteries running lengthwise in the y-coordinate, the fifth-level artery has eight arteries branching from the eight ends of the fourth-level arteries running

lengthwise in the x-direction, there are 16 vessels in the sixth-level artery running length wise in the z-direction, and finally there are 32 vessels in the seventh-level artery running length wise in the y-direction. The vein network has the same number of blood vessels as its counterpart artery in corresponding levels. In sum, there are 128 blood vessels in total in the considered skin structure.

To determine the diameters of these many level blood vessels, we followed the constructal theory of multiscale tree-shaped heat exchangers, and assumed that the diameters of arteries are decreasing by a constant ratio γ between successive levels of branched vessels, which is given by Bejan [8]

$$\gamma = \frac{NL_{\mathrm{b}}^{m+1}}{NL_{\mathrm{b}}^{m}} = \frac{NW_{\mathrm{b}}^{m+1}}{NW_{\mathrm{b}}^{m}} = 2^{-\frac{1}{3}}, \quad m = 1, \ldots, 6 \tag{9.1}$$

where NL_{b}^{m} and NW_{b}^{m} are the length and width of the cross section of a blood vessel in level m, respectively. The length of blood vessel is assumed to double after two consecutive construction steps, which can be expressed in the length-doubling rule by da Silva and Bejan [11] as $L_{\mathrm{b}}^{m} = 2^{\frac{1}{2}} L_{\mathrm{b}}^{m-1}, m = 1, \ldots, 6$, where L_{b}^{m} is the length of the blood vessel in level m. The mass flow of blood in the mth level vessel, $M_m = v_m F_m$, satisfies $M_m = 2M_{m+1}$ [11], where v_m is the blood flow velocity and F_m is the area of the cross section in the mth level vessel.

Furthermore, the blood temperature in the cross section of a vessel was assumed to be uniform. We further assumed that a steady-state energy balance in the blood vessel can be reached because the length of the considered blood vessel is relatively short and the blood velocity is relatively high. However, one may use a transient heat transfer equation for a more accurate solution. Hence, the convective energy balance equations, which were used to calculate the artery (levels 1 through 6) blood temperatures, can be expressed as [17, 18]

$$C_{\mathrm{B}} M_m \frac{\partial T_{\mathrm{b}}^{m}}{\partial x_i} - \alpha P_m (T_{\mathrm{w}}^{m} - T_{\mathrm{b}}^{m}) = 0, \tag{9.2}$$

where $x_i = y, x, z$ is given in order, C_{B} is the heat capacity of blood, α is the heat transfer coefficient between blood and tissue, and P_m is the vessel perimeter. In addition, T_{w}^{m} and T_{b}^{m} are the wall temperature and the blood temperature in the mth level vessel. For the smallest, terminal arterial vessels (level 7), a decreased blood flow rate (P) is included in the energy balance equation [17]

$$C_{\mathrm{B}} M_7 \frac{\partial T_{\mathrm{b}}^{7}}{\partial y} - \alpha P_7 (T_{\mathrm{w}}^{7} - T_{\mathrm{b}}^{7}) - P C_{\mathrm{B}} F_7 T_{\mathrm{b}}^{7} = 0. \tag{9.3}$$

The venous network was assumed to be similar to the arterial network, except that the blood flow direction in each vein is opposite of that in the artery, i.e., countercurrent flow occurs in these two kinds of vessels as shown in Fig. 9.1. Also, the diameter ratio, length ratio, and mass flow ratio of the blood between the

successive levels of the branched veins take the same form as described in those equations for the arteries. It should be pointed out that at the last two levels, the diameter does not change because the vessels do not branch, but only change direction [17]. The last level vessels of the arterial and venous beds are interconnected by the capillary system. Moreover, the convective energy balance equations (9.2)–(9.3) used to calculate the blood temperature in the artery domain are applied to the vein domain at the corresponding levels.

9.3 Application to Skin Burn Prediction

We [13, 16] applied the above designed vascular countercurrent network to the development of a mathematical model for skin burn injury induced by intense radiation heating. The model was obtained by modifying the Pennes equation and taking into account the thermal relaxation time of biological tissue. In particular, we employed the Maxwell–Cattaneo flux law as described in [19–21], namely, $(1+\tau\frac{\partial}{\partial t})\vec{q}=-k\nabla T$, in conjunction with the fourth power law, to model the effects of high thermal radiation on such skin. Here, $\vec{q}$, k, and T denote the thermal flux vector, thermal conductivity, and tissue temperature, respectively, τ is the thermal relaxation (or lag) time [22], which represents the time required to establish steady thermal conduction in a material volume element once a temperature gradient is imposed across it. In addition, the skin is modeled as a 3D triple-layered structure with embedded the seven-level dendritic countercurrent vascular network as shown in Fig. 9.1.

Based on the above Maxwell–Cattaneo flux law, a modified Pennes equation that governs bioheat transport in a 3D triple-layered skin structure, where each layer is assumed to be a thermally conducting rigid body, can be written as follows [13]:

$$\rho_l C_l\left(\frac{\partial T_l}{\partial t}+\tau\frac{\partial^2 T_l}{\partial t^2}\right)+\tau W_{\mathrm{b}}^l C_{\mathrm{b}}^l\frac{\partial T_l}{\partial t}=k_l\Delta T_l+W_{\mathrm{b}}^l C_{\mathrm{b}}^l(T_{\mathrm{out}}-T_l)+Q_l,\quad l=1,2,3. \tag{9.4}$$

Here, T_l is the temperature of the lth skin tissue layer; T_{out} is the blood temperature at exit or entrance of the seventh level vessel for the artery or vein; p_l, c_l, and k_l denote the density, specific heat, and thermal conductivity of the lth skin tissue layer, respectively; τ is the thermal relaxation time; C_{b}^l is the specific heat of blood; and W_{b}^l is the blood perfusion rate. Because in this model we considered only radiation heating, all other internal heat sources Q_l were assumed negligible. Note that when τ is zero, the above equation reduces to the Pennes equation.

Assume that heat exchange on the surface of the skin with the surroundings includes the heat loss from convection and radiation [23], and is expressed as follows:

$$-k_1 \frac{\partial T_1}{\partial z} = h(T_a - T_1) + \varepsilon\sigma(T_a^4 - T_1^4), \quad z = 0. \tag{9.5}$$

Here, h is the convective heat transfer coefficient, T_a is the ambient temperature, σ is the Stefan–Boltzmann constant, and ε is the emissivity. Because we considered radiation heating, the temperature T_a is much higher than T_1. For simplicity, we further assumed that the heat flux approaches zero as the tissue depth increases, which is realistic for a biological body [20]. The other boundary conditions in the tissue are $\frac{\partial T_1}{\partial \vec{n}} = 0$, where $\vec{n}$ is the unit outward normal vector on the boundary. At the entrance to the first level vessel, we assume that $T_b^1 = T_{in}$, where T_{in} is the blood temperature at the entrance of the artery. At the exit of the artery, the blood temperature is equal to the surrounding tissue temperature $T_b^7 = T_{out}$. The continuity of heat transfer between the lateral blood vessel and the tissue requires [13, 17] $\frac{\partial T_b^m}{\partial \vec{n}} = B_i(T_w^m - T_b^m), \quad m = 1, \ldots 7$. The interfacial conditions between three skin tissue layers were assumed to be perfectly thermal contact.

Because the blood flow in the vein is oriented against the arterial flow, the entrance of the blood to the vein is located at the seventh level, and the blood temperature is equal to the surrounding tissue temperature. The initial conditions are $T_l = T_0, \quad l = 1, 2, 3$ where T_1, T_2, and T_3 are the tissue temperature in skin layer one, two and three, respectively, and T_0 is the initial temperature in the tissue. A quantitative description of thermal damage to skin, as suggested by [24], can be written as

$$\frac{\partial \Omega}{\partial t} = \zeta \exp(-\frac{\Delta E}{RT_l}), \quad l = 1, 2, 3 \tag{9.6}$$

where ζ is the frequency factor, ΔE is the activation energy controlling the development of tissue injury, and R (=8.314 JK^{-1} mol^{-1}) is the gas constant. The temperature T_l is determined using (9.4). Here, we note that $\Omega = 0.53, 1.0, 10^4$ correspond to first, second, and third degree burn injuries, respectively [25].

Equations (9.1)–(9.6) with initial and boundary conditions constitute the basic equations used to describe the thermo-mechanical behavior of skin tissues at high temperature. Due to the complex nature of the above governing equations, the whole system was solved by a finite difference method.

To illustrate the use of the above method, we chose a 3D skin structure with the dimensions 1.62 cm × 1.62 cm × 1.542 cm and with embedded seven-level dendritic countercurrent vascular network, as shown in Fig. 9.1. The values of the biological parameters used are listed in Table 1 in [16]. We assumed heat convection occurring on the skin surface ($h = 0.001$ W/cm^2 [17]), where the surface is exposed to an ambient temperature of 200°C, in addition to radiation heating. The thermal relaxation time and emissivity were taken to be $\tau = 20$ s [20] and $\varepsilon = 0.9$ [25], respectively. Three meshes of 162 × 162 × 771, 162 × 324 × 771, and 162 × 162 × 1,542 were chosen in order to test the convergence of the

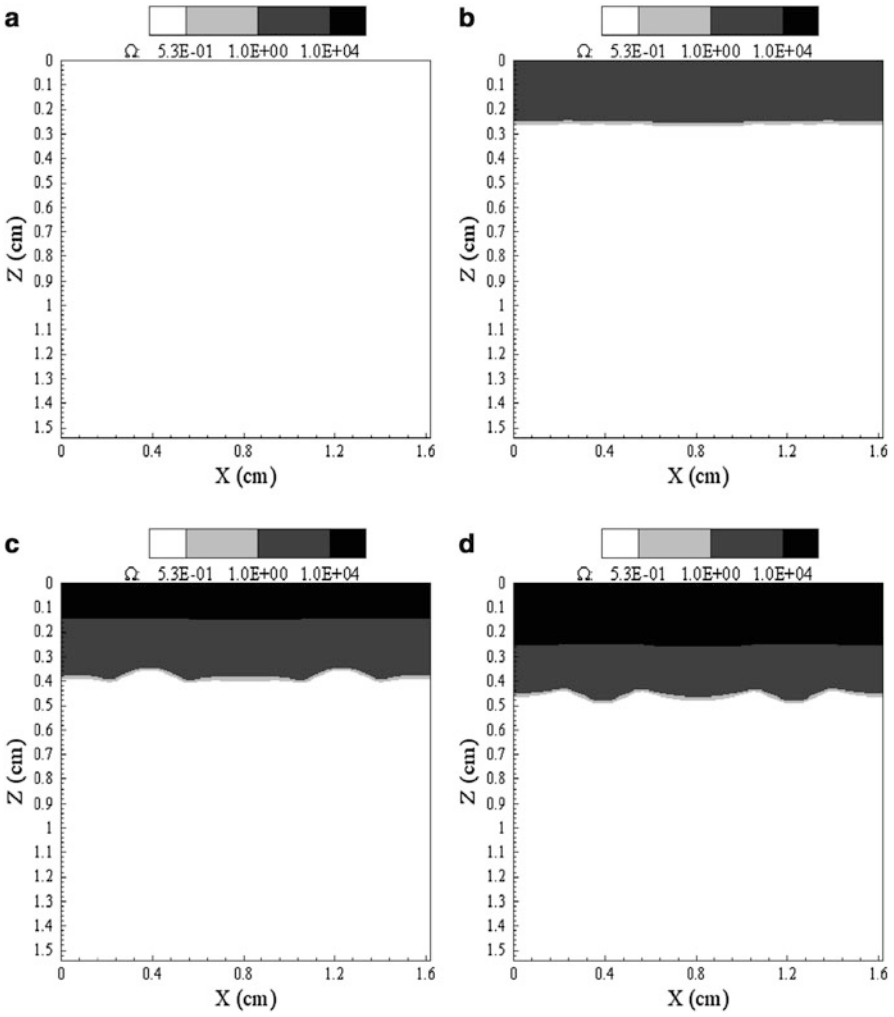

Fig. 9.2 Contours of skin burn distribution in the *xz* cross-section at $y = 0.76$ cm, where levels 1, 5, 6, and 7 of artery, and levels 4 and 7 of vein appear [16]

numerical solution. Other parameters used in these computations can be seen in Tables 2–3 in [16].

Figures 9.2 and 9.3 show the contours of the tissue damage distributions in various cross sections at (a) $t = 100$ s, (b) $t = 200$ s, (c) $t = 300$ s, and (d) $t = 400$ s. Because the values of $\Omega = 0.53, 1.0, 10^4$ correspond to the first, second, and third degree burn injuries, respectively, these two figures show that the skin appears to be the second degree burn at $t = 200$ s, and the third degree burn at $t = 300$ s and $t = 400$ s.

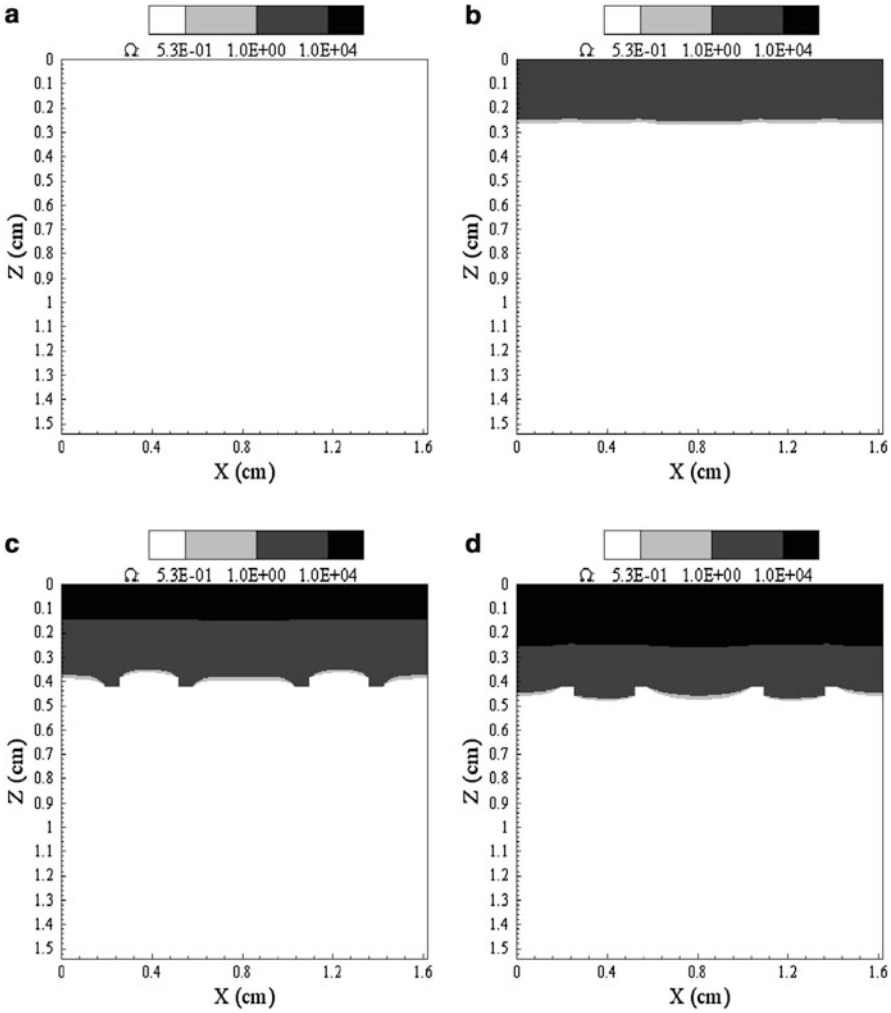

Fig. 9.3 Contours of skin burn distribution in the *xz* cross-section at $x = 0.7$ cm, where levels of 1, 4, and 7 of artery, and levels 5, 6, and 7 of vein appear [16]

9.4 Application to Skin Laser Radiation

There has been interest in research related to hyperthermia combined with radiation and cytotoxic drugs to enhance the killing of tumors. Conventional hyperthermia (target temperatures of 42–46 °C in conjunction with radiation) has demonstrated increased effectiveness in the treatment of certain types of cancer, such as those of liver metastases. The objective is to control laser heating or electromagnetic radiation of the tumor so that the temperature of the normal tissue surrounding the tumor remains low enough so as not to cause damage to the tissue. Hence, for process

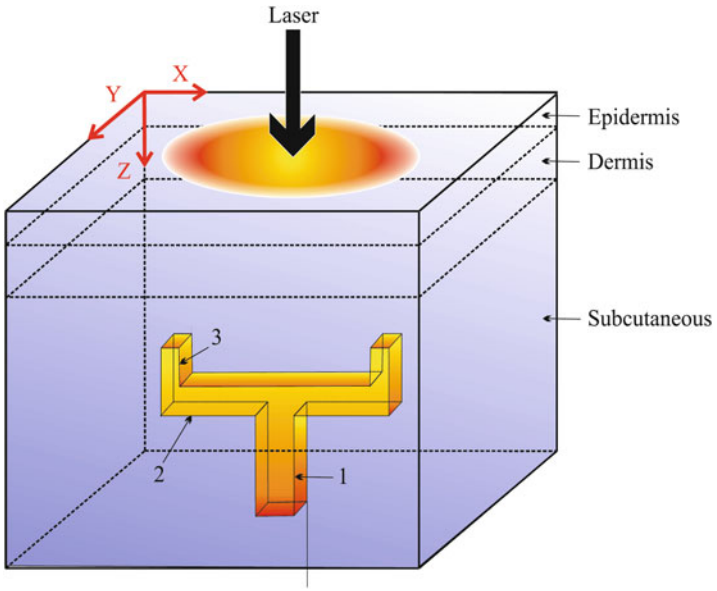

Fig. 9.4 3D triple-layered skin structure [12]

control, it is important to obtain a temperature field of the entire treatment region. With knowledge of the entire temperature field in the treatment region, clinical personnel can potentially control the heating source to deliver energy to the treatment target volume to raise its minimum temperature above 42 °C, while limiting the temperatures in the normal tissue to prevent damage. However, it is not easy to obtain an accurate determination of the temperature field over the entire treatment region during clinical hyperthermia treatments, because the number of invasive temperature probes that can be used is limited due to the pain tolerance of patients. Understanding the effect of high thermal radiation on biological tissues, specifically, thermomechanical damage to tissue, requires the accurate description of bioheat transfer. Hence, it is important to determine mathematically the laser or electromagnetic intensity and pattern of laser or electromagnetic exposure in order to optimize the temperature distribution in the treated region.

We considered the target region to be a rectangular structure embedded with only last three-level blood vessels as shown in Fig. 9.4 for simplification. The Pennes equation, (9.4) with $\tau = 0$, that describes the thermal behavior of the triple-layered skin structure when irradiated by the laser was used, where the laser power is assumed to be continuous and spatial with a normal distribution. Consequently, the heat source can be written as follows [26]:

$$Q = \frac{\alpha}{\sqrt{2\pi d^2}} P_0 (1 - \text{Reff}) \exp(-\alpha z) \exp\left[-\frac{(x - x_0(t))^2 + (y - y_0(t))^2}{2d^2} \right], \quad (9.7)$$

where α is the laser absorptivity and Reff is the laser reflectivity of the skin, d is the standard deviation of the width of a normally distributed laser beam. Here, $(x_0(t), y_0(t))$ is the location where the laser is focused at time t. P_0 is the laser intensity, which will be determined later on so that an optimal temperature distribution can be obtained. Optimality is achieved by minimizing the sum of square deviations between observed and prespecified temperature elevations at different locations on the skin surface.

We tested our method in the 3D skin structure where the parameter values are listed in Table 1 in [12] and the dimensions of the skin structure are given in Table 2 in [12]. The laser absorptivity and reflectivity are 1.8 cm^{-1} and 0.1, respectively [12]. A mesh of 50 × 50 × 1,208 in (x, y, z) was employed in the computation. The blood temperature elevation at entrance is assumed to be 1 °C. The temperature elevation was prespecified to be 8 °C at the center of the skin surface and 2 °C at the midpoint on each edge of the surface.

The pattern of laser irradiation was as follows: the laser with a beam width of 0.01 cm is focused at the center of the skin surface. When the temperature of the skin surface at the center rises to 8 °C, the laser is turned off to allow heat to diffuse from the center towards the perimeter of the region. The laser is then turned on when the temperature at the center of the skin surface decreases to 4 °C. The whole process lasts 400 s.

In our computation, we first considered the case where there is no heat convection on the skin surface. In this case, we started with an initial value P_0 of 1.2 W/cm and an increment of P_0 equal to 1 % of P_0. We optimized P_0 and obtained that P_0 converges to 1.1947 W/cm. Thus, we used the convergent value of P_0 to obtain the temperature distribution in the 3D skin structure as shown in Fig. 9.5. We then considered the case where there is a heat convection ($h = 0.001$ W/cm^2) on the skin surface. In this case, we started with an initial value P_0 of 1.1947 W/cm and an increment of P_0 equal to 1 % of P_0. We optimized P_0 and obtained that P_0 converges to 1.3166 W/cm. Thus, we used the convergent value of P_0 to obtain the temperature distribution in the 3D skin structure as shown in Fig. 9.6. It can be seen from these two figures that the temperature elevations at the center and at the edge of the skin surface reached 8 °C and 2 °C, respectively.

9.5 Application to Skin Electromagnetic Radiation

We extended our research to the electromagnetic radiation heating case [15]. To obtain the heat source, one need to obtain the distribution of electromagnetic fields in space and time, that is governed by the "normalized" Maxwell's equations as follows:

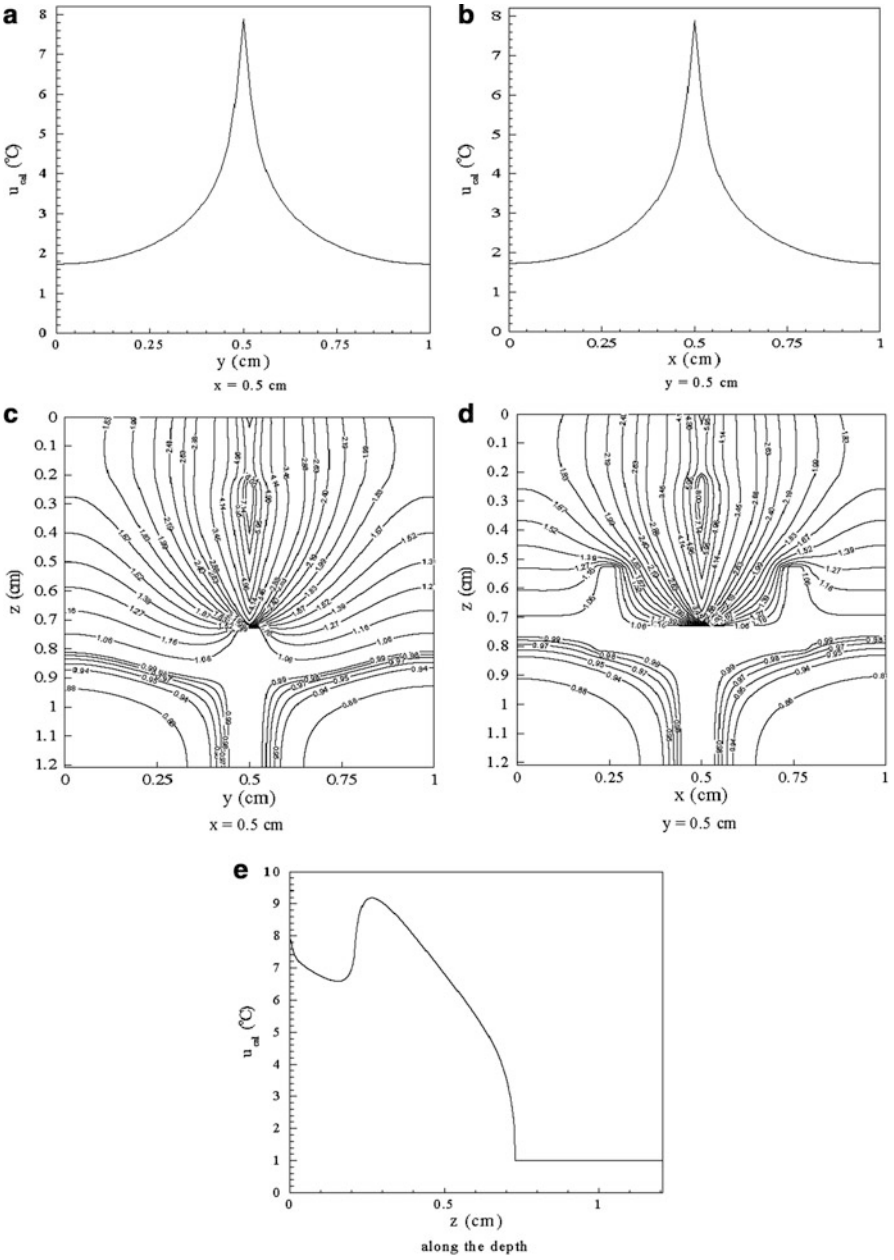

Fig. 9.5 Profiles of temperature elevations and contours at $t = 400$ s with no heat convection [12]

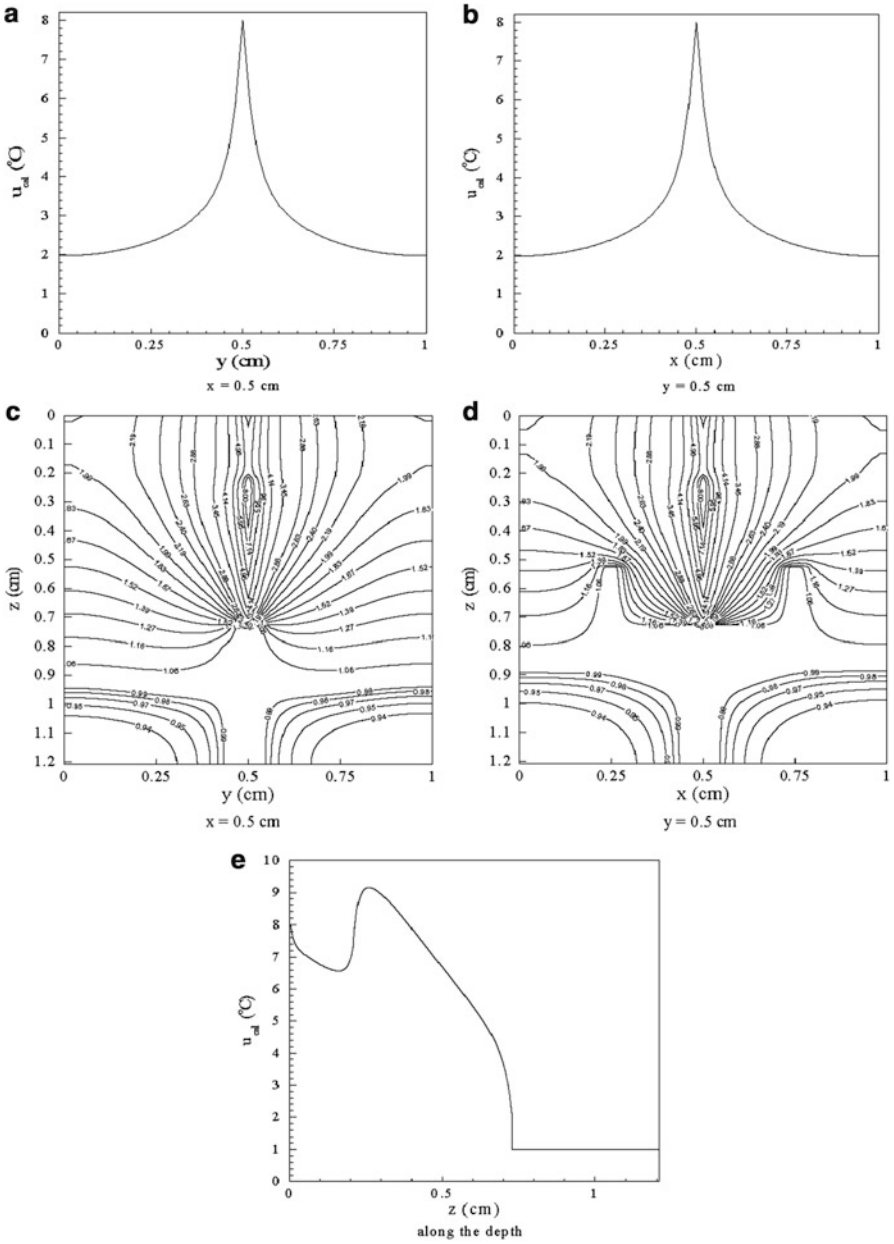

Fig. 9.6 Profiles of temperature elevations and contours at $t = 400$ s with a heat convection [12]

$$\begin{aligned}\frac{\partial \vec{D}}{\partial t} &= \frac{1}{\sqrt{\varepsilon_0 \mu_0}} \vec{\nabla} \times \vec{H},\\ \vec{D}(\omega) &= \varepsilon_r^*(\omega)\vec{E}(\omega),\\ \frac{\partial \vec{H}}{\partial t} &= -\frac{1}{\sqrt{\varepsilon_0 \mu_0}} \vec{\nabla} \times \vec{E},\end{aligned} \tag{9.8}$$

where $\vec{D}$ is the electric flux density, $\vec{E}$ is the electric density, $\vec{H}$ is the magnetic density, ε_0 is the permittivity of free space, μ_0 is the permeability of free space, ω is the angular frequency, and $\varepsilon_r^*(\omega)$ is the relative dielectric constant which can be expressed [27, 28]:

$$\varepsilon_r^*(\omega) = \varepsilon_\infty + \sum_{m=1}^{4} \frac{\Delta\varepsilon_m}{1 + (j\omega\tau_m)^{1-\alpha_m}} + \frac{\sigma_1}{j\omega\varepsilon_0}, \tag{9.9}$$

where ε_∞ is the permittivity in the terahertz frequency range, σ_1 is the ionic conductivity, and $j = \sqrt{-1}$; and for each dispersion region m, τ_m is the relaxation time, α_m is an adjustable parameter between 0 and 1, and $\Delta\varepsilon_m$ is the drop in permittivity in the frequency range. Equation (9.9), which is called the Cole-Cole expression, is based on the well-known dispersive properties of biological matter and their expression as a summation of terms corresponding to the main polarization mechanisms. The dielectric spectrum extends from Hz to GHz and shows four major regions of dispersion [28]. Solving Maxwell's equations coupled with the Cole-Cole expression by using the finite-difference time-domain (FDTD) method, however, is difficult because it is not easy to convert the equations from the frequency domain to the time domain when $0<\alpha_m<1$.

The dissipated density is the electromagnetic wave energy absorbed in the material. It is eventually converted into thermal energy. The dissipated power density is influenced by the field intensity distribution and electric properties. The heat function, which will be included as a source term in the bio-heat transfer equation, (9.4) with $\tau = 0$, can be expressed as [29] $Q = \omega\varepsilon_0\varepsilon''_{\text{eff}}\left|\vec{E}\right|^2 + \omega\mu_0\mu''_{\text{eff}}\left|\vec{H}\right|^2$, where $\varepsilon''_{\text{eff}}$ and μ''_{eff} are relative loss factors related to dipolar, electronic, atomic, space charge, and conduction losses. In our study, a sinusoidal wave was considered as $E_z = E_0 \sin(2\pi f \cdot t)$, where E_0 is the amplitude of the incident wave, f is the frequency of the wave, and t is time. Consequently, the volumetric heating rate can be computed from peak field amplitudes as $Q = \frac{1}{2}\omega\varepsilon_0\varepsilon''_{\text{eff}}\left|\vec{E}_{\max}\right|^2$ [29], where $\varepsilon''_{\text{eff}}$ is obtained based on (9.9) as follows:

$$\varepsilon''_{\text{eff}} = \sum_{m=1}^{4} \frac{\Delta\varepsilon_m(\omega\tau_m)^{1-\alpha_m}\cos(\frac{1}{2}\alpha_m\pi)}{1 + 2(\omega\tau_m)^{1-\alpha_m}\sin(\frac{1}{2}\alpha_m\pi) + (\omega\tau_m)^{2(1-\alpha_m)}} + \frac{\sigma_1}{\omega\varepsilon_0}. \tag{9.10}$$

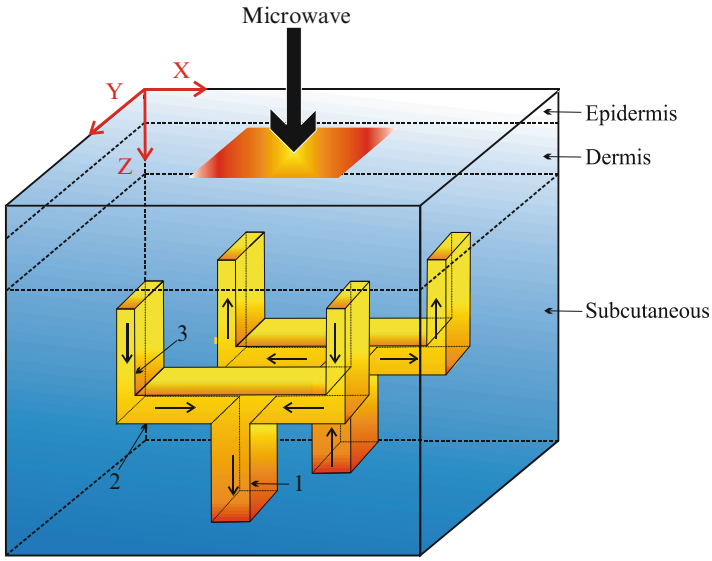

Fig. 9.7 3D triple-layered skin structure [15]

Since $\varepsilon_r^*(\omega)$ given by (9.9) is a complicated expression, we employed the z-transform described in [30] to simplify the situation. Finally, we used the FDTD method coupled with the perfectly matched layer technique [30] to obtain the EM fields. On the other hand, the finite difference scheme used for the bioheat transfer model is similar to that described in the previous section.

We tested our method in a 3D skin structure as shown in Fig. 9.7, where the parameter values of the 3D skin structure and dielectric properties of human skin can be seen in Tables 1–3 in [15]. The test was conducted by using the plane wave to illuminate the skin. The plane wave was driven at 10 GHz. The computational domain, which includes the plane wave and was used to obtain the EM fields, was computed in a lattice with grid points $75 \times 75 \times 320$ in (x, y, z). The plane wave resides in a lattice with dimensions $3 \times 3 \times 310$ in (x, y, z) along the center line of the z-direction. On the other hand, the computational domain for obtaining the temperature distribution in the 3D skin structure was placed in a lattice with grid points $60 \times 60 \times 604$ in (x, y, z). The temperature elevation of blood at entrance was assumed to be 1 °C. The temperature elevation at the center of the skin surface was prespecified to be 8 °C and the temperature elevation at the midpoint on each edge of the skin surface was prespecified to be 2 °C. In our computation, we considered that there was heat convection on the skin surface ($h = 0.001$ W/cm^2).

We started with an initial value E_0 of 2,000 V/m and an increment of E_0 equal to 1% of E_0. We optimized E_0 and obtained that E_0 converges to 1,941.8456 V/m.

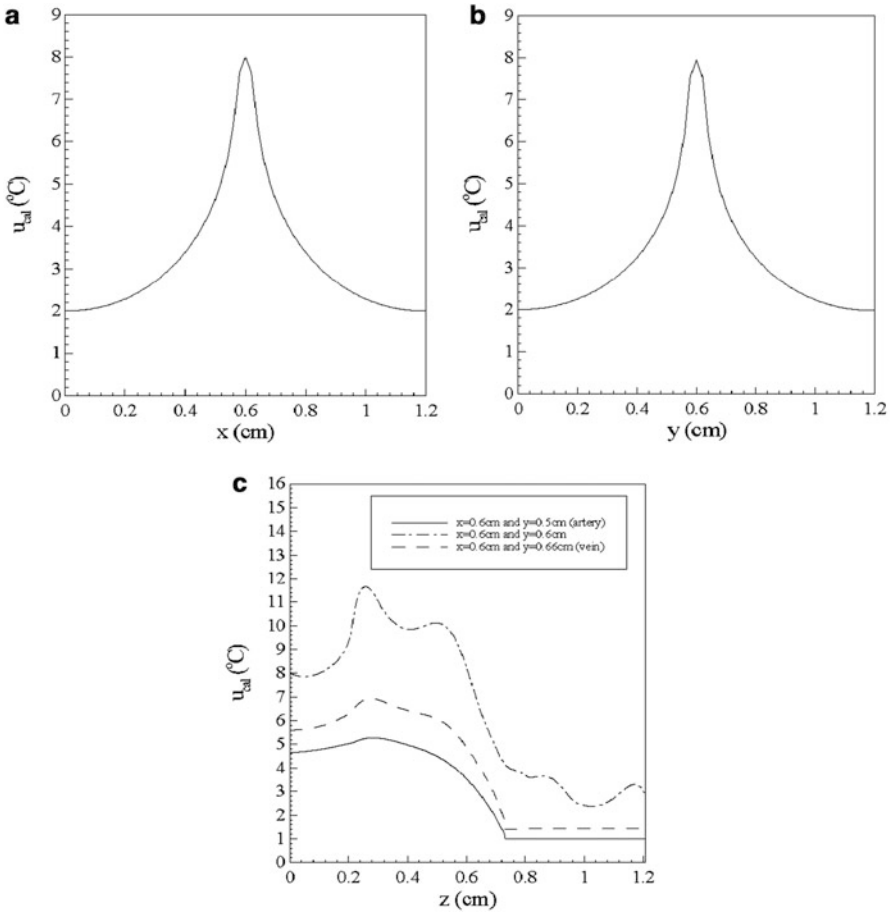

Fig. 9.8 Profiles of temperature elevations at $t = 400$ s [15]

Thus, we used the convergent value of E_0 to obtain the temperature distribution in the 3D skin structure. Figure 9.8 shows the temperature elevation profiles at $t = 400$ s along the lines (a) $y = 0.6$ cm and (b) $x = 0.6$ cm on the skin surface, and (c) along the depth (the z-direction), respectively. It can be seen that the temperature elevation at the center of the skin surface rises to 8 °C while the temperature elevation at the edge rises to 2 °C. Figure 9.9 shows contours of temperature elevations at in the cross sections of (a) $y = 0.50$ cm, (b) $y = 0.60$ cm, (c) $y = 0.66$ cm, and (d) $x = 0.6$ cm.

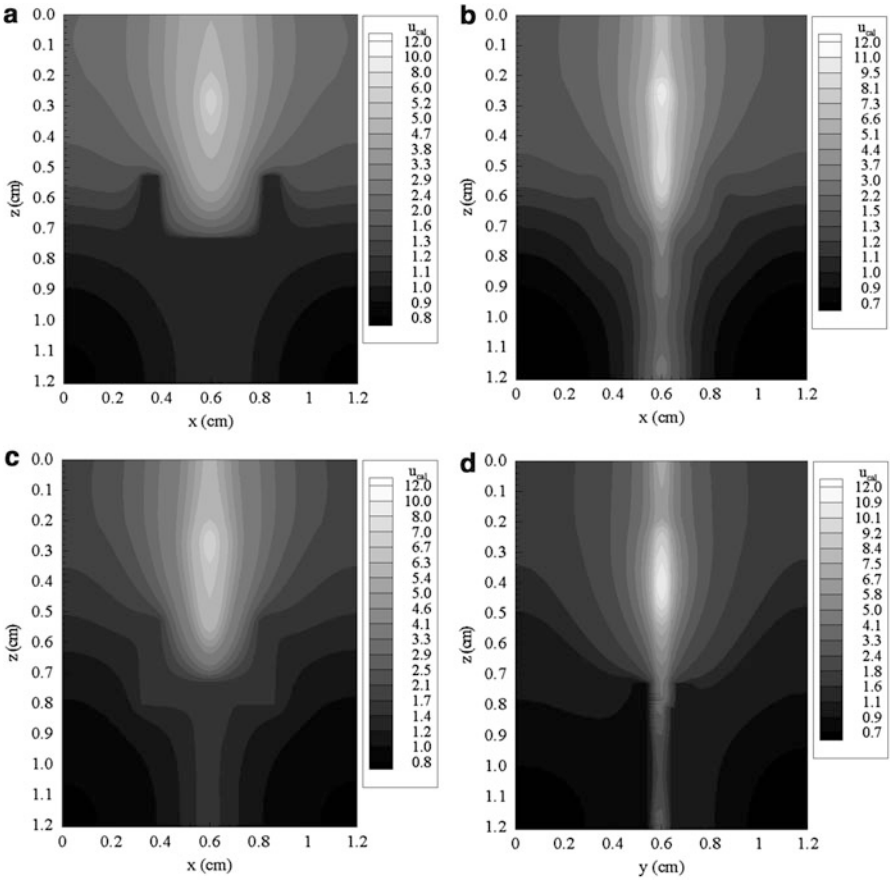

Fig. 9.9 Contours of temperature elevations at $t = 400$ s in the various cross sections [15]

9.6 Conclusions

The constructal theory of multiscale tree-shaped heat exchangers has been applied to the vascular countercurrent network embedded in a three-dimensional triple layered skin structure. Based on the designed vascular countercurrent network, we present our mathematical models and numerical results for predicting skin burn injury induced by intense radiation heating and for optimizing skin temperature induced by laser or electromagnetic radiations related to hyperthermia cancer treatments.

References

1. Borkebak RC. Heat transfer in biological systems. Int Rev Gen Exper Zool. 1966;2:269–344.
2. Bowman HF, Cravalho EG, Woods M. Theory, measurement and application of properties of biomaterials. Annu Rev Biophys Bioeng. 1975;4:43–80.

3. Bergman TL, Faghri A, Viskanta R. Frontiers in transport phenomena research and education: energy systems, biological systems, security, information technology and nanotechnology. Int J Heat Mass Tran. 2008;53:4599–613.
4. Lubashevsky IV, Gafiychuk V. Mathematical description of heat transfer in living tissue. Unpublished book
5. Chato JC. Fundamentals of bioheat transfer. In: Gautherie M, editor. Clinical thermology: thermal dosimetry and treatment planning. Berlin: Springer; 1990.
6. Gartner LP. Color atlas of histology. 3rd ed. Philadelphia: Lippincott Williams and Wilkins; 2000.
7. Bejan A. Shape and structure, from engineering to nature. Cambridge: Cambridge University Press; 2000.
8. Bejan A. The tree of convective heat streams: its thermal insulation function and the predicted 3/4-power relation between body heat loss and body size. Int J Heat Mass Tran. 2001;44:699–704.
9. Bejan A, Lorente S. Constructal theory of generation of configuration in nature and engineering. J Appl Phys. 2006;100:041301.
10. Bejan A, Lorente S. Design with constructal theory. Hoboken: Wiley; 2008.
11. da Silva AK, Lorente S, Bejan A. Constructal multi-scale tree-shaped heat exchangers. J Appl Phys. 2004;96:1709–18.
12. Dai W, Bejan A, Tang X, Zhang L, Nassar R. Optimal temperature distribution in a 3D triple layered skin structure with embedded vasculature. J Appl Phys. 2006;99:104702.
13. Dai W, Wang H, Jordan PM, Mickens RE, Bejan A. A mathematical model for skin burn injury induced by radiation heating. Int J Heat Mass Tran. 2008;51:5497–510.
14. Tang X, Dai W, Nassar R, Bejan A. Optimal temperature distribution in a 3D triple layered skin structure embedded with artery and vein vasculature. Numer Heat Transfer A. 2006;50:809–43.
15. Wang H, Dai W, Bejan A. Optimal temperature distribution in a 3D triple layered skin structure embedded with artery and vein vasculature and induced by electromagnetic radiation. Int J Heat Mass Tran. 2007;50:1843–54.
16. Zeng X, Dai W, Bejan A. Vascular countercurrent network for 3D triple-layered skin structure with radiation heating. Numer Heat Transfer A. 2010;57:369–91.
17. Huang H, Chen ZP, Roemer R. A counter current vascular network model of heat transfer in tissues. J Biomech Eng. 1996;118:120–9.
18. Majchrzak E, Mochnacki B. Numerical model of heat transfer between blood vessel and biological tissue. Comput Assist Mech Eng Sci. 1999;6:439–47.
19. Liu J. Preliminary survey on the mechanisms of the wave-like behaviors of heat transfer in living tissues. Forschung im Ingenieurwesen. 2000;66:1–10.
20. Liu J, Chen X, Xu LX. New thermal wave aspects on burn evaluation of skin subjected to instantaneous heating. IEEE Trans Biomed Eng. 1999;46:420–8.
21. Tzou DY. Macro-to-microscale heat transfer: the lagging behavior. Washington: Taylor and Francis; 1996.
22. Mitra K, Kumar S, Vedavarz A, Moallemi MK. Experimental evidence of hyperbolic heat conduction in processed meat. Trans ASME J Heat Transfer. 1995;117:568–73.
23. Sturesson C, Andersson-Engels A. A mathematical model for predicting the temperature distribution in laser-induced hyperthermia: experimental evaluation and applications. Phys Med Biol. 1995;40:2037–52.
24. Henriques FC, Mortiz AR. Studies of thermal injury in the conduction of heat to and through skin and the temperature attained therein: a theoretical and experimental investigation. Am J Pathol. 1947;23:531–49.
25. Diller KR. Modeling of bioheat transfer processes at high and low temperature. In: Cho YI, Hartnett JP, Irvine Jr TF, editors. Advanced in heat transfer, 22. New York: Academic; 1992. p. 157–357.
26. Jaesung H, Klavs FJ. Combined experimental and modeling studies of laser-assisted chemical vapor deposition of copper from copper (I)-hexafluoroacetylacetonate-trimethylviny-lsilane. J Appl Phys. 1994;75:2240–50.

27. Cole KS, Cole RH. Dispersion and absorption in dielectrics I. alternating current characteristics. J Chem Phys. 1941;9:341–51.
28. Gabriel S, Lau RW, Gabriel C. The dielectric properties of biological tissues: III. parametric models for the dielectric spectrum of tissues. Phys Med Biol. 1996;41:2271–93.
29. Dincov DD, Parrott KA, Pericleous KA. A new computational approach to microwave heating of two-phase porous materials. Int J Numer Method Heat & Fluid Flow. 2004;14:783–802.
30. Sullivan DM. Electromagnetic simulation using the FDTD method. New York: IEEE; 1999.

Chapter 10
Constructal Design of Animate and Inanimate Systems: An Answer to Consumerism?

J.V.C. Vargas

10.1 Introduction

After the Industrial Revolution, the average income and population began to exhibit unprecedented sustained growth. The world's average per capita income increased over tenfold, while the world's population increased over sixfold in the two centuries that followed [1, 2]. As a result, a consumption society appeared in the period post industrial revolution, in which the new industrial machinery allowed for the automation of the production of consumption items. The immediate consequence was the appearance of the worker in replacement of the artisan, i.e., less qualified individuals started to do the same tasks as more qualified ones, with greater productivity. Wisdom and creativity lost power to the factory owners. Therefore, the great corporations started to decide when, where, how, and to whom a service would be provided [3].

Such a scenario gave birth to consumerism, which is a social and economic order based on fostering a desire to purchase goods and services in ever greater amounts. The newly emergent middle class arising at the turn of the twentieth century comes to full fruition by the end of the twentieth century through the process of globalization. Critics of consumerism often state that consumerist societies cause damage to the environment, contribute to global warming, and use resources at a higher rate than other societies, and others say [4]: "Trying to reduce environmental pollution without reducing consumerism is like combating drug trafficking without reducing the drug addiction." Not all anti-consumerists oppose consumption in itself, but they argue against increasing the consumption of resources beyond what is environmentally sustainable. Some ecological economists recognize the inherent conflict between consumer-driven consumption and planet-wide ecological degradation [4].

J.V.C. Vargas (✉)
Departamento de Engenharia Mecânica, Universidade Federal do Paraná, C. P. 19011, Curitiba, Paraná 81531-990, Brazil
e-mail: vargasjvcv@gmail.com

L.A.O. Rocha et al. (eds.), *Constructal Law and the Unifying Principle of Design*, Understanding Complex Systems, DOI 10.1007/978-1-4614-5049-8_10,

Actually, such analyses are needed to treat the question of energy and natural resources availability with more scientific depth.

The conservation laws of mass, momentum, energy, and species have been known for centuries. Those principles state that mass, momentum, energy, and chemical species are conserved in the universe, continuously transforming into other forms, through different physical and chemical processes. These transformations occur irreversibly, thus reducing energy availability for use, i.e., with thermodynamic losses according to the second law of thermodynamics, which in turn could and should be minimized. Therefore, as humanity advanced scientific knowledge, theoretically it would be possible, by means of appropriate technological development, to make use of energy and natural resources perennially.

In sum, the concept that should be invoked for the increase or reduction of consumerism could be summarized in one very popular word currently, i.e., sustainability. So, what is necessary for mankind survival and of the world as we know it is the search for the balance between consumerism and the available technology in the moment we live. On the other hand, the imbalance between these two variables could definitely lead to catastrophic consequences. Therefore, the question to be answered is as follows: Is it possible to reach such balance as society evolves in time?

Another interesting aspect is that part of the scientific community tends to separate animate from inanimate systems making clear distinctions between them, mainly those scientists that work with biological sciences. In fact, evolution theory was originally conceived for biological organisms by Darwin [5]. Given that both animate and inanimate systems are made of the same chemical elements, i.e., matter, and therefore with a directly related energy level, it is well recognized that the conservation laws apply to all physical systems, indistinctively. Essentially, such separation tendency is a result of the lack of scientific knowledge regarding the creation of an animated system, i.e., life. Currently, it is clear how to go from an animate to an inanimate system, by killing the being for example, but the road that leads from inanimate to animate is not yet known. However, based on such observations, it is reasonable to pose the question: Is it appropriate to separate animate from inanimate systems?

Possible answers to the questions posed in the previous two paragraphs could lie on constructal theory [6], which is the thought that geometry (flow architecture) is generated by the pursuit of global performance subject to global constraints, in flow systems the geometry of which is free to vary. According to constructal theory, the optimization of flow architecture starts at the smallest (elemental) scale, in which the system still preserves its identity (e.g., a creek in a river basin; the single polymer electrolyte membrane fuel cell, PEMFC, in a fuel cell stack; a cell in a multicellular living organism). Irreversibilities due to all flow resistances (e.g., pressure drops, charge transfer, electrical resistances, mass diffusion) are minimized together for maximum global performance at the whole system level. Any physical system is a combination of several flow systems (e.g., electrical; chemical; fluid and heat flows). In sum, the optimization of flow-system architecture is common in engineering and nature.

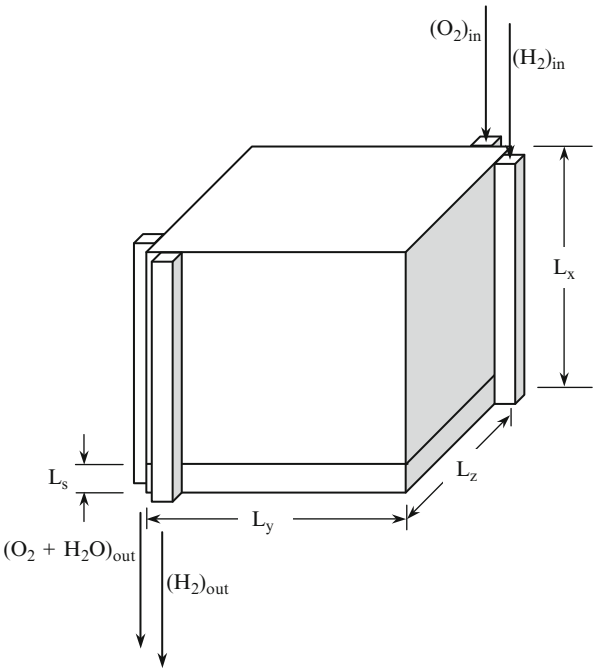

Fig. 10.1 The configuration of a PEMFC stack

Prediction entirely based on the constructal law could lead man to evolve to the sustainable equilibrium between consumerism and the available technology in time, in a self-regulatory process for all species survival. In conclusion, constructal law unifies all systems design.

The next sections present an example of Constructal design of a physical system, i.e., a PEMFC stack. The results are then utilized to identify common trends between the analyzed (inanimate) system and other animate systems.

10.2 The Example System

A PEMFC stack is shown schematically in Fig. 10.1. The stack is fed by two input headers, one carries fuel and the other oxidant, which are delivered to each single PEMFC in the stack. After the fuel and oxidant streams sweep the single PEMFC gas channels in the stack, two output headers collect the used gases and the water that is produced by the reactions in the fuel cells. Electrical power is produced by the stack, and a fraction is used to pump the fuel and oxidant across the PEMFC stack, through the input and output headers, and through very narrow gas channels in each single fuel cell. For simplicity, the model is based on the assumption that the fuel stream is pure hydrogen, and that the oxidant is pure oxygen.

A single PEMFC is divided into seven control volumes that interact energetically with one another. In the present model, the existence of a cooling channels system that irrigates the bipolar plates is assumed, and that the cooling fluid (e.g., water, air) is kept at an average specified temperature, T_∞, between single cells and around the stack. In this way, the electrical power delivered by the entire stack results from the analysis of one single cell, i.e., the electrical power produced by the stack is the electrical power produced by a single cell multiplied by the number of cells in the stack, which is a variable in the PEMFC stack constructal design procedure. However, the required pumping power depends on the flow structure of the entire PEMFC stack.

The mathematical model for a single cell operating at steady state was introduced in a previous study by Vargas et al. [7] and extended for the PEMFC stack dynamic and steady state analysis [8]. Therefore, the reader is directed to those references for assessing the complete details of the model.

Figure 10.2 shows schematically the division of a single PEMFC into seven control volumes. In addition, there are two bipolar plates (interconnects) that have the function of allowing the electrons produced by the electrochemical oxidation reaction at the anode to flow to the external circuit or to an adjacent cell. The control volumes (CV) are the fuel channel (CV1), the anode diffusion backing layer (CV2), the anode reaction layer (CV3), the polymer electrolyte membrane (CV4), the cathode reaction layer (CV5), the cathode diffusion backing layer (CV6), and the oxidant channel (CV7).

The model consists of the complete conservation equations for each control volume, and the equations accounting for electrochemical reactions. The reversible electrical potential and power of the fuel cell are then computed (based on the reactions) as functions of the temperature and pressure fields determined by the model. The instantaneous electrical potential and power of the fuel cell are obtained as functions of each compartment temperature, by subtracting from the reversible potential the losses due to surface overpotentials (poor electrocatalysis), slow diffusion, and internal ohmic losses through the cell (resistance of individual cell components, including electrolyte membrane, bipolar plates, interconnects, and any other cell components through which electrons flow). These are functions of the total cell current (I), which is directly related to the external load (or the cell voltage), and time. In sum, the total cell current and time are considered the independent variables.

10.3 Constructal Design

The previously published model [7, 8] allows the calculation of the electrical power output of a single PEMFC when its geometry and operating parameters change. The model accounts for internal temperature and pressure gradients and potential losses. An important step in constructal design is the identification of realistic design constraints. The total PEMFC stack volume, V_T, is fixed in the optimization

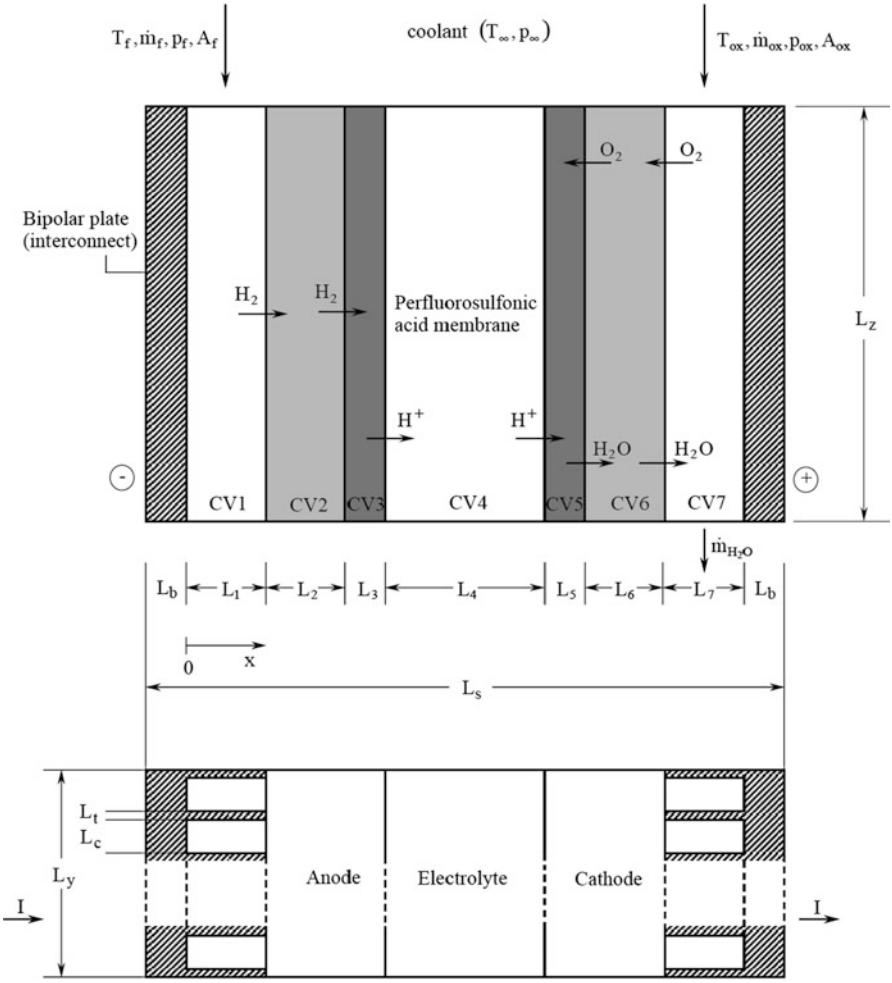

Fig. 10.2 The internal structure of a single PEMFC

process. In dimensionless terms, the volume constraint reads as $\xi_x \xi_y \xi_z = 1$. According to Fig. 10.1, in the PEMFC stack, the number of single cells is given by $n_s = \xi_x / \xi_s$, and L_s is the total length (or thickness) of a single cell, as it is shown in Fig. 10.2. All dimensionless lengths are defined by $\xi_i = L_i / V_T^{1/3}$.

Proceeding with the analysis, it is necessary to account for the pressure drops in the gas channels of the single cells, and also in the input and output headers, as shown schematically in Fig. 10.3. The calculation of the total pressure drops in the fuel cell stack will lead to the required total pumping power to supply the stack with fuel and oxidant at any current level.

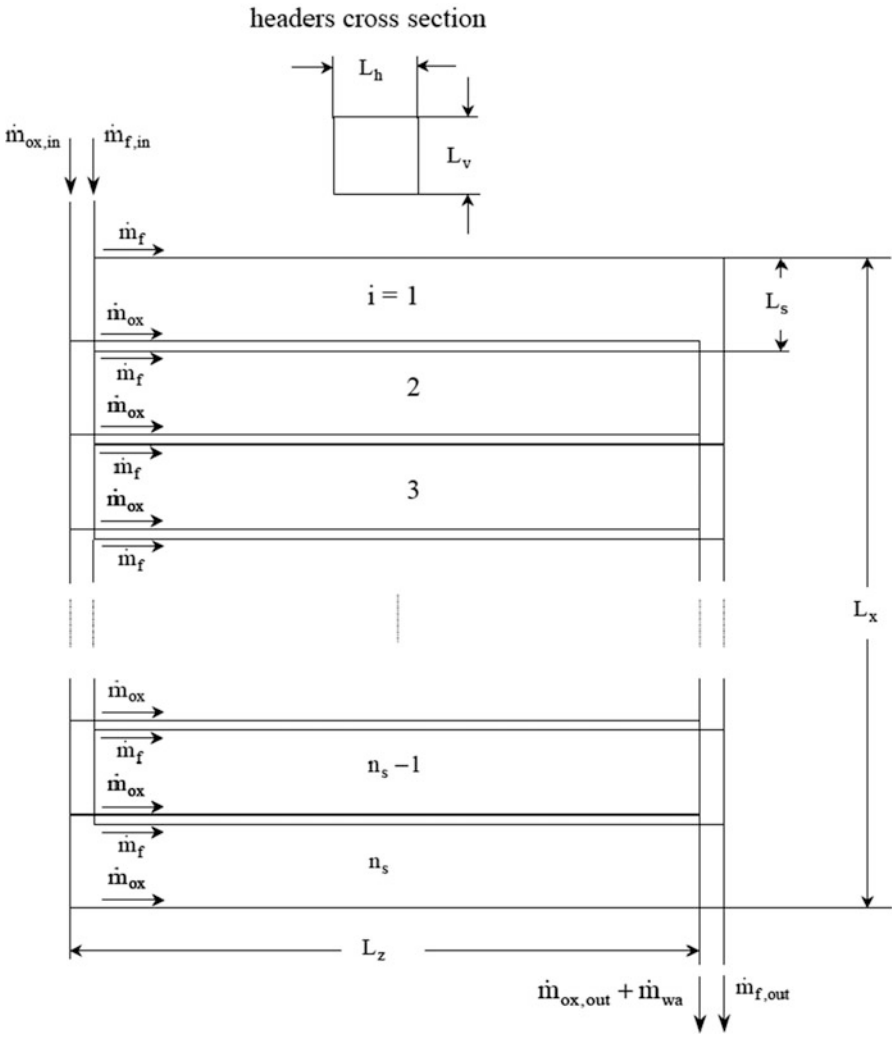

Fig. 10.3 Flow structure sketch of headers and gas channels in a PEMFC stack

The stoichiometric ratios in the fuel and oxidant channels, ζ_1 and ζ_7, are assumed known as specified operating parameters. Therefore, the inlet mass flow rates are $\psi_f = \zeta_1 \psi_{H_2}$ and $\psi_{ox} = \zeta_7 \psi_{O_2}$.

The pressure drops in the gas channels, from the input headers to the output headers, are given by the pressure drops in a single cell only, because they are in parallel (Fig. 10.3). The resulting dimensionless expression for rectangular shaped gas channels, accounting for the flow directional change (90° at the cell inlet and outlet), contraction (inlet), and expansion (outlet), together with the ideal gas

model, was calculated by Vargas et al. [8] and is not shown here for the sake of brevity.

According to Fig. 10.2, the architecture of the single fuel cell is determined completely by the internal structure ($L_s = 2L_b + \sum_{i=1}^{7} L_i$). The fuel cell stack external shape is given by (L_x, L_y, L_z) for a constrained total volume, V_T. The optimization objective is to determine the entire system architecture: the optimal volume allocation such that the PEMFC stack total net power is maximized. The determination of the total stack net power starts with the single PEMFC polarization curve, i.e., the fuel cell total potential as a function of current and the total net power (available for utilization) of a single fuel cell in the stack are given by

$$\tilde{V}_i = \tilde{V}_{i,a} + \tilde{V}_{i,c} - \tilde{\eta}_{ohm}, \quad \tilde{W}_{net,s} = \tilde{W}_s - \tilde{W}_p, \tag{10.1}$$

where $\tilde{W}_s = \tilde{V}_i \tilde{I}$, and $\tilde{W}_p = \psi_f S_f \theta_1 \Delta P_1 / P_1 + \psi_{ox} S_{ox} \theta_7 \Delta P_7 / P_7$, with $S_j = \dot{m}_{ref} T_\infty R_j / (V_{ref} I_{ref})$, $j = f,ox$ $(V_{ref} I_{ref})$, $j = f,ox$.

Additional power is required to pump fuel, oxidant, and produced water in and out of the headers shown in Fig. 10.3. The dimensionless pumping power required for the gases at the fuel cell level i and for the produced water out of the oxidant output header are given by

$$\tilde{W}_{i,k} = S_j \left[\frac{\psi \theta \Delta P}{P} \right]_{i,k}, \quad j = f,ox, \quad \tilde{W}_{wa,i} = \frac{S_f}{\tilde{\rho}_{wa}} [\psi \Delta P]_{wa,i}. \tag{10.2}$$

The total PEMFC stack power available for utilization is therefore obtained from

$$\tilde{W}_{net} = n_s \left(\tilde{W}_s - \tilde{W}_p \right) - \sum_{k} \sum_{i=1}^{n_s} \tilde{W}_{i,k} - \sum_{i=1}^{n_s} \tilde{W}_{wa,i}, \tag{10.3}$$

where $k = h_{f,in}$, $h_{ox,in}$, $h_{f,out}$, and $h_{ox,out}$. The objective function defined by (10.3) depends on the internal structure and thickness of each single cell, and on the external shape of the PEMFC stack. The mathematical model allows the computation of the total net power of the PEMFC stack, $\tilde{W}_{net}$. This is possible to achieve as soon as the physical values and a set of geometric internal ($1 = 2\,\xi_b/\xi_s + \sum_{i=1}^{7} \xi_i/\xi_s$ and ξ_s) and external (ξ_y/ξ_x and ξ_z/ξ_x) parameters are chosen for the overall system.

The constructal procedure seeks the PEMFC stack optimal internal structure, length (or thickness) of the single fuel cell, and external shape (ξ_y/ξ_x and ξ_z/ξ_x) based on the general configuration presented in Fig. 10.1, and according to the following algorithm:

1. Fix total PEMFC stack volume, $\tilde{V}_T$, and assume a fuel cell square section, i.e., $\frac{\xi_y}{\xi_x} = \frac{\xi_z}{\xi_x}$.
2. Select the lowest value for $\frac{\xi_y}{\xi_x} = \frac{\xi_z}{\xi_x}$ within a prespecified range of variation.

3. Compute ξ_x, ξ_y, ξ_z.
4. For $\tilde{A}_s = \xi_y \xi_z$, vary the thickness of a single fuel cell, ξ_s, within a prespecified range.
5. For each ξ_s, find the optimal internal structure that delivers a maximum value for $\tilde{W}_{net}$.
6. The result of the process of step 5 is $\xi_{s,opt}$ for $\tilde{W}_{net,m}$, which is the maximum value of $\tilde{W}_{net}$ found for all tested ξ_s in step 5.
7. Compute the resulting number of single cells in the stack: $n_{s,opt} = \frac{\xi_x}{\xi_{s,opt}}$, increment $\frac{\xi_y}{\xi_x} = \frac{\xi_z}{\xi_x}$, and return to step 2 until the entire $\frac{\xi_y}{\xi_x} = \frac{\xi_z}{\xi_x}$ prespecified range is covered.
8. The result of the outer loop (2–7) is the optimized configuration of the PEMFC stack for maximum net power density that is possible to be obtained in a constrained total volume, V_T, given by (10.3): $\left(\frac{\xi_y}{\xi_x} = \frac{\xi_z}{\xi_x}, \begin{Bmatrix} n_s \\ \xi_s \end{Bmatrix} \right)_{opt} \Rightarrow \tilde{W}_{net,mm}$.

The optimization of internal structure mentioned in step 5 of the optimization algorithm is executed following the procedure introduced by Vargas et al. [7] for a single PEMFC. First, the anode and cathode are assumed to have the same thickness. The thicknesses of the diffusion and reaction layers of the cathode and anode are varied simultaneously subject to fixed ratios of cathode thickness (y_2) and anode thickness (y_6) to total single cell length, i.e., $\xi_2/\xi_s + \xi_3/\xi_s = y_2$, $\xi_5/\xi_s + \xi_6/\xi_s = y_6$, where y_4 is the ratio of membrane thickness to total single cell length. The ratio of overall thickness to total length of the single fuel cell is also fixed, $y_2 + y_4 + y_6 = 0.8$. Under the simplifying hypotheses assumed, the internal structure optimization problem is reduced to one degree of freedom, i.e., the ratio $\xi_3/\xi_s = \xi_5/\xi_s$. The end result is the optimized configuration of the single fuel cell electrodes $(\xi_2, \xi_3, \xi_5, \xi_6)_{opt}$, for which the PEMFC stack net power, given by (10.3), is maximum.

The model equations and the specified initial conditions form a system of seven ordinary differential equations and two algebraic equations. The unknowns are θ_i and P_i, i.e., the dimensionless temperatures in the seven control volumes, and the dimensionless gas pressures in CV2 and CV6. Once the temperatures and pressures are known, the electrical potentials, electrical power, and PEMFC stack net power can be calculated for any current level.

10.4 Results and Discussion

In the procedure described by the algorithm presented in Sect. 10.3, the PEMFC stack net power is calculated by starting from open circuit ($\tilde{I} = 0$) and proceeding in prespecified increments $\Delta\tilde{I}$ (e.g., 2, 5, 10) until the net power is zero, the membrane limiting operating temperature is achieved, T_{Lim}, or the limiting current level is reached. This procedure is illustrated in Fig. 10.4, which shows simulation results for one selected PEMFC stack external shape $\left(\xi_y/\xi_x = \xi_z/\xi_x = 0.3\right)$, which has

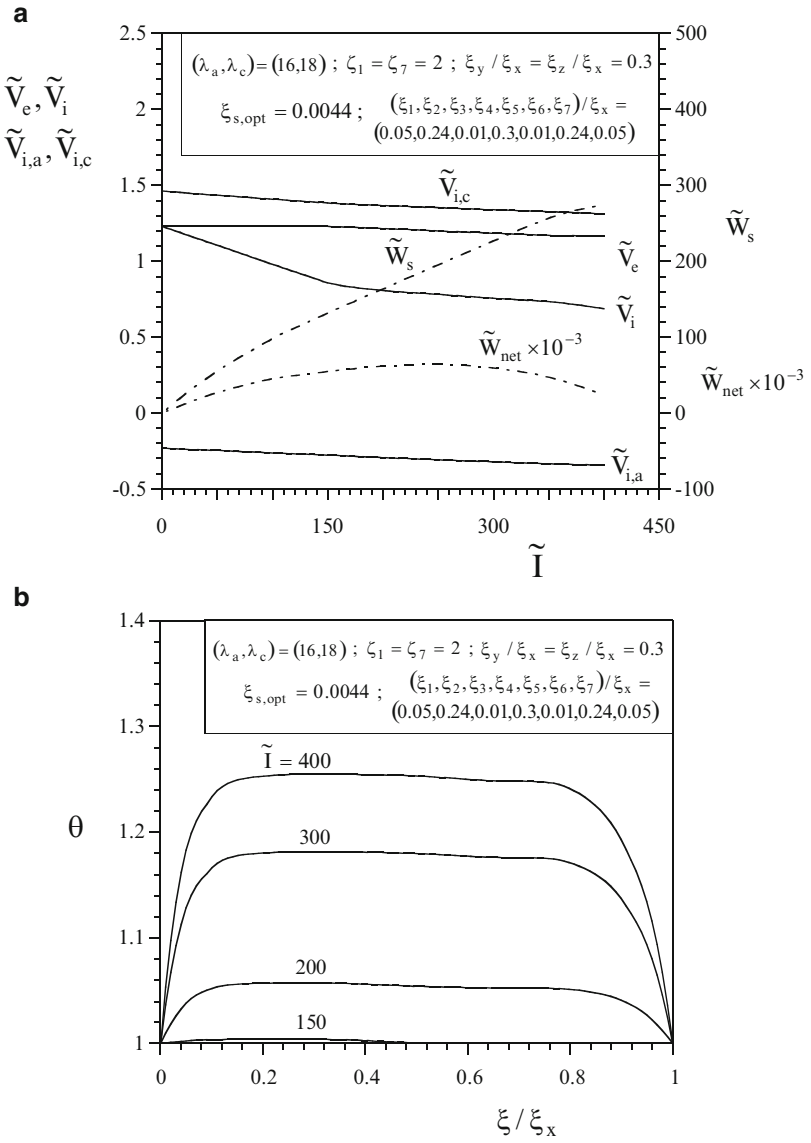

Fig. 10.4 (**a**) Example of single PEMFC polarization, total electrical power, and PEMFC stack net power output curves, and (**b**) the behavior of temperature versus flow length for several current levels, in a single PEMFC for the stack considered in Fig. 10.4a

been optimized according to step 5 of the algorithm of Sect. 10.3, i.e., an optimal internal structure and single cell thickness $(\xi_s = 0.0044)$ were found for that particular external shape. The resulting electrical power, and polarization curves of a single cell, and the PEMFC stack net power curves are shown in Fig. 10.4a.

According to the model, the actual open circuit voltage is equal to the reversible cell potential, because it has been assumed that no losses result from species crossover from one electrode through the electrolyte, and from internal currents. The change in the Gibbs free energy of reaction decreases as the temperature increases. Therefore, the reversible electrical potential decreases as the temperature increases, which happens when the current increases.

In Fig. 10.4a, the simulation stopped when the temperature at any compartment of the single fuel cell reached the limiting membrane operating temperature, i.e., $\theta_i \leq \theta_{\text{Lim}}$, and at this point $\tilde{W}_{\text{net}}>0$ for the selected configuration under analysis. The other ending criterion is $\tilde{W}_{\text{net}} = 0$, i.e., up to the point where the electrical power produced by the PEMFC stack matched the required pumping power to supply fuel and oxidant to the stack at any specified stoichiometric ratios $\zeta_1 = \zeta_7$. Under such selected operating conditions and geometry $\left(\xi_y/\xi_x = \xi_z/\xi_x = 0.3\right)$, the PEMFC stack did not reach the concentration polarization region as $\tilde{V}_{\text{e,a}}$ or $\tilde{V}_{\text{e,c}}$ would approach zero. The net power curve exhibits a maximum at $\tilde{I} \approx 250$, which is central in the evaluation of global performance, by balancing total electrical power produced with required pumping power to supply fuel and oxidant to the PEMFC stack. The maximum net power is the quantity maximized during the constructal procedure described by the algorithm presented in Sect. 10.3.

The fuel flow rate increases as the current increases; therefore more heat is generated by the reactions at the anode and cathode, increasing the temperature. The temperatures in the single fuel cell compartments shown in Fig. 10.2 increase as the current increases, as shown in Fig. 10.4b, because more heat is generated by the electrochemical reaction and by Joule effect (ohmic heating). The higher the current, the more accentuated are the temperature spatial gradients between the single fuel cell compartments, even for the single fuel cell considered in Fig. 10.4, with the selected high geometric aspect ratio $\xi_y, \xi_z \gg \xi_{\text{s,opt}}$ $\left(\xi_y/\xi_s = \xi_z/\xi_s = 152\right)$, i.e., with a small thickness compared to width and height. Therefore, the PEMFC stack net power and polarization curves produced by the present model take into account all the internal spatial temperature gradients, which affect the polarization curve and the total electrical power output. Most importantly, the spatial temperature distribution results of Fig. 10.4b show that although a cooling system is considered across the bipolar plates with an externally controlled and monitored average temperature T_∞, the actual single cell internal temperature is substantially higher than that. This finding should be considered in fuel cell design.

Figure 10.5 illustrates the constructal procedure for one set of external parameters of Fig. 10.4, $\zeta_1 = \zeta_7 = 2$, $(\lambda_a, \lambda_c) = (16, 18)$, and $\tilde{V}_T = 1.16$. The graphical results follow the steps of the algorithm presented in Sect. 10.3. Figure 10.5a shows the results of steps 4, 5, and 6, which identify $\xi_{\text{s,opt}}$ for several PEMFC stack external shapes, $\xi_y/\xi_x = \xi_z/\xi_x$. For each value of ξ_s, a corresponding fuel cell optimal internal structure is found, but this is not shown in Fig. 10.5 for the sake of brevity. However, the bulk of results of this study for the optimized internal structure corroborate the results discussed and documented in the constructal design of a single PEMFC [7], i.e., $\xi_3/\xi_s = \xi_5/\xi_s \cong 0.01$. The optimal single cell thickness $\xi_{\text{s,opt}}$ results from the

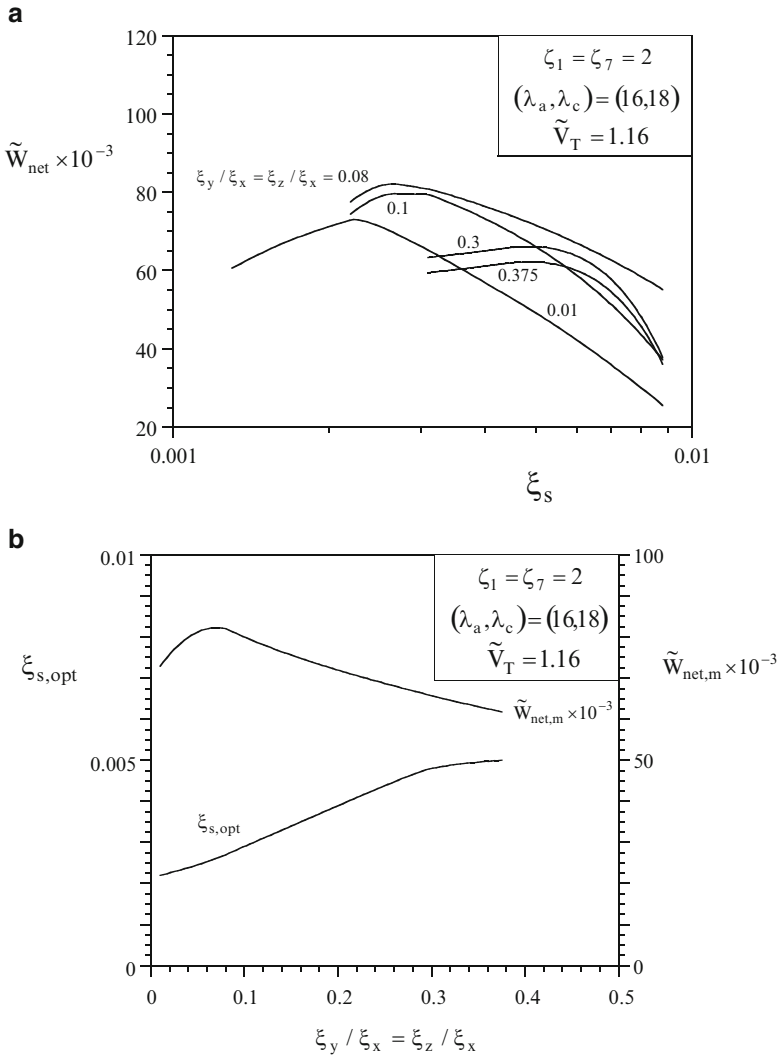

Fig. 10.5 (**a**) The internal structure and single cell thickness optimization according to Fig. 10.2 and the dependence on external shape of the PEMFC stack, and (**b**) the existence of a maximum PEMFC stack net power and the corresponding optimized single cell thickness with respect to external shape of the stack

trade-off between two effects: activation polarization losses and ohmic losses. As ξ_s increases, the electrode wetted areas increase; thus the activation losses decrease. On the other hand, the ohmic losses increase as thickness increases. Another interesting phenomenon is that the ionomer electrical conductivity increases as temperature increases at higher current levels, and with water content increase as well, therefore reducing ohmic loss at higher temperatures. The results of those trade-offs observed

during single cell thickness variation in the optimization process are shown in Fig. 10.5a, which shows net power maxima for five PEMFC stack external geometric aspect ratios. Note that the single cell thickness is optimized for the maximum PEMFC stack net power, i.e., the optimization of the component shape for maximum performance of the global system. The maxima are sharp, stressing the importance of these optima found in future fuel cell design.

The results of Fig. 10.5a are summarized in Fig. 10.5b, which also shows the existence of a second maximum for the PEMFC stack net power, this time with respect to external geometric aspect ratios. The curves document the final steps of the optimization algorithm presented in Sect. 10.3, pinpointing the optimal single cell thickness and stack external shape for maximum net power output. The maximum is sharp, and therefore important in fuel cell design. The existence of a PEMFC stack net power maximum with respect to stack external shape is explained by analyzing two extremes: (1) small $\xi_y/\xi_x = \xi_z/\xi_x$ implies that ξ_x is large, $\tilde{W}_\mathrm{s}$ is small due to large flow resistances in the x-direction, the number of single cells n_s is high, and therefore the resulting total stack electrical power is still high, but the headers pumping power increases as ξ_x increases, and therefore $\tilde{W}_\mathrm{net,m} \to 0$, and (2) large $\xi_y/\xi_x = \xi_z/\xi_x$ implies that ξ_x is small, $\tilde{W}_\mathrm{s}$ is large due to small flow resistances in the x-direction and also large wetted areas at the electrodes, the headers pumping power decreases as ξ_x decreases, but $\tilde{W}_\mathrm{p}$ is also large due to a large swept length ξ_x and small hydraulic diameters D_h, and therefore $\tilde{W}_\mathrm{net,m} \to 0$ in this extreme as well. In conclusion, there must exist an intermediate and optimal $\xi_y/\xi_x = \xi_z/\xi_x$ geometric configuration such that $\tilde{W}_\mathrm{net,m}$ is maximum, which balances the trade-off between electrical power output and pumping power to supply fuel and oxidant to the PEMFC stack, according to (10.3).

The investigation of the variation of the volume constraint is conducted in Fig. 10.6, where $\tilde{V}_\mathrm{T}$ $\tilde{V}_\mathrm{T}$ was varied over the range 0.1–1.16, for stoichiometric ratios $\zeta_1 = \zeta_7 = 2$. This variation is indicated by the three curves of Fig. 10.6a. All curves exhibit PEMFC stack maxima with respect to the external shape aspect ratios. The fuel cell stack net power increases as $\tilde{V}_\mathrm{T}$ increases. Additional results were produced to cover the entire range $0.1 \leq \tilde{V}_\mathrm{T} \leq 1.16$, which allowed the twice maximized stack net power and the optimized external shape aspect ratios to be plotted in Fig. 10.6b as functions of $\tilde{V}_\mathrm{T}$. The twice maximized stack net power increases monotonically with total volume, i.e., $\tilde{W}_\mathrm{net,mm}$ increases approximately as $\tilde{V}_\mathrm{T}^{3/4}$. The optimized external shape aspect ratios are robust with respect to the fuel cell stack total volume, staying approximately within the range $0.03 \leq \left(\xi_y/\xi_x = \xi_z/\xi_x\right)_\mathrm{opt} \leq 0.07$. Therefore, the optimization results obtained for a so-called inanimate system (the PEMFC stack) show the same trend as the long known allometric law in plotting an animal's basal metabolic rate (BMR) against the animal's own body mass, which is known as Kleiber's law, posed in 1932 [9], i.e., a proportionality between net power output and total volume with a slope of ¾ in a log-log plot.

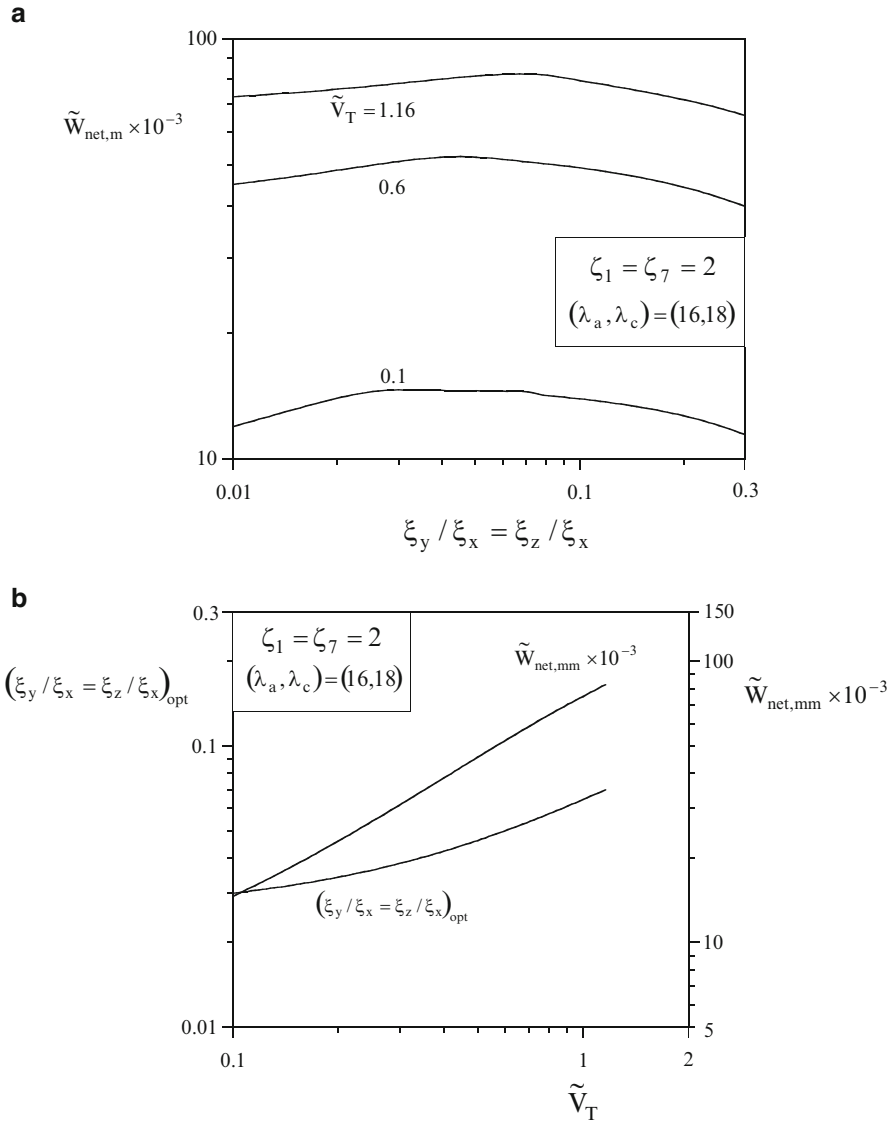

Fig. 10.6 (**a**) The external shape optimization and the dependence on total stack volume for $\zeta_1 = \zeta_7 = 2$, and (**b**) the results of the external shape optimization with respect to total stack volume, $\tilde{V}_T$

10.5 Conclusions

In this paper, the constructal design of a PEMFC stack was conducted so that maximum stack net power output was obtained. The procedure started with the construction of a mathematical model for fluid flow, mass and heat transfer in a

PEMFC stack, which takes into account spatial temperature and pressure gradients in a single PEMFC (Fig. 10.2), and pressure drops in the headers and all gas channels in the entire PEMFC stack (Fig. 10.3). The single PEMFC internal structure has an optimal allocation, and total thickness being such that wetted area in the reaction layers and electrical resistance are optimally balanced for maximum electrical power, and maximum global stack net power. Additionally, a three-dimensional flow space with the dimensions L_z and L_y in the plane perpendicular to L_x was considered and the total volume was fixed (Fig. 10.1). The new degrees of freedom, i.e., the aspect ratios L_y/L_x and L_z/L_x, allowed for the optimization of the PEMFC stack external shape, in addition to the single PEMFC internal structure and total thickness. As a result, an external shape was found such that electrical and pumping power are optimally balanced for maximum PEMFC stack net power. Dimensionless optimization results were presented graphically for the sake of generality.

A parametric analysis investigated the effect of total PEMFC stack volume on the optima found. The optimal PEMFC stack external shape was shown to be "robust" with respect to the analyzed parameters, i.e., $0.1 \leq \tilde{V}_T \leq 1.16$, and the twice maximized stack net power increases monotonically with total volume, i.e., $\tilde{W}_{net,mm}$ increases approximately as $\tilde{V}_T^{3/4}$, similarly to metabolic rate and body size in animals [6, 9]. This is an important finding for the purpose of "scaling up" or "scaling down" PEMFC stack design.

Fundamentally, it was shown that electrical and fluid flow trade-offs exist, and that from them results the single cell internal structure and total thickness, and the PEMFC stack external shape—the relative sizes and spacings—of flow systems, in accordance with other features of constructal design [6].

Furthermore, prediction entirely based on the constructal law could lead man to evolve to optimal engineering design in a continuous evolutionary technological process so that sustainable equilibrium between consumerism and the available technology is reached in time, in a self-regulatory process for all species survival. Such evolutionary process is long known to happen with animate systems in nature [5]. In conclusion, constructal law unifies all systems design.

References

1. Ashton TS. The industrial revolution (1760–1830). Oxford: Oxford University Press; 1948.
2. Berlanstein LR. The industrial revolution and work in nineteenth-century Europe. New York: Routledge; 1992.
3. Veblen T. The theory of the leisure class: an economic study of institutions. NY: Dover Publications; 1994.
4. Majfud J. The pandemic of consumerism. UN Chronicle. 2009
5. Darwin C. On the origin of species by means of natural selection, or the preservation of favoured races in the struggle for life. London: John Murray; 1859.
6. Bejan A. Shape and structure, from engineering to nature. Cambridge: Cambridge University Press; 2000.

7. Vargas JVC, Ordonez JC, Bejan A. Constructal flow structure for a PEM fuel cell. Int J Heat Mass Tran. 2004;47(19–20):4177–93.
8. Vargas JVC, Ordonez JC, Bejan A. Constructal PEM fuel cell stack design. Int J Heat Mass Tran. 2005;48:4410–27.
9. Willmer P, Stone G, Johnston I. Environmental physiology of animals. 2nd Ed. Malden, Mass., USA: Blackwell Pub.; 2005.

Chapter 11
Constructal Design of Rectangular Conjugate Cooling Channels

T. Bello-Ochende, O.T. Olakoyejo, and J.P. Meyer

11.1 Introduction

The new trend in modern heat transfer for thermal performance is shape and geometric optimization. Constructal theory and design [1, 2], ideally, have been adopted as an optimisation technique for the development of a procedure that is sufficiently allocating and optimising a fixed global space constraint using physical law.

The application of this theory started with Bejan and Sciubba [3], who obtained a dimensionless pressure difference number for optimal spacing of board to board of an array of parallel plate to channel length ratio and a maximum heat transfer density that can be fitted in a fixed volume in an electronic cooling application using the method of intersection asymptotes.

This body of knowledge has been applied to all facets of our lives; from humanity and nature to science and engineering [4–8].

In nature, water always takes the path of least flow resistance in the course of navigation in the river basin [4]. Thermodynamically, every system exhibits a level of imperfection due to entropy generation and leads to the degradation of performance of the system [5]. However, a system must adjust itself to operate maximally by optimising the process and geometric configuration of the system to reduce the generation of entropy.

In medicine [6], this physical law can also be applied to the treatment of cancer. The spreading of cancer can be controlled by maintaining the temperature field of the unaffected tissues in the neighbourhood of the turmoil below the temperature that the cancer virus can survive. In the business world [7, 8], constructal theory shows that the transportation cost can also be minimised by optimising the

T. Bello-Ochende (✉) • O. Olakoyejo • J. Meyer
Department of Mechanical and Aeronautical Engineering, University of Pretoria,
Pretoria Private Bag X20Hatfield 0028, South Africa
e-mail: Tunde.Bello-Ochende@up.ac.za; olakoyejo@yahoo.com; josua.meyer@up.ac.za

L.A.O. Rocha et al. (eds.), *Constructal Law and the Unifying Principle of Design*,
Understanding Complex Systems, DOI 10.1007/978-1-4614-5049-8_11,

transportation routes of goods and products from one area to another in a dendritic form in order to get shortest and easier distance.

In heat transfer [9], the peak temperature must be minimised at every hot spot of a system for better thermal performance and to avoid thermal stress by optimising shape and geometry.

In academia [10, 11], the constructal law was used to optimise the hierarchal rankings of universities in the global flow of knowledge. Also in military defence, the constructal law was used to provide insight information on the optimisation of warfare tactics and strategy [12].

The recent comment by Meyer [13] on the latest review of constructal theory by Bejan and Lorente [14] shows that the constructal law's application in all fields of educational design is a wide road to future advances.

In this chapter our focus is on the original engineering application of constructal theory, which is the geometric and shape optimisation especially in heat transfer analysis (Bello-Ochende et al.) [15–20]. The applications of this theory have been reviewed by Bejan [2], in which under certain global constraints, the best architecture of a flow system can be archived as the one that gives less global flow resistances or allows high global flow access. In other words, the shapes of the channels and unit structure that is subject to global constraint are allowed to morph. The optimisation of heat exchangers and multiscale devices by constructal theory was also recently reviewed and summarised by Reis [21] and Fan and Luo [22].

da Silva et al. [23] optimised the space allocation on a wall occupied by discrete heat sources with a given heat generation rate by forced convection using the method of constructal theory in order to minimise the temperature of the hot spot on the wall.

Also, Bello-Ochende et al. [24] conducted a three-dimensional optimisation of heat sinks and cooling channels with heat flux using scale analysis and the intersection of asymptotes method based on constructal theory to investigate and predict the design and optimisation of the geometric configurations of the cooling channels. Rocha et al.[25] and Biserni et al. [26] applied the theory to optimise the geometry of C- and H-shaped cavities, respectively, that intrude into a solid conducting wall in order to minimise the thermal resistance between the solid and the cavities.

This chapter focuses on the study of three-dimensional, laminar forced convection cooling of rectangular solid structures. It examines the optimisation of a fixed and finite global volume of solid materials with an array of rectangular cooling channels, which experience a uniform internal heat generation which will result in the minimal global thermal resistance. The objective is the building of a smaller construct to form a larger construct body that will lead to the minimisation of the global thermal resistance or, inversely, the maximisation of the heat transfer rate density (the total heat transfer rate per unit volume). This is achieved by forcing a coolant to the heated spot in a fast and efficient way so as to drastically reduce the peak temperature at any point inside the volume that needs cooling. The optimisation process is carried out numerically under total fixed volume and manufacturing constraints.

This study is an extension of our previous work [27] on the constructal theory for the cylindrical and square configurations with internal heat generation, where we showed that the minimised peak temperature is a function of the geometry and shape. The rectangular shape is considered separately because of the unique nature of the configuration in terms of the internal and external aspect ratios.

11.2 Computational Model

The physical configuration is shown schematically in Fig. 11.1. The system consists of parallel rectangular cooling channels in a solid structure of fixed global volume V. The solid material is generating an internal heat q_s'''. The body is cooled by forcing a single-phase cooling fluid (water) from the left side into the parallel cooling channels by a specified pressure difference ΔP, in a transverse direction. An elemental volume shown in Fig. 11.2 consisting of a cooling channel and the surrounding solid was used for analysis because of the assumption of the symmetrical heat distribution inside the structure. The heat transfer in the elemental volume is a conjugate problem that combines heat conduction in the solid and the convection in the working fluid. These two modes of heat transfer are coupled together through the continuity of heat flux at the solid–fluid interface.

11.2.1 Design Variables

In Fig. 11.2 an elemental volume constraint is considered to be composed of an elemental cooling channel of width w_c, height h_c, and the surrounding solid of thickness $s_1$and s_2 defined as:

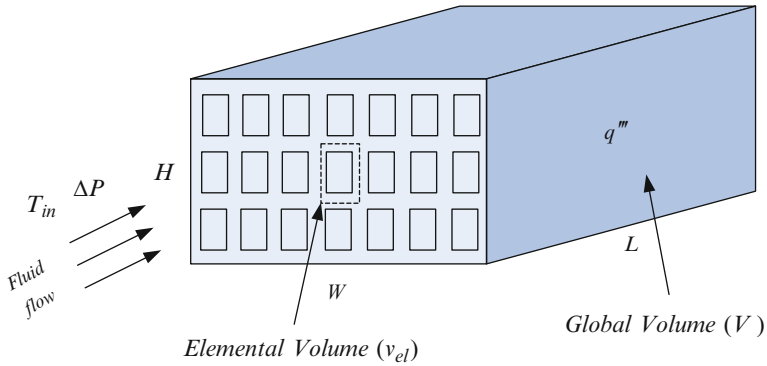

Fig. 11.1 Three-dimensional parallel rectangular channels across a solid body with internal heat generation and forced flow

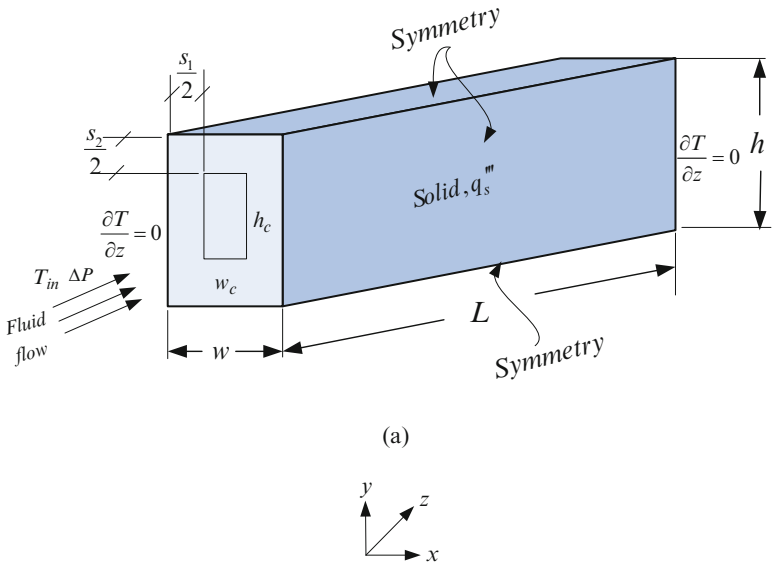

Fig. 11.2 The boundary conditions of the three-dimensional computational domain of the cooling channel

$$v_{\mathrm{el}} = whL, \quad w = w_{\mathrm{c}} + s_1, \quad h = h_{\mathrm{c}} + s_2. \tag{11.1}$$

The volume of the unit rectangular channel is:

$$v_{\mathrm{c}} = w_{\mathrm{c}} h_{\mathrm{c}} L. \tag{11.2}$$

Therefore the number of channels in the structure arrangement can be defined as:

$$N = \frac{HW}{hw} = \frac{HW}{(h_{\mathrm{c}} + s_2)(w_{\mathrm{c}} + s_1)}. \tag{11.3}$$

However, the porosity or void fraction of the unit structure is defined as:

$$\phi = \frac{v_{\mathrm{c}}}{v_{\mathrm{el}}} = \frac{h_{\mathrm{c}} w_{\mathrm{c}}}{hw}. \tag{11.4}$$

The aspect ratio of the unit structure and the elemental channel are defined as:

$$\mathrm{AR_s} = \frac{h}{w}, \quad \mathrm{AR_c} = \frac{h_{\mathrm{c}}}{w_{\mathrm{c}}}. \tag{11.5}$$

The fundamental problem under consideration is the numerical optimisation of $\mathrm{AR_c}$, d_{h}, s_1 and s_2 that correspond to the minimum resistance of a fixed volume for a given

pressure difference. The optimisation is evaluated from the analysis of the extreme limits of zero (0) less than or equal to design variables and the design variables less than or equal to infinity (∞). The optimal values of the design variables within the prescribed interval of the extreme limits exhibit the minimum thermal resistance.

The cooling fluid considered is water, which was forced through the cooling channels by a specified pressure difference ΔP across the axial length of the structure. The fluid is assumed to be in single phase, steady and Newtonian with constant properties. Water is more promising than air, because air-cooling techniques are not likely to meet the challenge of high heat dissipation in electronic packages [28, 29]. The temperature distribution in the model was determined by solving the governing differential equations for the conservation of mass, momentum and energy numerically. The governing differential equations used for the fluid flow and heat transfer analysis in the unit volume of the structure are:

$$\nabla \cdot \vec{u} = 0, \tag{11.6}$$

$$\rho(\vec{u} \cdot \nabla \vec{u}) = -\nabla p + \mu \nabla^2 \vec{u}, \tag{11.7}$$

$$\rho_{\mathrm{f}} C_{\mathrm{Pf}}(\vec{u} \cdot \nabla T) = k_{\mathrm{f}} \nabla^2 T. \tag{11.8}$$

The energy equation for a solid with internal heat generation is given as:

$$k_{\mathrm{s}} \nabla^2 T + q_{\mathrm{s}}''' = 0. \tag{11.9}$$

The continuity of the heat flux at the interface between the solid and the liquid is given as:

$$k_{\mathrm{s}} \left.\frac{\partial T}{\partial n}\right| = k_{\mathrm{f}} \left.\frac{\partial T}{\partial n}\right|. \tag{11.10}$$

A no slip boundary condition is specified at the wall of the channel, $\vec{u} = 0$, at the inlet ($x = 0$), $u_x = u_y = 0, T = T_{\mathrm{in}}$ and

$$P = \frac{\mathrm{Be}\alpha u}{{V_{\mathrm{el}}}^{2/3}} + P_{\mathrm{out}}, \tag{11.11}$$

where Be is the dimensionless pressure difference number based on elemental volume which was later called Bejan number by Bhattacharjee and Grosshandler [30] and Petrescu [31].

At the outlet ($x = L$), zero normal stress, $P_{\mathrm{out}} = 1$ atm

At the solid boundaries,

$$\nabla T = 0. \tag{11.12}$$

The measure of performance is the minimum global thermal resistance, which could be expressed in a dimensionless form as:

$$R_{\min} = \frac{k_f (T_{\max} - T_{in})_{\min}}{q'''_s L^2}. \tag{11.13}$$

This is a function of the optimised design variables and the peak temperature.

$$R_{\min} = f\left(\mathrm{AR}, d_h, s_1, s_2, j, (T_{\max})_{\min}\right). \tag{11.14}$$

$R_{\min}$ is the minimised thermal resistance for the optimised design variables. The inverse of $R_{\min}$ is the optimised overall global thermal conductance.

11.3 Numerical Procedure and Grid Analysis

The simulation work began by fixing the length of the channel, applied pressure difference, porosity, heat flux and material properties and we kept varying the values of the aspect ratio and hydraulic diameter of the channel in order to identify the best (optimal) internal configuration that minimised the peak temperature. The numerical solution of the continuity, momentum and energy equations (11.6)–(11.9) along with the boundary conditions (11.10)–(11.12) was obtained by using a three-dimensional commercial package FLUENT™ [32], which employs a finite volume method. The details of the method were explained by Patankar [33]. FLUENT™ was coupled with geometry and mesh generation package GAMBIT [34] using MATLAB [35] to allow the automation and running of the simulation process. After the simulation had converged, an output file was obtained containing all the necessary simulation data and results for the post-processing and analysis. The computational domain was discretised using hexahedral/wedge elements. A second-order upwind scheme was used to discretise the combined convection and diffusion terms in the momentum and energy equations. The SIMPLE algorithm was then employed to solve the coupled pressure–velocity fields of the transport equations. A flow chart representing the numerical procedure is shown in Fig. 11.3. The solution is assumed to have converged when the normalised residuals of the mass and momentum equations fall below 10^{-6} and while the residual convergence of energy equation was set to less than 10^{-10}. The number of grid cells used for the simulations varied for different elemental volume and porosities. However, grid independence tests for several mesh refinements were carried out to ensure the accuracy of the numerical results. The convergence criterion for the overall thermal resistance as the quantity monitored is:

$$\gamma = \frac{\left|(T_{\max})_i - (T_{\max})_{i-1}\right|}{\left|(T_{\max})_i\right|} \leq 0.01, \tag{11.15}$$

where i is the mesh iteration index. The mesh is more refined as i increases. The $i - 1$ mesh is selected as a converged mesh when the criterion (11.15) is satisfied.

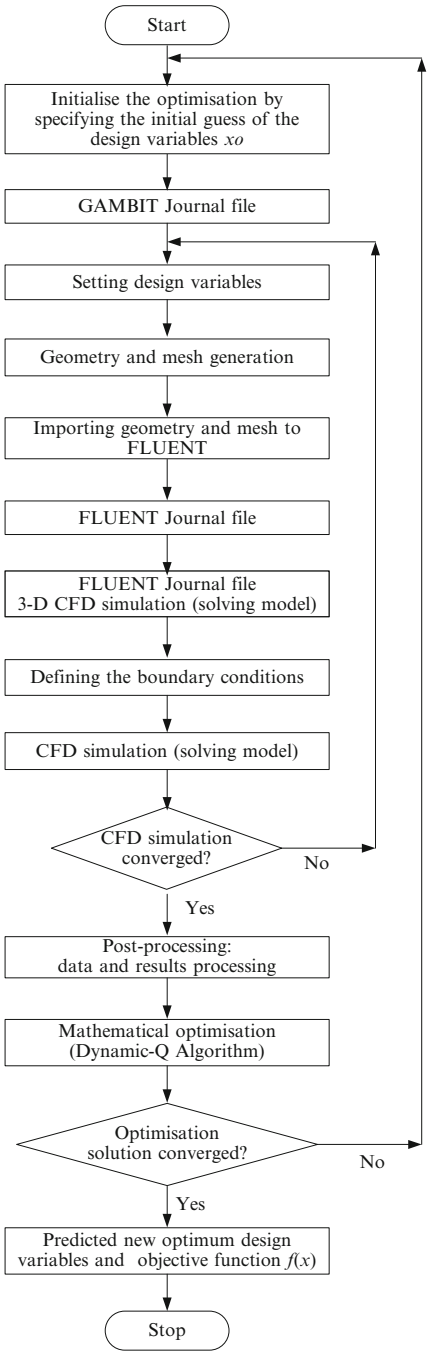

Fig. 11.3 Flow chart of numerical simulation process cooling channels embedded inside a high conducting solid

11.4 Numerical Results

In this section, we show that there is an optimal geometry that minimised the peak temperature. The results was presented for the case where $w = 150$ μm, $h = 1{,}200$ μm, $\emptyset = 0.2$ and a fixed length of $L = 10$ mm and fixed applied pressure differences of $\Delta P = 50$ kPa. The thermal conductivity of the solid structure (silicon) is 148 W/m K, and the internal heat generation within the solid was taken to be fixed at 100 W/cm^3. The thermophysical properties of water [36] used in this study were based on water at 300 K and the inlet water temperature was fixed at this temperature.

Figures 11.4 and 11.5 show the existence of an optimum aspect ratio and optimum hydraulic diameter of the cooling channel in which the peak temperature is minimised at any point in the channel. Figure 11.4 shows that peak temperature strongly depends on aspect ratio. The peak temperature decreases as the aspect ratio increases. However, at higher AR, the peak temperature increases.

Figure 11.5 is the graph of peak temperature as a function of the channel hydraulic diameter. It shows the existence of an optimum hydraulic diameter of the cooling channel where the peak temperature is minimised at any point in the channel. The channel hydraulic diameter has a significant effect on the peak temperature and the overall thermal resistance. It shows that there exists an optimal channel hydraulic diameter which lies in the range $0.005 \leq d_h/L \leq 0.015$ that minimised the peak temperature. These indicate that peak temperature decreases as d_h/L decreases and that a minimum value is reached beyond which the peak temperature begins to increase. Therefore, the global thermal resistance decreases

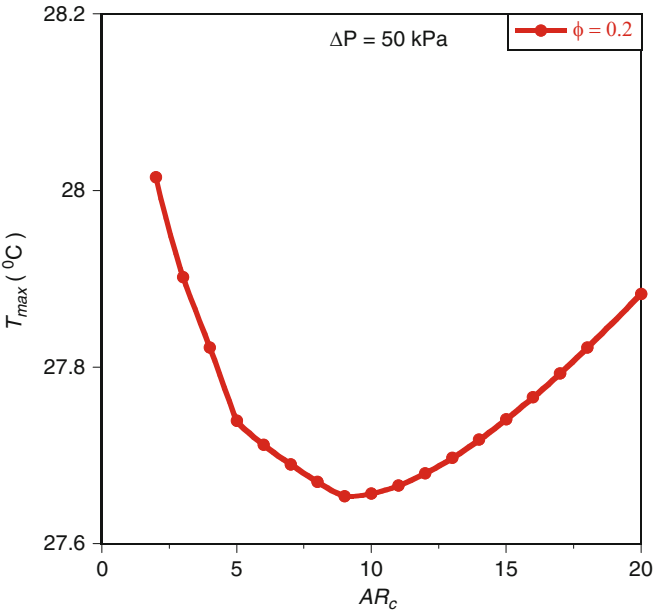

Fig. 11.4 Effect of optimised dimensionless channel aspect ratio AR_c on the peak temperature

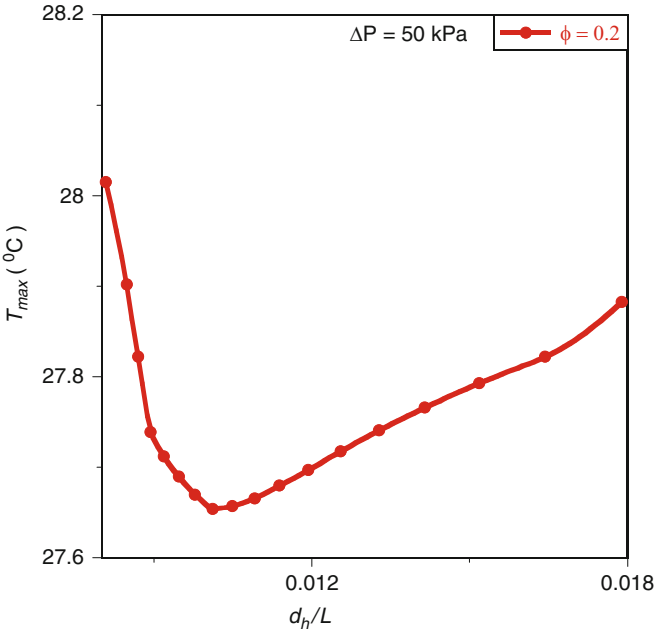

Fig. 11.5 Effect of optimised hydraulic diameter d_h, on the peak temperature

as the hydraulic diameter increases. Also, the global thermal resistance decreases as the hydraulic diameter decreases. Any hydraulic diameter values above or below the optimal ranges, will cause the working fluid not to properly engaged in the cooling process which is detrimental to the global performance of the system.

11.5 Mathematical Optimisation

In this section, we introduce an optimisation algorithm that will search and identify the optimal design variables at which the system will perform at an optimum. A numerical algorithm, Dynamic-Q [37], was employed and incorporated into the finite volume solver and grid (geometry and mesh) generation package by using MATLAB as shown in Fig. 11.3 for more efficient and better accuracy in determining the optimal performance.

The Dynamic-Q is a multidimensional and robust gradient-based optimisation algorithm, which does not require an explicit line search. The technique involves the application of a dynamic trajectory LFOPC optimisation algorithm to successive quadratic approximations of the actual problem [38, 39]. The algorithm is also specifically designed to handle constrained problems where the objective and constraint functions are expensive to evaluate. The details of the Dynamic-Q and applications can be found in open literature [37–42].

11.5.1 Design Variable Constraints

The constraint ranges for the optimisation are:

$$0.1 \leq \phi \leq 0.2, \quad 1 \leq \mathrm{AR_s} \leq 20, \quad 1 \leq \mathrm{AR_c} \leq 20, \quad v_{\mathrm{el}} = 1.8\,\mathrm{mm}^3, \quad 0 \leq w \leq L,$$
$$0 \leq w_{\mathrm{c}} \leq w, \quad 0 \leq h_{\mathrm{c}} \leq h, \quad 0 \leq s_1 \leq w, \quad 0 \leq s_2 \leq h. \tag{11.16}$$

The design and optimisation technique involves the search for and identification of the best channel layout that minimises the peak temperature, $T_{\max}$, such that the minimum thermal resistance between the fixed volume and the cooling fluid is obtained with the desired objectives function. The aspect ratio (external and internal), hydraulic diameter and the channel spacing and elemental volume were considered as design variables. The length of the channel and the elemental volume were fixed. However, the fixed cross-sectional shape of the structure is allowed to morph. Also the internal architecture of the cooling channel is allow to vary in aspect ratio, hydraulic diameter, channel spacing in horizontal and vertical direction. A number of numerical optimisations and calculations were carried out within the design constraint ranges given in (11.16) and the results are presented in the succeeding section in order to show the optimal behaviour of the entire system. The optimisation process was repeated for applied dimensionless pressure differences (Be) that correspond to $\Delta P = 10$ kPa to $\Delta P = 50$ kPa.

We reprocess all the results obtained from the numerical optimisation by reprojecting the objective function and the optimal design variable in dimensionless form as shown in Figs. 11.6, 11.7, 11.8 and 11.9.

Figure 11.6 shows the minimised dimensionless global thermal resistance as a function of dimensionless pressure difference at optimised design variables for the configuration. The results show that the dimensionless minimised global thermal resistance decreases as the dimensionless pressure difference increases. Equation (11.17) is the correlations for minimised dimensionless thermal resistance and the dimensionless pressure difference that is obtained when the cooling geometry is optimised in order to achieve cooling.

$$R_{\min} = \alpha \mathrm{Be}^{-\beta}, \tag{11.17}$$

where α and β are constant that depend on porosity and scale effects. For porosity of 0.2, α and β are 62.07 and 0.59, respectively, within the error of less than 0.01.

Figures 11.7, 11.8 and 11.9. show the optimal behaviours of the geometry with respect to applied pressure difference (or Bejan number). These show that unique optimal design geometries exist for each applied dimensionless pressure difference. Figure 11.7 shows that the optimised channel aspect increases as the applied dimensionless pressure difference and porosity increase. Also, in Figs. 11.6 and 11.7, the global dimensionless thermal resistance decreases as channel aspect ratio

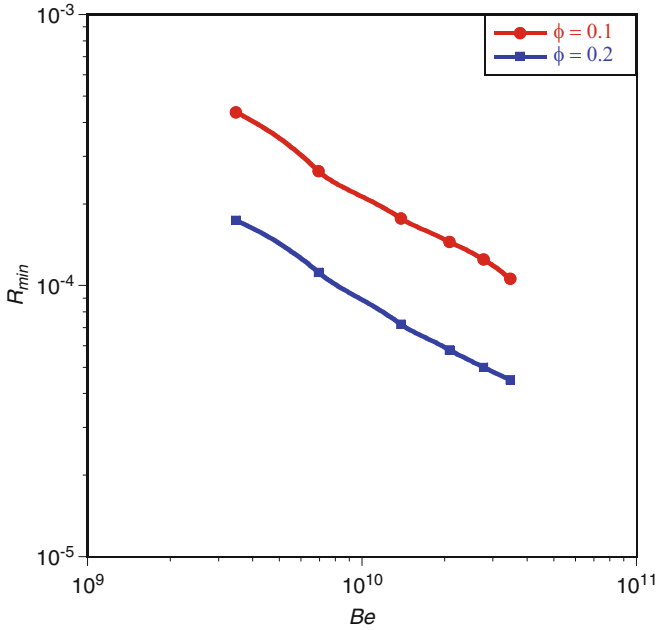

Fig. 11.6 Effect of dimensionless pressure difference on the minimised dimensionless global thermal resistance

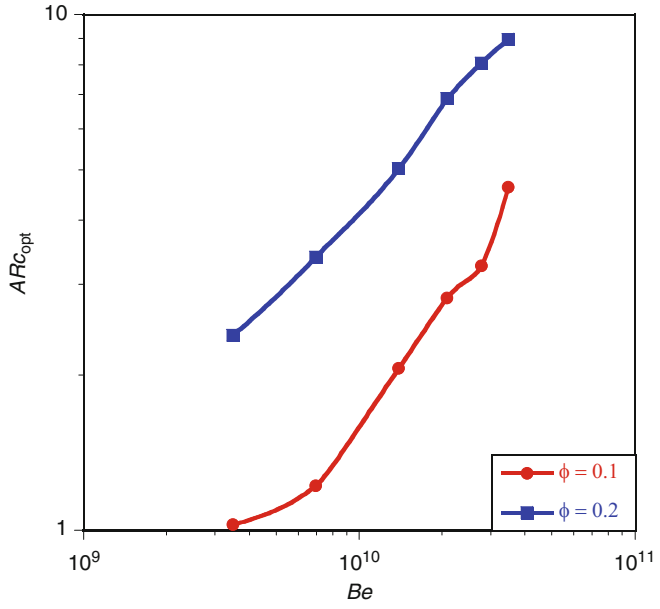

Fig. 11.7 Effects of dimensionless pressure difference on the optimised aspect ratio

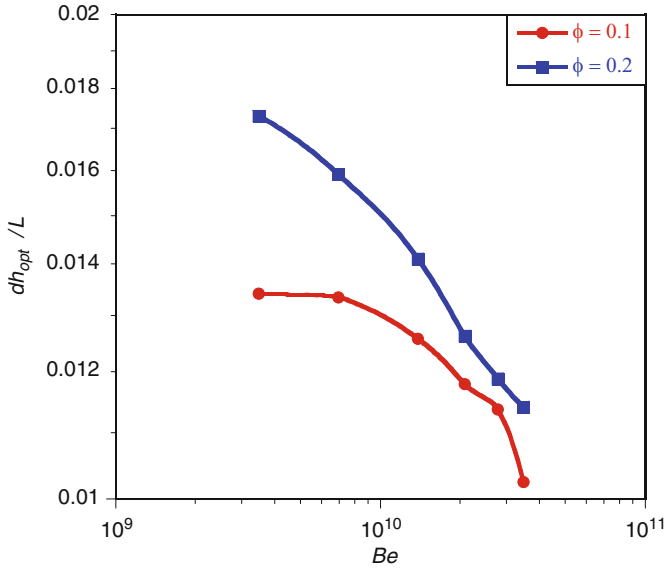

Fig. 11.8 Effect of dimensionless pressure difference on the optimised hydraulic diameter

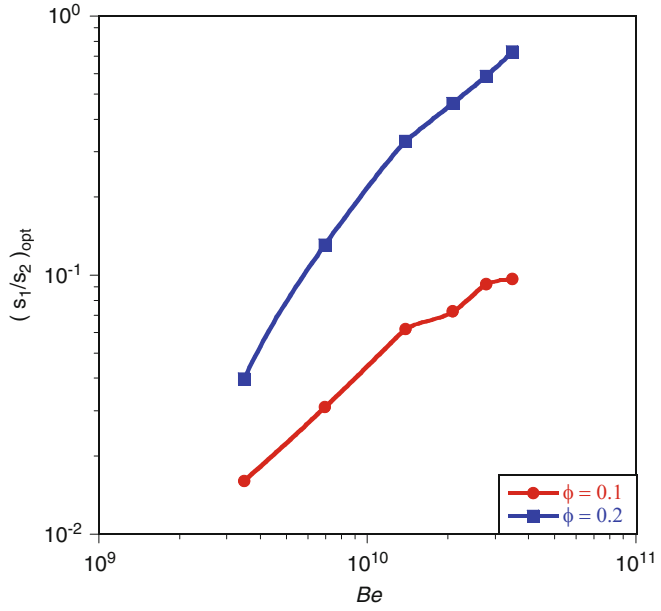

Fig. 11.9 Effect of dimensionless pressure difference on the optimised channel spacing ratio

increases. However, it is recognised that the optimal design scheme could lead to a design which could be impractical at very high channel aspect ratios due to the channel being too thin to manufacture.

Figures 11.8 and 11.9 show the effect of the dimensionless pressure difference on the optimised dimensionless design variable. Figure 11.8 shows that the optimal hydraulic diameter decreases as the pressure differences increase. Also, Fig. 11.9 shows the optimal behaviours of the channel spacing ratio $(s_1/s_2)_{\text{opt}}$. The $(s_1/s_2)_{\text{opt}}$ increases as the dimensionless pressure difference increases. We can say that there exists a unique optimal geometry for each of the applied pressure differences. The trend is in agreement with previous work. The trends of these results are also in agreement with previous work [24, 27].

11.6 Method of Intersection of Asymptotes

This section investigated further the numerical solution of the optimisation of flow and heat transfer with the analytical solution. The theoretical analysis for the configurations followed the application of the intersection of asymptotes method and scale analysis [2–4, 24] to provide the existence of an optimal geometry that minimised the peak temperature and global thermal resistance. The method of intersection of asymptotes outlined by Bello-Ochende et al. [24] was used to determine the optimal geometric shape. The objective was to provide the relationship between the global objective function in terms of global thermal resistance, R, and the varying hydraulic diameter, d_{h}, in the two extremes at $d_{\text{h}} \to 0$ and $d_{\text{h}} \to \infty$. The optimal geometry value, $d_{\text{h}_{\text{opt}}}$, that corresponds to R_{min}, is located approximately where the two asymptotes intercept. The following assumptions were made throughout the analysis: inlet temperature and the pressure difference, ΔP, driving the pump are fixed with a uniform flow distribution in all the channels, laminar flow, constant cross-sectional area of the channels, negligible inlet and exit plenum losses, negligible axial conduction. An elemental volume is treated because of the symmetry of the heat distribution. The analysis of a rectangular volume element is completely analogous to what is presented in Bello-Ochende et al. [24], using the same procedure as outlined by Bello-Ochende et al. [24]. We have that the dimensionless thermal resistance, R, behaviour in the extreme limit of a small rectangular channel is given as:

$$R = \left[\frac{k_{\text{f}}(T_{\text{max}} - T_{\text{in}})}{q''' L^2}\right] \cong 4P_{o_{d_{\text{h}}}} \beta \left(\frac{d_{\text{h}}}{L}\right)^{-2} \text{Be}^{-1}. \tag{11.18}$$

From (11.18) for a smaller channel $d_{\text{h}} = L$, the thermal resistance is inversely proportional to ${d_{\text{h}}}^2$. Keeping β (which is a function of porosity), it shows that the global thermal resistance increases as the hydraulic diameter decreases.

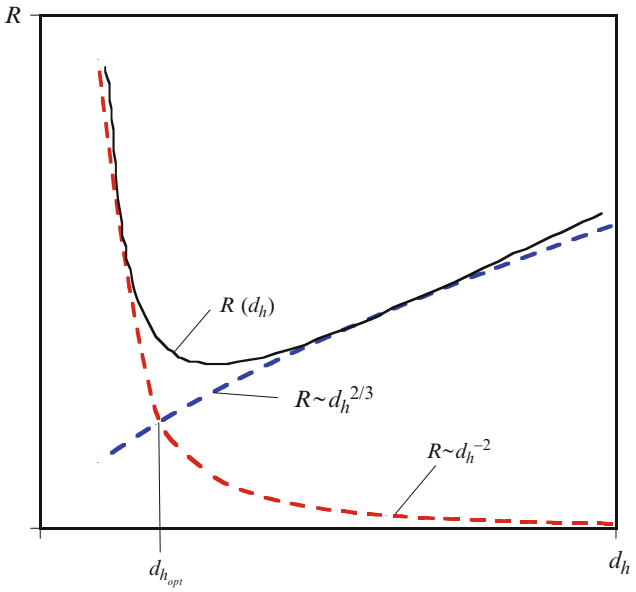

Fig. 11.10 Method of intersection of asymptotes: global thermal resistance

In the opposite extreme limit of large channel, the dimensionless global thermal resistance is defined in terms of dimensionless pressure difference as:

$$R = \left[\frac{k_{\mathrm{f}}(T_{\max} - T_{\mathrm{in}})}{q''' L^2}\right] \cong 0.7643\,\beta \left(\frac{d_{\mathrm{h}}}{L}\right)^{2/3} \mathrm{Be}^{-1/3}. \tag{11.19}$$

From (11.19), for a larger channel, the global thermal resistance is directly proportional to ${d_{\mathrm{h}}}^{2/3}$. Keeping β (which is a function of porosity) constant, confirms that as the hydraulic diameter becomes lager, the global thermal resistance increases.

The geometric optimisation in terms of channel could be achieved by combining (11.18) and (11.19) using the intersection of asymptotes method as shown in Fig. 11.10.

The optimal dimension can be generally approximated for the two configurations as hydraulic diameter where the two extreme curves intersect. The intersection result is:

$$\left(\frac{d_{\mathrm{h}}}{L}\right)_{\mathrm{opt}} \approx 1.8602\, {P_{o_{d_{\mathrm{h}}}}}^{3/8} \mathrm{Be}^{-1/4}, \tag{11.20}$$

where $d_{h_{\mathrm{opt}}}$ is the optimal hydraulic diameter for rectangular channel. Poiseuille number can be approximated as

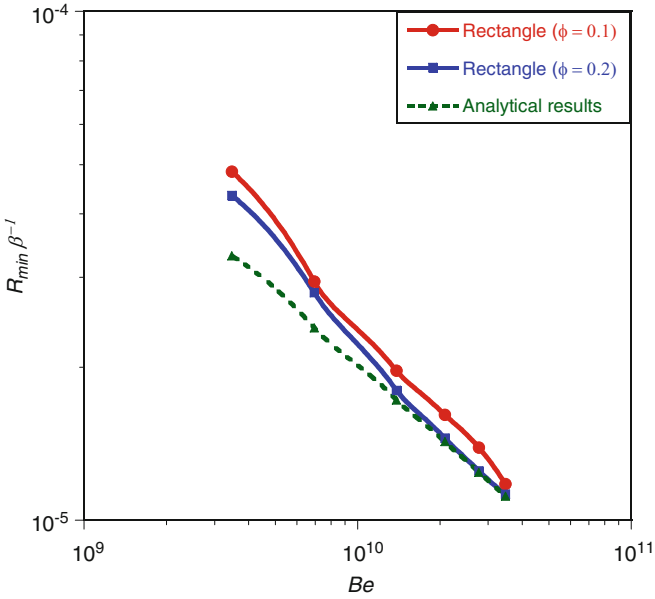

Fig. 11.11 Correlation of numerical and analytical solutions for the minimised global thermal resistance

$$P_{o_{d_h}} = \frac{12}{\left(1 + \mathrm{AR_c}^{-1}\right)^2 \left[1 - \frac{192}{\pi^5}\mathrm{AR_c}^{-1}\tanh\left(\frac{\pi}{2}\mathrm{AR_c}\right)\right]}, \tag{11.21}$$

hence (11.20) combines with (11.21) can be rewritten as

$$\left(\frac{d_h}{L}\right)_{opt} \approx 4.7234\left[\left(1 + \mathrm{AR_c}^{-1}\right)^2\left[1 - \frac{192}{\pi^5}\mathrm{AR_c}^{-1}\tanh\left(\frac{\pi}{2}\mathrm{AR_c}\right)\right]\right]^{-3/8}\mathrm{Be}^{-1/4}. \tag{11.22}$$

The minimum dimensionless global thermal resistance can be obtained for an elemental volume for the configurations that correspond to the optimal geometries by substituting (11.20) into (11.18) as:

$$R_{min} = 1.156\beta {P_{o_{d_h}}}^{1/4}\mathrm{Be}^{-1/2}. \tag{11.23}$$

Equation (11.23) shows that the thermal resistance decreases monotonically as Be increases for a fixed porosity. Therefore, the minimised dimensionless global thermal resistance of a rectangular channel with $P_{o_{d_h}}$ of (11.21) is:

$$R_{\min} = 2.1516\left[\left(1 + \mathrm{AR_c}^{-1}\right)^2\left[1 - \frac{192}{\pi^5}\mathrm{AR_c}^{-1}\tanh\left(\frac{\pi}{2}\mathrm{AR_c}\right)\right]\right]^{-1/4}\beta \mathrm{Be}^{-1/2}. \tag{11.24}$$

The analytical result of (11.23) was used to validate the numerical solutions. The numerical and approximate solutions based on scale analysis at optimal geometry dimensions are in good agreement and the solutions have similar trends as shown in Fig. 11.11. Although the analytical results are lower than numerical results, the theoretical and numerical values agree within a factor of 1.5 for the worst case. However, this deviations from the numerical result are attributed to simplifying assumptions made in the formulation of the theoretical solution. These results are also in agreement with the past research work [24].

11.7 Conclusion

This chapter studies the numerical optimisation of geometric structures of the cooling volume with internal heat generation for rectangular channel cross section based on constructal theory. The results showed that there is an optimal geometry for the configuration which minimises the thermal resistance. The numerical analysis also showed that the optimised geometry is a function of the dimensionless pressure difference. The results also showed that the minimised peak temperature decreases as the porosity increases.

The numerical results obtained are in good agreement with results obtained in the approximate solutions based on scale analysis at optimal geometry dimensions. The approximate dimensionless global thermal resistance predicts the trend obtained in the numerical results. This shows that there are unique optimal design variables (geometries) for a given applied dimensionless pressure number for fixed porosity. The use of the optimisation algorithm coupled with the CFD package made the numerical results to be more robust with respect to the selection of optima structure geometries, internal configurations of the flow channels and dimensionless pressure difference.

Therefore, when designing the cooling structure, the internal and external geometries of the structure, and pump power requirements are very important parameters to be considered in achieving efficient and optimal designs for the best performance.

Acknowledgements The funding obtained from the NRF, TESP, Stellenbosch University/University of Pretoria, SANERI/SANEDI, CSIR, EEDSM Hub and NAC is acknowledged and duly appreciated.

References

1. Bejan A. Advanced engineering thermodynamics. 2nd ed. New York: Wiley; 1997.
2. Bejan A. Shape and structure, from engineering to nature. Cambridge: Cambridge University Press; 2000.
3. Bejan A, Sciubba E. The optimal spacing of parallel plates cooled by forced convection. Int J Heat Mass Tran. 1992;35:3259–64.
4. Bejan A, Lorente S. Design with constructal theory. Hoboken: Wiley; 2008.
5. Bello-Ochende T, Bejan A. Fitting the duct to the "body" of the convective flow. Int J Heat Mass Tran. 2003;46:1693–701.
6. Wang H, Dai W, Bejan A. Optimal temperature distribution in a 3D triple-layered skin structure embedded with artery and vein vasculature and induced by electromagnetic radiation. Int J Heat Mass Tran. 2007;50:1843–54.
7. Bejan A, Badescu V, De Vos A. Constructal theory of economics structure generation in space and time. Energ Convers Manage. 2000;4:1429–51.
8. Bejan A, Badescu V, De Vos A. Constructal theory of economics. Appl Energ. 2000;67:37–60.
9. Bejan A. Optimal internal structure of volumes cooled by single phase forced and natural convection. J Electron Packaging. 2003;125:200–7.
10. Bejan A. Why university rankings do not change: education as a natural hierarchical flow architecture. Int J Des Nat Ecodyn. 2007;2(4):319–27.
11. Bejan A. Two hierarchies in science: the free flow of ideas and the academy. Int J Des Nat Ecodyn. 2009;4:86–94.
12. Weinerth G. The constructal analysis of warfare. Int J Des Nat Ecodyn. 2010;5(3):268–76.
13. Meyer JP. Constructal law in technology, thermofluid and Energy Systems, and in design education. Phys Life Rev. 2011;8(3):247–8.
14. Bejan A, Lorente S. The constructal law and the evolution of design in nature. Phys Life Rev. 2011;8(3):209–40.
15. Bello-Ochende T, Meyer JP, Bejan A. Constructal ducts with wrinkled entrances. Int J Heat Mass Trans. 2009;52:3628–33.
16. Muzychka YS. Constructal design of forced convection cooled micro-channel heat sinks and exchangers. Int J Heat Mass Trans. 2005;48(15):3119–24.
17. Rocha LAO, Lorenzini E, BiserniGeometric C. Optimization of shapes on the basis of Bejan's constructal theory. Int Commun Heat Mass. 2005;32:1281–8.
18. Kim SW, Lorente S, Bejan A. Vascularised materials with heating from one side and coolant forced from the other side. Int J Heat Mass Trans. 2007;50:3498–506.
19. Salimpour MR, Sharifhasan M, Shirani E. Constructal optimization of the geometry of an array of micro-channels. Int Commun Heat Mass. 2010;38:93–9.
20. Olakoyejo OT, Bello-Ochende T, Meyer JP. Geometric optimisation of forced convection in a vascularised material. Proceedings of the 8th International Conference on Heat Transfer, Fluid Mechanics and Thermodynamics; 2011; Pointe Aux Piments, Mauritius. p. 666–74
21. Reis AH. Constructal theory: from engineering to physics, and how flow systems develop shape and structure. Appl Mech Rev. 2006;59(5):269–82.
22. Fan Y, Luo L. Recent applications of advances in microchannel heat exchangers and multi-scale design optimization. Heat Transfer Eng. 2008;29(5):461–74.
23. da Silva AK, Lorente S, Bejan A. Optimal distribution of discrete heat sources on a plate with laminar forced convection. Int J Heat Mass Trans. 2004;47(11–12):2139–48.
24. Bello-Ochende T, Liebenberg L, Meyer JP. Constructal cooling channels for micro-channel heat sinks. Int J Heat Mass Trans. 2007;50(21–22):4141–50.
25. Rocha LAO, Lorenzini E, Biserni C, Cho Y. Constructal design of a cavity cooled by convection. Int J Des Nat Ecodyn. 2010;5(3):212–20.
26. Biserni C, Rocha LAO, Stanescu G, Lorenzini E. Constructal H-shaped cavities according to Bejan's theory. Int J Heat Mass Trans. 2007;5:2132–8.

27. Olakoyejo OT, Bello-Ochende T, Meyer JP. Geometric optimisation of forced convection in cooling channels with internal heat generation. Proceedings of the 14th International Heat Transfer Conference; 2010 Washington DC, USA. Paper: IHTC14-22230
28. Chu RC. "Thermal management roadmap cooling electronic products from handheld device to supercomputers,". Proceedings of the MIT Rohsenow Symposium; 2002 Cambridge, MA
29. SEMATECH. The National Technology Roadmap For Semiconductors: Technology Need SEMATECH, Austin, TX; 1997
30. Bhattacharjee S, Grosshandler WL. The formation of wall jet near a high temperature wall under microgravity environment. ASME HTD. 1998;96:711–6.
31. Petrescu S. Comments on the optimal spacing of parallel plates cooled by forced convection. Int J Heat Mass Trans. 1994;37:1283.
32. Fluent Inc.. Fluent version 6 manuals. Centerra resource park, 10 Cavendish Court, Lebanon, New Hampshire, USA, (http:\crwww.fluent.com). 2001
33. Patankar SV. Numerical heat transfer and fluid flow. New York: Hemisphere; 1980.
34. Fluent Inc. Gambit version 6 manuals. Centerra resource park, 10 Cavendish court, Lebanon, New Hampshire, USA. (http:\crwww.fluent.com). 2001
35. The MathWorks, Inc. MATLAB and Simulink Release notes for R2008a. 3 Apple Hill Drive, Natick, MA. (http:\crwww.mathworks.com), 2008
36. White FM. Viscous fluid flow. 2nd ed. Singapore: McGraw-Hill; 1991.
37. Snyman JA, Hay AM. The DYNAMIC-Q optimisation method: an alternative to SQP? Comput Math Appl. 2002;44:1589–98.
38. Snyman JA. Practical mathematical optimisation: an introduction to basic optimisation theory and classical and new gradient-based algorithms. New York: Springer; 2005.
39. Bello-Ochende T, Meyer JP, Ighalo FU. Combined numerical optimization and constructal theory for the design of microchannel heat sinks. Numer Heat Trans A. 2010;58:882–99.
40. Morris RM, Synyman JA, Meyer JP. Jets in crossflow mixing analysis using computational fluid dynamics and mathematical optimization. AIAA J Propulsion Power. 2007;23:618–28.
41. Motsamai OS, Synyman JA, Meyer JP. Optimisation of gas turbine combustor mixing for improved exit temperature profile. Heat Transfer Eng. 2010;31:402–18.
42. Olakoyejo OT, Bello-Ochende T, Meyer JP. Mathematical optimisation of laminar forced convection heat transfer through a vascularised solid with square channels. Int J Heat Mass Trans. 2012;55(9–10):2402–11.

Chapter 12
Flow of Stresses: Constructal Design of Perforated Plates Subjected to Tension or Buckling

L.A. Isoldi, M.V. Real, A.L.G. Correia, J. Vaz, E.D. dos Santos, and L.A.O. Rocha

12.1 Introduction

It is possible to state that improving systems configuration for achieving better performance is the major goal in engineering. In the past, the scientific and technical knowledge combined with practice and intuition has guided engineers in the design of man-made systems for specific purposes. Soon after, the advent of the computational tools has permitted to simulate and evaluate flow architectures with many degrees of freedom. However, while system performance was analyzed and evaluated on a scientific basis, system design was kept at the level of art [1].

The Constructal Theory was created by Adrian Bejan, in 1996, when a new geometric solution philosophy was applied to the conductive cooling of electronics [2, 3]. These studies have a significant importance because they played a basic and starting point role for the extension and application of Constructal Theory to problems in engineering and other branches of science [4, 5]. Moreover, Constructal Theory has been employed to explain deterministically the generation of shapes in nature [3].

The Constructal Law states that "for a flow system to persist in time (to survive) it must evolve in such a way that it provides easier and easier access to the currents that flow through it." It is not only a principle from which geometric shape and structure are deduced in Nature, but also an engineering method, Constructal

L.A. Isoldi • M.V. Real • A.L.G. Correia • J. Vaz • E.D. dos Santos
Universidade Federal de Rio Grande (FURG), Escola de Engenharia (EE), Rio Grande-RS CP 474, Brazil

L.A.O. Rocha (✉)
Departamento de Engenharia Mecânica (DEMEC), Universidade Federal do Rio Grande do Sul (UFRGS), Porto Alegre-RS, Brazil
e-mail: laorocha@gmail.com

L.A.O. Rocha et al. (eds.), *Constructal Law and the Unifying Principle of Design*, Understanding Complex Systems, DOI 10.1007/978-1-4614-5049-8_12,

Design, for optimizing the paths for flows through finite-size open systems [6]. This is a major step toward making system design a science. This Law indicates that if a system is free to morph under global constraints, the better flow architecture is the one that minimizes the global flow resistances, or maximizes the global flow access. A basic outcome of the Constructal Theory is that system shape and internal flow architecture do not develop by chance, but they result from the permanent struggle for better performance and therefore must evolve in time. As in engineered systems, in nature the competition is permanent (e.g., river basins, global circulations, trees and animals morph and improve in time under changing constraints) [1].

Concerning the engineering problems, the applicability of Constructal Design (Method for optimization of several systems, e.g., engineering) has been discussed largely in the recent literature: [7–11]. As it can be observed, these studies have been dominantly applied for the study of fluid mechanics and heat transfer.

In the heat transfer realm, Constructal Design has been employed for the optimization of cooling cavities intruded into conducting solids with uniform heat generation. Several shapes for the cavities have been studied. Since geometries with few degrees of freedom, C-shaped, elliptical, triangular, and T-shaped ones intruded into rectangular walls [12, 13], to those with a higher level of complexity, H and T–Y shaped cavities [14, 15]. The study of fins has also been the subject of optimization by means of Constructal Design. Optimal shapes and performance of T-shaped [16], Y-shaped [17], twice Y-shaped [18], T–Y-shaped [19], and T–Y-shaped fins with lateral extended surfaces [20] have been performed in the literature.

Concerning the fluid mechanics, [2, 3, 21] showed that the pressure drop for flows in ducts with round cross section are minimal in comparison with the pressure drops reached for other several regular polygonal cross sections. Examples of vascular tree-shaped flow architectures employed to guide river basin design are also presented in [22, 23]. Reference [24] studied the configuration of vascular channels when the flow is turbulent. Moreover, Constructal Design has also been employed for the optimization of internal and external flows submitted to convection heat transfer [10, 25, 26].

However, few studies in the field of mechanics of materials have been developed. In this subject, it is worthy to mention the studies of [27, 28]. The first paper draws attention to a specific class of thermal design problems, in which the system architecture is derived from a combination of heat transfer and mechanical strength considerations. In the latter work, it was studied the analogy between the geometric configuring of heat and fluid flow and the configuring of the stress distribution ("flow of stresses").

The present work analyses the behavior of thin perforated plates subjected to uniaxial load (tension or compression). The objective was to seek for the optimal geometry of rectangular perforated thin plates with three different centered hole shapes: elliptical, diamond, and rectangular by means of Constructal Design.

Thin plates are common structural elements widely used in buildings, bridges, ships, airplanes, and automobiles. Besides, cutouts are often provided in plate structures such as cold formed steel members, plate and box girders, box pylons, and ship grillages for

the purposes of access, services, and even aesthetics. The presence of holes in such structures results in a change in the mechanical behavior of the plates [29].

When these panels are used as structural elements, it is very common that they are subject to axial forces. If the axial force is tensile, the presence of the hole will cause a stress concentration in the plate. On the other hand, if the axial force is compression, the perforated plate could buckle if this load exceeds the critical load.

Therefore, the objective of this study was to obtain the optimal geometry that minimizes the maximal stress concentration along the plate or supports the higher critical buckling load for the plate. For this, the degree of freedom H_0/L_0 for elliptical, rectangular, and diamond holes (Fig. 12.1) was optimized for several ratios of volume fraction between the hole and the plate. It is expected that these mechanical behaviors can be optimized according to Constructal Law, similarly to what is observed for the optimization of heat and fluid flows. This optimization process was accomplished in the most fundamental sense, without application to a particular device or field. This explains why the values adopted for the degree of freedom H_0/L_0 were not limited only to the range of practical interest.

12.2 Flow Analogy

The lesson taught by Bejan's Constructal theory is this: geometry matters. The principle is the same in engineering and nature: the search for easier access by flow systems subjected to constraints generates shape and structure [3].

Reference [30] states that in mechanics of materials a qualitative understanding about stress concentration can be obtained by an analogy with a fluid flow, called flow analogy. Intuitive methods like the flow analogy are sometimes helpful to the engineer that needs to reduce stress concentrations in structural designs.

The governing field equations for ideal irrotational fluid flow are quite similar to those for stress. Thus, there exists an analogy between fluid flow lines, velocity, and pressure gradients on the one hand, and stress trajectories, magnitudes, and principal stresses on the other hand. The flow analogy for the plate in Fig. 12.2a is shown in Fig. 12.2b, where stress-free surface boundaries are replaced by solid-channel boundaries for the fluid (wherever stress cannot exist, fluid flow cannot exist). The uniformly applied loads are replaced by a uniform fluid flow field. Along the entrance section A–A of Fig. 12.2b, the flow is uniform, and, owing to symmetry, the flow is uniform at the exit of the channel. However, as the fluid particles approach section B–B, the streamlines need to adjust to move around the circular obstacle. In order to accomplish this, particles close to streamline 1 must make the greatest adjustment and must accelerate until they reach section B–B, where they reach maximum velocity, and then decelerate to their original uniform velocity some distance from B–B. Thus, the velocity at point c is the maximum. The compaction of the streamlines at c will lead to the development of a pressure gradient, which will actually cause the velocity of point b to be less than that of the incoming velocity of streamline 6 at A–A. Note also that when a particle on

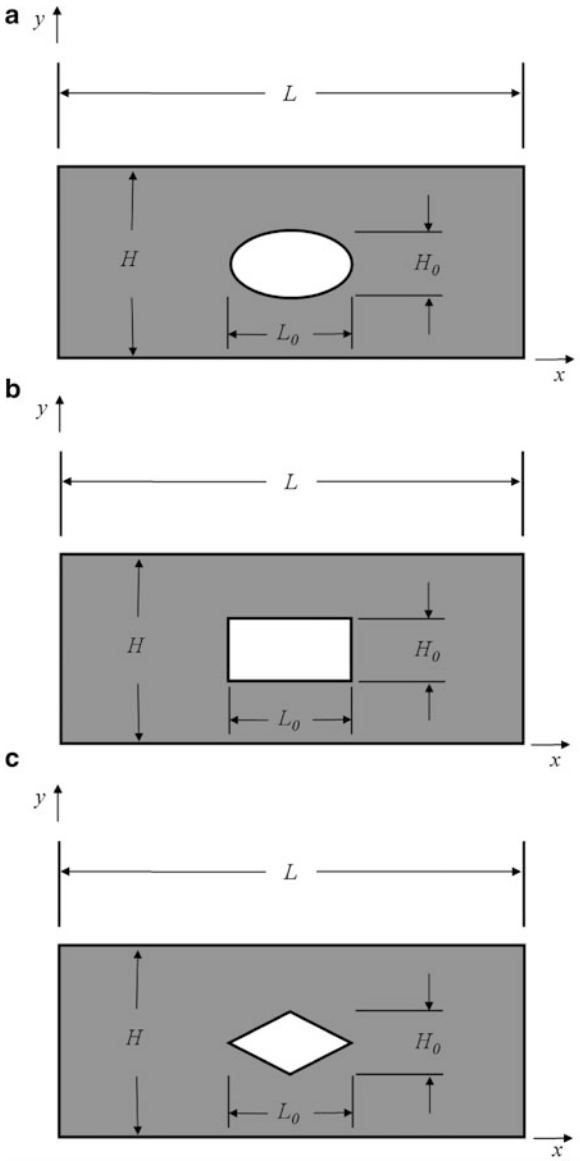

Fig. 12.1 Plate with centered hole: (**a**) elliptical, (**b**) rectangular, and (**c**) diamond

streamline 1 reaches point d, the particle theoretically takes on a velocity perpendicular to the net flow. This analogy agrees with that of the plate loaded in tension with a centrally located hole. The stress is a maximum at the edge of the hole corresponding to point c in Fig. 12.2b. The stress in the plate corresponding to point b is lower than the applied stress, and for point d the stress in the plate is compressive perpendicular to the axial direction. This analogy can be used to suggest improvements to reduce stress concentrations. For example, for the plate

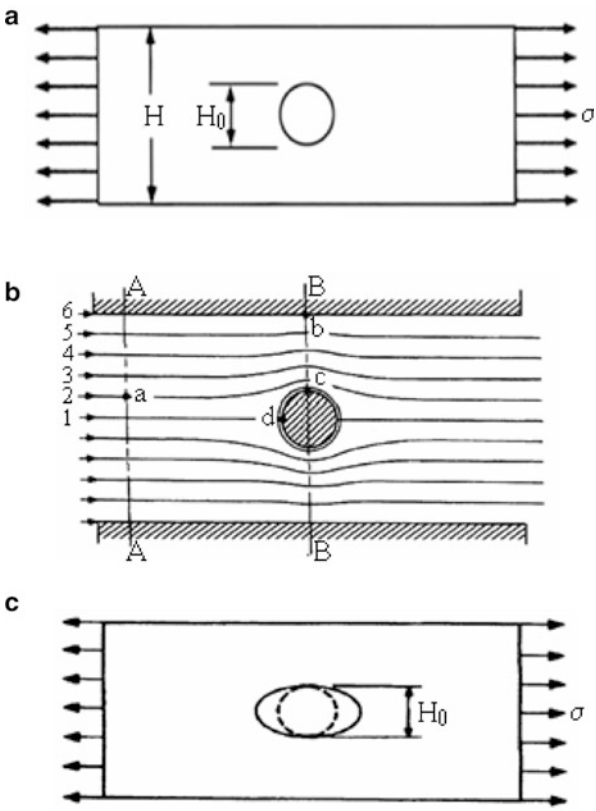

Fig. 12.2 Analogy between the fluid flow and stress concentration [30]

with the hole, the hole can be elongated to an ellipse as shown in Fig. 12.2c, which will improve the flow transition into section B–B (note that this is a reduction of material).

Therefore, considering that there is an analogy among the generation of geometric configuration for problems of heat, fluid, and stress flows, it is possible to develop studies in the area of mechanics of materials with focus in the structural optimization by means of Constructal Design.

12.3 Stress Concentration in Perforated Plates

When a large stress gradient occurs in a small, localized area of a structure, the high stress is referred to as a stress concentration. Near changes in geometry of a loaded structure, the flow of stress is interfered with, causing high stress gradients where the maximum stress and strain may greatly exceed the average or nominal values based on simple calculations. Rapid geometry changes disrupt the smooth flow of

stresses through the structure between load application areas. Plates in tension or bending with holes, notches, steps, etc., are simple examples involving direct normal stresses [30].

Therefore, if a structural member contains a discontinuity, such as a hole or a sudden change in cross section, high localized stresses can occur near the discontinuity. However, the values of the stress concentration are independent of the size of the member and of the material used; they depend only upon the ratios of the geometric parameters involved. Furthermore, the designer is more interested in the maximum value of the stress in a given section, than in the actual distribution of stresses in that section, since his main concern is to determine whether the allowable stress will be exceeded under a given loading, and not where the allowable stress will be exceeded [31].

There are several researches concerning the stress concentration in perforated plates, as in [32–34]. Thus, considering the Constructal design and using a numerical approach, the geometric optimization of a thin plate with a centered hole subjected to uniform longitudinal tensile stress at one end and clamped at the other end was accomplished. The objective was to obtain the optimal geometry that produces the minimal stress concentration value.

12.4 Buckling in Perforated Plates

Buckling is an instability phenomenon that can occur if a slender and thin-walled plate (plane or curved) is subjected to axial compression. At a certain given critical load the plate will buckle very sudden in the out-of-plane transverse direction [35].

In the analysis of the behavior of slender members, equilibrium and compatibility conditions are used in order to find the internal forces and deformations. In the simplest cases, a structure's safety is evaluated by confirming that the maximum values computed for the stresses are lower than the allowable stress defined for the material the structure is made of. This is a necessary condition for structural safety, but it may not be sufficient, either because the deformations are limited for some reason, or because there is the risk that the equilibrium configuration of the structure is not stable, i.e., that buckling may occur. In fact, while tensile forces may only do work if the material deforms or ruptures, for the case of compression there is a third possibility—buckling—which consists of a lateral deflection of the material, in relation to direction of actuation of the compressive forces. In accordance with these considerations, the stability of a structure may be analyzed by computing its critical load, i.e., the load corresponding to the situation in which a perturbation of the deformation state does not disturb the equilibrium between the external and internal forces [36].

Besides, the presence of holes in the plates results in a redistribution of the flow of stresses (membrane stresses) accompanied by a change in the mechanical behavior of these structural members. Actually, a significant reduction in elasto-plastic ultimate strength, when compared to solid plate (i.e., imperforated plate),

has always been found in perforated plates notwithstanding the occasionally occurring increase in elastic buckling critical load as reported in previous articles [29].

The buckling behavior of perforated plates has been the object of a large number of researches in the last decade. The main objective of the published articles can be divided into two categories: elastic buckling [37–39] and elasto-plastic buckling [40–45].

In summary, most of the previous researches focused on the changes in buckling behavior of perforated plates due to the presence of cutouts. The optimal hole shape and hole size to the plate buckling performance has not yet been systematically investigated. This task can be appropriately performed by using the principles of the Constructal Theory. Therefore, the Constructal Design coupled with a computational model were employed to define the optimal hole shape and size to the elastic buckling performance of perforated rectangular plates under uniaxial compression loading. For this, the optimal geometry is the one which supports the maximal load without to suffer buckling, i.e., the one which reach the highest critical buckling load.

12.5 Constructal Design Applied to Perforated Plates

The geometric optimization for thin plates with centered holes was investigated considering three different hole shapes: elliptical, rectangular, and diamond. The characteristic dimensions of each hole can vary, while the plate dimensions are constant. The hole variation is governed by the optimization parameter called hole volume fraction (ϕ). This parameter represents the relation between the hole volume (V_0) and the total plate volume without hole (V). The hole volume fraction can be understood as a constraint of the problem. In Constructal Design, this constraint is part of mechanism for generating the optimal geometric form that fills a given space. This parameter allows comparing different geometric shapes in an adequate way.

Therefore, for the plate with a centered elliptical perforation (Fig. 12.1a) the hole volume fraction is defined as:

$$\phi = \frac{V_0}{V} = \frac{(\pi H_0 L_0 t)/4}{HLt} = \frac{\pi H_0 L_0}{4HL} \tag{12.1}$$

where π is the mathematical constant; H_0 and L_0 are the characteristic dimensions of hole in y and x directions, respectively; H is the height of plate, L is the length, and t is the plate thickness.

When the thin plate has a hole with a rectangular shape (Fig. 12.1 b) the hole volume fraction is obtained by:

$$\phi = \frac{V_0}{V} = \frac{H_0 L_0 t}{HLt} = \frac{H_0 L_0}{HL} \tag{12.2}$$

and for the plate with centered diamond hole (Fig. 12.1c) the hole volume fraction is given by:

$$\phi = \frac{V_0}{V} = \frac{(H_0 L_0 t)/2}{HLt} = \frac{H_0 L_0}{2HL} \tag{12.3}$$

The objective in all analyses was to determine the optimal hole geometry (H_0/L_0) that is characterized by the minimum stress concentration value for the tensioned plate or by the maximization of critical buckling load for the compressed plate. For this, based on Constructal Design, the variables of the problems were considered dimensionless:

$$\tilde{x}, \tilde{y}, \tilde{t}, \tilde{H}, \tilde{L}, \tilde{H}_0, \tilde{L}_0 = \frac{x, y, t, H, L, H_0, L_0}{A^{1/2}} A \tag{12.4}$$

A is the area of plate without hole defined as:

$$A = HL \tag{12.5}$$

12.6 Computational Models

The numerical solutions for the problems studied here were carried out by the general-purpose program ANSYS, based on the Finite Element Method (FEM)

The FEM is a numerical procedure for obtaining approximate solutions to many of the problems encountered in engineering analysis with reasonable accuracy. In the field of structural analysis, the FEM is usually adopted in its displacement formulation. In this way, the structure continuum is divided into a number of small regions—the so-called finite elements. These elements are assumed to be interconnected at a discrete number of nodal points located on their boundaries [46].

12.6.1 Stress Concentration Model

For thin plates one can assume the plane stress approximation where all the stress components in the direction perpendicular to the plate surface vanish. Thus, the static equilibrium state is defined by:

$$\frac{\partial \sigma_x}{\partial x} + \frac{\partial \tau_{xy}}{\partial y} + F_x = 0 \tag{12.6}$$

Table 12.1 Numerical tests showing the achievement of grid independence

Number of elements	$\sigma^{j}_{\max}$(MPa)	$\left\|\frac{(\sigma^{j}_{\max}-\sigma^{j+1}_{\max})}{\sigma^{j}_{\max}}\right\|(\times 10^{-3})$
647	6.94	36.02
1,856	7.19	12.51
4,302	7.28	6.86
17,503	7.33	1.36
70,503	7.34	-

and

$$\frac{\partial \tau_{xy}}{\partial x} + \frac{\partial \sigma_y}{\partial y} + F_y = 0 \tag{12.7}$$

being σ_x and σ_y the normal stresses in the x and y axes, respectively, τ_{xy} the shear stresses acting in the x–y plane and F_x and F_y the body forces in the x and y directions, respectively. Since in the present analysis the effects of gravity are neglected, there are no body forces to be considered.

Therefore, (12.6) and (12.7) were numerically solved by means of ANSYS software. The element PLANE42 was adopted characterizing a quadrilateral 2D numerical model [47].

It was assumed that the plate's material is isotropic (steel), with Young's modulus, E, and Poisson's ratio, ν, with values of 210.00 GPa and 0.3, respectively. In all situations the left end of the perforated plate is clamped while a constant tension, σ, of 1.00 MPa, is applied in the right end.

The appropriate mesh size was determined by successive refinements (h-refinement), increasing the number of elements from the current mesh size to the next mesh size, until to satisfy the criterion:

$$\left| \left(\frac{\sigma^{j}_{\max} - \sigma^{j+1}_{\max}}{\sigma^{j}_{\max}} \right) \right| \leq 2.00 \times 10^{-3} \tag{12.8}$$

where $\sigma^{j}_{\max}$ represents the maximum stress calculated using the current mesh size, and $\sigma^{j+1}_{\max}$ corresponds to the maximum stress using the next mesh. The grid was non-uniform and varied from one geometry to the next.

The grid independence was tested with a particular case of elliptical hole, when the ellipse axes have the same value, i.e., the hole is a circumference. So, a plate with a circular hole ($H/L = 0.50$; $\phi = 0.20$; $H_0/L_0 = 1.00$) was used. Table 12.1 shows the results of numerical simulations employed to obtain the independent mesh. Based on Table 12.1 and in accordance with (12.8), it is possible to affirm that the grid independence is achieved with 17,503 elements. This mesh was generated with an element size of 10 mm.

With the purpose of validating the numerical model, the results obtained using the independent mesh are compared with the analytical solution. This comparison is

made considering the plate used in grid independence test. The analytical result for this case is given by [30]:

$$\sigma_{max} = \left[C_1 + C_2\left(\frac{H_0}{H}\right) + C_3\left(\frac{H_0}{H}\right)^2 + C_4\left(\frac{H_0}{H}\right)^3\right]\left(\frac{\sigma H}{H - H_0}\right) \tag{12.9}$$

being the coefficients: $C_1 = 3.00$, $C_2 = -3.13$, $C_3 = 3.66$ and $C_4 = -1.53$.

Equation (12.9) gives a stress concentration of 7.22 MPa while the numerical solution of this problem was 7.33 MPa (see Table 12.1), i.e., the numerical results found with the present methodology agreed within 1.50% with those of the literature [30].

In order to reinforce the numerical evaluation, other case for the plate with elliptical hole was considered with the following parameters: $H/L = 0.50$; $\phi = 0.20$; $H_0/L_0 = 1.50$. The analytical solution is defined by (12.9), considering the following coefficients: $C_1 = 4.00$, $C_2 = -4.08$, $C_3 = 4.01$ and $C_4 = -1.91$. The analytical result is 17.63 MPa while the numerical one is 17.50 MPa, showing a difference of only 0.74% between the solutions. The close agreement between analytical and numerical results show the validity of the computational modeling adopted in this research.

The theory of elasticity states that an infinite stress arises at a sharp corner. In a computational modeling this can be proved if the stress concentration is evaluated with successive mesh refinements around the sharp corner. Reference [34] confirmed this behavior, showing that the stress increases as the mesh is refined for an L-bracket finite element plane stress solution.

To eliminate such numerical problem, rounded corners are usually employed in the computational domain. However, the process to round the sharp corners would bring a greater complexity to the construction of geometries, especially in an optimization process where several cases must be studied.

For this reason the sharp corners in rectangular and diamond holes were considered. However, the mesh adopted produces stress concentration results close to those that would be obtained if the sharp corners have been rounded. Some cases were compared and differences lower than 9.0% were encountered, justifying the geometrical simplification used in this first approach to the problem.

12.6.2 Buckling Model

The computational model used to evaluate the critical buckling load of plates was developed in the general-purpose finite element program ANSYS, as already mentioned. In all buckling numerical simulations the ANSYS SHELL93 reduced integration eight-node thin shell element was adopted. This element has six degrees-of-freedom at each node: three translations (u,v,w) and three rotations ($\theta_x, \theta_y, \theta_z$) [47].

The approach adopted for buckling analysis was the eigenvalue buckling (linear). This numerical procedure is used for calculating the theoretical buckling load of a linear elastic structure. Since it assumes the structure exhibits linearly elastic behavior, the predicted buckling loads are overestimated. Therefore, if the component is expected to exhibit structural instability, the search for the load that causes structural bifurcation is referred to as a buckling load analysis. Because the buckling load is not known a priori, the finite element equilibrium equations for this type of analysis involve the solution of homogeneous algebraic equations whose lowest eigenvalue corresponds to the buckling load, and the associated eigenvector represents the primary buckling mode [48].

The strain formulation used in the analysis includes both the linear and nonlinear terms. Thus, the total stiffness matrix, $[K]$, is obtained by summing the conventional stiffness matrix for small deformation, $[K_E]$, with another matrix, $[K_G]$, which is the so-called geometrical stiffness matrix. The matrix $[K_G]$ depends not only on the geometry but also on the initial internal forces (stresses) existing at the start of the loading step, $\{P_0\}$. Therefore, the total stiffness matrix of the plate with load level $\{P_0\}$ can be written as [49]:

$$[K] = [K_E] + [K_G] \tag{12.10}$$

When the load reaches the level of $\{P\} = \lambda\{P_0\}$, where λ is a scalar, the stiffness matrix can be defined as:

$$[K] = [K_E] + \lambda[K_G] \tag{12.11}$$

Now, the governing equilibrium equations for the plate behavior can be written as:

$$[[K_E] + \lambda[K_G]]\{U\} = \lambda\{P_0\} \tag{12.12}$$

where $\{U\}$ is the total displacement vector that may therefore be determined from:

$$\{U\} = [[K_E] + \lambda[K_G]]^{-1}\lambda\{P_0\} \tag{12.13}$$

At buckling, the plate exhibits a large increase in its displacements with no increase in the load. From the mathematical definition of the matrix inverse as the adjoint matrix divided by the determinant of the coefficients it is possible to note that the displacements $\{U\}$ tend to infinity when:

$$\det \rightleftarrows [[K_E] + \lambda[K_G]] = 0 \tag{12.14}$$

Equation (12.14) represents an eigenvalue problem, which when solved provides the lowest eigenvalue, λ_1, that corresponds to the critical load level $\{P_{cr}\} = \lambda_1\{P_0\}$ at which buckling occurs. In addition, the associated scaled displacement vector $\{U\}$ defines the mode shape at buckling. In the finite element program ANSYS, the eigenvalue problem is solved by using the Lanczos numerical method [47].

Table 12.2 Comparison of critical buckling load for plate with centered circular hole

Hole diameter (m)	P_{cr} (kN/m) [37]	P_{cr} (kN/m)—Present work	Difference (%)
0.10	766.19	763.56	−0.34
0.20	789.36	786.50	−0.36
0.30	825.08	820.87	−0.51
0.40	849.26	847.78	−0.17
0.50	901.54	898.79	−0.31
0.60	986.46	981.22	−0.53

The first validation of this numerical procedure was carried out comparing its result with the analytical critical buckling load. A solid plate, i.e., a plate without perforation was used. The plate was simply supported on four edges in the out-of-plane direction. In this case, the plate's analytical critical buckling load is given by [50]:

$$P_{cr} = k\frac{\pi^2 E t^3}{12H^2(1-\nu^2)} \tag{12.15}$$

being t the plate thickness.

Thus, considering a solid steel plate with the same properties described earlier and with a thickness of 10.00 mm, the analytical critical buckling load is 759.20 kN/m.

For the numerical solution the plate was discretized adopting a triangular element with side size of 50.00 mm ($H/20$), generating a mesh with 1,814 finite elements, resulting in a critical buckling load of 755.30 kN/m.

Therefore, comparing the analytical and numerical solutions a difference of −0.51% was found, showing a good agreement.

Another validation was performed with the same plate used in the first validation; however, centered circular holes were considered. In Table 12.2 the results for the critical buckling load were compared with those obtained by the numerical study developed by Ref. [37].

Again an excellent agreement was obtained, being −0.53% the maximal difference encountered.

12.7 Results

After the validation of the computational models, they are employed in the geometric optimization process based on Constructal Design. The results of the mechanical behavior for thin rectangular plates with centered perforations subjected to a uniaxial load, i.e., tension or compression, are presented below, allowing to define the optimal geometry in each case.

The present numerical investigation consisted of determining the stress distribution in a large number of perforated plate configurations. The studied structures have two degrees of freedom: H/L and H_0/L_0. In this study H/L is kept constant ($H/L = 0.50$, being $H = 1.00$ m and $L = 2.00$ m). The optimization was performed

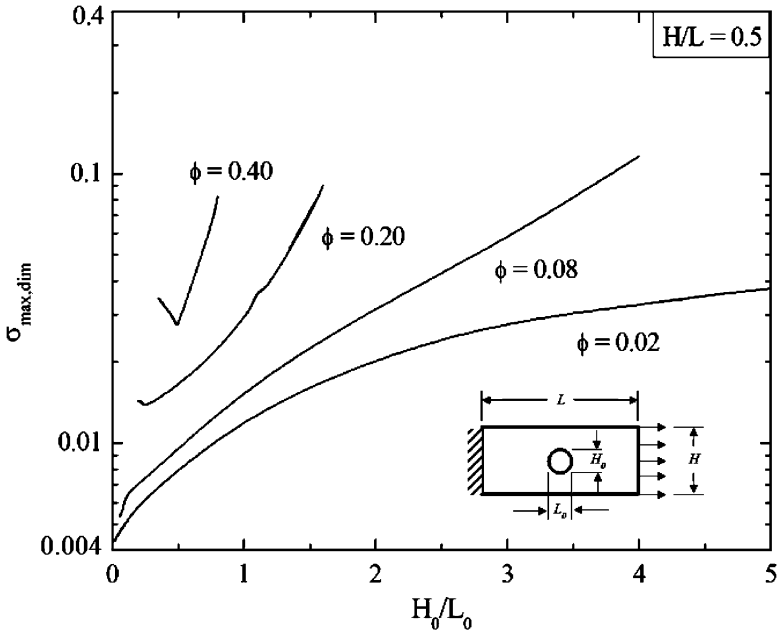

Fig. 12.3 Plate with elliptical hole: optimization of the stress concentration for several values of H_0/L_0

varying H_0/L_0 to obtain the geometry that generates a minimal dimensionless maximum stress concentration, if the clamped-free plate is subjected to a tension of 1.00 MPa. Several hole volume fractions, ϕ, were considered for each hole shape studied.

Figure 12.3 shows the optimization reached for the plate with centered elliptical hole. The optimal dimensionless maximum stress, $\sigma_{\max,\dim}$, was defined by dividing the optimal maximum von Mises stress (numerically evaluated) by the steel yielding stress, $\sigma_{ys} = 250.00$ MPa.

As expected, lower values for the hole volume fraction produce lower stress concentration levels. An important observation of Fig. 12.3 is that for lower values of ϕ the optimal geometries are reached for the lower ratios of H_0/L_0, i.e., for the higher intrusion of the hole in the longitudinal direction. As the volume fraction increases, $\phi \geq 0.20$, the optimal shape is not obtained for the minimal or the maximal ratio of H_0/L_0, i.e., there is an optimal geometry that leads to the minimal dimensionless maximum stress concentration. Differences between the optimal and the worst geometries of approximately 594 and 200% are noticed for the volume fractions of $\phi = 0.02$ and $\phi = 0.40$, respectively. The results show that Constructal Design can be employed for the minimization of stress concentration ("flow of stresses"), as previously observed in [28]. This behavior is similar to those found in the heat transfer problems, e.g., optimization of elliptical cavities intruded into solids with internal heat generation [13].

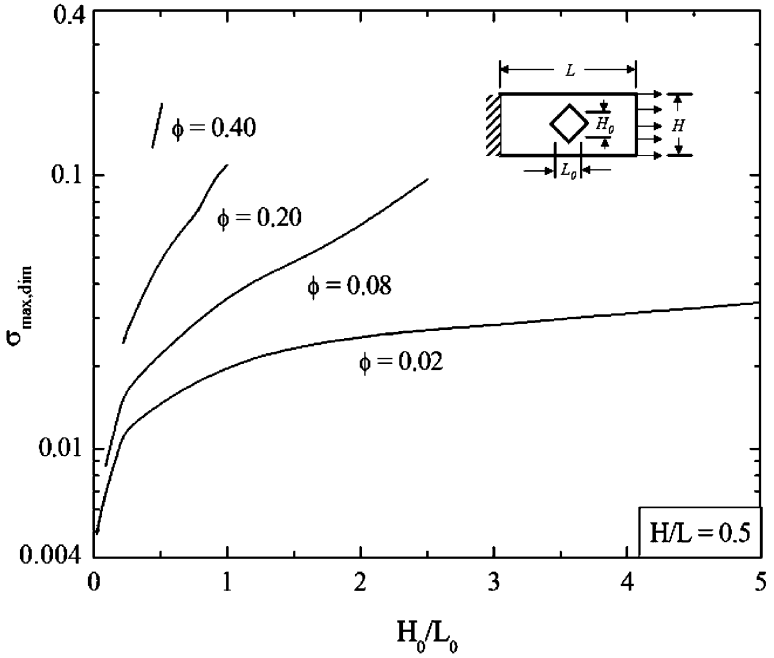

Fig. 12.4 Plate with diamond hole: optimization of the stress concentration for several values of H_0/L_0

The results evaluated for the tensioned plate with centered diamond hole are presented in Fig. 12.4. For all volume fractions, the dimensionless maximum stress increases with the increase of the ratio H_0/L_0. For higher values of volume fractions, the behavior is dissimilar to that observed for the plates with elliptical holes. This fact is related to the geometric restriction of the increase of the transversal (vertical) diagonal of the diamond hole.

The stress variation for plates with rectangular holes is showed in Fig. 12.5. In this case, only for $\phi = 0.02$ the optimal shape is reached for the minimal extreme of H_0/L_0. For the other values of ϕ, the optimal values are not placed in the extremes of H_0/L_0. This behavior is more similar to that found for plates with elliptical holes than that obtained for the diamond holes.

The procedure to reach the minimal dimensionless maximum stress used in Figs. 12.3, 12.4, and 12.5 for elliptical, rectangular, and diamond holes, respectively, was repeated for several values of the volume fraction ϕ. The optimal values achieved for each volume fraction are summarized in Fig. 12.6 where the once minimized dimensionless maximum stresses $(\sigma_{max,dim})_m$ are plotted as function of ϕ for the three hole shapes: elliptical, diamond, and rectangular. As expected, the best shape is the elliptical for the ratio $(H_0/L_0)_o = 0.014$. However, contrary to the common sense, where it is intuitively believed that the elliptical hole is universally better than other geometrical shapes, for hole volume fractions higher

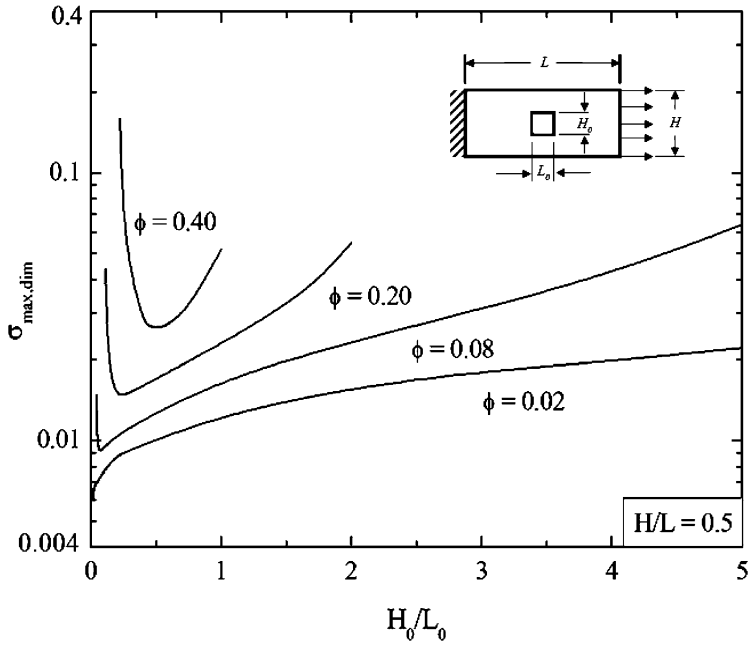

Fig. 12.5 Plate with rectangular hole: optimization of the stress concentration for several values of H_0/L_0

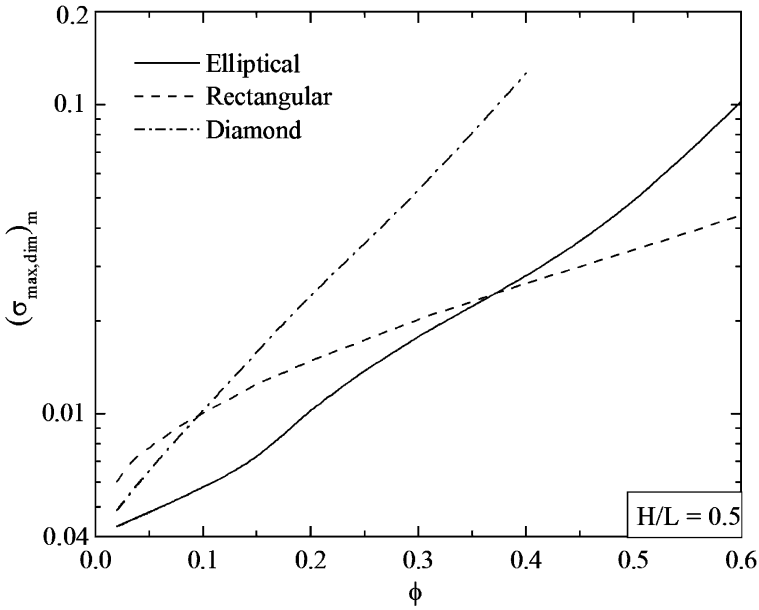

Fig. 12.6 The once minimized dimensionless maximum stress $(\sigma_{max,dim})_m$ as a function of the hole volume fraction ϕ for all hole shapes

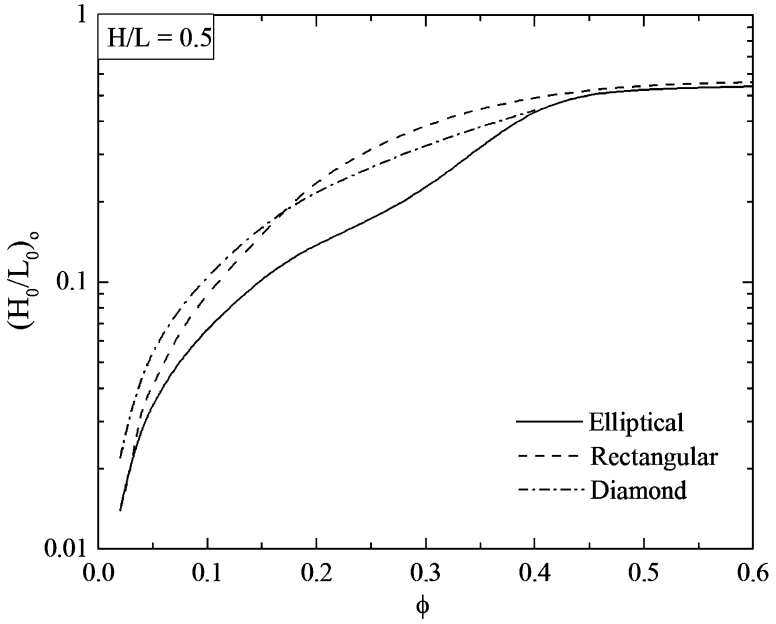

Fig. 12.7 The once optimized $(H_0/L_0)_o$ as a function of the hole volume fraction ϕ for all hole shapes

than approximately 0.40, the once minimized dimensionless maximum stresses for rectangular holes are lower than those found for the elliptical ones. Even the diamond hole, which in general leads to the worst results, in the range $0.02 \leq \phi \leq 0.09$ is better than the rectangular hole.

In Fig. 12.7 it is depicted the once optimized ratio $(H_0/L_0)_o$, as a function of ϕ for the three hole shapes: elliptical, diamond, and rectangular. For all kinds of hole, the lower possible ratio H_0/L_0 lead to the best shapes. For volume fractions lower than $\phi \approx 0.45$, the once optimized ratio $(H_0/L_0)_o$ increases with the increase of the volume fraction ϕ. As the volume fraction increases, the load generates higher stress concentrations in the transversal direction. Then, the increase of the ratio H_0/L_0 does not benefit the mechanical performance of the system. Due to this fact, the optimal ratio $(H_0/L_0)_o$ stabilizes after $\phi \approx 0.45$ for the elliptical and rectangular holes. For diamond holes, there are no geometries for volume fractions higher than $\phi \approx 0.40$.

The investigation about the critical buckling load of perforated plates was developed considering different values for the hole volume fraction, ϕ, for each hole shape. So, a variation of the degree of freedom H_0/L_0 was performed for each case. The other degree of freedom, H/L, was kept constant at 0.50 ($H = 1.00$ m and $L = 2.00$ m) for all numerical simulations. Besides, these values of critical buckling load numerically obtained were normalized by the analytical result for the critical buckling load of a non perforated plate (12.15).

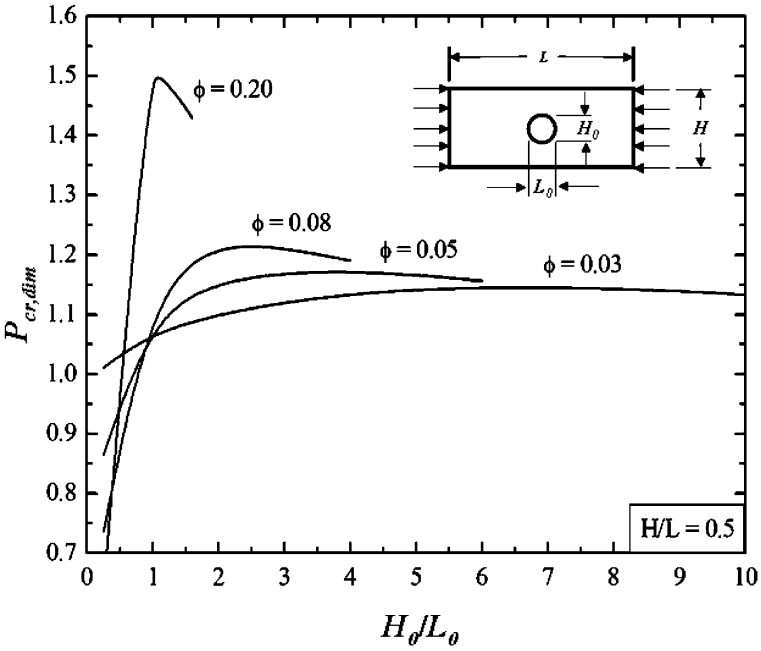

Fig. 12.8 Plate with centered elliptical perforation: optimization of the critical buckling load

Figure 12.8 presents the behavior of dimensionless critical buckling load versus the degree of freedom H_0/L_0 of the plate with centered elliptical hole. It is possible to note in Fig. 12.8 that for each hole volume fraction there is a maximum value of critical buckling load placed in an intermediate range of the ratio H_0/L_0. Another important observation is concerned with the increasing of the maximum critical buckling load with the increasing of the hole volume fraction.

Now, the results for the plate with rectangular centered perforation are showed in Fig. 12.9. The evolution of dimensionless critical buckling load is plotted as a function of degree of freedom H_0/L_0 for the same values of hole volume fraction already mentioned. Analogous behaviors in comparison with those of Fig. 12.8 are observed, i.e., when the value of hole volume fraction grows there is an increase in maximum $P_{\mathrm{cr,dim}}$.

Finally, the plate with centered diamond hole was studied and the results for the dimensionless critical buckling load depending on the H_0/L_0 for specific hole volume fractions are presented in Fig. 12.10. Comparing the behavior illustrated in Fig. 12.10 with those presented in Fig. 12.8 and in Fig. 12.9, it is possible to identify the same trend, i.e., only one value for the maximal critical buckling load is obtained as a function of the degree of freedom H_0/L_0.

Beyond the already mentioned hole volume fractions, others values of ϕ were numerically investigated. Figure 12.11 exhibits the effect of the hole volume fraction over the once maximized dimensionless buckling load for the three hole

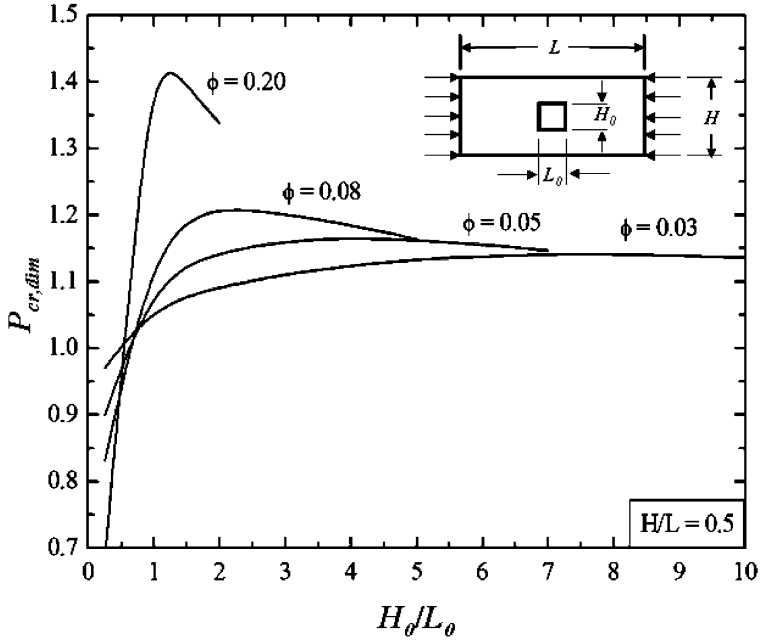

Fig. 12.9 Plate with centered rectangular perforation: optimization of the critical buckling load

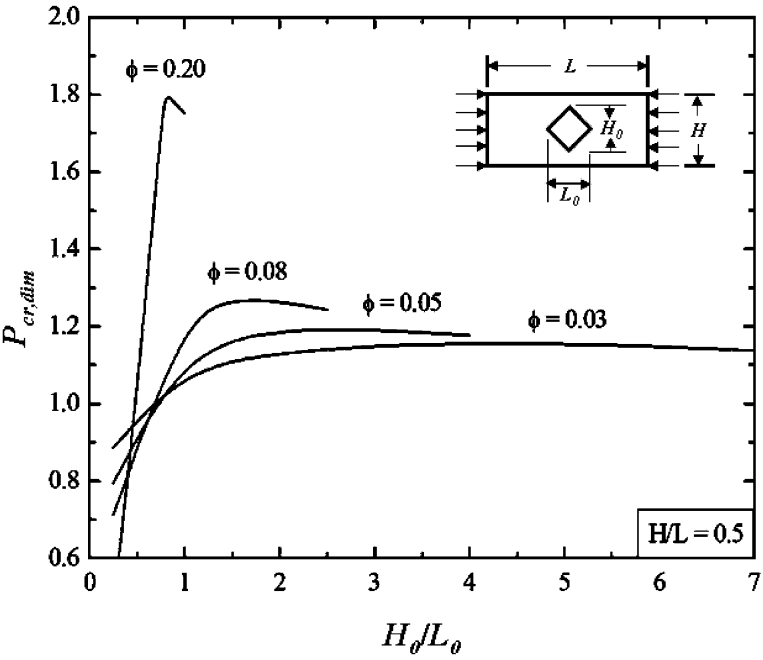

Fig. 12.10 Plate with centered diamond perforation: optimization of the critical buckling load

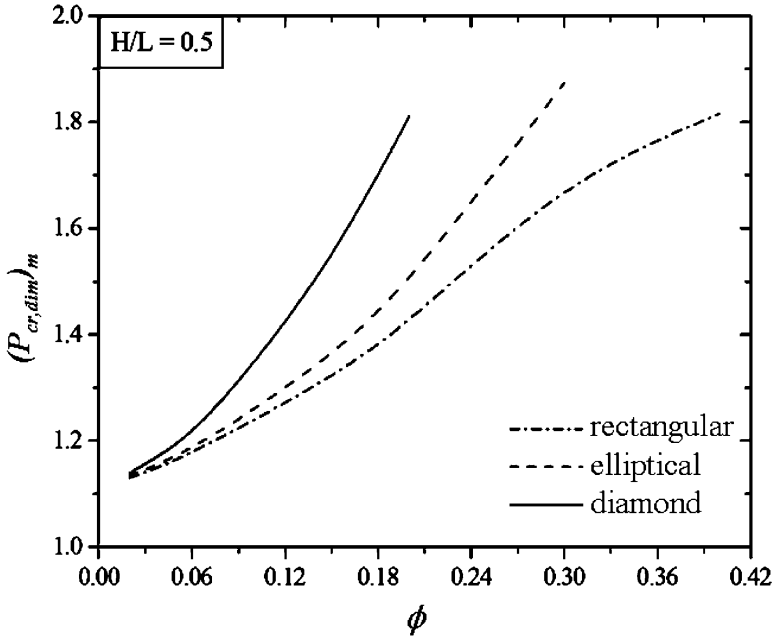

Fig. 12.11 The once maximized dimensionless critical buckling load $(P_{cr,dim})_m$ as a function of the hole volume fraction ϕ for all hole shapes

shapes studied. It is emphasized that, it is not possible to obtain geometries for the diamond and elliptical holes at values of $\phi > 0.2$ and $\phi > 0.3$, respectively. Figure 12.11 also indicates that, for $\phi \leq 0.20$, higher values of critical buckling loads are obtained for plates with centered diamond hole, i.e., in the range where the comparison between the three geometries is allowed, the diamond hole leads to the best performance. For $\phi = 0.20$, the highest dimensionless buckling load is $P_{cr,dim} = 1.8112$, which is approximately 17.4 and 21.5% better than the best elliptical and rectangular shapes, respectively. For the range $0.20 < \phi \leq 0.30$, the elliptical shape is better than the rectangular one, reaching a maximum $P_{cr,dim} = 1.8741$, which is approximately 10% higher than the $P_{cr,dim}$ found for the best rectangular shape. For $0.3 < \phi \leq 0.4$, it is only possible to intrude rectangular holes into the plate. In spite of this fact, the maximum dimensionless buckling load reached for the rectangular hole at $\phi = 0.4$ is $P_{cr,dim} = 1.8160$, which is 3.0% lower than the optimal elliptical shape for $\phi = 0.3$. The results make evident the importance of applying the Constructal Design for the geometric optimization of engineering structures.

Finally, in Fig. 12.12 it is depicted the once optimized ratio $(H_0/L_0)_o$ as a function of ϕ for the three hole shapes: elliptical, rectangular, and diamond. One can observe that the same trend is exhibited for all kinds of hole: the once optimized ratio $(H_0/L_0)_o$ decreases with the increase of the hole volume fraction ϕ. For the

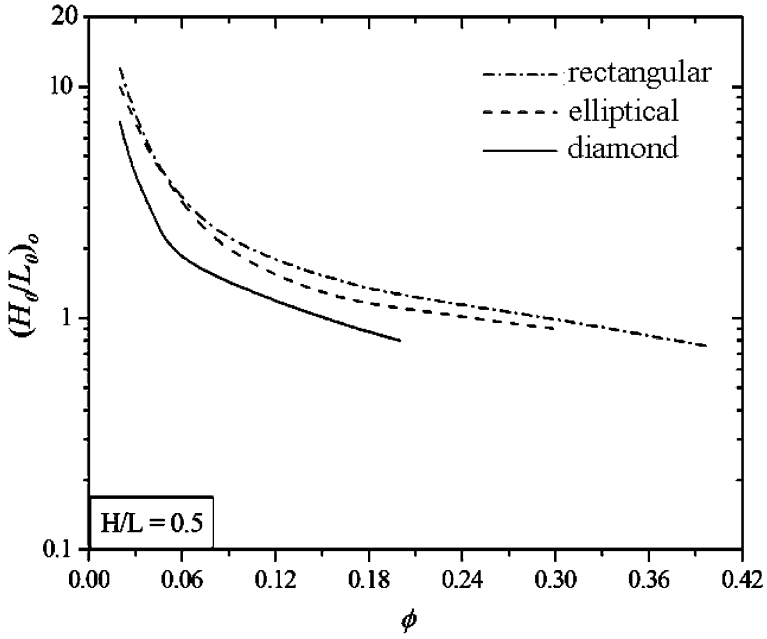

Fig. 12.12 The once optimized rate of $(H_0/L_0)_o$ as a function of the hole volume fraction ϕ for all hole shapes

same value of ϕ, the results indicate that the best performance is reached for the geometry with the lowest once optimized ratio of $(H_0/L_0)_o$.

Here it is important to note that the method used in the determination of the plate's buckling load assumes a linear elastic material behavior. Thus, the results here presented are rigorously valid only if the calculated critical buckling load does not cause normal stresses above the material's yielding stress, when it is applied to the plate. If the yielding stress limit is surpassed, a nonlinear finite element analysis should be performed, including geometrical and material nonlinearities.

12.8 Conclusions

Constructal Design has been successfully applied to the geometric optimization of engineering problems involving heat transfer and fluid flow. However, the Constructal method has not yet been consolidated for the geometric optimization of mechanic of materials problems. Few publications involving these problems and Constructal Theory are found, especially for a problem only concerning the mechanic of materials concepts. Therefore, in this chapter a study is presented that employs the Constructal design to define the optimal geometries of perforated thin plates subjected to a uniaxial load.

In this chapter we apply Constructal Theory to optimize the geometry of perforated thin plates subjected to uniform longitudinal mechanical load, causing tensile stresses or compressive stresses. The purpose was to obtain the optimal geometry which minimizes the maximal stress concentration or maximizes the critical buckling load of rectangular perforated plates with three different centered hole shapes: elliptical, rectangular, and diamond. One degree of freedom, the ratio between the height and length of the holes (H_0/L_0), was optimized to minimize the maximal stress concentration or to maximize the critical buckling load for several holes volume fractions (ϕ). Computational models based on the Finite Element Method (FEM) were used to solve these problems.

The results showed that Constructal Design can be employed not only for the geometric optimization of heat and fluid flow problems but also for the geometric optimization of the flow of stresses in pure mechanic of materials problems.

The best elliptical shape is 39.81 and 12.96% better than the best rectangular and diamond shapes, respectively for the tensile plate considering the minimal value of ϕ. The plates with rectangular holes became the best geometry to minimize the stress concentration for higher values of ϕ .

The results showed that, for $\phi \leq 0.20$ the optimum geometry is the diamond hole for the plate subjected to compression reaching a maximum buckling load around 80.0, 21.5, and 17.4% higher than a plate without perforation, plate with elliptical and rectangular holes, respectively. The elliptical and rectangular holes, respectively, led to the best performance for intermediate and higher values of ϕ.

Thus, for the continuity of this work it is suggested to evaluate the effect of the degree of freedom H/L on the problems discussed here. It is also proposed the geometric optimization of additional structural elements subject to other types of loads.

References

1. Bejan A, Lorente S. The constructal law (La loi constructale). Int J Heat Mass Tran. 2006;49:445–5.
2. Bejan A. Constructal-theory network of conducting paths for cooling a heat generating volume. Int J Heat Mass Tran. 1997;40:799–816.
3. Bejan A. Shape and structure, from engineering to nature. Cambridge: Cambridge University Press; 2000.
4. Bejan A, Lorente S. Design with constructal theory. Hoboken: Wiley; 2008.
5. Ghodoossi L. Conceptual study on constructal theory. Energy conversion and management. 2004;45:1379–95.
6. Bejan A, Lorente S. Constructal theory of generation of configuration in nature and engineering. J Appl Phys. 2006;100:041301.
7. Azad AV, Amidpour M. Economic optimization of shell and tube heat exchanger based on constructal theory. Energy. 2011;36:1087–96.
8. Beyene A, Peffley J. Constructal theory, adaptive motion, and their theoretical application to low-speed turbine design. J Energ Eng-ASCE. 2009;135:112–8.

9. Kang D-H, Lorente S, Bejan A. Constructal dendritic configuration for the radiation heating of a solid stream. J Appl Phys. 2010;107:114910.
10. Kim Y, Lorente S, Bejan A. Constructal multi-tube configuration for natural and forced convection in cross-flow. Int J Heat Mass Tran. 2010;53:5121–8.
11. Kim Y, Lorente S, Bejan A. Steam generator structure: continuous model and constructal design. Int J Energ Res. 2011;35:336–45.
12. Biserni C, Rocha LAO, Bejan A. Inverted fins: geometric optimization of the intrusion into a conducting wall. Int J Heat Mass Tran. 2004;47:2577–86.
13. Rocha LAO, Montanari GC, dos Santos ED, Rocha AS. Constructal design applied to the study of cavities into a solid conducting wall. Therm Eng. 2007;6:41–7.
14. Biserni C, Rocha LAO, Stanescu G, Lorenzini E. Constructal H-shaped cavities according to Bejan's theory. Int J Heat Mass Tran. 2007;50:2132–8.
15. Lorenzini G, Rocha LAO. Geometric optimization of T-Y-shaped cavity according to constructal design. Int J Heat Mass Tran. 2009;52:4683–8.
16. Bejan A, Almogbel M. Constructal T-shaped fins. Int J Heat Mass Tran. 2000;43:2101–15.
17. Lorenzini G, Rocha LAO. Constructal design of Y-shaped assembly of fins. J Heat Mass Tran. 2006;49:4552–7.
18. Xie ZH, Chen LG, Sun FR. Constructal optimization of twice Y-shaped assemblies of fins by taking maximum thermal resistance minimization as objective. Sci China Technol Sci. 2010;53:2756–64.
19. Lorenzini G, Rocha LAO. Constructal design of T-Y assembly of fins for an optimized heat removal. Int J Heat Mass Tran. 2009;52:1458–63.
20. Lorenzini G, Correa RL, dos Santos ED, Rocha LAO. Constructal design of complex assembly of fins. J Heat Tran-T ASME. 2011;133:1-1–7.
21. Bejan A, Lorente S. The constructal law and the thermodynamics of flow systems with configuration. Int J Heat Mass Tran. 2004;47:3203–14.
22. Bejan A. Advanced engineering thermodynamics. Hoboken: Wiley; 2006.
23. Reis AH. Constructal view of scaling laws of river basins. Geomorphology. 2006;78:201–6.
24. Cetkin E, Lorente S, Bejan A. Natural constructal emergence of vascular design with turbulent flow. J Appl Phys. 2010;107:114901-1–9.
25. Bello-Ochende T, Meyer JP, Ogunronbi OI. Constructal multiscale cylinders rotating in cross-flow. Int J Heat Mass Tran. 2011;54:2568–77.
26. Rocha LAO, Lorente S, Bejan A. Tree-shaped vascular wall designs for localized intense cooling. Int J Heat Mass Tran. 2009;52:4535–44.
27. Lorente S, Bejan A. Combined 'flow and strength' geometric optimization: internal structure in a vertical insulating wall with air cavities and prescribed strength. Int J Heat Mass Tran. 2002;45:3313–20.
28. Lorente S, Lee J, Bejan A. The "flow of stresses" concept: the analogy between mechanical strength and heat convection. Int J Heat Mass Tran. 2010;53:2963–8.
29. Cheng B, Zhao J. Strengthening of perforated plates under uniaxial compression: Buckling analysis. Thin Wall Struct. 2010;48:905–14.
30. Young WC, Budynas RG. Roark's formulas for stress and strain. New York: McGraw-Hill; 2002.
31. Beer FP, Johnston Jr ER, Dewolf JT, Mazurek D. Mechanics of materials. 5th ed. New York: McGraw-Hill; 2009.
32. She C, Guo W. Three-dimensional stress concentrations at elliptic holes in elastic isotropic plates subjected to tensile stress. Int J Fatigue. 2007;29:330–5.
33. Rezaeepazhand J, Jafari M. Stress analysis of perforated composite plates. Compos Struct. 2005;71:463–8.
34. Rencis JJ, Terdalkar S. Stress concentrations and static failure for common elements used in finite element stress analysis. Proceedings of the 2007 Midwest Section Conference of the American Society for Engineering Education; 2007. p. 1–17

35. Åkesson B. Plate buckling in bridges and other structures. New York: Taylor and Francis; 2007.
36. Silva VD. Mechanics and strength of materials. Berlin: Springer; 2006.
37. El-Sawy KM, Nazmy AS. Effect of aspect ratio on the elastic buckling of uniaxially loaded plates with eccentric holes. Thin Wall Struct. 2001;39:983–98.
38. El-Sawy KM, Martini MI. Elastic stability of bi-axially loaded rectangular plates with a single circular hole. Thin Wall Struct. 2007;45:122–33.
39. Moen CD, Schafer BW. Elastic buckling of thin plates with holes in compression or bending. Thin Wall Struct. 2009;47:1597–607.
40. El-Sawy KM, Nazmy AS, Martini MI. Elasto-plastic buckling of perforated plates under uniaxial compression. Thin Wall Struct. 2004;42:1083–101.
41. Paik JK. Ultimate strength of perforated steel plates under edge shear loading. Thin Wall Struct. 2007;45:301–6.
42. Paik JK. Ultimate strength of perforated steel plates under axial compressive loading along short edges. *Ships and Offshore Structures*,2007;2:355–60
43. Paik JK. Ultimate strength of perforated steel plates under combined biaxial compression and edge shear loads. Thin Wall Struct. 2008;46:207–13.
44. Maiorana E, Pellegrino C, Modena C. Linear buckling analysis of perforated plates subjected to localized symmetrical load. Eng Struct. 2008;30:3151–8.
45. Maiorana E, Pellegrino C, Modena C. Non-linear analysis of perforated steel plates subjected to localized symmetrical load. J Constr Steel Res. 2009;65:959–64.
46. Real M de V, Isoldi LA. Finite element buckling analysis of uniaxially loaded plates with holes. Proceedings of Southern Conference on Computational Modeling, Furg; 2010; Rio Grande
47. ANSYS, User's manual (version 10.0). Swanson analysis system Inc, Houston; 2005
48. Madenci E, Guven I. *The finite element method and applications in engineering using ANSYS®*. Ed., Springer; 2006
49. Przemieniecki JS. Theory of matrix structural analysis. Ed. Dover Publications; 1985
50. Wang CM, Wang CY, Reddy JN. Exact solutions for buckling of structural members. Florida: CRC; 2005.

Chapter 13
Equipartition of Joulean Heat in Thermoelectric Generators

Achintya Kumar Pramanick

13.1 Introduction

The crisis of totalitarian victory is, from the perspective of history, an intellectual crisis characterized by intellectual sloth, lack of imagination, and wishful thinking [1]. It is well known that no science develops systematically from one single starting point according to a definite preconceived plan, but its development depends upon practical considerations and proceeds more or less simultaneously along different lines, corresponding to the many ways of looking at the problems, and to the time and views of the investigator. Thus the science cannot attain its objective by direct means, but only gradually along numerous and devious paths, and therefore a wide scope is provided for the individuality of the worker [2, 3].

Admittedly, if we do not succeed in solving a mathematical or a physical problem, it is often because we have failed to recognize the more general standpoint from which the problem before us appears as a single link in a chain of related problems. This way to find generalized methods is certainly the most practical and the surest, for he who seeks the method without having a definite problem in mind seeks in vain [4]. For reasons, in this present endeavor, it is preferable to choose a topical problem which is of common interest both to the physicists and engineering community. This effort is inspired by the seminal call of Bejan [5] through a letter which appeared in the journal of American Physics Teachers' Association.

In the history of science and engineering thermoelectric phenomena is old and prevalent [6–10]. Thermoelectric device was considered to verify the second law of thermodynamics [11] and to model the heat engine [12–14]. It is generally postulated [12] or observed [15, 16] that exactly half of the Joulean heat produced

A.K. Pramanick (✉)
Department of Mechanical Engineering, National Institute of Technology Durgapur, West Bengal 713209, India
e-mail: acp@hrz.tu-chemnitz.de

L.A.O. Rocha et al. (eds.), *Constructal Law and the Unifying Principle of Design*, Understanding Complex Systems, DOI 10.1007/978-1-4614-5049-8_13,

in a thermoelectric device arrives equally both at the hot and cold junction. In the present study some of the conditions and consequences of this equipartitioned Joulean heat are reported.

Since it is pointed out in a treatise [17] that different assumptions can lead to different results, the role of assumptions in describing the model is also stressed. It has become fashionable [18–20] to publish volumes of empirical material such as figures, photographs, computer-generated images, and essays on the observation that both natural and engineered systems display geometric similarity. In contrast, the present report is a submission against such strategies that may eventually open up the vision of contemporary as well as next generation of researchers. This is at any rate in the opinion of the author, lack or even absence of figures accompanying the analysis or description actually stimulates abstract thinking process which is eventually the key to problem-solving aspect.

Lastly, there are at least two distinct ways by which a subject field can be developed. One is the *"horizontal"* expansion into the more remote fields intersected by the subject. Another is the *"vertical"* expansion, that is, a deepening of our present understanding (inception, conception, and perception) that defines the subject. The methodology adopted in the present study is the so-called *vertical* one [21]. There remains not only a merit in questioning the established point of view, but also there lies the fact that a true research frontier is, quite often, the territory overlooked by the crowd [22].

13.2 Conditions of Equipartitioned Joulean Heat

First we will seek the temperature distribution along the device leg, as it is one of chief importance for the evaluation of thermal efficiency of the device. Under steady-state condition for the divergence of the flux vector, total energy remains constant along any coordinate direction of a dimensional space. Specializing along x-direction for each leg we obtain [23]

$$TJ_x\left(\frac{\partial\alpha}{\partial x}\right)_{\mathrm{T}} + \tau J_x\frac{\mathrm{d}T}{\mathrm{d}x} - \rho {J_x}^2 - \frac{\mathrm{d}}{\mathrm{d}x}\left(\kappa\frac{\mathrm{d}T}{\mathrm{d}x}\right) = 0, \tag{13.1}$$

where J_x is the electrical current density vector along x-direction, T is the temperature distribution function, κ is the thermal conductivity of the conductor, ρ is the electrical resistivity of the conductor, α and τ are the Seebeck and the Thomson coefficients, respectively.

The solution of this equation for temperature distribution demands a specification of the dependence of α, κ, ρ, and τ on x or T. One viable approximation consists of replacing all transport coefficients by their averages [24]. In this spirit, the first term in (13.1) drops out and we arrive at the equation

$$\langle \kappa \rangle \frac{\mathrm{d}^2 T}{\mathrm{d}x^2} - \langle \tau \rangle J_x \frac{\mathrm{d}T}{\mathrm{d}x} + \langle \rho \rangle {J_x}^2 = 0, \tag{13.2}$$

where the symbol $\langle\rangle$ represents an averaged quantity.

Before attempting to solve the resulting simplified equation, it is to be noted that the approximation method is valid only if

$$T_{\mathrm{HC}} \approx T_{\mathrm{LC}}, \tag{13.3a}$$

but

$$T_{\mathrm{HC}} > T_{\mathrm{LC}}, \tag{13.3b}$$

such that the temperature difference across the thermoelectric element is $\Delta T = T_{\mathrm{HC}} - T_{\mathrm{LC}} > 0$. Here T_{HC} and T_{LC} are the temperatures of the thermoelectric module for the high and low temperature side, respectively. These mathematical restrictions are of little practical interest, since for operation of the device at higher efficiency, temperature difference should be as high as possible [25] on the whole of the thermoelectric device. On the contrary, for very high temperature, the phenomenological representation of irreversible process is inappropriate. Hence, the assumption of negligible temperature gap is at least consistent with the physical theory developed in literature [26]. In the real world of engineering design it represents a cascaded system, where power generation takes place discretely in successive stages in series with each other and the power is extracted at each stage. With the increase in number of modules, the temperature gap across any module is reduced and the discrete power generation mimics the continuous power production from a single module.

Now, we will nondimensionalize (13.2) using

$$\theta = \frac{T - T_{\mathrm{LC}}}{T_{\mathrm{HC}} - T_{\mathrm{LC}}} = \frac{T - T_{\mathrm{LC}}}{\Delta T} \tag{13.4a}$$

and

$$\xi = \frac{x}{L}. \tag{13.4b}$$

The resulting equation takes the form

$$\frac{\mathrm{d}^2 \theta}{\mathrm{d}\xi^2} - \Lambda \frac{\mathrm{d}\theta}{\mathrm{d}\xi} + \lambda = 0, \tag{13.5}$$

where

$$\Lambda = \frac{\langle \tau \rangle J_x L}{\langle \kappa \rangle} \tag{13.6a}$$

and

$$\lambda = \frac{\langle \rho \rangle (J_x L)^2}{\langle \kappa \rangle \Delta T}. \tag{13.6b}$$

The boundary conditions transform into

$$\theta = 1 \quad \text{at } \xi = 0 \tag{13.7a}$$

and

$$\theta = 0 \quad \text{at } \xi = 1. \tag{13.7b}$$

Solution of (13.5) subjected to boundary conditions (13.7a) and (13.7b) reads as

$$\theta^* = \frac{\lambda}{\Lambda}\xi + \left[\frac{1 + \frac{\lambda}{\Lambda}}{1 - \exp(\Lambda)}\right] \exp(\Lambda\xi) + \frac{\exp(\Lambda\xi) + \frac{\lambda}{\Lambda}}{\exp(\Lambda) - 1}. \tag{13.8}$$

Now, we would like to locate the regime of maximum temperature. This is an important observation when we mimic a thermoelectric device with that of heat engine [27]. In a finite-time [5] heat engine model there is a continuous variation of temperature from heat source to heat sink along the physical path of energy transport. When both the legs of the thermoelectric device are of the same length, the location of maximum temperature in either leg of the thermoelectric generator is obtained by setting $\frac{\mathrm{d}\theta^*}{\mathrm{d}\xi} = 0$, which yields

$$\xi^* = \frac{1}{\Lambda} \ln\left\{\frac{1}{1 + \frac{\Lambda}{\lambda}}\left[\frac{\exp(\Lambda) - 1}{\Lambda}\right]\right\}. \tag{13.9}$$

Now, we would like to prescribe some design conditions that will lead the temperature maximum to pass through the geometrical mid-point of the module of a cascaded thermoelectric device. Each individual module can be thought of an independent heat engine or an equivalent one-dimensional insulation system. For a narrow temperature gap across the module, the temperature maximum passes through the mid-point of the device and it experiences a minimum entropy generation or equivalently maximum power condition [28].

The design criterion $\frac{\Lambda}{\lambda} \to 0$ transforms (13.9) into the form

$$\xi^* = \frac{1}{\Lambda} \ln\left[\frac{\exp(\Lambda) - 1}{\Lambda}\right]. \tag{13.10a}$$

Expanding the left side of (13.10a) analytically around the singular point $\Lambda = 0$ and then passing to the limit, we have

$$\lim_{\Lambda\to 0}\xi^* = \lim_{\Lambda\to 0}\frac{1}{\Lambda}\ln\left\{\frac{1}{\Lambda}\left[\left(1+\Lambda+\frac{\Lambda^2}{2!}+\frac{\Lambda^3}{3!}+\cdots\right)-1\right]\right\} = \frac{1}{2}. \tag{13.10b}$$

Thus (13.10b) clearly demonstrates that for $\Lambda \to 0$, temperature maximum passes through the geometric mid-point of the conductor as the electrical current changes the direction. As long as (13.3a) and (13.3b) are valid the result obtained in (13.10b) is physically realistic. So, in order to construct a cascaded system the length of the first junction (construct) should be at half of the total permissible length of the assembly of the thermocouples. The geometric mid-point will act as a heat source for the next junction and so on.

Heat flow towards the hot end $\dot{Q}^*_{\mathrm{H}}$ is calculated by invoking Fourier conduction law as

$$\dot{Q}^*_{\mathrm{H}} = -\kappa A\left.\frac{\partial T}{\partial x}\right|_{x=0} = -\dot{Q}_{\mathrm{k}}\left.\frac{\partial\theta^*}{\partial\xi}\right|_{\xi=0} = \dot{Q}_{\mathrm{J}}\left[\frac{\Lambda-\exp(\Lambda)+1}{\Lambda\exp(\Lambda)-\Lambda}\right], \tag{13.11}$$

where the conducted heat through cross-sectional area A and of length L is

$$\dot{Q}_{\mathrm{k}} = \frac{\kappa A\Delta T}{L}, \tag{13.12}$$

and the Joulean heat source of cross-sectional area A and length L is

$$\dot{Q}_{\mathrm{J}} = \rho {J_x}^2 AL \tag{13.13}$$

such that as $\Lambda \to 0$

$$\lambda \approx \frac{\dot{Q}_{\mathrm{J}}}{\dot{Q}_{\mathrm{k}}}. \tag{13.14}$$

We calculate the ratio $\left|\frac{\dot{Q}^*_{\mathrm{H}}}{\dot{Q}_{\mathrm{J}}}\right|$ in the limit $\Lambda \to 0$ in order to examine that what proportion of Joulean heat moves to the hot end. On calculating the limit, using L' Hospital's theorem, we have

$$\lim_{\Lambda\to 0}\left|\frac{\dot{Q}^*_{\mathrm{H}}}{\dot{Q}_{\mathrm{J}}}\right| = \lim_{\Lambda\to 0}\left|\frac{\Lambda-\exp(\Lambda)+1}{\Lambda\exp(\Lambda)-\Lambda}\right| = \frac{1}{2}. \tag{13.15}$$

From (13.15) we observe that exactly half of the Joulean heat proceeds to the hot end. The first law of thermodynamics asserts that precisely fifty percent of the Joulean heat contributes to the cold junction.

13.3 Consequences of Equipartitioned Joulean Heat

In order to maintain a consistency with the standard notation of analysis prevailing in the literature we will define the relationship between electrical resistance and resistivity, thermal conductance and conductivity of the thermoelectric element introduced in the foregoing section. Electrical resistance R is related to its counterpart resistivity ρ through

$$R = \frac{\rho L}{A}. \tag{13.16a}$$

Thermal conductance K is dependent on conductivity κ as

$$K = \frac{\kappa A}{L}. \tag{13.16b}$$

First law of thermodynamics analysis neglecting Thomson effect enables us to write down the following heat transport equations in algebraic forms. Employing Newton's law of heat transfer [29] finite-time heat transfer rate to the hot junction $\dot{Q}_{\mathrm{H}}$ is given by

$$\dot{Q}_{\mathrm{H}} = K_{\mathrm{H}}(T_{\mathrm{H}} - T_{\mathrm{HC}}) = \alpha I T_{\mathrm{HC}} + K(T_{\mathrm{HC}} - T_{\mathrm{LC}}) - F_{\mathrm{H}} I^2 R, \tag{13.17}$$

where K and K_{H} are the thermal conductances across the compartment containing thermoelectric components and the hot junction, respectively. T_{H} is the temperature of the high temperature source and T_{HC} is that of thermoelectric element such that $T_{\mathrm{HC}} \leqslant T_{\mathrm{H}}$. Fraction of Joulean heat entering into the hot junction is F_{H}. Equation (13.17) can be rearranged as

$$(K + K_{\mathrm{H}} + \alpha I)T_{\mathrm{HC}} - K T_{\mathrm{LC}} - (K_{\mathrm{H}} T_{\mathrm{H}} + F_{\mathrm{H}} I^2 R) = 0. \tag{13.17a}$$

Similarly, finite-time heat transfer rate to the cold junction $\dot{Q}_{\mathrm{L}}$ with Newton's law of heat transfer [29] is obtained as

$$\dot{Q}_{\mathrm{L}} = K_{\mathrm{L}}(T_{\mathrm{LC}} - T_{\mathrm{L}}) = \alpha I T_{\mathrm{LC}} + K(T_{\mathrm{HC}} - T_{\mathrm{LC}}) + F_{\mathrm{L}} I^2 R, \tag{13.18}$$

where K_{L} is the thermal conductance across the cold junction. T_{L} is the temperature of the low temperature sink and T_{LC} is that of thermoelectric component such that $T_{\mathrm{LC}} \geqslant T_{\mathrm{L}}$. Fraction of Joulean heat entering into the cold junction is F_{L}.

Equation (13.18) can be rewritten as

$$K T_{\mathrm{HC}} - (K + K_{\mathrm{L}} - \alpha I)T_{\mathrm{LC}} + (K_{\mathrm{L}} T_{\mathrm{L}} + F_{\mathrm{L}} I^2 R) = 0. \tag{13.18a}$$

For the Joulean heat distribution it is obvious that

$$F_{\mathrm{H}} + F_{\mathrm{L}} = 1. \tag{13.19}$$

Now, the system of (13.17a), (13.18a), and (13.19) has four variables T_{HC}, T_{LC}, F_{L}, and F_{H} rendering single degree of freedom. Choosing F_{H} to be that degree of freedom we solve for T_{HC} and T_{LC} to obtain

$$T_{\mathrm{HC}} = \frac{K[(K_{\mathrm{H}}T_{\mathrm{H}} + K_{\mathrm{L}}T_{\mathrm{L}}) + I^2R] + (K_{\mathrm{L}} - \alpha I)(K_{\mathrm{H}}T_{\mathrm{H}} + F_{\mathrm{H}}I^2R)}{K(K_{\mathrm{H}} + K_{\mathrm{L}}) + (K_{\mathrm{H}} + \alpha I)(K_{\mathrm{L}} - \alpha I)} \tag{13.20a}$$

and

$$T_{\mathrm{LC}} = \frac{K[(K_{\mathrm{H}}T_{\mathrm{H}} + K_{\mathrm{L}}T_{\mathrm{L}}) + I^2R] + (K_{\mathrm{H}} + \alpha I)(K_{\mathrm{H}}T_{\mathrm{H}} + F_{\mathrm{H}}I^2R)}{K(K_{\mathrm{H}} + K_{\mathrm{L}}) + (K_{\mathrm{H}} + \alpha I)(K_{\mathrm{L}} - \alpha I)}. \tag{13.20b}$$

Presently, we proceed to seek possible set of solutions for the assumed unknown variable F_{H} or F_{L}. Eliminating T_{HC} between (13.17a) and (13.18a) and providing an expression for T_{LC} from (13.20b) we obtain

$$\begin{aligned}&[K(K_{\mathrm{H}}T_{\mathrm{H}} + K_{\mathrm{L}}T_{\mathrm{L}}) + K_{\mathrm{H}}K_{\mathrm{L}}T_{\mathrm{L}}] + \alpha K_{\mathrm{L}}T_{\mathrm{L}}I + R[K + F_{\mathrm{L}}K_{\mathrm{H}}]I^2 + \alpha F_{\mathrm{L}}RI^3 \\ &= [K(K_{\mathrm{H}}T_{\mathrm{H}} + K_{\mathrm{L}}T_{\mathrm{L}}) + K_{\mathrm{H}}K_{\mathrm{L}}T_{\mathrm{L}}] + \alpha K_{\mathrm{L}}T_{\mathrm{L}}I + R[F_{\mathrm{L}}(K + K_{\mathrm{H}}) + F_{\mathrm{H}}K]I^2 + \alpha F_{\mathrm{L}}RI^3.\end{aligned} \tag{13.21}$$

Comparing like powers of I, we have for the term I^2

$$K + F_{\mathrm{L}}K_{\mathrm{H}} = (K + K_{\mathrm{H}})F_{\mathrm{L}} + KF_{\mathrm{H}}. \tag{13.22}$$

Analogously, T_{LC} eliminant of (13.17a) and (13.18a) with the insertion of the expression for T_{HC} from (13.20a) we get

$$\begin{aligned}&[K(K_{\mathrm{H}}T_{\mathrm{H}} + K_{\mathrm{L}}T_{\mathrm{L}}) + K_{\mathrm{L}}K_{\mathrm{H}}T_{\mathrm{H}}] - \alpha K_{\mathrm{H}}T_{\mathrm{H}}I + R[K + F_{\mathrm{H}}K_{\mathrm{L}}]I^2 - \alpha F_{\mathrm{H}}RI^3 \\ &= [(K + K_{\mathrm{L}})K_{\mathrm{H}}T_{\mathrm{H}} + KK_{\mathrm{L}}T_{\mathrm{L}}] - \alpha K_{\mathrm{H}}T_{\mathrm{H}}I + R[F_{\mathrm{H}}(K + K_{\mathrm{L}}) + F_{\mathrm{L}}K]I^2 - \alpha F_{\mathrm{H}}RI^3.\end{aligned} \tag{13.23}$$

Equating similar powers of I on both sides, we have for I^2

$$K + F_{\mathrm{H}}K_{\mathrm{L}} = (K + K_{\mathrm{L}})F_{\mathrm{H}} + KF_{\mathrm{L}}. \tag{13.24}$$

Any particular solution of two identities (13.22) and (13.24) must have general functional form involving K, K_{H}, and K_{L}, that is

$$F_{\mathrm{H}} = F_{\mathrm{H}}(K, K_{\mathrm{H}}, K_{\mathrm{L}}) \tag{13.25a}$$

and

$$F_{\mathrm{L}} = F_{\mathrm{L}}(K, K_{\mathrm{H}}, K_{\mathrm{L}}). \tag{13.25b}$$

On following symmetry we assume a trial solution of the form

$$F_{\mathrm{H}} = \frac{1}{2}\left(\frac{K_{\mathrm{H}}K_{\mathrm{L}} + KK_{\mathrm{H}} + KK_{\mathrm{H}}}{K_{\mathrm{H}}K_{\mathrm{L}} + KK_{\mathrm{H}} + KK_{\mathrm{L}}}\right) = \frac{1}{2}\left(\frac{K_{\mathrm{H}}K_{\mathrm{L}} + 2KK_{\mathrm{H}}}{K_{\mathrm{H}}K_{\mathrm{L}} + KK_{\mathrm{H}} + KK_{\mathrm{L}}}\right). \tag{13.26a}$$

Employing (13.26a) in (13.19) we obtain

$$F_{\mathrm{L}} = \frac{1}{2}\left(\frac{K_{\mathrm{H}}K_{\mathrm{L}} + KK_{\mathrm{L}} + KK_{\mathrm{L}}}{K_{\mathrm{H}}K_{\mathrm{L}} + KK_{\mathrm{H}} + KK_{\mathrm{L}}}\right) = \frac{1}{2}\left(\frac{K_{\mathrm{H}}K_{\mathrm{L}} + 2KK_{\mathrm{L}}}{K_{\mathrm{H}}K_{\mathrm{L}} + KK_{\mathrm{H}} + KK_{\mathrm{L}}}\right). \tag{13.26b}$$

Substituting (13.26a) and (13.26b) into the identity (13.22) we have for both sides a common expression:

$$C_1 = \frac{4KK_{\mathrm{H}}K_{\mathrm{L}} + 2K^2(K_{\mathrm{H}} + K_{\mathrm{L}}) + K_{\mathrm{H}}^2K_{\mathrm{L}}}{2(K_{\mathrm{H}}K_{\mathrm{L}} + KK_{\mathrm{H}} + KK_{\mathrm{L}})}. \tag{13.27a}$$

Similarly, inserting (13.26a) and (13.26b) into the other identity, (13.24), we obtain another common expression:

$$C_2 = \frac{4KK_{\mathrm{H}}K_{\mathrm{L}} + 2K^2(K_{\mathrm{H}} + K_{\mathrm{L}}) + K_{\mathrm{H}}K_{\mathrm{L}}^2}{2(K_{\mathrm{H}}K_{\mathrm{L}} + KK_{\mathrm{H}} + KK_{\mathrm{L}})}. \tag{13.27b}$$

Equations (13.27a) and (13.27b) confirm that (13.26a) and (13.26b) are a set of possible solutions for the identities (13.22) and (13.24). Further by simple inspection we observe that (13.22) and (13.24) admit the following numerical values:

$$F_{\mathrm{H}} = 0 \quad \text{and} \quad F_{\mathrm{L}} = 1; \tag{13.28a}$$

$$F_{\mathrm{H}} = 1 \quad \text{and} \quad F_{\mathrm{L}} = 0; \tag{13.28b}$$

$$F_{\mathrm{H}} = \frac{1}{2} \quad \text{and} \quad F_{\mathrm{L}} = \frac{1}{2}. \tag{13.28c}$$

Lastly, we will examine for what combinations of K, K_{H}, and K_{L} these numeric values are returned for the functional relations (13.22) or (13.24). Equations (13.26a) and (13.26b) along with (13.28a) say that

$$K_{\mathrm{H}}K_{\mathrm{L}} = -2KK_{\mathrm{H}}. \tag{13.29a}$$

For (13.28b) to be tantamount with (13.26a) and (13.26b) one requires that

$$K_H K_L = -2KK_L. \tag{13.29b}$$

Equivalency of (13.26a) and (13.26b) with (13.28c) demands that

$$K_{\mathrm{H}} = K_{\mathrm{L}}. \tag{13.29c}$$

13.4 Results and Discussions

In order to discover the physical meaning underlying with the design criteria presented in second section we undertake the following analysis. The design prescription $\frac{\Delta}{\lambda} \to 0$ leading to (13.10a) is better realized when the limit is treated as an inequality. The fact that in the limiting case the denominator has to be quite higher than the numerator leads to the result

$$L \gg \frac{\langle \tau \rangle}{\langle \rho \rangle} \frac{\Delta T}{J_x}, \tag{13.30a}$$

with reference to the definitions (13.6a) and (13.6b). Similarly, the design criterion $\Lambda \to 0$ rendering (13.10b) reads as

$$L \ll \frac{\langle \kappa \rangle}{\langle \tau \rangle} \frac{1}{J_x}. \tag{13.30b}$$

Thus combining (13.30a) and (13.30b) we see that the largest and smallest scale of permissible length of a thermoelectric module is bounded by the inequality

$$\frac{\langle \tau \rangle}{\langle \rho \rangle} \frac{\Delta T}{J_x} \ll L \ll \frac{\langle \kappa \rangle}{\langle \tau \rangle} \frac{1}{J_x}. \tag{13.30c}$$

Further, we inspect the design criteria $\frac{\Delta}{\lambda} \to 0$ and $\Lambda \to 0$ simultaneously that have returned (13.10a) and (13.10b), respectively. Invoking definitions (13.6a) and (13.6b) it is substantiated that $\tau \to 0$, $\kappa \to 0$, and $\rho \to 0$. Literal meanings of such stipulations are negligible Thomson effect, low thermal conductivity, and poor electrical resistivity of the thermoelectric material, respectively. It requires special mention that such prescriptions are physically ideal and material development should proceed in this direction [30].

13.5 Conclusions

It is interesting to report that in a cascaded thermoelectric device placing the second module along the longitudinal center of the first module and proceeding from the maximum considered length to the minimum considered length we actually

generated a fractal-like pattern in space which is deterministic and the first construct is a T-shaped region in space. Thus it is worthy to mention that better design appeals to be more natural. Such deduced design procedure is recognized through constructal theory in pertinent literature [31, 32].

Now, we look back to the third section. Since K, K_H, and K_L are all nonnegative quantities [28] only (13.28c) and (13.29c) are physically realistic. Thus the sufficient condition for the equipartition of Joulean heat produced is the equipartition of conductance allocation between high and low temperature heat sources. Furthermore, when one of the three conductances run to a very high value leaving other two in a moderate range, Joulean heat distribution again becomes unequal. In pertinent literature [12] thermoelectric generator is treated as a natural heat engine. It is interesting to report that the question of optimal allocation of heat exchange equipment [33–35] is a mere consequence of equipartition of Joulean heat in a thermoelectric generator.

The physical (constructal) solution presented in this work actually pertains to Steiner-like [36, 37] problems in mathematics that has defeated the fastest computers [38]. The elegant variational solution [39] of such branching network is practically very complex even in one dimension [40]. Thus it echoes Bejan [41] that it is too early to give up pencil on paper.

It frequently happens that in a scientific enquiry we merely investigate either the conditions or the consequences of a phenomenon. It has been demonstrated that simultaneous study of conditions and consequences of an event is more revealing and rewarding. Further, from the chronology of the cited references it disseminates that natural scientists and engineers should work together towards a sustainable development of the field that Bejan preached since about two decades back [5].

In sum, the present chapter is devoted to the study of a thermoelectric generator from the perspective of a heat engine. Two important dimensionless parameters are identified to designate negligible Thomson effect, low thermal conductivity, and poor electrical resistivity of a good semiconductor or semimetal. For ideal values of these parameters it has been demonstrated that the temperature maximum passes through the longitudinal center of a one-dimensional thermoelectric element while exactly half of the Joulean heat arrives at both hot and cold junction. When half the Joulean heat affects hot end and half the cold side, thermal conductance inventory (heat exchanger) is allocated equally between the high and low temperature side. The final architecture of a cascaded assembly of thermoelectric module exhibits a fractal-like but deterministic (constructal) pattern that develops from the largest to the smallest scale with the fundamental construct being a T-shaped region in space. The physicists' knowledge of equipartitioned Joulean heat and the engineers' wisdom of equipartitioned heat exchanger allocation are unified with reference to a thermoelectric generator. The chief objective of this contribution is to draw the attention of the colleagues of cross disciplines that Bejan advocated for a possible cross-fertilization of the field.

References

1. Bridgman PW. A challenge to physicists. J Appl Phys. 1942;13:209.
2. Planck M. A survey of physical theory. Jones R, Williams DH, Trans. Dover: New York, 1993. p. 82
3. Truesdell C. The tragicomedy of classical thermodynamics. International Centre for Mechanical Sciences, Udine, Courses and Lectures, No. 70, Springer, New York, 1983
4. Hilbert D. Mathematical problems. Archive for Mathematical Physics. 1901;3:1, 44–63, 213–37
5. Bejan A. Engineering advances on finite-time thermodynamics. Am J Phys. 1994;62:11–2.
6. Thomson W. Thermoelectric currents. In: Mathematical and physical papers-I. London: Cambridge University Press. 1882. p. 232–91
7. Bridgman PW. Thermoelectric phenomena in crystals and general electrical concepts. Phys Rev. 1928;31:221–35.
8. Ioffe AF. The revival of thermoelectricity. Sci Am. 1958;199:31–7.
9. Robert R Heikes, Roland W. Ure Jr. Editors, Mullin AA (Rev.). Thermoelectricity: science and engineering. Am J Phys. 1962;30:78
10. Pramanick AK, Das PK. Constructal design of a thermoelectric device. Int J Heat Mass Tran. 2006;49:1420–9.
11. Gupta VK, Gauri Shander, Sarat B, Sharma NK. Experiment to verify the second law of thermodynamics using a thermoelectric device. Am J Phys. 1984;52:625–8.
12. Gordon JM. Generalized power versus efficiency characteristics of heat engines: the thermoelectric generator as an instructive illustration. Am J Phys. 1991;59:551–5.
13. Yan Z, Chen J. Comment on "Generalized power versus efficiency characteristics of heat engine: the thermoelectric generator as an instructive illustration. Am J Phys. 1993;61:380.
14. Gordon JM. A response to Yan and Chen's "Comment on 'Generalized power versus efficiency characteristics of heat engine: the thermoelectric generator as an instructive illustration',". Am J Phys. 1993;61:381.
15. Noon JH, O'Brien BJ. Sophomore experiment in thermoelectricity. Am J Phys. 1958;26:373–5.
16. Luke WH. Reply to experiment in thermoelectricity. Am J Phys. 1960;28:563.
17. De Vos A, Desoete B. Equipartition principle in finite-time thermodynamics. J Non-Equil Thermody. 2000;25:1–13.
18. Bejan A. Advanced engineering thermodynamics. New York: Wiley; 1997. p. X.
19. J. le R. d' Alembert. Nouvelles experiences sur la resistance des fluides. Paris: Jambert; 1777
20. Truesdell C. Six lectures on modern natural philosophy. Berlin: Springer; 1966. p. 100–1.
21. Bejan A. Advanced engineering thermodynamics. New York: Wiley; 1997. p. XV.
22. Feyerabend P. Against method. London: Verso; 1978.
23. Harman TC, Honig JM. Thermoelectric and thermomagnetic effects and applications. New York: McGraw Hill; 1967. p. 276.
24. Sherman B, Heikes RR, Ure Jr RW. Calculation of efficiency of thermoelectric device. J Appl Phys. 1960;31:1–16.
25. Gross ETB. Efficiency of thermoelectric devices. Am J Phys. 1961;29:729–31.
26. Hatsopoulos GN, Keenan JH. Analysis of the thermoelectric effects by methods of irreversible thermodynamics. Trans ASME. 1958;80:428.
27. Bejan A. Entropy generation minimization: the new thermodynamics of finite-size devices and finite-time processes. J Appl Phys. 1996;79:1191–218.
28. Bejan A. Models of power plants that generate minimum entropy while operating at maximum power. Am J Phys. 1996;64:1054–9.
29. De Vos A. Efficiency of some heat engines at maximum power conditions. Am J Phys. 1985;53:570–3.
30. Min G, Rowe DM. Thermoelectric figure-of-merit barrier at minimum lattice thermal conductivity. Appl Phys Lett. 2000;77:860–2.

31. Bejan A. Shape and structure, from engineering to nature. UK: Cambridge University Press; 2000.
32. Pramanick AK. Natural philosophy of thermodynamic optimization. Doctoral thesis; Indian Institute of Technology, Kharagpur, India, 2007.
33. Bejan A. Theory of heat transfer-irreversible power plants–II. The optimal allocation of heat exchange equipment. Int J Heat Mass Tran. 1995;38:433–44.
34. Bejan A. Power and refrigeration plants for minimum heat exchanger inventory. J Energ Resour Tech. 1993;115:148–50.
35. Pramanick AK, Das PK. Assessment of Bejan's heat exchanger allocation model under the influence of generalized thermal resistance, relaxation effect, bypass heat leak and internal irreversibility. Int J Heat Mass Tran. 2008;51:474–84.
36. Gray A. Tubes. Basel: Birkhäuser; 2004.
37. Hwang FK, Richards DS, Winter P. The steiner tree problem. Amsterdam: Elsevier; 1992.
38. Bern MW, Graham RL. The shortest network problem. Sci Am. 1989;260:84–9.
39. Rubinstein JH, Thomas DA. A variational approach to the steiner network problem. Ann Oper Res. 1991;33:481–99.
40. Ivanov AO, Tuzhilin AA. Branching solution to one-dimensional variational problems. Singapore: World Scientific; 2001.
41. Bejan A. Advanced engineering thermodynamics. New York: Wiley; 1997. p. 811.

Chapter 14
Constructal Design of Refrigeration Devices

H. Zhang, X. Liu, R. Xiong, and S. Zhu

14.1 Refrigeration, Flow and Design

The objective of refrigeration is to achieve and maintain a temperature below that of the surroundings. The refrigeration industry is expanding worldwide to fulfill the increasing needs to ensure living conditioning of humans. For example, in China, about ten million domestic refrigerators and freezers were manufactured in 2009 [1]. The adverse aspect is that refrigeration devices consume a large amount of energy in the world, which invokes more efficient and economical design. The design of refrigeration devices involves many aspects, in which fluid flow is a key mechanism. Due to the complexity of flow process in refrigeration applications, to a large extent, trial-and-error method has been the mainstream technique for a long time. Since Bejan proposed the constructal law in 1996 [2], principle-based flow system optimization technique has been practiced by many engineers in diverse fields [3, 4]. Like in other flow engineering fields, constructal theory is playing a more and more important role in improving the design of refrigeration devices [3–12]. In this chapter, we present our recent advances in constructal optimization in refrigeration devices through two case studies, i.e., domestic freezers and heat pump water heaters.

14.2 Temperature Nonuniformity in Domestic Freezers

One important requirement for decreasing energy consumption and improving food quality in compartments of refrigerators or freezers is to keep the temperature nonuniformity under specified level. For forced-flow cooling devices, this

H. Zhang (✉) • X. Liu • R. Xiong • S. Zhu
School of Energy and Power Engineering, Nanjing University of Science and Technology, Nanjing, Jiangsu 210094, China
e-mail: houlei_zhang@yahoo.com.cn; nj167@sina.com.cn; njxrhui@gmail.com; zhushuguang@tsinghua.org.cn

L.A.O. Rocha et al. (eds.), *Constructal Law and the Unifying Principle of Design*, Understanding Complex Systems, DOI 10.1007/978-1-4614-5049-8_14,

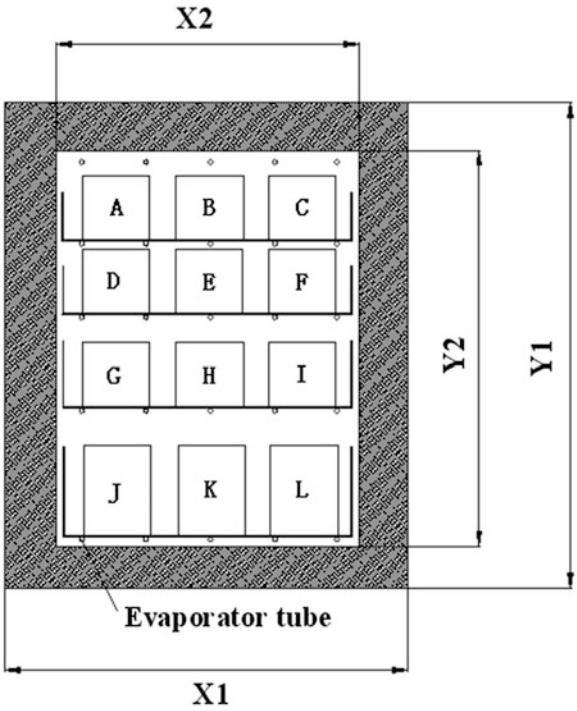

Fig. 14.1 Two-dimensional freezer model, X1 = 550, X2 = 390, Y1 = 795, Y2 = 655. Drawers: width × height × wall thickness = 376 × 73 × 2.6 for Drawers I and II, 376 × 128 × 2.6 for Drawer III and 376 × 173 × 2.3 for Drawer IV. Loads: width × height = 100 × 100 for Loads A, B, C, D, E, F, 100 × 125 for Loads G, H, I, and 100 × 175 for Loads J, K, L. Unit: mm

requirement is of no significance. But for direct cooling devices (i.e., fanless) where natural convection induced by internal cold surfaces (i.e., evaporator surfaces) dominates the cooling performance, the temperature nonuniformity becomes an important problem. Greater temperature nonuniformity means greater internal thermal/flow resistance (or irreversibility) in the compartments. By changing the internal configuration, the irreversibility may be redistributed to get better flow access. So for specified design constraints, in order to obtain minimum temperature nonuniformity, the generation of flow configuration becomes the key that has been indicated by the constructal law [2]: For a finite size flow system to persist in time (to survive) it must evolve in such a way that it provides easier and easier access to the currents that flow through it. Therefore the goal is to replace the existing drawings of the compartments by easier-flowing drawings.

A two-compartment device with one top refrigerator compartment and one bottom freezer compartment is selected for discussion. In this chapter only the temperature nonuniformity in the freezer compartment is investigated. We start with the simple case of a two-dimensional freezer compartment (Fig. 14.1) in which

there are five layer evaporator tubes with a uniform tube diameter d, four drawers (i.e., I, II, III, and IV from top to bottom in Fig. 14.1) with three dimensions (Fig. 14.1), and 12 loads (i.e., A, B, ... , L in Fig. 14.1) with three dimensions (Fig. 14.1). The shadow area in Fig. 14.1 represents the insulation walls of the freezer. We set the geometry in Fig. 14.1 as the reference structure and the temperatures at the center positions of A, B, ... , L (T_i, i = A, B, ... , L) as the characteristic temperatures that are used for evaluating the temperature nonuniformity in the freezer compartment. For a specified d, the total number of evaporator tubes N_t is an equivalent of the evaporator area A or the consumed evaporator materials or cost. Assume that the length of the evaporator tubes is 1

$$A = N_t \pi d. \tag{14.1}$$

Besides the evaporator area A in (14.1), another critical design constraint is the evaporating temperature T_e, which is relevant to the coefficient of performance (COP) of the refrigeration system,

$$\mathrm{COP} = f(T_e). \tag{14.2}$$

For simplicity, we neglect the heat conduction resistance in the evaporator tube walls, therefore the surface temperature of the evaporator tubes equals T_e. Small A and high T_e are always welcomed by designers. In some cases due to the nonuniform temperature distribution in the freezer compartment some characteristic temperatures may exceed the specified value even A and T_e are appropriate. To solve the problem, in this chapter we try to change the internal constraints to minimize the temperature nonuniformity in the freezer compartment under specified constraints (A and T_e) and analyze the effects of the modified designs on the cooling capacity.

For the compartment in Fig. 14.1, cold flow is transferred from the evaporator surfaces to external surroundings. The temperature field in the compartment is simulated numerically using a model for two-dimensional conjugated heat transfer. The equations governing the natural convection in the freezer compartment are written with the following assumptions: The flow is steady and turbulent, there is no variation in the fluid properties except density, and thermal radiation is negligible. The turbulent flow assumption will be checked later. Here we select standard k–ε model to simulate the turbulent flow and heat transfer process. The time averaged continuity, momentum, and energy equations along with standard k–ε model equations for fluid flow can be found in fluid dynamics literatures [13–17]. In our simulations, the constants used in the k–ε model equations are determined according to ref. [15]. The equation for heat conduction in the solid (e.g., loads, drawers, and insulation walls) is

$$\frac{\partial^2 T_s}{\partial x^2} + \frac{\partial^2 T_s}{\partial y^2} = 0, \tag{14.3}$$

where T_s is solid temperature, x and y are coordinates in the width and height directions respectively. The boundary conditions for the problem (velocity u, v in x and y directions, temperature T, and heat flux q) are specified as follows:

$$u = 0, \quad v = 0, T = T_e, \quad \text{evaporator surfaces} \tag{14.4a}$$

$$q = h_0(T_r - T_{wo}), \quad \text{top exterior wall} \tag{14.4b}$$

$$q = h_0(T_0 - T_{wo}), \quad \text{left, right, and bottom exterior wall,} \tag{14.4c}$$

where T_r, $T_{0,}$ and T_{wo} are the refrigerator compartment temperature (=2°C), the ambient temperature (=25°C) and the exterior surface temperature respectively. The external convective coefficient h_0 is assumed constant [=10 W/(m^{2}K)]. For checking the flow regime assumption, we calculate the Rayleigh number Ra after each simulation

$$Ra = \frac{g\beta\Delta TL^3}{\alpha\upsilon}, \tag{14.5}$$

where ΔT is the temperature difference between the interior surfaces of insulation walls and evaporator tube surfaces, L is the characteristic size (=X2), g is gravitational acceleration, α, β, and υ are thermal diffusivity, isobaric cubical expansion coefficient, and kinematic viscosity of fluid respectively.

The temperature nonuniformity ΔT_m is quantitatively defined as the maximum temperature difference among the 12 characteristic temperatures at the center positions of A, B, ... , and L, where T_{max} and T_{min} represent the maximum and minimum values respectively,

$$\Delta T_m = T_{max} - T_{min}. \tag{14.6a}$$

Assume that the evaporating temperature for reference $T_{e,ref}$ is constant (−28°C) and define the dimensionless temperature nonuniformity ω as

$$\omega = \frac{T_{max} - T_{min}}{T_0 - T_{e,ref}}. \tag{14.6b}$$

The cooling capacity Q_e is obtained via integrating heat flux q based on the simulating results:

$$Q_e = \int_{top} q\mathrm{d}A + \int_{bottom} q\mathrm{d}A + \int_{left} q\mathrm{d}A + \int_{right} q\mathrm{d}A, \tag{14.7}$$

where top, bottom, left, and right correspond to the top, bottom, left, and right exterior surfaces of the freezer compartment respectively.

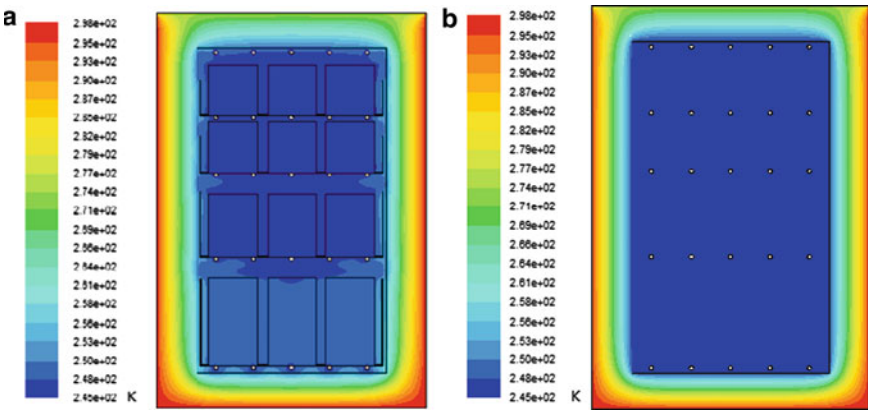

Fig. 14.2 Temperature fields of the two-dimensional freezer compartment, mode (5, 5, 5, 5, 5), $d_{II}/d_I = 1$, $\lambda_{in} = 0.018$ W/(mK), $T_e = -28°C$ [18]: (**a**) With loads, $\lambda_{drawer} = 0.17$ W/(mK), $\lambda_{load} = 1$ W/(mK); (**b**) Without loads

Some properties (density ρ, isobaric specific heat c_P, and thermal conductivity λ) used in the numerical simulations are listed below: $\rho_{drawer} = 1{,}050$ kg/m^3, $c_{P,drawer} = 1{,}800$ J/(kg K) for drawers, $\rho_{in} = 35$ kg/m^3, $c_{P,in} = 1{,}045$ J/(kgK) for insulation walls, $\rho_{load} = 1{,}000$ kg/m^3, $c_{P,load} = 1{,}000$ J/(kg K) for loads, and $c_{P,air} = 1{,}006$ J/(kg K), $\lambda_{air} = 0.0242$ W/(m^{2}K) for air. To generate the temperature field and calculate the temperature nonuniformity we use a finite-volume computational package [16] with pressure-based solver, cell-based gradient evaluation, SIMPLE algorithm for pressure–velocity coupling, and second order upwind scheme for momentum and energy equations. The simulating results show that $Ra \sim 10^9$, which corresponds to transitional flow regime. According to Ma [17], it is acceptable in engineering sense to adopt k–ε turbulent model to simulate natural convection process in freezer compartments for the magnitude of scale $Ra \sim 10^9$.

We start from checking the difference between loaded and unloaded freezer compartments. Figure 14.2 shows the temperature fields of the compartment with drawers and loads (i.e., loaded compartment) and that without drawers and loads (i.e., unloaded compartment). The temperature field in the loaded compartment (Fig. 14.2a) is more nonuniform ($\omega \approx 0.0555$ or $\Delta T_m \approx 2.94$ K) than that in the unloaded compartment (Fig. 14.2b, $\omega \approx 0.001$ or $\Delta T_m \approx 0.054$ K). From the viewpoint of engineering, the temperature nonuniformity in Fig. 14.2b is completely negligible. In fact, for an empty freezer compartment without internal drawers and loads, the fluid can flow freely with very little internal resistance. When the freezer compartment is loaded as shown in Fig. 14.2a, the fluid flow and heat-flow paths in the compartment are greatly blocked by the drawers and loads. Seen in Fig. 14.2a, the high-temperature region appears in the space between the fourth-layer and fifth-layer evaporator tubes (or in Drawer IV), where the load size is larger than that in other drawers (Drawers I, II, and III). We can also see that due to the existence of Drawer IV the space near the fifth-layer evaporator tubes

becomes narrow and that weakens the natural convection heat transfer to its neighbors, e.g., Loads J, K, and L. For the tubes in the same layer, due to the heat dissipation to the surroundings through insulation walls, the center temperature is lower than that near the insulation walls, e.g., $T_K < T_J = T_L$. This indicates that the temperature distribution is nonuniform in both two directions, x and y.

For simplicity, we keep the distance equal between two neighbor evaporator tubes in the same layer. In Fig. 14.2, we adopt the assumption temporarily that the number of the evaporator tubes of each layer N_i is the same, i.e., $N_i = N_t/5$ (i = 1–5), which we call reference mode (5, 5, 5, 5, 5), i.e., five tubes per layer. According to constructal theory, we can vary the internal constraints (e.g., geometry and materials) of a system to evolve our design toward achieving greater flow access, e. g., in this chapter, more uniform temperature distribution in the freezer compartment.

In Figs. 14.3 and 14.4 we show the first way to change the internal constraints through optimizing the distribution of the evaporator area. Figure 14.3 shows the effects of nonuniform distribution of the evaporator area with fixed evaporator tube diameter d on the dimensionless temperature nonuniformity ω, the cooling capacity Q_e, and the characteristic temperatures T_i. The results show that under the specified design constraints, nonuniform evaporator area distribution may provide greater or less temperature nonuniformity than uniform distribution. If we evolve from reference mode (5, 5, 5, 5, 5) toward the right direction (Fig. 14.3a), we can obtain the decreasing ω but nearly constant Q_e. For example, the temperature nonuniformity ω of mode (4, 3, 4, 7, 7), i.e., from top to bottom, 4, 3, 4, 7, and 7 evaporator tubes, is decreased 22.3% from reference mode (5, 5, 5, 5, 5), while the cooling capacity Q_e increases only 0.3%. This means that in the specified range of Fig. 14.3a, the thermal resistance of insulation walls is dominant along the heat transfer path from the evaporator tubes to the surroundings. We can also find that increasing both the fourth-layer and fifth-layer evaporator areas [e.g., mode (4, 4, 4, 7, 6)] is better than just increasing one of them [e.g., mode (4, 4, 4, 8, 5)] because in the former case the heat transfer to Loads J, K, and L is enhanced through both the top natural convective path and the bottom conduction path. Nevertheless, note that nonuniform mode (5, 4, 4, 5, 7) receives greater temperature nonuniformity than reference mode (5, 5, 5, 5, 5) that is a reminder that two opposite directions exist, one towards better and one towards worse. Figure 14.3b documents the 12 characteristic temperatures: T_A, T_B, . . . , and T_L. For all the modes in Fig. 14.3b, in the same y position the center temperatures are lower than that of their neighbors near the insulation walls which is in agreement with the image in Fig. 14.2a. But lower ω is not equivalent to lower characteristic temperatures at all locations. Simple monotonic relationship does not exist. The important feature we should care is the highest characteristic temperature T_{max}. In design practices, T_{max} less than specified temperature ($T_{specified}$) is a mandatory criterion required by test standards [19]. Therefore we have to keep both ω and T_i (i = A, B,. . ., L) under control. To summarize, we need to move a part of the evaporator area from lower-temperature region to high-temperature region in order to make the cooling ability match the corresponding cooling task.

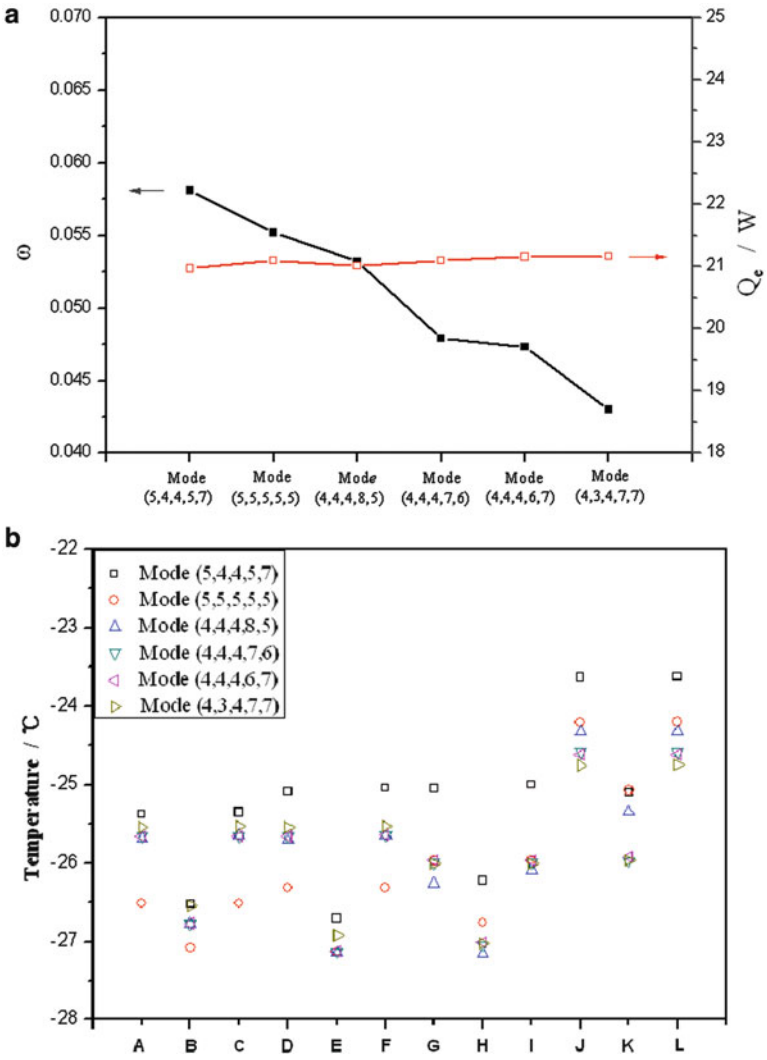

Fig. 14.3 Constructal optimization of temperature nonuniformity via nonuniform evaporator area distribution, $d_{II}/d_I = 1$, $\lambda_{drawer} = 0.17$ W/(mK), $\lambda_{in} = 0.018$ W/(mK), $\lambda_{load} = 1$ W/(mK), $T_e = -28°C$ [18]: (**a**) Temperature nonuniformity and cooling capacity; (**b**) Characteristic temperatures

Multiscale design inspired by constructal theory offers an alternative to optimizing the distribution of evaporator area. Assume that the diameter of the ith-layer evaporator tubes is d_i, for a specified evaporator area A

$$A = N_t \pi d = \sum_{i=1}^{5} (N_i \pi d_i). \tag{14.8}$$

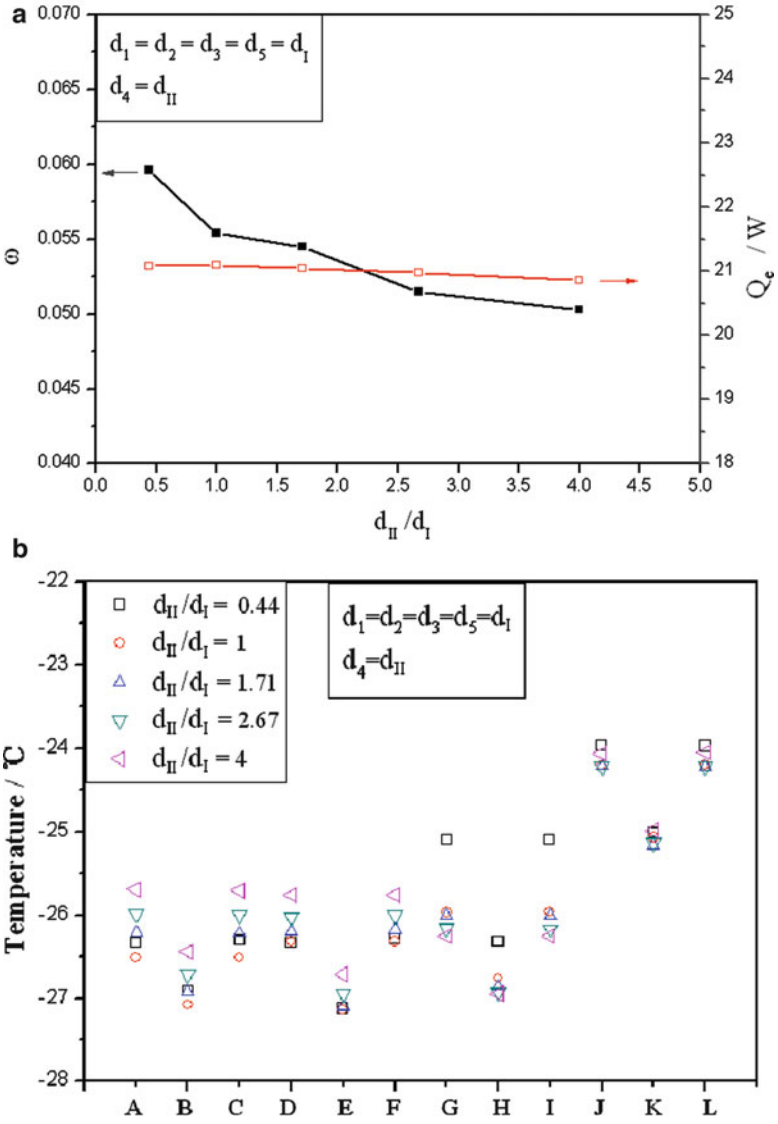

Fig. 14.4 Constructal optimization of temperature nonuniformity via two-size design, mode (5, 5, 5, 5, 5), $\lambda_{drawer} = 0.17$ W/(mK), $\lambda_{in} = 0.018$ W/(mK), $\lambda_{load} = 1$ W/(mK), $T_e = -28$ °C [18]: (**a**) Temperature nonuniformity and cooling capacity; (**b**) Characteristic temperatures; (**c**) Temperature nonuniformity and cooling capacity; (**d**) Characteristic temperatures

Figure 14.4 shows the simulating results of two-size (evaporator tube diameter: d_I, d_{II}) design compared with one-size (evaporator tube diameter: d) design. Two configurations are considered. For $d_1 = d_2 = d_3 = d_5 = d_I$ and $d_4 = d_{II}$ (Figs. 14.4a and 14.4b), ω decreases with the increasing in d_{II}/d_I while Q_e keeps nearly constant.

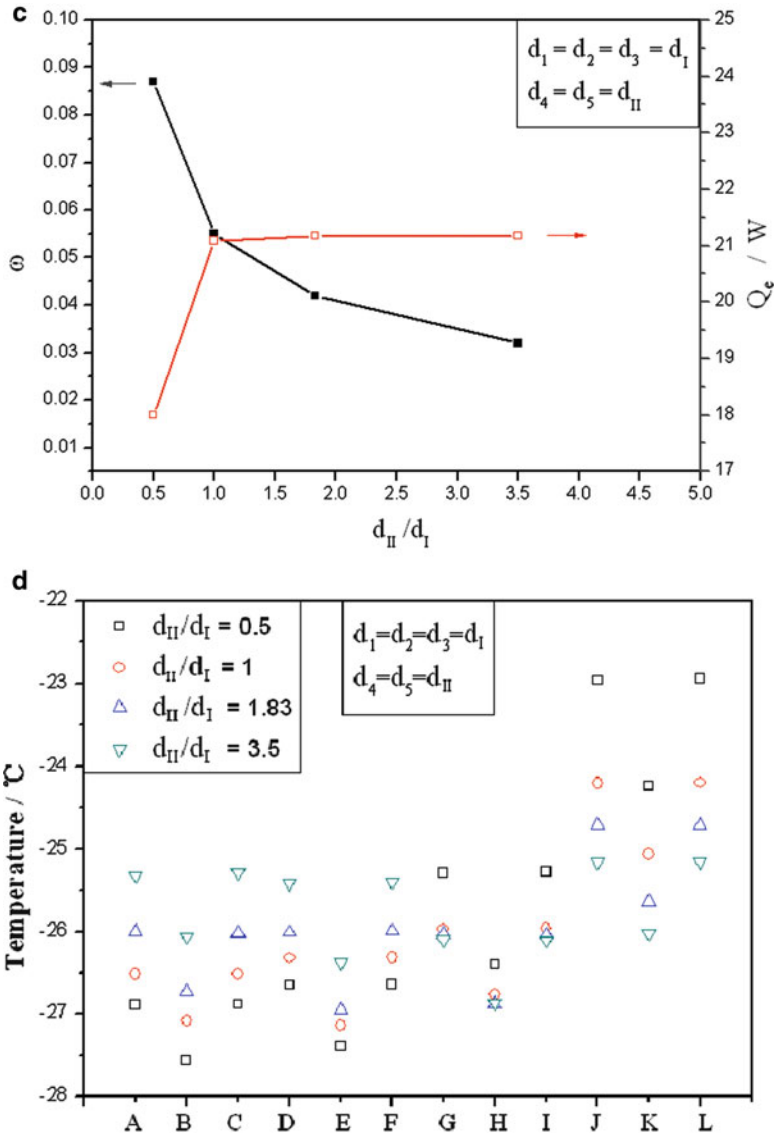

Fig. 14.4 (continued)

For instance, $d_{II}/d_I = 4$, ω decreases 9.3% from the uniform-diameter geometry $d_{II}/d_I = 1$ with only 1% decreasing in Q_e. For $d_1 = d_2 = d_3 = d_I$ and $d_4 = d_5 = d_{II}$ (Figs. 14.4c and 14.4d), ω decreases with the increasing in d_{II}/d_I. Compared with Fig. 14.4a, for fixed d_{II}/d_I, $\omega_{\text{Fig. 14.4c}} < \omega_{\text{Fig. 14.4a}}$ due to more area that is moved downward in Fig. 14.4c. This conclusion is the same as that shown in Fig. 14.3 for one-size situation. Undoubtedly, the two-size analysis can be extended to multisize

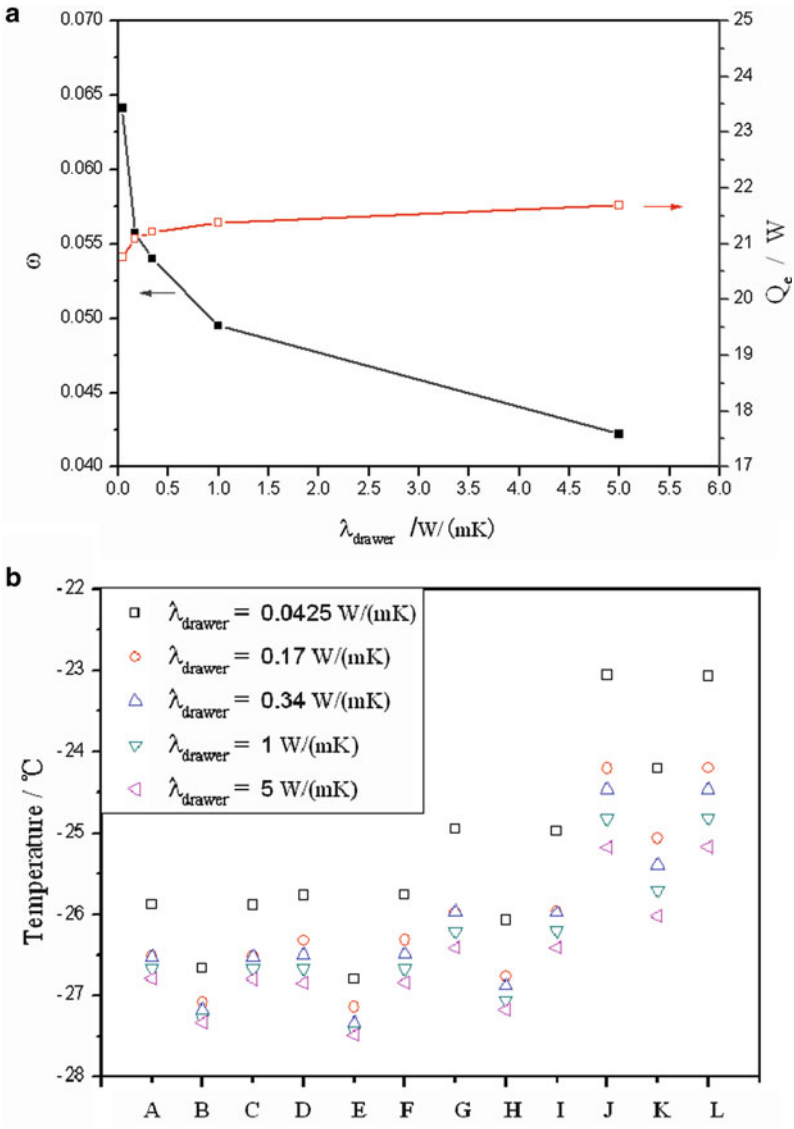

Fig. 14.5 The effects of thermal conductivity of drawers, mode (5, 5, 5, 5, 5), $d_{II}/d_I = 1$, $\lambda_{in} = 0.018$ W/(mK), $\lambda_{load} = 1$ W/(mK), $T_e = -28$ °C [18]: (**a**) Temperature nonuniformity and cooling capacity; (**b**) Characteristic temperatures

optimization. Note that either the one-size design or the two-size design mainly involves the evaporator area redistribution in the y direction. The temperature nonuniformity in the x direction can be decreased using the same idea.

The second way to vary the internal constraints is to adopt new alternative materials. Figure 14.5 shows the effects of the thermal conductivities of drawers

λ_{drawer} on ω, Q_{e}, and T_i. In designs of domestic refrigerators/freezers, drawers are commonly made of plastics with low thermal conductivity [e.g., 0.17 W/(mK)]. Seen in Fig. 14.5a, when λ_{drawer} is small, ω descends significantly with the increasing in λ_{drawer}, and when λ_{drawer} is large, the tendency approaches smooth. This indicates that selecting more conductive materials for drawers is an efficient way to decrease ω. In this situation, the cooling capacity Q_{e} increases with λ_{drawer} weakly. Figure 14.5b shows an important feature different from that shown in Figs. 14.3 and 14.4, i.e., the lower λ_{drawer}, the lower T_i at all 12 locations.

Figure 14.6 shows the effects of the thermal conductivities of insulation walls λ_{in} on ω, Q_{e}, and T_i. Seen in Fig. 14.6a, better heat insulation decreases the heat loss to the surroundings and the temperature nonuniformity ω. The cooling capacity Q_{e} decreases significantly with the decreasing in λ_{in}, which corresponds to a lower energy consumption of the freezer. Also seen in Fig. 14.6b, with the decreasing in λ_{in}, T_i drops significantly. Therefore for the same temperature requirement in freezer compartments, the features of T_i in Figs. 14.5 and 14.6 provide more space to lift the evaporating temperature T_{e} and corresponding COP. This reminds us that developing new advanced materials for drawers and insulation walls is a straightforward striving for improving the performance of domestic freezers.

In the above analysis, we fixed the evaporating temperature T_{e} and the evaporator area A [$= \sum_{i=1}^{5} (N_i \pi d_i)$]. These two parameters are commonly determined based on the required compartment temperature and the cooling capacity. For example, for two-star and three-star freezers, $-12°\text{C}$ and $-18°\text{C}$ in the compartment are required, respectively. So for a three-star freezer, $T_{\text{e}} = -28°\text{C}$ is acceptable, but for a two-star freezer, higher T_{e} is more economical. Figures 14.7a and 14.7b illustrate the effects of T_{e} on ω, Q_{e}, and T_i. The higher the evaporating temperature T_{e} the lesser the temperature nonuniformity ω and the cooling capacity Q_{e}. This observation means that the temperature nonuniformity issue is more important for a freezer with lower temperature requirement.

Figure 14.8 shows the effects of the evaporator area A (or N_{t}) with specified d on ω, Q_{e}, and T_i, where we assume that all layers have the same evaporator tubes. With the increasing in N_{t}, ω decreases while Q_{e} increases significantly (Fig. 14.8a). As N_{t} and Q_{e} correspond to the evaporator material cost and the energy consumption of the freezer, a compromise should be made in design practice. Figure 14.8b reminds us that the compromise should fulfill the requirement $T_i \leq T_{\text{specified}}$, where $T_{\text{specified}}$ is specified by test standards. For example, in Fig. 14.8b 8 characteristic temperatures in the 12 of mode (1, 1, 1, 1, 1) are higher than $-18°\text{C}$ specified for three-star freezers [19]. In this case, mode (1, 1, 1, 1, 1) should be abandoned although it costs the least.

According to test standards of domestic refrigerating appliances [19], the properties of loads used for product tests are specified. Figure 14.9 shows the effects of the thermal conductivity of loads λ_{load} on ω, Q_{e}, and T_i. Seen in Fig. 14.9a, the temperature nonuniformity ω drops with the increasing in λ_{load}. When λ_{load} is larger than 1 W/(mK), ω descends slowly. The cooling capacity changes less than 5% in the range $\lambda_{\text{load}} = 0.1$–$10$ W/(mK). This result is important for temperature-sensitive loads in use. The feature of T_i in Fig. 14.9b is similar to that of drawers (Fig. 14.5b).

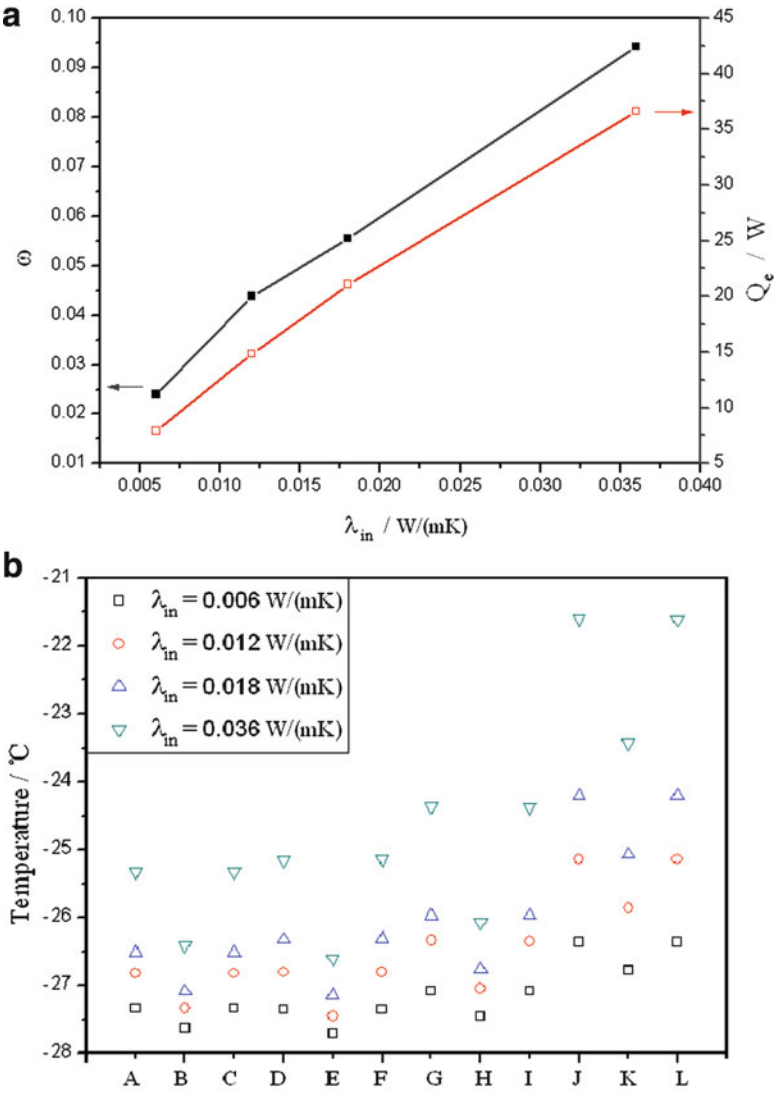

Fig. 14.6 The effects of thermal conductivity of insulation materials, mode (5, 5, 5, 5, 5), $d_{II}/d_I = 1$, $\lambda_{drawer} = 0.17$ W/(mK), $\lambda_{load} = 1$ W/(mK), $T_e = -28°C$ [18]: (**a**) Temperature nonuniformity and cooling capacity; (**b**) Characteristic temperatures

In the above analysis we have shown how to decrease the temperature nonuniformity based on constructal theory. Here we continue to discuss three-dimensional problems. Up to now a lot of work including numerical simulation-based trial-and-error optimization has been performed for refrigerators and freezers [20–24], while we formulate the three-dimensional problem briefly using constructal design

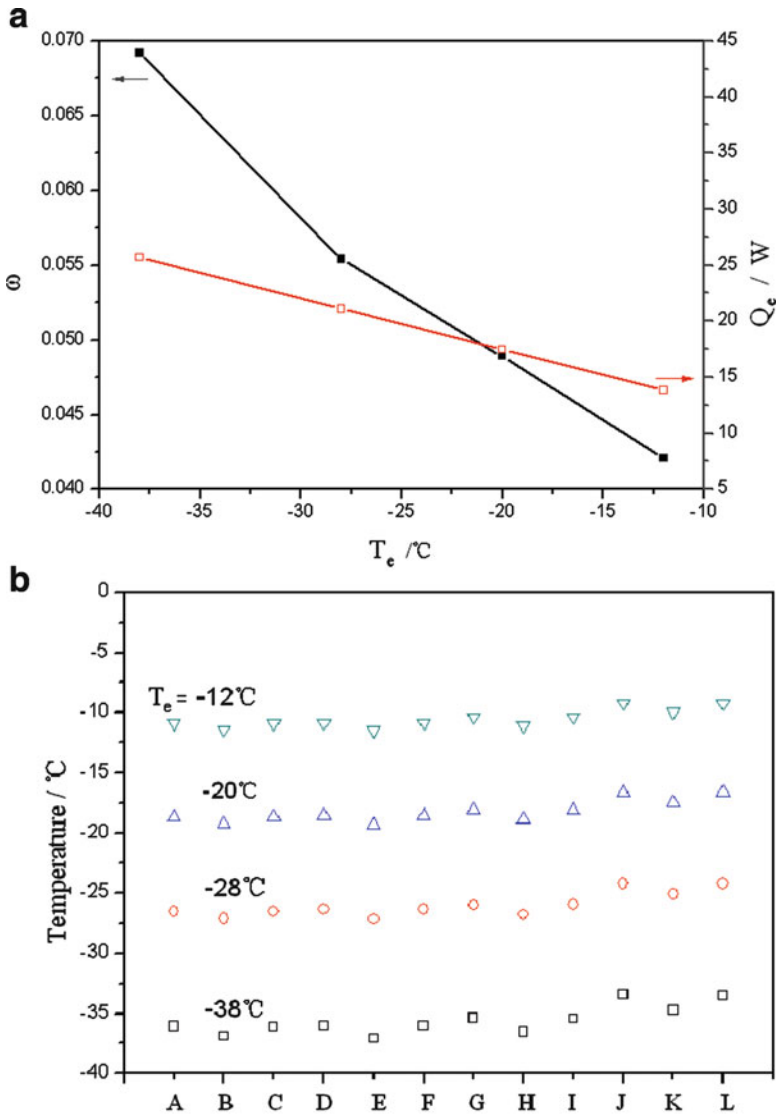

Fig. 14.7 The effects of evaporating temperature, mode (5, 5, 5, 5, 5), $d_{II}/d_I = 1$, $\lambda_{drawer} = 0.17$ W/(mK), $\lambda_{in} = 0.018$ W/(mK), $\lambda_{load} = 1$ W/(mK) [18]: (**a**) Temperature nonuniformity and cooling capacity; (**b**) Characteristic temperatures

method. The three-dimensional freezer compartment is shown in Fig. 14.10 in which the loads are arranged based on the test standard [19].

According to the test requirements specified by ref. [19], six characteristic temperatures at the centers of M1, M2, M3, M4, M5, and M6 (Fig. 14.10) are used for evaluating the temperature nonuniformity. The definitions of (14.6a, 14.6b) with

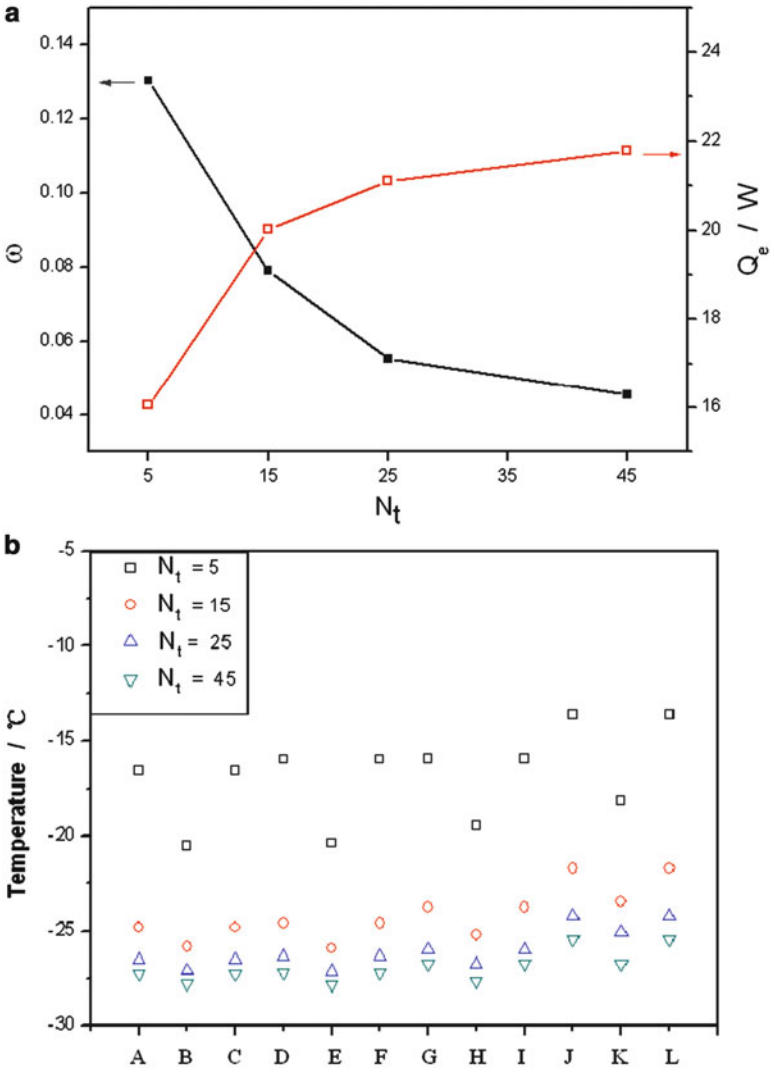

Fig. 14.8 The effects of evaporator area, $d_{II}/d_I = 1$, $\lambda_{drawer} = 0.17$ W/(mK), $\lambda_{in} = 0.018$ W/(mK), $\lambda_{load} = 1$ W/(mK), $T_e = -28$ °C [18]: (**a**) Temperature nonuniformity and cooling capacity; (**b**) Characteristic temperatures

six temperatures are adopted here. The evaporator consists of five layer steel evaporator tubes with thin steel bars welded on the surfaces of the evaporator tubes. As an example, one layer is shown in Fig. 14.11. The steel bars function as the shelves of the drawers and the loads, and as the extended heat transfer surfaces (i.e., fins) of the evaporator tubes. Therefore the total heat transfer area A_{ht} is composed of evaporator tubes area A_{tube} and steel bars area A_{bar}.

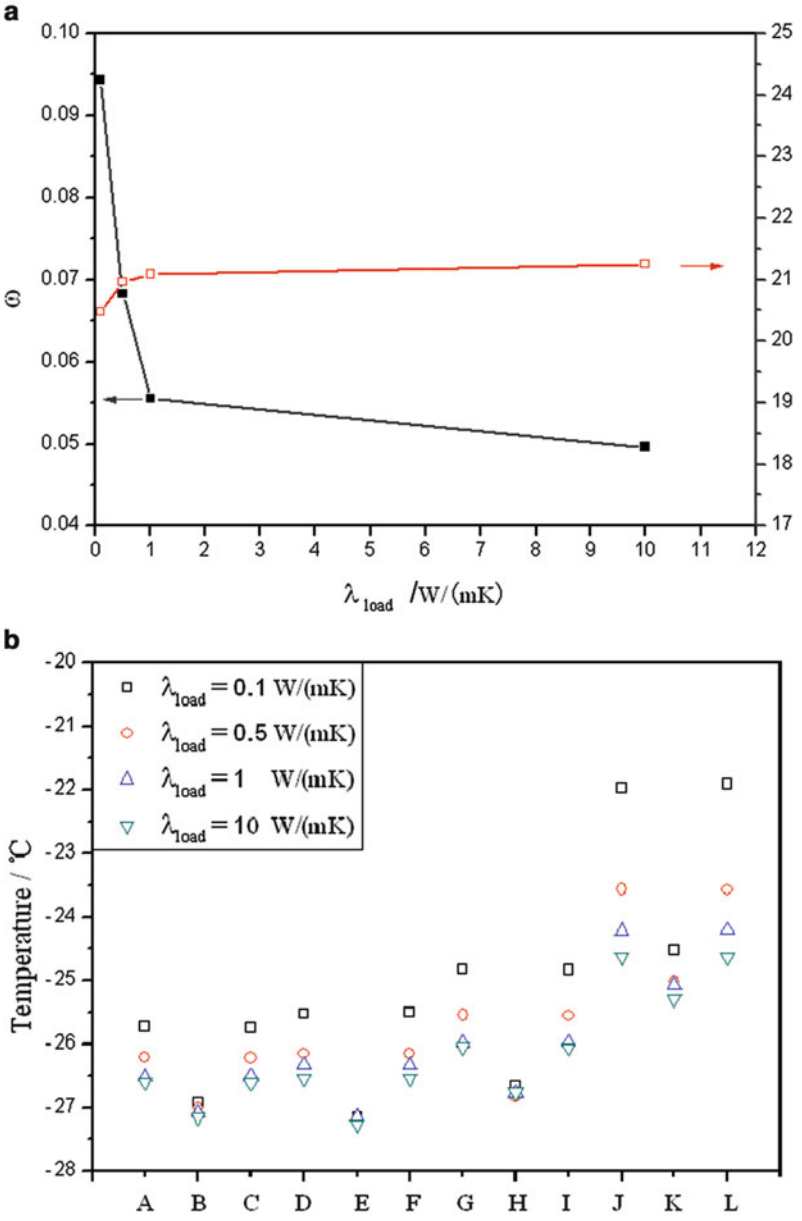

Fig. 14.9 The effects of thermal conductivity of loads, mode (5, 5, 5, 5, 5), $d_{II}/d_I = 1$, $\lambda_{drawer} = 0.17$ W/(mK), $\lambda_{in} = 0.018$ W/(mK), $T_e = -28$ °C [18]: (**a**) Temperature nonuniformity and cooling capacity; (**b**) Characteristic temperatures

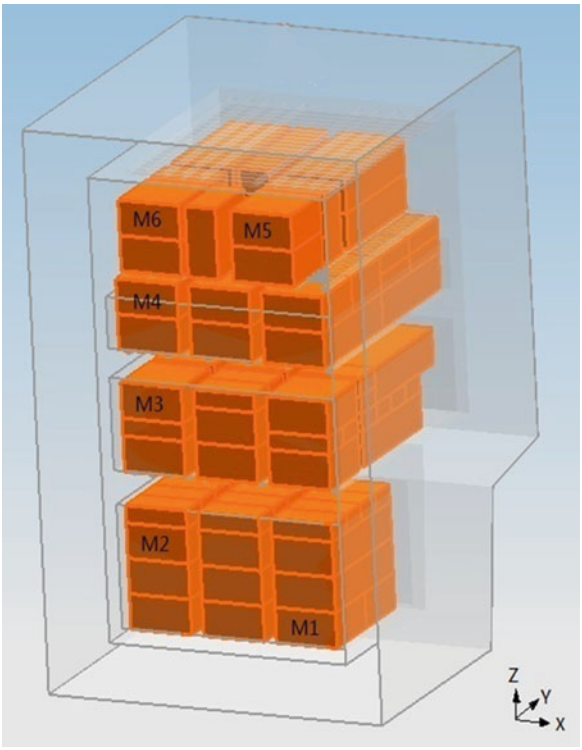

Fig. 14.10 Three-dimensional domestic freezer compartment

$$A_{\mathrm{ht}} = \sum_{i=1}^{5} \left(\phi_{\mathrm{tube},i}\phi_{\mathrm{tube}}A_{\mathrm{ht}}\right) + \sum_{i=1}^{5} \left(\phi_{\mathrm{bar},i}\phi_{\mathrm{bar}}A_{\mathrm{ht}}\right), \tag{14.9}$$

where $\phi_{\mathrm{tube},i}$, ϕ_{tube}, $\phi_{\mathrm{bar},i}$, and ϕ_{bar} are area fractions that are defined as follows.

$$\phi_{\mathrm{tube},i} = \frac{A_{\mathrm{tube},i}}{A_{\mathrm{tube}}}, \tag{14.10a}$$

$$\phi_{\mathrm{tube}} = \frac{A_{\mathrm{tube}}}{A_{\mathrm{ht}}}, \tag{14.10b}$$

$$\phi_{\mathrm{bar},i} = \frac{A_{\mathrm{bar},i}}{A_{\mathrm{bar}}}, \tag{14.10c}$$

$$\phi_{\mathrm{bar}} = \frac{A_{\mathrm{bar}}}{A_{\mathrm{ht}}}. \tag{14.10d}$$

In (14.10a)–(14.10d), subscript i denotes the ith-layer evaporator tubes.

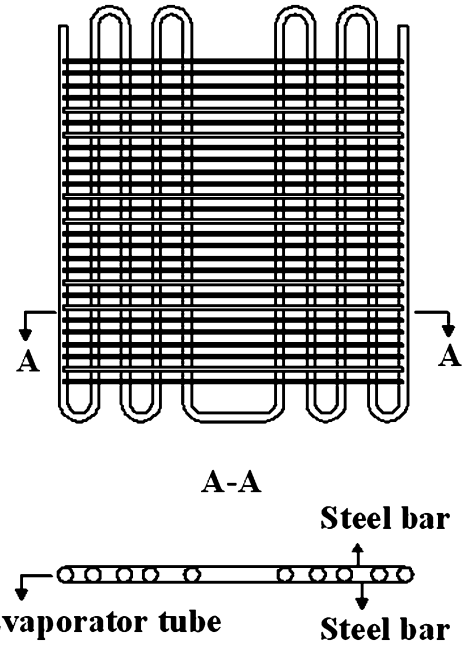

Fig. 14.11 Evaporator geometry

Although the three-dimensional geometry is more irregular and the corresponding CFD simulations are more time-consuming, there is no obstacle to perform the same constructal optimization procedure as formulated for the two-dimensional cases. For example, if we are pursuing a modification of an old product, the cheapest way is to fix the total heat transfer area A_{ht} and find optimal ϕ_{tube}, ϕ_{bar}, $\phi_{tube,i}$, and $\phi_{bar,i}$ (Fig. 14.12) without other changes. Note that although we focus our attention on decreasing the temperature nonuniformity in the freezer compartment, the design is multiobjective (see Fig .14.12 and more in Chap. 7 of ref. [4]). In conclusion, the constructal design method provides an optimization tool for real three-dimensional domestic refrigerators/freezers.

14.3 Reciprocating Flow Heating-Based Heat Pump Water Heaters

Air-source heat pump water heaters have attracted a lot of attention due to its great energy saving potential [25, 26]. Heat pump water heaters with forced convection heating can be classified into two types, i.e., constant temperature heating type (CTHT) and variable temperature heating type (VTHT). If the condensing temperature in the water heating process does not change, it is called CTHT system; otherwise it is called VTHT system. For CTHT system, cold water is heated by one time flowing through the condenser to specified temperature with a very high and

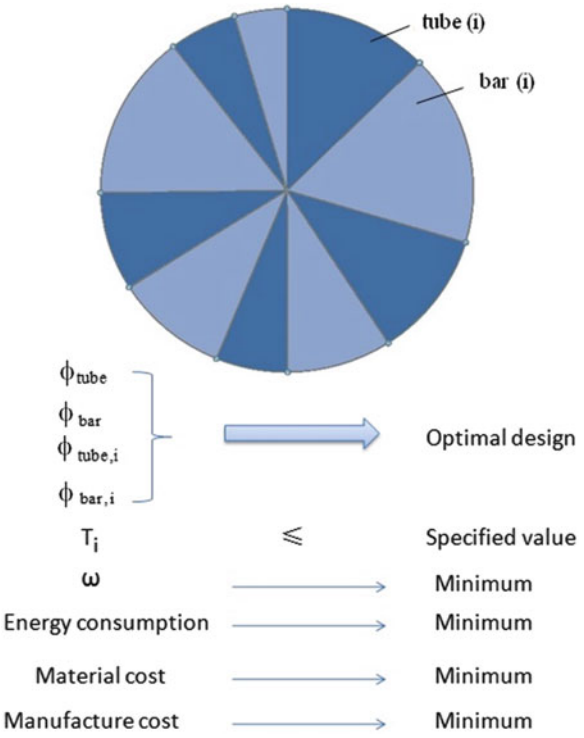

Fig. 14.12 Three-dimensional domestic freezer optimization

constant condensing temperature of refrigerant. Such system can supply hot water instantaneously; however, the coefficient of performance (COP) is low due to the high condensing temperature. For VTHT system, cold water is heated to specified temperature by multi-time flowing through the condenser with eventually increased condensing temperature. Due to the lower average condensing temperature, the COP of VTHT system is higher than that of CTHT system.

In many VTHT systems, water tanks are commonly-used equipments. One drawback of normal water tanks is the direct contact of cold and hot water, which causes irreversible heat loss. One way to weaken the direct contact of cold and hot water is to adopt float plate to separate cold and hot water in water tanks [27]. In the present work we add flexible furl-canister to the float plate in order to avoid the cold and hot water contact loss in water tanks. Another aspect we are concerned about is to keep the hot water supply continuously. This requirement is equivalent to the maximization of hot water mass that is supplied in a specified period. Either providing more hot water in the same period or decreasing the internal heat leak (i.e., irreversibility) in water tanks corresponds to generating configurations with greater flow access that is what the constructal law aims at. Inspired by the constructal law of the generation of flow configuration, in this section we investigate a VTHT-based air-source heat pump water heater system which considers the above two aspects.

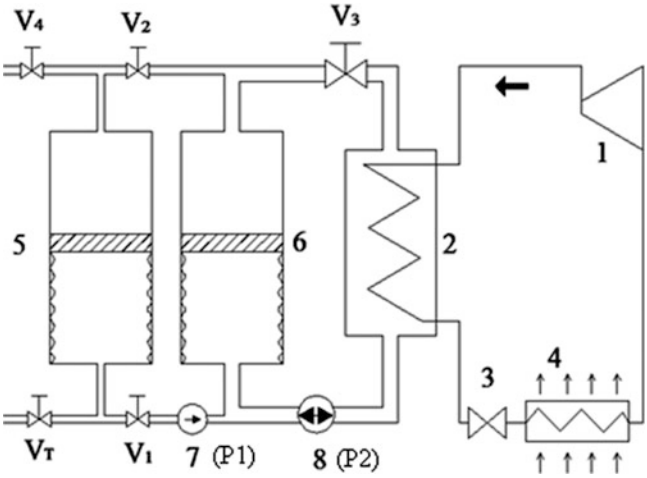

Fig. 14.13 Scheme of heat pump water heater system [30]: 1-Compressor; 2-Condenser; 3-Expansion valve; 4-Evaporator; 5-Storage tank; 6-Heating tank; 7-Pump (P1); 8-Water flow direction alteration device (P2); V_1, V_2, V_3, V_4, V_T-Valve

Table 14.1 Logic of heat pump system operation

No.	Operating stage	V_1	V_2	V_3	V_4	V_T	P_1	P_2
1.	Cold water charging process	Off	Off	Off	On	On	Off	Off
2.	Cold water exchange process	On	On	Off	Off	Off	On	Off
3.	Water recharging process	Off	Off	Off	On	On	Off	Off
4.	Water heating process I	Off	Off	On	Off	Off	Off	Rightward
5.	Water heating process II	Off	Off	On	Off	Off	Off	Leftward
6.	Hot water exchange process	On	On	Off	Off	Off	On	Off
7.	Hot water supplying and cold water charging process	Off	Off	On/off	On	On	Off	On/off

The system, shown in Fig. 14.13, includes conventional refrigeration part and water loop part. The water loop part consists of two water tanks (i.e., heating tank and storage tank), water flow direction alteration device and connectors (e.g., pipes and valves). In order to avoid or reduce internal heat leak caused by the direct contact or mixing of cold and hot water, each water tank is separated into two cavities by a floating plate connected with flexible water proof furl-canister. Such structure (i.e., the water proof furl-canister) prevents the mass transfer between cold and hot water (i.e., mass leak) that cannot be fully avoided by only using floating plates [27]. If the heat insulation of the floating plate with furl-canister is well-designed, heat leak will be very small.

We assume that at the first start of the operating process the floating plate sits at the bottom dead center of the corresponding water tank. The system operating logic from the first start is given in Table 14.1. Apparently, in the water heating process,

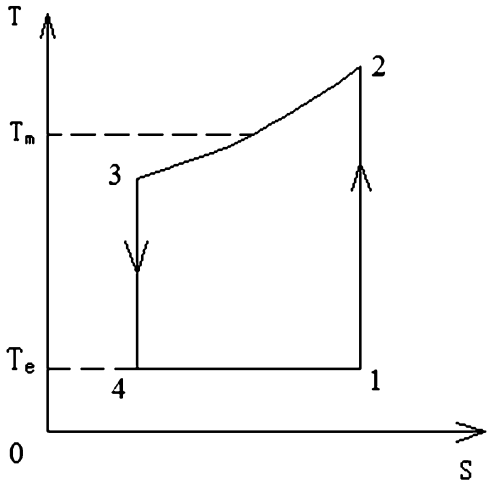

Fig. 14.14 Temperature-entropy diagram (*T*–*S*) of reversed half-Lorenz cycle

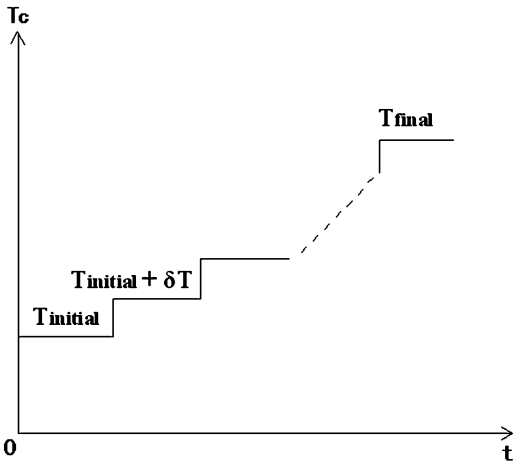

Fig. 14.15 Condensing temperature variation with time (*T*–*t*) of reciprocating heating cycle

the condensing temperature increases discretely with the increasing water temperature and water flow direction varies alternatively until the water is heated to a specified temperature.

An ideal temperature-dependent heat source based heating and cooling heat pump cycle is reversed Lorenz cycle [28, 29]. If the evaporating temperature T_e is kept constant, it becomes reversed half-Lorenz cycle in Fig. 14.14. In space-based ideal reversed half-Lorenz cycle, the condensing temperature T_c matches the water temperature with zero temperature difference along the fluid flow direction in the condenser, although finite temperature difference always exists in real cycles. Under ideal conditions for the system shown in Fig. 14.13, the condensing temperature (T_c) varies with time (t). Figure 14.15 gives the scheme of the condensing temperature variation, where $T_{initial}$ and T_{final} denote initial and final water

temperatures, respectively, and δT represents temperature increment. Every step change represents one time flow direction alteration which is realized by P2 in Fig. 14.13.

Assume that the heating process includes n_t (total heating times, $n_t = n + 1$, n: water flow direction alternation number) times of heating from initial cold water temperature T_0 to final hot water temperature T_{final} for fixed time duration and water mass. Based on the heat transfer rate Q and power consumption W, the average coefficient of performance $\overline{COP}$ is then determined by

$$\overline{\text{COP}} = \frac{\int Q\mathrm{d}t}{\int W\mathrm{d}t} = \frac{n+1}{\sum_{i=1}^{n+1} \frac{1}{\text{COP}_i}}, \tag{14.11}$$

where COP_i represents the coefficient of performance in once flow heating process. If $n = 0$, the cold water flows through the condenser only once to arrive at the final temperature T_{final}. If $n > 0$, the cold water flows through the condenser $n + 1$ times. Reciprocating flowing heating method in the present work, among others, provides one way to realize the above multi-time heating process. If n (or n_t) approaches infinite and the temperature difference between water and refrigerant in the condenser is neglected, the time-based ideal heating process "evolves" to space-based reversed half-Lorenz cycle. It is clear that the present heating process is just analogous to reversed half-Lorenz cycle, which does not mean it is a real reversed half-Lorenz cycle.

Based on (14.11), we give an example (in Fig. 14.16) how flow direction alternation number n (or the heating times n_t) affects $\overline{\text{COP}}$. Figure 14.16 shows that $\overline{\text{COP}}$ increases with the increasing in n and when n is small, $\overline{\text{COP}}$ increases faster than that when n is large. When n is large enough (e.g., $n > 7$ and evaporating temperature $T_e = 5°\text{C}$), $\overline{\text{COP}}$ only varies with n slightly. The effect of the evaporating temperature T_e is also documented in Fig. 14.16. The higher the evaporating temperature the greater the $\overline{\text{COP}}$, which obeys the common rule of typical vapor compression cycles.

In order to check if the system in Fig. 14.13 can work in principle, we built an experimental setup with two 70 L water tanks [30]. The mechanical parts worked as expected. We measured the condensing pressure and the evaporating pressure of the refrigerant (R22) of the system that is shown in Fig. 14.13 under different operating conditions. Figure 14.17 gives one case of the time-dependent condensing temperature and evaporating temperature, which are derived from the measured pressure data. In Fig. 14.17, the range $t < 6$ min corresponds to the first start process in which the evaporating temperature is time-dependent. When t is larger than 6 min, the evaporating temperature approaches stable (i.e., time-independent). Different from T_e, the condensing temperature rises step-by-step in the water heating process. Unlike the ideal process shown in Fig. 14.15, the flow direction alteration process is not a pure step change due to the finite time needed by changing the fluid flow direction in the condenser.

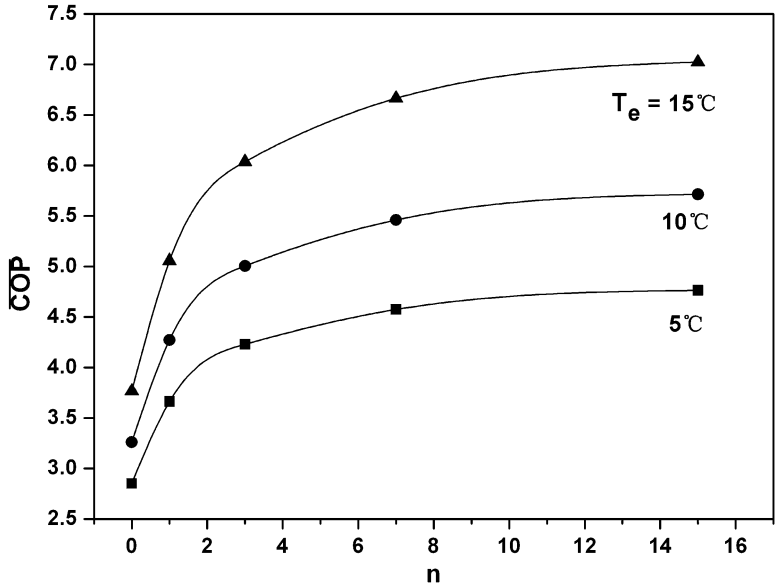

Fig. 14.16 The effect of n on $\overline{\text{COP}}$ for different T_e [31]

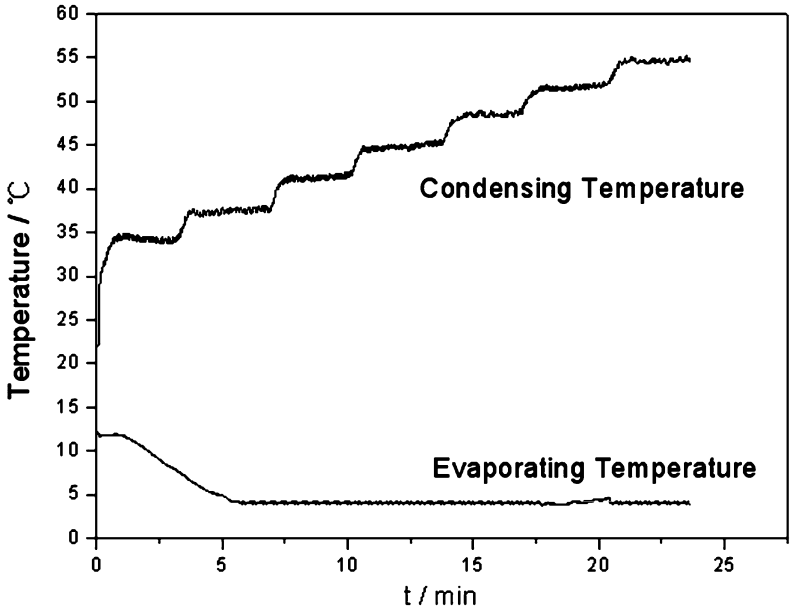

Fig. 14.17 Experimental refrigerant temperatures [30]

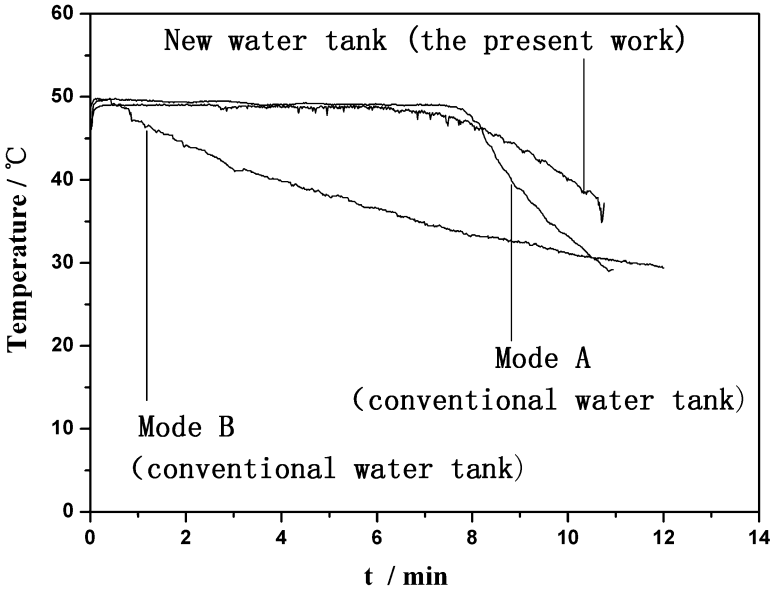

Fig. 14.18 The effect of heat leak on hot water discharging temperature [30]

The heat leak with a water tank includes internal heat leak and external heat leak. The external heat leak refers to the heat loss to the surroundings due to imperfect external heat insulation of the water tank. The internal heat leak infers the heat loss existing inside the water tank, i.e., the heat loss caused by direct contact or mixing of cold and hot water in conventional water tanks. The design of floating plate with furl-canister in Fig. 14.13 provides a way to eliminate or reduce such internal heat leak.

In order to check the internal heat insulation performance of floating plate with furl-canister in water tanks, we performed an experiment for the storage tank (Fig. 14.13) that works in the operating stage No. 7 in Table 14.1 [30, 31]. The hot water discharging temperature is recorded and compared with that of conventional water tanks without floating plate with furl-canister. The results are shown in Fig. 14.18.

In Fig. 14.18, mode A of conventional water tanks means that cold water flows into the water tank from bottom inlet and mode B of conventional water tanks means that cold water flows into the water tank from top inlet. The water tank used in the present work displays better internal heat insulation performance than that of conventional water tanks. For instance, if the acceptable final hot water temperature is 40°C, the new water tank can persist for about 10 min, but conventional water tanks can only persist for about 8.8 min for mode A and 4 min for mode B. Longer discharging time corresponds to more hot water supply and less internal heat leak because the discharging hot water flow rate and the volume of the water tank are the same. It should be mentioned that the design of the floating plate with furl-canister in the experimental prototype [30] is not fully optimized and there is space for

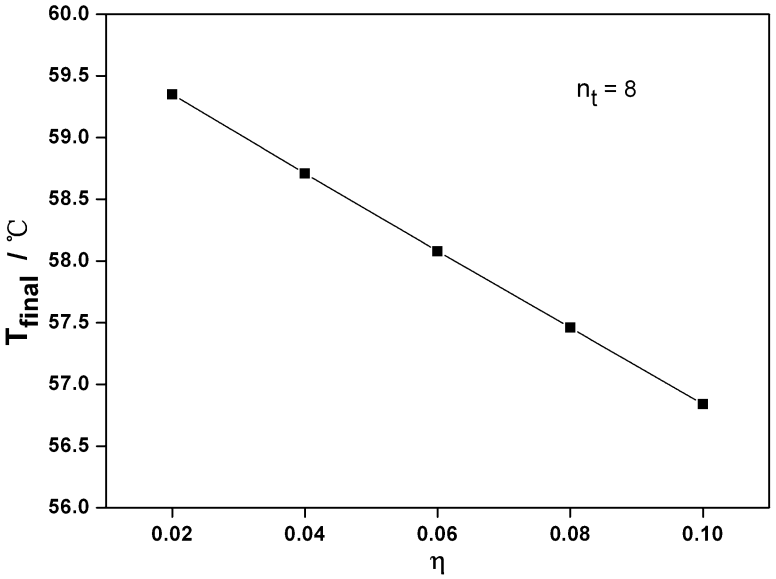

Fig. 14.19 The effect of V_c on final water temperature (T_{final}) [31]

further improvement. Here we only show the results of the storage tank, while the performance of the heating tank is similar. In addition, the measured $\overline{COP}$ of the prototype is nearly the same as that with conventional water tanks and unidirectional flow heating in the condenser [30]. Therefore in principle it is safe to conclude that the present system is better than those conventional ones.

The floating plate with furl-canister configuration can avoid or greatly reduce the internal heat leak in water tanks, while it causes the clearance volume problem due to reciprocating flow heating process. The clearance volume V_c is defined as the sum of the minimum volumes formed in the water tank (with volume V) when the floating plate moves to the top dead center and the bottom dead center, respectively. One example of the effect of dimensionless clearance volume η ($=V_c/V$) on final temperature T_{final} is given in Fig. 14.19 [31, 32]. In Fig. 14.19, the water flow rate and the heating times ($n_t = 8$) are kept constant. It is seen that the final hot water temperature T_{final} decreases with the increasing in dimensionless clearance volume η linearly. In practical systems, the clearance volume may also exist in the condenser, connectors, and tubes, so V_c or η is a generalized concept. The results here emphasize the necessity of reducing the clearance volume and increasing the compactness of condenser, connectors, and tubes.

The improvement of the heat pump water heater in the present work verified the constructal design idea once more: The performance of a flow system can be improved by optimizing its internal constraints (geometry and materials). The present case can also be reviewed by using entropy generation minimization (EGM) method [33, 34]. Less entropy generation means less irreversibility or better design. For the reciprocating heating process shown above, larger heating times n_t

corresponds to lower average condensing temperature (T_c) or less temperature difference between the condensing temperature and the evaporating temperature ΔT_{ce} ($=T_c - T_e$). Less ΔT_{ce} means less entropy generation for the heat pump system, so using multi-time flow heating method to decrease ΔT_{ce} becomes a natural choice. The system in the present work offers one way to achieve our objective.

Heat leak in water tanks is another important irreversibility source. The feature in the present design is to use the floating plate with furl-canister to eliminate or reduce the heat transfer entropy generation in water tanks. If the internal heat leak is zero (i.e., ideal heat insulation), the entropy generation becomes zero, which is the objective that we optimize our water tank design. The effect of clearance volume can also be explained from the viewpoint of EGM. Actually, the cold water in the clearance volume does absorb heat from the system that produces entropy generation, but the heated water in the clearance volume cannot be provided to users. Such entropy generation is unwanted and harmful.

In the above analysis, only the heat transfer entropy generation is taken into account while another important entropy generation source-fluid flow friction is not included. Nevertheless, because in most heat pump systems pumping power for driving water flow is much less than power consumption of compressors, the heat transfer entropy generation is more important. If we do not consider the effects of fluid friction and equipment details, the above discussion shows us the clear direction of constructal optimization, i.e., toward more heating times, less internal heat leak (or better water tank design) and less clearance volume.

For forced convection based heat pump water heaters, multi-time reciprocating flow heating method, among others, provides a feasible way to increase the average coefficient of performance. This new system demonstrates advantages compared with typical conventional systems in a few aspects. First, in the cold water heating process or hot water discharging process, cold water charging is not affected that means the operating process is continuous. Second, the structure of floating plate with furl-canister in water tanks helps reduce the internal heat loss that has been confirmed by experimental results. Although the developed prototype is not perfect, the constructal theory-inspired results do point out the evolution direction of further design optimization qualitatively. The work can be easily extended to water coolers.

14.4 From “Cool” to “Cooler”

In this chapter we have demonstrated two examples of constructal optimization of refrigeration devices. The two case studies drop to the same conclusion that refrigeration devices with flow processes can be optimized through changing the internal constraints (geometry and materials) to improve their performance. Although it is difficult to predict the details of the future of refrigeration engineering and devices due to uncertain constraints, the history of refrigeration has told us how physics laws pushed the technology and the industry forward. From the very

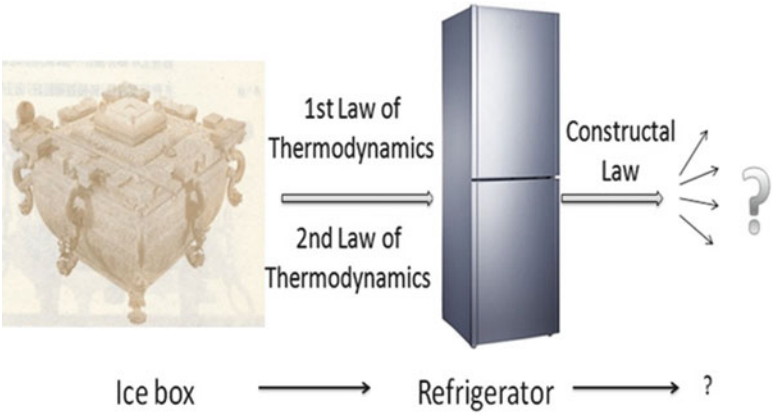

Fig. 14.20 From ancient ice box to constructal refrigeration tree. *Ice box*: from Li [36]

beginning of using natural ice, Ling Ren (pronunciation of Chinese, i.e., ice person) [35], based on their "cool" but empirical knowledge, stored ice in insulated houses and used it in different ways, e.g., cooling drinks in an ice box (left part of Fig. 14.20) [36] in hot summer days. Since thermodynamics laws were proposed, engineers got deep insight on the mechanism how refrigeration systems and devices ran and helped develop the modern refrigeration industry. Now constructal law, as thermodynamics laws did before, is expected to change the shape and structure of refrigeration products toward better performance [37].

Same important, constructal law is changing our way of working, e.g., in formulating our problems better and optimizing our design more efficiently. The constructal design thought is reshaping the refrigeration engineers (i.e., the designers) and help them explore new frontiers in refrigeration engineering (Fig. 14.20). The new equilibrium architecture is unknown to us now, but we know the direction and how to generate the new and optimal structure. Such a process may not be smooth, but as Lu (a Chinese writer) said: "For actually the earth had no roads to begin with, but when many men pass one way, a road is made" [38]. Constructal law is playing such a role to make great contributions to refrigeration future, from "cool" to "cooler."

References

1. National Bureau of Statistics of China. http://www.stats.gov.cn/ (2011)
2. Bejan A. Constructal-theory network of conducting paths for cooling a heat generating volume. Int J Heat Mass Tran. 1997;40:799–816.
3. Bejan A. Shape and structure, from engineering to nature. Cambridge: Cambridge University Press; 2000.
4. Bejan A, Lorente S. Design with constructal theory. New York: Wiley; 2008.
5. Shiba T, Bejan A. Thermodynamic optimization of geometric structure in the counterflow heat exchanger for an environmental control system. Energy. 2001;26:493–511.

6. Vargas JVC, Bejan A. Integrative thermodynamic optimization of the environmental control system of an aircraft. Int J Heat Mass Tran. 2001;44:3907–17.
7. Bejan A, Siems DL. The need exergy analysis and thermodynamic optimization in aircraft development. Exergy Int J. 2001;1:14–24.
8. Zamfirescu C, Bejan A. Constructal tree-shaped two-phase flow for cooling a surface. Int J Heat Mass Tran. 2003;46:2785–97.
9. Zamfirescu C, Bejan A. Tree-shaped structures for cold storage. Int J Refrig. 2005;28:231–41.
10. Reis AH, Miguel AF, Bejan A. Constructal theory of particle agglomeration and design of air-cleaning devices. J Phys D: Appl Phys. 2006;39:2311–8.
11. Bi Y, Guo T, Zhang L, Chen L, Sun F. Entropy generation minimization for charging and discharging processes in a gas-hydrate cool storage system. Appl Energ. 2010;87:1149–57.
12. Revellin R, Bonjour J. Entropy generation during flow boiling of pure refrigerant and refrigerant-oil mixture. Int J Refrig. 2011;34:1040–7.
13. Launder BE, Spalding DB. Lectures in mathematical models of turbulence. London: Academic; 1972.
14. Launder BE, Spalding DB. The numerical computation of turbulent flows. Comput Method Appl M. 1974;3:269–89.
15. Tao WQ. Numerical heat transfer. 2nd ed. Xi'an: Xi'an Jiao Tong University Press; 2001. Ch. 9.
16. ANSYS FLUENT (Version 12.0) User's Manual. Fluent Inc
17. Ma H. Numerical simulations for the laminar and the turbulent natural convection of high Rayleigh number (Ra) in an enclosure (in Chinese). Master Thesis. Wuhan: Huazhong University of Science and Technology; 2004
18. Zhang H, Liu X, Xiong R, Zhu S. Constructal optimization in refrigeration devices: case studies. Constructal Law Conference; 2011 Dec 1–2; Porto Alegre, Brazil
19. China Light Industry Association. Household refrigerating appliances – refrigerators (GB/T 8059.1-1995). Beijing: Standard Press of China; 1995.
20. Laguerre O, Flick D. Heat transfer by natural convection in domestic refrigerators. J Food Eng. 2004;62:79–88.
21. Laguerre O, Amara SB, Moureh J, Flick D. Numerical simulation of air flow and heat transfer in domestic refrigerators. J Food Eng. 2007;81:144–56.
22. Hermes CJL, Melo C, Knabben FT, Gonclaves JM. Prediction of the energy consumption of household refrigerators and freezers via steady-state simulation. Appl Energ. 2009;86:1311–9.
23. Borges BN, Hermes CJL, Goncalves JM, Melo C. Transient simulation of household refrigerators: a semi-empirical quasi-steady approach. Appl Energ. 2011;88:748–54.
24. Yoon WJ, Jung HW, Chung HJ, Kim Y. Performance optimization of a two-cycle with parallel evaporators for a domestic refrigerator-freezer. Int J Refrig. 2011;34:216–24.
25. Hepbasli A, Kalinci Y. A review of heat pump water heating systems. Renew Sust Energ Rev. 2009;13:1211–29.
26. Lohani SP, Schmidt D. Comparison of energy and exergy analysis of fossil plant, ground and air source heat pump building heating system. Renew Energ. 2010;35:1275–82.
27. Stene J. A method for increasing the energy efficiency of residential CO2 heat pump water heater systems. Preliminary Proc of the 5th IIR-Gustav Lorentzen Conference on Natural Working Fluids; 2002, Guangzhou; p. 276–83
28. Cavallini A. Working fluids for mechanical refrigeration. Int J Refrig. 1996;19:485–96.
29. Chen J, Zhu FQ, Xu SQ. Lorenz cycle and non-azeotropic refrigerants- Investigation on refrigeration cycles with variable temperature heat source (in Chinese). Refrigeration Technology. 1999;4:33–6.
30. Zhang H, Liu X, Chen S, Xiong R. Experimental investigation on air source heat pump water heater with two water tanks based on reciprocating flow heating (in Chinese). Fluid Machinery. 2010;38:61–66, 71.
31. Chen S. Theoretical analysis and experimental investigation on dual-tank heat pump water heater based on reciprocating heating process (in Chinese). Master Thesis. Nanjing: Nanjing University of Science and Technology; 2008

32. Chen S, Zhang H, Liu X. Design of a water tank with floating plate and furl-canister and research on its internal moving, heating and mass transfer performance (in Chinese). Refrigeration Air Conditioning and Electric Power Machinery. 2009;30:20–4.
33. Bejan A. Entropy generation through heat and fluid flow. New York: Wiley; 1982.
34. Bejan A. Entropy generation minimization. Boca Raton: CRC Press; 1996.
35. Pan Q, editor. The history of refrigeration in China (ch. 1). Beijing: Sci and Tech Press of China; 2008
36. Li X. Listen to the ancient footsteps (ch. 2). Chongqing: Chongqing Publishing Group; 2006
37. IIR. IIR listings of refrigeration research priorities. International Institute of Refrigeration; Paris; 2005
38. Lu X. My old home (in Chinese). New Youth.1921;9. Translated into English by Yang X, Yang G. In: Lu Xun: selected works. Beijing: Foreign Languages Press; 2003

Chapter 15
Constructal Design of Vortex Tubes

E.D. dos Santos, C.H. Marques, G. Stanescu, L.A. Isoldi, and L.A.O. Rocha

15.1 Introduction

The vortex tube (also known as Ranque-Hilsch vortex tube) is a mechanical device which splits a compressed high-pressure gas stream into cold and hot lower pressure streams without any chemical reactions or external energy supply [1–3]. Such a separation of the flow into regions of low and high total temperature is referred to as the temperature (or energy) separation effect. The device consists of a simple circular tube, one or more tangential nozzles, and a throttle valve. Figure 15.1 depicts schematically two types of vortex tubes: Counter flow (Fig. 15.1a) and parallel flow (Fig. 15.1b). The operational principle of a counter flow vortex tube, which is the scope of the present work, Fig. 15.1a, consists of a high-pressure gas that enters the vortex tube and passes through the nozzle(s). The gas expands through the nozzle and achieves a high angular velocity, causing a vortex-type flow in the tube. There are two exits: the hot exit that is placed near the outer radius of the tube at the end away from the nozzle and the cold exit that is placed at the center of the tube at the same end as the nozzle. By adjusting a throttle valve (cone valve) downstream of the hot exit it is possible to vary the fraction of the incoming flow that leaves

E.D. dos Santos (✉) • C.H. Marques • L.A. Isoldi
Escola de Engenharia (EE), Universidade Federal de Rio Grande (FURG), CP 474,
Rio Grande-RS, Brazil
e-mail: elizoldodosantos@furg.br; cristoferhood@gmail.com; liercioisoldi@furg.br

G. Stanescu
Departamento de Engenharia Mecânica, Centro Politécnico, Universidade Federal do Paraná,
Jardim das Américas, CP. 19011 Curitiba, Pr, Brazil
e-mail: stanescu@ufpr.br

L.A.O. Rocha
Departamento de Engenharia Mecânica (DEMEC), Universidade Federal do
Rio Grande do Sul (UFRGS), Porto Alegre-RS, Brazil
e-mail: luizrocha@mecanica.ufrgs.br

L.A.O. Rocha et al. (eds.), *Constructal Law and the Unifying Principle of Design*,
Understanding Complex Systems, DOI 10.1007/978-1-4614-5049-8_15,

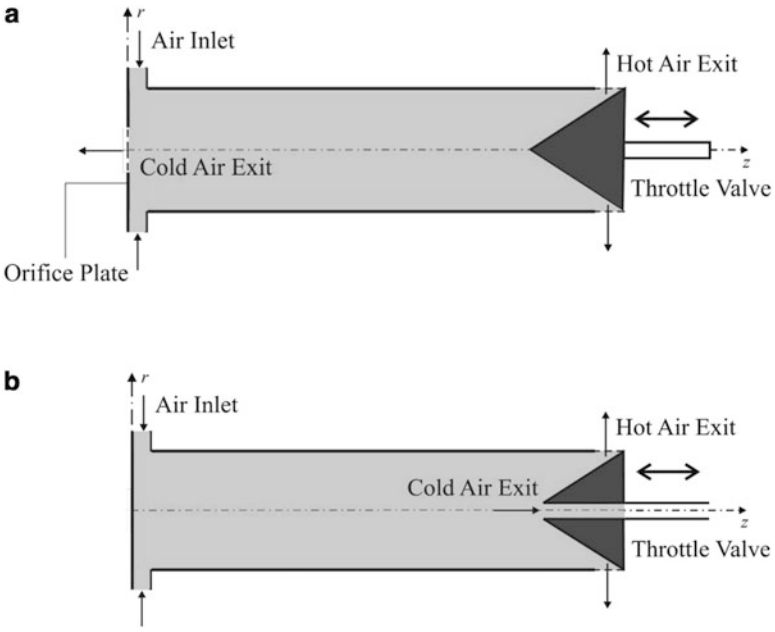

Fig. 15.1 Operating principle of two types of vortex tubes: (**a**) counter flow and (**b**) parallel flow

through the cold exit, referred as cold fraction. This adjustment affects the amount of cold and hot energy that leaves the vortex tube in the device exits.

The vortex tube has been a subject of studies due to its enormous applications in engineering, such as cooling of machine parts, refrigeration, cool electric or electronic control cabinets, cooling of equipment in laboratories dealing with explosive chemicals, chill environmental chambers, cool foods, liquefaction of natural gas, and cooling suits [3–7]. Moreover, the lack of moving parts, electricity, and other advantages make the device attractive for a number of specialized applications where simplicity, robustness, reliability, and general safety are desired [8].

Another important motivation for the study of vortex tube is the complexity of the energy separation phenomenon in the compressible and turbulent flow. Several studies have been performed to explain the phenomena occurring during the energy separation inside the vortex tube. For example, Harnet and Eckert [9] invoked turbulent eddies. Stephan et al. [10] stated that the drive of fluid motion is related with Goërtler vortices. Ahlborn and Groves [11] presented the theory of secondary circulation to explain energy separation. Lewis and Bejan [8] suggested that angular velocity gradients in the radial direction give rise to frictional coupling between different layers of the rotating flow resulting in a migration of energy via shear work from the inner layers to the outer layers.

Recently, computational fluid dynamics (CFD) modeling has been utilized to improve the comprehension about the energy separation. For instance, Schlenz [12] numerically investigated the energy separation for an axisymmetric compressible flow.

The turbulence was treated with a zero-equation turbulence model and the calculations agreed only qualitatively with the experimental data. Cockerill [13] presented a mathematical model for the simulation of a compressible turbulent flow in a vortex tube. He observed that the formation of forced vortex and a strong radial pressure gradient were the two driving forces behind energy separation. Aljuwayhel et al. [14] investigated the energy separation mechanism using the commercial code FLUENT, based on the finite volume method (FVM). They observed that the standard k–ε turbulence model predicted the velocity and temperature separation better than the RNG k–ε turbulence model. Dutta et al. [7] studied the influence of different Reynolds Averaged Navier-Stokes (RANS) turbulence models: standard k–ε, RNG k–ε, standard k–ω, and SST k–ω. A comparison of the temperature separation obtained numerically and experimentally corroborates the previous findings of Aljuwayhel et al. [14]. Farouk and Farouk [15] used large eddy simulation (LES) and compared with previous experimental results of Skye et al. [16] and k–ε predictions. The authors noticed that temperature separation predicted with LES was closer to the experimental results in comparison with those reached with RANS model. It is worthy to mention that the computational effort for LES is, in general, several times higher than that observed for RANS simulations. This fact prevents the use of LES for optimization studies, since several simulations are required.

Concerning the optimization of the vortex tube, according to Eiamsa-ard and Promvonge [3] two important parameters must be taken into account. The first is the geometrical characteristics of the vortex tube (diameter and length of the hot and cold tubes, diameter of the cold orifice, shape of the hot tube, number of inlet nozzles, and others). The second is focused on the thermo-physical parameters such as inlet gas pressure, cold mass fraction, and type of gas (air, oxygen, helium, and methane). Studies in this subject have been presented in the literature. For example, Promvonge and Eiamsa-ard [17] reported the effects of the number of inlet tangential nozzles, the cold orifice diameter and the tube insulations on the temperature reduction and isentropic efficiency of the vortex tube. Aydin and Baki [18] investigated experimentally the energy separation in a counter flow vortex tube having various geometrical and thermo-physical parameters. Pinar et al. [19] investigated the effects of inlet pressure, nozzle number, and fluid type factors on the vortex tube performance by means of Taguchi method. However, as long as we know, it has not been presented in studies concerned with the geometric optimization of the vortex tube by means of constructal design [20, 21].

Constructal theory has been used to explain deterministically the generation of shape in flow structures of nature (river basins, lungs, atmospheric circulation, animal shapes, vascularized tissues, etc) based on an evolutionary principle of flow access in time. That principle is the Constructal law: for a flow system to persist in time (to survive), it must evolve in such way that it provides easier and easier access to the currents that flow through it [21]. This same principle is used to yield new designs for electronics, fuel cells, and tree networks for transport of people, goods, and information [22]. The applicability of this method/law to the physics of engineered flow systems has been widely discussed in recent literature [23–26].

In the present work it is considered as the numerical optimization of a vortex tube device by means of constructal design. It is evaluated in a vortex tube with axisymmetric computational domain. The compressible and turbulent flows are solved with a commercial CFD package code based on the Finite Volume Method, FLUENT [27]. The turbulence is tackled with the standard k–ε model into the Reynolds Averaged Navier-Stokes (RANS) approach. The geometry evaluated here has one global restriction, the total volume of the cylindrical tube, and four degrees of freedom: d/D (the ratio between the diameter of the cold outlet and the diameter of the vortex tube, cold orifice ratio), d_1/D (the ratio between the nozzle diameter of the entering air and the diameter of the vortex tube), L_1/L (the ratio between the length of the hot exit annulus and the length of the vortex tube), and D/L (the ratio between the diameter of the vortex tube and its length). However, only the degree of freedom d/D is optimized while the other degrees of freedom are kept fixed. The purpose is to maximize the amount of energy extracted from the cold region (cooling effect) for several geometries. All evaluated geometries are simulated for several ratios between the fixed inlet pressure (p_1) and the pressure of the hot exit (p_2), which is adjusted to obtain several cold mass fractions.

15.2 Mathematical Model

The analyzed physical problem consists of a two dimensional axisymmetric cylindrical cavity, as illustrated in Fig. 15.2. The air entering the tube is modeled as an ideal gas with constant specific heat capacity, thermal conductivity, and viscosity. The inlet stagnation conditions are fixed at $p_1 = 300$ kPa and $T_1 = 300$ K for the verification case and $p_1 = 700$ kPa for the optimization cases. The intake air enters with an angle of $\alpha = 9°$ with respect to tangential direction. The static pressure at the cold exit boundary is fixed at atmospheric pressure. For the hot exit boundary, several simulations are performed with various pressures in order to simulate the effect of throttle valve. For each fixed pressure of the hot exit boundary, one specific value of cold mass fraction ($y_c = m_c/m$) is reached. Once it is considered as a two-dimensional axisymmetric domain, an

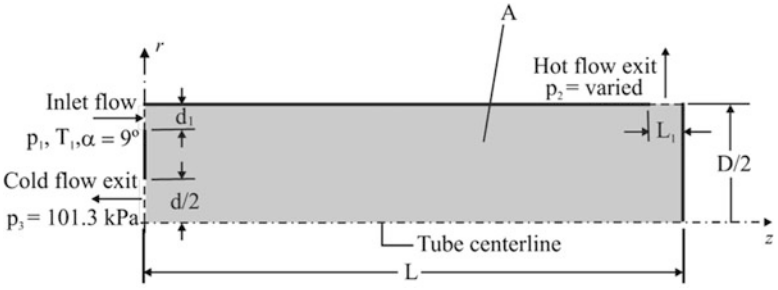

Fig. 15.2 Domain of the vortex tube

axis is imposed in the lower surface of the domain, Fig. 15.2. The other surfaces present the no-slip and adiabatic conditions. The vortex tube dimensions are assumed: $L = 1.0 \times 10^{-1}$ m, $L_1 = 1.5 \times 10^{-3}$ m, $D = 2 \times 10^{-2}$ m, $d_1 = 1.0 \times 10^{-3}$ m, and $d = 6.0 \times 10^{-3}$ m for the verification case. The degrees of freedom are also fixed: $d_1/D = 0.05$, $L_1/L = 0.015$, and $D/L = 0.2$. The objective of the analysis is to determine the optimal remaining geometry d/D that leads to the maximum cooling heat transfer rate (Q_c).

According to constructal design [21], optimization can be subjected to the total volume constraint,

$$V = \pi D^2 L/4. \tag{15.1}$$

For all evaluated cases, it solved the time-averaged conservation equations of mass, momentum, and energy for the turbulent flow, which is given respectively by:

$$\frac{\partial \bar{\rho}\bar{v}_i}{\partial x_i} = 0 \quad (i = 1, 2 \text{ and } 3) \text{ in } t \times \Omega, \tag{15.2}$$

$$\frac{\partial \bar{\rho}\bar{v}_i}{\partial t} + \frac{\partial \left(\bar{\rho}\bar{v}_i\bar{v}_j\right)}{\partial x_j} = -\frac{\partial \bar{p}}{\partial x_j}\delta_{ij} + \frac{\partial}{\partial x_j}\left\{\mu\left(\frac{\partial \bar{v}_i}{\partial x_j} + \frac{\partial \bar{v}_j}{\partial x_i}\right) - \tau_{ij}\right\} \quad (i,j = 1, 2 \text{ and } 3) \text{ in } t \times \Omega, \tag{15.3}$$

$$\frac{\partial \bar{\rho}\bar{T}}{\partial t} + \frac{\partial}{\partial x_j}\left(\bar{\rho}\bar{v}_j\bar{T}\right) = \frac{\partial}{\partial x_j}\left\{\frac{k}{c_p}\frac{\partial \bar{T}}{\partial x_j} - q_j\right\} \quad (i,j = 1, 2 \text{ and } 3) \text{ in } t \times \Omega, \tag{15.4}$$

where $\overline{()}$ represents the time-averaged variables, ρ is the density of the fluid (kg·m^{-3}), μ is the dynamical viscosity (kg·m^{-1}·s^{-1}), k is the thermal conductivity of the fluid (W·m^{-1}·K^{-1}), v_i is the velocity in i-direction, i = 1, 2 and 3 (m·s^{-1}), p is the pressure (N·m^{-2}), T is the temperature (K), δ_{ij} is the Kronecker delta, Ω is the spatial domain (m), and t is the temporal domain (s).

The turbulent tensor can be written by [28]:

$$\tau_{ij} = \mu_t\left(\frac{\partial \bar{v}_i}{\partial x_j} + \frac{\partial \bar{v}_j}{\partial x_i}\right) \quad (i,j = 1, 2 \text{ and } 3). \tag{15.5}$$

The turbulent transport of temperature is obtained through an analogy with the Reynolds tensor [28] and is given by:

$$q_j = \bar{\rho}\alpha_t\frac{\partial \overline{T}}{\partial x_j} \quad (j = 1, 2 \text{ and } 3). \tag{15.6}$$

The time-averaged fields of velocity, pressure, and temperature are obtained by means of standard k–ε model [29, 30]. According to this model it is required that the

Table 15.1 Model constants appearing in the governing equations

C_μ	$C_{\varepsilon 1}$	$C_{\varepsilon 2}$	σ_k	σ_ε	Pr_t
0.09	1.44	1.92	1.0	1.3	1.0

solution of two additional equations for the turbulent kinetic energy k and its dissipation rate ε, which can be expressed as follows:

$$\frac{\partial k}{\partial t} + \bar{v}_j \frac{\partial k}{\partial x_j} = \tau_{ij} \frac{\partial \bar{v}_i}{\partial x_j} + \frac{\partial}{\partial x_j}\left[\left(\upsilon + \frac{\upsilon_t}{\sigma_k}\right)\frac{\partial k}{\partial x_j}\right] - \varepsilon \quad (i,j = 1,2 \text{ and } 3), \tag{15.7}$$

$$\frac{\partial \varepsilon}{\partial t} + \bar{v}_j \frac{\partial \varepsilon}{\partial x_j} = \frac{\partial}{\partial x_j}\left[\left(\upsilon + \frac{\upsilon_t}{\sigma_\varepsilon}\right)\frac{\partial \varepsilon}{\partial x_j}\right] + C_{\varepsilon 1}\frac{\varepsilon}{k}\tau_{ij}\frac{\partial \bar{v}_i}{\partial x_j} - C_{\varepsilon 2}\frac{\varepsilon^2}{k} \quad (i,j = 1,2 \text{ and } 3), \tag{15.8}$$

where:

$$\upsilon_t = C_\mu \frac{k^2}{\varepsilon}, \tag{15.9}$$

$$\alpha_t = \frac{\upsilon_t}{\mathrm{Pr}_t}. \tag{15.10}$$

The model constants appearing in the governing equations, (15.7)–(15.10), are given in Table 15.1. In order to calculate turbulence quantities accurately in the near-wall region, wall functions for velocity and temperature fields are employed.

15.3 Numerical Model

We simulate the compressible turbulent flows by solving (15.2)–(15.4) using a CFD package based on rectangular finite volume method [27]. The solver is density based and all simulations were performed with the second-order upwind advection scheme. More details about the finite volume method can be found in Patankar [31] and Versteeg and Malalasekera [32].

The spatial discretization is performed with rectangular finite volumes. The grid is more refined for the highest velocity and temperature gradients regions. The grid independence is reached according to the criterion $|(T^j_{\min} - T^{j+1}{}_{\min})/T^j_{\min}| < 5 \times 10^{-4}$, where $T^j_{\min}$ represents the minimal temperature along the domain for the actual grid and $T^{j+1}{}_{\min}$ corresponds to the minimal temperature for the following grid. The number of volumes is increased approximately two times from one grid to the next. The grid sensibility study is presented for the verification case in Table 15.2. The independent grid was obtained with 11,760 volumes.

Table 15.2 Grid independence study

Number of volumes	T^j_{min} (K)	$\lvert(T^j_{min} - T^{j+1}_{min})/T^j_{min}\rvert$
5,460	285.4661	1.1570×10^{-3}
11,760	285.1358	4.7350×10^{-5}
27,730	285.0008	

15.4 Results and Discussion

Firstly, the accuracy of the numerical code is evaluated. A qualitatively evaluation is performed in Fig. 15.3, where the stream function obtained in the present work (Fig. 15.3a) is compared with that numerically predicted in ref. [14] (Fig. 15.3b). It can be observed that there is a similarity between both topologies. For both simulations a steep gradient of velocity near the intake region is noticed. Besides, it is observed that the split of the flux is in three different regions: periphery region (flux that leaves the domain by the hot outlet), central region (fluid that leaves the domain by the cold outlet), and the recirculation region. It is also observed that there are minor differences for the recirculation, such as the lower deformation of the recirculation near the cold exit in the simulation performed in the present study.

For the quantitative analysis, the temperature profiles as a function of the vortex tube radius obtained with the present work are compared with those predicted by Aljuwayhel et al. [14] for two different placements of azimuthal coordinates: $z = 0.06$ m and $z = 0.08$ m. Figure 15.4 shows for both placements that the temperature profiles have the same tendency. However, the magnitude of the temperature is higher for the simulations of the present work than that predicted in the literature. The highest differences are 2.36% and 1.70% for $z = 0.06$ m and 0.08 m, respectively. These differences were not expected, since both solutions are obtained with the same numerical code [27]. One possible explanation for the deviations is related with the selection of numerical parameters used in the solution, such as, the advection scheme or the residuals of convergence. In spite of this fact, the results showed a very good agreement.

After the numerical verification, the effect of the cold mass fraction (y_c) on the heat transfer rate that leaves the cold exit (Q_c) is investigated. Figure 15.5 shows the effect of y_c on the heat transfer rate in the cold exit for $p_1 = 700$ kPa, $d/D = 0.3$, $d_1/D = 0.05$, $L_1/L = 0.015$, and $D/L = 0.2$. There is one optimal cold mass fraction, $y_{c,o} = 0.56$ and the corresponding maximal heat transfer rate obtained for this cold mass fraction is $Q_{c,m} = 221.61$ W, which is 39.39% and 9.10% higher than that found for $y_c = 0.24$ (lower extreme) and $y_c = 0.72$ (upper extreme), respectively. This is an important result and shows that there is one opportunity for geometric optimization. Note that the cold mass fraction is directly linked with the adjustment of the throttle valve, i.e., with the opening area of the valve. In the present study, the cold mass fraction is varied as a function of the hot outlet pressure, but the same effect would be obtained for a fixed hot exit pressure and varying the degree of freedom L_1/L.

Figure 15.6 shows the effect of the cold mass fraction (y_c) on the temperatures of cold (T_C) and hot (T_H) outlets. The results show that T_C and T_H increase with the augment of the cold mass fraction. The results of Figs. 15.5 and 15.6 also show that

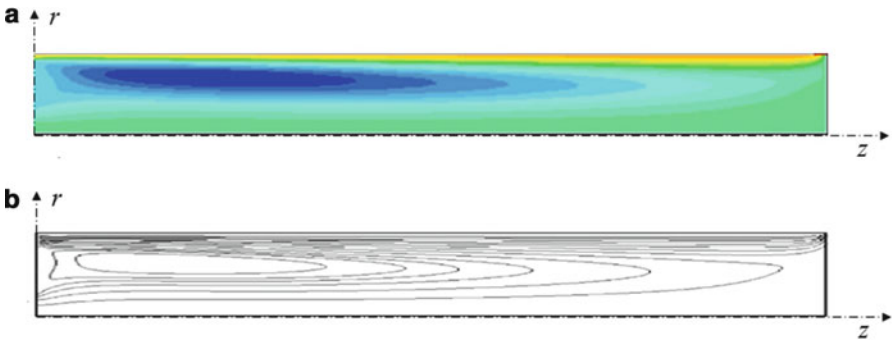

Fig. 15.3 Comparison of the stream function obtained numerically: (**a**) present work, (**b**) ref. [14]

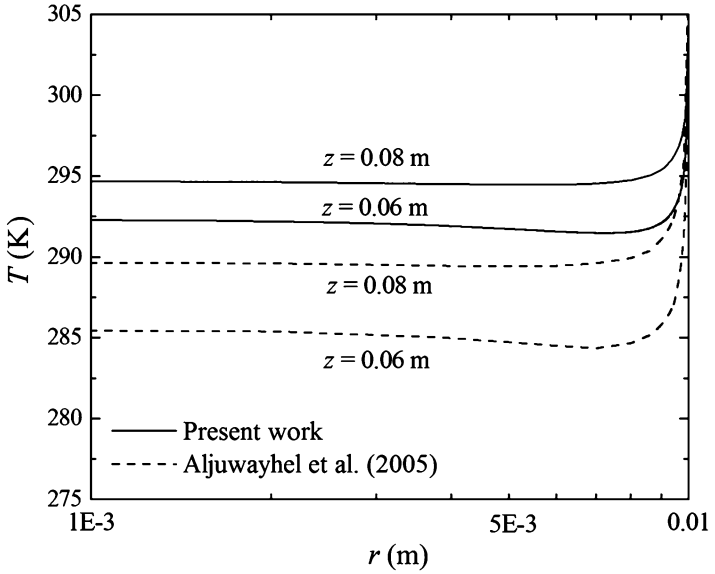

Fig. 15.4 Comparison of the static temperature profiles as a function of the vortex tube radius for the azimuthal coordinates ($z = 0.06$ m and 0.08 m) obtained in the present work and predicted in ref. [14]

the optimal adjustment of the throttle valve, which leads to the maximal cold heat transfer rate $Q_{c,m}$ is not obtained for the highest cold air temperature drop (ΔT_C) nor for the highest mass flow rate that leaves the cold boundary (m_c).

Figure 15.7 illustrates the temperature distribution in the vortex tube for the following cold mass fractions: $y_c = 0.24$ (Fig. 15.7a), $y_{c,o} = 0.56$ (Fig. 15.7b), and $y_c = 0.72$ (Fig. 15.7c) that represent the lower extreme, the optimal and the upper extreme of the curve shown in Fig. 15.5, respectively. For the lower extreme (Fig. 15.7a) it is observed that the steepest temperature gradients is in the radial

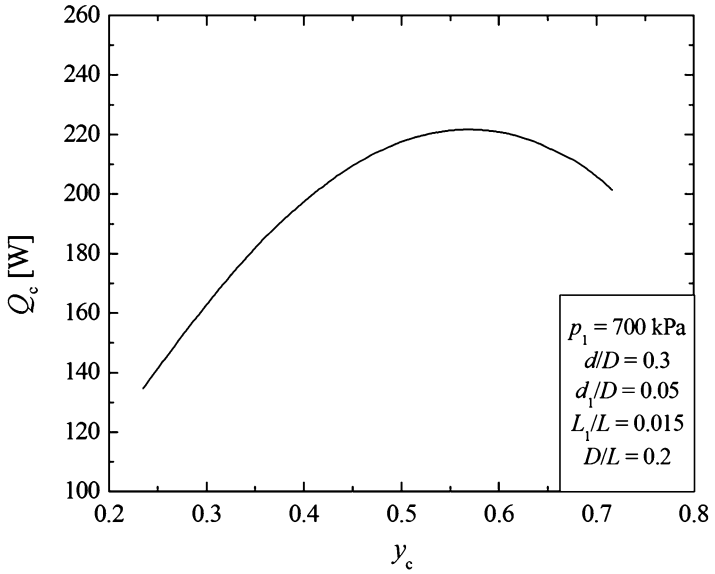

Fig. 15.5 First maximization of the cold heat transfer rate (Q_c) as function of the cold mass fraction (y_c)

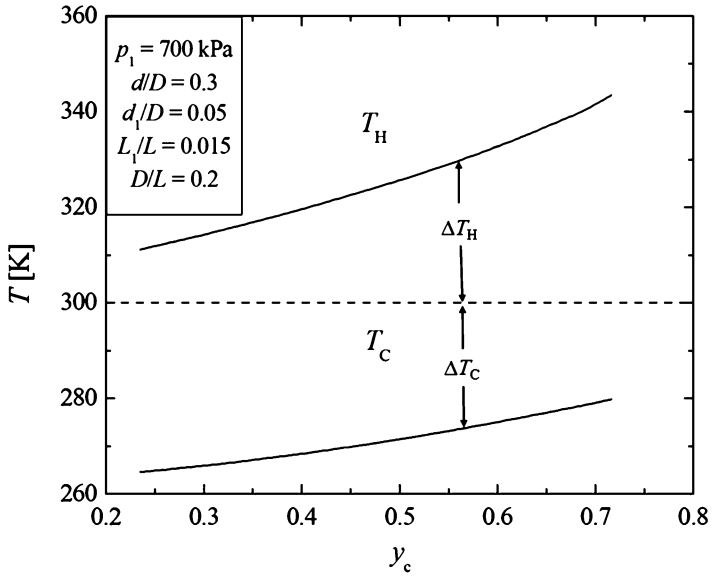

Fig. 15.6 The effect of the cold mass fraction (y_c) over the temperatures of cold (T_C) and hot (T_H) outlets

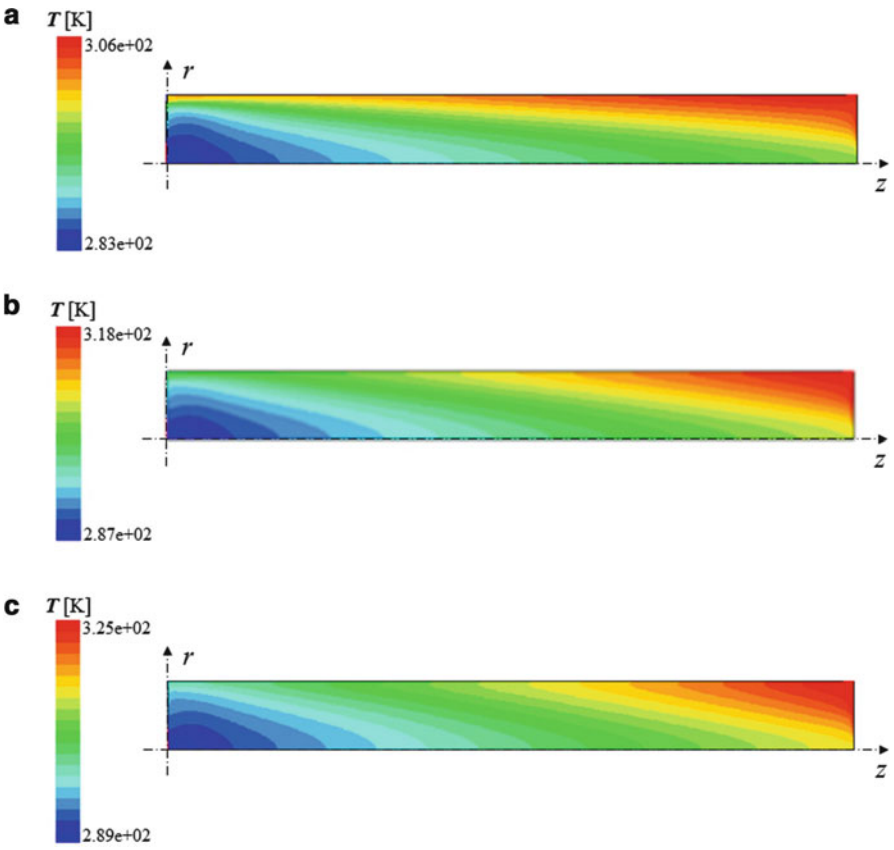

Fig. 15.7 Temperature distribution when $d/D = 0.3$ for several cold mass fractions: (**a**) $y_c = 0.24$, (**b**) $y_{c,o} = 0.56$, (**c**) $y_c = 0.72$

direction. With the increase of y_c the heat flux became more intense in the azimuthal direction (Fig. 15.7b and c). It is interesting to notice that the optimal shape (Fig. 15.7b) has the best distribution of temperature between the hottest and coldest regions, i.e., in agreement with the constructal principle of optimal distribution of imperfections.

Figure 15.8 shows the effect of the cold mass fraction (y_c) on the cooling heat transfer rate (Q_c) for several ratios of d/D. In general, one optimal intermediate value of $y_{c,o}$ is observed for each curve d/D and its corresponding $Q_{c,m}$, with exception of the curve $d/D = 0.6$, where the maximum is reached in the higher extreme of y_c. An interesting behavior is noticed for curves of $d/D = 0.3$ and $d/D = 0.6$. For the range $0.47 \leq y_c \leq 0.56$ the geometry with $d/D = 0.3$ leads to a better performance than that reached for $d/D = 0.6$, while the opposite effect is obtained for the range $0.56 \leq y_c \leq 0.68$. In other words, one ratio of d/D does not lead necessarily to the best thermal performance for all ranges of y_c evaluated.

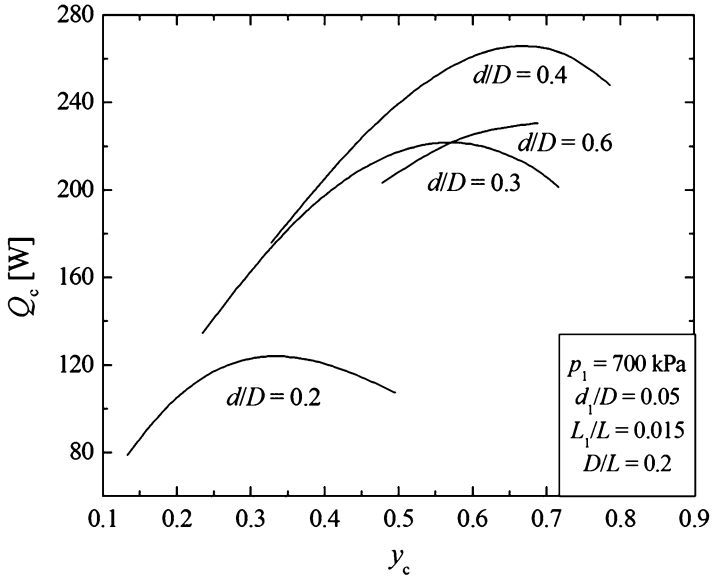

Fig. 15.8 The maximization of the cooling heat transfer rate (Q_c) as function of the of the cold mass fraction (y_c) for several ratios of d/D

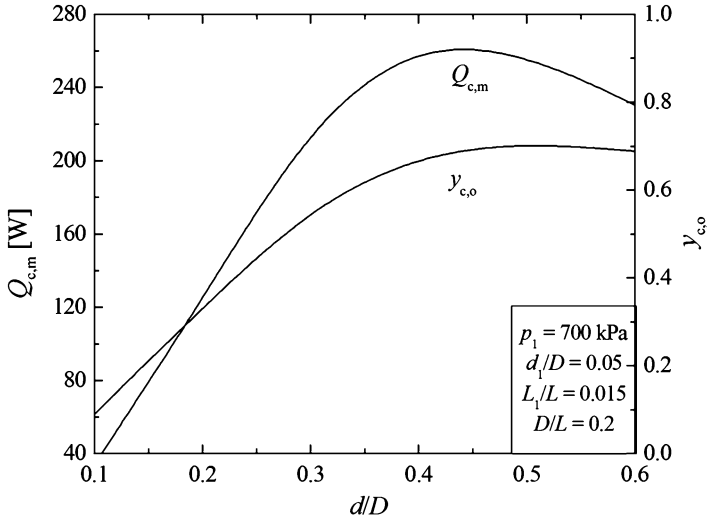

Fig. 15.9 Second optimization of the cooling heat transfer rate ($Q_{c,m}$) and the optimal cold mass fraction ($y_{c,o}$) as function of d/D

The best ratios d/D obtained in Fig. 15.8 are compiled in Fig. 15.9. In this figure it is possible to observe that there is one optimal ratio of $(d/D)_o = 0.43$, which conducts to the second maximization of $Q_{c,mm} = 270$ W and its corresponding $y_{c,oo} = 0.685$, where the subscripts mm and oo mean that the cold heat transfer rate

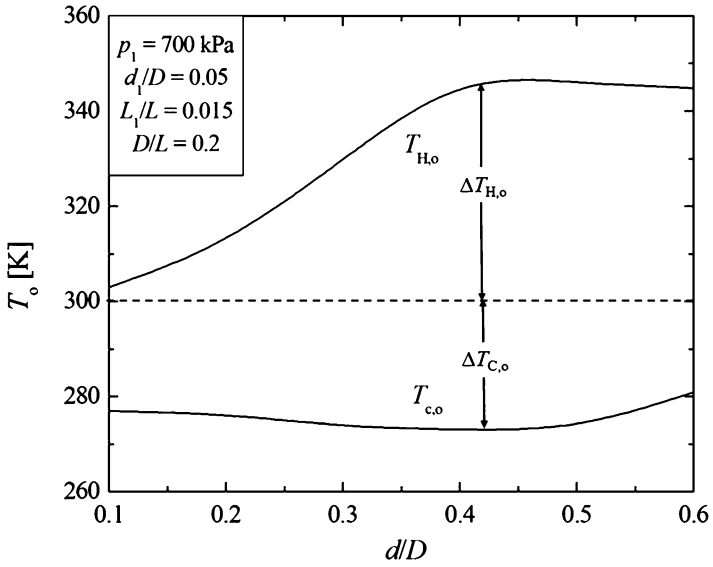

Fig. 15.10 The effect of d/D over the optimal temperature of cold $T_{C,o}$ and hot $T_{H,o}$ outlets

and the cold mass fraction are optimized twice. Other important observation is that the twice maximized cooling heat transfer rate $Q_{c,mm}$ is 87.33% and 14.63% better than the $Q_{c,m}$ obtained for the ratios $d/D = 0.1$ and 0.6, respectively. Moreover, the best cold mass fractions curve $y_{c,o}$ has the same tendency observed for the cooling heat transfer rate curve $Q_{c,m}$. Nonetheless, the ratio of d/D that leads to the highest value of y_c is not the same that leads to the optimal Q_c.

Figure 15.10 shows the effect of the ratio d/D on the temperature of cold $T_{C,o}$ and hot $T_{H,o}$ outlets. Differently from the effect of y_c on the cold air temperature drop (ΔT_C), Fig. 15.6, there is one minimal cold temperature $T_{C,o}$, for $(d/D)_o = 0.43$. In other words, the same ratio d/D that once maximizes the cold heat transfer rate ($Q_{c,m}$) is the same for determination of the maximum cold air temperature drop $\Delta T_{C,o}$. Figure 15.11 shows the vortex tube temperature distribution for the following ratios d/D: $d/D = 0.1$ (Fig. 15.11a), $(d/D)_o = 0.43$ (Fig. 15.11b) and $d/D = 0.6$ (Fig. 15.11c). For the lower ratio $d/D = 0.1$, the temperature gradient is more intense in the radial direction. Similarly to the results observed for the simulations with lower cold mass fractions (Fig. 15.7c). For $(d/D)_o = 0.43$, Fig. 15.11b, the heat flux became more intense in the azimuthal direction, as it occurred when the $y_{c,o}$ is increased (Fig. 15.7b). As the ratio d/D increases, Fig. 15.11c, the temperature gradients are again more intense in the radial direction, reflecting the decrease of $y_{c,o}$ as a function of d/D observed in the Fig. 15.9. It is important to reinforce that, independent of the parameter used for the improvement of the thermal performance (y_c or d/D), the best vortex tube shape is the one that distributes the imperfections better, i. e., the shape that has the best distribution of temperature between the hot and cold outlets.

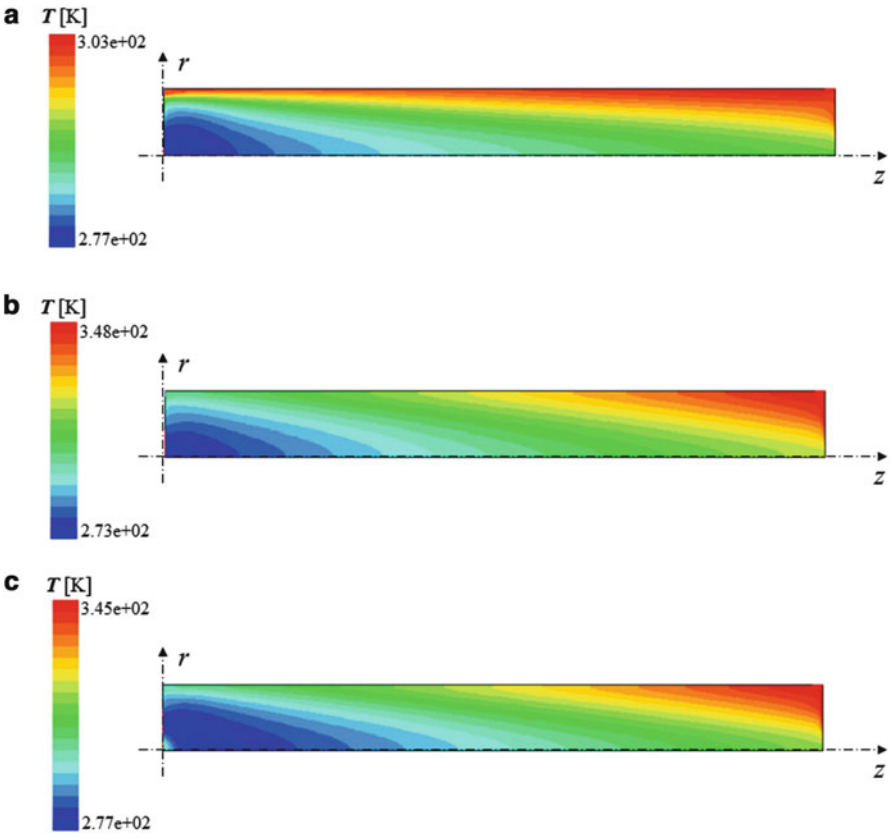

Fig. 15.11 Temperature distribution obtained for several ratios of d/D: (**a**) $d/D = 0.1$, (**b**) $(d/D)_o = 0.43$, and (**c**) $d/D = 0.6$

15.5 Conclusions

In the present work the numerical optimization of a vortex tube device by means of constructal design was considered. A vortex tube with axisymmetric computational domain was evaluated. The compressible and turbulent flows were numerically solved with a commercial CFD package code based on the Finite Volume Method [27]. The turbulence was tackled with the standard k–ε model into the Reynolds Averaged Navier-Stokes (RANS) approach. The cold heat transfer rate Q_c was maximized twice : First, with respect to the cold mass fraction y_c and later with respect to the degree of freedom d/D (the ratio between the diameter of the cold outlet and the diameter of the vortex tube). The other degrees of freedom (d_1/D, L_1/L, and D/L) and the total volume of the vortex tube were kept fixed. It was observed that one optimal ratio $y_{c,o}$ led to the maximum heat transfer rate $Q_{c,m}$ when the ratio d/D was fixed.

The results showed that the best thermal performance of the vortex tube was obtained as a function of the product of the cold mass (m_c), which increases with the increase of y_c, and the cold air temperature drop (ΔT_C), which decreases with the increase of y_c.

The results also showed one optimal geometry given by the ratio $(d/D)_o = 0.43$. The twice maximized cold heat transfer rate ($Q_{c,mm}$) was approximately 87% and 15% better than the lower and upper studied extremes of d/D and its corresponding cold mass fraction was $y_{c,oo} = 0.685$. The same optimal ratio $(d/D)_o = 0.43$ that maximized the cold heat transfer rate was also obtained for the maximization of the cold air temperature drop $\Delta T_{C,o}$. Another important observation was that, independent of the parameter used for the improvement of the thermal performance (y_c or d/D), the best shapes were reached according to the constructal principle of optimal distribution of imperfections.

References

1. Ranque GJ. Expériences sur la détente giratoire avec productions simultanées d'um échappement d'air chaud et d'um échappement d'air froid. J Phys Radium. 1933;4:112S–5. United States Patent No. 1,952,281 (1934).
2. Hilsch R. The use of the expansion of gases in a centrifugal field as a cooling process. Rev Sci Instrum. 1947;18:108–13.
3. Eiamsa-ard S, Promvonge P. Review of Ranque–Hilsch effects in vortex tubes. Renew Sust Energ Rev. 2008;12:1822–42.
4. Fin'ko VE. Cooling and condensation of a gas in a vortex flow. Sov Phys Tech Phys. 1983; 28 (9):1089–93
5. Bruno TJ. Applications of the vortex tube in chemical analysis Part I: introductory principle. Am Lab. 1993;25:15–20.
6. Kirmaci V. Exergy analysis and performance of a counter flow Ranque–Hilsch vortex tube having various nozzle numbers at different inlet pressures of oxygen and air. Int J Refrig. 2009;32:1626–33.
7. Dutta T, Sinhamahapatra KP, Bandyopdhyay SS. Comparison of different turbulence models in predicting the temperature separation in a Ranque-Hilsch vortex tube. Int J Refrig. 2010;33 (4):783–92.
8. Lewis J, Bejan A. Vortex tube optimization theory. Energy. 1999;24:931–43.
9. Harnett JP, Eckert ERG. Experimental study of the velocity and temperature distribution in a high-velocity vortex-type flow. Trans ASME. 1957;79(4):751–8.
10. Stephan K, Lin S, Durst M, Huang F, Seher D. An investigation of energy separation in a vortex tube. Int J Heat Mass Tran. 1983;26(3):341–8.
11. Ahlborn B, Groves S. Secondary flow in a vortex tube. Fluid Dyn Res. 1997;21:73–86.
12. Schlenz D. Kompressible strahlgetriebene drallstromung in rotationssymmetrischen kanalen. Ph.D thesis, Technische Fakultat Universtitat: Erlangen–Nurnberg; 1982
13. Cockerill. Thermodynamics and fluid mechanics of a Ranque–Hilsch vortex tube. Master thesis, University of Cambridge: England; 1995
14. Aljuwayhel NF, Nellis GF, Klein SA. Parametric and internal study of the vortex tube using a CFD model. Int J Refrig. 2005;28:442–50.
15. Farouk T, Farouk B. Large eddy simulations of the flow field and temperature separation in the Ranque-Hilsch vortex tube. Int J Heat Mass Trans. 2007;50:4724–35.

16. Skye HM, Nellis GF, Klein SA. Comparison of CFD analysis to empirical data in a commercial vortex tube. Int J Refrig. 2006;29:71–80.
17. Promvonge P, Eiamsa-ard S. Investigation on the vortex termal separation in a vortex tube refrigerator. ScienceAsia. 2005;31(3):215–23.
18. Aydin O, Baki M. An experimental study on the design parameters of a counter flow vortex tube. Energy. 2006;31(14):2763–72.
19. Pinar AM, Uluer O, Kirmaci V. Optimization of conter flow Ranque–Hilsch vortex tube performance using Taguchi method. Int J Refrig. 2009;32(6):1487–94.
20. Bejan A. Shape and structure, from engineering to nature. Cambridge: Cambridge University Press; 2000.
21. Bejan A, Lorente S. Design with constructal theory. New York: John Wiley and Sons Inc; 2008.
22. Bejan A, Lorente S. Constructal theory of generation of configuration in nature and engineering. J Appl Phys. 2006;100:041301.
23. Beyene A, Peffley J. Constructal theory, adaptive motion, and their theoretical application to low-speed turbine design. J Ener Eng-ASCE. 2009;135(4):112–8.
24. Kim Y, Lorente S, Bejan A. Constructal multi-tube configuration for natural and forced convection in cross-flow. Int J Heat Mass Tran. 2010;53:5121–8.
25. Kim Y, Lorente S, Bejan A. Steam generator structure: continuous model and constructal design. Int J Energ Res. 2011;35:336–45.
26. Azad AV, Amidpour M. Economic optimization of shell and tube heat exchanger based on constructal theory. Energy. 2011;36:1087–96.
27. FLUENT (version 6.3.16). ANSYS Inc; 2007
28. Bejan A. Convection heat transfer. Durhan: Jhon Wiley; 2004.
29. Launder AE, Spalding DB. Lectures in mathematical models of turbulence. London: Academic; 1972.
30. Wilcox AC. Turbulence modeling for CFD. La Canada: DCW Industries; 2002.
31. Patankar SV. Numerical heat transfer and fluid flow. New York: McGraw Hill; 1980.
32. Versteeg HK, Malalasekera W. An introduction to computational fluid dynamics – the finite volume method. England: Longman; 1995.

Chapter 16
Constructal Design of Wave Energy Converters

E.D. dos Santos, B.N. Machado, N. Lopes, J.A. Souza, P.R.F. Teixeira, M.N. Gomes, L.A. Isoldi, and L.A.O. Rocha

16.1 Introduction

The augmentation of energy demand and the Kyoto agreement to reduce the greenhouse gas emissions have increased the interest for the study of renewable energy [1]. The growth and interest in expanding the wave energy sector are based on its potential estimated to be up to 10 TW. Depending on what is considered to be exploitable, this covers from 15 to 66 % of the total world energy consumption referred to 2006 [2–4]. According to ref. [5] the wave energy level is usually expressed as power per unit length (along the wave crest or along the shoreline direction). Typical values for "good" offshore locations (annual average) range between 20 and 70 kW/m and occur mostly in moderate to high latitudes. In this sense, the southern coasts of South America, Africa, and Australia are particularly attractive for wave energy exploitation.

E.D. dos Santos (✉) • B.N. Machado • N. Lopes • P.R.F. Teixeira • L.A. Isoldi
Escola de Engenharia (EE), Universidade Federal de Rio Grande (FURG),
Rio Grande-RS CP 474, Brazil
e-mail: elizaldosantos@furg.br; biancanevesmachado@gmail.com; nathaliapel@hotmail.com; pauloteixeira@furg.br; liercioisoldi@furg.br

J.A. Souza
Department of Mechanical Engineering and Center for Advanced Power Systems
Florida State University, 2525 Pottsdamer St, Room 229, Tallahassee,
FL 32310-6046, USA
e-mail: jasouza1974@gmail.com

M.N. Gomes
Departamento de Engenharia Mecânica, Centro Politécnico, Universidade Federal do Paraná,
Jardim das Américas, Curitiba, Pr CP. 19011, Brazil
e-mail: mateusufpel.gomes@gmail.com

L.A.O. Rocha
Departamento de Engenharia Mecânica (DEMEC), Universidade Federal do
Rio Grande do Sul (UFRGS), Porto Alegre-RS, Brazil
e-mail: laorocha@gmail.com

L.A.O. Rocha et al. (eds.), *Constructal Law and the Unifying Principle of Design*,
Understanding Complex Systems, DOI 10.1007/978-1-4614-5049-8_16,

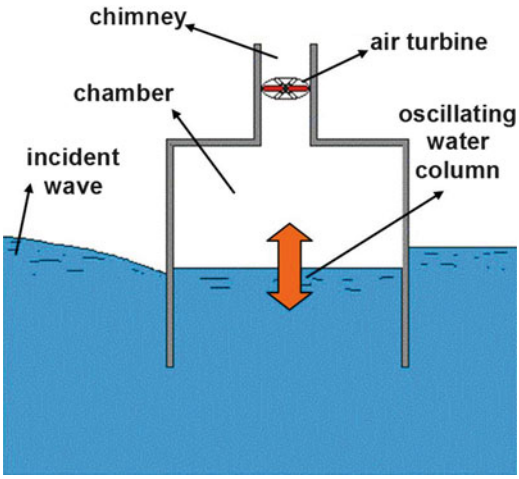

Fig. 16.1 Sketch of an OWC converter

This enormous energy potential of ocean waves has been recognized throughout history. However, it is only in recent times, following the oil crises of the 1970s when attention was focused on the possibility of extracting increased amounts of power from natural energy sources, that the exploitation of ocean waves in the production of electricity was explored in more detail. Experiments on wave energy conversion have indicated that several methods were feasible, and many areas of the world were shown to have the potential coastal wave energy that could be converted into useful power [2].

The wave energy converters (WECs) can be classified according to their placement on the coast [6]: (1) onshore, (2) nearshore (devices placed at depths lower than 20 m), and (3) offshore (devices placed at depths higher than 20 m). The WECs can also be classified according to its main operational principle in three main classes: (1) oscillating water column (OWC), (2) body oscillating (point absorbers or surging devices), and (3) overtopping devices [3]. Important reviews about the technologies employed for wave energy conversion, as well as the progress around the world, have been presented [5, 7–10]. In the next subsections, it will be presented a description of OWC and overtopping devices as well as a brief review of some studies presented in the literature.

16.1.1 Oscillating Water Column

An OWC is a steel or concrete structure with a chamber presenting at least two openings, one in communication with the sea and the other one with the atmosphere, Fig. 16.1. Under the action of waves the free surface inside the chamber oscillates and displaces the air above the free surface. The air is thus forced to flow through a turbine that generates electrical power [11]. Usually a Wells turbine is

employed; such ones, once started, turn in the same direction to extract power from air flowing in either axial direction, i.e., the turbine motion is independent of the fluid direction [12].

The greatest disadvantage of the OWC converter is the large dimensions of its structure. As a result, the cost of a single device is, in general, expensive [5, 12]. An advantage of using the OWC device for power extraction is that the air speed is increased by reduction in the cross-sectional area of the channel approaching the turbine. This couples the slow motion of the waves to the fast rotation of the turbine without mechanical gearing [12]. Another important advantage is that the moving mechanical parts, that is, the turbine and the generator, are not in direct contact with water [5, 12].

Besides, the OWC is one of the most common and most maturated WEC devices. The conceptual studies on OWC started in the 1970s. Up to date, several plants were built in different countries. The most important large-scale OWCs are in service in Portugal (1999) and in UK (2000), which are called Pico and Limpet power plants, respectively.

Several studies have been performed in the literature about OWC. For example, Falcão and Justino [13] developed a theoretical model to simulate the energy conversion, from wave to turbine shaft, of an OWC plant equipped with a Wells air-turbine and with a valve for air-flow control. Brito-Melo et al. [14] investigated numerically the influence of the Wells turbine aerodynamic design on the overall OWC plant performance, as affected by the turbine peak efficiency and the range of flow rates that the turbine can operate efficiently. Conde and Gato [15] presented a numerical study of air-flow in a typical pneumatic chamber geometry of an OWC-WEC, equipped with two vertical-axis air turbines, asymmetrically placed on the top of the chamber. Jayashankar et al. [16] proposed a new topology that uses twin unidirectional turbines for an OWC using data from near shore plants in India and Japan to arrive at the design. Concerning the evaluation of the OWC chamber geometry, Dizadji and Sajadian [17] performed an extensive experimental research evaluating various geometrical designs of an OWC chamber which yield to the maximum conversion of wave energy into useful energy. However, in this work, the evaluation of geometry did not followed Constructal Design, since any restriction for the geometry was not imposed.

This study applies Constructal Design to the geometric optimization of an OWC converter allowing it reaches its best performance, i.e., the maximum conversion between wave energy and electrical energy.

Therefore, employing a 2D computational modeling of an OWC converter, the geometric optimization of the ratio between its chimney and chamber lengths (l/L) was investigated. The ratio between the height and the length of the OWC chamber was kept constant ($H/L = 0.2$). The total volume of the OWC device is also fixed and the ratio between the volume of the chimney and the total device volume ($\phi = 0.15$) is a problem restriction. Maximize the air mass flow rate that crosses the chimney was the objective of the optimization process.

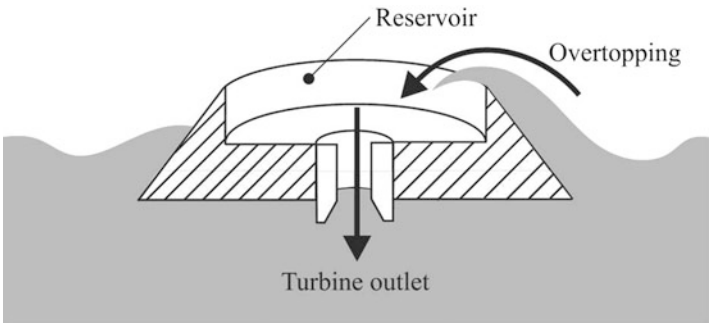

Fig. 16.2 Sketch of an overtopping converter

16.1.2 Overtopping

The overtopping device, which is the other scope of the present chapter, Fig. 16.2, consists of a ramp that captures the water that is close to the wave crest and introduces it, by over spilling, into a reservoir where it is stored at a level higher than the average free-surface level of the surrounding sea. The potential energy of water trapped in the reservoir is then converted to electrical energy through a low head turbine connected to a generator. Examples of important installed overtopping devices are the Wave Dragon (WD) and the Sea Slot-cone Generator (SSG). The SSG structure consists of a number of reservoirs one on the top of each other above the mean water level in which the water of incoming waves is stored temporary.

Concerning the employment of overtopping devices for wave energy conversion, experimental studies have been reported in the literature. For example, Kofoed et al. [18] performed several tests in a WD energy converter prototype, planning for deployment of a 4 MW power production unit. In this study, the prototype was instrumented in order to monitor power production, wave climate, forces in mooring lines, stresses in structure, and movements of WD. The authors established the background to obtain optimal design of the structure and regulation of the power take off system. Tedd and Kofoed [19] studied overtopping flow series on the WD prototype with the aim to maximize the flow in low crested structures. Moreover, a simulation algorithm is tested by comparison with an overtopping flow. Margheritini et al. [20] obtained experimental results to improve the knowledge about the characteristics of a SSG overtopping WEC. The pilot plant studied was an onshore full-scale module in three levels with an expected power production of 320 MWh/year. Margheritini et al. [4] presented the development of a classification of WECs based on the different impact of the technologies to the environment.

Into the numerical framework, Beels et al. [1] employed time-dependent mild-slope equations to model single and multiple WD WECs. The results indicated that a farm of five Wave Dragon WECs installed in a staggered grid with a distance of 2D is preferred, when taking cost and space into account. Neves et al. [21] compared three numerical methods for estimative of the mean volume that

overcomes the ramp: Amazonia (based on the solution of nonlinear equations for shallow waves), Cobras-UC (an eulerian model which uses volume of fluid (VOF) for the multiphase flow), and SPHysics. Besides that, Iahnke [22] evaluated the ramp inclination of an overtopping device for a two-dimensional flow. It was considered a wave climate similar to that found in the southern of Brazil (Rio Grande city, placed at approximately 32°S and 52°W). In that work, the best geometry was reached for an angle of 30º ($H_1/L_1 = 0.58$). It is also worthy to mention that the investigation of overtopping flow over breakwaters and dams has also been subject of several studies [23–26].

The present work aims to discover, by means of the constructal law, the geometrical optimization of an overtopping energy converter. The basic idea here developed is similar to that performed in ref. [22], but now taking into account the total volume and the volume fraction of the ramp as constraints.

16.1.3 Constructal Design Applied for WECs

Constructal theory has been used to explain deterministically the generation of shape in flow structures of nature (river basins, lungs, atmospheric circulation, animal shapes, vascularized tissues, etc.) based on an evolutionary principle of flow access in time. That principle is the Constructal law: for a flow system to persist in time (to survive), it must evolve in such a way that it provides easier and easier access to the currents that flow through it [27, 28].

This same principle is used to yield new designs for electronics, fuel cells, and tree networks for transport of people, goods, and information [29]. The applicability of this method/law to the physics of engineered flow systems has been widely discussed in recent literature [30–33]. However, Constructal law has not been employed yet into the wave energy framework.

16.2 Mathematical Model

16.2.1 Oscillating Water Column Modeling

The optimization process was developed considering a two-dimensional OWC device (Fig. 16.3), being the objective the maximization of the mass flow rate of air passing through the OWC chimney. The wave flow is generated by imposing a velocity field in the left surface of the tank. For the geometric optimization, two constraints were selected: the total volume of OWC converter and the volume fraction of the chimney.

The total volume of OWC, composed by the chamber volume and the chimney volume, is defined by:

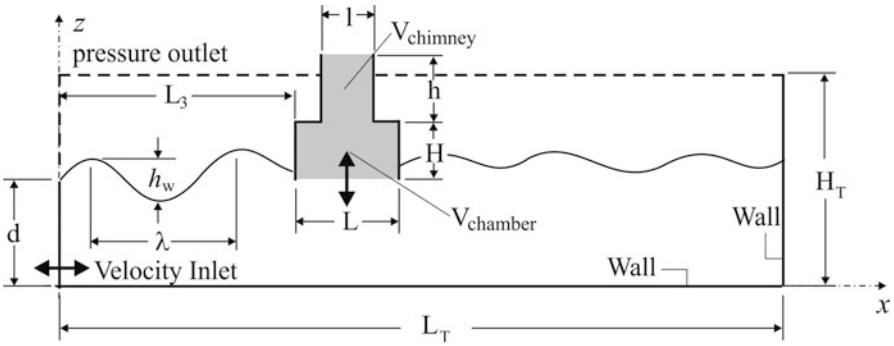

Fig. 16.3 Domain of the OWC device

$$V_{\text{Total}} = V_{\text{Chamber}} + V_{\text{Chimney}} = HLW + hlW, \tag{16.1}$$

where H and L are the height and the length of the chamber, respectively, and h and l are the height and the length of the chimney, respectively. W is the width of the converter (dimension perpendicular to the figure plane). The volume fraction of the chimney is given by:

$$\phi = \frac{V_{\text{Chimney}}}{V_{\text{Total}}} = \frac{hlW}{(HLW + hlW)} = \frac{hl}{(HL + hl)}. \tag{16.2}$$

Completing the requirements to apply the Constructal Design, the degree of freedom l/L (ratio between the chimney and the chamber lengths) was varied, keeping fixed the other parameters: $H/L = 0.2$, $L/\lambda = 2.06$ (the ratio between the chamber and the wave lengths), and $d/\lambda = 0.5$ (the ratio between the depth and the wave length, relative depth). Moreover, the following dimensions and parameters are assumed: $H_{\text{T}} = 1.0$ m, $L_{\text{T}} = 8.0$ m, $L_3 = 3.0$ m, $d = 0.5$ m, $h_{\text{w}} = 0.14$ m, $\lambda = 1.0$ m, $T = 0.8$ s, and a total time of simulation of $t = 8.0$ s.

16.2.2 Overtopping Modeling

The analyzed physical problem for this case consists of a two-dimensional overtopping device placed in a wave tank, as depicted in Fig. 16.4. The third dimension W is perpendicular to the plane of the figure. The wave flow for this case is also generated by imposing a velocity field in the left surface of the tank. The generated waves reach the ramp and the crest water can be spilled into the reservoir.

The objective of the analysis is to determine the optimal geometry (h_{w}/λ, d/λ, h_{w}/d, and H_1/L_1) that leads to the maximum mass flow rate of water entering in the reservoir. As previously mentioned, the degree of freedom H_1/L_1 is optimized, keeping fixed the other parameters: $\phi = 0.02$, $d/\lambda = 0.5$ (the ratio between the

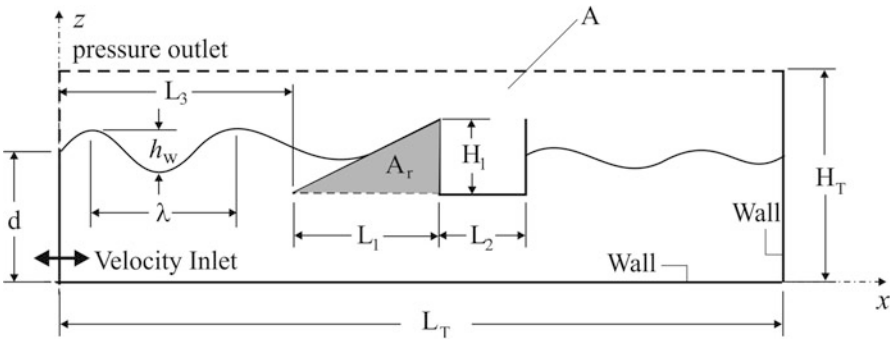

Fig. 16.4 Domain of the overtopping device

depth and the wave length), $h_w/\lambda = 0.12$, and $h_w/d = 0.23$ (the ratio between the wave height and the wave length). Moreover, the following dimensions and parameters are assumed: $H_T = 1.0$ m, $L_T = 8.0$ m, $L_2 = 0.5$ m, $L_3 = 3.0$ m, $h_w = 0.14$ m, $\lambda = 1.2$ m, $d = 0.6$ m, $T = 0.88$ s and a total simulation time of $t = 20.0$ s. In the constructal design framework, the optimization of the present problem is subjected to two constraints, namely, the total area of the wave tank constraint,

$$A = H_T L_T \tag{16.3}$$

and the area of the ramp constraint

$$A_r = \frac{H_1 L_1}{2}, \tag{16.4}$$

where H_T is the wave tank height (m), L_T is the wave tank length (m), H_1 is the ramp height (m), and L_1 is the ramp length (m). Equation (16.4) can be expressed as the device volume (area) fraction

$$\phi = \frac{A_r}{A}. \tag{16.5}$$

16.2.3 The Multiphase Volume of Fluid

The analysis consists in finding the solution of a water–air mixture flow. For the treatment of this kind of flow, the VOF formulation, which is based on the hypothesis of two or more impenetrable phases, is employed. Since the ratio of the density between water and air on the mixture is much higher than unity, it is

expected that this treatment leads to excellent predictions of the phenomenon. It is worth to mention that for each control volume, the sum of the volumetric fractions for all involved phases is unity.

The variable and property fields are shared by the phases and represent averaged values on the volume. It is necessary to know each volumetric fraction of the mixture. The variables and properties for a specific volume represent one of the phases or a mixture of phases, depending on the values of the volume fraction. For a qth volumetric fraction of the fluid, named α_q, three configurations are presented [34]:

$\alpha_q = 0$: the volume is empty (for a q_0 fluid)
$\alpha_q = 1$: the volume is full (for a q_0 fluid)
$0 < \alpha_q < 1$: the volume of q_0 fluid has interface with other phases

For each volume domain, the properties are obtained as a function of the local value of α_q. The placement among the phases is defined from the mass equation solution for the fraction of one or more phases. For the phase q_0, the continuity equation is given by [34]:

$$\frac{\partial}{\partial t}\left(\alpha_q \rho_q\right) + \nabla\left(\alpha_q \rho_q \vec{v}_q\right) = S_{\alpha_q} + \sum_{p=1}^{n}\left(\dot{m}_{pq} - \dot{m}_{qp}\right), \tag{16.6}$$

where $\dot{m}_{qp}$ is the rate of mass transfer from phase q to phase p (kg m^{-3} s^{-1}), $\dot{m}_{pq}$ is the rate of mass transfer from phase p to phase q (kg m^{-3} s^{-1}), and $S_{\alpha q}$ is the mass source term, which is null in the present study. The volume fraction equation is not solved for the primary phase, being computed based on the following restriction:

$$\sum_{q=1}^{n} \alpha_q = 1. \tag{16.7}$$

For a system with n phases, the density is obtained from the weighting of the related phases. Therefore, density can be written by:

$$\rho = \sum \alpha_q \rho_q. \tag{16.8}$$

The momentum equations are solved for the mixture water–air and the velocity fields are shared among the phases. The momentum equations can be written in its vectorial notation by:

$$\frac{\partial}{\partial t}(\rho \vec{v}) + \nabla(\rho \vec{v}\vec{v}) = -\nabla p + \nabla\left(\bar{\bar{\tau}}\right) + \rho \vec{g} + \vec{F}, \tag{16.9}$$

where p is the static pressure (N m^{-2}), $\bar{\bar{\tau}}$ is the viscous stress tensor (N m^{-2}), $\vec{g}$ is the gravitational acceleration (m s^{-2}), and $\vec{F}$ represents external body forces (N m^{-3}).

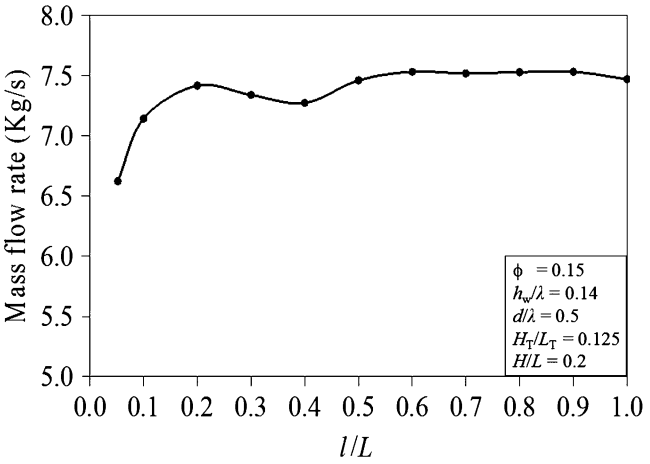

Fig. 16.5 Mass flow rate variation as a function of degree of freedom *l*/*L*

Concerning the waves generation, it is employed a user defined function (UDF) for the entrance velocity of the channel, simulating the wavemaker behavior [35]. The velocities in x and z directions for the entrance channel are, respectively, given by:

$$u = Agk\frac{\cosh(kz+kd)}{\omega\cosh(kd)}\cos(kx-\omega t)+\frac{3}{4}A^2\omega k\frac{\cosh 2k(d+z)}{\sinh^4(kd)}\cos 2(kx-\omega t), \tag{16.10}$$

$$w = Agk\frac{\sinh(kz+kd)}{\omega\cosh(kd)}\sin(kx-\omega t)+\frac{3}{4}A^2\omega k\frac{\sinh 2k(d+z)}{\sinh^4(kd)}\sin 2(kx-\omega t), \tag{16.11}$$

where A is the wave amplitude (m), k is the wave number given by $k = 2\pi/\lambda$ (m^{-1}), d is the water depth (m), T is the wave period (s), ω is the frequency given by $\omega = 2\pi/T$ (rad/s), x is the streamwise coordinate (m), t is the time (s), and z is the normal coordinate (m).

For other boundary conditions, the upper region of the left surface, as well as the upper surface, has prescribed atmospheric pressure (see the dashed surfaces in Figs. 16.5 and 16.6). In the other surfaces of the tank (lower and right surfaces) and in the device (OWC and overtopping) surfaces the velocities are prescribed as null.

For the initial conditions, it is considered that the fluid is still and the free water surface is $d = 0.5$ m for the OWC simulation and $d = 0.6$ m for the overtopping case.

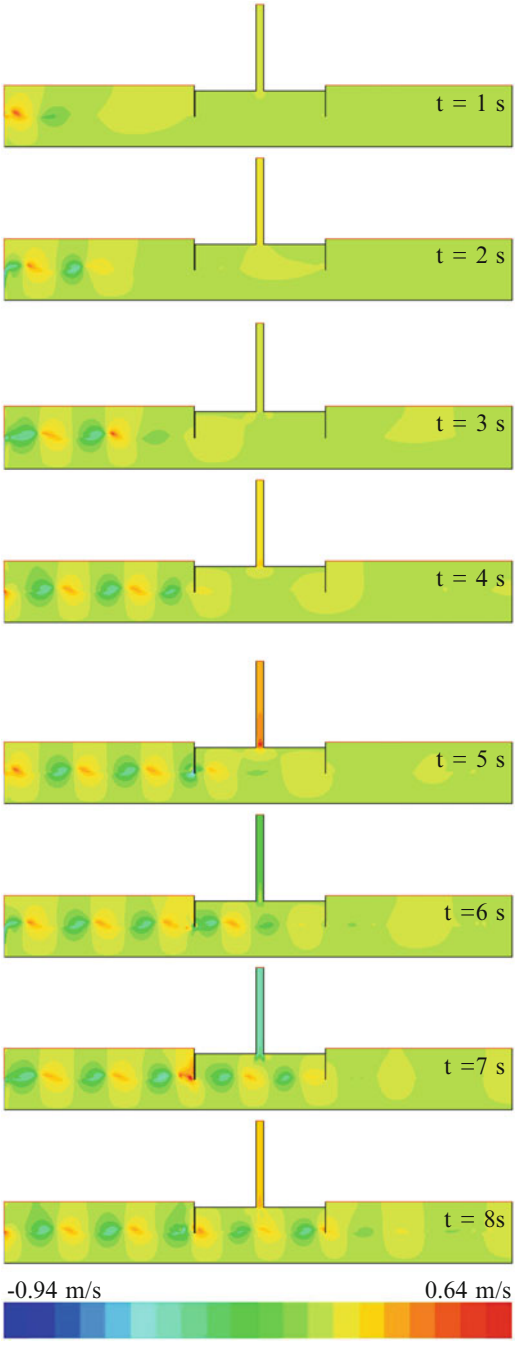

Fig. 16.6 The transversal velocity topology for the worst ratio of $l/L = 0.052$

16.3 Numerical Model

For the numerical simulation of the conservation equations of mass and momentum, a commercial code based on the finite volume method (FVM) [36] is employed. The solver is pressure based and all simulations were performed by upwind and PRESTO! for spatial discretizations of momentum and pressure, respectively. The velocity–pressure coupling is performed by the PISO method, while the GEO-RECONSTRUCTION method is employed to tackle with the volumetric fraction. Moreover, under-relaxation factors of 0.3 and 0.7 are imposed for the conservation equations of continuity and momentum, respectively. More details concerned with the numerical methodology can be obtained in refs. [36–38].

The numerical simulations were performed using a computer with two dual-core Intel processors with 2.67 GHz clock and 8 GB RAM memory. The computations were parallelized by means of Message Passing Interface (MPI). The time processing of each simulation was approximately 3.2×10^4 s (9 h).

It is important to emphasize that this numerical methodology was already validated in previous studies of this research group: Gomes et al. [39] and Gomes [40]. Therefore, for the sake of brevity this validation will not be re-presented in this chapter.

16.4 Results and Discussion

16.4.1 Optimization of the OWC Device

The geometric optimization process, based on the Constructal Design, of the OWC converter was developed considering the following constraints: the volume fraction, $\phi = 0.15$, the design parameters ($L/\lambda = 2.06$, $d/\lambda = 0.5$), and the ratio between height and length of the OWC chamber, $H/L = 0.2$. Several numerical simulations were performed, varying the degree of freedom l/L, as shown in Table 16.1. The OWC dimensions L and H are kept constants and equal to 2.0616 m and 0.4123 m. Hence, to obey the problem constraints, the value of h also varies, as indicated in Table 16.1. Therefore, with these considerations, the influence of this parameter in the mass flow rate of air passing through the OWC chimney was investigated.

Figure 16.5 shows the results for the time-averaged mass flow rate versus the degree of freedom l/L. The maximum value obtained for the time-averaged mass flow rate is nearly 7.54 kg/s and is noticed for the optimal ratio of $(l/L)_o = 0.6$. Moreover, the optimal shape is approximately 12 % better than the worst one, showing the applicability of constructal design for the optimization of OWC-WECs. The time-averaged mass flow rate is almost constant in the range $0.5 \leq l/L \leq 1.0$. For instance, the best shape is only 0.8 % higher than the time-averaged mass flow rate obtained for the ratio $l/L = 1.0$. This behavior can be related with the

Table 16.1 Variable parameters in the optimization process

Simulation	l/L	l (m)	h (m)
1	0.0520	0.1072	1.3992
2	0.1000	0.2062	0.7276
3	0.2000	0.4123	0.3638
4	0.3000	0.6185	0.2425
5	0.4000	0.8246	0.1819
6	0.5000	1.0308	0.1455
7	0.6000	1.2369	0.1213
8	0.7000	1.4431	0.1039
9	0.8000	1.6492	0.0910
10	0.9000	1.8554	0.0808
11	1.0000	2.0616	0.0728

larger ratio of $L/\lambda = 2.06$ employed in the present simulations. More defined points of maximum could be obtained for lower ratios of L/λ and other investigations are required. Other interesting behavior is observed for the range $0.052 \leq l/L \leq 0.4$, where it is noticed an increase of the mass flow rate in the range $0.052 \leq l/L \leq 0.2$ and a subsequent decrease until a local point of minimal mass flow rate for the ratio $l/L = 0.4$.

Figures 16.6 and 16.7 show the transient normal velocity for the ratios: $l/L = 0.052$ (worst) and $(l/L)_o = 0.6$ (optimal), respectively. For the lower ratio of $l/L = 0.052$ (Fig. 16.5) there are large oscillations of the velocity field magnitude inside the chimney as a function of time. However, the cross-sectional area restricts significantly the amount of mass flow rate at the chimney leading to low values of time-averaged mass flow rate ($\dot{m} = 6.6\,\mathrm{kg/s}$). As the ratio l/L increases, the cross-sectional area also increases and the magnitude of the velocity field inside the chimney decreases. However, in the range between $0.2 \leq l/L \leq 0.4$ the decrease of velocity field is more intensive than that observed for the lower ratios of l/L, explaining the local minimum point for the mass flow rate at $l/L = 0.4$. For ratios $l/L \geq 0.6$, the velocity field turns to decrease compensating the augment of the cross-sectional area and leading to time-averaged mass flow rates almost constant.

16.4.2 Optimization of the Overtopping Device

The optimization process consists in the simulation of several geometries with different ratios of H_1/L_1. To evaluate the effect of H_1/L_1 over the overtopping behavior, Fig. 16.8 shows the instantaneous mass flow rate of water that enters the reservoir as a function of time for some values of H_1/L_1. For all analyzed cases, a step inlet of water into the reservoir for specific instants of time is observed. It is worthy of mention that, for $t \geq 15.0$ s the overtopping is not observed for any simulation. For the lower ratios of H_1/L_1 ($H_1/L_1 = 0.4$ and 0.6) the peaks of mass flow rate occur at $t = 5.6$ s and $t = 9.2$ s, while for the higher ratios of H_1/L_1 ($H_1/L_1 = 0.8$ and 1.0) one peak of mass flow rate is observed for $t = 8.3$ s.

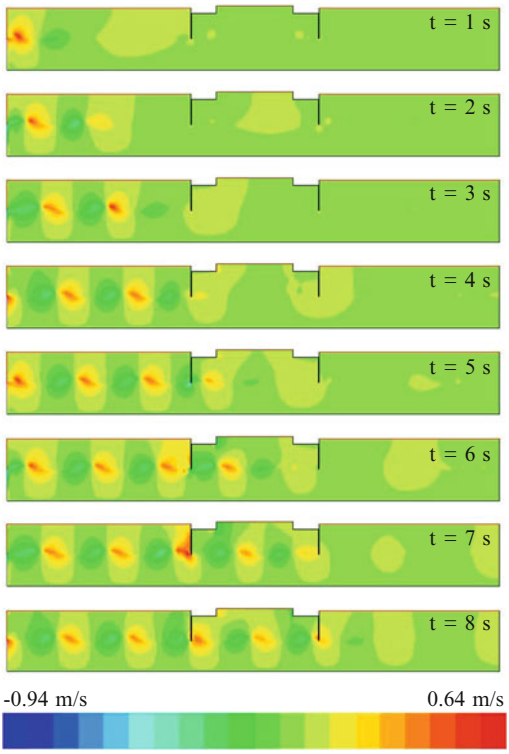

Fig. 16.7 The transversal velocity topology for the optimal ratio of $l/L = 0.60$

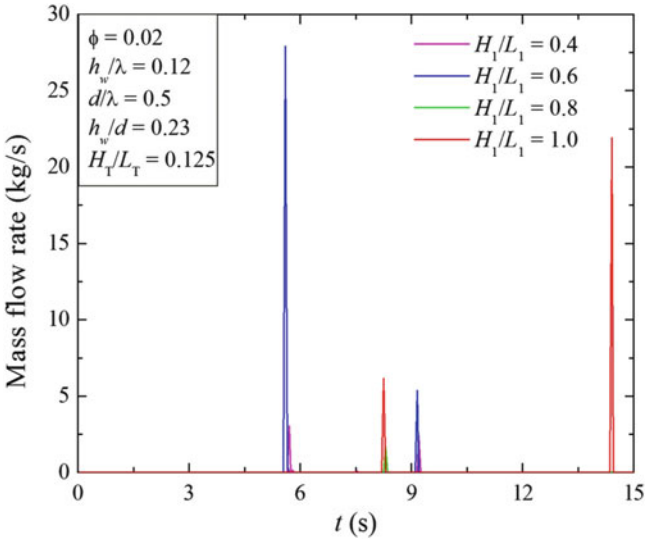

Fig. 16.8 Instantaneous mass flow rate of water in the overtopping device as a function of time for several rates of H_1/L_1

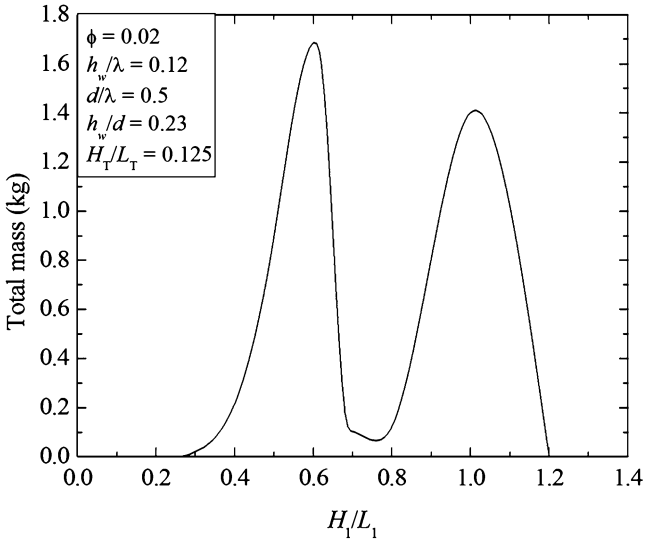

Fig. 16.9 The effect of H_1/L_1 over the amount of mass of water that enters the reservoir

For $t = 14.3$ s, the peak is observed only for $H_1/L_1 = 1.0$. Another important observation is that the mass flow rate peaks reached for $H_1/L_1 = 0.6$ and 1.0 are higher than those observed for $H_1/L_1 = 0.4$ and 0.8. For example, the highest peak obtained for $H_1/L_1 = 0.6$ ($\dot{m} = 27.89\,\text{kg/s}$) and its second peak ($\dot{m} = 5.35\,\text{kg/s}$) are approximately 820 and 76 % higher than the highest peak observed for $H_1/L_1 = 0.4$.

Figure 16.9 exhibits the effect of the ratio H_1/L_1 over the total amount of mass that enters the reservoir along the time. An optimal ratio of $(H_1/L_1)_o = 0.6$ which maximizes the mass that enters into the reservoir along the time ($m_m = 1.6845$ kg) is observed. As expected, the lower and upper extremes of the ratio H_1/L_1 lead to the worst geometries. An interesting behavior is observed for $H_1/L_1 = 1.0$, in which a local point of maximum is obtained ($m = 1.4010$ kg). Moreover, constructal design allowed a significant increase of the device performance. For example, the overtopped amount of mass for the optimal ratio is approximately 20 times higher than the one observed for the ratio $H_1/L_1 = 0.75$, which is the case with the minimal amount of mass among the cases in which overtopping occurs.

Figure 16.10 shows the transient behavior of the wave generated in the wave tank over the ramp for the lowest ratio of $H_1/L_1 = 0.1$. The topologies are presented for the following time steps: $t = 1.0$ s, 4.0 s, 5.6 s, 8.5 s and 9.2 s, and they are shown, respectively, in Fig. 16.10a–e. Note that the initial formation of the first wave due to the imposition of the velocity fields in the inlet surface of the wave tank is observed for $t = 1.0$ s (Fig. 16.10a). The incidence of the wave over the ramp can also be seen for $t = 4.0$ s (Fig. 16.10b). Afterwards, for $t = 5.6$ s (Fig. 16.10c), the flow is meagered and the dissipation of the wave can also be observed. As a consequence, the water of the wave remains far from the reservoir. It is possible

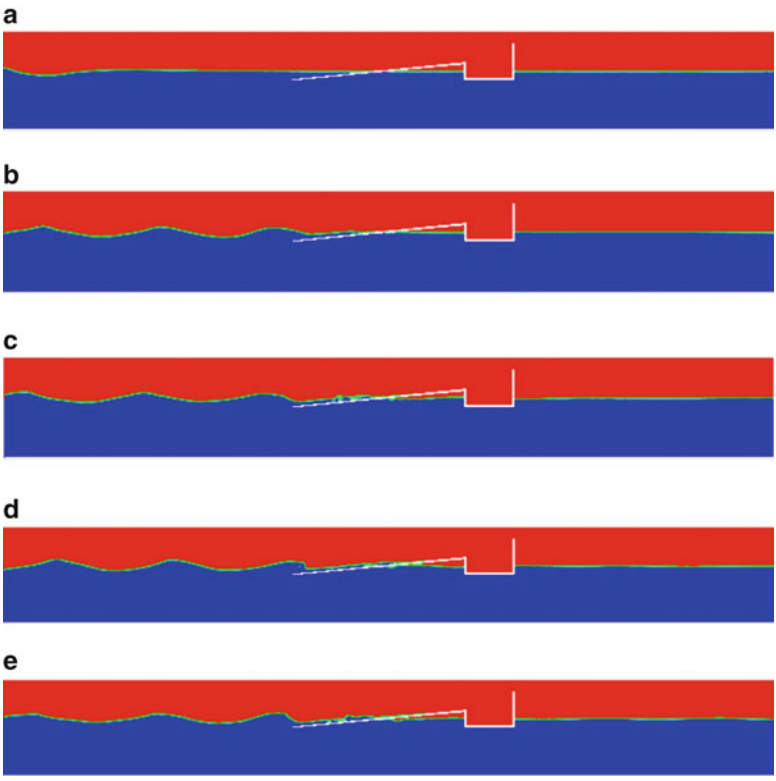

Fig. 16.10 The transient wave flow with the ratio $H_1/L_1 = 0.1$ for the following time steps: (**a**) $t = 1.0$ s, (**b**) $t = 4.0$ s, (**c**) $t = 5.6$ s, (**d**) $t = 8.5$ s, (**e**) $t = 9.2$ s

to observe the wave reflection caused by the overtopping device for Fig. 16.10d and e, $t = 8.5$ s and 9.2 s. In spite of the lower height of the ramp for the case $H_1/L_1 = 0.1$, the water does not spill the reservoir due to the kinetic energy dissipation imposed by the larger length of the ramp. The behavior in this case is similar to that observed for the flow in a beach.

Figure 16.11 shows the transient behavior of the wave generated in the wave tank over the ramp for the highest ratio of $H_1/L_1 = 1.2$. The topologies of the flow are obtained for the same time steps of the earlier case, i.e., $t = 1.0$ s, $t = 4.0$ s, $t = 5.6$ s, $t = 8.5$ s, and $t = 9.2$ s (Fig. 16.11a–e). For this case, the height of the ramp increases significantly and the ramp behaves like a wall. Figure 16.11a and b show the initial formation of waves besides incoming waves over the ramp. Figure 16.11c and d show the conversion of kinetic into potential energies, change which is observed in its amplitude. However, for any evaluated time steps, the increase of the wave height is not enough to allow the overtopping of the water flow. Afterwards, the reflection caused by the ramp induces the smoothing of the wave (Fig. 16.11e). Therefore, the mechanisms which avoid the overtopping are different for the lowest and highest ratios of H_1/L_1. In the former case

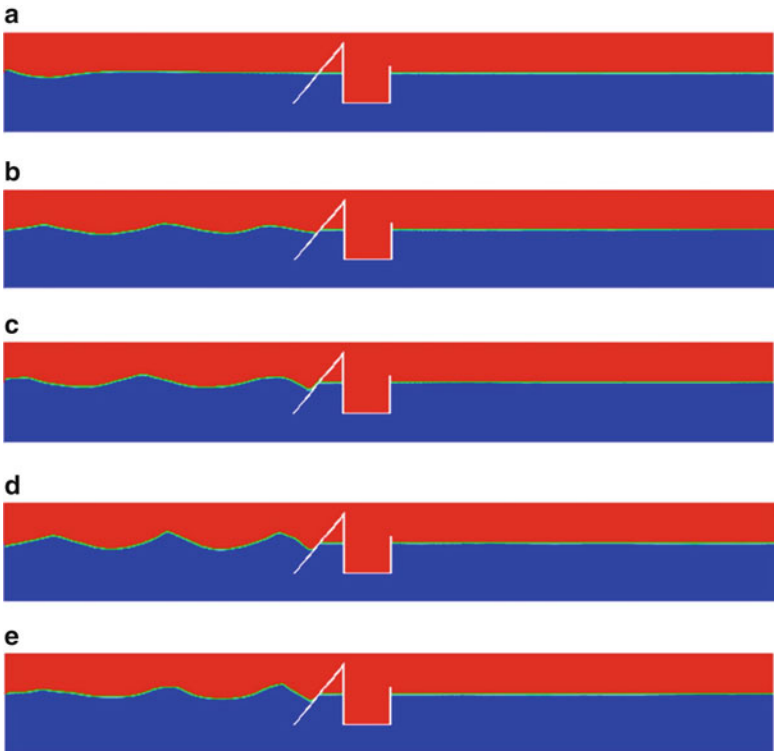

Fig. 16.11 The transient wave flow with the ratio $H_1/L_1 = 1.2$ for the following time steps: (**a**) $t = 1.0$ s, (**b**) $t = 4.0$ s, (**c**) $t = 5.6$ s, (**d**) $t = 8.5$ s, (**e**) $t = 9.2$ s

($H_1/L_1 = 0.1$), the fact that overtopping does not occur is concerned with the kinetic energy dissipation in the ramp, while in the latter case ($H_1/L_1 = 1.2$) the nonoccurrence of overtopping is related to the conversion of part of kinetic energy into potential energy, generating waves with amplitudes lower than the height of the ramp.

Figure 16.12 shows the transient wave flow for the optimized ratio of H_1/L_1. The topologies of the flow are obtained for the following time steps: $t = 1.0$ s, $t = 4.0$ s, $t = 5.6$ s, $t = 8.2$ s, and $t = 9.2$ s (Fig. 16.12a–e). For the initial time steps, Fig. 16.12a and b, the behavior obtained for the earlier cases is also noted here. For $t = 5.6$ s, the overtopping of the water wave flow is observed. In comparison with lower ratios of H_1/L_1 geometries, the optimal ratio of $(H_1/L_1)_o = 0.6$ leads to a lower suppression of the wave kinetic energy. For $t = 8.2$ s, Fig. 16.12d, the overtopping occurs again with a minor intensity. This decrease of the amount of mass that enters into the reservoir can be related to the conversion of kinetic energy into potential energy before the wave overtops the ramp, i.e., the wave reaches the devices with lower kinetic energy and does not go into the reservoir again.

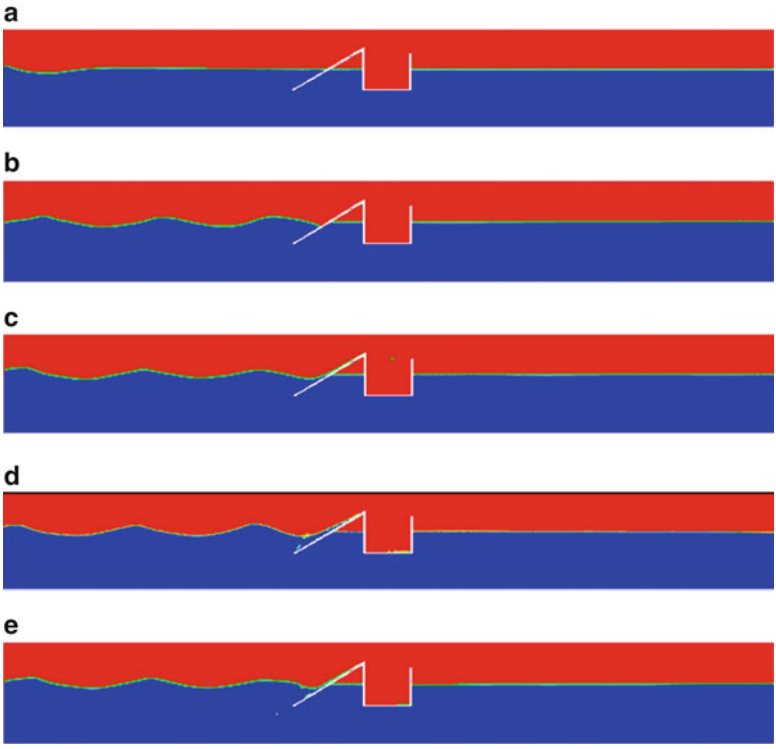

Fig. 16.12 The transient wave flow with the ratio $H_1/L_1 = 0.6$ for the following time steps: (**a**) $t = 1.0$ s, (**b**) $t = 4.0$ s, (**c**) $t = 5.6$ s, (**d**) $t = 8.2$ s, (**e**) $t = 9.2$ s

Figure 16.13 exhibits the transient wave flow for the ratio $H_1/L_1 = 1.0$, in which a local maximum mass entering into the reservoir is observed. For initial time steps, Fig. 16.13a and b, the same behavior for the previous cases is observed here. For $t = 5.6$ s, Fig. 16.13c, the water does not have enough kinetic energy to overtop the ramp. Afterwards, the reflection caused by the ramp (Fig. 16.13d) increases the wave amplitude up to a point where the overtopping is observed, for $t = 14.3$ s. Unlike the optimal case, in which the increase of the wave amplitude minimizes the magnitude of the mass flow rate from the first to the second peak, in this case ($H_1/L_1 = 1.0$), the increase of the wave potential energy also increases the magnitude of the mass flow rate from the first to the second peak.

16.5 Conclusions

Nowadays it is evident the requirement to employ alternative and renewable energy sources. One of these sources is in the oceans, more specifically in wave energy. Several devices were proposed to convert the energy from the ocean waves into

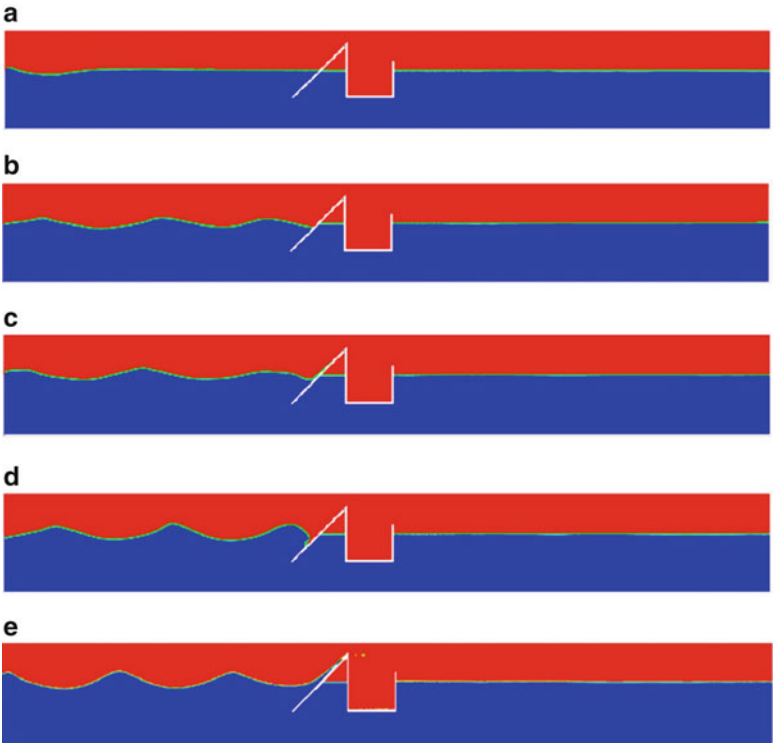

Fig. 16.13 The transient wave flow with the ratio $H_1/L_1 = 1.0$ for the following time steps: (**a**) $t = 1.0$ s, (**b**) $t = 4.0$ s, (**c**) $t = 5.6$ s, (**d**) $t = 8.5$ s, (**e**) $t = 14.3$ s

electricity. As a consequence, the geometric optimization of these devices, which will lead to a rationalization of energy resources, is also important.

The present study showed a numerical evaluation of the geometry of OWC and overtopping energy converters by means of Constructal Design. The geometric optimization of the OWC was performed varying the degree of freedom l/L, while the total volume of the OWC device was kept constant. Besides, all numerical simulations were performed with $H/L = 0.2$, $\phi = 0.15$, $L/\lambda = 2.06$, and $d/\lambda = 0.5$. Concerning the overtopping device, the degree of freedom H_1/L_1 was optimized, keeping the device volume fraction, $\phi = 0.02$, and the wave flow parameters: $h_w/\lambda = 0.12$, $d/\lambda = 0.5$, and $h_w/d = 0.23$ fixed. The conservation equations of mass and momentum were solved with a commercial code based on the finite volume method (FVM). The multiphase VOF model and a wavemaker were adopted to generate regular incident waves in the tank.

The numerical results presented in this chapter illustrated the applicability of Constructal Design for the optimization of WECs (rationalization of energetic resources). It was also observed that the shape which leads to the best conversion of energy is the same one which minimizes the resistances of the fluid flow (imperfections).

The results indicated that the highest mass flow rate of air in the chimney was achieved for an optimal ratio of $(l/L)_o = 0.6$ for the OWC device. This optimal geometry was 12 % better than the worst geometry ($l/L = 0.052$). Moreover, in the range $0.5 \leq l/L \leq 1.0$ the mass flow rate results showed a pattern quite similar. This behavior can be related with the larger ratio of $L/\lambda = 2.06$ employed in the present study.

Concerning the overtopping device, the differences were more evident. For example, the amount of mass that entered into the reservoir for the optimal geometry, $(H_1/L_1)_o = 0.6$, was 20 times higher than the one found for the ratio $H_1/L_1 = 0.75$, which was the case with the minimal amount of mass among the cases in which overtopping occurs. Another interesting observation was that there was one local point of maximum for $H_1/L_1 = 1.0$. Moreover, the lower and upper extremes of the ratio H_1/L_1 conducted to worst performances.

References

1. Beels C, Troch P, De Visch K, Kofoed JP, De Backer G. Application of time-dependent mild slope equations for the simulation of wake effects in the lee of a farm of wave dragon wave energy converters. Renew Energ. 2010;35:1644–61.
2. Engineering Committee on Oceanic Resources – Working Group on Wave Energy Conversion. Wave energy conversion. John Brooke, editor. Oxford: Elsevier; 2003
3. Cruz J, Gunnar M, Barstow S, Mollison D. Green energy and technology. In: Ocean wave energy. Joao Cruz, editor. Heidelberg: Springer; 2008
4. Margheritini L, Hansen AM, Frigaard P. A method for EIA scoping of wave energy converters – based on classification of the used technology. Environ Impact Asses. 2012;32:33–44.
5. Falcão AFO. Wave energy utilization: a review of the technologies. Renew Sust Energ Rev. 2010;14:899–918.
6. Cruz J, Sarmento A. Wave energy – introduction to technological, economical and environmental aspects (in portuguese). Portugal Instituto do Ambiente Alfragide; 2004
7. Clément A, McCullen P, Falcão A, Fiorentino A, Gardner F, Hammarlund K, Lemonis G, Lewis T, Nielsen K, Petroncini S, Pontes MT, Schild P, Sjöström BO, Sørensen HC, Thorpe T. Wave energy in Europe: current status and perspectives. Renew Sust Energ Rev. 2002;6:405–31.
8. Zhang D, Li W, Lin Y. Wave energy in chine: current status and perspectives. Renew Energ. 2009;34:2089–92.
9. Bahaj A. Generating electricity from the oceans. Renew Sust Energ Rev. 2011;15:3399–416.
10. Zabihian F, Fung AS. Review of marine renewable energies: case study of Iran. Renew Sust Energ Rev. 2011;15:2461–74.
11. Nielsen FG, Andersen M, Argyriadis K, Butterfield S, Fonseca N, Kuroiwa T, Le Boulluec M, Liao S-J, Turnock SR, Waegter J. Ocean wind and wave energy utilization. Southampton: ISSC; 2006
12. Twidell J, Weir T. Renewable energy resources. London: Taylor and Francis; 2006.
13. Falcao AFO, Justino PAP. OWC wave energy devices with air flow control. Ocean Eng. 1999;26:1275–95.
14. Brito-Melo A, Gato LMC, Sarmento AJNA. Analysis of wells turbine design parameters by numerical simulation of the OWC performance. Ocean Eng. 2002;29:1463–77.
15. Condenad JMP, Gato LMC. Numerical study of the air-flow in an oscillating water column wave energy converter. Renew Energ. 2008;33:2637–44.

16. Jayashankar V, Anand S, Geetha T, Santhakumar S, Jagadeesh Kumar V, Ravindran M, Setoguchi T, Takao M, Toyota K, Nagata S. A twin unidirectional impulse turbine topology for OWC based wave energy plants. Renew Ener. 2009;34:692–8.
17. Dizadji N, Sajadian SE. Modeling and optimization of the chamber of OWC system. Energy. 2011;36:2360–6.
18. Kofoed JP, Frigaard P, Friis-Madsen E, Sørensen HC. Prototype testing of the wave energy converter wave dragon. Renew Energ. 2006;31:181–9.
19. Tedd J, Kofoed JP. Measurements of overtopping flow time series on the wave dragon, wave energy converter. Renew Energ. 2009;34:711–17.
20. Margheritini L, Vicinanza D, Frigaard P. SSG wave energy converter: design, reliability and hydraulic performance of an innovative overtopping device. Renew Energ. 2009;34:1371–80.
21. Neves MG, Reis MT, Didier E. Comparison of wave overtopping at coastal structures calculated with AMAZON, COBRAS-UC and SPHysics. Proceedings of the V European Conference on Computational Fluid Dynamics, ECCOMAS CFD; Lisbon, Portugal; 2010
22. Iahnke SLP. State of the art and development of an numerical simulation model for the overtopping principle (in Portuguese). MSc. thesis. Universidade Federal do Rio Grande; Rio Grande, Brasil; 2010
23. Van der Meer JW, Janssen JPFM. Wave run-up and wave overtopping at dikes. In: Kobayashi N, Dermirbilek, editors. Wave forces on inclined and vertical wall structures. ASCE, p.1–27. Also Delft Hydraulics, Publication. 487, 1994
24. Franco L, Gerloni M de, Van der Meer JW. Wave overtopping on vertical and composite breakwaters. In: Proceedings of the 24th International Conference on Coastal Engineering; 1995 Kobe, Japan. pp. 1030–44
25. Briganti R, Bellotti G, Franco L, De Rouck J, Geeraerts J. Field measurements of wave overtopping at the rubble mound breakwater of Rome–Ostia yacht harbour. Coast Eng. 2005;52:1155–74.
26. Cáceres I, Stive MJF, Sánchez-Arcilla A, Trung LH. Quantification of changes in current intensities induced by wave overtopping around low-crested structures. Coast Eng. 2008;55:113–24.
27. Bejan A. Shape and Structure, from Engineering to Nature. Cambridge: Cambridge University Press; 2000.
28. Bejan A, Lorente S. Design with constructal theory. New York: John Wiley and Sons Inc; 2008.
29. Bejan A, Lorente S. Constructal theory of generation of configuration in nature and engineering. J Appl Phys. 2006;100:041301.
30. Beyene A, Peffley J. Constructal theory, adaptive motion, and their theoretical application to low-speed turbine design. J Energ Eng-ASCE. 2009;135(4):112–8.
31. Kim Y, Lorente S, Bejan A. Constructal multi-tube configuration for natural and forced convection in cross-flow. Int J Heat Mass Tran. 2010;53:5121–8.
32. Kim Y, Lorente S, Bejan A. Steam generator structure: continuous model and constructal design. Int J Energ Res. 2011;35:336–45.
33. Azad AV, Amidpour M. Economic optimization of shell and tube heat exchanger based on constructal theory. Energy. 2011;36:1087–96.
34. Ling L, Yongcan C, Yuliang L. Volume of fluid (VOF) method for curved free surface water flow in shallow open channel. Department of hydraulic engineering, Tsinghua University, Beijing; 2001
35. Horko M. CFD Optimization of an oscillating water column energy converter. MSc thesis. School of mechanical engineering, The University of Western. Australia; 2007
36. FLUENT (version 6.3.16). ANSYS Inc; 2007
37. Patankar SV. Numerical heat transfer and fluid flow. New York: McGraw Hill; 1980.
38. Versteeg HK, Malalasekera W. An introduction to computational fluid dynamics – the finite volume method. England: Longman; 1995.
39. Das M, Gomes N, Olinto CR, Rocha LAO, Souza JA, Isoldi LA. Computational modeling of a regular wave tank. Engenharia Térmica. 2009;8:44–50.
40. Das M, Gomes N. Computational modeling of na oscillating water column device to conversion of wave energy into electrical energy (in Portuguese). MSc thesis. Universidade Federal do Rio Grande; Brasil; 2010

Chapter 17
Constructal Design of Thermal Systems

L.A.O. Rocha, E.D. dos Santos, D.C. Cunha, F.L. Garcia, G. Lorenzini, C. Biserni, M. Letzow, J.A.V. Costa, J.A. Souza, and L.A. Isoldi

17.1 Introduction

Constructal theory and design accounts for the universal phenomenon of generation and evolution of design [1, 2]. Constructal theory has been used to explain deterministically the generation of shape in flow structures of nature (river basins, lungs, atmospheric circulation, animal shapes, vascularized tissues, etc.) based on an evolutionary principle of flow access in time. That principle is the Constructal law: "for a flow system to persist in time "to survive," it must evolve in such way that it provides easier and easier access to the currents that flow through it" [2]. This same principle is used to yield new designs for electronics, fuel cells, and tree networks for transport of people, goods, and information [3]. The applicability of

L.A.O. Rocha (✉) • F.L. Garcia
Departamento de Engenharia Mecânica (DEMEC), Universidade Federal do Rio Grande do Sul (UFRGS), Porto Alegre, RS, Brazil
e-mail: laorocha@gmail.com; feulink@gmail.com

E.D. dos Santos • L.A. Isoldi
Escola de Engenharia (EE), Universidade Federal de Rio Grande (FURG), CP 474, Rio Grande, RS, Brazil
e-mail: elizoldodosantos@furg.br; liercioisoldi@furg.br

D.C. Cunha
Instituto Federal de Educação, Ciência e Tecnologia do Rio Grande do Sul, Campus Rio Grande, Rua Eng. Alfredo Huch, 475, Rio Grande 96201-460, RS, Brazil
e-mail: daniele.cunha@riogrande.ifrs.edu.br

G. Lorenzini
Dipartimento di Ingegneria Industriale, Università degli Sudi di Parma, Parco Area delle Scienze 181/A, 43124 Parma, Italy
e-mail: giulio.lorenzini@libero.it

C. Biserni
Dipartimento di Ingegneria Energetica, Nucleare e del Controllo Ambientale, Università degli Studi di Bologna, Viale Risorgimento 2, 40136 Bologna, Italy
e-mail: cesare.biserni@mail.ing.unibo.it

L.A.O. Rocha et al. (eds.), *Constructal Law and the Unifying Principle of Design*, Understanding Complex Systems, DOI 10.1007/978-1-4614-5049-8_17,

this method/law to the physics of engineered flow systems has been widely discussed in recent literature [4–7].

One important subject in engineering is the study of fins arrays. This fact is concerned with its employability in many applications, such as heat exchangers, microelectronics, cooling of internal combustion engines, and electric motors [8, 9]. The study of fins has also been the subject of optimization by means of Constructal Design. Bejan and Almogbel [10] optimized a T-shaped assembly of fins. The objective was to maximize the global thermal conductance subject to total volume and fin material constraints. After that, several configurations of assembly of fins were extensively studied [11–14].

As cavities can be considered as spaces between adjacent fins, they also play an important role in the heat transfer field and Constructal Design has been successfully applied to the study of cooling cavities intruded into conducting solids with uniform heat generation. Several shapes, from the elemental C-shaped cavity to the complex T-Y cavity, have been investigated [15–19].

Recently, Constructal design has also been applied to bioreactors in solid-state fermentation to discover the shape of the bioreactor that allows heat currents to be removed easily from the hot medium [20, 21].

This chapter considers the constructal design of three thermal systems: T-shaped cavity, electric motor fins, and hollow bioreactor for solid-state fermentation. Giving freedom to the thermal systems, the best shapes will emerge according to the Constructal Law.

17.2 T-Shaped Cavity

This section studies an open cavity shaped as T intruding into a solid conducting wall, as shown in Fig. 17.1. The structure has four degrees of freedom: L_0/L_1 (ratio between the lengths of the stem and bifurcated branches), H_1/L_1 (ratio between the thickness and length of the bifurcated branches), H_0/L_0 (ratio between the thickness and length of the stem), and H/L (ratio between the height and length of the conducting solid wall) and two restrictions, the ratio between the cavity

M. Letzow
Programa de Pós-Graduação em Modelagem Computacional, Universidade Federal do Rio Grande, Avenida Itália, km 8, CP. 474Rio Grande, RS, Brazil
e-mail: max.letzow@bol.com.br

J.A.V. Costa
Escola de Química e Engenharia de Alimentos, Universidade Federal do Rio Grande, CP 474Rio Grande, RS 96201-900, Brazil
e-mail: v_costa@mec.ua.pt

J.A. Souza
Department of Mechanical Engineering and Center for Advanced Power Systems
Florida State University, 2525 Pottsdamer St, Room 229, Tallahassee, FL 32310-6046, USA
e-mail: jasouza1974@gmail.com

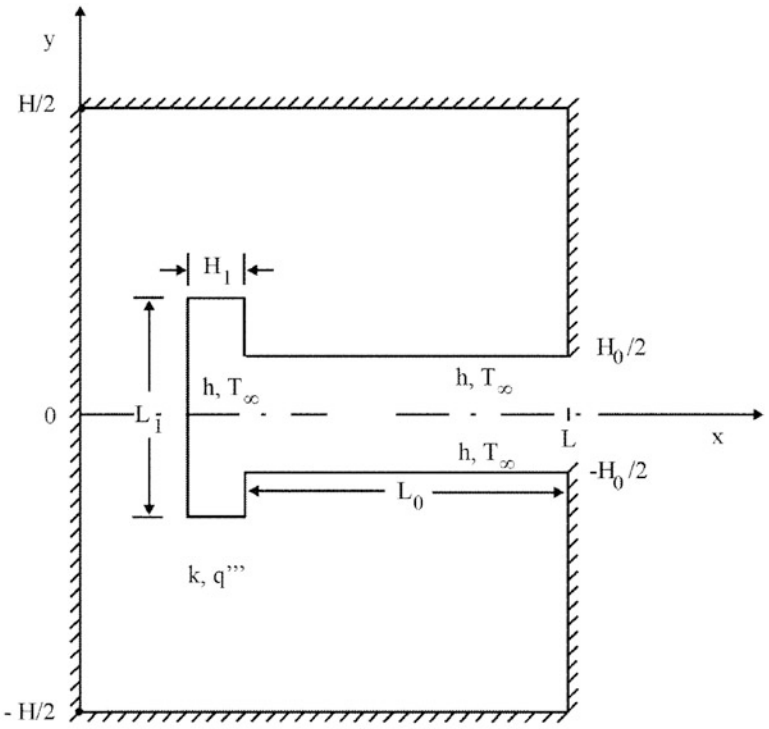

Fig. 17.1 T-shaped cavity cooled by convection

volume and solid volume (ϕ) and the total volume. The purpose of the numerical investigation is to minimize the dimensionless global thermal resistance between the cavity and the ambient. The configuration is two-dimensional, with the third dimension (W) sufficiently long in comparison with the height H and the length L of the volume occupied by the body. The solid is isotropic with the constant thermal conductivity k. It generates heat uniformly at the volumetric rate q''' (W/m^3). The outer surfaces of the solid are perfectly insulated. The generated heat current ($q'''A$) is removed by convective heat transfer through the cavities' walls. The heat transfer coefficient h is uniform over all the exposed surfaces.

The objective of the analysis is to determine the geometry (L_0/L_1, H/L, H_0/L_0, H_1/L_1) that minimizes the dimensionless global thermal resistance $\theta_{\max} = \frac{T_{\max} - T_\infty}{q'''A/k}$. According to constructal design, this optimization can be subjected to two constraints, namely, the total area constraint,

$$A = HL, \tag{17.1}$$

and the cavity area constraint,

$$A_c = H_0 L_0 + H_1 L_1. \tag{17.2}$$

Equations (17.1)–(17.2) can be expressed as the cavity area fraction:

$$\phi = \frac{A_c}{A}. \tag{17.3}$$

The analysis that delivers the global thermal resistance as a function of the geometry consists of solving numerically the heat conduction equation along the solid region,

$$\frac{\partial^2 \theta}{\partial \tilde{x}^2} + \frac{\partial^2 \theta}{\partial \tilde{y}^2} + 1 = 0, \tag{17.4}$$

where the dimensionless variables are

$$\theta = \frac{T - T_\infty}{q''' A/k} \tag{17.5}$$

and

$$\tilde{x}, \tilde{y}, \tilde{H}_0, \tilde{L}_0, \tilde{H}_1, \tilde{L}_1, \tilde{H}, \tilde{L} = \frac{x, y, H_0, L_0, H_1, L_1, H, L}{A^{1/2}}. \tag{17.6}$$

The outer surfaces are insulated, i.e.,

$$\frac{\partial \theta}{\partial \tilde{x}} = 0 \text{ or } \frac{\partial \theta}{\partial \tilde{y}} = 0. \tag{17.7}$$

The boundary conditions on the cavity surfaces come from balancing the conduction and convection heat transfer, and their dimensionless resulting values are given by

$$-\frac{\partial \theta}{\partial \tilde{x}} = \frac{a^2 \theta}{2} \text{ or } -\frac{\partial \theta}{\partial \tilde{y}} = \frac{a^2 \theta}{2}. \tag{17.8}$$

The parameter (a) that emerged in (17.8) was already used by Bejan and Almogbel [10] and it is defined as

$$a = \left(\frac{2hA^{1/2}}{k} \right)^{1/2}. \tag{17.9}$$

The dimensionless forms of (17.1) and (17.3) are

$$\tilde{H}\tilde{L} = 1, \tag{17.10}$$

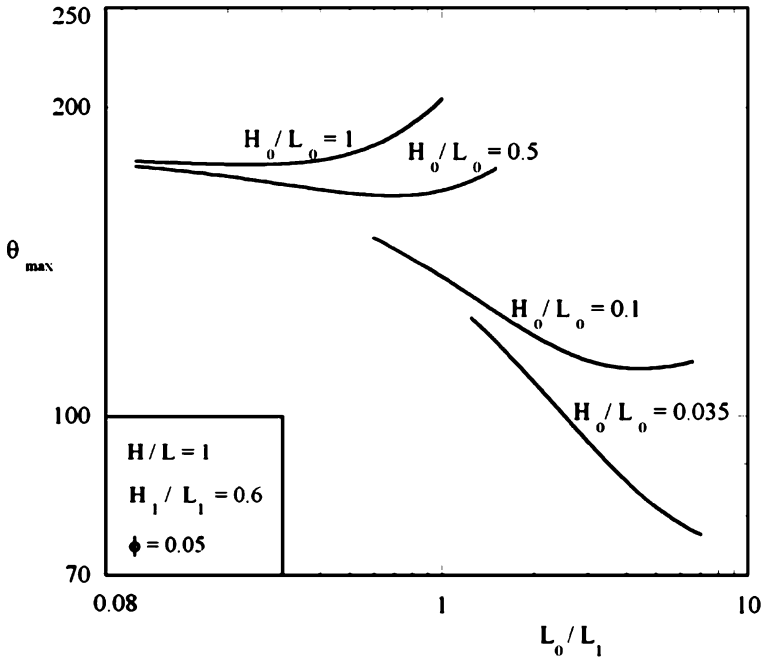

Fig. 17.2 The optimization of the dimensionless global thermal resistance as a function of the ratio L_0/L_1 for several values of the ratio H_0/L_0

$$\phi = \tilde{H}_0\tilde{L}_0 + \tilde{H}_1\tilde{L}_1. \tag{17.11}$$

The dimensionless global thermal resistance, $\theta_{\max}$, is our objective function and is defined as

$$\theta_{\max} = \frac{T_{\max} - T_\infty}{q'''A/k}. \tag{17.12}$$

The function defined by (17.12) can be determined numerically, by solving (17.4) for the temperature field in every assumed configuration (L_0/L_1, H/L, H_0/L_0, H_1/L_1) of the type shown in Fig. 17.1 and calculating $\theta_{\max}$ to see whether $\theta_{\max}$ can be minimized by varying the configuration. Details about the numerical method, grid independence, and validation of the numerical method can be found in references [15–19]. In all simulations, we used the value $a = 0.1$ according to the example illustrated in ref. [10]: under forced convection it has been demonstrated that this number agrees with practical values used by the industry.

Figure 17.2 shows the optimization of the global thermal resistance, $\theta_{\max}$, for several values of the ratio H_0/L_0 as a function of the ratio L_0/L_1: there is an optimal ratio L_0/L_1 that minimizes $\theta_{\max}$ when the parameters (ϕ and a) and the degrees of freedom (H/L, H_0/L_0, H_1/L_1) are fixed.

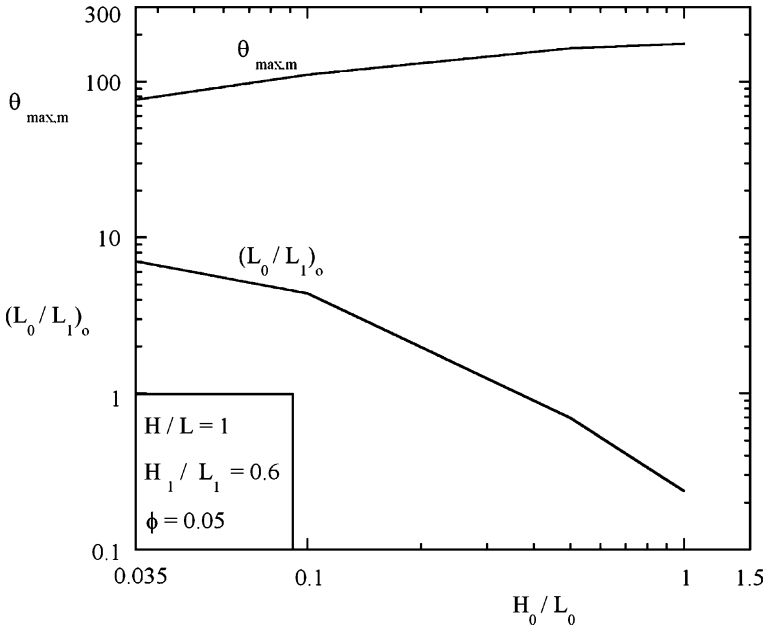

Fig. 17.3 The once optimized dimensionless global thermal resistance and the once optimized ratio (L_0/L_1)o as a function of the ratio H_0/L_0

The same results of Fig. 17.2 have been highlighted in Fig. 17.3: the ratio L_0/L_1, optimized with reference to one degree of freedom, decreases when H_0/L_0 increases. Figure 17.3 also shows that θ_{max} decreases as the ratio (H_0/L_0) also decreases and it reaches its minimal value when ratio H_0/L_0 is the smallest geometrically possible: we named these optimal values $\theta_{max,mm} = 76.7$, $(L_0/L_1)_{oo} = 7.04$, and $(H_0/L_0)_o = 0.035$, where the subscript "mm" means minimized twice, "oo" optimized twice, and "o" optimized once.

The search for best geometric shapes continues in Fig. 17.4: now the second optimization of the degree of freedom L_0/L_1 performed in Fig. 17.3 is repeated for several values of the cavity area fraction ϕ. Figure 17.4 shows that the optimal ratio $(H_0/L_0)_o$ is almost insensitive to changes in the value of the area fraction ϕ. However, $\theta_{max,mm}$ and $(L_0/L_1)_{oo}$ decrease steadily as the area fraction increases. It can be noticed from Fig. 17.4 that the value $\theta_{max,mm}$ when $\phi = 0.3$ is 51% smaller than the value of $\theta_{max,mm}$ when $\phi = 0.05$.

We continue our search for better configurations exploring the effect of the degree of freedom H_1/L_1 in the optimization process. Figure 17.5 shows that $\theta_{max,mm}$ decreases when H_1/L_1 also decreases and reaches its minimal value when H_1/L_1 is the smallest possible: the global thermal resistance value $\theta_{max,mm}$ calculated when $H_1/L_1 = 0.01$ is approximately 33% smaller than its value calculated when $H_1/L_1 = 1$.

Figure 17.5 also shows that $(L_0/L_1)_{oo}$ is approximately constant and equal to 2 when H_1/L_1 is smaller than 0.3. For H_1/L_1 greater than 0.3 the ratio $(L_0/L_1)_{oo}$

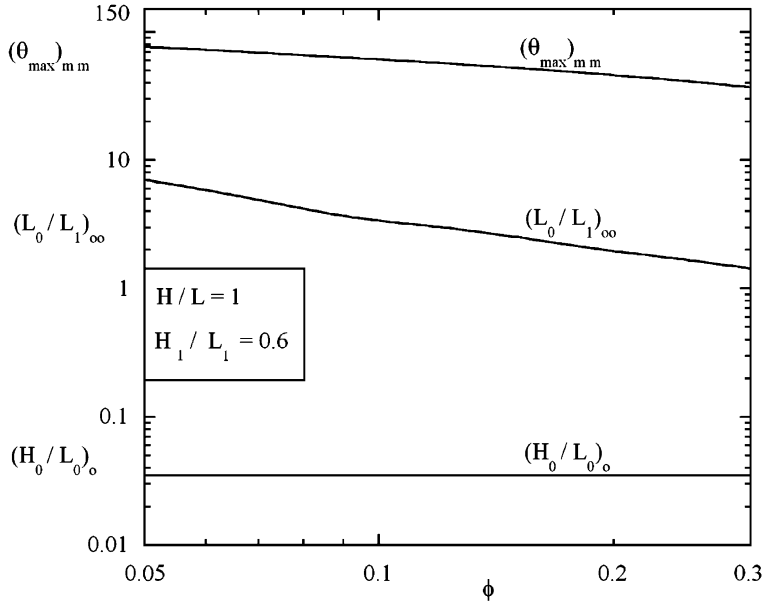

Fig. 17.4 The twice optimized dimensionless global thermal resistance, the twice optimized ratio $(L_0/L_1)_{oo}$, and the once optimized ratio $(H_0/L_0)_o$ as a function of the area fraction ϕ

increases as the ratio H_1/L_1 also increases. In the other side, the optimal ratio $(H_0/L_0)_o$ does not change much and can be roughly approximated as 0.1.

The best shapes calculated in Fig. 17.5 are shown in scale in Fig. 17.6. We can notice that the hot spots are all concentrated in the right side of Fig. 17.6. It is also important to notice that the best configurations are the ones where the cavity penetrates completely into the solid body and the vertical branch of T occupies all the vertical length of the solid body.

When compared to the C-shaped cavity [19], the T-shaped cavity performs approximately 45% better under the same thermal and geometric conditions. We found these results because we optimized completely the three degrees of freedom: L_0/L_1, H_0/L_0, and H_1/L_1. The performance of the T-shaped cavity can be improved if we optimize the degree of freedom H/L and study the effect of the parameter "a." These issues will be addressed in future works.

17.3 Electric Motors Fins

Consider the geometry of the electric motor frame, shown in Fig. 17.7. The configuration is two-dimensional with the third dimension sufficiently long in comparison with the radius of the external side of the electric motor frame (R_2).

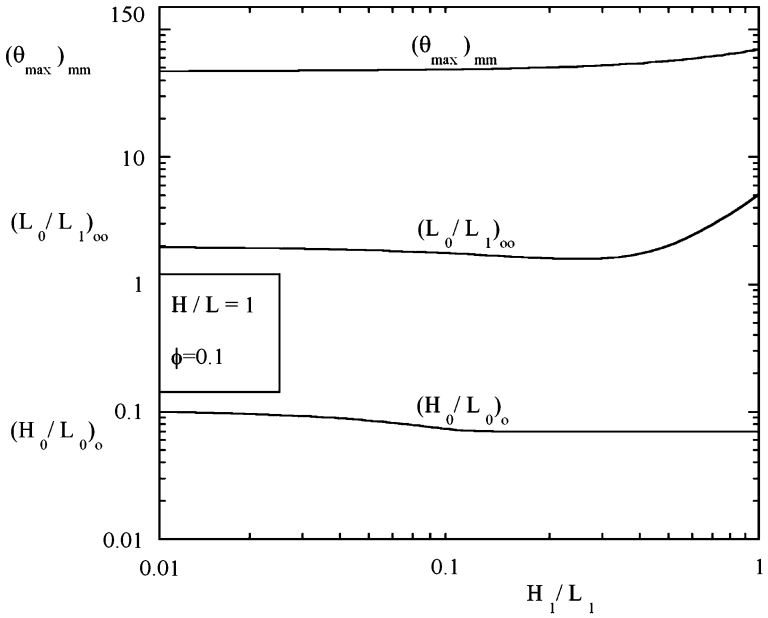

Fig. 17.5 The twice optimized dimensionless global thermal resistance, the twice optimized ratio $(L_0/L_1)_{oo}$, and the once optimized ratio $(H_0/L_0)_o$ as a function of the ratio (H_1/L_1)

The convection heat transfer coefficient (h) is uniform over all the external surfaces. Besides, the temperature of the external flow is known (T_∞). The heat current through the root section (q_1) is also known. The maximum temperature (T_{max}) occurs at the internal section of the frame, i.e., for $r = R_0$, and varies with the geometry.

The purpose of the analysis is to determine the optimal geometry (t_1/H_1, t_1/t_2, and N) that is characterized by the minimum global thermal resistance ($(T_{max} - T_\infty)/q_1$). According to the Constructal design [1, 2] this optimization can be subjected to constraints, namely, the total volume of the electric frame without fins, i.e., frame area constraint

$$A = \pi R_1^2, \tag{17.13}$$

the fin-material volume (with a cross-sectional trapezoidal area) constraint

$$A_f = \frac{N}{2}(t_1 + t_2)H_1, \tag{17.14}$$

and the volume of the cavity where it is inserted the rotor-stator set

$$A_r = \pi R_0^2. \tag{17.15}$$

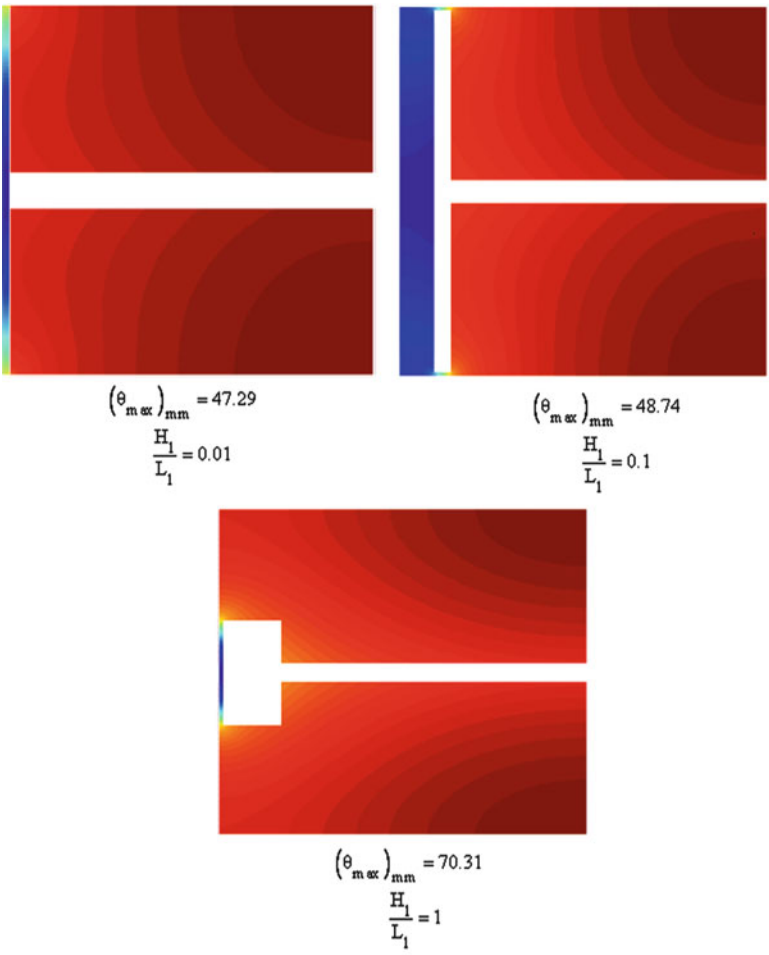

Fig. 17.6 The best shapes of Fig. 17.5

Equations (17.14)–(17.15) can be expressed as the fin volume fraction,

$$\phi_{\mathrm{f}} = \frac{A_{\mathrm{f}}}{A}, \tag{17.16}$$

and the rotor-stator cavity volume fraction,

$$\phi_{\mathrm{r}} = \frac{A_0}{A}. \tag{17.17}$$

It is worth mentioning that R_2 varies with the geometry of fins. Thus, the total area, given by (17.13), is selected as a function of the radius of the frame without fins (R_1), which is kept fixed for all performed simulations.

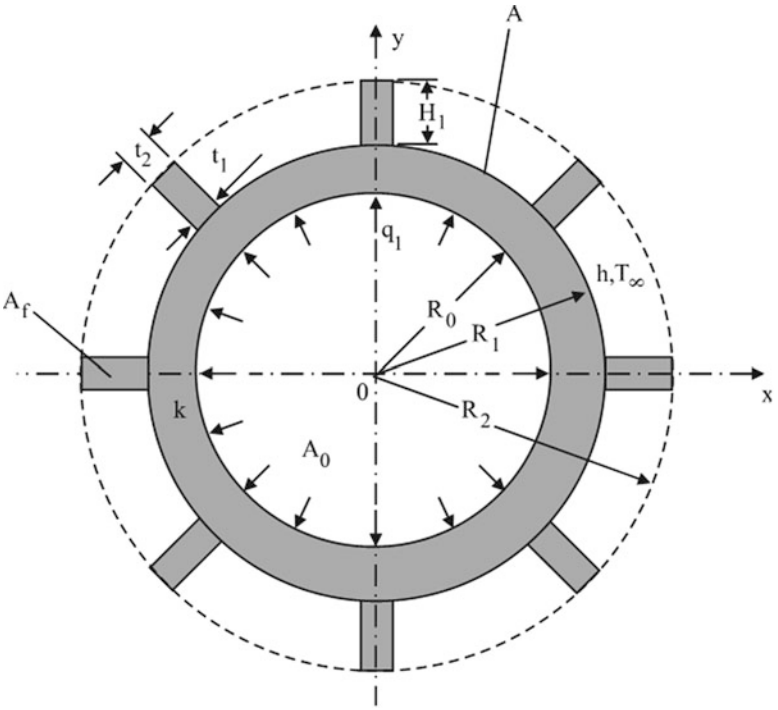

Fig. 17.7 Domain of the electric motor frame

The analysis that delivers the global thermal resistance as a function of the frame electric motor geometry consists in solving numerically the heat conduction equation along the entire domain of the solid annulus with fins, which is considered isotropic with constant thermal conductivity k,

$$\frac{\partial^2\theta}{\partial\tilde{x}^2}+\frac{\partial^2\theta}{\partial\tilde{y}^2}=0, \tag{17.18}$$

where the dimensionless variables are

$$\theta=\frac{T-T_\infty}{q_1/kW} \tag{17.19}$$

and

$$\tilde{x},\tilde{y},\tilde{r},\tilde{R}_0,\tilde{R}_1,\tilde{R}_2,\tilde{H}_1,\tilde{t}_1,\tilde{t}_2=\frac{x,y,r,R_0,R_1,R_2,H_1,t_1,t_2}{A^{1/2}}. \tag{17.20}$$

The boundary conditions are given by

$$-\frac{\partial\theta}{\partial\tilde{r}}=\frac{q_1}{2k\pi\tilde{R}_0}, \tag{17.21}$$

where $\tilde{r}$ is the dimensionless radius and

$$-\frac{\partial\theta}{\partial\tilde{x}}=\frac{a}{2}\theta \text{ or } -\frac{\partial\theta}{\partial\tilde{y}}=\frac{a}{2}\theta \text{ at the outer surfaces.} \tag{17.22}$$

The parameter (a) that emerged in (17.22) was defined in (17.9).
The dimensionless forms of (17.13) and (17.16)–(17.17) are

$$\pi\tilde{R}_1^2=1, \tag{17.23}$$

$$\phi_\mathrm{f}=\frac{N}{2}(\tilde{t}_1+\tilde{t}_2)\tilde{H}_1, \tag{17.24}$$

$$\phi_\mathrm{r}=\pi\tilde{R}_0^2. \tag{17.25}$$

The maximal excess temperature, $\theta_{\max}$, is also the dimensionless global thermal resistance between the volume of the entire system (cavity and solid) and the surroundings:

$$\theta_{\max}=\frac{T_{\max}-T_\infty}{q_1/kW}. \tag{17.26}$$

The numerical work consisted of determining the temperature field in a large number of configurations of the type shown in Fig. 17.7. The structure depicted in Fig. 17.7 has three degrees of freedom: N, t_1/t_2, and t_2/H_1. The first degree to be optimized by minimizing $\theta_{\max}$ is the ratio t_1/H_1. Afterwards, other degrees of freedom are optimized in the following sequence: t_1/t_2 and N. The procedure of optimization, grid independence, and validation of the numerical method are better depicted in the study of Biserni et al. [12].

Figure 17.8 shows the dimensionless global thermal resistance as a function of the ratio t_1/H_1 for several ratios t_1/t_2 and for the following parameters: $N=5$, $\phi_\mathrm{r}=0.6$, and $\phi_\mathrm{f}=0.05$. In general, the optimal shapes were observed for the lower ratios t_1/H_1, except for the value $t_1/t_2=50$, where the optimal shape is not obtained for the extreme ratios of t_1/H_1. For the ratio $t_1/t_2=100$, where the optimal geometry was found, the best shape that emerged in Fig. 17.8 was found to be at $t_1/H_1=0.008$.

The procedure for obtaining the minimal overall thermal resistance presented in Fig. 17.8 is repeated for several values of t_1/t_2. The once minimized global thermal resistance $(\theta_{\max})_\mathrm{m}$ as well as the corresponding once optimized ratio $(t_1/H_1)_\mathrm{o}$ as a function of the ratio t_1/t_2 are presented in Fig. 17.9. For $N=5$, $\phi_\mathrm{r}=0.6$, and $\phi_\mathrm{f}=0.05$, it is shown that there is a second opportunity of optimization, i.e., there

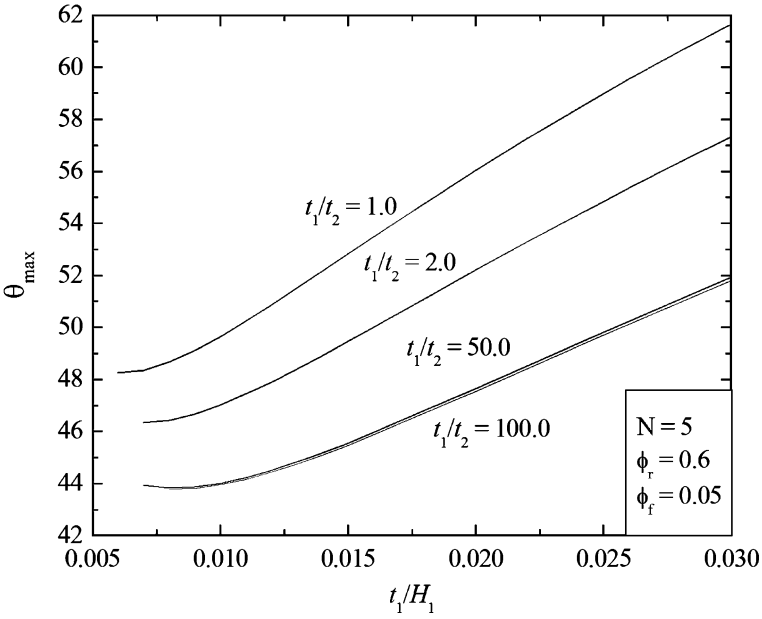

Fig. 17.8 The optimization of the global thermal resistance as a function of t_1/H_1 for several values of the ratio t_1/t_2

is an optimal $(t_1/t_2)_o$ that minimizes global thermal resistance. It is also observed that the increase of the $(\theta_{max})_m$ for $t_1/t_2 \geq 90$ is related with the increase of $(t_1/H_1)_o$. Figure 17.10 presents the once minimized global thermal resistance for several values of the fin volume fraction: $\phi_f = 0.05$, $\phi_f = 0.1$, and $\phi_f = 0.2$. For all performed simulations the parameters N and ϕ_r were kept fixed ($N = 5$ and $\phi_r = 0.6$). As expected, lower values of $(\theta_{max})_m$ are obtained for higher values of ϕ_f. Besides, for $\phi_f = 0.1$ and $\phi_f = 0.2$, the optimal shapes are achieved for higher values of t_1/t_2, on the contrary to previously observed for $\phi_f = 0.05$. The optimal shape obtained with $\phi_f = 0.2$ has a once minimized global thermal resistance 19.54% and 42.39% lower than that calculated for $\phi_f = 0.1$ and $\phi_f = 0.05$, respectively.

Figure 17.11 shows the once optimized ratio $(t_1/H_1)_o$ as a function of the ratio t_1/t_2 for several values of the fin volume fraction: $\phi_f = 0.05$, $\phi_f = 0.1$, and $\phi_f = 0.2$. It can be noticed that, for $\phi_f = 0.1$ and $\phi_f = 0.2$, the ratio $(t_1/H_1)_o$ is constant for higher values of t_1/t_2, differently of the behavior observed for $\phi_f = 0.05$. This difference for the evaluated fin volume fractions is reflected in the once minimized global thermal resistance.

Figure 17.12 presents the twice minimized global thermal resistance, $(\theta_{max})_{mm}$, as a function of the number of fins N for several fin-material volume fractions: $\phi_f = 0.05$, 0.1, and 0.2. It is shown that the $(\theta_{max})_{mm}$ decreases when both the number of fins N and the fin-material volume fractions ϕ_f increase. It is also noticed that the twice minimized global thermal resistance has an asymptotic tendency as a

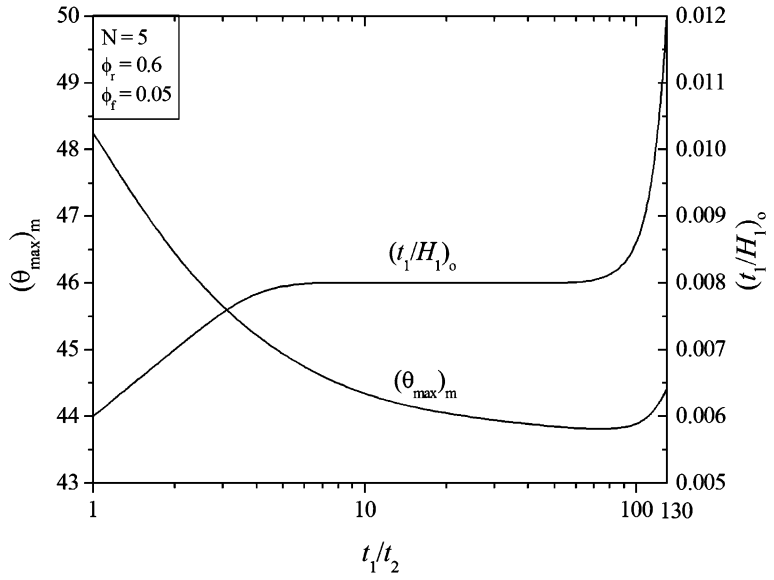

Fig. 17.9 The optimization of the once minimized global thermal resistance and the corresponding once minimized ratio $(t_1/H_1)_o$ as a function of the ratio t_1/t_2

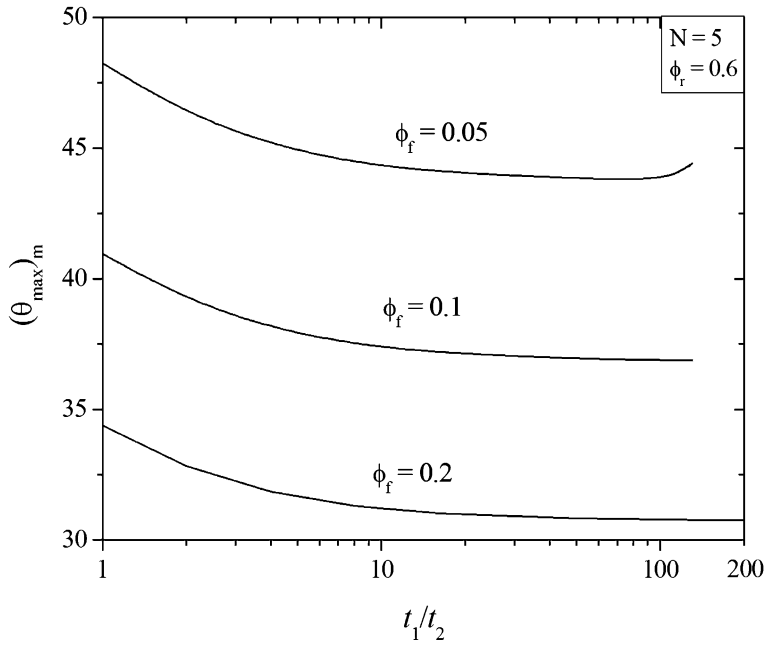

Fig. 17.10 The optimization of the once minimized global thermal resistance as a function of the ratio t_2/t_2 for several values of ϕ_f

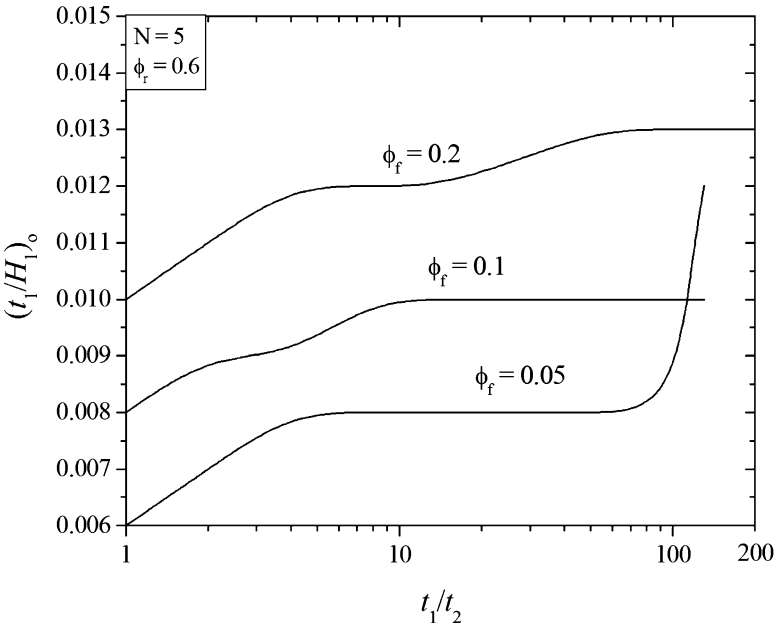

Fig. 17.11 The once minimized ratio $(t_1/H_1)_o$ as a function of the ratio t_1/t_2 for several values of ϕ_f

function of the number of fins, i.e., the increase of complexity will not indefinitely lead to an increase of the thermal performance. The increase of N from 5 to 8 leads to an improvement of 23.8%, 25.0%, and 20.5% in the thermal performance for $\phi_f = 0.05$, 0.1, and 0.2, respectively. When N is augmented from 8 to 10, the thermal performance increases only 12.5%, 13.2%, and 12.0%.

The optimal ratios $(t_1/t_2)_o$ and $(t_1/H_1)_{oo}$ for several values of N and ϕ_f are shown in Figs. 17.13 and 17.14, respectively. Figure 17.13 shows that the optimal ratio $(t_1/t_2)_o$ increases with the increase of N until the stabilization of the ratio $(t_1/t_2)_o$ for $\phi_f = 0.05$, while the ratio $(t_1/t_2)_o$ increases with the increase of N for $\phi_f = 0.1$. For $\phi_f = 0.2$, the optimal ratio $(t_1/t_2)_o$ increases from $N = 5$ to 8 and decreases from $N = 8$ to 10. Figure 17.14 shows that the twice optimized ratio $(t_1/H_1)_{oo}$ decreases from $N = 5$ to 8 for all evaluated fin-material volume fractions ϕ_f. For higher values of N the ratio $(t_1/H_1)_{oo}$ continues to decrease for $\phi_f = 0.2$, while a stabilization for the other values of $\phi_f = 0.05$ and 0.1 is observed.

Figure 17.15 shows the optimal shapes for several values of $N = 5$, 8, and 10 and $\phi_f = 0.2$. The best shape is obtained for $N = 10$. The best shape obtained with $N = 10$ and $\phi_f = 0.2$ is 46.1% and 21.3% better than the best shapes reached for $\phi_f = 0.05$ and $\phi_f = 0.1$, respectively. Other important observation is that the optimal shapes reached with higher values of N ($N = 8$ or 10) can lead to a better thermal performance, even for lower values of ϕ_f, i.e., the increase of the geometry complexity can compensate the lower amount of fin-material (ϕ_f) (for example, see the twice minimized global thermal resistance, $(\theta_{max})_{mm}$, obtained for $N = 5$ and

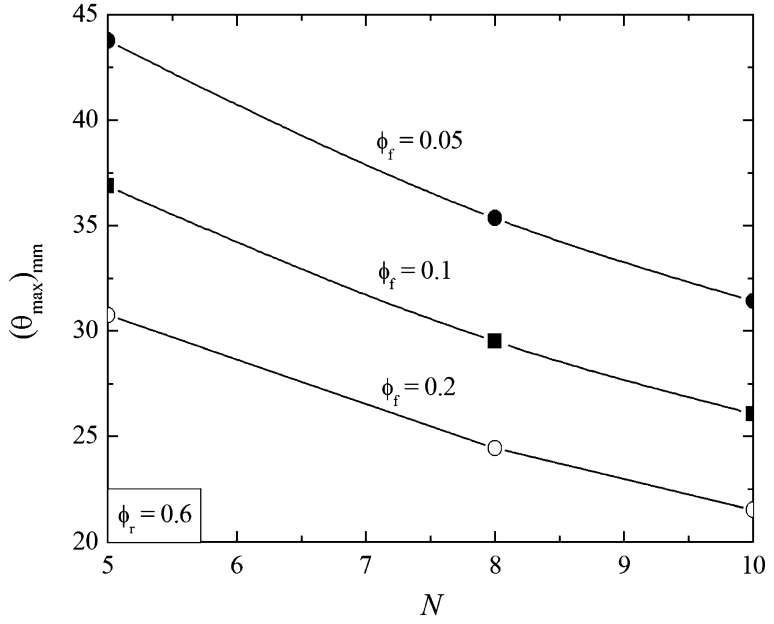

Fig. 17.12 The effect of the number of fins N and ϕ_f in the twice minimized global thermal resistance

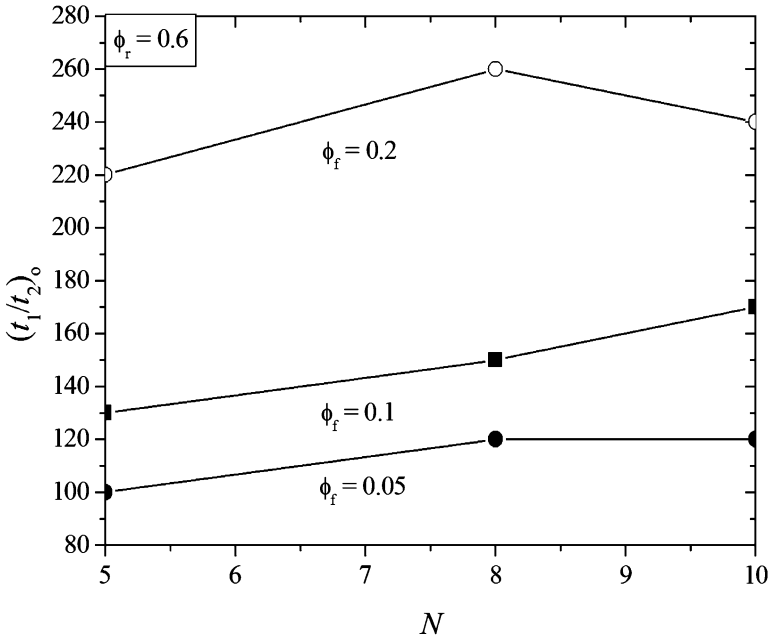

Fig. 17.13 The effect of the number of fins N and ϕ_f in the once optimized ratio $(t_1/t_2)_o$

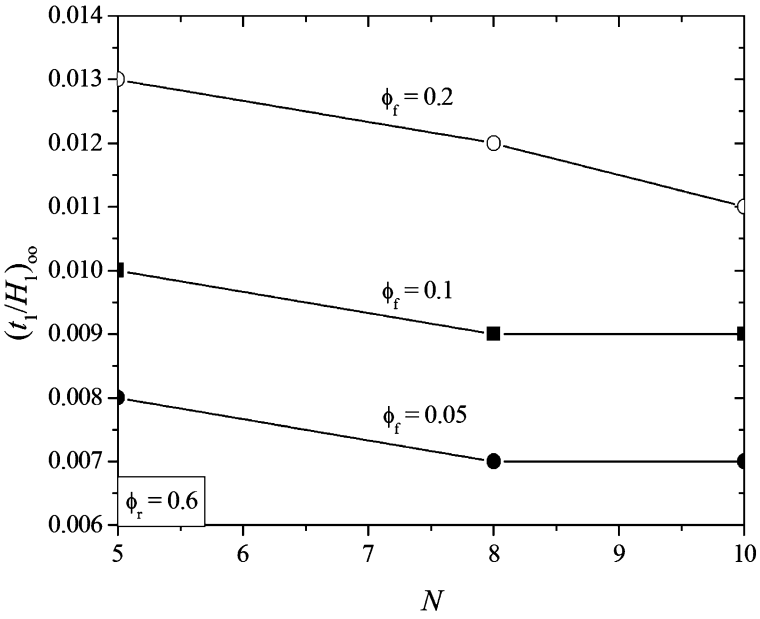

Fig. 17.14 The effect of the number of fins N and ϕ_f in the twice optimized ratio $(t_1/H_1)_{oo}$

$\phi_f = 0.1$). The results reinforce that not only the increase of the heat exchange area of the assembly of fins conducts to the better thermal performance but also the geometry design. The geometries with more uniform temperature distribution led to the best thermal performance according to the constructal principle of optimal distribution of imperfections [1, 2].

17.4 Hollow Bioreactor for Solid-State Fermentation

The proposed bioreactor is a column with an aeration system through which air is fed via an internal duct that has a fully perforated wall (promoting, therefore, the entry of air perpendicularly to it). There are walls in the area around the inlet and the exit of the internal duct, which allows the air to flow through the porous medium. Figure 17.16 shows the layout of the bioreactor and the domain studied (axisymmetrical).

The hollow bioreactor has two degrees of freedom: the ratio between the diameter and height of the bioreactor (D/L) and the ratio between the diameters of the internal duct at its entrance and exit (D_{in}/D_{out}). These parameters were studied, as well as the fraction of volume occupied by the internal duct (φ), which is given by (17.28)

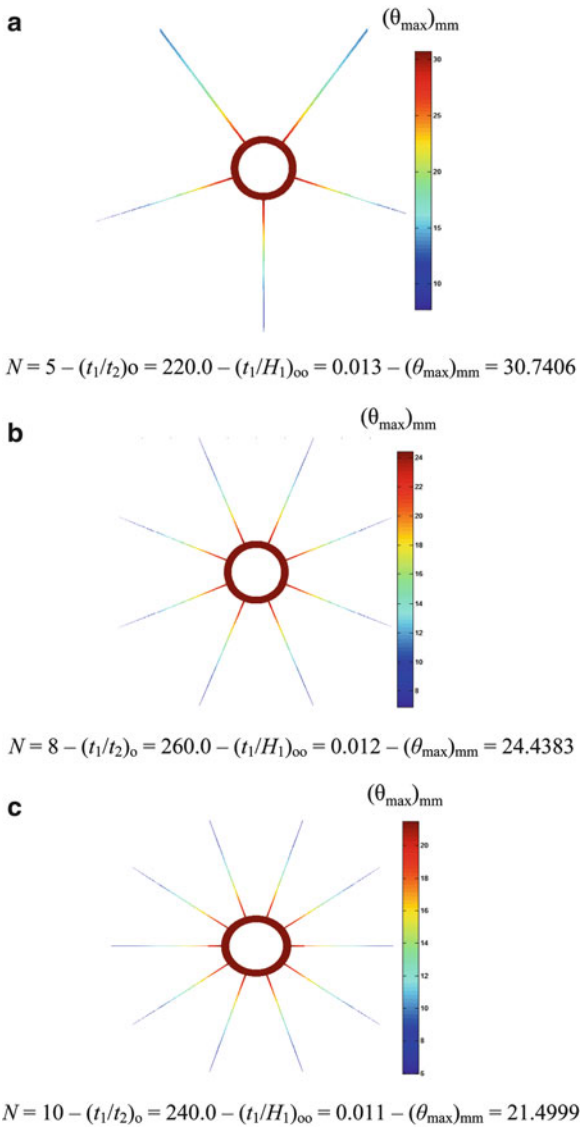

Fig. 17.15 The optimal shapes as function of N for $\phi_f = 0.2$

$$\varphi = \frac{V_d}{V}, \tag{17.27}$$

where V_d is the volume of the internal duct (defined by (17.29)) and V is the total volume of the bioreactor,

$$V_d = \frac{\pi}{12} L(D_{in} + D_{out})^2. \tag{17.28}$$

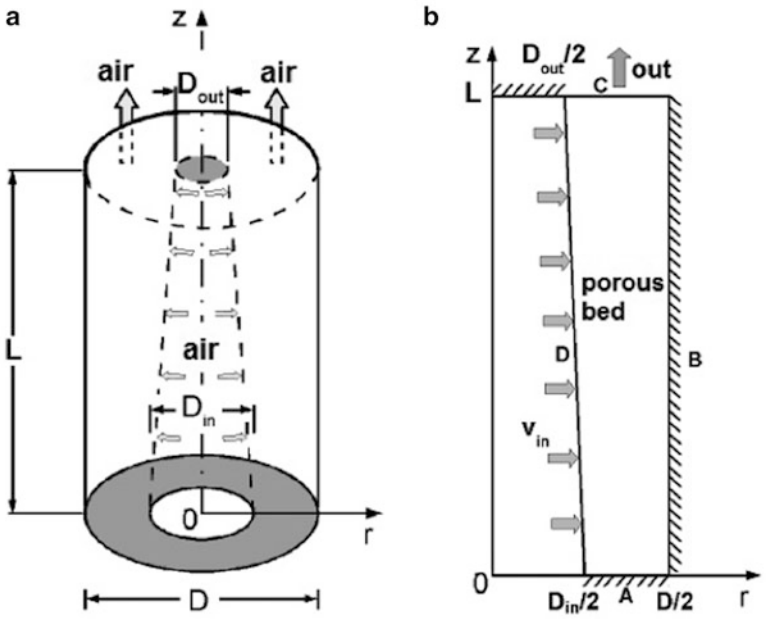

Fig. 17.16 Diagram of hollow bioreactor and computational domain

The mathematical and numerical models, grid independence, validation, and details of the numerical model are presented and discussed in refs. [20, 21]. The computational domain that represents the bioreactor was generated, discretized, and exported to the Fluent software (v. 6.3.26–ANSYS, Inc., USA) for numerical resolution of the mathematical model through the finite volume method. Simulations were performed to examine the temperature and velocity profiles inside the porous bed for two different configurations of the bioreactor: with an internal duct of air supplier with a constant cross-section ($(D_{in}/D_{out}) = 1$) and with a nonconstant cross-section duct ($(D_{in}/D_{out}) \neq 1$).

The Constructal design allows the hollow bioreactor to work without external equipment to cool the bed, since Constructal design minimizes the maximum temperature of the bioreactor (objective function) through the Constructal principle. The maximum temperature was set at 308 K, as this is considered ideal for the growth of the *Aspergillus* fungus [22, 23]. By keeping the total volume of the bioreactor (V) constant, the numerical model was resolved for different (D/L) ratios to obtain the optimum geometry ($(D/L)_{opt}$), which corresponds with the minimized maximum temperature, $T_{max,m} = 308$ K. This procedure was repeated for different volume fractions of the internal duct (φ), ratios between the diameters of entry and exit of the internal duct (D_{in}/D_{out}), volumetric flow rates (Q), and air temperatures at entry (T_{in}).

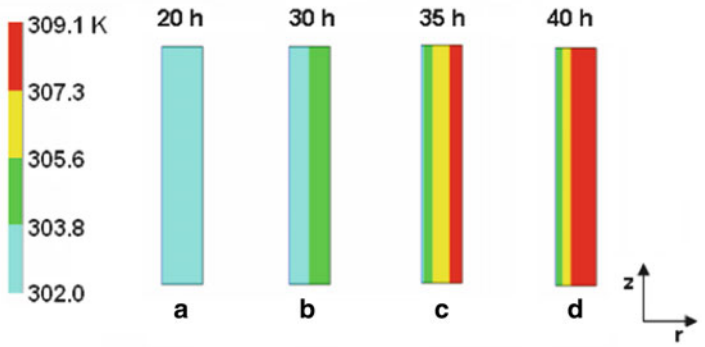

Fig. 17.17 Field of temperatures of the computational domain at 20 h (**a**), 30 h (**b**), 35 h (**c**), and 40 h (**d**) of fermentation ($(D/L) = 0.5$, $\varphi = 0.1$, $(D_{in}/D_{out}) = 1$, $T_{in} = 302$ K, and $Q = 3 \times 10^{-7}$ m^3 s^{-1})

Figure 17.17 shows the temperature field for the bioreactor with internal duct constant cross section. As the configuration is not optimal, temperatures above the optimum level established in this work (308 K) can be seen (Fig. 17.17d).

The initial 20 h of the cultivation (Fig. 17.17a) shows that the porous bed temperature is arising slowly, indicating that the organism is in the *lag* phase of growth. After 20 h (Fig. 17.17b), the *lag* phase of growth has been exceeded and the concentration of microorganisms begins to grow faster, fostering a small radial gradient of temperature. At 35 and 40 h (Fig. 17.17c, d), the bed temperature rises rapidly, characterizing the exponential phase of growth, where rapid generation of heat occurs.

Figure 17.17 also shows that the hollow bioreactor with constant cross-section internal duct presents radial and constant gradients of temperature throughout the bioreactor. This profile is due to a set of factors made up of the constant cross section of the internal duct, the insulated external walls of the bioreactor, and by the air inlet in the direction r. Conventional column bioreactors, unlike the hollow, have axial gradients of temperature throughout the bioprocess [24].

The maximum temperature of the hollow bioreactor at 35 and 40 h (about 309 K) is low, when compared with the maximum temperature of conventional column bioreactors under the same configurations and operating conditions, because the conventional bioreactor reaches temperatures higher than 323 K. Therefore, the aeration system of the hollow proves to be efficient at cooling the porous medium.

Figure 17.18 shows the temperature profiles in the two cases in which the cross section of the internal duct is not constant ($(D_{in}/D_{out}) \neq 1$). These examples include two configurations: a configuration where $(D_{in}/D_{out}) < 1$ and another in which $(D_{in}/D_{out}) > 1$.

Unlike the temperature profile of the hollow bioreactor with a constant cross-section internal duct (Fig. 17.17), the bioreactors with $(D_{in}/D_{out}) \neq 1$ (Fig. 17.18) do not have radial gradients of temperature constant along the length (z direction).

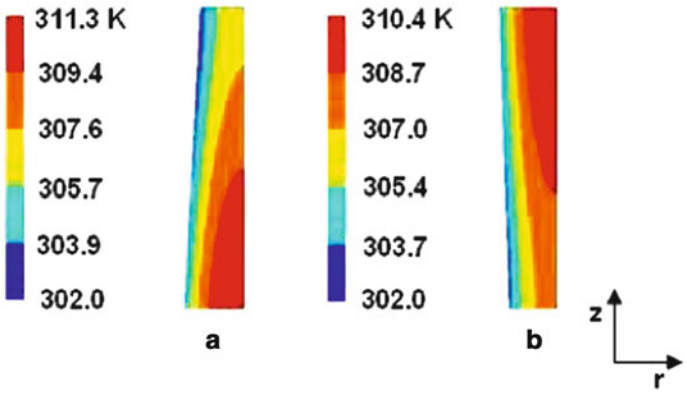

Fig. 17.18 Temperature profiles of the hollow bioreactor with ratio $(D_{in}/D_{out}) = 0.5$ (**a**) and $(D_{in}/D_{out}) = 1.5$ (**b**) at 40 h of bioprocess ($(D/L) = 0.5$, $\varphi = 0.1$, $T_{in} = 302$ K, and $Q = 3 \times 10^{-7}$ m^3 s^{-1})

It can also be seen that, despite the two examples shown in Fig. 17.18 having the same ratio (D/L), the same volume fraction of the internal duct (φ), the same volumetric flow rate (Q), and air temperature of inlet air (T_{in}), the temperature profiles are different due to the ratios (D_{in}/D_{out}). It can be confirmed, in Fig. 17.18a, that when $(D_{in}/D_{out}) < 1$, the region of the maximum temperature of the bioreactor is located next to the wall around the top of the internal duct. In contrast, when $(D_{in}/D_{out}) > 1$ (Fig. 17.18b), there is a maximum temperature near the bioreactor's exit.

The value of the maximum temperature differs between the two cases. The ratio $(D_{in}/D_{out}) > 1$ provides a lower maximum temperature, when compared to the maximum temperature of the bioreactor with $(D_{in}/D_{out}) < 1$ under the same conditions. However, when compared with the maximal temperature for the case where $(D_{in}/D_{out}) = 1$ (which has the temperature profile shown in Fig. 17.17d under the same configurations and operating conditions), the minimum–maximum temperature is in the configuration of the bioreactor with the constant cross-section internal duct.

Regarding the fluid velocity through the porous medium (Fig. 17.19), it was found that the use of bioreactors with ratio $(D_{in}/D_{out}) > 1$ (Fig. 17.19c) provides a better distribution of air velocity along the bioreactor and reduces the areas of low aeration (located next to the wall around the beginning of the internal duct). Since the flow of air converges to the exit of the bioreactor, in this area the fluid velocity is maximal.

After the bioreactor was defined with a constant cross-section internal duct $((D_{in}/D_{out}) = 1)$, different fractions of volume of the internal duct (φ) were tested to verify its effect on the bioreactor's maximum temperature, as shown in Fig. 17.20.

It is worth noting that, as the fraction of volume of the internal duct increases, higher ratios (D/L) are needed to maintain the maximal temperature of 308 K. Larger volume fractions of the internal duct (φ) diminish the useful capacity of the

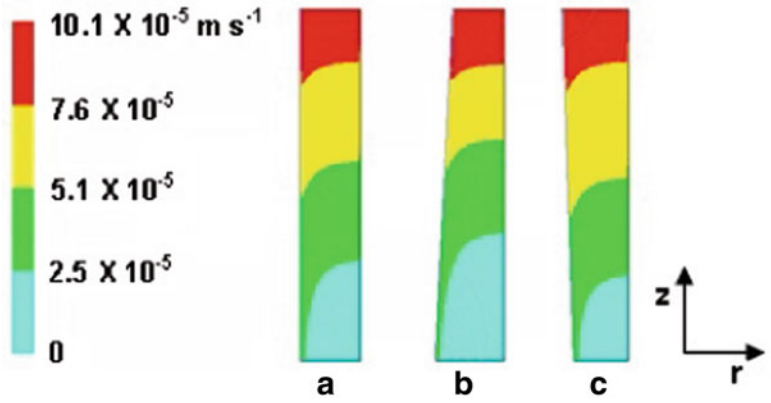

Fig. 17.19 Velocity profiles of the hollow bioreactor with ratio $(D_{in}/D_{out}) = 0.5$ (**a**) and $(D_{in}/D_{out}) = 1.5$ (**b**) at 40 h of bioprocess $((D/L) = 0.5,\ \varphi = 0.1,\ T_{in} = 302$ K, and $Q = 3 \times 10^{-7}$ m^3 s^{-1})

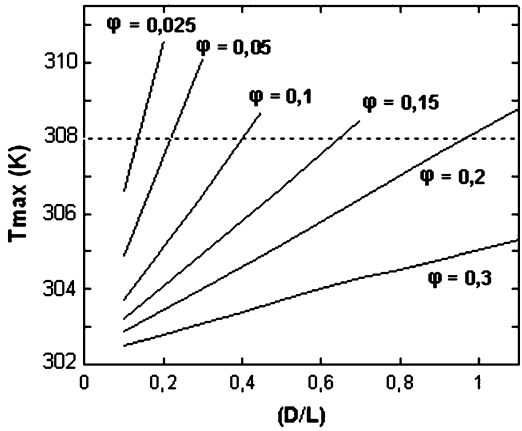

Fig. 17.20 Maximum temperature of the bioreactor according to (D/L) for various φ ($Q = 3 \times 10^{-6}$ m^3 s^{-1}, $T_{in} = 302$ K, $(D_{in}/D_{out}) = 1$)

bioreactor, and therefore also reduce the volumetric heat generation. There is then the need for higher ratios (D/L), as the temperature profile of the hollow bioreactor with $(D_{in}/D_{out}) = 1$ is characterized by the radial gradient of temperature. In other words, bioreactors with higher φ have less heat generation and, therefore, may be wider (higher ratio (D/L)).

It can also be seen that, for the same volume fraction of the internal duct (φ), there is an increase in the maximum temperature of the bioreactor with the increase in the (D/L) ratio, and this increase is more pronounced at lower values of φ. The increase in maximum temperature in greater (D/L) ratios can also be explained by the radial gradient of temperature characteristic of the hollow bioreactor with $(D_{in}/D_{out}) = 1$.

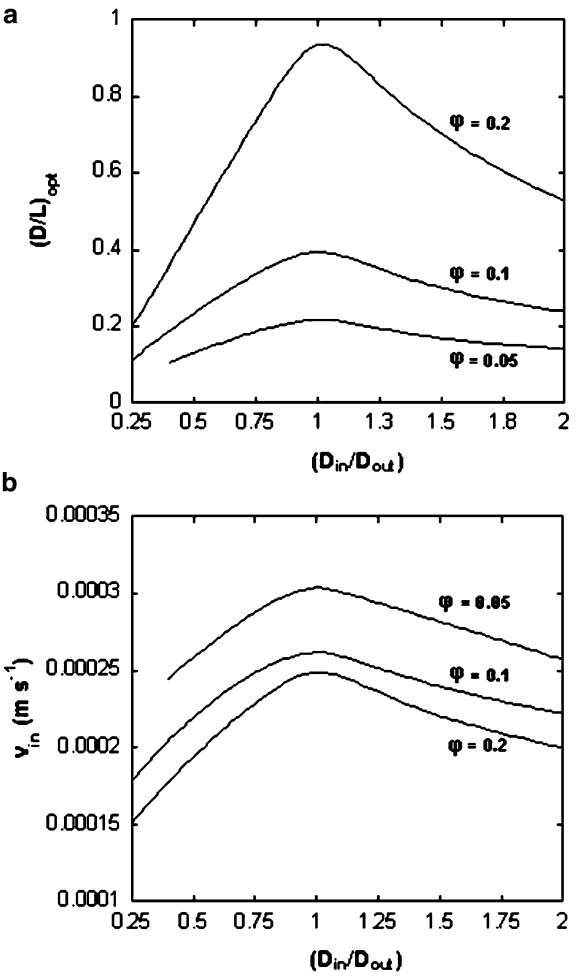

Fig. 17.21 Geometric optimization of the hollow bioreactor as a function of (D_{in}/D_{out}) for different φ ($T_{in} = 302$ K and $Q = 3 \times 10^{-6}$ m^3 s^{-1}) (**a**) and corresponding velocity of fluid for each optimization (**b**)

After observing the effect of the volume fraction φ on the maximum temperature of the bioreactor, geometric optimization was carried out according to the ratio (D_{in}/D_{out}). Figure 17.21a shows the configurations of bioreactor $((D/L)_{opt})$ for different (D_{in}/D_{out}) and φ, under the operational conditions of $T_{in} = 302$ K and $Q = 3 \times 10^{-6}$ m^3 s^{-1}.

Figure 17.21a, b shows peaks located at $(D_{in}/D_{out}) = 1$. The peaks in Fig. 17.21a indicate that the bioreactor which has the internal duct with constant section is the configuration with the highest ratio $(D/L)_{opt}$ for a particular value of φ. The peaks in Fig. 17.21b, in turn, justify the higher ratio $(D/L)_{opt}$ for bioreactors with $(D_{in}/D_{out}) = 1$, because this configuration has the maximum velocities of air inlet, which increase the cooling of the bed and thus enable the bioreactor to have a larger diameter and, therefore, a larger ratio (D/L) for the same volumetric flow rate.

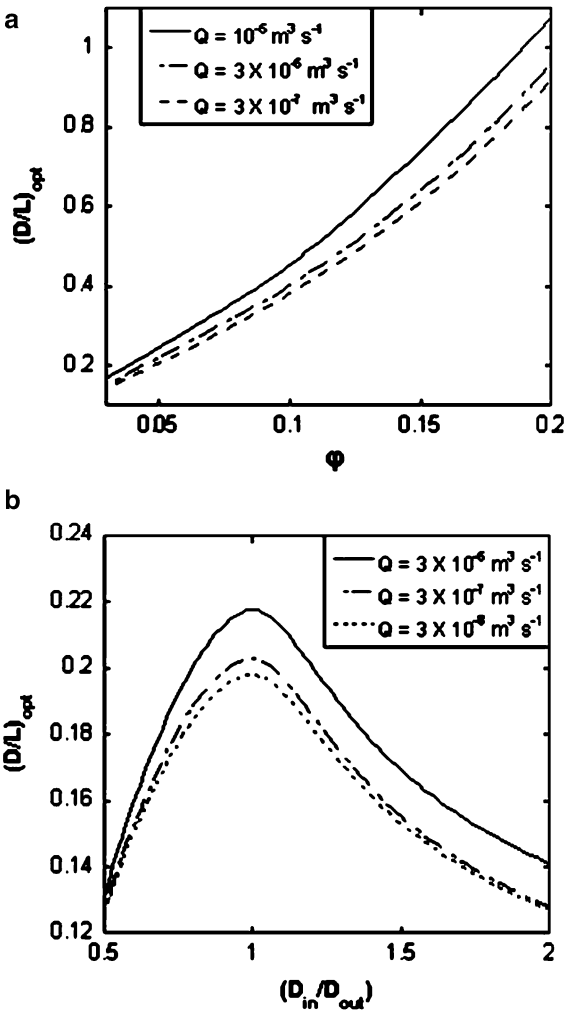

Fig. 17.22 Geometric optimization of the hollow bioreactor for different Q ($T_{in} = 302$ K). (**a**): as a function of φ, and (D_{in}/D_{out}) = 1. (**b**): as a function of (D_{in}/D_{out}) and $\varphi = 0.05$

Figure 17.22a shows the configurations $(D/L)_{opt}$ of the hollow bioreactor with constant section internal duct as a function of φ for different volumetric flow rates of air inlet (Q). The flows of inlet air have been set not to exceed the maximum velocity in the bed of 0.006 m s^{-1}. This level of velocity was previously tested successfully in bioprocesses with the *Aspergillus* fungus using the same bed of substrate [22].

Within the interval of volumetric flow rate studied, it can be noted that the flow of air (Q) has a more pronounced effect on the configuration $(D/L)_{opt}$ of the bioreactors with larger volume fractions of the internal duct (φ). Bioreactors with small internal duct volume fractions ($\varphi \leq 0.04$) have a $(D/L)_{opt}$ configuration almost independent of the volumetric flow rate of air. On the other hand, $(D/L)_{opt}$

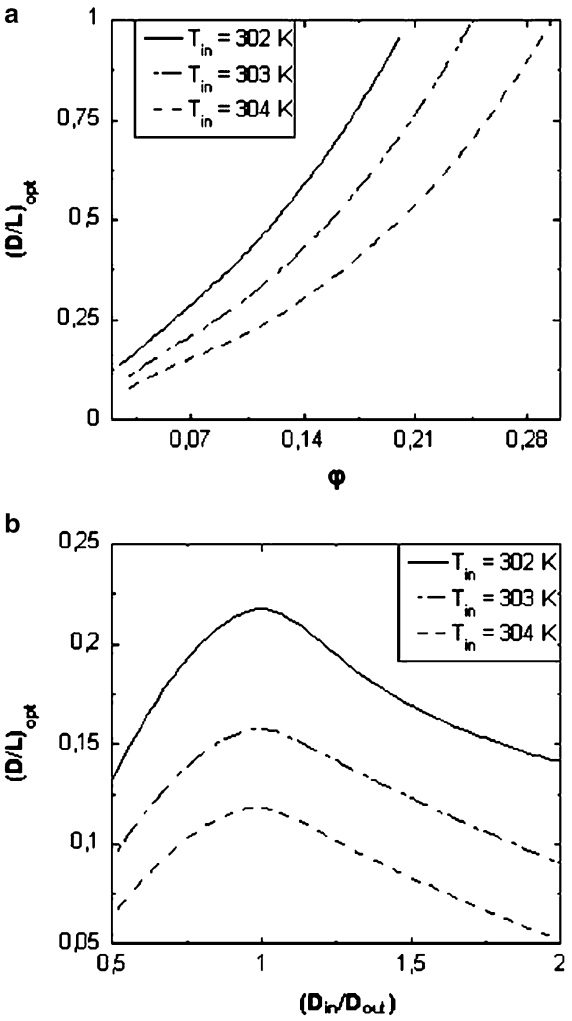

Fig. 17.23 Geometric optimization of the hollow bioreactor for different T_{in} ($Q = 3 \times 10^{-6}$ m^3 s^{-1}). (**a**): as a function of φ, with (D_{in}/D_{out}) = 1. (**b**): as a function of (D_{in}/D_{out}), with $\varphi = 0.05$

increases with the value of φ and with increasing volumetric flow rate. In Fig. 17.22b, it can be seen that, regardless of the (D_{in}/D_{out}) ratio, the increase in the volumetric flow rate of air (Q) provides configurations with higher $(D/L)_{opt}$ when φ is kept constant.

The general observation of the effect of the flow of air on $(D/L)_{opt}$ highlights the importance of experimental data on the acceptable maximum velocity of air inside the porous bed that is not detrimental to the growth of fungus. This parameter is important and there is a shortage of information on the practical limits of this data [24].

The constructal design of the bioreactor for different temperatures of air-supply (T_{in}) is also presented in Fig. 17.23. The temperature of inlet air has a strong effect on the configuration ($(D/L)_{opt}$) of the hollow bioreactor. Mitchell et al. [25] also

observed the effect of T_{in} on the optimization of the conventional column bioreactor. The authors report that T_{in} must be carefully defined, since it must be high enough to provide reasonable rates of growth, especially in the entry region of a conventional bioreactor, which is kept near the T_{in}.

The effect of T_{in} on the geometry $(D/L)_{opt}$ of the hollow bioreactor is more pronounced with larger internal duct volume fractions (φ) (Fig. 17.23a). For a bioreactor with the same φ, the use of lower temperatures establishes configurations with higher $(D/L)_{opt}$ ratios to operate under the temperature of 308 K. The greatest cooling provided by the lower temperature is reflected in the increased diameter of the bioreactor and thus at higher $(D/L)_{opt}$ ratios. The observation of the effect of T_{in} in the $(D/L)_{opt}$ value was also verified by Cunha et al. [20] in their work about modular bioreactor for SSF.

Figure 17.23b shows the optimization of the hollow bioreactor as a function of the (D_{in}/D_{out}) ratio. The figure confirms that the use of lower T_{in} provides higher $(D/L)_{opt}$, regardless of the (D_{in}/D_{out}) ratio.

17.5 Conclusions

This chapter shows how to apply Constructal design to discover configurations that facilitates the access of heat currents in thermal systems.

Firstly, we studied an open T-shaped cavity intruding into a solid conducting wall. The results showed that the cavity performs better when it penetrates almost completely into the solid body and the vertical branch of the T cavity occupies almost all the vertical length of the cavity. The optimal geometry has the smallest possible value of H_1/L_1 ($\phi = 0.01$), while the optimal value (H_0/L_0) was set approximately 0.1 and the optimal (L_0/L_1) was roughly approximate as 2. The T-shaped cavity performed approximately 45% better when compared to the C-shaped cavity under the same thermal and geometric conditions. This result only was able to be achieved because we optimized completely all the three degrees of freedom. We also noticed that the hot spots moved from one side to the other of the solid body depending on the changes in the geometry in the search for the better distribution of imperfections in the solid body.

Secondly the Constructal method was applied to the geometry similar to that find in electrical motor frames. Two degrees of freedom are investigated, t_1/H_1 and t_1/t_2, for several number of fins ($N = 5$, 8, and 10) and fin-material volume fractions ($\phi_f = 0.05$, 0.1, and 0.2). The results showed that the twice minimized dimensionless thermal resistance, $(\theta_{max})_{mm}$, decreases with the increase of the number of fins N, as well as the fin-material volume fraction ϕ_f. It was also observed that the $(\theta_{max})_{mm}$ tends to stabilize when N increases. However, more studies with the simulation of number of fins higher than $N = 10$ are required to corroborate this finding. Another important observation was that the increase of the geometry complexity can compensate the lower amount of fin-material fraction (ϕ_f). For example, the twice minimized global thermal resistance, $(\theta_{max})_{mm}$, obtained for

$N = 5$ and $\phi_f = 0.1$ was approximately 4 and 15% higher than the ones reached with $N = 8$ and $\phi_f = 0.05$ and with $N = 10$ and $\phi_f = 0.05$.

Finally, this chapter presents a new type of bioreactor for solid-state bioprocesses: the hollow bioreactor. The geometry of the bioreactor was examined, which allows the bioprocess to occur under the temperature of 308 K, without the use of external cooling equipment. The possibility of using less equipment shows how constructal design can be used as a tool for the ecologically correct management of energy. The hollow bioreactor has a lower maximum temperature than that observed in the conventional column bioreactor with the same configurations and same operational conditions, which demonstrates that the method is efficient at cooling the porous medium. The ratio between the diameters of the internal duct's entry and exit (D_{in}/D_{out}) of the hollow bioreactor influences the maximum temperature observed during the bioprocess. Bioreactors with (D_{in}/D_{out}) ratio >1 have a maximum temperature lower than the maximum temperature of bioreactors with (D_{in}/D_{out}) < 1 (under the same operational conditions and configurations). Moreover, they provide better distribution of air velocity along the bioreactor, thus reducing areas that are less favored by aeration. The configuration of the hollow bioreactor—$(D/L)_{opt}$—depends on the volume fraction of the internal duct (φ). Bioreactors with higher volume fractions of the internal duct have lower useful capacity and, therefore, generate less heat, which demands wider configurations of the bioreactor (higher ratio $(D/L)_{opt}$), when compared to the bioreactors with smaller volume fractions of the internal duct. The volumetric flow of air inlet (Q) also affects the configuration $(D/L)_{opt}$ of the bioreactor. The increase in volumetric flow rate increases the ratio $(D/L)_{opt}$. The use of lower temperatures of air inlet (T_{in}) leads to bioreactor configurations with higher $(D/L)_{opt}$ ratios, regardless of the volume fraction of the internal duct and the (D_{in}/D_{out}) ratio used in the bioreactor.

References

1. Bejan A. Shape and structure, from engineering to nature. UK: Cambridge University Press; 2000.
2. Bejan A, Lorente S. Design with constructal theory. New York: John Wiley and Sons Inc; 2008.
3. Bejan A, Lorente S. Constructal theory of generation of configuration in nature and engineering. J Appl Phys. 2006;100:041301.
4. Beyene A, Peffley J. Constructal theory, adaptive motion, and their theoretical application to low-speed turbine design. J Energ Eng-ASCE. 2009;135:112–8.
5. Kim Y, Lorente S, Bejan A. Constructal multi-tube configuration for natural and forced convection in cross-flow. Int J Heat Mass Tran. 2010;53:5121–8.
6. Azad AV, Amidpour M. Economic optimization of shell and tube heat exchanger based on constructal theory. Energy. 2011;36:1087–96.
7. Kim Y, Lorente S, Bejan A. Steam generator structure: continuous model and constructal design. Int J Energ Res. 2011;35:336–45.
8. Aziz A. Optimum dimensions of extended surfaces operating in a convective environment. Applied Mechanics Reviews. 1992;45:155–73.

9. Kraus AD. Developments in the analysis of finned arrays. Donald Q. Kern Award lecture, National Heat Transfer Conference; Aug11; 1997, Baltimore, MD; Int J Transport Phenomena. 1999;1141–164
10. Bejan A, Almogbel M. Constructal T-shaped fins. Int J Heat Mass Tran. 2000;43:2101–15.
11. Lorenzini G, Rocha LAO. Constructal design of Y-shaped assembly of fins. Int J Heat Mass Tran. 2006;49:4552–7.
12. Xie ZH, Chen LG, Sun FR. Constructal optimization of twice Y-shaped assemblies of fins by taking maximum thermal resistance minimization as objective. Sci Chine Tech Sci. 2010;53:2756–64.
13. Lorenzini G, Rocha LAO. Constructal design of T-Y assembly of fins for an optimized heat removal. Int J Heat Mass Tran. 2009;52:1458–63.
14. Lorenzini G, Correa RL, dos Santos ED, Rocha LAO. Constructal design of complex assembly of fins, J Heat Trans-T ASME, Vol. 2011;133:1-1–1-7
15. Biserni C, Rocha LAO, Bejan A. Inverted fins: geometric optimization of the intrusion into a conducting wall. Int J Heat Mass Tran. 2004;47:2577–86.
16. Rocha LAO, Montanari GC, dos Santos ED, Rocha AS. Constructal design applied to the study of cavities into a solid conducting wall. Therm Eng. 2007;6:41–7.
17. Biserni C, Rocha LAO, Stanescu G, Lorenzini E. Constructal H-shaped cavities according to Bejan's theory. Int J Heat Mass Tran. 2007;50:2132–8.
18. Lorenzini G, Rocha LAO. Geometric optimization of T-Y-shaped cavity according to constructal design. Int J Heat Mass Tran. 2009;52:4683–8.
19. Rocha LAO, Lorenzini G, Biserni C, Cho Y. Constructal design of a cavity cooled by convection. Int J Des Nat Ecodyn. 2010;3:212–20.
20. Cunha DC, Souza JA, Rocha LAO, Costa JAV. Hexahedral modular bioreactor for solid state bioprocesses. World J Microbiol Biotech. 2009;25:2173–8.
21. Cunha DC, Souza JA, Costa JAV, Rocha LAO. Constructal design of solid state fermentation bioreactors. Int J Energ Tech. 2009;1:1–8.
22. Mitchell D, Parra R, Aldred D, Magan N. Water and temperature relations of growth and ochratoxin A production by *Aspergillus carbonarius* strains from grapes in Europe and Israel. J Appl Microbiol. 2004;97:439–45.
23. Parra R, Aldred D, Archer DB, Magan N. Water activity, solute and temperature modify growth and spore production of wild type and genetically engineered *Aspergillus niger* strains. Enzyme and Microbial Technology. 2004;35:232–7.
24. Mitchell DA, von Meien OF, Krieger N. Recent developments in modeling of solid- state fermentation: heat and mass transfer in bioreactors. Biochem Eng J. 2003;13:137–47.
25. Mitchell DA, Pandey A, Sangsurasak P, Krieger N. Scale-up strategies for packed-bed bioreactors for solid-state fermentation. Process Biochemistry. 1999;35:167–78.

Index

L.A.O. Rocha et al. (eds.), *Constructal Law and the Unifying Principle of Design*, Understanding Complex Systems, DOI 10.1007/978-1-4614-5049-8,